На премию им. И.М. Копылова 2021

О.В. Егоров (ГАИШ МГУ, САО РАН):

Т.А. Лозинская (ГАИШ МГУ) :

А.В. Моисеев (САО РАН):

Цикл статей не тему
“Изучение воздействия звездообразования на газовую среду карликовых галактик ”, основанный на выполненных авторами наблюдениях на телескопе БТА

Аннотация

Из-за малой глубины потенциальной ямы, большой толщины газовых дисков и отсутствия спиральных волн плотности, карликовые иррегулярные галактики являются замечательным ``полигоном'' для рассмотрения процессов воздействия молодых звездных группировок на межзвездную среду. Здесь взаимодействие звезд и газа можно изучать во всей полноте пространственных и временных масштабов, вплоть до гигантских оболочек, сравнимых по размерам с диском галактики. Такому исследованию и посвящен данный цикл работ. В течение более чем 20 лет наблюдений на БТА со сканирующим интерферометром Фабри-Перо (ИФП) авторами была получена информация о пространственно разрешенной кинематике ионизованного газа с высоким спектральным разрешением для ряда близких карликовых галактик, что существенно обогатило наши представления о взаимодействии массивных звезд с межзвездной средой по сравнению. Оптические наблюдения в линии Hα с ИФП имеют в 3-10 раз лучшее пространственное разрешение, чем радиоданные в линии HI 21 см, что принципиально важно для выделения мелкомасштабных (до 10 пк) структур. Наблюдения с ИФП дополнялись как архивной фотометрией в других диапазонах (HST и GALEX), так и длиннощелевой и панорамной спектроскопией на БТА. Были разработаны и применены новые методы обработки данных. Впервые в практике работы с данными ИФП, стала использоваться техника диаграмм позиция-скорость с одновременным анализом кубов данных HI в линии 21 см (Лозинская и др. 2003 и последующие работы). Метод диаграмм интенсивность-дисперсия скоростей (I-σ) был существенно дополнен и применен для поиска уникальных эмиссионных объектов (Moiseev & Lozinskaya, 2012). Для исключения влияния кругового вращения при измерении скоростей расширения оболочек был разработан метод “деротации” кубов данных (Egorov et al 2014). Среди основных результатов, следует отметить следующие:

1) Впервые удалось измерить скорость расширения и оценить возраст гигантской (110x220 пк) биполярной туманности вокруг уникальной звезды WO в IC 1613. Необычная морфология туманности была объяснена тем, что звезда сформировалась в плотной газовой стенке на краю суперкаверны HI, так что звездный ветер прорывался в двух направлениях из плотного слоя газа. Последующий анализ данных радионаблюдений галактики на телескопе VLA подтвердил это предположение.
2) Изучена система оболочек нейтрального и ионизованного газа, связанных с комплексами современного звездообразования в галактиках IC 10, IC 1613, IC 2574, Holmberg I, Holmberg II, DDO 53. Исследована их кинематика, измерены скорости расширения и динамический возраст. Показано, что взаимодействие

гигантских (более 1 кпк диаметром) сверхоболочек HI может стимулировать формирование локальных комплексов звездообразования в их стенках, которые, в свою очередь, приводят к разрушению этих килопарсековых структур.

3) Исследована структура, кинематика и спектр свечения ионизованного газа в уникальной синхротронной сверхоболочке в галактике IC 10. Показано, что вспышка Гиперновой является более правдоподобным механизмом образования сверхоболочки, чем принятая ранее модель вспышки десятка сверхновых. В качестве компактного остатка Гиперновой Lozinskaya & Moiseev (2007) предложили темный компаньон рентгеновского источника IC10 X-1. Сразу после выхода этой статьи Prestwich et al. (2007) показали, что здесь пнаходится один из самых массивых (23-43 Mʘ) кандидатов в черные дыры звездных масс.
4) Обнаружена четкая связь между поверхностной яркостью в линии Hα, и дисперсией лучевых скоростей (σ): с уменьшением яркости растет разброс возможных значений σ, максимальная дисперсия скоростей наблюдается в областях малой яркости, а минимальная - в центрах областей HII. Такое поведение объяснено наличием у гигантских областей HII корон возмущенного диффузного газа низкой плотности с высокими турбулентными скоростями.
5) Успехом методики диаграммы I-σ является обнаружение уникальной звезды - кандидата LBV в галактике UGC 8508 и кандидата в остаток сверхновой в Holmberg I.
6) Наблюдения на БТА туманности, связанной с ультраярким рентгеновским источником (ULX) в Holmberg II, выявили в распределении лучевых скоростей структуру, интерпретированную как проявление головной ударной волны, вызванной быстрым полетом ULX через межзвездную среду и воздействием его горячего ветра на туманность. Это является первым прямым наблюдением вылета ULX из родительского скопления и подтверждает точку зрения о том, что многие ULX являются аккрецирующими черными дырами звездных масс.
7) На выборке более 50 карликовых галактик продемонстрировано существование глобального соотношения между текущим темпом звездообразования и средневзвешенной по яркости дисперсией скоростей. Moiseev et al (2015) интерпретировали это как аргумент в пользу того, что дисперсия скоростей ионизованного газа в карликовых галактиках не отражает вириальные движения, а в основном определяется энергией, впрыскиваемой в межзвездную среду в процессе звездообразования. Полученные на БТА данные о турбулентных движениях газа теперь используются для построения унифицированных моделей галактических дисков (Krumholz et al. 2018).
8) В галактиках Holmberg II, DDO53, IC 2574 выявлен и исследован новый феномен - диффузные оболочечные структуры ионизованного газа низкой яркости, часто находящиеся внутри каверн нейтрального водорода. Показано, что для их ионизации достаточно "утечки" Лайман-квантов от наблюдаемых в направлении их стенок О-звезд.
9) Показано, что аномальный внешний "хвост" нейтрального водорода вокруг галактики DDO 53 является, скорее всего, аккреционным потоком - остатком от слияния со спутником более 1 млрд. лет назад. Падение нейтрального газа на галактику формирует ударные волны в межзвездной среде и поддерживает текущее звездообразование в наиболее ярком звездном комплексе галактики.

Список статей

1) **Egorov, O. V., Lozinskaya T. A.**, Vasiliev K. I., Yarovova A. D., Gerasimov I. S., Kreckel K., **Moiseev A. V.,** "Star formation in the nearby dwarf galaxy DDO 53: interplay between gas accretion and stellar feedback", 2021, MNRAS, accepted, DOI:10.1093/mnras/stab2710, arXiv:2109.08526
2) **А.В. Моисеев,** "Сканирующий интерферометр Фабри-Перо на 6-м телескопе САО РАН", 2021, Астрофизический бюллетень, т. 76, с. 380
3) **Egorov Oleg V., Lozinskaya Tatiana A., Moiseev Alexei V.**, Smirnov-Pinchukov Grigory V., "Star-formation complexes in the `galaxy-sized' supergiant shell of the galaxy Holmberg I", 2018,Monthly Notices of the Royal Astronomical Society, v. 478, p. 3386
4) **Egorov O.V., Lozinskaya T.A., Moiseev A.V.**, Shchekinov, "Complexes of triggered star formation in supergiant shell of Holmberg II ", 2017, Monthly Notices of the Royal Astronomical Society, v. 464, p. 1833
5) **Egorov O.V., Lozinskaya T.A., Moiseev A.V.,** "The ultraluminous X-ray source HoII X-1: kinematical evidence of its escape from the cluster", 2017, Monthly Notices of the Royal Astronomical Society, v. 467, L1
6) **Moiseev Alexei V.,** Tikhonov Anton V., Klypin Anatoly, "What controls the ionized gas turbulent motions in dwarf galaxies?", 2015, Monthly Notices of the Royal Astronomical Society, v. 449, p. 3568
7) **Egorov O.V., Lozinskaya T.A., Moiseev A.V**., "Triggered star formation in giant HI supershells: ionized gas", 2015, Astronomical and Astrophysical Transactions, v. 29, p. 17
8) **Egorov O. V., Lozinskaya T.A., Moiseev A.V.**, Smirnov-Pinchukov G.V., "The supergiant shell with triggered star formation in Irr galaxy IC~2574: neutral and ionized gas kinematics", 2014, Monthly Notices of the Royal Astronomical Society, v. 444, p. 376
9) **Egorov O.V., Lozinskaya T.A., Moiseev A.V.** "Emission spectrum of ionized gas in the irregular galaxy Holmberg II", 2013, Monthly Notices of the Royal Astronomical Society, v. 429, p. 1450
10) **Moiseev A.V., Lozinskaya T.A.,** ``Ionized gas velocity dispersion in nearby dwarf galaxies: looking at supersonic turbulent motions", 2012, Monthly Notices of the Royal Astronomical Society, v. 423, p. 1831
11) **Егоров О.В., Лозинская Т.А, Моисеев А.В.,** ``Область бурного звездообразования в Irr галактике IC 10: структура и кинематика ионизованного и нейтрального газа", 2010, Астрономический Журнал, т. 87, с. 316
12) **Лозинская Т.А., Моисеев А.В.,** Подорванюк Н.Ю., Буренков А.Н.,``Спектр свечения газа в Irr галактике IC 10", 2009, Письма в Астрономический Журнал, т. 35, с. 811
13) **Lozinskaya T.A., Moiseev A.V.**, ``Synchrotron Superbublle in the IC 10 Galaxy: A Hypernova Remnant?", 2007, Monthly Notices of the Royal Astronomical Society, v. 381, p. L26
14) **Лозинская Т.А., Моисеев А.В.,** Авдеев В.Ю., **Егоров О.В.,** ``Структура и кинематика межзвездной среды в области звездообразования в BCD галактике VII Zw 403 (UGC 6456)", 2006, Письма в Астрономический журнал, т. 32, с. 403
15) **Лозинская Т.А., Моисеев А.В.,** Подорванюк Н.Ю., ``Кинематика

ионизованного и нейтрального газа в комплексе звездообразования в галактике IC 1613", 2003, Письма в Астрономический журнал, т. 29, с. 95
16) **Лозинская Т.А.,** Архипова В.П., **Моисеев А.В.,** Афанасьев В.Л., ``Наблюдения звездных объектов на границе оболочек в комплексе звездообразования в галактике IC 1613", 2002, Астрономический журнал, т. 79, с. 19
17) **Лозинская Т.А., Моисеев А.В.,** Афанасьев В.Л., Вилкотс Э., Госс М., ``Межзвездная среда вокруг WO звезды в галактике IC 1613: новые наблюдения в оптическом и радио диапазонах", 2001, Астрономический журнал, т. 78, с. 235
18) Афанасьев В.Л., **Лозинская Т.А., Моисеев А.В.,** Блантон Е., ``Гигантская биполярная оболочка вокруг WO-звезды в галактике IC1613: структура и кинематика", 2000, Письма в Астрономический журнал, т. 26, с. 190
19) **Lozinskaya T. A.** Silchenko O. K., Helfand D. J., Goss W. M. ``Resolving the Source of X-Rays in the Local Group Dwarf IC 1613: X-Ray, Radio, and Optical Observations of a Luminous Supernova Remnant'', 1998, The Astronomical Journal, Volume 116, Issue 5, pp. 2328

Краткий обзор выполненных работ приведен в статье Моисеева (2021). Также часть перечисленных выше результатов вошли в докторскую диссертацию А.В. Моисеева (защищена в 2012 г.) и в монографию Т.А. Лозинской “Взрывы звезд и звездный ветер в галактиках” (Москва, 2012)

Сведения об авторах:

Егоров Олег Владимирович:
Кандидат физико-математических наук, старший научный сотрудник отдела радиоастрономии Государственного Астрономического Института имени П.К. Штернберга Московского государственного университета имени М.В. Ломоносова и
имени М.В.Ломоносова
Почтовый адрес: Россия, 119234, Москва, Университетский проспект. д. 13, ГАИШ МГУ

Лозинская Татьяна Александровна:
Профессор, доктор физико-математических наук, ведущий научный сотрудник отдела радиоастрономии Государственного Астрономического Института имени П.К. Штернберга Московского государственного университета имени М.В. Ломоносова и
имени М.В.Ломоносова
Почтовый адрес: Россия, 119234, Москва, Университетский проспект. д. 13, ГАИШ МГУ

Моисеев Алексей Валерьевич:
Доктор физико-математических наук, ведущий научный сотрудник
Лаборатория спектроскопии и фотометрии внегалактических объектов
Специальной астрофизической обсерватории Российской академии наук
Почтовый адрес: Россия, 369167,Карачаево-Черкесская республика, Зеленчукский район, Нижний Архыз, САО РАН

Monthly Notices of the ROYAL ASTRONOMICAL SOCIETY

MNRAS **508,** 2650–2667 (2021) https://doi.org/10.1093/mnras/stab2710
Advance Access publication 2021 September 22

Star formation in the nearby dwarf galaxy DDO 53: interplay between gas accretion and stellar feedback

Oleg V. Egorov [1,2]★ Tatiana A. Lozinskaya,[2] Konstantin I. Vasiliev,[3] Anastasiya D. Yarovova,[2,3] Ivan S. Gerasimov,[3] Kathryn Kreckel [1] and Alexei V. Moiseev [4,2]

[1]*Astronomisches Rechen-Institut, Zentrum für Astronomie der Universität Heidelberg, Mönchhofstraße 12-14, D-69120 Heidelberg, Germany*
[2]*Lomonosov Moscow State University, Sternberg Astronomical Institute, Universitetsky pr. 13, Moscow 119234, Russia*
[3]*Lomonosov Moscow State University, Faculty of Physics, Leninskie gory 1-2, Moscow 119991, Russia*
[4]*Special Astrophysical Observatory, Russian Academy of Sciences, Nizhnii Arkhyz 369167, Russia*

Accepted 2021 September 16. Received 2021 September 14; in original form 2021 July 27

ABSTRACT

We present the results of a multiwavelength study of the nearby dwarf galaxy DDO 53 – a relatively isolated member of the M 81 group. We analyse the atomic and ionized gas kinematics (based on the observations with Fabry–Perot interferometer in H α line and archival data in H I 21 cm line), distribution, excitation, and oxygen abundance of the ionized gas (based on the long-slit and integral-field spectroscopy and on imaging with narrow-band filters), and their relation with the young massive stars (based on archival *HST* data). We detect a faint 2-kpc sized supershell of ionized gas surrounding the galaxy. Most probably, this structure represents a large-scale gas outflow, however, it could be also created by the ionizing quanta leaking from star-forming regions to the marginally detected atomic hydrogen surrounding the galactic disc. We analyse the properties of the anomalous H I in the north part of the galaxy and find that its peculiar kinematics is also traced by ionized gas. We argue that this H I feature is related to the accreting gas cloud captured from the intergalactic medium or remaining after the merger event occurred >1 Gyr ago. The infalling gas produces shocks in the interstellar medium and could support the star formation activity in the brightest region in DDO 53.

Key words: ISM: bubbles – ISM: kinematics and dynamics – galaxies: individual: DDO 53 – galaxies: irregular – galaxies: star formation.

1 INTRODUCTION

Feedback from massive stars has far-reaching effects on a galaxy's interstellar medium (ISM) and is thought to play a crucial role in the life cycle of the molecular material and the regulation of star formation on global scales. Through three main channels (ionizing radiation, stellar winds, and supernovae explosions) massive stars carve out low-density bubbles and shells (see e.g. Krumholz et al. 2014; Rahner et al. 2019). These processes are especially important in dwarf irregular (dIrr) galaxies, where their thick gas-rich discs and a lack of spiral density waves allow the development of prominent structures in the ISM formed as a result of stellar feedback. Moreover, because of their shallow gravitation potential, feedback in dIrr galaxies can easily launch galactic winds in comparison with more massive systems, and thus dwarf galaxies appear to be a major pollutants of the intergalactic medium (IGM; e.g. Ferrara & Tolstoy 2000; Emerick, Bryan & Mac Low 2019). Thus, nearby dIrr galaxies are ideal laboratories for studying the effects of massive stellar feedback on the surrounding material and could provide important constraints on the feedback parameters crucial for reproducing realistic galaxies in the cosmological simulations (e.g. Ceverino & Klypin 2009; Keller, Wadsley & Couchman 2015; Schaye et al. 2015).

Beyond the Local Group, the galaxies from the nearest M81 group ($D \sim 3.5$ Mpc) appear to be a perfect test-bed for studies of the feedback processes and the interactions of the galaxies with the IGM at the scales of individual H II regions and massive stars. The group is reach in neutral hydrogen (Sorgho et al. 2019) and thus provides a large diversity between the member galaxies in terms of their star formation rates (SFR), morphologies, masses, and metallicities (e.g. Karachentsev et al. 2002; Weisz et al. 2008; Croxall et al. 2009). Based on the observations performed with high-resolution Fabry–Perot interferometer (FPI) and long-slit or integral field unit (IFU) spectrographs, we previously analysed in details the kinematics, morphology, and chemical abundance of the ISM and their relation with the ongoing star formation activity in several individual galaxies of the M81 group: VII Zw 403 (Lozinskaya et al. 2006; Arkhipova et al. 2007; Egorov & Lozinskaya 2011), IC 2574 (Egorov et al. 2014), Holmberg I (Egorov et al. 2018), Holmberg II (Egorov, Lozinskaya & Moiseev 2013; Wiebe et al. 2014; Egorov et al. 2017), and NGC 3077 (Oparin, Egorov & Moiseev 2020). All these galaxies are gas rich and reveal extended complexes of star formation with prominent feedback-driven superbubbles, and in most of them the long duration of star formation activity led to the creation of so-called supergiant shells (SGSs), having sizes up to 2 kpc, the interaction of which could be a driver of star formation propagation (Egorov et al. 2017; Vasiliev, Shchekinov & Koval' 2020). H I observations revealed a presence of gaseous tidal tails

★ E-mail: oleg.egorov@uni-heidelberg.de

© 2021 The Author(s)
Published by Oxford University Press on behalf of Royal Astronomical Society

Downloaded from https://academic.oup.com/mnras/article/508/2/2650/6373944 by Special Astrophysical Observatory of the Russian Academy of Sciences user on 15 October 2021

Table 1. General parameters of the galaxy DDO 53.

Parameters	Value
Names[a]	DDO 53, UGC 4459, VII Zw238, PGC 24050, VV 499
Distance[b]	3.68 Mpc
M_B^a	-13.49^m
Optical radius[a], R_{25}	24 arcsec = 425 pc
log (SFR)[c]	$-2.2... - 2.3$
$12 + \log(\mathrm{O/H})^d$	7.67 ± 0.04
$M_{\mathrm{H\,I}}^e$	7.1×10^7 M$_\odot$
$M_\star^f$	1.0×10^7 M$_\odot$
Inclination[g], i	37°
PA_{kin}^g	123°
V_{rot}^g	20 km s^{-1}

Notes. [a]HyperLEDA Data base (Makarov et al. 2014, http://leda.univ-lyon1.fr/). [b]Tully et al. (2009), Karachentsev, Makarov & Kaisina (2013). [c]Hunter, Elmegreen & Ludka (2010), Sabbi et al. (2018). [d] This work. [e]Hunter et al. (2012). [f]Weisz et al. (2011). [g]Iorio et al. (2017).

or surrounding high-velocity clouds around some of the mentioned galaxies thus indicating their interaction with the IGM in the M81 group (Ashley et al. 2017; Sorgho et al. 2019, 2020).

Here, we analyse the ISM and ongoing star formation in the quiescent and metal-poor dIrr galaxy DDO 53, which is located at the periphery of the M81 group at a distance of 3.68 Mpc (the general parameters derived in this paper or adopted from previous studies are given in Table 1). In contrast with the previously mentioned galaxies, DDO 53 does not exhibit SGS in its ISM, or clear signs of tidal/accretion tails or surrounding gas clouds in its H I maps. The nearest galaxy to DDO 53 – blue compact dwarf (BCD) galaxy UGC 4483 – is located at ∼223 kpc from it (Karachentsev et al. 2002), which makes DDO 53 a fairly isolated galaxy. Despite that, several observational findings have drawn our attention to this galaxy and motivated us to perform a detailed analysis of its ISM: peculiar kinematics in the H I at the periphery of the galactic disc and the presence of extended H α emission surrounding the galaxy (first reported in this paper).

Modelling the kinematics of atomic hydrogen, Iorio et al. (2017) found extra emission in the H I 21 cm line in the north part the galaxy and suggested that it could be related to a gas outflow or inflow. In their recent work, Hunter et al. (2019) have found only one region of strong non-circular motions of H I in DDO 53, which is also located there, and one of the 7 H I holes detected in this galaxy by Pokhrel, Simpson & Bagetakos (2020) also coincides with this region. From earlier analysis of the galaxy's environment, Pustilnik et al. (2003) suggested that the current starburst in DDO 53 could be triggered by the tidal disturbance by the M 81 group as whole, or by the interaction with the IGM. On the other hand, Begum et al. (2006) showed that the IGM ram pressure is unlikely to influence the gas distribution and kinematics in the galaxy because the estimated gas density in the vicinity of DDO 53 is much lower than demanded to explain the observed peculiarities. The authors speculated that DDO 53 may be a product of a recent merger between two faint dwarf galaxies. However, as was found by Weisz et al. (2008) from the analysis of the resolved star formation history, such a merger event should have occurred more than 1 Gyr ago, which means it is unlikely to be responsible for the observed non-circular motions and peculiarities in the H I morphology, or for the recent burst of star formation that occurred about 25 Myr ago. The question on the origin of ongoing star formation and of non-circular motions remains unsolved.

The optical appearance of DDO 53 is dominated by a few bright blue clumps, which emit copious amounts of H α and are observed towards the two high-density peaks of the H I distribution (Begum et al. 2006). The kinematics of ionized gas of DDO 53 was first investigated with a scanning Fabry–Perot interferometer (FPI) by Dicaire et al. (2008), but the authors were only able to measure the distribution of radial velocities in the bright H II regions. Moiseev & Lozinskaya (2012) presented much deeper observations of this galaxy with FPI and identified three areas of elevated velocity dispersion in DDO 53. Among them, only one is observed towards the bright H II regions and demonstrates a shell-like morphology and thus could be easily interpreted as a feedback-driven superbubble. Two other structures are rather embedded in the diffuse ionized gas (DIG) between the bright H II regions, and since the information about the mechanism of gas excitation in these regions was unavailable, their origin remained uncertain. Beside these features in the ionized gas, we also discovered a faint 2-kpc-sized H α shell-like structure surrounding the galaxy (we describe it further in the current paper). All these features point to the far reaching impact of stellar feedback on the DDO 53 morphology.

In this study, we perform an in-depth analysis of the ISM of DDO 53 and its relation to the ongoing star formation and the surrounding IGM. We use new data from long-slit and integral-field spectroscopy and narrow-band imaging, as well as the the data obtained earlier with a scanning FPI, and the archival data of H I observations from LITTLE THINGS survey (Hunter et al. 2012). The aim of this analysis is to reveal the nature of the observed features in neutral and ionized gas morphology and kinematics mentioned above. The paper is organized as follows: Secton 2 contains the description of observational data; in Section 3 we report the results of the observations. Namely, Sections 3.1 describes the morphology of ionized gas in DDO 53; Section 3.2 is dedicated to the morphology and kinematics of atomic component; Section 3.3 presents our analysis of the small-scale kinematics of ionized gas; and in Section 3.4 we focus on the analysis of the gas excitation and metallicity using the spectral data. In Section 4, we discuss the results obtained considering the potential role of the gas accretion and stellar feedback in the creation of the observed peculiarities in DDO 53's appearance. Section 5 summarizes our results.

2 OBSERVATIONS AND DATA REDUCTION

2.1 Optical FPI-observations

The observations were performed at the prime focus of the 6-m telescope of Special Astrophysical Observatory of the Russian Academy of Sciences (SAO RAS) using a scanning FPI mounted inside the SCORPIO multimode focal reducer (Afanasiev & Moiseev 2005). These data were previously analysed and described in Moiseev & Lozinskaya (2012), Moiseev (2014), and Moiseev, Tikhonov & Klypin (2015). The log of these observations and the parameters of other data sets is given in Table 2, where T_{exp} is the exposure time, field of view (FOV) , arcsec/*px* – pixel size on the final images, θ – the final angular resolution, λ_c – the central wavelength of the used filters, and $\delta\lambda$ is the final spectral resolution.

The result of the FPI observations and data reduction was a large-scale data cube containing 36-channel spectra in the region around the red-shifted H α line. The analysis of the emission line profiles was carried out using multicomponent Voigt fitting (Moiseev & Egorov 2008), which yields flux, line-of-sight velocity, and velocity dispersion (corrected for instrumental broadening) for each component as an output. The measured values of the H α velocity dispersion

Downloaded from https://academic.oup.com/mnras/article/508/2/2650/6373944 by Special Astrophysical Observatory of the Russian Academy of Sciences user on 15 October 2021

Table 2. Log of observational data.

Data set	Date of obs	T_{exp}, s	FOV	arcsec/*px*	θ, arcsec	Sp. range	λ_c, Å	$\delta\lambda$ or FWHM, Å
FPI	2009 Feb 26	36 × 200	6.1 arcmin × 6.1 arcmin	0.71	3.3	13 Å around H α	–	0.8 (35 km s^{-1})
LS PA=198	2019 Feb 11	8400	1 arcsec × 6.1 arcmin	0.36	2.8	3600–7070	–	4.8
LS PA=211	2013 Nov 12	5400	1 arcsec × 6.1 arcmin	0.36	1.5	3600–7070	–	4.8
LS PA=259	2013 Nov 12	7200	1 arcsec × 6.1 arcmin	0.36	1.0	3600–7070	–	4.8
LS PA=323	2013 Nov 11	9600	1 arcsec × 6.1 arcmin	0.36	1.7	3600–7070	–	4.8
Image FN655	2013 Dec 04	3000	6.1 arcmin × 6.1 arcmin	0.36	1.8	H α +[N II]	6559	97
Image FN655	2019 Dec 18	3060	6.1 arcmin × 6.1 arcmin	0.36	1.7	H α +[N II]	6559	97
Image FN674	2013 Dec 04	3000	6.1 arcmin × 6.1 arcmin	0.36	1.8	[S II] 6717+6731	6733	60
Image FN641	2013 Dec 04	1500	6.1 arcmin × 6.1 arcmin	0.36	1.8	Continuum	6413	179
Image FN641	2019 Dec 18	1020	6.1 arcmin × 6.1 arcmin	0.36	1.7	Continuum	6413	179
Image FN712	2019 Dec 18	1020	6.1 arcmin × 6.1 arcmin	0.36	1.7	Continuum	7137	209
PPAK IFU	2013 Dec 15	3 × 400	1 arcmin × 1 arcmin	1.00	2.5	3700–7000	–	10

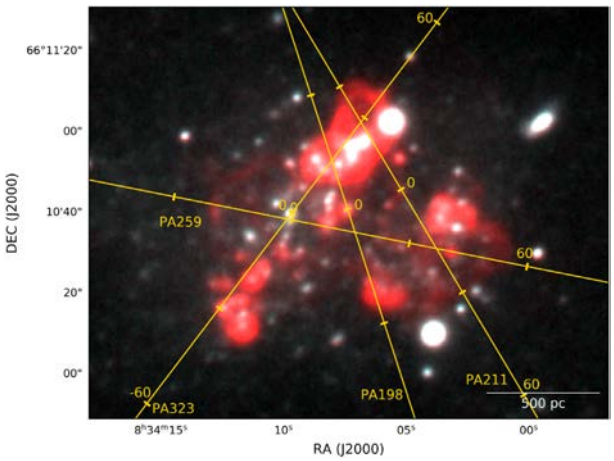

Figure 1. Position of the SCORPIO-2 slits overlaid on the image of DDO 53, where the red channel shows the distribution of H α emission (observed with FN655 filter) and the white colour traces the underlying continuum (in FN641 filter).

were additionally corrected for natural and thermal broadening by quadratically subtracting $\sigma_{th} = 9.6$ km s^{-1}.

2.2 Long-slit spectroscopic observations

The long-slit observations were carried out with the SCORPIO-2 multimode focal reducer (Afanasiev & Moiseev 2011) at the 6-m telescope of SAO RAS. Four spectra with different slit positions were obtained (see Fig. 1 and Table 2).

The data reduction was performed in a standard way using the SCORPIO-2 IDL-based pipeline as described in Egorov et al. (2018). The observations of the spectrophotometric standards BD+28d4211 at a close zenith distance immediately after or before the DDO 53 observations were used to calibrate its spectra to an absolute intensity scale.

To measure the fluxes of emission lines, our own IDL software based on the MPFIT (Markwardt 2009) routine was used. Gaussian fitting was applied to measure the integrated line fluxes of each studied region. For estimating the final uncertainties of the line fluxes, we quadratically added the errors propagated through all data reduction steps to the uncertainties returned by MPFIT. We did not performed any modelling or subtraction of the underlying stellar population because of its negligible contribution to the emission spectra.

A reddening correction was applied to each spectrum before estimating the lines flux ratios listed in this paper. For that we derived the colour excess $E(B-V)$ from the observed Balmer decrement and then used a Cardelli, Clayton & Mathis (1989) curve parametrized by Fitzpatrick (1999) to perform a reddening correction. In this paper, we use the following abbreviations for emission line flux ratios: [S II]/H α is F([S II] λ6717 + 6731 Å)/F(H α); [N II]/H α is F([N II] λ6584 Å)/F(H α); [O III]/H β is F([O III] 5007 Å)/F(H β).

2.3 IFU spectroscopy

The galaxy DDO 53 was observed with the Postdam Multi Aperture Spectrograph (PMAS) spectrograph (Roth et al. 2005) in the PPak mode (Verheijen et al. 2004; Kelz et al. 2006) at the Calar Alto 3.5-m telescope. This instrument samples a ∼1 arcmin hexagonal FOV with 331 fibres of 2.7 arcsec diameter. Observations were taken using the V300 grating, which provides full coverage of the optical spectral range (3700–7000 Å) while avoiding vignetting from the instrument.

Our data reduction follows the procedure described in detail in Kreckel et al. (2013), and is summarized here. All data are reduced using the P3D package (Sandin et al. 2010), v2.2.5.1 'Serenity'. Due to the low ∼65 per cent filling factor of the fibres, the science field was observed in three dither positions. Arc and calibration lamp images are also obtained at the position of the science field in order to trace the dispersed fibre positions across the CCD. Spectrophotometric standards were observed at the beginning and end of the night. Sky subtraction is carried out using simultaneously observed dedicated sky fibres placed ∼75 arcsec from the centre of the FOV (see Kelz et al. 2006). Emission line maps were constructed assuming a Gaussian line profile shape and fit using the same way as for long-slit data.

These IFU data provide the ability to trace the spatial distribution of the spectral properties of ionized gas, however, we can perform such an analysis only for a few of the brightest lines (H α, [O III], and H β to some extent), while the signal-to-noise (S/N) of the fainter lines (including, [N II], [S II]) is too small outside the brightest H II regions. Since the long-slit spectra provide higher S/N, we utilize the IFU data only to analyse the spatial distribution of the [O III]/H β in the brightest star-forming complex, and to measure the metallicities in a few bright regions not crossed by any of the slits.

2.4 Narrow-band imaging

Deep optical images of DDO 53 in the H α and [S II] emission lines were taken at the prime focus of the 6-m telescope of SAO RAS with SCORPIO-2 using narrow-band filters FN655 and FN674,

Downloaded from https://academic.oup.com/mnras/article/508/2/2650/6373944 by Special Astrophysical Observatory of the Russian Academy of Sciences user on 15 October 2021

respectively. The transmission curves of each filter can be found on the SCORPIO-2 web site.[1]

To construct the final image in Hα emission, we combine the images obtained on different years at the same instrument and with the same set of filters. Each individual exposure is reduced separately. After standard data reduction processes including bias subtraction, flat-fielding, correction for variations of atmospheric extinction and seeing, all different exposures were aligned and combined using sigma-clipping to remove the cosmic hits and artefacts.

We use the broader band FN641 and FN712 filters centred on the continuum to subtract the stellar contamination from the obtained emission line images. The data reduction for the continuum images is performed in the same way as for the emission line images. The final images are aligned to the reference Hα image using the ASTROALIGN procedure (Beroiz, Cabral & Sanchez 2020). We combine both continuum images with the weights proportional to the distance of the central wavelength of the corresponding filter from that for the Hα or [S II] image. These final continuum images were subtracted from those obtained with the FN655 and FN674 filters to obtain our final pure Hα and [S II] emission line images. The ASTROMETRY.NET service (Lang et al. 2010) is used to do an astrometric calibration of the images.

We also observed spectrophotometric standards AGK+81d266 and BD+25d4655 during the same night in FN655 and FN674 filters, respectively, and use them for further flux calibration of our Hα and [S II] images. Our final narrow-band images show surface brightness value at the 1σ level corresponding to (1.8, 4.8) $\times$ 10^{-18} erg s^{-1} cm^{-2} arcsec^{-2} in Hα and [S II] emission lines, respectively, as measured by the standard deviation of the background intensities.

Note that because the full width at half-maximum (FWHM) of the FN655 filter is broader than the distance between the Hα and [N II] emission lines, the image in this filter is contaminated by [N II] 6548, 6584 Å emission. According to our spectral observations, the [N II]/Hα flux ratio is 0.03–0.06 for DDO 53 (see Section 3.4). Because of the transmission of the FN655 filter is lower at the region of [N II] emission lines than for Hα, we conclude that the [N II] contamination of the Hα images does not exceed 4 per cent.

2.5 Other observational data used

We use archival JVLA data of the H I 21 cm line from the LITTLE THINGS survey (Hunter et al. 2012) to study the H I gas distribution and kinematics. In this work, we analyse both the natural-weighted (NA) and robust-weighted (RO) data cubes that have a velocity scale of 2.6 km s^{-1} per channel and angular resolution of $beam_{\rm NA}$ = 11.8 $\times$ 9.5 arcsec and $beam_{\rm RO}$ = 6.3 $\times$ 5.7 arcsec, respectively.

The selection of the main-sequence O-stars presented in this paper is based on the LEGUS catalogue (Sabbi et al. 2018) providing photometry in five wide-band filters *F275W*, *F336W*, *F438W*, *F555W*, and *F814W* (corresponding to the *NUV*, *U*, *B*, *V*, *I* bands) as observed with the *Hubble space telescope* (*HST*) using the ACS/WFC3 camera. We use the same criteria as in Kahre et al. (2018), namely – we limit the reddening-free parameter $Q = (m_{NUV} - m_B) - \frac{E(NUV-B)}{E(V-I)}(m_V - m_I)$ to the range of $-2.1 \leq Q \leq 0$. We also apply additional criteria following the model parameters for O-stars from Martins, Schaerer & Hillier (2005): $M_V < -3.9$ and $(m_V - m_I) \leq 0.5$. Thus, we select 85 O-star candidates that meet these criteria and consider further their distribution and properties. Their localization is shown in Fig. 2. Note that we use version 2.0 of the LEGUS catalogue, containing only stars with the highest quality photometry, and hence the estimated number of O-stars is rather a lower limit. Using a less strict selection criteria would add about 40 additional O-stars candidates, but the general picture of their distribution remains unchanged. In addition, some stars towards the H II regions might still be missed because of contamination of the measurements in the filters by line emission.

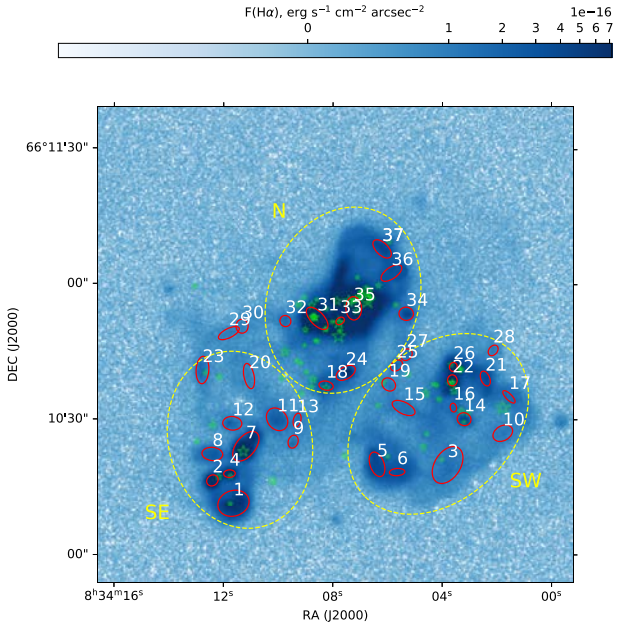

Figure 2. The location of H II regions identified by the ASTRODENDRO routine overlaid on Hα images. The yellow ellipses encircle the complexes of H II regions according to our designation in the text. The pale green asterisks show the location of the main-sequence O-stars identified in the *HST* LEGUS catalogue; the size of the symbols correlate with M_V of the star.

3 RESULTS OF OBSERVATIONS

3.1 Morphology of the H II regions and diffuse ionized gas

Optical images of DDO 53 reveal a few star-forming clumps emitting Hα (see Figs 1 and 2). The brightest northern H II complex has a size of about 450 pc and consists of a number of resolved H II regions and an extended ionized shell-like structure having a size of 270 pc. Other star-forming regions in the galaxy are remarkably fainter. A net of extended faint filamentary structures is observed in Hα connecting the relatively bright H II regions.

Strobel, Hodge & Kennicutt (1990) analysed their early images of DDO 53 in Hα and identified 18 H II regions in the galaxy. Since our images reveal much fainter structures, we perform a new selection of the H II regions using the ASTRODENDRO[2] routine, with the following parameters: the minimum level was set to be equal to 5σ on our images, the minimal intensity difference between regions was set to 1σ, and the minimal size of the regions was set to the seeing value. We identified 37 H II regions as shown in Fig. 2. All these regions could be roughly combined into three larger complexes denoted further as N, SE, and SW.

[1] https://www.sao.ru/hq/lsfvo/devices/scorpio-2/filters_eng.html

[2] http://www.dendrograms.org/

Downloaded from https://academic.oup.com/mnras/article/508/2/2650/6373944 by Special Astrophysical Observatory of the Russian Academy of Sciences user on 15 October 2021

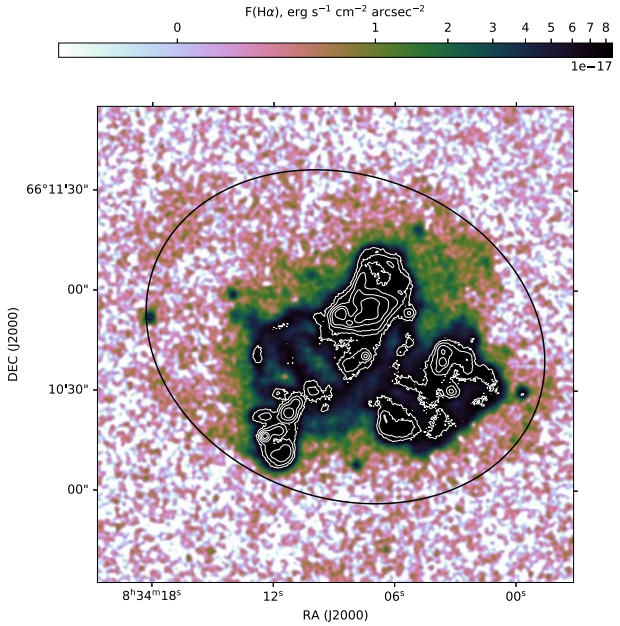

Figure 3. An Hα image of the galaxy demonstrates the low surface brightness ionized structures outside the regions of ongoing star formation. A black ellipse encompasses the identified surrounding shell-like structure. The white contours trace the inner Hα isophotes.

Beside the bright H II regions and filamentary structures connecting them, we detect very faint diffuse emission extending to distances up to 1.2 kpc from the centre of DDO 53 (see Fig. 3). This feature has a surface brightness of about (2.0–3.8) $\times$ 10^{-18} erg s^{-1} cm^{-2} arcsec^{-2} at the southern and north-eastern parts of the galaxy, while they reach a level of about 1.1 $\times$ 10^{-17} erg s^{-1} cm^{-2} arcsec^{-2} towards the north-west from the galaxy centre. Only the brightest clump of the north-eastern part of this structure is marginally detected in FPI data. Also, this clump is well aligned with the extended H I blue-shifted emission in 21 cm (see Section 3.2). We can encompass all the DIG clumps by an ellipse having position angle of $PA \sim 60^\circ$, major semi-axis of $R_{\rm maj} \sim 1070$ pc, and axial ratio of $R_{\rm min}/R_{\rm maj} \sim 0.8$ that corresponds to the inclination of $i \sim 35^\circ$, close to the inclination of the galaxy. Hence, the observed diffuse ionized structure has the form of a supershell with size of about 2 kpc. We will check further in Section 4.1 if this structure could be a large-scale outflow driven by stellar feedback.

Comparing the Hα luminosity of the individual star-forming complexes with the deposit of Lyman continuum (LyC) quanta from the identified O-stars within them (see Fig. 2 and Section 2.5), we may judge the ionization balance in these regions, as well as for the whole galaxy. From the LEGUS catalogue, we can derive the M_V of each star, which can then be translated to the produced number of ionizing quanta Q^0 according to the model by Martins et al. (2005). Summing Q^0 for all stars within each complex, we find that an available number of $Q^0_* = (5.45, 0.83, 1.76) \times 10^{50}$ s^{-1} for complexes N, SE, and SW, respectively. At the same time, the number of quanta required to produce the observed Hα flux in these complexes could be estimated as $Q^0_{\rm H\alpha} \simeq \frac{L(H\alpha)}{0.45h\nu} = (4.07, 1.23, 1.52) \times 10^{50}$ s^{-1} (Osterbrock & Ferland 2006). Thus, the identified O-stars alone produce enough quanta for gas ionization within each complex. Note that lower $Q^0_*/Q^0_{\rm H\alpha}$ in the SE complex is related to the rather arbitrary separation between the complexes SE and N – some O-stars are observed close to the border between them and were counted in the ionization balance for complex N. Calculating the escape fraction $f_{\rm esc} = 1 - Q^0_{\rm H\alpha}/Q^0_*$ for these complexes together we obtain $f_{\rm esc} = 0.16$, similar to that of the SW complex ($f_{\rm esc} = 0.14$). These estimates of the escape fraction from the star-forming complexes are lower than those for other dwarf galaxies (e.g. $f_{\rm esc} \sim 0.5{-}0.7$ for Holmberg I (Egorov et al. 2018) and Holmberg II (Egorov et al. 2017) derived from a similar analysis; $f_{\rm esc} > 0.2$ in LMC according to MUSE data in McLeod et al. 2019). Such a discrepancy is probably because of the underestimation of the number of O-stars, since the LEGUS catalogue we used contains only the stars with the highest quality photometry (see Section 2.5). However, even with this number we measure that the total number of available LyC quanta $Q^0_* \sim 8.1 \times 10^{50}$ s^{-1} is enough to explain the total Hα luminosity of the galaxy (resulting to $Q^0_{\rm H\alpha} \simeq 7.2 \times 10^{50}$ s^{-1}), including its diffuse structures like the previously mentioned 2 kpc-sized supershell.

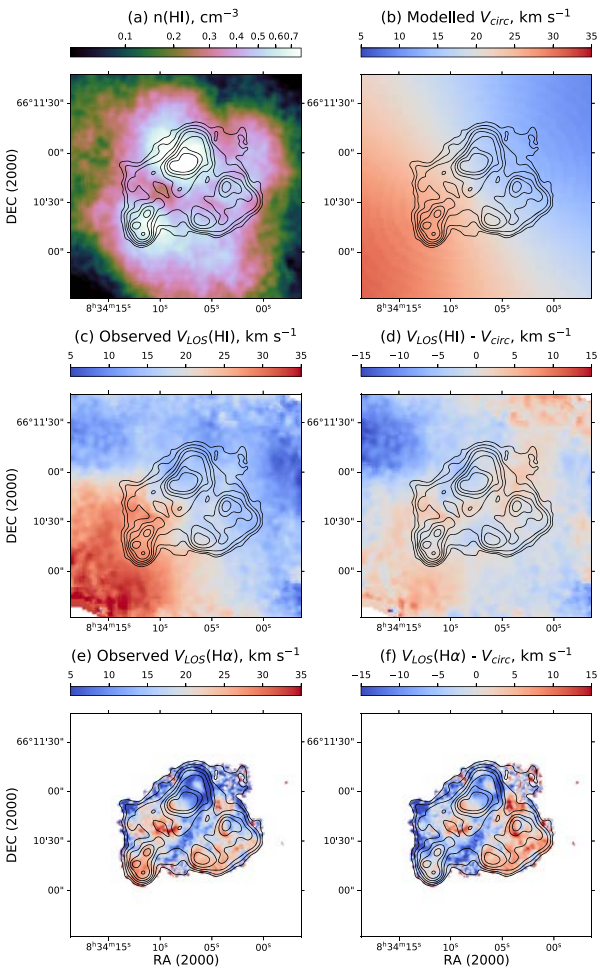

Figure 4. Distribution of the volume density of H I (a) and the velocity fields in H I 21 cm and Hα lines. Panel (b) shows the modelled velocity field of circular rotation for DDO 53; panels (c) and (d) – the observed velocity field in H I and residuals after subtraction of the circular rotation model; panels (e) and (f) – the same information for the ionized gas in the Hα line. Contours on each panel are lines of constant Hα surface brightness.

3.2 Morphology and kinematics of the atomic gas

The H I distribution in DDO 53 reveals two high-density peaks in the integrated 21-cm map (see Fig. 4a). These peaks coincide with the brightest complexes of star formation – N and SE (see Fig. 2). The third star-forming complex – SW – resides in the lower density

Downloaded from https://academic.oup.com/mnras/article/508/2/2650/6373944 by Special Astrophysical Observatory of the Russian Academy of Sciences user on 15 October 2021

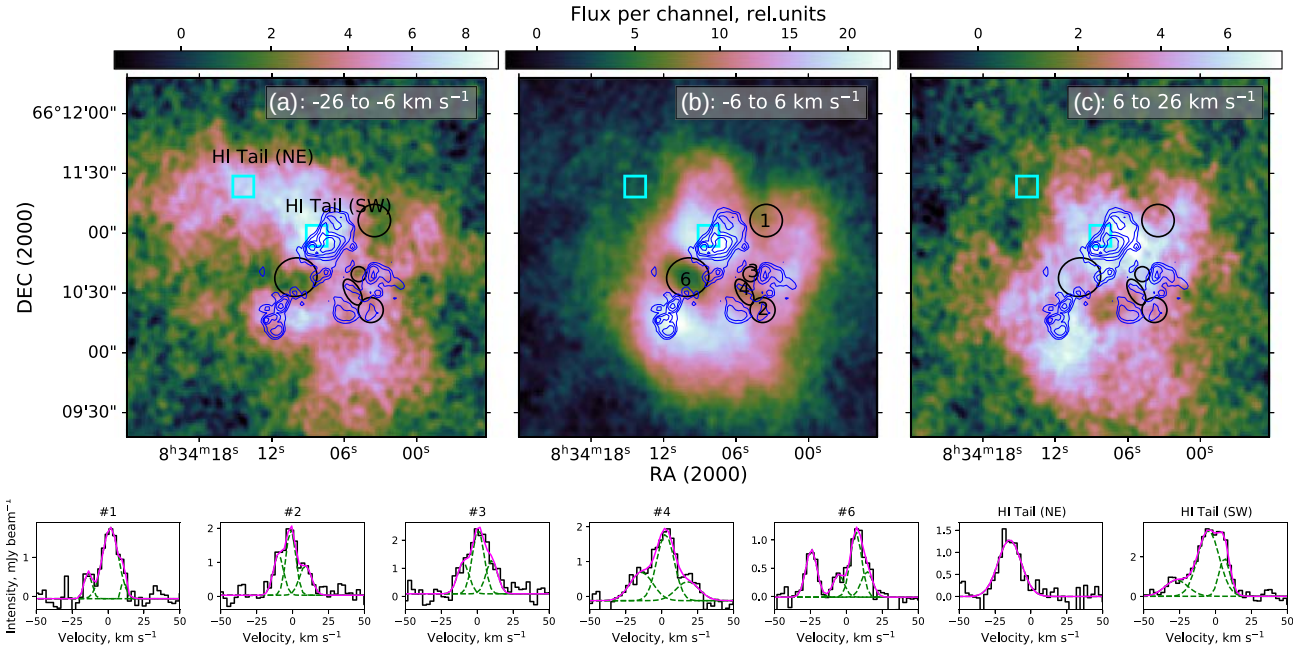

Figure 5. Atomic hydrogen in DDO 53 at different velocities as obtained by integration of several channels in the H I data cube after extraction of the circular rotation model: (a) blue-shifted gas motions at the velocities of $-26...-6$ km s^{-1}; (b) not shifted motions within $-6...6$ km s^{-1}; (c) red-shifted motions at the velocities of $6...26$ km s^{-1}. Contours on each panel are the lines of constant Hα surface brightness. The black ellipses show the location of the H I holes identified by Pokhrel et al. (2020). The bottom row shows the H I line profiles extracted towards the centres of the H I holes and towards the cyan squares (in two places in the H I tail) and the results of their approximation by 1–3 Gaussians. Individual Gaussian components are shown by the green-dashed lines, while the magenta colour is their sum.

environment, while its brightest nebulae are observed towards the regions with locally enhanced H I volume density.

To obtain the distribution of H I volume density (shown in Fig. 4a), we rely on the NA H I data assuming a constant scale height of the H I disc $h = 290$ pc as estimated by Bagetakos et al. (2011), with the following relation between the column density $N_{\rm H\,I}$ and volume density $n_{\rm H\,I}$:

$$N_{\rm HI} = \int_{-\infty}^{+\infty} n_{\rm HI} \exp\left(\frac{-z^2}{2h^2}\right) {\rm d}z = \sqrt{2\pi} h n_{\rm HI}. \quad (1)$$

The $n_{\rm H\,I}$ is corrected for inclination by multiplying by $\cos(i)$ to take into account the longer path along the line of sight than expected in equation (1). The resulting volume density of H I reaches a value of $n_{\rm H\,I} \sim 0.8$ cm^{-3} in the N and SE complexes, while a typical value of $n_{\rm H\,I} = 0.3$–0.5 cm^{-3} is found in the SW region and outside the bright star-forming complexes. These values translated into a gas mass densities are typical for other nearby dwarfs and the outskirts of massive galaxies (e.g. Abramova & Zasov 2011; Bacchini et al. 2019, 2020), however, the derived values depend on two very uncertain parameters – disc scale height and inclination. In particular, the inclination angle estimates for DDO 53 vary significantly in the literature – from $i = 27°$ Oh et al. (2011) to $i = 56°$ Boisvert & Rhee (2016). Here, we adopt a value of $i = 37°$ measured by Iorio et al. (2017).

Using the kinematic centre, position angle $PA_{\rm kin}$ and inclination angle (see Table 1) derived by Iorio et al. (2017) we reconstruct a model for circular rotation (Fig. 4b) and subtract it from the observed data cubes in both H I 21 cm and Hα lines (following the 'derotation' procedure described in Egorov et al. 2014). The observed line-of-sight H I velocity field (the first statistical moment of NA LITTLE THINGS data cube) is shown in Fig. 4(c), and the residuals after subtracting the circular motions are shown in Fig. 4(d). Similarly, the observed velocity field in Hα and the residuals after subtraction of the circular rotation model are given in Figs 4(e) and (f); we consider them in Section 3.3.

The recovered simple model of circular rotation well describes the gas kinematics of the H I in the central part of DDO 53, while significant residual velocities are observed to the north-east from the star-forming regions. Iorio et al. (2017) mentioned the extra emission in the H I 21 cm line in this area; Hunter et al. (2019) found the only one region of strong non-circular motions in DDO 53, which is also located there. Below, we try to describe its morphology and kinematics by analysing the H I data cube after subtraction of the circular motions.

We demonstrate in Fig. 5 the H I intensity maps of (a) blue-shifted, (b) not shifted, and (c) red-shifted emission. These maps were obtained by integration of the 'derotated' H I data cube within the velocity range of $-26...-6$, $-6...6$, and $6...26$ km s^{-1}, respectively. A long north-eastern tail in the H I emission appears only in the blue channels and almost does not contribute to the signal in the central and red-shifted channels. We refer further to this anomalous H I gas as the 'H I tail'.

As it is clearly seen in Fig. 6, the H I tail is connected with the brightest star-forming region in complex N. The 'position–velocity' diagram shown in the bottom panel is constructed along the whole extent of the tail. It demonstrates that the tail is not connected with the bulk of the galaxy in velocity space. The H I 21 cm line profile of this tail can be fit by a single Gaussian with a velocity offset of about 20 km s^{-1}, while its contribution in the integrated line profile is still visible at the same velocity towards the region of star formation (see the two right-hand profiles in Fig. 5). Thus, we may conclude that the gas in the area of non-circular motions of atomic hydrogen mentioned by Iorio et al. (2017) and Hunter et al. (2019) has elongated tail-

Downloaded from https://academic.oup.com/mnras/article/508/2/2650/6373944 by Special Astrophysical Observatory of the Russian Academy of Sciences user on 15 October 2021

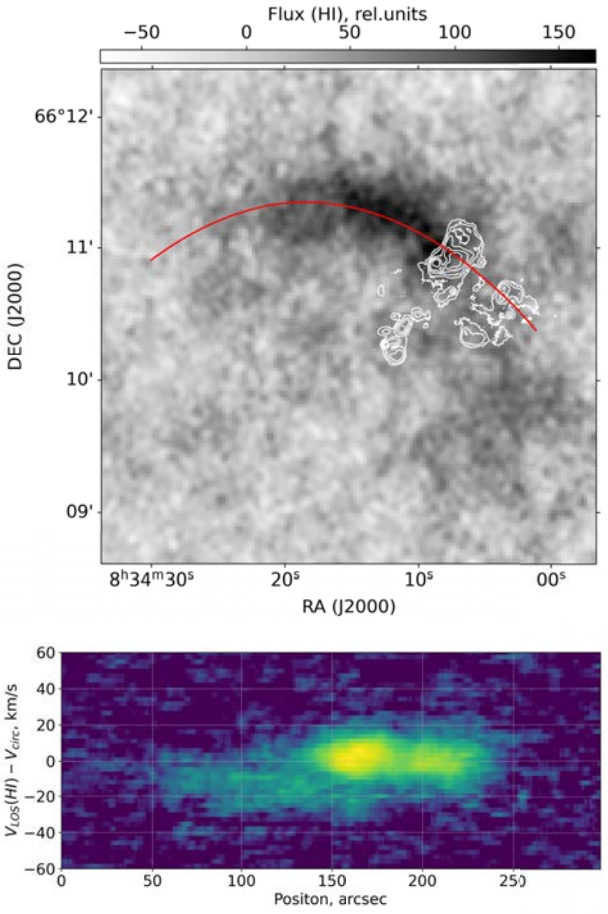

Figure 6. Map of DDO 53 in the blue-shifted H I channels (−29... −16 km s^{-1}) and the localization of the 'position–velocity' (PV) diagram constructed along the H I tail (top panel). This PV diagram is shown on the bottom panel and demonstrate a clear separation in velocity space of the H I tail (left half) from the bulk gas motions (right half). Contours on the top panel are lines of constant H α surface brightness.

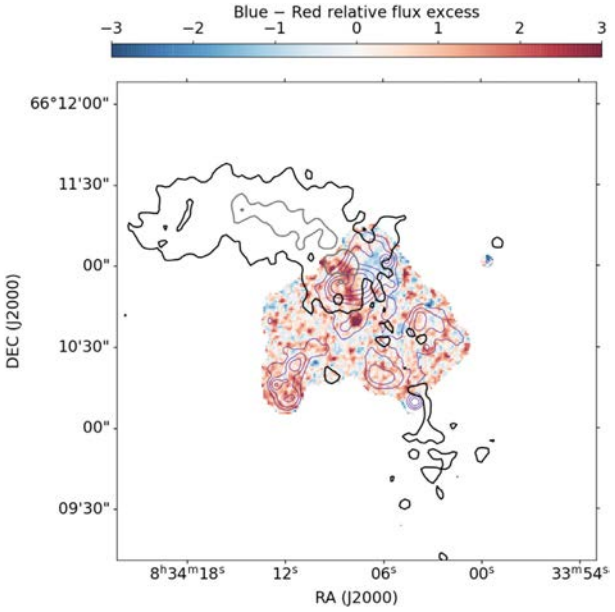

Figure 7. A map of the asymmetry of the H α line profile (computed as the difference of the flux excess in the blue- and red-shifted wings after single-component Voigt fitting normalized to the noise level), with overlaid contours of the H I flux in the blue-shifted channels (black colour). The violet contours correspond to the H α flux distribution.

like form, kinematically detached from the galaxy and probably appears to be an external gas cloud. We discuss this finding further in Section 4.2.

The small-scale morphology and kinematics of atomic hydrogen in DDO 53 were previously analysed by Bagetakos et al. (2011) and Pokhrel et al. (2020) who identified several expanding H I holes (or supershells) despite the rather poor angular resolution of the available H I 21 cm data (in comparison with the galaxy size). They identified three and seven holes, respectively, having diameters of 170–340 pc and ages of 6–18 Myr. We show the location of the H I supershells with their names according to Pokhrel et al. (2020) list (as it is the more complete one) in Fig. 5 with the black ellipses. Note that we exclude from consideration supershell #5 (it is located much further north from complex N and does not correspond to any prominent H I structure) and #7 (which coincides with the H I tail – both studies misidentified it as a H I hole).

As expected, all the H I supershells in DDO 53 are located outside the bright H II regions, but star-forming regions are observed towards their edges. An exception is the supershell #2, which coincides with H II region #3 in the SW complex. Based on the decomposition of the H I 21 cm line profiles observed towards the central parts of each shell (Fig. 5), we may conclude that clear signs of expansion are indeed visible in all supershells, and the estimated expansion velocities are the same as derived by Pokhrel et al. (2020). Note that the prominent blue-shifted component at ~ -24 km s^{-1} in the centre of supershell #6 in principle could also be related to the gas in the H I tail given the similarity of the line-of-sight velocities.

3.3 Small-scale kinematics of the ionized gas

In contrast with the H I data, high residuals after subtracting the model of circular rotation are still prominent in the velocity field of the ionized gas [panels (e) and (f) in Fig. 4]. We do not observe any significant correlation of the residuals distribution with the H I volume density or H α surface brightness, however, it seems that the red-shifted non-circular motions are more frequent in the SW complex. Tilted-rings modelling of the ionized gas velocity field using the H α FPI data revealed a very similar distribution in the residual velocities (Moiseev 2014). Hence, we suggest that the significant non-circular motions result from the stellar feedback influencing scales smaller than the resolution of H I data rather than from the general differences between atomic and ionized gas kinematics. Since the effects of the galaxy rotation contribute to the observed gas kinematics of DDO 53 to the same extent as the stellar feedback, we further use the 'derotated' data for the H α kinematics to concentrate mostly on the local gas motions.

The observed shape of the H α line in the FPI data is highly symmetric and well described by a single Voigt profile in most of the galaxy, however, noticeable asymmetry is present in complex N where the H I tail connects with the brightest H II regions. To explore this, we fit the whole data cube with a single Voigt profile and analyse the residuals. As a proxy for the line asymmetry we use the difference of the flux excess in the blue- and red-shifted wings normalized to the noise level at the corresponding pixel. The resulting map is shown in Fig. 7. The reddest colour shows the regions where the intensity of the

Downloaded from https://academic.oup.com/mnras/article/508/2/2650/6373944 by Special Astrophysical Observatory of the Russian Academy of Sciences user on 15 October 2021

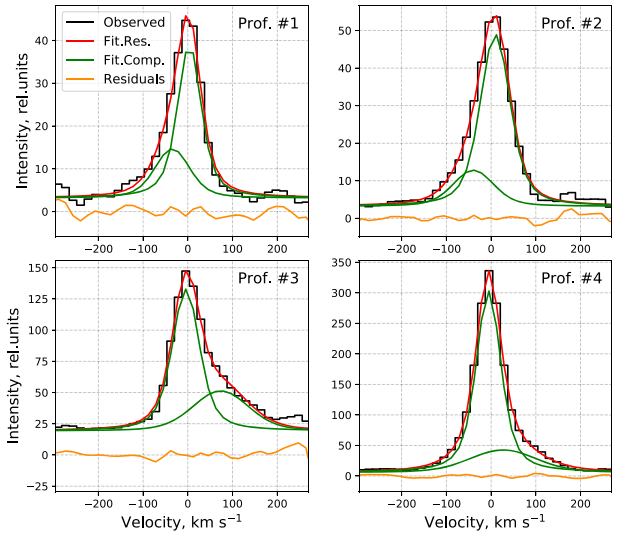

Figure 8. Example of Hα line profiles extracted from FPI data within the regions shown by the green squares in Fig. 9(c), and the results of their fitting with 1- or 2-component Voigt functions. Profile #1 corresponds to the H II region #2 and appears as single component line profile with $\sigma(\mathrm{H}\alpha) = 18.5$ km s^{-1} that is typical for DDO 53. Other profiles are from the only three regions in the galaxy where kinematically distinct components were detected. The most prominent of these (profile #2) corresponds to region #24 discussed in Section 3.4.

red-shifted component exceeds the 3σ level, while the bluest colour corresponds to the same for the blue-shifted component relative to the result of a single-component fitting. The only extended region with a large contribution of the shifted component to the integrated Hα line profile is elongated from the H II region #24 (see Fig. 2) towards the brightest regions #31, 33, 35, and coincides well with the direction of the H I tail (shown by the black contours). Hence, we may suggest that the shifted component in the Hα line and the H I tail are related to each other.

Visual inspection of the FPI data cube reveal only four regions where the Hα line profile could be reliably decomposed on to two kinematically distinct components, and all these regions are present on the map of Hα asymmetry as the red or blue spots that confirm the result presented in Fig. 7. Examples of the line profiles towards such regions and the results of their decomposition are given in Fig. 8. The exact borders over which the profiles were integrated are shown in Fig. 9(c) with a green colour. In all these cases, the second component is broader than the central one. Several other spots in the map of Hα line asymmetry also could be in principle decomposed into two components (in particular – in the shell to the north-west of the brightest H II region), but the S/N or the separation between components is too low there to get a reliable result.

From the analysis of the Hα data cube, Moiseev & Lozinskaya (2012) previously identified three regions of high velocity dispersion of ionized gas (see their fig. 1) that were considered to be probable unresolved expanding superbubbles, however, the origin of such supersonic motions remained unknown. Here, we reproduce their analysis using a slightly different criteria and selection algorithm. For that we use the so-called $I-\sigma$ diagrams, showing the dependence of the velocity dispersion $\sigma(\mathrm{H}\alpha)$ on the logarithm of the Hα line flux in each corresponding pixel (see Fig. 9b). Such diagrams were introduced by Muñoz-Tuñon et al. (1996) and further improved by Moiseev & Lozinskaya (2012). Different components of the ionized ISM occupy different places on the $I-\sigma$ diagram. First, we exclude all the pixels with Hα flux below the median value for DDO 53 as probably corresponding to the DIG – $\Sigma(\mathrm{H}\alpha) \simeq 10^{39}$ erg s^{-1} kpc^{-2} that was considered by Zhang et al. (2017) as demarcating surface brightness between DIG and H II regions). H II regions are a dominant features on the rest of the diagram and appear as having relatively high Hα flux and $\sigma(\mathrm{H}\alpha)$ close to the flux-weighted mean value in the galaxy ($\sigma_m = 18.6 \pm 3.4$ km s^{-1}). We classify a pixel as related to an H II region (blue colour) if its $\sigma(\mathrm{H}\alpha)$ lies within the normal distribution around σ_m at each I value. As follows from the classification map (panel a) and its comparison with Hα map (panel c), the prominent faint filaments that physically are not H II regions, but do not demonstrate elevated velocity dispersion, are also classified as H II regions following our criteria. Finally, the regions having $\sigma(\mathrm{H}\alpha)$ higher than defined by a normal distribution around σ_m with standard deviation equal to one or two times the uncertainties of σ_m (3 km s^{-1}) are considered either turbulent ISM (cyan colour) or superbubble candidates (red colour), respectively. According to Muñoz-Tuñon et al. (1996), the expanding superbubbles should appear on the $I-\sigma$ diagram as triangle-shaped features, as they appear in Fig. 9(b).

In Fig. 9(d), we show the distribution of the FPI pixels on the plane of the residual line-of-sight velocity $V_{\mathrm{Res}}(\mathrm{H}\alpha$; after circular rotation subtraction) versus $\log F(\mathrm{H}\alpha)$. The colours are the same as in the $I-\sigma$ diagram, but here we also introduce the area corresponding to the well detached blue-shifted ionized gas motions that do not show elevated velocity dispersion (encoded in green colours on both of these diagrams and on panel a). As follows from Fig. 9(a), this area is observed towards the brightest H II regions in complex N, exactly in the place where the H I tail is observed. It is connected with the area of large Hα line profile asymmetry. The absolute offset (~ 10 km s^{-1}) of these motions is slightly lower than for the H I tail, but they still might be related with each other (see Section 4.2).

We apply the ASTRODENDRO routine to select all spatially-connected pixels classified as turbulent ISM or superbubbles and having size not less than angular resolution of the data. As a result, we identify six regions approximated by ellipses; their numbers are given on panels (a) and (c). Among them, four regions contain the extended areas classified as expanding superbubbles (SB-2, 3, 5, 6), while the regions SB-1 and SB-4 have lower maximal velocity dispersion. We consider all the selected regions as superbubble candidates. Note that while only region SB-6 demonstrates a clear shell-like morphology, other regions (except the most compact SB-5) are still encircled by the Hα filamentary structures or H II regions that are typical for superbubbles in an inhomogeneous medium.

Three of the expanding superbubbles coincide with the regions selected by Moiseev & Lozinskaya (2012), while SB-5 was not identified previously. The latter region appears as a small H II region #24 (according to Fig. 2), demonstrating the most prominent asymmetry of the Hα line profile (Fig. 7 and also the orange contours in Fig. 9a) that could be reliably decomposed on to two kinematically distinct components, one of which is broad and red-shifted (prof. #3 in Fig. 8). Among the rest of the selected superbubble candidates, only SB-2 demonstrates a multicomponent Hα line profile at the current resolution (prof. #2). As follows from Fig. 9(c), all of the selected regions do not contain numerous OB stars, yet a few of them are encircled by these superbubble candidates. Such a picture was observed earlier in other dIrr galaxies (e.g. Egorov et al. 2017). In some cases (SB-4 and SB-6), the elevated velocity dispersion are observed just beyond the prominent star clusters located within the bright H II regions. We suggest that such regions appear to be

Downloaded from https://academic.oup.com/mnras/article/508/2/2650/6373944 by Special Astrophysical Observatory of the Russian Academy of Sciences user on 15 October 2021

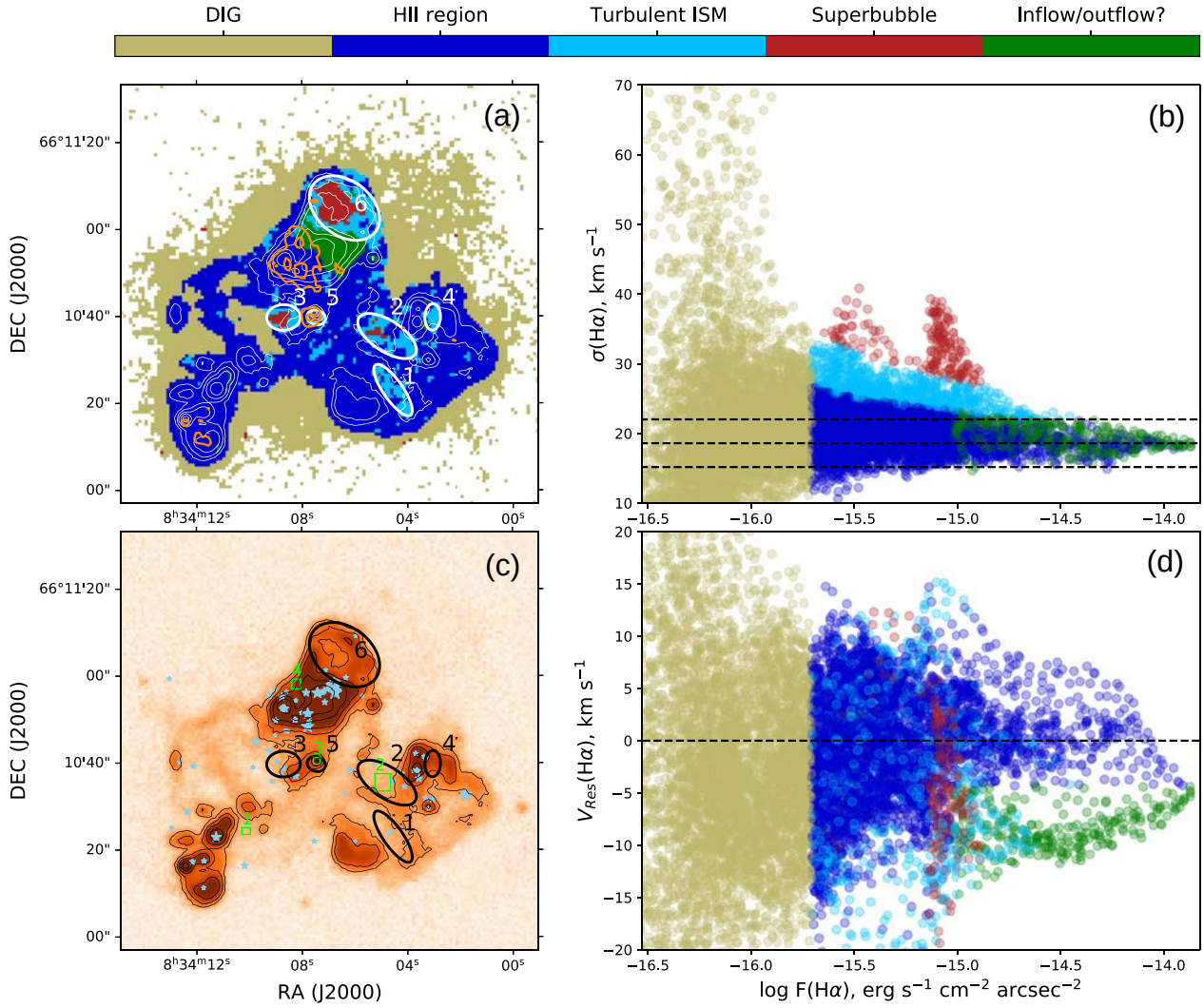

Figure 9. Analysis of the H α velocity dispersion σ(H α) in the FPI data. *Panel (a)* – classification map according to the diagrams presented on panels (b) and (c). Different colours encode several types of regions denoted on the colour-bar [colours are the same in panels (a), (b), and (d)]. The white ellipses are the superbubble candidates that have elevated σ(H α) and are selected with ASTRODENDRO. The orange contours correspond to the H α line profile asymmetry distribution as shown in Fig. 7. The white contours show the distribution of H α surface brightness. *Panel (b)* – 'I–σ' diagram of the H α line showing the pixel-by-pixel dependence of the σ(H α) on the logarithm of the line flux F(H α). The olive colours correspond to the DIG and is selected as having F(H α) less than the median value for the galaxy. The blue colours trace the areas with σ(H α) within the normally distributed values for the corresponding flux around the flux-weighted mean value σ_m(Hα) = 18.6 ± 3.5 km s^{-1} (shown by the dashed lines). The cyan colours are the regions having σ(H α) beyond this normal distribution, and the red colours are peaks in the diagram having σ(H α) larger than found for a normal distribution with twice the standard deviation around σ_m(H α). *Panel (c)* – H α image of the galaxy with overlaid ellipses from panel (a) and location of the main-sequence O-stars. The black contours trace the H α surface brightness. *Panel (d)* – pixel-by-pixel analysis of the line-of-sight residual velocity V_{res}(H α) versus log F(H α). The pixels with blue-shifted V(H α) and σ(H α) normally distributed around σ_m(H α) are denoted by the green colours on panels (a), (b), and (d). Note that on panel (d) the points from such blue-shifted regions smoothly turn into the points related to the superbubble SB-6.

superbubbles expanding into the lower density environment outside the star-forming regions under the influence of the energy and momentum ejection of the OB stars (and supernovae) residing in the bright H II regions.

Because the observed H α line profile does not show a clear separation into the components from the approaching and receding sides, we cannot precisely measure the expansion velocities V_{exp} of the identified superbubbles. However, we can still estimate it from the velocity dispersion σ_{int} derived from the integrated spectrum of the whole superbubble region. Smirnov-Pinchukov & Egorov (2021) demonstrated that V_{exp} can be expressed as $V_{exp} = k(\sigma_{int}^2 - \sigma_m^2)^\alpha + V_0$ with the coefficients k, α, and V_0 dependent on the mean value of velocity dispersion outside a superbubble σ_m and on the given FWHM of the instrumental profile.[3] We list the derived values for each superbubble in Table 3 together with their centres (RA, Dec.), minor and major diameters D_{min}, D_{maj} (measured as the size of the ellipses in Fig. 9, which enclose 80 per cent of the area with elevated velocity dispersion for each region), position angle PA, kinematic age, and kinetic energy consumption $\dot{E}_{kin}$. The kinematic age is derived assuming the Weaver et al. (1977)

[3]In case of DDO 53 we utilized FPI $k = 3.14$, $\alpha = 0.4$, $V_0 = -3$.

Downloaded from https://academic.oup.com/mnras/article/508/2/2650/6373944 by Special Astrophysical Observatory of the Russian Academy of Sciences user on 15 October 2021

Table 3. Derived parameters of the superbubbles selected from the I–σ diagram in Fig. 9.

#	RA (J2000)	Dec. (J2000)	$D_{\rm min}$, pc	$D_{\rm maj}$, pc	PA	$\sigma_{\rm int}$, km s^{-1}	$V_{\rm exp}$, km s^{-1}	Age, Myr	$\dot{E}_{\rm kin}$, 10^{36} erg s^{-1}
SB-1	128.51897	66.17306	80	251	35	21	18	2.4	1.5
SB-2	128.51990	66.17650	127	275	57	23	21	2.6	4.6
SB-3	128.53627	66.17770	106	138	92	28	33	1.1	6.8
SB-4	128.51268	66.17772	64	108	178	23	24	1.1	1.2
SB-5	128.53108	66.17770	60	77	72	26	30	0.7	1.6
SB-6	128.52660	66.18468	224	321	52	25	28	2.9	20.5

model of evolution of superbubbles from which we could derive $t = 0.6R/V_{\rm exp}$. The effective radius is derived as $R = 0.5\sqrt{D_{\rm min} \times D_{\rm maj}}$. The kinetic energy retained in the superbubbles is estimated as $\dot{E}_{\rm kin} = 0.5\dot{M}_{\rm sh}V^2_{\rm exp} = 2\pi n\mu m_{\rm H}R^2V^3_{\rm exp}$ assuming $\mu = 1.4$ (taking into account the helium contribution) and volume density $n = 0.4\,{\rm cm}^{-3}$ (see Fig. 4). As follows from Table 3, the identified superbubbles are relatively young and have ages of 1–3 Myr. That is consistent with the estimate made by Moiseev & Lozinskaya (2012) who roughly assumed the maximal velocity dispersion as a proxy of the expansion velocity. These values are also consistent with the estimates of the age of the H II regions derived in Section 3.4. Comparing the measured values of $\dot{E}_{\rm kin}$ with the mechanical wind luminosity of single O-star ($L_w \sim 0.8 \times 10^{36}\,{\rm erg\,s}^{-1}$ for an O3V star at a metallicity of $Z = 0.2\,{\rm Z}_\odot$, according to Smith, Norris & Crowther 2002), we may conclude that even the few OB stars residing in the centre or the edges of SB-1, SB-2, SB-3, and SB-4 produce enough energy to drive the expansion of the superbubbles, especially assuming that such a calculation does not take into account contribution of the radiation pressure and of the possible supernovae explosions. An additional source of energy beyond the winds of the OB stars (perhaps, supernovae, but see further discussion on the external gas flow and shocks in Section 4.2) are required to drive the expansion of SB-6.

3.4 Gas excitation and metallicity of the H II regions and superbubbles

From our long-slit and IFU spectroscopic observations, we were able to derive the excitation state and physical properties of more than half of 37 identified H II regions in DDO 53 and also in some diffuse emission structures related to the identified superbubbles. We analysed the integrated spectra of those parts of the H II regions crossed by the slit, or the integrated spectra over the whole extent of the H II region (within the borders shown in Fig. 2) in the case of the IFU observations. The results of the analysis are given in Table 4. All the listed flux ratios were corrected for reddening estimated from the measured Balmer decrement as described in Section 2.2; the corresponding colour excess $E(B-V)$ for each region are given in Table 4. We provide also measurements of the equivalent width of the H β line, EW(H β), the age of the H II regions as estimated from the EW(H β) according to the model of Levesque & Leitherer (2013), and the oxygen abundance 12 + log(O/H) measured using two methods (see below).

3.4.1 Measurements of oxygen abundance

For measurements of 12 + log(O/H) as indicator of the gas phase metallicity, we utilize the S calibration from Pilyugin & Grebel (2016) – an empirical method relying on the flux ratios of strong emission lines ([N II] 6584Å, [S II] 6717,6731Å, [O III] 5007Å and H β). For two bright H II regions (#33 and #35), we were able to also measure the faint auroral line [O III] 4363Å and thus to measure the electron temperature $T_{\rm e}$ and derive $12 + \log({\rm O/H})_{Te}$ with the $T_{\rm e}$-method following the relations in Izotov et al. (2006). Our measurements made using the S calibration show slightly higher values than those made using the $T_{\rm e}$ method.

Previous studies showed that DDO 53 has a low oxygen abundance $12 + \log({\rm O/H}) = 7.82 \pm 0.09$ (Croxall et al. 2009), however, earlier estimates differ significantly showing 12 + log (O/H) = 7.52−8.59 (Hunter & Gallagher 1985; Skillman, Kennicutt & Hodge 1989; Hunter & Hoffman 1999; Pustilnik et al. 2003; Saviane et al. 2008). The median and standard deviation of oxygen abundance derived in our study from a larger sample of H II regions $12 + \log({\rm O/H})_{\rm S} = 7.59 \pm 0.16$ is in good agreement with $12 + \log({\rm O/H}) = 7.52 \pm 0.08$ obtained by Pustilnik et al. (2003) and with estimates made using the $T_{\rm e}$ method for the brightest H II regions, however, it is lower than all other measurements in the literature. The distribution of the O/H measurements across different H II regions show significant variations in the range of ∼7.3–7.8 dex without any sign of a radial gradient. We find that our measured values of $12 + \log({\rm O/H})_{\rm S}$ strongly correlate with the surface brightness of corresponding H II region (and anticorrelate with [S II]/H α) and hence we expect that the faint nebulae might be biased by a significant DIG contribution. Given that, we also derive the flux-weighted mean value $12 + \log({\rm O/H})_{\rm S} = 7.67 \pm 0.04$. This latter value is in a perfect agreement with its absolute magnitude M_B according to the luminosity–metallicity reference relation (e.g. Berg et al. 2012) and still lower than measured by Croxall et al. (2009). Thus, we estimate the mean gas phase metallicity of DDO 53 to be $Z \sim 0.08$–$0.10\,{\rm Z}_\odot$, depending on whether we consider the probable contamination by DIG or not.

In Fig. 10, we compare the photoionization models from Gutkin, Charlot & Bruzual (2016) with the measured line flux ratios for individual H II regions shown on the BPT diagnostic diagrams (Baldwin, Phillips & Terlevich 1981). We find that the model for $Z \sim 0.13\,{\rm Z}_\odot$ (orange line) could explain most of the data points, and there is a lack of agreement with the models for lower metallicity. Those points with [O III]/H β below the lower limit for the modelled curve have lower ionization parameter than considered in the Gutkin et al. (2016) models, but could be fit by other models at the same metallicity providing we assume the low ionization parameter values. Taking into account the well-known problem of the discrepancy between oxygen abundance measurements made by empirical and model-based calibrations (e.g. Kewley & Ellison 2008), we may conclude that our flux-weighted metallicity estimate is in agreement with the photoionization models and that the nebulae with significantly lower values of 12 + log(O/H) in Table 4 are highly contaminated by DIG, and do not reflect real chemical inhomogeneity due to accretion of metal-poor gas or another process.

Downloaded from https://academic.oup.com/mnras/article/508/2/2650/6373944 by Special Astrophysical Observatory of the Russian Academy of Sciences user on 15 October 2021

Table 4. Results of the analysis of the spectra for individual H II regions according to Fig. 2. For each region, we provide the source of the data (IFU or long slit with corresponding position angle) and the ranges within with the spectra were integrated (for IFU – the elliptical aperture shown in Fig. 2). Regions with names that start with SB are the superbubbles identified in Section 3.3 (see Fig. 9).

Region	1	2	2	3	5	7	7
Slit	IFU	PA323	IFU	PA211	PA198	PA323	IFU
Pos.(arcsec)	–	−32 – −27	–	25–31	16–27	−21–−16	–
E(B-V)	0.00 ± 0.04	0.37 ± 0.03	0.00 ± 0.03	0.21 ± 0.12	0.03 ± 0.02	0.18 ± 0.04	0.09 ± 0.04
[O II] 3727,3729/H β	1.42 ± 0.16	–	0.21 ± 0.23	–	2.27 ± 0.67	–	2.36 ± 0.37
[O III] 5007/H β	2.41 ± 0.11	4.45 ± 0.11	3.74 ± 0.14	0.56 ± 0.11	1.51 ± 0.03	1.56 ± 0.08	2.61 ± 0.14
[N II] 6583/H α	0.027 ± 0.010	0.011 ± 0.003	<0.003	<0.055	0.034 ± 0.003	0.035 ± 0.006	0.024 ± 0.009
[S II] 6717,6731/H α	0.090 ± 0.009	0.030 ± 0.003	0.072 ± 0.014	0.193 ± 0.029	0.120 ± 0.003	0.131 ± 0.009	0.106 ± 0.011
[Ar III] 7136/H α	–	–	–	–	0.016 ± 0.002	0.033 ± 0.017	–
EW(H β)	114.9 ± 9.9	72.5 ± 6.3	199.3 ± 20.8	19.4 ± 7.4	61.6 ± 3.4	60.6 ± 9.2	56.4 ± 3.4
Age (Myr)	4.3 ± 0.1	4.8 ± 0.1	3.4 ± 0.3	6.5 ± 0.7	4.9 ± 0.1	5.0 ± 0.1	5.0 ± 0.1
$12 + \log(O/H)_S$	7.71 ± 0.10	7.76 ± 0.08	–	–	7.61 ± 0.03	7.63 ± 0.06	7.71 ± 0.11

Region	8	10	11	14	14	15	18
Slit	PA323	PA259	PA323	PA211	PA259	PA259	PA259
Pos.(arcsec)	−24 – −22	46–56	−9 – −5	17–21	38–43	20–29	6–12
E(B-V)	0.14 ± 0.07	0.07 ± 0.05	0.00 ± 0.13	0.00 ± 0.10	0.09 ± 0.02	0.08 ± 0.06	0.04 ± 0.03
[O III] 5007/H β	0.86 ± 0.10	0.80 ± 0.06	0.12 ± 0.08	0.39 ± 0.09	1.02 ± 0.02	0.29 ± 0.09	0.81 ± 0.04
[N II] 6583/H α	0.051 ± 0.012	0.056 ± 0.014	0.072 ± 0.021	<0.044	0.031 ± 0.004	0.052 ± 0.008	0.039 ± 0.006
[S II] 6717,6731/H α	0.145 ± 0.018	0.117 ± 0.014	0.226 ± 0.030	0.237 ± 0.030	0.128 ± 0.004	0.238 ± 0.012	0.198 ± 0.009
[Ar III] 7136/H α	–	–	–	–	0.008 ± 0.004	–	–
EW(H β)	24.9 ± 4.6	54.4 ± 13.0	15.6 ± 4.5	38.2 ± 8.3	112.4 ± 9.4	35.8 ± 4.9	34.0 ± 3.1
Age (Myr)	6.2 ± 0.3	5.0 ± 0.3	6.9 ± 0.4	5.4 ± 0.3	4.3 ± 0.1	5.5 ± 0.2	5.6 ± 0.2
$12 + \log(O/H)_S$	7.53 ± 0.10	7.52 ± 0.08	–	–	7.43 ± 0.04	7.18 ± 0.09	7.44 ± 0.05

Region	20	22	23	24	27	31	31
Slit	PA259	PA211	PA259	PA198	PA211	PA198	PA323
Pos.(arcsec)	−14 – −5	9–16	−22 – −17	−4 – 2	−4 – 3	−24 – −19	12–16
E(B-V)	0.13 ± 0.07	0.09 ± 0.06	0.08 ± 0.07	0.30 ± 0.02	0.05 ± 0.08	0.01 ± 0.02	0.07 ± 0.01
[O II] 3727,3729/H β	–	–	–	–	–	1.20 ± 1.26	1.59 ± 0.55
[O III] 5007/H β	0.39 ± 0.08	0.49 ± 0.07	0.73 ± 0.07	0.94 ± 0.02	0.23 ± 0.07	1.40 ± 0.04	1.58 ± 0.02
[N II] 6583/H α	0.052 ± 0.016	0.044 ± 0.010	0.031 ± 0.011	0.026 ± 0.003	<0.043	0.041 ± 0.005	0.029 ± 0.002
[S II] 6717,6731/H α	0.220 ± 0.022	0.238 ± 0.017	0.152 ± 0.013	0.068 ± 0.003	0.241 ± 0.025	0.165 ± 0.007	0.123 ± 0.003
[Ar III] 7136/H α	–	–	–	0.006 ± 0.002	–	0.012 ± 0.005	0.012 ± 0.001
EW(H β)	24.7 ± 7.5	20.9 ± 4.0	58.2 ± 10.7	39.7 ± 2.1	32.4 ± 6.2	45.6 ± 3.6	87.4 ± 2.5
Age (Myr)	6.2 ± 0.6	6.5 ± 0.3	5.0 ± 0.2	5.4 ± 0.1	5.7 ± 0.3	5.3 ± 0.1	4.6 ± 0.0
$12 + \log(O/H)_S$	7.28 ± 0.12	7.32 ± 0.09	7.32 ± 0.12	7.34 ± 0.03	–	7.65 ± 0.04	7.57 ± 0.02

Region	31	33	33	33	35	35	35
Slit	IFU	PA198	PA323	IFU	PA211	PA323	IFU
Pos.(arcsec)	–	−16 – −7	17–19	–	−19 – −10	20–28	–
E(B-V)	0.00 ± 0.02	0.00 ± 0.01	0.17 ± 0.02	0.00 ± 0.03	0.01 ± 0.02	0.05 ± 0.01	0.00 ± 0.02
[O II] 3727,3729/H β	1.72 ± 0.22	1.63 ± 0.17	–	1.46 ± 0.12	–	2.25 ± 0.46	1.59 ± 0.10
[O III] 5007/H β	2.06 ± 0.06	2.39 ± 0.04	2.00 ± 0.05	3.05 ± 0.10	2.48 ± 0.05	1.75 ± 0.02	2.64 ± 0.05
[N II] 6583/H α	0.030 ± 0.009	0.027 ± 0.002	0.031 ± 0.003	0.021 ± 0.007	0.025 ± 0.004	0.028 ± 0.002	0.025 ± 0.006
[S II] 6717,6731/H α	0.131 ± 0.007	0.114 ± 0.002	0.121 ± 0.004	0.108 ± 0.004	0.094 ± 0.004	0.105 ± 0.002	0.108 ± 0.003
[Ar III] 7136/H α	–	0.014 ± 0.001	0.015 ± 0.002	–	0.020 ± 0.004	0.015 ± 0.001	–
EW(H β)	79.1 ± 2.5	108.5 ± 2.5	116.5 ± 7.9	170.6 ± 7.1	50.9 ± 2.6	147.3 ± 7.6	149.1 ± 3.7
Age (Myr)	4.7 ± 0.0	4.3 ± 0.0	4.3 ± 0.1	3.8 ± 0.1	5.1 ± 0.1	4.0 ± 0.1	3.9 ± 0.0
$12 + \log(O/H)_{Te}$	–	7.59 ± 0.06	–	–	–	7.55 ± 0.15	7.50 ± 0.05
$12 + \log(O/H)_S$	7.68 ± 0.08	7.71 ± 0.02	7.69 ± 0.03	7.72 ± 0.09	7.69 ± 0.05	7.60 ± 0.02	7.72 ± 0.06

Region	36	37	37	SB-3	SB-6	SB-6	–
Slit	IFU	PA323	IFU	PA323	PA211	PA323	–
Pos.(arcsec)	–	33–39	–	4–9	−30 – −22	29–31	–
E(B-V)	0.00 ± 0.07	0.03 ± 0.02	0.16 ± 0.10	0.12 ± 0.08	0.13 ± 0.07	0.00 ± 0.06	–
[O II] 3727,3729/H β	2.15 ± 0.79	–	2.88 ± 1.17	–	–	–	–
[O III] 5007/H β	1.09 ± 0.12	0.68 ± 0.03	1.00 ± 0.13	0.39 ± 0.09	0.71 ± 0.07	0.96 ± 0.08	–
[N II] 6583/H α	0.044 ± 0.022	0.044 ± 0.005	0.031 ± 0.022	0.042 ± 0.013	0.046 ± 0.007	0.056 ± 0.011	–
[S II] 6717,6731/H α	0.295 ± 0.051	0.170 ± 0.005	0.202 ± 0.045	0.245 ± 0.019	0.194 ± 0.011	0.201 ± 0.016	–
[Ar III] 7136/H α	–	–	–	–	–	0.034 ± 0.010	–
EW(H β)	1.9 ± 0.3	144.4 ± 24.5	73.9 ± 6.7	12.6 ± 2.8	80.0 ± 14.8	88.9 ± 19.2	–
Age (Myr)	9.2 ± 0.1	4.0 ± 0.3	4.8 ± 0.1	7.2 ± 0.3	4.7 ± 0.2	4.6 ± 0.2	–
$12 + \log(O/H)_S$	7.62 ± 0.17	7.41 ± 0.04	7.45 ± 0.22	7.22 ± 0.12	7.44 ± 0.07	7.62 ± 0.08	–

Downloaded from https://academic.oup.com/mnras/article/508/2/2650/6373944 by Special Astrophysical Observatory of the Russian Academy of Sciences user on 15 October 2021

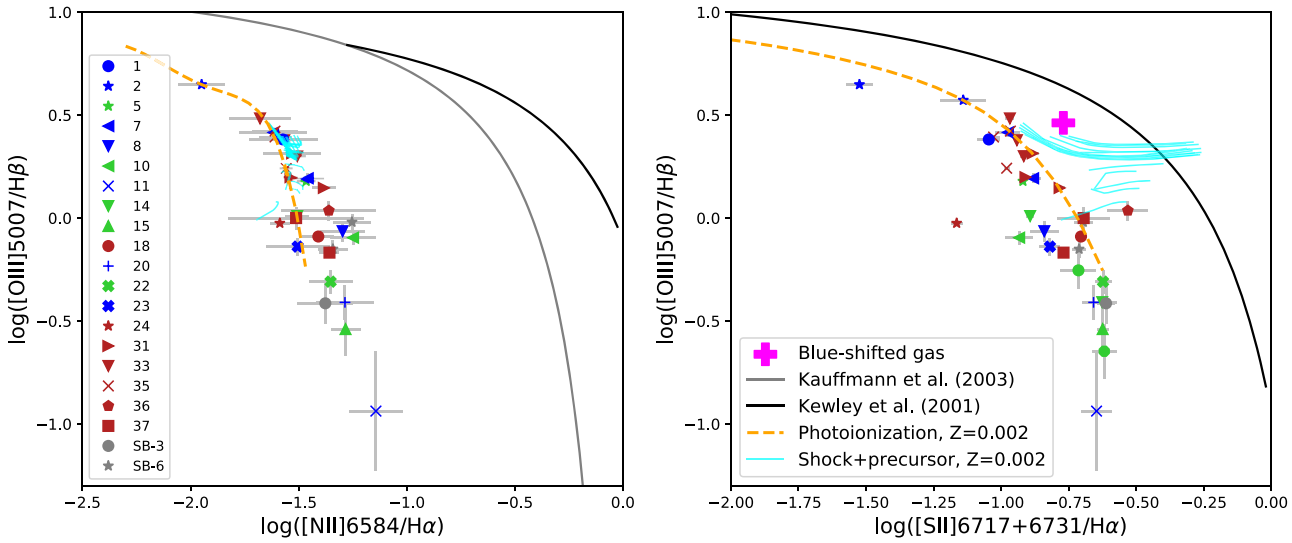

Figure 10. The diagnostic BPT diagram (Baldwin et al. 1981) together with its extension (Veilleux & Osterbrock 1987) showing the line ratios of [O III]/H β versus [N II]/H α (left-hand panel) and [S II]/H α (right-hand panel) for different H II regions according to their numbers in Fig. 2 and Table 4. The grey points for SB-3 and SB-6 correspond to the emission inside the identified superbubbles according to Fig. 9. The magenta cross on the right-hand panel corresponds to the area of elevated [O III]/H β towards the region of the blue-shifted H I and H α motions (see Fig. 12). The black and grey curves represent the demarcation lines between photoionized regions (to the left of them) and those having high contribution of other excitation mechanisms (for solar metallicity, taken from Kewley et al. 2001 and Kauffmann et al. 2003, respectively). The orange-dashed line is the polynomial approximation of the grid of photoionization model from Gutkin et al. (2016) constructed for metallicity Z = 0.002 (12 + log(O/H) $\simeq$ 7.8), and the cyan lines are the model of shocks+precursor for the same metallicity and for shock velocities V = 100–500 km s^{-1} as given from Alarie & Morisset (2019).

3.4.2 *Indication of shocks in the ISM*

The estimated ages of the H II regions demonstrate quite a uniform distribution around a value of 5.0 $\pm$ 1.1 Myr, with the older ages towards the low brightness area where we find signs of expanding superbubbles, and slightly younger ages for the brightest H II regions. This is in agreement with the estimates made by Pustilnik et al. (2003), yet we do not confirm their findings on the older age of the H II regions towards the SE complex. Comparing the ages of the H II regions and the estimates of the kinematic ages of the superbubbles (see Table 3), we may expect that the latter were developed when the H II regions were relatively evolved and hence the supernovae explosions should have already occurred. Hence, the energy of supernovae explosions should contribute significantly to the energy balance of superbubbles, and we may expect to find signs of shock excitation towards them.

The map of [S II]/H α obtained from our narrow-band images (Fig. 11) shows that all H II regions have this flux ratio well below the typical value of 0.4 that is usually used for separation of supernovae remnants from photoionized nebulae (Blair, Kirshner & Chevalier 1981; Blair & Long 2004). At the same time, the [S II]/H α is slightly increased towards the identified superbubbles (the same also follows from the long-slit spectra for SB-3 and SB-6, see Table 4). This is especially evident for superbubble SB-2 where the [S II]/H α reaches values above 0.5. In principle, the enhanced ratio of [S II]/H α and other low-excitation ions is also usually observed in the DIG, probably related with the leaking ionizing quanta from H II regions [e.g. Hidalgo-Gámez (2007) and Haffner et al. (2009) specifically for DIG in DDO 53]. However, since we also observe the presence of a blue-shifted broadened component in the H α profile in the centre of superbubble SB-2 (prof. #2 in Fig. 8), we suggest there is a high contribution of shocks from supernovae there.

As is already mentioned, Fig. 10 demonstrates the measurements of the line flux ratios made for the integrated spectra of the H II regions as given in Table 4 on the BPT diagrams, which are usually considered as the main diagnostic instrument allowing us to distinguish between different excitation mechanisms for ionized nebulae. Different symbols correspond to different regions, and the grey symbols denoted with 'SB' letters are related to the measurements made within the corresponding superbubbles. Those

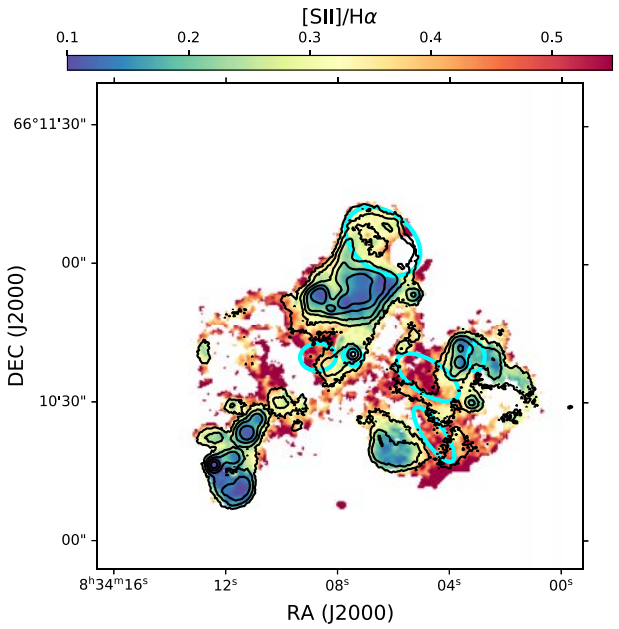

Figure 11. The flux ratio of [S II]/H α as measured from narrow-band imaging observations. The black contours trace the levels of constant H α surface brightness. The cyan ellipses denote the borders of superbubbles as identified in Fig. 9.

Downloaded from https://academic.oup.com/mnras/article/508/2/2650/6373944 by Special Astrophysical Observatory of the Russian Academy of Sciences user on 15 October 2021

symbols sharing the same colour correspond to the same star-forming complex according to Fig. 2 (red colour = complex N; green colour = SW; blue colour = SE). We do not find any significant difference in ionization properties of the H II regions within different complexes except that [O III]/H β (which could be considered as a proxy of hardness of the ionizing radiation) is slightly lower for complex SW. As follows from the diagrams, all analysed nebulae in DDO 53 lie far below the demarcation lines from Kewley et al. (2001) and Kauffmann et al. (2003) within the photoionization domain. However, it is important to remember that the parametrization of these lines were obtained assuming solar metallicity, while DDO 53 is low-metallicity galaxy.

On the BPT diagram we overlay (as the cyan lines) the grid of shocks models at $Z \sim 0.13\,Z_{\odot}$ that were computed by Alarie & Morisset (2019) for the same chemical abundance prescription as is in the Gutkin et al. (2016) models. Different lines correspond to different shock velocities. One may see that while in principle all the data points are well described by pure photoionization, at least for bright regions in complex N the shocks acting in such a low-metallicity environment could produce the same line ratios, and hence it is impossible to distinguish between the contribution of these two mechanism without considering additional source of information (e.g. local gas kinematics as described in Section 3.3). Since we detected the presence of a prominent H α line asymmetry and a blue-shifted cloud (Figs 7 and 9), as well as the underlying broad component between the bright H II regions #31, 33, 35 (prof. #4 in Fig. 8), we suggest that shocks contribute to the overall gas excitation in this area where the most intense ongoing star formation occurs. The origin of these shocks could be related to either feedback from O-stars, or from the interaction with the H I tail.

We also consider the ionization structure of the brightest complex N in more details. We do not see any significant enhancement of the [S II]/H α flux ratio beyond the H II regions (Fig. 11), but the IFU data reveal elevated [O III]/H β at the edge of the bright nebulae rather than towards the central part (Fig. 12). The highest [O III]/H β flux ratio in the galaxy (after the H II region #2) is observed here, exactly at the place where all three peculiarities in gas kinematics (the beginning of the H I tail, the extended region of H α line profile asymmetries, and the area of blue-shifted non-circular motions in the ionized gas) were detected. Note that while the largest number of identified O-stars concentrate in this complex, they are located outside the area of the highest [O III]/H β allowing us to suggest that these stars are unlikely to be the only sources for the observed gas excitation. Since shocks could also elevate [O III]/H β (Allen et al. 2008), we consider this scenario. The position of the most prominent extended region of enhanced [O III]/H β line ratio (coinciding with the area of the blue-shifted ionized gas) on the [O III]/H β versus [S II]/H α diagram is shown by the magenta cross in Fig. 10. This region is shifted towards the top-right part of the diagram compared to the rest of the H II regions in the complex and is better explained by the grid of shock models rather than by the models of pure photoionization. From this and from the analysis of the gas kinematics, we conclude that the shocks are observed at the south-western part of complex N.

3.4.3 *Peculiar H II regions*

Finishing the analysis of the excitation state of the ionized gas, we describe two H II regions having peculiarities in their spectra – #2 and #24. Their spectra integrated over the area crossed by the slits PA = 323 and PA = 198, respectively, are given in Fig. 13.

Region #2 demonstrate the highest [O III]/H β in the galaxy and deviates to the top left from the rest H II regions on BPT diagrams, yet it still could be well fit by the same photoionization model. A local peak of $E(B-V)$ is also observed towards this region, however, it is not detected by IFU observations (probably because of the different area of spectra extraction). Together with a high [O III]/H β, this region has the lowest [S II]/H α and [N II]/H α line ratios in DDO 53, thus suggesting that most of the gas there is in a high excitation state. From IFU observations we reveal high [O III]/[O II]$\sim$18. Such a large value is indicative that the region is density-bounded and hence should produce a significant amount of leaking LyC quanta (Jaskot & Oey 2013).

Region #24 was already mentioned in Section 3.3 as having the most prominent two-component H α line profile with the second component broadened and red-shifted (prof. #3 in Fig. 8). This region coincides with the peak of the H α line asymmetry map (Fig. 7) and with one of the detected superbubbles (SB-5). The long-slit spectrum also clearly reveals a broadened component under the Balmer lines. On the BPT diagrams the [S II]/H α ratio for the region stands out remarkably from the rest of H II regions towards lower values, and thus points to probably having lower gas metallicities. However, the estimates given in Fig. 10 and Table 4 were obtained for integral fluxes in each involved lines, without decomposition on to the components. Assuming that the true flux ratio comes from the narrow components, we decompose the H α on to two Gaussian (as shown in Fig. 13) and estimate the resulting values of [S II]/H $\alpha_{\rm narrow} \simeq 0.13$ and [N II]/H $\alpha_{\rm narrow} \simeq 0.06$. With these values this region would occupy the same area on BPT diagrams as the H II regions #8 and #10 and thus it should have higher oxygen abundance consistent with the photoionization model. Given that the second broad component of the H α line is significantly red-shifted and extended well beyond the H II region (as traced by H α asymmetry map), we may suggest that this underlying component is not related with the H II region and the observed picture is a result of the projection along the line of sight of the regular H II region and the faint region of non-circular motions.

4 DISCUSSION

4.1 A supergiant shell of ionized gas: large-scale outflow or the result of leaking LyC quanta?

Our H α narrow-band images revealed faint ionized gas encircling the galaxy (Section 3.1). This emission appears as an SGS of ionized gas. Its size (about 2 kpc) is significantly larger than for the biggest ionized supershell in the LMC (Book, Chu & Gruendl 2008), and comparable with the one discovered in the galaxy Holmberg II (Egorov et al. 2017). In this section, we discuss the possible origin of such a giant emission structure.

Through the influence of the winds and supernovae, massive stars create superbubbles of about 100 pc size in the ISM, while the merging of such structures could produce the kpc-sized SGSs observed in many nearby galaxies in both ionized and neutral gas. Continuous ejection of momentum and energy leads to the development of large-scale outflows in the form of galactic fountains or winds. Comparing the optical and H I maps for 12 dwarf galaxies, McQuinn, van Zee & Skillman (2019) found that many of them demonstrate an excess of H α emission at their periphery – this was interpreted as a signature of galactic fountains or winds (depending on the escape velocities of the gas). The discovered supershell of ionized gas in DDO 53 is also observed at the periphery of the galaxy and surrounds the stellar disc and bright H I clouds, thus producing

Downloaded from https://academic.oup.com/mnras/article/508/2/2650/6373944 by Special Astrophysical Observatory of the Russian Academy of Sciences user on 15 October 2021

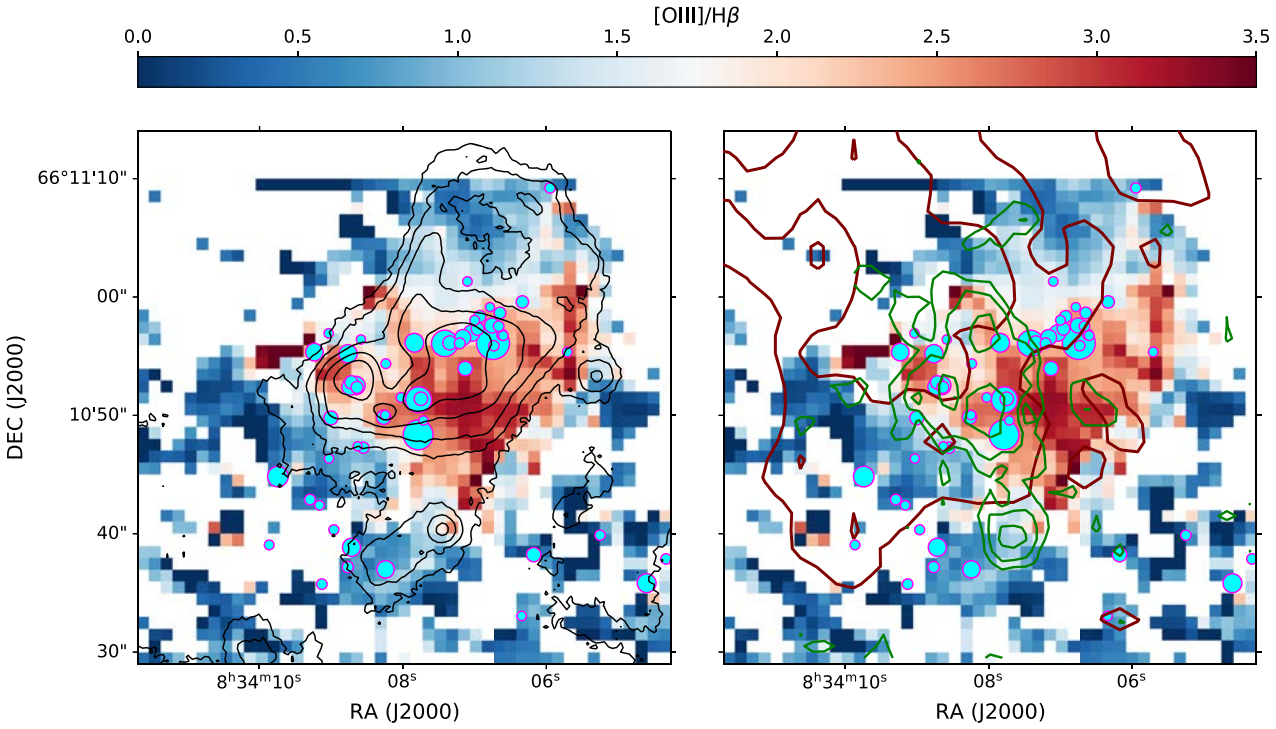

Figure 12. The distribution of the [O III]/H β lines flux ratio in the star-forming complex N as derived from IFU (PPAK/PMAS) data. *Left-hand panel*: The black contours show the lines of constant H α surface brightness; the cyan circles show the locations of identified O-stars (size of the symbols correlate with their M_V). *Right-hand panel*: The brown contours show the lines of the constant H I density of the H I tail; the green contours correspond to the asymmetry of the H α profile as given in Fig. 7.

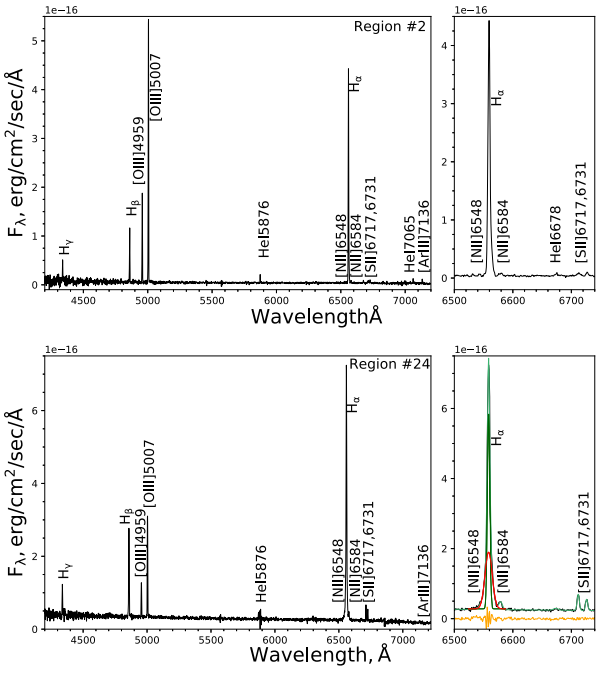

Figure 13. Example of the spectra for H II regions # 2 (top) and #24 (bottom) extracted from the long-slit spectra. The H α line of the spectrum of region #2 was fit with both narrow and broad Gaussians.

an excess of H α emission in the same way as in McQuinn et al. (2019).

Assuming that the detected ionized supershell in the galaxy DDO 53 is indeed an outflow, we estimate the mass-loss rate ($\dot{M}_{\rm out}$) and mass-loading factor ($\eta = \dot{M}_{\rm out}/SFR$) to check if the ongoing star formation is sufficient to drive such an outflow. With our angular resolution and S/N ratio in the H α line we cannot trace precisely the shape of the supershell. Since its brightest parts could be encircled by an ellipse having axial ratio and position angle in accordance with inclination and PA of the galaxy (see Section 3.1 and Fig. 3), we can assume a spherically symmetrical outflow in the form of a thin shell having radius of $R \sim 1$ kpc and thickness of $h \sim 0.2R$ that is typical for superbubbles (e.g. Churchwell et al. 2006; Krause et al. 2013) and consistent with our estimates derived from the smoothed H α map. We can estimate $\dot{M}_{out}$ from the total mass of the outflow dividing it by the time required for crossing the shell ($\tau = h/v_{\rm out}$ where $v_{\rm out}$ is the outflow velocity):

$$\dot{M}_{\rm out} = 4\pi R^2 \mu m_{\rm H} < n_{\rm p} > v_{\rm out}, \quad (2)$$

where $m_{\rm H}$ is the mass of hydrogen atoms, $\mu = 1.4$ to account for the Helium contribution, $<n_{\rm p}>$ is the average number density of ionized hydrogen atoms that has an unknown value. However, it could be derived from the surface brightness of the H α line I(H α) in the following way:

$$I(\mathrm{H}\,\alpha) = \frac{h\nu_{\mathrm{H}\,\alpha}}{4\pi} \int n_{\rm p} n_{\rm e} \alpha^{eff}_{\mathrm{H}\,\alpha} \mathrm{d}s \simeq \frac{h\nu_{\mathrm{H}\,\alpha}\alpha^{eff}_{\mathrm{H}\,\alpha} L}{4\pi} \left\langle n_{\rm e}^2 \right\rangle, \quad (3)$$

where I(H α) is expressed in erg cm^{-2} s^{-1} sr^{-1}, the effective recombination coefficient is $\alpha^{eff}_{\mathrm{H}\,\alpha} \simeq 1.17 \times 10^{-13}$ cm^3 s^{-1} for electron temperature $T_{\rm e} = 10\,000$ K (Osterbrock & Ferland 2006), and L is the

Downloaded from https://academic.oup.com/mnras/article/508/2/2650/6373944 by Special Astrophysical Observatory of the Russian Academy of Sciences user on 15 October 2021

optical path towards the supershell rim where we measure the surface brightness. Taking into account the spherical thin-shell geometry, we can derive that $L = 2h\sqrt{1+2R/h} \simeq 1.33R$ with our assumption of $h \sim 0.2R$. Due to clumping of the ISM, $< n_e^2 > \neq < n_e >^2$, but they are related with each other through the filling factor. According to Kado-Fong et al. (2020), $< n_e > \simeq 0.2\sqrt{< n_e^2 >}$ for the DIG. Hence,

$$< n_p > \simeq < n_e > \simeq 1.23 \times 10^8 \sqrt{I(\mathrm{H}\,\alpha)/R}, \quad (4)$$

where $I(\mathrm{H}\,\alpha)$ is in erg cm^{-2} s^{-1} arcsec^{-2} and R is in pc.

Only the few brightest clumps in the supershell were detected in our FPI data making it impossible to measure the outflow velocity. We can only roughly estimate its upper limit as $v_{\rm out} \sim 20$ km s^{-1} assuming that the earlier mentioned H I 'tail' (separated by this value from the bulk of the H I) is related to the supershell (see the next section for a discussion on that), or that the maximum deviations of the map of residual velocities in H α line are related with such a large-scale outflow (see Fig. 4).

Combining the estimates of all involved parameters together, we derive $\dot{M}_{\rm out} \simeq 0.06\,\mathrm{M}_\odot$ and $\log(\eta) \simeq 1.05$, which is slightly higher than the values derived by McQuinn et al. (2019) for several other dwarf galaxies of similar circular velocity, but in a good agreement with the simulations by Christensen et al. (2016). Note that the usage of a lower filling factor like in McQuinn et al. (2019) will bring our estimate into perfect agreement with their results.

Thus, we conclude that the 2 kpc sized supershell-like structure of ionized gas could be a large-scale outflow driven by the ongoing star formation. However, this scenario still might be challenged by comparison of the H α and H I flux maps. As it follows from Fig. 5, there is prominent H I emission visible in blue-shifted channels at the periphery of DDO 53 beyond the H I tail and the known H I supershells. Some of these gas clouds correlate with peaks in the H α emission of the ionized supershell under discussion. Hence, we may expect that at least in part the H α emission could also be related to the ionization of the surrounding atomic gas by leaking quanta. As we demonstrated in Section 3.1, the amount of leaking ionizing quanta from the star-forming complexes is enough to explain the emission of such diffuse structures. In reality, both effects might contribute, and deeper H I data and more accurate measurements of H α velocities are required to distinguish between them. It is worthwhile to also note that the ionization of the faint outer H I gas in principle might also take place in other studies of some of the dwarf galaxies lacking the deep H I data at their periphery, but having deep enough H α data.

4.2 Star formation history and its relation to the blue-shifted H I tail

The kinematics and the localization of the H I tail allow one to suggest two explanations of its origin. It might be an external gas cloud falling on to the galaxy, or it might be resulted from a feedback-driven outflow due to the massive stars in complex N, and thus it contains outflowing gas rather than inflowing gas. The blue-shifted velocities of the cloud are more consistent with the latter scenario, and the observed shocks could thus be related to the influence of the stellar winds and possible supernovae on the surrounding ISM, rather then with infalling gas. However, it is hard to explain such a large extent and elongated shape in the H I tail, which is more consistent with a gas accretion scenario. Moreover, the observed SFR in the region N (see estimates below) is an order of magnitude less than it follows from equation (1) in Veilleux, Cecil & Bland-Hawthorn (2005) for the mass-loss rate from the region resulting from feedback $\dot{M}_* \sim 0.26$ SFR. Thus, the observed star formation in complex N is insufficient to drive such an outflow, and the external origin of the H I tail remains our favourable scenario.

DDO 53 is a rather isolated member of the M 81 group – it has no known neighbouring galaxy within several tens of its optical radius (Karachentsev et al. 2002). Despite that, as we describe above, both the morphology and kinematics of its ISM are perturbed. Since DDO 53 is located nearly between two subgroups of the M 81 group, Pustilnik et al. (2003) suggested that the current starburst there could be triggered by a tidal disturbance by the M 81 group as a whole, or by the interaction with the IGM, and these effects could be responsible for the observed peculiarities in the appearance of DDO 53. Estimating the density of the IGM at the periphery of the M 81 group to be too low, Begum et al. (2006) showed that ram pressure is unlikely to influence the gas in the galaxy. Instead they suggested that DDO 53 may be a product of a recent merger between two faint dwarf galaxies. From an analysis of the resolved *HST* images, Weisz et al. (2008) found that the SFR was enhanced about 1 Gyr ago. A dwarf–dwarf merger scenario can explain all the mentioned effects, including the presence of the blue-shifted H I 'tail' at the north part of the galaxy. However, according to estimates by Weisz et al. (2008), this event should have taken place not less than 1 Gyr ago. It is unclear whether the imprints of such interaction in the gaseous disc could survive for that time, as it is much longer than the dynamical time-scale for the galaxy (about 120 Myr).

Numerical studies shows that dwarf–dwarf mergers should not be rare, in particular for isolated galaxies, yet observational support of this process still remains very scarce – only few low mass dwarf galaxies with evidences for a recent major merger are known (see e.g. Rich et al. 2012; Amorisco, Evans & van de Ven 2014; Egorova et al. 2021). Deason, Wetzel & Garrison-Kimmel (2014) found that ∼15–20 per cent of 'field' dwarf galaxies with $M_\star > 10^6\,\mathrm{M}_\odot$ in the Local Group likely experienced a major merger since $z \sim 1$. However, the authors note that it is unclear for how long major mergers would have significant residual impact on star formation, stellar kinematics, or morphology. According to simulations performed by Lotz et al. (2008) for more massive galaxies, the asymmetry of morphology could be observed at time-scales of 0.3–1.1 Gyr. A simulation of two gas-rich merging dwarf galaxies (Bekki 2008) also shows similar time-scales and reproduces the morphology more or less consistently with that observed in DDO 53 (centrally concentrated regions of star formation surrounded by old stars and H I envelope), but the expected SFR is much higher than what is observed in DDO 53. That author showed that such a scenario reproduces BCD galaxies. In the case of DDO 53, an interaction in the past with a less massive companion (like it was established for DDO 68, see Annibali et al. 2019) seems to be a more favourable scenario. Starkenburg, Helmi & Sales (2016) showed in their models that the residuals of minor mergers for low-mass galaxies can demonstrate a disturbed morphology in both gas and stars, and that this process leads to a modest enhancement of SFR that is comparable with the values observed in DDO 53. In their models, features like the H I tail in DDO 53 could survive long enough, but the prominent stellar shells should also appear at the same time. They were not clearly detected in DDO 53, however the distribution of the red stars is asymmetrical (Weisz et al. 2008).

According to Weisz et al. (2008), the SFR of DDO 53 was almost uniform and rather shallow during the last 1 Gyr, and the current burst of star formation occurred 25 Myr ago. While its morphological appearance could be explained by a minor merger that occurred >1 Gyr ago, the ongoing starburst is unlikely to be driven by this event. Alternatively, it could be triggered by the more recent accretion of a gas cloud from the IGM. It could be a remnant of the proposed merger event, or a gas cloud that resided in the galaxy vicinity.

Downloaded from https://academic.oup.com/mnras/article/508/2/2650/6373944 by Special Astrophysical Observatory of the Russian Academy of Sciences user on 15 October 2021

Despite the fact that DDO 53 is rather isolated galaxy, the later option does not appear to be unlikely. Thus, a perfect example of a starburst in an isolated galaxy driven by accretion of a gas cloud is IC 10 – a nearby dwarf galaxy from the Local Group (Ashley et al. 2014). In such a scenario, the northern blue-shifted H I tail might be directly related with the infalling gas cloud. Indeed, as it follows from Figs 5(a) and 6, the tail is connected with the brightest star-forming complex N in the galaxy, accounting for about half of the current star formation in the galaxy, which allows us to speculate that neutral gas from this filament may provide the fuel for star formation.

We can roughly check whether accretion from the H I tail is able to provide enough gas to sustain star formation in the brightest H II complex. We assume a simple geometrical model, in which the 'tail' is located in the galactic plane along the minor axis and has a cylindrical shape width $D = 285$ pc (measured from blue-shifted channels in 'derotated' RO H I data). As it follows from H I 21 cm line profile fitting and from the PV diagrams (Fig. 5, 6), the velocity of the 'tail' is $V_{\rm LOS} \sim -20$ km s^{-1}, with respect to the bulk H I motions. This value can be transformed to the falling gas velocity in the galaxy plane $V_{\rm gas} = V_{\rm LOS} \times \cos(i)^{-1} \sim 25$ km s^{-1}, assuming an inclination of $i = 37^{\circ}$ (see Section 3.2). Given the estimated H I volume density $n_{\rm H\,I} \sim 0.25$ cm^{-3} (assuming a constant scale height of the H I disc, see Fig. 4(a)), we estimate the gas infall rate as

$$\dot{M}_{\rm gas} \simeq 1.43 \times 10^{-8} n_{\rm H\,I} D^2 V_{\rm gas}\ ({\rm M}_{\odot}\ {\rm yr}^{-1}), \quad (5)$$

which give us a value $\dot{M}_{\rm gas} \sim 0.007\,{\rm M}_{\odot}\ {\rm yr}^{-1}$. The value of $n_{\rm H\,I}$ might be underestimated if the size of the 'tail' along the line of sight is significantly smaller than the adopted scale height of the H I disc, which would lead to a higher value of $\dot{M}_{\rm gas}$. Converting the Hα line flux observed from the brightest complex of star formation to SFR we obtain ${\rm SFR_N} \sim 0.002\,{\rm M}_{\odot}\ {\rm yr}^{-1}$. Hence, comparing with the estimate of $\dot{M}_{\rm gas}$ we may conclude that such an infalling gas cloud will provide enough gas to sustain star formation at the observed rate.

From the analysis of the small-scale ionized gas kinematics in complex N, we find that the highly asymmetrical Hα line profile, together with the area of the kinematically detached ionized gas motions, are observed towards the place where the H I tail connects with the brightest H II region (see Section 3.3, Figs 7 and 9). The spectral diagnostics reveal that the line ratios are consistent with gas excitation by shocks in that area (Section 3.4, Figs 10 and 12). These findings are consistent with a scenario where the H I tail is a gas cloud falling on to the galactic disc and thus producing shock waves and triggering a burst of star formation in complex N. It is also interesting that almost all main-sequence O-stars in this region of the galaxy are located along the shape encircling this H I cloud (see right-hand panel of Fig. 12). Note that despite the presence of oxygen abundance variations in our measurements (see Section 3.4), we find neither any strong indications of dilution by accreted low-metallicity gas, nor expelled metals driven by a large-scale outflow (Section 4.1) – higher quality IFU data are required to clarify the small-scale oxygen abundance variations.

5 SUMMARY

We present results from an observational analysis of the interplay between massive stars, the interstellar and IGM, and ongoing star formation in the nearby relatively isolated low-metallicity dwarf galaxy DDO 53. Our multiwavelength analysis is based on narrow-band optical imaging and long-slit and Fabry–Perot spectroscopy performed with the 6-m telescope BTA (SAO RAS), integral-field spectroscopy with PPAK/PMAS at 3.5-m telescope (Calar Alto) and archival data of JVLA (in H I 21 cm line) and *HST* observations. We obtain the following results:

(i) Six expanding superbubbles of ionized gas were identified in the galaxy by the elevated velocity dispersion in the Hα emission line. In general, their location is consistent with the presence of previously detected H I supershells (Pokhrel et al. 2020). We demonstrate that the mechanical energy input from the winds of the observed O-stars within the superbubbles is enough to drive their expansion, but supernovae should also play a significant role, at least in part of the superbubbles, as follows from the diagnostic emission line ratios.

(ii) We analysed the excitation state and measured the oxygen abundance in more than half of 37 detected H II regions in the galaxy. Since the metallicity estimate derived from the empirical S calibration (Pilyugin & Grebel 2016) correlates with the Hα surface brightness and with the [S II]/Hα line ratio, we suggest that the measurements could be highly contaminated by the presence of DIG in the galaxy, which is also responsible for large variation of the estimated oxygen abundance. To get rid of this, we measure an Hα flux-weighted mean value of $12 + \log({\rm O/H})_S = 7.67 \pm 0.04$ that is consistent with the photoionization and shocks model grids that could describe our observations. Without the weighting the measurements by the Hα flux we get a mean value of $12 + \log({\rm O/H})_S = 7.59 \pm 0.16$ that is in a good agreement with the estimates made using $T_{\rm e}$ method for two brightest nebulae. Our measurements give a lower oxygen abundance than was adopted previously (Croxall et al. 2009) and is more consistent with the lowest estimates obtained by Pustilnik et al. (2003).

(iii) The brightest complex of star formation in DDO 53 demonstrates excitation from shocks both in emission line ratios diagnostics and in its ionized and neutral gas kinematics. We suggest that the shocks originate from the interaction of the ISM in the galaxy with the anomalous H I cloud that is detected there, rather than by the influence of the feedback from massive stars.

(iv) We investigated the origin of the anomalous H I gaseous tail to the north of the galaxy. From the analysis of its H I kinematics and its relation to the kinematics and excitation of the ionized gas, we argue that it represents a gas cloud falling on to the galaxy. This gas accretion event might be a reason for the enhanced star formation in the galaxy ∼25 Myr ago and it also could supply the fuel for sustaining star formation in the brightest Hα complex of DDO 53. The origin of the gas cloud still remains unknown, but it could be the remnant of a previous merger event that occurred more than 1 Gyr ago, or it could be captured from the IGM since the M 81 group is gas rich.

(v) We discover a faint giant 2-kpc sized ionized supershell surrounding the galaxy. It is likely that this structure represents a large-scale feedback-driven outflow. Under this assumption we estimate the mass-loading factor and find a value of $\log(\eta) \simeq 1.05$ that is slightly higher than the values obtained by McQuinn et al. (2019) for four other dwarf galaxies of the same circular velocity as for DDO 53, and in better agreement with the simulations by Christensen et al. (2016). However, we also suggest that, at least in part, this extended Hα emission could originate from the ionization of the dispersed H I at the periphery of DDO 53 by the leaking quanta from the star-forming regions.

(vi) We detected two small-size H II regions exhibiting broad underlying Balmer lines and peculiarities in their spectra. One of them has a high line flux ratio of [O III]/[O II]∼18 and appears to be a density bounded nebula, which could produce significant amount of leaking ionizing quanta. The other H II region is probably a regular

Downloaded from https://academic.oup.com/mnras/article/508/2/2650/6373944 by Special Astrophysical Observatory of the Russian Academy of Sciences user on 15 October 2021

H II region projected on to the extended region of diffuse gas excited by shocks.

As follows from the presented analysis, both stellar feedback and external gas accretion are important processes regulating the appearance of the ISM, its gas kinematics, and the ongoing star formation in the DDO 53 galaxy. At the same time, the galaxy DDO 53 appears to be quite rare object where one can observe the interplay between the star formation activity and the ongoing gas accretion. A growing number of observational studies report the discoveries of the the anomalous H I gas towards the bright H II regions (e.g. Sancisi et al. 2008; Lelli et al. 2012), or dynamical and excitation peculiarities of the ionized gas (e.g. Sánchez Almeida et al. 2014; Egorova, Moiseev & Egorov 2019; Sil'chenko, Moiseev & Egorov 2019), as indications of the recent gas accretion fuelling the star formation activity. Our results suggest that in DDO 53 we observe all these effects simultaneously.

ACKNOWLEDGEMENTS

The authors thank A. Burenkov, D. Oparin, and R. Uklein for their assistance in the SCORPIO-2 observations, and B. Groves and K. Sandstrom for their contribution in acquiring the PPAK IFU data. The analysis of the gas kinematics and overall discussion presented in this work was supported by the Russian Science Foundation (projects no. 19-72-00149). KK and OE gratefully acknowledge funding from the Deutsche Forschungsgemeinschaft (DFG, German Research Foundation) in the form of an Emmy Noether Research Group (grant number KR4598/2-1, PI Kreckel) for support of the gas excitation measurements. Observations with the 6-m telescope of the SAO RAS carried out with the financial support of the Ministry of Science and Higher Education of the Russian Federation (including agreement No 05.619.21.0016, project ID RFMEFI61919X0016). The renovation of telescope equipment is currently provided within the national project 'Science'. Based on observations collected at the Centro Astronómico Hispano-Alemán (CAHA) at Calar Alto, operated jointly by Junta de Andalucía and Consejo Superior de Investigaciones Científicas (IAA-CSIC). This research used ASTROPY (http://www.astropy.org) a community-developed core PYTHON package for Astronomy (Astropy Collaboration 2013, 2018), and of ASTRODENDRO, a PYTHON package to compute dendrograms of Astronomical data (http://www.dendrograms.org). We acknowledge the usage of the Hyperleda data base (http://leda.univ-lyon1.fr).

DATA AVAILABILITY

The data underlying this article will be shared on reasonable request to the corresponding author. The reduced FPI data are available in SIGMA-FPI data base[4] (Egorov et al., in preparation).

REFERENCES

Abramova O. V., Zasov A. V., 2011, Astron. Rep., 55, 202
Afanasiev V. L., Moiseev A. V., 2005, Astron. Lett., 31, 194
Afanasiev V. L., Moiseev A. V., 2011, Balt. Astron., 20, 363
Alarie A., Morisset C., 2019, Rev. Mex. Astron. Astrofís., 55, 377
Allen M. G., Groves B. A., Dopita M. A., Sutherland R. S., Kewley L. J., 2008, ApJS, 178, 20
Amorisco N. C., Evans N. W., van de Ven G., 2014, Nature, 507, 335
Annibali F. et al., 2019, ApJ, 883, 19
Arkhipova V. P., Lozinskaya T. A., Moiseev A. V., Egorov O. V., 2007, Astron. Rep., 51, 871
Ashley T., Elmegreen B. G., Johnson M., Nidever D. L., Simpson C. E., Pokhrel N. R., 2014, AJ, 148, 130
Ashley T., Simpson C. E., Elmegreen B. G., Johnson M., Pokhrel N. R., 2017, AJ, 153, 132
Astropy Collaboration, 2013, A&A, 558, A33
Astropy Collaboration, 2018, AJ, 156, 123
Bacchini C., Fraternali F., Iorio G., Pezzulli G., 2019, A&A, 622, A64
Bacchini C., Fraternali F., Pezzulli G., Marasco A., 2020, A&A, 644, A125
Bagetakos I., Brinks E., Walter F., de Blok W. J. G., Usero A., Leroy A. K., Rich J. W., Kennicutt R. C., 2011, AJ, 141, 23
Baldwin J. A., Phillips M. M., Terlevich R., 1981, PASP, 93, 5
Begum A., Chengalur J. N., Karachentsev I. D., Kaisin S. S., Sharina M. E., 2006, MNRAS, 365, 1220
Bekki K., 2008, MNRAS, 388, L10
Berg D. A. et al., 2012, ApJ, 754, 98
Beroiz M., Cabral J., Sanchez B., 2020, Astron. Comput., 32, 100384
Blair W. P., Kirshner R. P., Chevalier R. A., 1981, ApJ, 247, 879
Blair W. P., Long K. S., 2004, ApJS, 155, 101
Boisvert J. H., Rhee G., 2016, AJ, 152, 15
Book L. G., Chu Y.-H., Gruendl R. A., 2008, ApJS, 175, 165
Cardelli J. A., Clayton G. C., Mathis J. S., 1989, ApJ, 345, 245
Ceverino D., Klypin A., 2009, ApJ, 695, 292
Christensen C. R., Davé R., Governato F., Pontzen A., Brooks A., Munshi F., Quinn T., Wadsley J., 2016, ApJ, 824, 57
Churchwell E. et al., 2006, ApJ, 649, 759
Croxall K. V. et al., 2009, ApJ, 705, 723
Deason A., Wetzel A., Garrison-Kimmel S., 2014, ApJ, 794, 115
Dicaire I. et al., 2008, MNRAS, 385, 553
Egorov O. V., Lozinskaya T. A., 2011, Astrophys. Bull., 66, 293
Egorov O. V., Lozinskaya T. A., Moiseev A. V., 2013, MNRAS, 429, 1450
Egorov O. V., Lozinskaya T. A., Moiseev A. V., Shchekinov Y. A., 2017, MNRAS, 464, 1833
Egorov O. V., Lozinskaya T. A., Moiseev A. V., Smirnov-Pinchukov G. V., 2014, MNRAS, 444, 376
Egorov O. V., Lozinskaya T. A., Moiseev A. V., Smirnov-Pinchukov G. V., 2018, MNRAS, 478, 3386
Egorova E. S., Egorov O. V., Moiseev A. V., Saburova A. S., Grishin K. A., Chilingarian I. V., 2021, MNRAS, 504, 6179
Egorova E. S., Moiseev A. V., Egorov O. V., 2019, MNRAS, 482, 3403
Emerick A., Bryan G. L., Mac Low M.-M., 2019, MNRAS, 482, 1304
Ferrara A., Tolstoy E., 2000, MNRAS, 313, 291
Fitzpatrick E. L., 1999, PASP, 111, 63
Gutkin J., Charlot S., Bruzual G., 2016, MNRAS, 462, 1757
Haffner L. M. et al., 2009, Rev. Mod. Phys., 81, 969
Hidalgo-Gámez A. M., 2007, AJ, 134, 1447
Hunter D. A. et al., 2012, AJ, 144, 134
Hunter D. A., Elmegreen B. G., Ludka B. C., 2010, AJ, 139, 447
Hunter D. A., Gallagher J. S. III, 1985, ApJS, 58, 533
Hunter D. A., Hoffman L., 1999, AJ, 117, 2789
Hunter D. A., Laufman L., Oh S.-H., Levine S. E., Simpson C. E., 2019, AJ, 158, 23
Iorio G., Fraternali F., Nipoti C., Di Teodoro E., Read J. I., Battaglia G., 2017, MNRAS, 466, 4159
Izotov Y. I., Stasińska G., Meynet G., Guseva N. G., Thuan T. X., 2006, A&A, 448, 955
Jaskot A. E., Oey M. S., 2013, ApJ, 766, 91
Kado-Fong E., Kim J.-G., Ostriker E. C., Kim C.-G., 2020, ApJ, 897, 143
Kahre L. et al., 2018, ApJ, 855, 133
Karachentsev I. D. et al., 2002, A&A, 383, 125
Karachentsev I. D., Makarov D. I., Kaisina E. I., 2013, AJ, 145, 101
Kauffmann G. et al., 2003, MNRAS, 346, 1055
Keller B. W., Wadsley J., Couchman H. M. P., 2015, MNRAS, 453, 3499
Kelz A. et al., 2006, PASP, 118, 129
Kewley L. J., Dopita M. A., Sutherland R. S., Heisler C. A., Trevena J., 2001, ApJ, 556, 121
Kewley L. J., Ellison S. L., 2008, ApJ, 681, 1183

[4] http://sigma.sai.msu.ru

Downloaded from https://academic.oup.com/mnras/article/508/2/2650/6373944 by Special Astrophysical Observatory of the Russian Academy of Sciences user on 15 October 2021

Krause M., Fierlinger K., Diehl R., Burkert A., Voss R., Ziegler U., 2013, A&A, 550, A49
Kreckel K. et al., 2013, ApJ, 771, 62
Krumholz M. R. et al., 2014, in Beuther H., Klessen R. S., Dullemond C. P., Henning T., eds, Protostars and Planets VI. Univ. Arizona Press, Tucson, AZ, p. 243
Lang D., Hogg D. W., Mierle K., Blanton M., Roweis S., 2010, AJ, 139, 1782
Lelli F., Verheijen M., Fraternali F., Sancisi R., 2012, A&A, 537, A72
Levesque E. M., Leitherer C., 2013, ApJ, 779, 170
Lotz J. M., Jonsson P., Cox T. J., Primack J. R., 2008, MNRAS, 391, 1137
Lozinskaya T. A., Moiseev A. V., Avdeev V. Y., Egorov O. V., 2006, Astron. Lett., 32, 361
Makarov D., Prugniel P., Terekhova N., Courtois H., Vauglin I., 2014, A&A, 570, A13
Markwardt C. B., 2009, in Bohlender D. A., Durand D., Dowler P., eds, ASP Conf. Ser. Vol. 411, Astronomical Data Analysis Software and Systems XVIII. Astron. Soc. Pac., San Fransisco, p. 251
Martins F., Schaerer D., Hillier D. J., 2005, A&A, 436, 1049
McLeod A. F., Dale J. E., Evans C. J., Ginsburg A., Kruijssen J. M. D., Pellegrini E. W., Ramsay S. K., Testi L., 2019, MNRAS, 486, 5263
McQuinn K. B. W., van Zee L., Skillman E. D., 2019, ApJ, 886, 74
Moiseev A. V., 2014, Astrophys. Bull., 69, 1
Moiseev A. V., Egorov O. V., 2008, Astrophys. Bull., 63, 181
Moiseev A. V., Lozinskaya T. A., 2012, MNRAS, 423, 1831
Moiseev A. V., Tikhonov A. V., Klypin A., 2015, MNRAS, 449, 3568
Muñoz-Tuñon C., Tenorio-Tagle G., Castañeda H. O., Terlevich R., 1996, AJ, 112, 1636
Oh S.-H., de Blok W. J. G., Brinks E., Walter F., Kennicutt R. C., Jr, 2011, AJ, 141, 193
Oparin D. V., Egorov O. V., Moiseev A. V., 2020, Astrophys. Bull., 75, 361
Osterbrock D. E., Ferland G. J., 2006, Astrophysics of Gaseous Nebulae and Active Galactic Nuclei, 2nd edn. University Science Books, Mill Valley, CA
Pilyugin L. S., Grebel E. K., 2016, MNRAS, 457, 3678
Pokhrel N. R., Simpson C. E., Bagetakos I., 2020, AJ, 160, 66
Pustilnik S., Zasov A., Kniazev A., Pramskij A., Ugryumov A., Burenkov A., 2003, A&A, 400, 841
Rahner D., Pellegrini E. W., Glover S. C. O., Klessen R. S., 2019, MNRAS, 483, 2547
Rich R. M., Collins M. L. M., Black C. M., Longstaff F. A., Koch A., Benson A., Reitzel D. B., 2012, Nature, 482, 192
Roth M. M. et al., 2005, PASP, 117, 620
Sabbi E. et al., 2018, ApJS, 235, 23
Sánchez Almeida J., Elmegreen B. G., Muñoz-Tuñón C., Elmegreen D. M., 2014, A&AR, 22, 71
Sancisi R., Fraternali F., Oosterloo T., van der Hulst T., 2008, A&AR, 15, 189
Sandin C., Becker T., Roth M. M., Gerssen J., Monreal-Ibero A., Böhm P., Weilbacher P., 2010, A&A, 515, A35
Saviane I., Ivanov V. D., Held E. V., Alloin D., Rich R. M., Bresolin F., Rizzi L., 2008, A&A, 487, 901
Schaye J. et al., 2015, MNRAS, 446, 521
Sil'chenko O. K., Moiseev A. V., Egorov O. V., 2019, ApJS, 244, 6
Skillman E. D., Kennicutt R. C., Hodge P. W., 1989, ApJ, 347, 875
Smirnov-Pinchukov G. V., Egorov O. V. 2021, Astrophys. Bull., in press
Smith L. J., Norris R. P. F., Crowther P. A., 2002, MNRAS, 337, 1309
Sorgho A., Chemin L., Kam Z. S., Foster T., Carignan C., 2020, MNRAS, 493, 2618
Sorgho A., Foster T., Carignan C., Chemin L., 2019, MNRAS, 486, 504
Starkenburg T. K., Helmi A., Sales L. V., 2016, A&A, 587, A24
Strobel N. V., Hodge P., Kennicutt R. C. J.Jr, 1990, PASP, 102, 1241
Tully R. B., Rizzi L., Shaya E. J., Courtois H. M., Makarov D. I., Jacobs B. A., 2009, AJ, 138, 323
Vasiliev E. O., Shchekinov Y. A., Koval' V. V., 2020, in Romanyuk I. I., Yakunin I. A., Valeev A. F., Kudryavtsev D. O., eds, Ground-Based Astronomy in Russia. 21st Century. Special Astrophys. Obser. Russian Acad. Sci., Nizhny Arkhyz, Russia, p. 284
Veilleux S., Cecil G., Bland-Hawthorn J., 2005, ARA&A, 43, 769
Veilleux S., Osterbrock D. E., 1987, ApJS, 63, 295
Verheijen M. A. W., Bershady M. A., Andersen D. R., Swaters R. A., Westfall K., Kelz A., Roth M. M., 2004, Astron. Nachr., 325, 151
Weaver R., McCray R., Castor J., Shapiro P., Moore R., 1977, ApJ, 218, 377
Weisz D. R. et al., 2011, ApJ, 739, 32
Weisz D. R., Skillman E. D., Cannon J. M., Dolphin A. E., Kennicutt R. C. Jr, Lee J. C., Walter F., 2008, ApJ, 689, 160
Wiebe D. S., Khramtsova M. S., Egorov O. V., Lozinskaya T. A., 2014, Astron. Lett., 40, 278
Zhang K. et al., 2017, MNRAS, 466, 3217

This paper has been typeset from a TEX/LATEX file prepared by the author.

Downloaded from https://academic.oup.com/mnras/article/508/2/2650/6373944 by Special Astrophysical Observatory of the Russian Academy of Sciences user on 15 October 2021

Mon. Not. R. Astron. Soc. **381,** L26–L29 (2007) doi:10.1111/j.1745-3933.2007.00359.x

A synchrotron superbubble in the IC 10 galaxy: a hypernova remnant?

T. A. Lozinskaya[1⋆] and A. V. Moiseev[2⋆]

[1]*Sternberg Astronomical Institute, Universitetskii pr. 13, Moscow, 119992 Russia*
[2]*Special Astrophysical Observatory, Nizhnii Arkhyz, Karachaevo-Cherkesia, 369167 Russia*

Accepted 2007 June 29. Received 2007 June 29; in original form 2007 June 4

ABSTRACT

The nature of the synchrotron superbubble in the IC 10 galaxy is discussed using the results of our investigation of its ionized gas structure, kinematics and emission spectrum from observations made with the 6-m telescope of the Special Astrophysical Observatory of the Russian Academy of Sciences, and based on our analysis of the radio emission of the region. The hypernova explosion is shown to be a more plausible mechanism of formation of the synchrotron superbubble compared with the earlier proposed model of multiple supernova explosions. A compact remnant of this hypernova may be identified with the well-known X-ray binary X-1 – an accreting black hole.

Key words: ISM: bubbles – ISM: kinematics and dynamics – supernova remnants – galaxies: individual: IC 10.

1 INTRODUCTION

The synchrotron superbubble in the IC 10 galaxy was discovered by Yang & Skillman (1993). They associated it with the explosion of about 10 supernovae. The synchrotron nature of the radio emission of this superbubble is corroborated by the high degree of its polarization (Chyzy et al. 2003). The multiple supernova explosions model was also adopted by Bullejos & Rozado (2002) and Thurow & Wilcots (2005).

We provide a detailed study of the structure, kinematics and emission spectrum of the ionized gas in the region of the synchrotron superbubble based on observations made with the 6-m telescope of the Special Astrophysical Observatory of the Russian Academy of Sciences (SAO RAS). We suggest, in accordance with our observations and based on our analysis of the radio emission of the region, that the synchrotron superbubble was produced by a hypernova explosion and not via multiple supernova explosions as was believed until now.

2 RESULTS OF OBSERVATIONS

We observed the ionized gas in the synchrotron superbubble region with the SAO RAS 6-m telescope using the SCORPIO focal reducer (Afanasiev & Moiseev 2005) operating in three modes: direct [S II] line images, long-slit spectroscopy, and observations with a scanning Fabry–Perot interferometer (FPI) in the Hα line. We report the detailed results of our observations in a separate paper (Lozinskaya et al. 2007). In this Letter we summarize the main results of these observations and the ensuing conclusions.

⋆E-mail: lozinsk@sai.msu.ru (TAL); moisav@sao.ru (AVM)

Fig. 1 shows the resulting [S II] 6717+31 Å line image of the region with 20-cm continuum radio emission contours from Yang & Skillman (1993) superimposed. Compared with Hα images [from Gil de Paz, Madore & Pevunova (2003) or from our FPI data], our continuum-subtracted [S II] image reveals a well-defined shell morphology which one can identify with the synchrotron superbubble.

The size of the filamentary [S II] shell is about 44 arcsec, which corresponds to 170 pc at the distance of 790 kpc (Vacca, Sheehy & Graham 2007). Its central coordinates [$\alpha_{(2000)} = 0^{\rm h}\ 20^{\rm m}\ 29^{\rm s}$, $\delta_{(2000)} = 59^{\circ}\ 16'\ 40''$] agree with those of the radio shell observed by Yang & Skillman (1993).

Our long-slit spectra are indicative of the enhanced [S II] emission in the synchrotron superbubble area, much stronger than in other star-forming regions in the galaxy. Indeed, the I([S II])/I(Hα) ratio in the superbubble lies in the 0.6–1.0 interval (see Fig. 2), and this is consistent with the corresponding ratios of supernova remnants (SNRs). Fig. 1 in Rosado et al. (1999) and fig. 4 in Hidalgo-Gamez (2005) also point to the bright [S II] emission in the region.

We have performed a very detailed Hα line study of the kinematics of ionized gas using a scanning FPI, and analysed more than 40 position–velocity (P–V) diagrams crossing the synchrotron superbubble in various directions. The FPI data have allowed us to estimate the characteristic expansion velocity of the system of bright knots and filaments to be 50–80 km s^{-1}. The measured expansion velocity fully agrees with the 50–70 km s^{-1} value mentioned by Bullejos & Rozado (2002).

We use the above expansion velocity, combined with the electron density of $n_{\rm e} \simeq 20$–30 cm^{-3} estimated from the [S II] 6717/6731-Å emission-line ratio, to evaluate the mass and kinetic energy of the optical shell to be about $M \simeq 8 \times 10^{38}$ g and $E_{\rm kin} \simeq (1$–$3) \times 10^{52}$ erg, respectively. (As is commonly adopted for SNRs, we assume that the shell thickness is about 0.1 of its radius.)

© 2007 The Authors. Journal compilation © 2007 RAS

Downloaded from https://academic.oup.com/mnrasl/article/381/1/L26/1068693 by Special Astrophysical Observatory of the Russian Academy of Sciences user on 13 October 2021

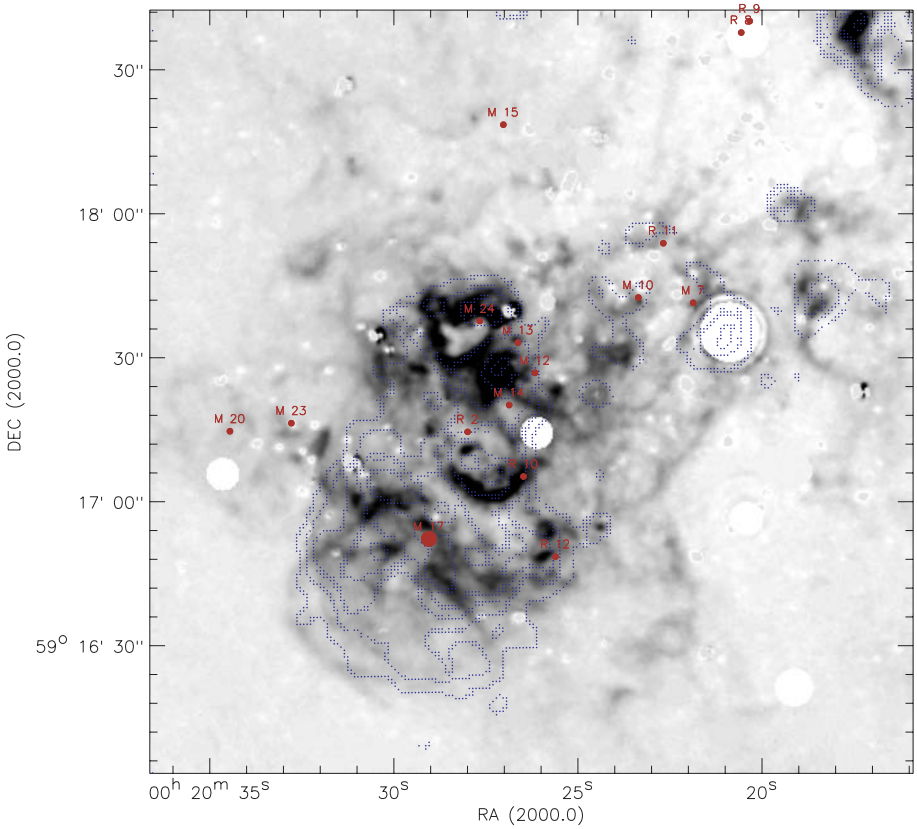

Figure 1. The [S II] 6717+31 Å lines image of the region taken with the 6-m telescope of the SAO RAS with the SCORPIO focal reducer. Small red circles show spectroscopically confirmed WR stars. The large red circle in the south-eastern part of the region is the WR star M17, a component of the brightest compact X-ray source X-1 in the IC 10 galaxy (see text). The blue lines show the superimposed 20-cm continuum radio emission contours from Yang & Skillman (1993).

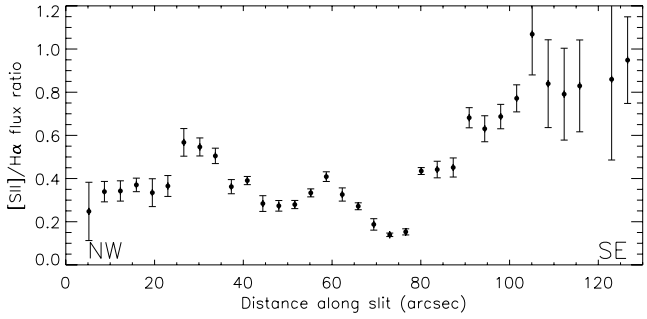

Figure 2. The variations of [S II]/Hα flux ratio along the spectrograph slit. The position angle of the slit was PA = 133°. The synchrotron superbubble corresponds to the distances 90–130 arcsec.

The energy obtained is between the value of $E_{\rm kin} \simeq (5–6) \times 10^{52}$ erg estimated by Thurow & Wilcots (2005) from the mean half-width of the Hα line in the synchrotron superbubble, and $E_{\rm kin} \simeq (0.6–1.2) \times 10^{51}$ erg reported by Bullejos & Rozado (2002) and Rosado et al. (2002).

3 THE NATURE OF THE SUPERBUBBLE

The kinetic energy of an old SNR is lower than about 30 per cent of the supernova explosion energy (Chevalier 1974). Thus our inferred kinetic energy for the optical shell in the synchrotron superbubble corresponds to the explosion of about a dozen supernovae plus stellar winds of their host OB association, or to a hypernova explosion.

However, our analysis of the synchrotron radiation of the superbubble leads us to suggest that a hypernova explosion explains better the nature of this radiation than do multiple supernovae.

First, the surface brightness $\Sigma_{(1\,\rm GHz)} = 10^{-20}$ W m^{-2} Hz^{-1} sr^{-1} for the size of the superbubble of 170–190 pc fits perfectly well the theoretical $\Sigma(D)$-dependence that Asvarov (2006) derived for a hypernova explosion with an initial energy of $E_0 = 5 \times 10^{52}$ erg in a medium with density $n_0 = 0.01$ cm^{-3} (see Fig. 3 where we show the superbubble in IC 10 by a red circle).

Secondly, and this is most important, we are the first to allow for the fact that explosions of 'recent' supernovae in the model of Yang & Skillman (1993) occur in a tenuous cavity inside the common shell swept out by the 'first' supernovae.

The first few supernova explosions may indeed have produced several times stronger radio emission compared with that of a single supernova. However, the situation changes radically as the first supernovae create the common swept-out supershell. The remnants of subsequent supernovae expand in a low-density medium inside the swept-out cavity, and their radio emission rapidly decays because of the adiabatic expansion of the cloud of relativistic particles with magnetic field.

The radio brightness of an SNR depends on the parameters of the ambient medium as

$$\Sigma(D) \propto n_0^{2/3} B_0^{1.5} \propto n_0^{2/3+1.5k_0},$$

where $B_0 \propto n_0^{k_0}$ (Asvarov 2006).

© 2007 The Authors. Journal compilation © 2007 RAS, MNRAS **381,** L26–L29

Downloaded from https://academic.oup.com/mnrasl/article/381/1/L26/1068693 by Special Astrophysical Observatory of the Russian Academy of Sciences user on 13 October 2021

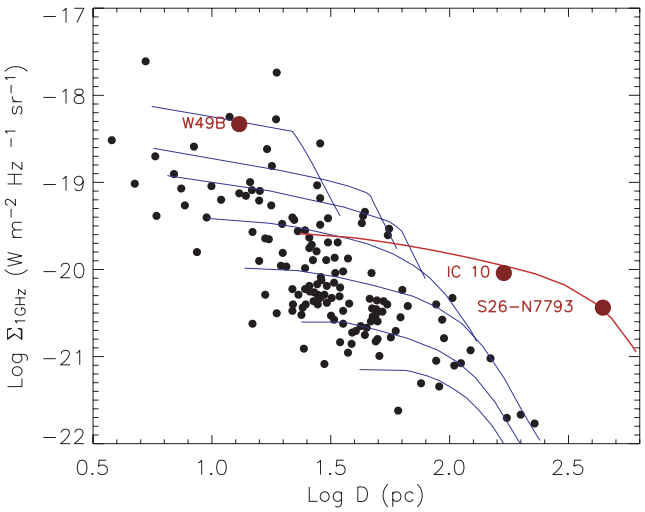

Figure 3. The $\Sigma_{1\,\mathrm{GHz}}-D$ diagram mainly based on data extracted from fig. 6 of Asvarov (2006). The black dots show the positions of SNRs in our Galaxy and several nearby galaxies. The red circles mark the positions of the hypernova remnant candidates including the synchrotron superbubble in IC 10. The red line is the theoretical $\Sigma-D$ relation constructed by Asvarov (2006) for a hypernova explosion with an initial energy of $E_0 = 5 \times 10^{52}$ erg in a medium with unperturbed density $n_0 = 0.01$ cm^{-3}. The blue curves in the figure show the $\Sigma-D$ dependences for SNRs with standard energy $E_0 = 10^{51}$ erg expanding in media of different densities.

The brightness of an SNR in the cavity where the density is 10 or 100 times lower than the ambient density can be easily seen to decrease by a factor of 5 or 20, respectively.

The allowance for the fact that the interstellar magnetic field is frozen in the gas further strengthens this conclusion, because the magnetic field inside the cavity is weaker than the ambient field. Correspondingly, the surface radio brightness of the SNR in the tenuous cavity mentioned above decreases by a factor of several tens or several hundred.

Of course, these are just qualitative estimates, because some supernovae may explode in the dense medium near the swept-out shell.

We nevertheless conclude that subsequent supernova explosions in the model of Yang & Skillman (1993) contribute little to the radio brightness of the synchrotron shell created by the first supernova explosions, implying a further increase of the required number of supernovae. That is why we believe a hypernova explosion to be a more plausible mechanism for the formation of the synchrotron superbubble than multiple supernova explosions.

The age of this hypernova remnant determined by its size and the expansion velocity of 50–80 km s^{-1} inferred in this Letter corresponds to $t \simeq$ (4–7) $\times\ 10^5$ yr if it is at the Sedov stage or $t \simeq$ (3–5) $\times\ 10^5$ yr for the case of the radiative cooling stage.

Such an age is also supportive of the hypernova hypothesis, because 10 supernova explosions require about two orders of magnitude longer time.

The anomalously high number of Wolf–Rayet (WR) stars in the galaxy IC 10 provides indirect evidence in support of the same conclusion. In the case of a normal initial mass function the anomalously high density of WR stars implies a virtually 'simultaneous' current burst of star formation covering most of the galaxy (see e.g. Massey et al. 2007, and references therein). We 'caught' IC 10 during the short stage of its evolution when massive WR progenitors are still alive, but the supermassive pre-hypernova has already finished its life, and we observe the remnant of its explosion as the synchrotron superbubble.

One can believe the compact remnant of this hypothetical hypernova to coincide with the brightest X-ray source in the galaxy X-1, discovered by Brandt et al. (1997). X-1 is a stellar-mass black hole accreting from WR star M17; the mass of this black hole is $\simeq 4\,M_\odot$ if it is not spinning, or up to ≈ 6 times higher if there is significant spinning (Bauer & Brandt 2004; Wang, Whitaker & Williams 2005).

If the synchrotron shell were indeed a hypernova remnant, one would expect to find extended X-ray emission in the region. Based on *Chandra* observations, Bauer & Brandt (2004) found evidence for faint extended X-ray emission 'cospatial' with the synchrotron superbubble. However, accurate reduction of *XMM–Newton* and *Chandra* observations (removing the X-ray CCD-readout streaks of X-1) led Wang et al. (2005) to conclude that the faint diffuse thermal X-ray emission appears to be associated with the intense star-forming region. New X-ray observations are highly desirable.

4 DISCUSSION AND CONCLUSION

Compared with the other two hypothetical hypernova remnants – W49B and S26–N7793 – shown in Fig. 3, the synchrotron supershell in IC 10 appears to be the most confidently identified object. Indeed, as Keohane et al. (2006) show in their paper, the progenitor of W49B was a supermassive star. At the same time, the location of the radio source in the $\Sigma-D$ relation agrees excellently with the results of the computations that Asvarov (2006) performed for an SNR with a standard energy of $E_0 = 10^{51}$ erg in a medium with density $n_0 = 5$ cm^{-3}.

The hypernova remnant S26–N7793 in the NGC 7793 galaxy was also earlier attributed to multiple supernova explosions (see Pannutti et al. 2002, and references therein). This S26–N7793 remnant is most probably at a later evolutionary stage than the synchrotron shell in IC 10. However, we still do not understand its shape: it appears as an SNR with a long filament as an extension.

NGC 5471B in the galaxy M101 is one of the most reliably identified hypernova remnants (Wang 1999), and was studied in detail in radio, optical and X-ray ranges [see Skillman (1985), Chu & Kennicutt (1986), Chen et al. (2002) and references therein]. Its kinetic energy reaches $E_{\mathrm{kin}} = 5 \times 10^{51}$ erg ($E_0 \geqslant 10^{52}$ erg), its kinematic age is no more than 10^5 yr, and it is characterized by a high [S II]/Hα ratio. The one problem of its identification is that NGC 5471B lies in an active star formation region in the giant H II complex NGC 5471, and contains a large number of faint clusters and two clusters as rich as R136 within the bright [S II] shell NGC 5471B (Chen, Chu & Johnson 2005).

The synchrotron superbubble in IC 10 does not have this difficulty. Hunter (2001) has distinguished two clusters near the southern border of the superbubble: 4–6 and 4–7. However, these are not the richest clusters in the galaxy and they could not host a dozen supernova explosions.

Note in conclusion that the synchrotron supershell in IC 10 can be identified as a hypernova remnant based on a combination of several criteria — first, the very high kinetic energy of the shell; secondly, the presence of a bright extended spherically symmetric source of synchrotron radio emission, which is difficult to explain by multiple supernova explosions; thirdly, the optical shell with high [S II] line brightness, which is 'cospatial' with the radio source and has a kinematical age of $t \simeq$ (3–7) $\times\ 10^5$ yr; and, fourthly, the presence of a compact remnant of the explosion of a very massive star.

Downloaded from https://academic.oup.com/mnrasl/article/381/1/L26/1068693 by Special Astrophysical Observatory of the Russian Academy of Sciences user on 13 October 2021

ACKNOWLEDGMENTS

We thank Alexander Burenkov and Azamat Valeev for their help in the observations, and also Gennadij Bisnovatyj-Kogan, Konstantin Postnov and Sergej Popov for fruitful discussions. We are grateful to the anonymous referee for useful comments. This work was supported by the Russian Foundation for Basic Research (projects 05–02–16454 and 07–02–00227) and is based on the observational data obtained with the 6-m telescope of the Special Astrophysical Observatory of the Russian Academy of Sciences funded by the Ministry of Science of the Russian Federation (registration number 01-43).

REFERENCES

Afanasiev V. L., Moiseev A. V., 2005, Astron. Lett., 31, 194
Asvarov A. I., 2006, A&A, 459, 519
Bauer F. E., Brandt W. N., 2004, ApJ, 601, L67
Brandt W. D., Ward M. J., Fabian A. C., Hodge P. W., 1997, MNRAS, 291, 709
Bullejos A., Rozado M., 2002, Rev. Mex. Astron. Astrofis. Ser. Conf., 12, 254
Chen C.-H. R., Chu Y.-H., Gruendl R., Lai S. P., Wang Q. D., 2002, AJ, 123, 2462
Chen C.-H. R., Chu Y.-H., Johnson K. E., 2005, ApJ, 619, 779
Chevalier R. A., 1974, ApJ, 188, 501
Chu Y.-H., Kennicutt R. C., 1986, ApJ, 311, 85
Chyzy K. T., Knapik J., Bomans D. J., Klein U., Beck R., Soida M., Urbanik M., 2003, A&A, 405, 513
Gil de Paz A., Madore B. F., Pevunova O., 2003, ApJS, 147, 29
Hidalgo-Gamez A. M., 2005, A&A, 442, 443
Hunter D. A., 2001, ApJ, 559, 225
Keohane J. W., Reach W. T., Rho J., Jarrett T. H., 2006, ApJ, 654, 938
Lozinskaya T. A., Moiseev A. V., Podorvanuk N. Yu., Burenkov A. N., 2007, Astron. Lett., submitted
Massey P., Olsen K., Hodge P., Jacoby G. H., McNeill R., Smith R., Strong Sh., 2007, AJ, 133, 2393
Pannuti T. G., Duric N., Lacey C. K., Ferguson A. M. N., Magnor M. A., Mendelowitz C., 2002, ApJ, 565, 966
Rosado M., Bullejos A., Valdez M., Georgiev L., Lacey C., Borissova J., Esteban C., 1999, in Chu Y.-H., Suntzeff N., Hesser J., Bohlender D., eds, Proc. IAU Symp. 190, New Views of the Magellanic Clouds. Astron. Soc. Pac., San Francisco, p. 168
Rosado M., Valdez-Gutierrez M., Bullejos A., Arias L., Georgiev L., Ambrocio-Cruz P., Borissova J., Kurtev R., 2002, in Rosado M., Binette L., Arias L., eds, ASP Conf. Ser. Vol. 282, Galaxies: The Third Dimension. Astron. Soc. Pac., San Francisco, p. 50
Skillman E. D., 1985, ApJ, 290, 449
Thurow J. C., Wilcots E. M., 2005, AJ, 129, 745
Vacca W. D., Sheehy C. D., Graham J. R., 2007, ApJ, 662, 272
Wang Q. D., 1999, ApJ, 517, L27
Wang Q. D., Whitaker K. E., Williams R., 2005, MNRAS, 362, 1065
Yang H., Skillman E. D., 1993, AJ, 106, 1448

This paper has been typeset from a TEX/LATEX file prepared by the author.

Downloaded from https://academic.oup.com/mnrasl/article/381/1/L26/1068693 by Special Astrophysical Observatory of the Russian Academy of Sciences user on 13 October 2021

АСТРОФИЗИЧЕСКИЙ БЮЛЛЕТЕНЬ, 2021, том 76, № 3, с. 380–406

УДК 520.872; 520-14(084.121); 520.84(084.121); 520.36

СКАНИРУЮЩИЙ ИНТЕРФЕРОМЕТР ФАБРИ–ПЕРО НА 6-М ТЕЛЕСКОПЕ САО РАН

© 2021 А. В. Моисеев[1*]

[1]Специальная астрофизическая обсерватория РАН, Нижний Архыз, 369167 Россия

Поступила в редакцию 14 мая 2021 года; после доработки 17 мая 2021 года; принята к публикации 17 мая 2021 года

Сканирующий интерферометр Фабри–Перо (ИФП) — старейший из методов оптической панорамной (3D) спектроскопии. Он до сих пор не потерял актуальности благодаря возможности обеспечить высокое спектральное разрешение в большом поле зрения. В данной работе рассматривается история применения этого метода для исследования протяженных объектов (туманностей и галактик). Обсуждаются методики обработки и анализа данных. Основное внимание уделяется реализации наблюдений со сканирующим ИФП на 6-м телескопе САО РАН. В настоящее время он применяется здесь в составе многорежимного редуктора светосилы SCORPIO-2. Выполнен краткий обзор результатов исследования различных галактических и внегалактических объектов с помощью сканирующего ИФП на 6-м телескопе: областей звездообразования и молодых звездных объектов, спиральных, кольцевых, карликовых и взаимодействующих галактик, газовых подсистем, связанных с конусами ионизации активных галактических ядер, галактическими ветрами и т.п. Обсуждаются дальнейшие перспективы исследований с помощью сканирующего ИФП в САО РАН.

Ключевые слова: *техника: интерферометрия — техника: обработка изображений — техника: спектроскопия изображений — инструменты: интерферометры*

1. ВВЕДЕНИЕ

Интерферометры Фабри–Перо (ИФП), основанные на принципах, впервые описанных в работе Fabry and Perot (1901), уже более столетия применяются для исследования движений ионизованного газа в различных астрофизических объектах. Успешные измерения распределения лучевых скоростей в туманности Ориона были выполнены с помощью интерферометра, состоящего их двух плоскопараллельных зеркал, незадолго до начала Первой мировой войны (Buisson et al. 1914). После некоторого перерыва эта техника изучения газовых туманностей была возрождена в Марсельской обсерватории (Courtès 1960) и стала широко распространяться и совершенствоваться. В практику советской астрономии такие наблюдения были введены во многом благодаря П. В. Щеглову (Sheglov 1963). На разработанных им ИФП с помощью 48-см и 125-см телескопов Крымской станции ГАИШ МГУ проводились многочисленные исследования кинематики остатков сверхновых и других эмиссионных туманностей (Lozinskaya 1969; 1973).

Результатом наблюдений ИФП с фиксированным расстоянием между пластинами («эталона Фабри–Перо») является изображение — интерферограмма, на которой смешана пространственная и спектральная информация, так что каждой точке (x, y) в плоскости изображения соответствует длина волны λ, меняющаяся с расстоянием от оптической оси (рис. 1). На таком кадре измерить доплеровские скорости можно только в отдельных областях туманности, для которых выполняется условие максимума интерференции:

$$n\lambda = 2l\mu\cos\theta, \qquad (1)$$

где l и μ — зазор и коэффициент преломления среды между пластинами интерферометра, а θ — угол падения лучей, пересчитываемый в радиус интерференционного кольца. Идея сканирующего интерферометра состоит в изменении величины правой части выражения (1). И хотя впервые возможность механического перемещения пластин ИФП была реализована еще в 1920-х гг., в наблюдениях сперва использовали более надежные схемы — наклон интерферометра к лучу зрения или же изменение давления, а следовательно, и μ среды, в которую помещен эталон. Подробное описание истории развития различных технических решений, завершившейся применением пьезоэлектрических сканирующих систем, обеспечивающим контролируемое изменение l, приведено в работе Atherton (1995).

*E-mail: moisav@sao.ru

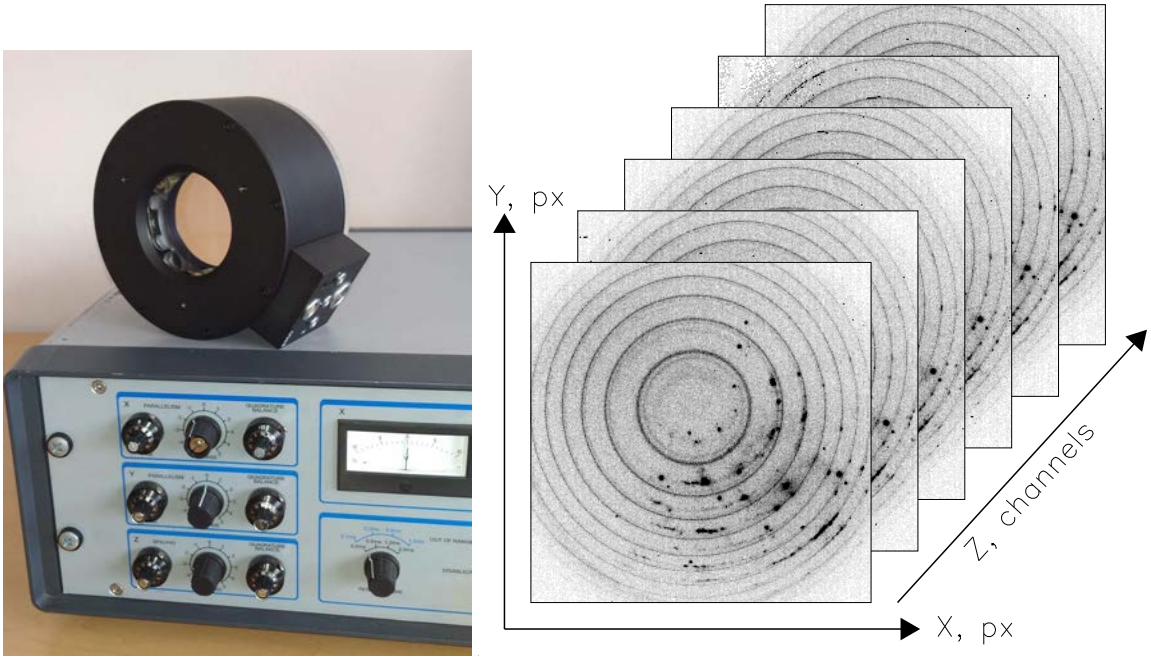

Рис. 1. Слева: сканирующий ИФП ET50-FS-100 и контроллер CS100, используемые в наблюдениях на 6-м телескопе. Справа: исходный куб «сырых» интерферограмм, полученных со SCORPIO-2 в феврале 2020 г. в линии Hα; показан каждый шестой канал. Кольца равномерной яркости — эмиссионные линии ночного неба в разных порядках интерференции. Видны области H II галактики NGC 4535.

В 1969 г. на 2.1-м телескопе обсерватории Kitt Peak с помощью ИФП, на котором сканирование осуществляется изменением давления, были выполнены наблюдения движений ионизованного газа в линии Hα в галактике M 51. Детектором являлись фотопластинки, которые затем сканировались на микроденситометре. В результате удалось построить набор спектров эмиссионной линии, заполняющих изображение этой галактики (Tully 1974). Сходные принципы применялись в приборе «Galaxymetr», использовавшимся для построения полей скоростей газа в галактиках различных типов (de Vaucouleurs and Pence 1980).

С этих наблюдений берет начало оптическая панорамная (называемая также 3D) спектроскопия, оперирующая понятием «куба данных» в пространстве (x, y, λ). Здесь длины волн λ (или доплеровские скорости в определенной спектральной линии) являются третьей (спектральной) координатой. По способу регистрации куба данных спектрографы делятся на два основных типа (Monnet 1995): с одновременной и последовательной регистрацией. В полевых (integral-field spectrographs — IFS) спектрографах одновременно регистрируются спектры от всех пространственных элементов, конструктивно выполненных в виде матрицы микролинз (Bacon et al. 1995), пучка световолокон (Arribas et al. 1991) или системы зеркал — резателей изображений (Bacon et al. 2014, Weitzel et al. 1996). Для решения спектрофотометрических задач оптимальной оказалась комбинация микролинз и световолокон (Courtes 1982), впервые реализованная в спектрографе MPFS на 6-м телескопе САО РАН (Afanasiev et al. 2001; 1990b).

В спектрометрах с последовательной регистрацией (ИФП и Фурье-спектрографы) третья координата в кубе данных появляется благодаря дополнительным экспозициям. В случае сканирующего ИФП речь идет о наборе интерферограмм, полученных при изменении оптического пути $l\mu$ между зеркалами (рис. 1). В этом случае возможно, хотя и в узком спектральном диапазоне, обеспечить большое поле зрение в комбинации с высоким спектральным разрешением. Последнее важно для изучения дисперсии лучевых скоростей газа по уширению эмиссионных линий в областях звездообразования (Melnick et al. 1987, Roy et al. 1986).

До конца прошлого века с помощью сканирующих ИФП было исследовано едва ли не больше туманностей и галактик, чем всеми остальными методами 3D-спектроскопии. Отметим вклад таких систем, как TAURUS (Taylor and Atherton 1980), TAURUS-2 (Gordon et al. 2000), HIFI (Bland and Tully 1989) и CIGALE (Boulesteix et al. 1984), работающих на телескопах диаметром от 3 метров. К сожалению, перечисление всех приборов и результатов выходит за рамки данного обзора. Отметим

Таблица 1. Системы со сканирующим ИФП на крупных и средних телескопах

Telescope/Device	FOV′	$\mathcal{R}$	Detector	References
10.4-m GTC/OSIRIS	8	400–800[1]	CCD	González et al. (2014)
10-m SALT/RSS	8	1 500	CCD	Mitchell et al. (2015)
6.5-m Magellan/MMTF	27	400–1 000[1]	CCD	Veilleux et al. (2010)
6-m BTA/SCORPIO-2	6.1	500[1], 4 000, 16 000	CCD	Afanasiev and Moiseev (2011)
4.2-m WHT/GHαFaS	4.7	15 000	IPCS	Hernandez et al. (2008)
4.1-m SOAR/SAM-FP	3	11 000	CCD	Mendes de Oliveira et al. (2017)
2.5-m SAI MSU/MaNGaL	5.6	500[1]	CCD	Moiseev et al. (2020)
2.1-m OAN/PUMA	10	16 000	CCD	Rosado et al. (1995)

[1] режим перестраиваемого фильтра

лишь две важные тенденции. Во-первых, необходимость выполнять сканирование в меняющихся атмосферных условиях делает выгодным стратегию многократного повторения циклов интерферограмм с короткими экспозициями. В таком случае эффективно себя показывают системы счета фотонов (Image Photon Counting System — IPCS), которые в других областях спектроскопии вытеснены ПЗС-матрицами с более высокой квантовой эффективностью. Во-вторых, сейчас сканирующие ИФП заметно менее популярны, сравнительно с IFS. Это связано как со значительно большей универсальностью последних при наблюдениях в небольших (менее 1′) полях зрения, так и с тем, что данные, получаемые с ИФП, часто считаются слишком «сложными и непривычными» с точки зрения анализа и интерпретации, сравнительно с классической спектроскопией[1]. Тем не менее в областях своей специализации, таких, как исследование кинематики и морфологии ионизованного газа, с ИФП возможно выполнять массовые однородные обзоры. Например, в ходе проекта GHASP была исследована кинематика 203 спиральных и иррегулярных галактик (Epinat et al. 2008).

В таблице 1 приводятся характеристики современных систем на базе сканирующих ИФП на телескопах средних и больших диаметров, результаты работы которых были опубликованы в последние годы: название телескопа и прибора, поле зрения, спектральное разрешение $\mathcal{R} = \lambda/\delta\lambda$, тип детектора и ссылка на описание. К сожалению, современный список содержит меньше позиций, чем аналогичный, составленный более 30 лет назад (Bland and Tully 1989), хотя ряда перечисленных в таблице 1 телескопов тогда еще не было. Более того, на момент написания данного обзора, согласно информации на сайтах соответствующих обсерваторий, часть перечисленных в таблице инструментов находится на реконструкции (система на SALT), либо выведена из эксплуатации (MMTF). Треть списка составляют ИФП низкого спектрального разрешения, работающие в режиме перестраиваемого фильтра (tunable filters) с шириной полосы 10–20 Å: здесь куб данных обычно содержит только несколько каналов (изображения в эмиссионной линии и в близком континууме).

Из таблицы 1 следует, что 6-м Большой Азимутальный Телескоп Специальной астрофизической обсерватории Российской академии наук (БТА САО РАН) остается крупнейшим в мире телескопом, на котором регулярно проводятся наблюдения методом 3D-спектроскопии со сканирующим ИФП высокого ($\mathcal{R} > 10\,000$) спектрального разрешения. Кроме того, здесь доступны варианты интерферометров низкого ($\mathcal{R} < 1\,000$) и умеренного ($\mathcal{R} \sim 5\,000$) разрешения. Неудивительно, что такой широкий набор возможностей для наблюдений вместе с более чем сорокалетней историей этого метода на 6-м телескопе способствовали выполнению множества интересных работ по исследованию межзвездной среды как в Галактике, так и за ее пределами. Ниже будет рассмотрена история смены поколений приборов, использующих сканирующие ИФП на 6-м телескопе, и характеристики этого метода в составе прибора SCORPIO-2 (раздел 2). Далее, после обсуждения особенностей обработки и анализа данных (раздел 3) рассматриваются конкретные опубликованные результаты, касающиеся изучения кинематики различных типов галактик (раздел 4) и воздействия

[1] Мы не рассматриваем здесь инструменты солнечных телескопов, где роль ИФП весьма значительна.

звездообразования на межзвездную среду на шкалах от нескольких парсек до десятка килопарсек (раздел 5). В Заключении (раздел 6) обсуждаются дальнейшие перспективы этого метода на нашем телескопе.

2. ИСТОРИЯ ИФП НА БТА

Идея применения на телескопе укорачивающей фокус оптической системы (фокального редуктора) предложена и реализована Г. Куртесом еще в 1950–60 гг. (Courtès 1960). Фокальный редуктор обеспечивает оптимальное соответствие угловых размеров изображений звезд и элементов детектора, увеличивает эквивалентную светосилу, что важно для исследования протяженных объектов. Оптика редуктора дает возможность установки в параллельном пучке между коллиматором и камерой диспергирующего элемента (гризм или ИФП), что превращает редуктор в многорежимный спектрограф. На 6-м телескопе изучение движений ионизованного газа в галактиках с помощью ИФП было начато группой из Марсельской обсерватории во взаимодействии с коллегами из САО РАН с помощью гостевого редуктора, обеспечивающего в первичном фокусе эквивалентную светосилу $F/1.5–F/1.6$. Первые интерферограммы галактики NGC 925 были получены напрямую на фотопластинки 28 октября 1978 г.; в наблюдениях в сентябре 1979 г. перед фотокассетой был установлен двухкаскадный электронно-оптический преобразователь производства RSA. На основе полученных данных было построено поле лучевых скоростей в линии Hα. Несмотря на усреднение наблюдаемых скоростей в довольно крупных «пикселях» размером $14'' \times 14''$, удалось не только построить кривую вращения галактики, но и оценить возмущения в движении газа, вносимые спиральной волной плотности (Marcelin et al. 1982). В октябре 1980 г. и январе 1981 г. были получены первые интерферограммы эмиссии ионизованного газа в M 33, NGC 925 и VV 551 с помощью марсельского IPCS «COLIBRI» (от «Comptage linéaire de Brillance», Boulesteix et al. 1982). По четырем интерферограммам было построено поле скоростей спиральной галактики NGC 2403 и ее кривая вращения (Marcelin et al. 1983).

С 1985 г. в САО РАН на основе коммерческих фотообъективов был создан фокальный редуктор для интерферометрических наблюдений, дающий эквивалентную светосилу $F/2.2$. ИФП с пьезоэлектрическим сканированием фирмы Queensgate Instruments Ltd. (Англия) был приобретен в рамках совместного проекта с CNRS (Франция). В качестве детектора использовался счетчик фотонов КВАНТ (Afanasiev et al. 1987) форматом 512×512 элементов с масштабом $0.46''$/px. Вся эта система, детально описанная в работе Dodonov et al. (1995), в публикациях обычно именовалась CIGALE (от «Cinématique des Galaxies») в честь её прототипа — автоматизированного редуктора со сканирующим ИФП и IPCS, созданного марсельской группой для 3.6-м телескопа CFHT (Boulesteix et al. 1984). По-видимому, первой публикацией, основанной на результатах наблюдения CIGALE на 6-м телескопе, является исследование кинематики активной галактики Mrk 1040 (Afanasiev et al. 1990a). Счетчик фотонов КВАНТ был в 1997 г. заменен ПЗС-матрицей с низким шумом считывания, форматом 1 К×1 К.

Также в рамках франко-советского сотрудничества были налажены наблюдения со сканирующим ИФП на 2.6-м телескопе Бюраканской астрофизической обсерватории (БАО) в Армении (Boulesteix et al. 1987). Первоначально французские коллеги привозили туда оригинальную систему CIGALE с CFHT, также побывавшую и на 6-м телескопе. Позже для 2.6-м телескопа был собран новый редуктор, а в качестве детектора применялась ПЗС со сдвигом изображения на закрытую половину чипа. При этом как сами ИФП, так и набор разделяющих светофильтров часто путешествовали из одной обсерватории в другую, по разные стороны Кавказского хребта. С 1991 г. речь шла уже о поездках между разными странами. В начале 2000-х годов по договоренности с коллегами из БАО интерферометр высокого разрешения и фильтры были переданы в САО РАН для проведения совместных исследований (см. раздел 5).

Несмотря на такие недостатки, как плохое качество изображений на краю поля зрения, невысокое пропускание оптики и отсутствие автоматизации, описанный выше фокальный редуктор использовался на БТА более десяти лет, пока не встал вопрос о его коренной модернизации. В 1999 г. в САО РАН под руководством В. Л. Афанасьева и при участии автора обзора были начаты работы по созданию нового редукторы светосилы SCORPIO (Afanasiev and Moiseev 2005), увидевшего «первый свет» 21 сентября 2000 г.

SCORPIO[2] представлял собой многорежимный прибор, в котором ИФП являлся лишь одним из вариантов наблюдений наряду с прямыми снимками, спектроскопией с гризмами и спектрополяриметрией. Эквивалентная светосила в первичном фокусе БТА — $F/2.6$ (первоначальная светосила до замены оптики в 2003 г. составляла $F/2.9$). В качестве детектора до 2003 г. использовалась ПЗС-матрица TK1024, размером 1024×1024, позже замененная на EEV 42-40

[2]После реконструкции, проведенной в 2019 г., прибор продолжил работу на БТА под названием SCORPIO-1.

форматом 2048 × 2048 пикселей. Поле зрения при этом изменилось незначительно (с 5′.4 до 6′.1), так как геометрический размер пикселя у данных ПЗС составлял 24 и 13.5 мкм соответственно. Обычно наблюдения с ИФП проводятся в режиме аппаратного биннинга с целью уменьшения времени считывания и повышения отношения S/N. В случае EEV 42-40 в основном применялся биннинг 4×4 или 2×2 px, что соответствует масштабу 0″.72 и 0″.36.

Универсальность прибора, высокая квантовая эффективность, возможность быстрой смены программы наблюдений в зависимости от текущих атмосферных условий привели к тому, что начиная с 2006 г. около 50% всех ночей на 6-м телескопе распределяются для наблюдений, выполняемых с помощью SCORPIO (Afanasiev and Moiseev 2011). Однако за более чем десять лет работы прибор заметно устарел, запросы и пожелания наблюдателей также постоянно росли. Поэтому под руководством В. Л. Афанасьева в САО РАН был разработан новый фокальный редуктор SCORPIO-2, первые наблюдения с которым состоялись 22 июня 2010 г.

С 2013 г. наблюдения с ИФП на БТА проводятся только в составе SCORPIO-2. Прибор имеет ту же эквивалентную светосилу. В качестве детектора до 2020 г. применялась ПЗС E2V 42-90 форматом 4612 × 2048 с тем же размером пикселя 13.5 мкм, что сохраняло тот же угловой масштаб изображений, что и на старом SCORPIO. С 2020 г. начаты наблюдения с новой камерой на базе ПСЗ E2V 261-84 форматом 4096 × 2048 с физическим размером пикселя 15 мкм, что дает масштаб 0″.8 и 0″.4 в режимах считывания с биннингом 4×4 и 2×2 соответственно. С обоими «прямоугольными» ПЗС полный формат детектора используется только при наблюдениях в спектральных режимах, а в случае ИФП или прямых снимков вырезается квадратный фрагмент 2048 × 2048 px.

Все перечисленные выше ПЗС-камеры с азотным охлаждением изготовлены в лаборатории перспективных разработок САО РАН, последняя версия этих камер описана в работе Ardilanov et al. (2020).

2.1. Набор ИФП в САО РАН

Список сканирующих пьезоэлектрических интерферометров типа ET50-FS-100 (световой диаметр 50 мм), доступных для наблюдений со SCORPIO-2, дан в таблице 2. Здесь: n — порядок интерференции по центру поля зрения для наблюдений в несмещенной линии Hα; $\Delta\lambda = \lambda/n$ — расстояние между соседними порядками, определяющее свободный спектральный диапазон; $\delta\lambda$ — полуширина аппаратного контура, которая определяет спектральное разрешение; $F = \Delta\lambda/\delta\lambda$ — добротность (finesse), в первую очередь, зависит от характеристик отражающих покрытий зеркал интерферометра; n_z — число каналов, на которое разбивается свободный спектральный интервал, задающее размерность куба данных по «спектральной» координате. Интерферометр самого низкого порядка (IFP20) используется для наблюдений в режиме перестраиваемого фильтра, когда выполняется сканирование только небольшой части от $\Delta\lambda$, поэтому параметр n_z здесь неактуален. Подробнее об этом виде наблюдений см. Moiseev et al. (2020).

Таблица 2. Параметры сканирующих ИФП в SCORPIO-2 (для $\lambda = 6563$ Å)

	IFP20	IFP186	IFP751	IFP501
n	20	188	751	501
$\Delta\lambda$, Å	328	34.9	8.7	13.1
$\delta\lambda$, Å	13	1.7	0.44	0.80
F	25	21	20	16
n_z	–	40	40	36

Интерферометры IFP751, IFP186 и IFP20 изготовлены для САО РАН английской фирмой IC Optical Systems Ltd.[3] (бывшая Queensgate Instruments) в 2009, 2012 и 2016 гг. соответственно. Интерферометр IFP501 использовался для наблюдений в системе CIGALE еще в 80–90 г. прошлого века, а после — в SCORPIO. Он все еще в рабочем состоянии, но IFP751 предпочтительнее для большинства задач, решаемых с высоким спектральным разрешением. Старый интерферометр, работающий в $n(\mathrm{H}\alpha) = 235$, применявшийся в CIGALE и SCORPIO, сейчас неработоспособен и заменен на IFP186.

Необходимость работать с разными n вызвана двумя основными причинами. Во-первых, как и в случае с классической спектроскопией, низкое разрешение — это возможность добиться с теми же экспозициями большего отношения S/N в каждом спектральном канале, т.е. наблюдать более слабые объекты, чем с высоким разрешением. Но, когда линия объекта практически совпадает по длине волны с линиями излучения ночного неба, более высокое разрешение может стать актуальным. Во-вторых, так как технически сложно добиться $F > 30$, для достижения высокого спек-

[3] https://www.icopticalsystems.com/

трального разрешения $\delta\lambda$ требуются высокие порядки интерференции n:

$$\mathcal{R} = \frac{\lambda}{\delta\lambda} = \frac{\lambda F}{\Delta\lambda} = nF.$$

Это, в свою очередь, приводит к уменьшению расстояния между соседними порядками $\Delta\lambda$, ограничивая доступный для однозначного измерения диапазон скоростей. Так, IFP751 обеспечивает в линии Hα инструментальный контур с $FWHM \approx 20$ км с$^{-1}$, что позволяет изучать распределение дисперсии скоростей и многокомпонентную структур эмиссионных линий в областях звездообразования (раздел 5). При этом рабочий диапазон наблюдаемых скоростей составляет всего $\Delta v \approx 390$ км с$^{-1}$, что меньше разброса скоростей во взаимодействующих или активных галактиках. Поэтому, используя только данные интерферометра, мы уже не можем отличить линию на длине волны λ от компонента с доплеровским смещением $\lambda + \Delta\lambda$. Иногда это удается сделать с привлечением дополнительной информации, например, длиннощелевой спектроскопии. Зато с IFP186 ($\Delta v \approx 1600$ км с$^{-1}$) интерпретация таких кинематических компонент будет практически однозначной, но ценой потери разрешения (здесь $FWHM \approx 77$ км с$^{-1}$).

Дополнительная проблема при наблюдениях со сканирующим ИФП возникает в «красном» спектральном диапазоне, где разница длин волн между яркими близкими линиями ионизованного газа составляет около 15 Å, что меньше $\Delta\lambda$ для $n > 400$. Речь идет о системах линий Hα+[N II]λ6548, 6583 и [S II]λ6716, 6731. Поскольку узкополосные фильтры с $FWHM = 12$–25 Å, описанные в следующем разделе, не полностью подавляют излучение соседних линий, важно, чтобы разница длин волн линий различалась на не целое число $\Delta\lambda$. Оптимальным является разделение линий с длинами волн λ_1 и λ_2 на полпорядка, т.е. условие:

$$|\lambda_2 - \lambda_1| = (0.5 + k)\Delta\lambda = (0.5 + k)\frac{\lambda_1}{n}, \quad (2)$$

где $k = 0, 1, 2....$ Рисунок 2 иллюстрирует проблему выбора n для оптимального разделения всех перечисленных выше пар близких спектральных линий, которым соответствуют различные наклонные линии на графике. Разумеется, добиться идеального выполнения соотношения (2) для всех пар невозможно, но если задаться более мягким критерием — разделением линий в пределах $(0.3$–$0.7)\Delta\lambda$, то ему удовлетворяют несколько диапазонов значений n. Первый соответствует $k = 0$ и $n \approx 150$–200. Параметры IFP186 были выбраны, исходя из этого критерия. Следующая «оптимальная» область с $n \approx 750$ соответствует интерферометру IFP751. В третьей области с $n \approx 1100$ почти для всех выбранных пар линий выполняется «жесткий» критерий (2). С такими интерферометрами ($n = 1051$, 1353) выполнялись первые наблюдения на БТА (Marcelin et al. 1982). Но при этом $\Delta v < 300$ км с$^{-1}$ в линии Hα, что слишком мало для многих задач внегалактической астрономии. Кроме того, поскольку с ростом $\mathcal{R}$ уменьшается ширина интерференционных колец, необходимо следить, чтобы по всему полю зрения кольца уверенно разрешались элементами детектора.

Разумеется, оптимальным было бы использование единственного ИФП, позволяющего точно менять зазор между пластинами от 10 до 500 мкм, что перекрывает весь требуемый диапазон n. К сожалению, это невозможно для доступных на рынке пьезоэлектрических интерферометров, а лабораторные разработки не были завершены (Marcelin et al. 2008).

2.2. Узкополосные фильтры

В соответствии с выражением (1), в случае немонохроматического излучения в каждом пикселе интерферограммы присутствует сигнал на длинах волн, соответствующих разным порядкам интерференции, так что $n\lambda = const$. При рассмотрении куба данных это означает «упаковку» излучения с разными длинами волн внутри узкого спектрального интервала (см. рис. 3, а также Fig. 2 в статье Daigle et al. 2006). Поэтому необходимо выделить изучаемый спектральный интервал, чтобы уменьшить паразитную засветку от изучаемого объекта, а также от линий ночного неба. Идеальным решением было бы применение узкополосного фильтра с прямоугольным профилем пропускания шириной $\Delta\lambda$, центрированного на требуемую эмиссионную линию. Близкой к этому идеальному варианту является система двух ИФП с сильно различающимися порядками интерференции, настроенными так, чтобы при сканировании их пики пропускания всегда совпадали на требуемой длине волны. Спектральное разрешение задается интерферометром с большим зазором ($n \approx 200$–1000), а свободный спектральный интервал определяется интерферометром с $n = 10$–30. Последнее дает для линии Hα $\Delta\lambda = 200$–600 Å. Выделение столь широкой полосы не представляет проблем для современных среднеполосных интерференционных фильтров и практически реализовано в случае ИФП в режиме перестраиваемого фильтра (Moiseev et al. 2020, Veilleux et al. 2010). Системы на базе сдвоенных ИФП давно и эффективно работают на солнечных телескопах (см., к примеру, Kentischer et al. 1998) и даже применялись для наблюдений ярких комет (Morgenthaler et al. 2001).

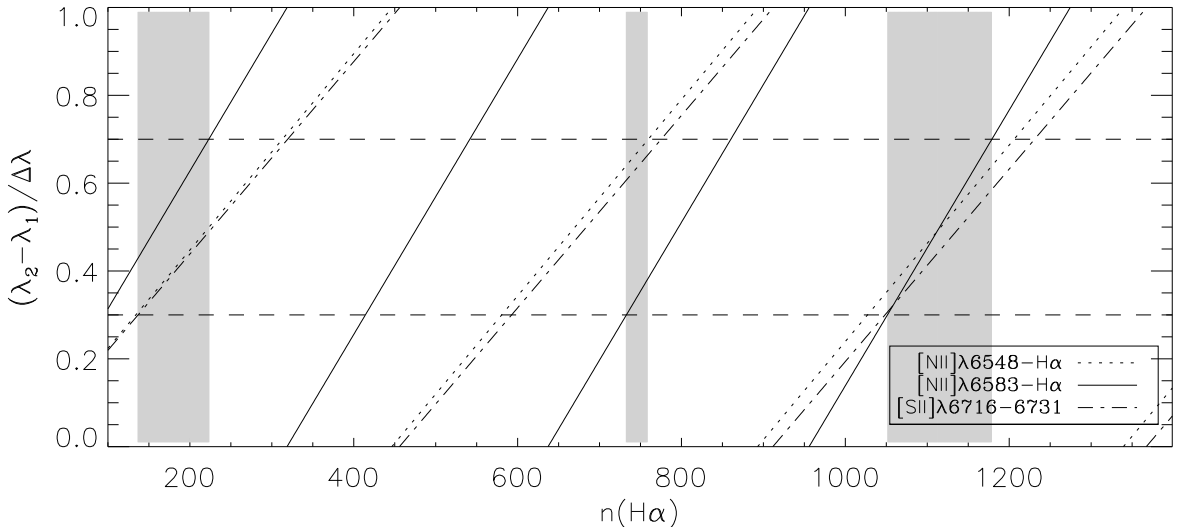

Рис. 2. График изменения относительного расстояния между близкими линиями в зависимости от порядка интерференции (на длине волны Hα). Линиями различного типа показаны разные варианты пар $\lambda_1-\lambda_2$. Горизонтальными штрихами выделена область «хорошего разделения», где наблюдаемое расстояние между линиями лежит в диапазоне $(0.5 \pm 0.2)\Delta\lambda$. Серая заливка соответствует диапазонам n, где данное условие выполняется.

К сожалению, автору не известны результативно работающие системы для ночных наблюдений с помощью сдвоенного сканирующего ИФП, хотя соответствующие проекты неоднократно анонсировались (Marcelin et al. 2008, Rangwala et al. 2008). В качестве частичного исключения можно рассматривать прибор WHAM, применявшийся для исследованию диффузного газа как Млечного Пути (Haffner et al. 2003), так и Большого Магелланового Облака (Ciampa et al. 2021). Высокое спектральное разрешение и чувствительность достигаются с помощью двух эталонов Фабри–Перо с фиксированным зазором, но низкое угловое разрешение (1°) не позволяет использовать его для исследования большинства галактик и туманностей.

Простым и распространенным решением для выделения требуемого участка спектра является применение узкополосных фильтров с полосой пропускания $FWHM \gtrsim \Delta\lambda$. Но при этом возникает сразу несколько причин, ограничивающих эффективность наблюдений. Во-первых, для выделения эмиссионных линий галактик в заданном диапазоне красных смещений необходим набор фильтров с перекрывающимися кривыми пропускания, центрированных на соответствующие системные скорости. Во-вторых, изготовление интерференционных фильтров достаточно большого диаметра с шириной полосы несколько нанометров, имеющих пропускание в максимуме не ниже 70–80%, сопряжено с рядом технических трудностей. Такие фильтры предлагаются лишь несколькими производителями в мире и весьма дороги. Набор из 10–15 таких фильтров близок по стоимости к сканирующему ИФП с тем же световым диаметром. В-третьих, профиль пропускания таких фильтров, как правило, близок к гауссову. Это может приводить к существенным вариациям пропускания внутри рабочего спектрального диапазона, а также к паразитной засветке из соседних порядков интерференции в крыльях профиля пропускания фильтра. Отметим также, что длина волны максимума пропускания узких фильтров заметно (в единицах $FWHM$) меняется с температурой окружающей среды.

Линии наблюдаемого объекта, «приходящие» из соседних порядков интерференции, часто рассматриваются наблюдателями как мешающий фактор. Автору известны статьи, в которых исследователи ошибочного принимали эмиссию [N II] из других порядков за вторую подсистему ионизованного газа в линии Hα. С другой стороны, если при выборе параметров интерферометра соблюдалось условие (2), а эмиссионные линии в исследуемом объекте достаточно узкие для их уверенного разделения, то возникает возможность исследования кинематики газа сразу в двух эмиссионных линиях. В случае Hα+[N II] речь идет о линиях с разным механизмом возбуждения. Становится возможным исследовать эффекты, связанные с ударными волнами, за фронтом которых возможно усиление наблюдаемого свечения в запрещенных линиях азота относительно линий серии Бальмера. Поэтому распределение яркости и лучевых скоростей в этих линиях могут различаться. Рисунок 3 показывает пример одновременного наблюдения линий азота и водорода в галактике NGC 1084 (см. также раздел 5). Такой режим наблюдений актуален и

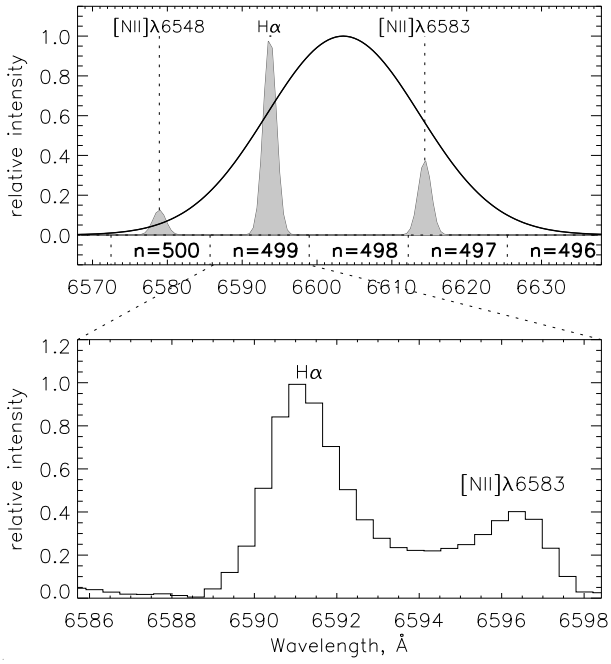

Рис. 3. Линии ионизованного газа в галактике NGC 1084 (Moiseev 2000). Вверху: схема взаимного расположения в шкале длин волн линий Hα+[N II] (серая заливка) и узкополосного фильтра (жирная линия). Подписаны порядки интерференции ($n = ..$), разделенные интервалами $\Delta\lambda$. Внизу: наблюдаемый с ИФП спектр.

при исследовании ионизованного газа в галактиках ранних типов, в центральных областях которых линия Hα скрывается в мощной абсорбционной подложке от спектра звездного населения, тогда как [N II] продолжает быть видимой. В то же время в областях H II на периферии звездного диска линия Hα значительно ярче, чем [N II]. Пример одновременного построения полей лучевых скоростей в этих линиях для галактики NGC 7742 приводится в работе Sil'chenko and Moiseev (2006).

С имеющимися в SCORPIO-2 фильтрами для наблюдений доступны объекты с лучевыми скоростями от -200 до 13 500 км с$^{-1}$ в линии Hα до примерно 6 000 км с$^{-1}$ в линии [S II]λ6717 и примерно до 17 000 км с$^{-1}$ в [O III]λ5007. Разумеется, с этим набором можно наблюдать и другие линии. Так, поле скоростей полярного кольца на $z = 0.06$ ($V_{\rm sys} \approx 18\,000$ км с$^{-1}$) было построено в линии Hβ (Finkelman et al. 2011). Актуальный список фильтров доступен на странице прибора[4], там же можно получить последнюю версию программы для подбора оптимального фильтра на выбранную линию с учетом красного смещения и температуры воздуха.

Этот набор светофильтров собирался в САО РАН в течение многих лет, благодаря различным совместным программам и грантам. Начало коллекции было положено несколькими фильтрами для наблюдения вблизи линии Hα, предоставленными коллегами из БАО и изготовленными фирмой Barr Associates Inc. (США) по заказу Марсельской обсерватории. Этот набор был расширен фильтрами, изготовленными для САО РАН в НИИПП (г. Москва). В дальнейшем из разных источников приобретались фильтры производства Andover Corporation (США). К сожалению, через 15 лет использования покрытия фильтров НИИПП частично деградировали. Сейчас эти фильтры практически все заменены на аналоги от Andover Corporation. Большинство фильтров имеют световой диаметр 50 мм (2 дюйма) — распространенный стандарт у многих производителей. К сожалению, этого размера не хватает, чтобы перекрыть поле зрения по диагонали, поэтому в углах кадров имеет место виньетирование, заметное на интерферограммах на рис. 1. Хорошим компромиссом между размером и стоимостью являются квадратные фильтры с шириной стороны 50 мм, изготовленные в Custom Scientific, Inc. (США). Они практически полностью перекрывают поле зрения SCORPIO-2.

На основе опыта по разделению близких линий из соседних порядков, наша команда в САО РАН сейчас отдает предпочтение фильтрам с $FWHM \approx 30$ Å, что в два раза шире, чем те, с которыми начинались наблюдения на БТА с ИФП. Одно из преимущество таких фильтров — близкий к прямоугольному профиль кривой пропускания, в отличие от гауссовского у более узких фильтров.

3. ОБРАБОТКА И АНАЛИЗ ДАННЫХ

Первичная обработка данных, получаемых со сканирующим ИФП, включает в себя как стандартные процедуры редукции ПЗС-кадров (учет тока смещения, плоского поля и удаление следов космических частиц), так и специфические: поканальная фотометрическая коррекция, переход в шкалу длин волн с помощью учета фазового смещения. Основные принципы и алгоритмы достаточно подробно описаны в ряде работ: Bland and Tully (1989), Gordon et al. (2000), Moiseev (2002). Подробное описание пакета программ IFPWID, используемого для обработки наблюдений с ИФП на SCORPIO, дано в работе Moiseev and Egorov (2008); там же рассмотрена методика вычитания бликов, приводится оценка точности измерения лучевых скоростей и дисперсии скоростей с разными ИФП. Дополнительные процедуры, используемые для повышения точности построения шкалы длин волн с помощь «Λ-куба», описаны в статье автора обзора в 2015 г.

[4] https://www.sao.ru/hq/lsfvo/devices/scorpio-2/

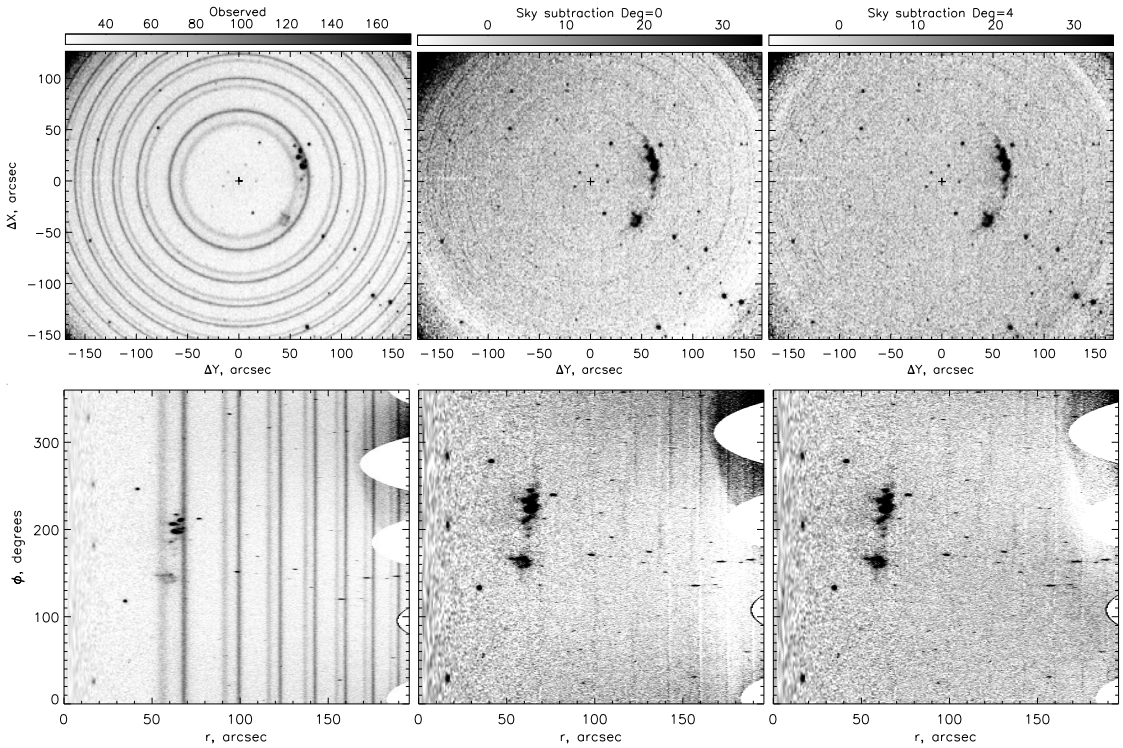

Рис. 4. Вычитание линий ночного неба на примере наблюдений галактики UGC 4115. Верхний ряд — наблюдаемые кадры, нижний — они же в полярной системе координат (r, ϕ). Слева направо: исходная интерферограмма, вычитание неба при простом усреднении (полиномом степени 0) и при описании линий неба полиномом 4-й степени.

3.1. Вычитание фона неба

Рассмотрим подробнее процедуру вычитания фона ночного неба в пакете IFPWID, в которую были внесены некоторые важные модификации, не описанные в статьях 2002–2015 гг. При наблюдениях с системой счета фотонов вариации яркости фона (эмиссионные линии верхней атмосферы Земли, рассеянный свет Луны и т.д.) усредняются в итоговом кубе благодаря многократному повторению циклов сканирования с короткими (10–30 с) временами накоплений отдельных интерферограмм. Это позволяет производить его вычитание из спектров, переведенных в шкалу длин волн, усредняя по площадкам, свободным от излучения объекта, подобно тому, как это обычно делается в классической спектроскопии. Такой принцип использовался в пакете ADHOC (J. Boulesteix), разработанном для обработки данных CIGALE. Современные модификации этого алгоритма описаны Daigle et al. (2006). Но в наблюдениях с ПЗС ненулевые шум и время считывания требуют экспозиций длительностью несколько минут. Здесь уже нельзя пренебречь вариациями фона внутри полученного куба, его необходимо вычитать в каждом кадре еще до перехода в шкалу длин волн, усредняя эмиссию неба по азимутальному углу φ в концентрических кольцах (Moiseev 2002). Важно точно определять центр системы интерференционных колец от линий неба. В пакета IFPWID предусмотрен режим автоматического поиска центра по минимуму отклонений усредненного профиля фона от наблюдаемого.

При наблюдениях объектов низкой яркости становятся существенными отклонения картины фона неба от простой концентрической модели из-за вариаций по полю аппаратного контура, связанного с аберрациями оптики, настройками ИФП, наклоном детектора и т.п. Отклонения возрастают к краю поля зрения, где интерференционные кольца тоньше, и важно как можно более точно построить модель фона. Ранее нами применялась методика усреднения фона в отдельных секторах по углу φ. Она работает хорошо для объектов, занимающих небольшое поле зрения (Moiseev and Egorov 2008). Лучший результат дает построение модели фона в полярной системе координат. Здесь интенсивность фона на данном радиусе r может быть представлена в виде простой функции $I_r(\varphi)$. На рис. 4 показаны примеры описания этой функции полиномом, где нулевая степень соответствует простому азимутальному усреднению $I_r(\varphi) = const$. Видно, что полином 4-й степени позволяет добиться лучшего результата вычитания фона.

В настоящий момент в связи с ростом числа задач по наблюдениям объектов, занимающих все поле зрения прибора (построение мозаик для близких галактик и т.п.), мы работаем над моделированием точного распределения интенсивности эмиссионных линий неба с учетом вариации аппаратного контура. Подобный подход применялся, например, для данных IFS MUSE (Soto et al. 2016, Streicher et al. 2011).

3.2. Представление и анализ куба данных

Проблема оптимальной визуализации и представления кубов данных как в процессе анализа, так и в публикациях, является общей для всех методов 3D-спектроскопии. Несмотря на известный прогресс в динамической визуализации «объемных» спектральных данных (Punzo et al. 2015), для их интерпретации и объяснения полученных результатов коллегам удобнее оперировать двумерными картами и графиками. Специфика кубов данных ИФП (большое поле зрения и малая протяженность по спектральной координате) позволяет использовать методы визуализации, сходные с теми, что применяются при анализе радионаблюдений молекулярного и атомарного газа. Рисунок 5 демонстрирует это на примере карликовой галактики NGC 428, исследованной с ИФП на SCORPIO-2 (Egorova et al. 2019). Покальные карты позволяют увидеть пространственное расположение областей с разной кинематикой. Диаграмма «позиция–скорость» (P–V) концентрирует внимание на лучевых скоростях и форме спектральных линий вдоль заданного направления. Карта распределения яркости в эмиссионной линии Hα полезна для выделения отдельных областей H II, профили которых можно рассматривать индивидуально. Распределение лучевых скоростей (поле скоростей) может описываться теми или иными модельными приближениями (раздел 4.1), а карта дисперсии лучевых скоростей σ позволяет изучить турбулентные движения газа (раздел 5). Для получения таких карт профиль спектральной линии подгоняется функцией Фойгта, представляющей собой свертку профилей Лоренца (описывающего инструментальный контур ИФП) и Гаусса (аппроксимация исходного профиля, не уширенного прибором). Ширина инструментального контура определяется по линиям калибровки. Подробнее методика построения карт дисперсии скоростей, свободных от аппаратного уширения, описана Moiseev and Egorov (2008).

3.3. Наблюдения в линиях поглощения

Выше обсуждалось только применение сканирующего ИФП для 3D-спектроскопии эмиссионных линий ионизованного газа. Это наиболее популярное приложение для данной техники. В то же время, очевидна возможность использовать ИФП для панорамных наблюдений в линиях поглощения. Определенную проблему составляют переналожение сигнала из соседних порядков и модуляция, вносимая в наблюдаемый спектр узкополосным фильтром (раздел 2.2). Поэтому важно, чтобы изучаемая спектральная линия была достаточно контрастна и не имела бленд внутри свободного спектрального диапазона ИФП. В 1990-х годах на 1.5-м и 4-м телескопах Cerro Tololo Inter-American Observatory была выполнена серия успешных массовых наблюдений звезд в шаровых скоплениях (Gebhardt et al. 1995) и избранных площадок в направлении на бар Млечного Пути (Rangwala et al. 2009) с помощью ИФП в линии Ca II λ8542. В последнем случае удалось измерить как лучевые скорости, так и оценить металличность по EW (Ca II) более чем 3000 звезд. В тот момент этот метод являлся серьезным конкурентом мультиобъектной спектроскопии в данном конкретном приложении. С аналогичной техникой на 0.9-м телескопе той же обсерватории было получено поле лучевых скоростей звездного компонента и измерена угловая скорость вращения бара в галактике раннего типа NGC 7079 (Debattista and Williams 2004). Отметим работы этого же коллектива на телескопе CFHT, где сканирующий ИФП сочетался с системой адаптивной оптики (Gebhardt et al. 2000) для исследования динамики звезд в центре шарового скопления M 15 .

В связи с отсутствием фильтров для выделения красной линии кальция на 6-м телескопе со SCORPIO мы пробовали измерять скорости звезд в скоплениях по абсорбции Hα. В тестовых наблюдениях шарового скопления M 71 одновременно были получены лучевые скорости около 700 звезд до $m_v \approx 18^{\rm m}$ с точностью индивидуальных измерений 2–4 км с$^{-1}$ (Moiseev 2002). В дальнейшем этот метод применялся для измерения лучевых скоростей и выделения членов рассеянных скоплений Млечного Пути по заявке А. С. Расторгуева (ГАИШ МГУ). В 2002–2003 гг. такие измерения были выполнены для нескольких скоплений. К сожалению, результаты не были доведены до публикации.

Мы также проводили на 6-м телескопе эксперименты по построению полей скоростей звезд в галактиках с помощью ИФП в линии Ca II λ6495, но из-за малого контраста линии точность измерений была невысока. С другой стороны, отражающие покрытия IFP186 и IFP751 оптимизированы для наблюдений в том числе в области 8500–9500 Å, а новый детектор E2V 261-84 обладает относительно высокой чувствительностью в этом диапазоне при практически полном отсутствии муара (фрингов). Поэтому в случае приобретения соответствующих фильтров задачи по картированию

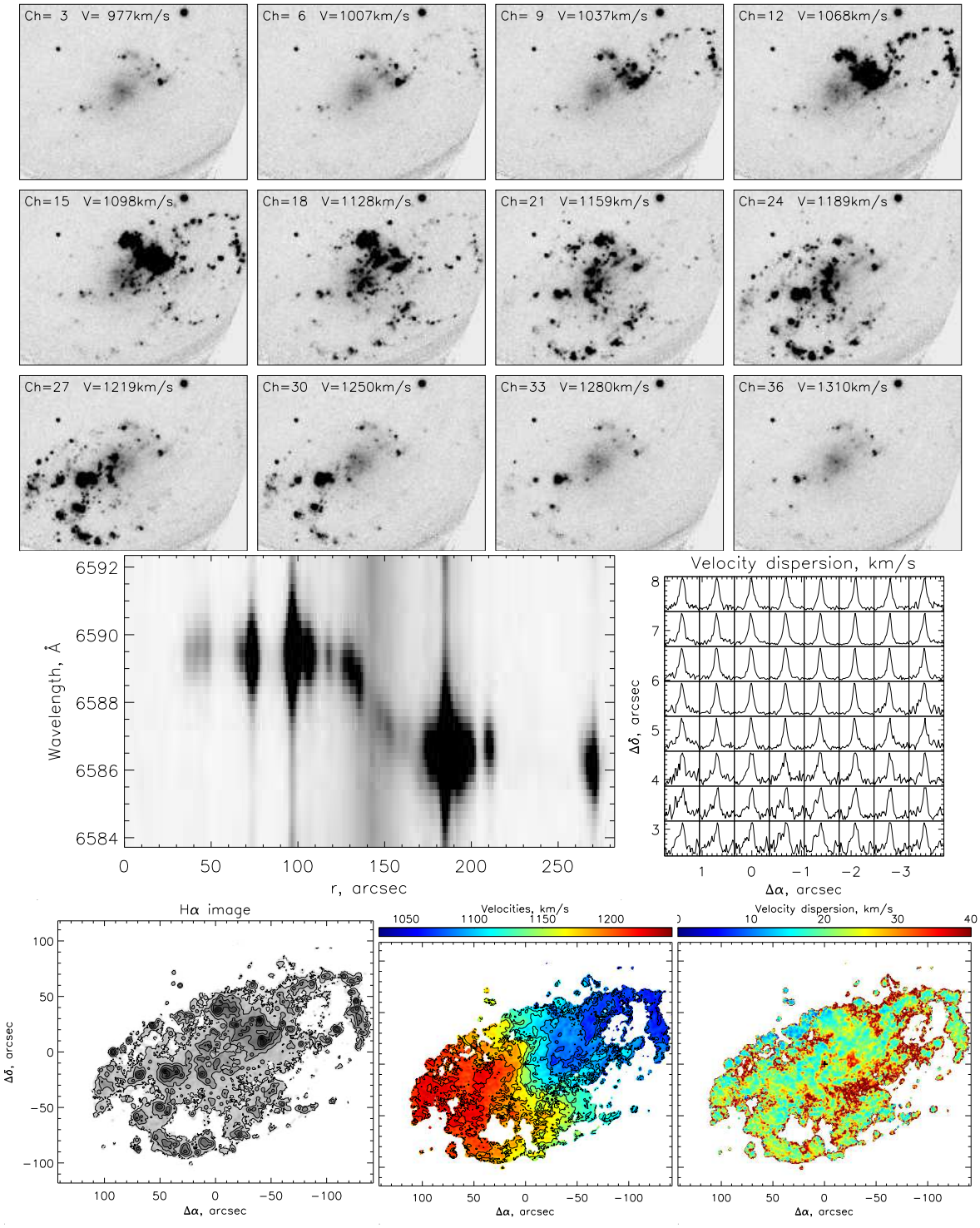

Рис. 5. Различные представления куба данных для галактики NGC 428. Вверху: поканальная карта. Показан каждый третий канал, указаны лучевые скорости. Посередине: PV-диаграмма вдоль большой оси галактики (слева) и примеры спектров эмиссионной линии Hα вблизи ядра (справа). Внизу: карты, построенные в результате аппроксимации спектров профилем Фойгта: поток в эмиссионной линии, поле лучевых скоростей и дисперсии скоростей.

протяженных объектов в линиях триплета Ca II со SCORPIO-2 могут иметь интересные перспективы.

4. НАБЛЮДАТЕЛЬНЫЕ РЕЗУЛЬТАТЫ: ОБЪЕКТЫ С ДОМИНИРОВАНИЕМ КРУГОВОГО ВРАЩЕНИЯ

В этом разделе кратко обсуждаются исследования с ИФП на БТА тех галактик, в которых в наблюдаемой кинематике газа доминирует регулярное круговое вращение. Часто целью их изучения являлся поиск отклонений от этой симметричной картины. Поэтому сперва разберем используемые нами методы выделения круговой составляющей из наблюдательных данных.

4.1. Анализ полей скоростей вращающихся дисков

Наблюдаемая лучевая скорость точки, вращающейся по орбите, наклоненной к картинной плоскости на угол i, определяется выражением:

$$V_{\rm OBS} = V_{\rm SYS} + V_R \sin\varphi \sin i + V_\varphi \cos\varphi \sin i + V_Z \cos i, \quad (3)$$

где R, φ — радиальная и азимутальная координаты в плоскости орбиты, $V_{\rm SYS}$ — системная скорость, а V_φ, V_R, V_Z — соответственно азимутальная, радиальная и вертикальная составляющие вектора скорости.

Методы определения параметров, описывающих движения ионизованного газа в дисках галактик по данным 3D-спектроскопии, можно условно разделить на несколько групп:

1. Независимый поиск параметров из выражения (3) в узких кольцах поля скоростей вдоль радиуса — метод «наклонного кольца».

2. Гармоническое разложение распределения лучевых скоростей по азимутальному углу в узких кольцах.

3. Одновременная подгонка моделью всего поля лучевых скоростей. Возможно использование карты других моментов, определяемых по профилю линии (поверхностная яркость и дисперсия скоростей), или же результатов численных расчетов.

4. Модельное описание всего куба данных в заданной эмиссионной линии.

Рассмотрим их подробнее.

4.1.1. Поиск параметров в узких кольцах

Относящийся к первой группе метод «наклонного кольца» (tilted-ring) изначально был применен для анализа полей скоростей по радиоданным H I в линии 21 см (Rogstad et al. 1974). Классическое его описание, ставшее основой популярной процедуры ROTCUR, вошедшей в пакеты анализа радиоданных GIPSY и AIPS, дано в ряде работ Begeman (1989), Teuben (2002). Ниже кратко излагаются основы этой методики, адаптированной для анализа полей скоростей ионизованного газа (Moiseev 2014b, Moiseev et al. 2004).

В предположении чисто кругового вращения тонкого плоского диска ($V_R = V_Z = 0, V_\varphi = V_{\rm ROT}$) выражение (3) трансформируется в:

$$V_{\rm OBS}(r, PA) = V_{\rm SYS} + V_{\rm ROT}(R(r)) \times \frac{\cos(PA - PA_{\rm kin}) \sin i}{(1 + \sin^2(PA - PA_{\rm kin}) \,{\rm tg}^2\, i)^{1/2}}, \quad (4)$$

где r — видимое расстояние от центра вращения в картинной плоскости, PA — позиционный угол. Расстояние до центра вращения в плоскости галактики:

$$R(r) = r(1 + \sin^2(PA - PA_0) \,{\rm tg}^2\, i)^{1/2}. \quad (5)$$

В формуле (4) $PA_{\rm kin}$ и PA_0 — позиционные углы кинематической оси и линии узлов диска. В случае чисто круговых движений $PA_{\rm kin} \equiv PA_0$. Наблюдаемое поле скоростей разбивается на эллиптические кольца, задаваемые уравнением (5) для $R = const$. В каждом кольце с помощью χ^2-минимизации выполняется аппроксимация наблюдаемой зависимости $V_{\rm OBS}(PA)$ модельной кривой (4). В результате на данном R получаем набор параметров, характеризующих ориентацию орбит ($PA_{\rm kin}$, i), скорости кругового вращения и системную.

Если есть уверенность, что в плоскости диска нет сильных изгибов, то можно положить наклон и системную скорость независимыми от радиуса ($i = i_0$, $V_{\rm SYS} = const$), в таком случае радиальные вариации $PA_{\rm kin}$ будут отражать особенности распределения некруговых компонент вектора скорости. В частности, радиальные потоки газа под действием гравитационного потенциала галактического бара приводят к «развороту» $PA_{\rm kin}$ относительно PA_0 диска. Сравнение с ориентацией эллиптических изофот позволяет отличить случай бара, т.е. изменение формы орбит в плоскости галактики, от наклонного или изогнутого диска, т.е. круговых орбит в другой плоскости (см. обсуждение и ссылки в Egorova et al. (2019), Moiseev et al. (2004)).

Метод «наклонного кольца» достаточно гибок и позволяет проверять гипотезы о характере движений газа, фиксируя различные комбинации параметров в уравнении (4). Можно также оценивать

амплитуду радиальных движений, полагая в формуле (3) $V_r \neq 0$, что актуально для столкновительных кольцевых галактик (Bizyaev et al. 2007). В работе Sil'chenko et al. (2019) использовалась модификация метода, позволяющая последовательными итерациями описать движение газа в сильно изогнутых дисках даже в случае плохого заполнения полей скоростей.

4.1.2. Гармоническое разложение

Возмущения кругового движения неосесимметричным гравитационным потенциалом (спиральная волна, бар, приливное взаимодействие) приводят к тому, что в правой части выражения (3) появляются гармонические члены вида $A_j \cos j\varphi$, $B_j \sin j\varphi$, $j = 1, 2...$ Иными словами, распределение лучевых скоростей в узком кольце на данном радиусе $V_{\rm OBS}(\varphi)$ раскладывается в ряд Фурье, в котором системная скорость — это коэффициент при нулевой гармонике и т.д. Sakhibov and Smirnov (1989) одними из первых применили эту идею для определения параметров спиральной волны плотности из полей скоростей, полученных с ИФП. Franx et al. (1994) использовали сходную методику для определения формы гравитационного потенциала галактик раннего типа. В работе Lyakhovich et al. (1997) последовательно изложена идея применения метода Фурье-анализа полей скоростей для восстановления полного трехмерного вектора скорости газа в диске при определенных предположениях о характере спиральной структуры (раздел 4.2). К сожалению, предложенная методика восстановления вектора скорости не получила широкого распространения. Возможной причиной являлась необходимость весьма кропотливого анализа с привлечением также фотометрических данных, так как результат часто оказывался чувствительным к выбору параметров ориентации диска. С другой стороны, само по себе применение Фурье-анализа для описания полей лучевых скоростей как газового, так и звездного компонента галактик стало в последнее время популярно благодаря программе Kinemetry (Krajnović et al. 2006). Здесь опыт гармонического разложения распределений поверхностной яркости обобщен на более высокие моменты функции распределения лучевых скоростей: на собственно лучевую скорость (1-й момент), дисперсию скоростей (2-й момент) и т.д. При этом не требуется даже допущения о плоском диске, метод может прилагаться даже к данным о кинематике звезд в галактиках ранних типов. А в случае газа в дисковых галактиках Kinemetry может использоваться как фильтр высоких пространственных частот, выделяющий регулярную компоненту поля скоростей.

4.1.3. Моделирование всего поля

Метод «наклонных колец» позволяет достаточно адекватно понять характер движений в плоском диске. Если же плоскость диска изгибается, то можно получить первое приближение для параметров изгиба. Однако оценка параметров при аппроксимации наблюдений в узком кольце выражением (4) бывает неустойчивой, особенно в случае неполного заполнения кольца точками с надежными измерениями скоростей. Прежде всего, имеет место вырождение по $V_{\rm ROT}{-}i$, особенно при малых углах наклона $i < 30{-}40°$. Действительно, для M-колец получаем, что полное поле скоростей при фиксированном динамическом центре описывается $4 \times M$ свободными параметрами. Для наблюдений с ИФП галактик размером несколько arcmin, как на рис. 5, это число может составлять несколько сотен (ширина колец близка к величине пространственного разрешения). Что, очевидно, чрезмерно. На практике $V_{\rm ROT}$, i, $PA_{\rm kin}$ плавно меняются с радиусом и можно задать простые аналитические выражения для радиальных изменений ориентации орбит и кривой вращения, положив также $V_{\rm SYS} = const$.

Описание поля скоростей в рамках единой двумерной модели с несколькими свободными параметрами сильно повышает устойчивость решения. Так, Coccato et al. (2007) смогли хорошо описать поле лучевых скоростей газа в галактиках NGC 2855 и NGC 7049 по данным прибора VIMOS, используя модель изогнутого диска всего с семью параметрами. Поскольку при сильных изгибах луч зрения мог несколько раз пересечь диск, то важно было одновременно принимать в расчет распределение яркости в эмиссионной линии. Сходный подход был применен нами для исследования ориентации орбит сильно наклоненного и изогнутого диска в галактике Arp 212 (Moiseev 2008). Удалось найти устойчивое модельное решение для описания кинематики ионизованного газа, распределенного в отдельных изолированных областях H II.

Для плоского слабовозмущенного диска двумерная модель позволяет надежно определить параметры его ориентации даже в случае положения «плашмя» (face-on, $i < 20°$). В качестве примера можно привести наше исследование с ИФП практически круглого газового кольца в Объекте Хога (рис. 6) с $i = 18 \pm 4°$. Здесь удалось сделать выбор между плоской и слегка изогнутой моделью кольца (Finkelman et al. 2011). В качестве другого примера моделирования плоских дисков можно привести работу Fathi et al. (2006), в которой используется параметризация кривой вращения моделью звездного экспоненциального диска.

Кроме того, возможно выполнять прямое сравнение данных численных гидродинамических расчетов с наблюдаемыми полями скоростей, например, для случая галактик с перемычками (Fathi et al. 2005).

4.1.4. Моделирование куба данных

Мощность современных компьютеров позволяет перейти от подгонки двумерных полей скоростей и распределений яркости к более информативной аппроксимации всего куба данных. Как и в случае метода наклонного кольца, впервые такие алгоритмы были применены к кубам радиоданных, поскольку при наблюдениях в линии 21 см пространственное разрешение обычно не велико и существенен эффект усреднения лучевых скоростей внутри синтезированной диаграммы направленности (beam smearing). А поскольку яркость в этой линии связана с плотностью H I, то распределение интенсивности часто можно задавать в виде гладкой функции по радиусу. Удачным примером является популярный пакет TiRiFiC (Józsa et al. 2007), позволяющий исследовать изгибы и другие особенности пространственной структуры газовых дисков.

В случае оптических кубов данных такое моделирование актуально, прежде всего, для кинематики газа в галактиках на больших красных смещениях, где так же важен эффект beam smearing, поскольку пространственное разрешение сравнимо с размерами изучаемых объектов. Отметим программные пакеты GalPak^{3D}(Bouché et al. 2015) и ^{3D}BAROLO (Di Teodoro and Fraternali 2015). Последний потенциально может быть применен и для анализа кубов, полученных с ИФП. В работе Bekiaris et al. (2016) уже демонстрировалась возможность такого анализа с помощью пакета GBKFIT на примере данных наблюдений дисковых галактик с ИФП в обзоре GHASP.

4.2. Спиральные галактики

Ещё в самых первых наблюдениях с ИФП на БТА (раздел 2) были обнаружены возмущения полей лучевых скоростей в NGC 925 и NGC 2903, связанные с их спиральными рукавами (Marcelin et al. 1982; 1983). Позже эти данные были проанализированы методом гармонического разложения (Sakhibov and Smirnov 1989), что позволило определить параметры двухрукавной волны плотности, понять направление радиальных движений газа в рукавах, измерить угловую скорость вращения спирального узора и бара (в NGC 925). Дальнейшее развитие этого метода анализа было инициированно исследованиями галактики Mrk 1040 (NGC 931), отличающейся двухпиковой кривой вращения с необычно резким скачком скорости вращения в 10 кпк от центра и заметными некруговыми движениями в диске. Эти пекулярности интерпретировались либо как необычно крупный (20 кпк размером) бар, невидимый из-за пылевого поглощения в сильно наклоненном диске (Amram et al. 1992), либо как присутствие вихревых структур (Afanasiev and Fridman 1993). Последняя интерпретация была связана с гипотезой о гидродинамической генерации спиральных волн в газовом диске (Morozov 1979), альтернативной классической теории волн плотности звездного диска. Для работы гидродинамического механизма требовался резкий скачок скорости вращения, подобный наблюдаемому в Mrk 1040, воспроизводимый также в лабораторных опытах на вращающейся мелкой воде (Fridman et al. 1985). Гигантские вихри, вращающиеся в противоположную сторону относительно вращения галактики (антициклоны), должны наблюдаться в системе координат, связанной со спиралями и в случае классического механизма генерации. Но их расположение отличается от предсказаний гидродинамической теории. Соответствующие критерии приведены в работе Lyakhovich et al. (1997), посвященной методу восстановления картины трехмерных движений газа на основе Фурье-анализа полей скоростей.

В рамках совместного проекта Vortex (САО РАН, Институт астрономии РАН, ГАИШ МГУ) на 6-м телескопе было получено несколько десятков полей скоростей, для которых был выполнен Фурье-анализ. К сожалению, до публикации были доведены только результаты восстановления трехмерных векторов скорости в дисках спиральных галактик NGC 157 (Fridmanet al. 2001a) и NGC 3631 (Fridmanet al. 2001b, Fridman et al. 1998). В обоих случаях были обнаружены гигантские вихревые структуры, связанные с классическим механизмом генерации волн плотности. Также были опубликованы результаты анализа кинематики еще 15 галактик выборки методом «наклонного кольца» (Fridman et al. 2005). Здесь были построены кривые вращения, свободные от влияния некруговых движений, а также выделены многочисленные области с пекулярной кинематикой ионизованного газа, в которых отличия от кругового вращения достигают 50–150 км с$^{-1}$. Иногда здесь наблюдается два кинематических компонента в проекции на луч зрения. Столь большие пекулярные скорости не связаны со спиральными волнами, а обусловлены, скорее всего, либо «галактическими фонтанами», вызванными звездообразованием (раздел 5), либо взаимодействием с окружением, включая аккрецию газовых облаков. Часть этих пекулярных областей была обнаружена еще в ранних наблюдениях с длиннощелевым спектрографом 6-м телескопа

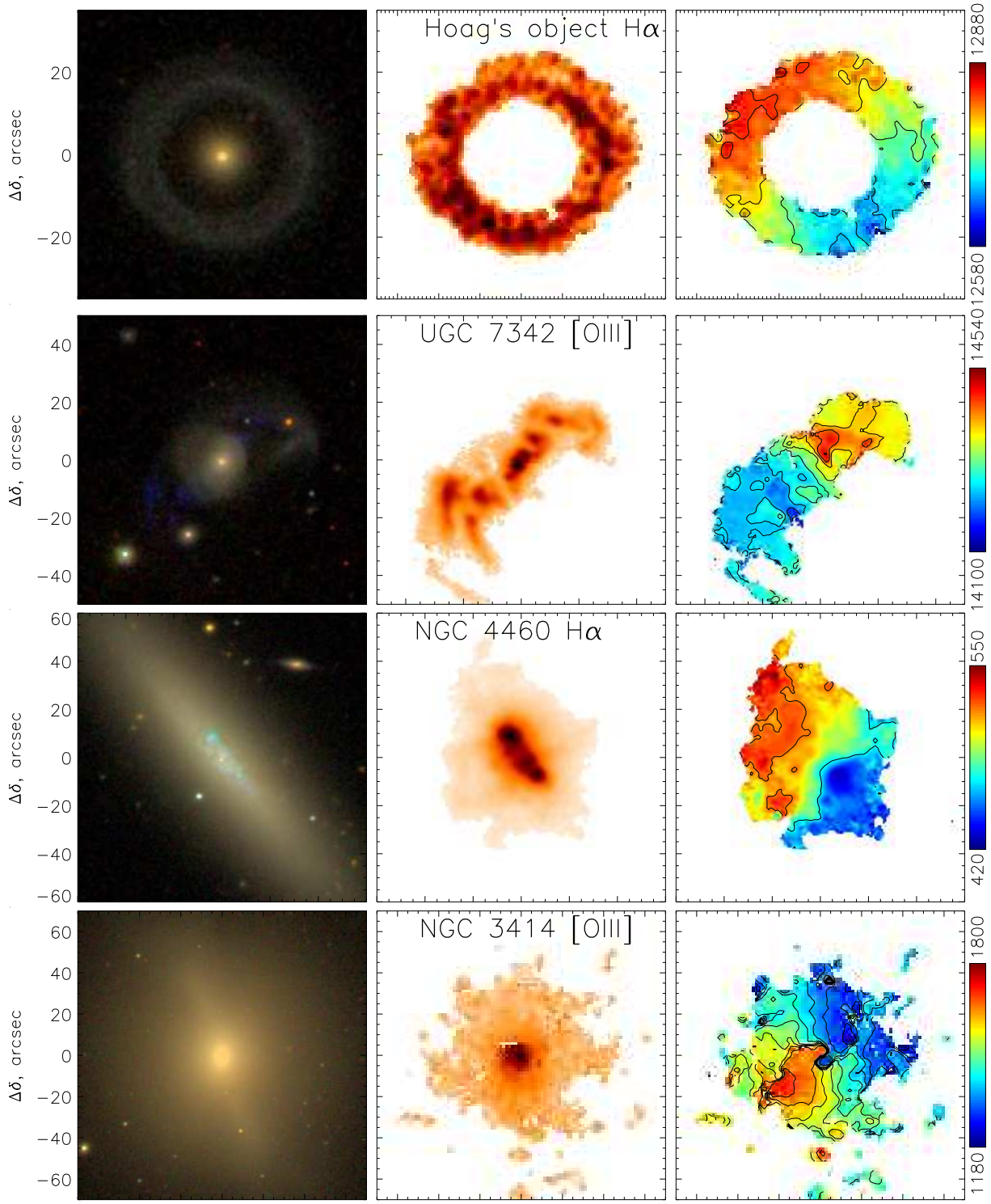

Рис. 6. Галактики с доминированием кругового вращения в кинематике газа. Слева направо: изображение из SDSS, распределения яркости в указанной эмиссионной линии и поле скоростей ионизованного газа, построенные из наблюдений с ИФП на БТА. Шкала — в км $с^{-1}$. Сверху вниз: объект Хога (Finkelman et al. 2011), активная галактика UGC 7342 (Keel et al. 2015), галактический ветер в NGC 4460 (Oparin and Moiseev 2015), внутренний полярный диск в линзовидной галактике NGC 3414 (Sil'chenko et al. 2019).

(Afanasiev et al. 1988; 1992). Карты ИФП позволили исследовать их в деталях.

Интересна галактика NGC 1084, на периферии которой обнаружена сложная структура профилей эмиссионных линий. Здесь от самой яркой в линии Hα сверхассоциации перпендикулярно спиральной ветви отходит эмиссионный «отрог»[5]. Пекулярный компонент в Hα, смещенный относительно основного на $-100...+150$ км с$^{-1}$, часто сопровождаемый ударным возбуждением линии [N II], наблюдается между областями H II. Moiseev (2000) предложил две интерпретации наблюдаемой картины, связанные как с галактическими фонтанами, так и со следами прошлых взаимодействий. Позже появились дополнительные аргументы в пользу как недавнего (менее 40 млн. лет, Ramya et al. 2007), так и более раннего (порядка 1 мрд. лет, Martínez-Delgado et al. 2010) поглощения карликового спутника.

Наряду со спиральными волнами плотности пекулярные некруговые движения газа возникают под воздействием трехосного гравитационного потенциала бара. Возмущение поля скоростей приводит к повороту $PA_{\rm kin}$ относительно PA внешних изофот, что воспроизводится в численных моделях (см. Moiseev and Mustsevoi 2000, Moiseev et al. 2004, и ссылки там). Это позволяет находить околоядерные бары (минибары) внутри центрального килопарсека даже в тех случаях, когда бар не виден на оптических изображениях. В одной из первых работ по поиску минибаров методом 3D-спектроскопии (Zasov and Sil'chenko 1996) использовались в том числе наблюдения с ИФП на БТА. Показателен случай галактики NGC 972. Здесь бар в сильно запыленной центральной области сперва был обнаружен по возмущению поля скоростей, а потом найден на снимках в ближнем ИК, свободных от пылевого поглощения (Zasov and Moiseev 1999). В этой же галактике обнаружена систематическая разница лучевых скоростей в эмиссионных линиях Hα и [N II], связанная с ударной волной на кромках бара (Afanasiev et al. 2001). Эффект замедления скоростей вращения в запрещенных линиях на кромках бара был описан ранее в работах Afanasiev et al. (1979), Afanasiev and Shapovalova (1994). К сожалению, это направление не получило дальнейшего развития. Автор считает, что сравнение лучевых скоростей в бальмеровских и запрещенных линиях может использоваться для изучения свойств галактических баров в современных обзорах, выполненных методом 3D-спектроскопии.

[5]Сейчас в базе NED эта область именуется как «NGC 1084 spur».

Отметим работу Smirnova et al. (2006), где по данным ИФП со SCORPIO была измерена угловая скорость вращения бара в галактике NGC 6104, а также исследование кандидатов в галактики с двойными барами, основанное на совместном использовании данных ИФП и MPFS (Moiseev et al. 2004).

Анализ поля лучевых скоростей позволяет строить достаточно надежные кривые вращения с уверенным определением угла наклона i, свободные от влияния областей некруговых движений. Это важно для построения моделей распределения массы в галактиках. В качестве одной из первых работ такого рода, выполненных на 6-м телескопе, отметим статью Ryder et al. (1998), которая является также одним из первых примеров одновременного использования в исследовании полей скоростей ионизованного газа (данные ИФП в Hα) и нейтрального водорода (наблюдения в линии 21 см). Эти данные хорошо дополняют друг друга, так как в H I более протяженный диск, но пространственное разрешение недостаточно для исследования внутренних областей, где помогают измерения в линии Hα. В работе Moiseev (2014b) такое совмещение кривых вращения выполнено для ряда близких карликовых галактик.

4.3. Галактики ранних типов (E-S0)

В последние десятилетия претерпевает изменения прежняя точка зрения о том, что эллиптические и линзовидные галактики лишены холодного и теплого газа. Важную роль здесь сыграла оптическая 3D-спектроскопия, в том числе на 6-м телескопе. В работах Plana and Boulesteix (1996), Plana et al. (1998) исследовались распределение и кинематика ионизованного газа в 11 E и S0 галактиках. В трех случаях были обнаружены две кинематически выделенные газовые подсистемы, возможно, располагающиеся в разных основных плоскостях эллипсоидов, что явно указывало на внешнее происхождение газа. Последующие наблюдения линзовидных галактик методами панорамной спектроскопии позволили существенно продвинуться в исследовании звездного населения и ионизованного газа галактик ранних типов, но относительно малое поле зрения не позволяло изучить их внешние части. Таких ограничений не было в работе Sil'chenko et al. (2019), представивших результаты наблюдений со SCORPIO/SCORPIO-2 протяженных газовых дисков в 18 линзовидных галактиках методами панорамной и длиннощелевой спектроскопии (см. пример NGC 3414 на рис. 6). Оказалось, что современное звездообразование обычно происходит там, где газ лежит точно в плоскости звездного диска и следует круговому вращению. В галактиках без текущего звездообразования протяженные

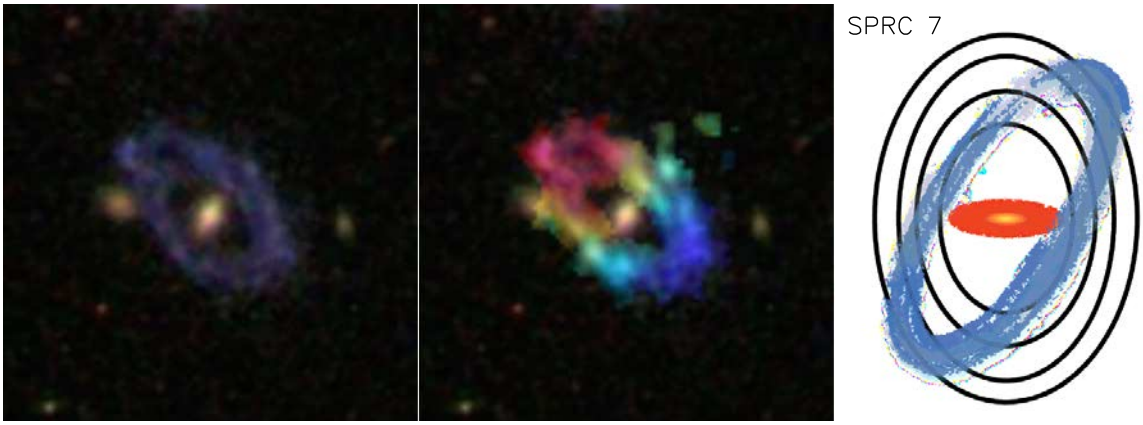

Рис. 7. Полярное кольцо в SPRC-7. Слева направо: цветное изображение из SDSS; совмещение данных SDSS с полем скоростей по данным ИФП, цвета соответствуют наблюдаемым лучевым скоростям, интенсивность шкалирована в соответствии с распределением яркости в эмиссионной линии Hβ; распределение гравитационного потенциала темного гало согласно численным расчетам. Схематично показаны центральный диск и полярное (наклонное) кольцо (Moiseev et al. 2015a).

газовые диски либо находятся в динамически стабильной квазиполярной ориентации, либо являются результатом захвата вещества с отличающимся направлением момента вращения, что приводит к ударной ионизации газа. Полученные данные указывают на существенное отличие геометрии аккреции газа в линзовидных и спиральных галактиках: аккреция в S0-галактиках обычно происходит вне плоскости звездного диска.

4.4. Галактики с полярными кольцами и родственные им объекты

Другой пример внешних газовых структур дают галактики с полярными кольцами (ГПК). Здесь протяженные кольца или диски из газа, пыли и звезд вращаются в плоскости примерно перпендикулярной к основному галактическому диску. Считается, что образование ГПК связано с событием, приносящем вещество с иным орбитальным моментом: слиянием двух галактик, аккрецией хозяйской галактикой вещества спутника или газовых филаментов. Фотометрическое и спектральное исследование ГПК на БТА началось группой из Санкт-Петербургского университета еще в 1990-х. Позже исследование наиболее сложных с точки морфологии кандидатов в ГПК из каталога Whitmore et al. (1990) начало проводится методами 3D-спектроскопии, причем сочетались оба доступных на БТА метода. С помощью MPFS исследовалась кинематика звездного населения центральной галактики в поле $16'' \times 16''$. Поле скоростей ионизованного газа картировалось на ИФП с большим полем зрения. При необходимости анализ дополнялся данными фотометрии и длиннощелевой спектроскопии (Hagen-Thorn et al. 2005, Merkulova et al. 2012; 2009). Характерен пример UGC 5600, в которой большая часть газа лежит вне плоскости звездного диска, причем во внутренних областях речь идет о полярном кольце, а во внешних — о сильном изгибе газового диска (Shalyapina et al. 2007). С помощью аналогичных наблюдений в галактике NGC 7468 (Shalyapina et al. 2004a) был обнаружен околоядерный полярный диск радиусом около 1 кпк. Каталог и характерные параметры таких структур, родственных ГПК, приводятся в работе Moiseev (2012). В некоторых случаях анализ полей скоростей газа и звезд приводил к исключению галактики из списка кандидатов в ГПК (Yakovleva et al. 2016).

В случае сплюснутого или трехосного гравпотенциала в полярной плоскости существуют устойчивые орбиты, поэтому захваченное вещество будет вращаться здесь достаточно долго. Если же плоскость орбиты заметно отличается от полярной, то формирующееся кольцо должно прецессировать к плоскости галактики. Так, наблюдения галактики Arp 212 с ИФП в Hα показали, что здесь сосуществуют сразу две вращающиеся подсистемы ионизованного газа: внутренний диск, совпадающий со звездным, и внешние области H II, орбиты которых сильно наклонены (Moiseev 2008). Учитывая опубликованные данные о распределении H I, мы пришли к выводу, что большая часть газа в галактике собрана в широком кольце радиусом около 20 кпк. Внешние части кольца вращаются в плоскости, ортогональной к звездному диску. Орбиты газовых облаков прецессируют с уменьшением радиуса и приближаются к плоскости диска. В диапазоне радиусов 2–3.5 кпк наблюдается столкновение между газом полярного кольца и внутренним диском, сопровождаемое вспышкой звездообразования.

Подробнее вопрос о некомпланарных, в том числе сталкивающихся газовых подсистемах в га-

лактиках поздних типов, рассматривался в работах Moiseev (2011; 2014a). Анализ карт ИФП для 25 близких карликовых галактик, представленный в статье Moiseev (2014b), показал, что доля объектов с наклонными газовыми структурами составляет более 10%, т.е. более чем на порядок превосходит имеющиеся оценки частоты встречаемости «классических» ГПК. Это указывает на важную роль аккреции внешнего вещества в современной эволюции галактик.

Новые цифровые обзоры неба привели к увеличению списка надежных кандидатов в ГПК, доступных для детального изучения (например, каталог SPRC Moiseev et al. 2011). Наблюдение вращения газа и звезд в двух взаимно перпендикулярных плоскостях дает возможность изучить трехмерное распределение массы в галактике, в том числе определить форму темного гало: сплюснутость, вытянутость, отклонения от осевой симметрии. Khoperskov et al. (2014) смогли восстановить форму темного гало галактики SPRC-7 на основании наблюдений Brosch et al. (2010) со SCORPIO, в том числе в режиме ИФП. Эта галактика обладает одним из самых больших полярных колец, диаметром около 50 кпк. Темное гало оказалось здесь заметно сплюснутым к плоскости кольца (рис. 7). Аналогичный анализ на основе наблюдений с ИФП выполнен для SPRC-260 (Khoperskov et al. 2013). Подробнее с результатами наблюдений объектов SPRC разными методами можно ознакомиться в работе Moiseev et al. (2015a). В последние годы на БТА с ИФП проведено картирование ионизованного газа еще в нескольких галактиках этого каталога. Данные готовятся к публикации.

Спектральное исследование на БТА известной кольцевой галактики Объект Хога (рис. 6) показало, что, хотя здесь центральная галактика и внешнее кольцо вращаются в одной плоскости, механизм формирования системы близок к тому, что предлагается для некоторых ГПК. Наблюдаемые характеристики Объекта Хога удается объяснить в предположении, что кольцо образовалось в результате «холодной» аккреции газа из филаментов межгалактической среды на прародительницу — эллиптическую галактику (Finkelman et al. 2011). С этой гипотезой согласуются и последующие наблюдения в линии 21 см (Brosch et al. 2013).

4.5. Взаимодействующие и пекулярные системы

Исследование полей скоростей столкновительных кольцевых галактик, в том числе с привлечением результатов численного моделирования, дает возможность определить скорость расширения кольцевой волны плотности. Интересным примером является Arp 10 с двумя кольцами звездообразования (Bizyaev et al. 2007). Анализ поля скоростей показал, что во внутреннем кольце имеют место значительные (более 30 км $с^{-1}$) вертикальные колебания газового диска. В то же время внешнее кольцо расширяется неравномерно, с $V_r = 30–110$ км $с^{-1}$, что и объясняет его эллиптическую форму. Показано, что кольцевая структура сформировалась в результате нецентрального столкновения с массивным спутником 85 млн. лет назад. Примеры полей скоростей других кольцевых столкновительных галактик, построенных с помощью ИФП на БТА, приведены в статье Moiseev and Bizyaev (2009).

Интересный и пока малоизученный аспект взаимодействия галактик был обнаружен в результате наблюдений на БТА Mrk 334 (Smirnova and Moiseev 2010), испытавшей недавнее слияние с массивным компаньоном. В диске галактики найдена каверна, заполненная ионизованным газом низкой плотности со значительными (до 70 км $с^{-1}$ по картам ИФП) отклонениями от кругового вращения. Мы интерпретировали эту область как места недавнего (примерно 12 млн. лет назад) пролета остатков разрушенного спутника через газовый диск основной галактики. Не менее интересны результаты совместного анализ фотометрических и спектральных данных для галактики Mrk 315 (Ciroi et al. 2005), которую мы застали в момент взаимодействия сразу с двумя спутниками, что привело к появлению нескольких кинематических компонент в кубе данных ИФП. При этом один из спутников, испытывающий быстрый пролет через газовое гало галактики, теряет собственный газ, формируя структуру, подобную инверсионному следу самолета.

Значительное внимание в исследованиях на БТА отводится изучению кинематики карликовых галактик и их взаимодействию с окружением. Moiseev et al. (2010) провели наблюдения с ИФП выборки из девяти галактик с экстремально низкой металличностью газа (от 1/35 до 1/10 от солнечного значения [O/H]). В большинстве галактик поля скоростей не могут быть описаны моделью одного вращающегося диска: наблюдаемые некруговые скорости указывают на различные стадии взаимодействия или слияния с компаньоном, в двух случаях удалось выделить по две независимо вращающиеся подсистемы. Все это указывает на то, что текущая вспышка звездообразования в этих галактиках индуцирована недавним взаимодействием. Характерным примером является DDO 68, отличающаяся рекордно низкой металличностью среди близких галактик и демонстрирующая признаки еще не закончившегося взаимодействия (см. Pustilnik et al. 2017, и ссылки там).

Сейчас на БТА завершается программа по картированию с ИФП выборки карликовых галактик низкой металличности, находящихся в близких

войдах. Принципы селекции объектов и анализ кинематики наиболее яркой из галактик выборки — NGC 428 (рис. 5) — приводятся в работе Egorova et al. (2019). Здесь, как и в рассмотренном выше примере, наблюдаются следы современного взаимодействия со спутниками или аккреции внешнего газа, несмотря на относительно бедное окружение. Так, оказалось, что сложная структура галактики Ark 18 является результатом двух последовательных слияний со спутниками, одно из которых, с отношением масс 1/5, сформировало внешний диск низкой поверхностной яркости (Egorova et al. 2021).

4.6. Активные галактические ядра

Исследование ионизованного газа в галактиках с активными ядрами является давним интересом нашей группы в САО РАН. Первые наблюдения выполнялись с помощью длиннощелевого спектрографа (см., например, Afanasiev et al. 1979, Afanasiev and Sil'chenko 1991). Но уже первые созданные приборы для 3D-спектроскопии показали высокую эффективность этих методов для исследования эмиссионных структур со сложной морфологией, возмущенной кинематикой и неоднозначным состоянии ионизации. При исследовании сейфертовской галактики Mrk 573 Afanasiev et al. (1996) применили одновременно оба типа 3D-спектрографов БТА: MPFS для спектроскопии центральной области в широком спектральном диапазоне и сканирующий ИФП для картирования кинематики ионизованного газа без ограничения по полю зрения. Этот подход был в дальнейшем применен в серии работ, исследующих как процессы поступления газа в центральные области галактик (Smirnova et al. 2006), так и воздействие активного ядра на межзвездную среду, связанное с радиоджетами Mrk 533 (Smirnova et al. 2007), истечениями типа галактического ветра (Smirnova and Moiseev 2010, см. также работу Афанасьев и др. 2020) или конусами ионизации (Kozlova et al. 2020, Smirnova et al. 2018). Во многих случаях речь идет о так называемых протяженных областях формирования узких эмиссионных линий (extended emission-line regions, EELR) размером от нескольких до десятков килопарсек.

В САО РАН в сотрудничестве с Волгоградским государственным университетом был разработан оригинальный сценарий, объясняющий формирование конусов ионизованного вещества в окрестностях ядер сейфертовских галактик, включая Z-образные структуры, наблюдаемые в ряде EELR.

Здесь предполагалось, что регулярные ионизованные структуры связаны с ударными волнами, порождаемые неустойчивостью Кельвина–Гельмгольца при вторжении джета активного ядра в окружающую среду (Afanasiev et al. 2007a). Были выполнены соответствующие численные расчеты (Afanasiev et al. 2007b), воспроизводящие морфологию EELR в NGC 5252. Но в большинстве случаев наблюдения указывают на то, что ионизация конусов обусловлена в первую очередь жестким ультрафиолетовым излучением ядра, коллимированного пылевым тором. Причем луч такого «ионизационного маяка» может освещать газ вдали от галактики. Так, в Mrk 6 эмиссионные филаменты наблюдаются на расстояниях до 40 кпк от ядра, а их поле скоростей показывает, что это не выброс газа из ядра, а аккреция внешнего вещества (Smirnova et al. 2018).

В случае удачного расположения относительно наблюдателя EELR являются своеобразным удаленным экраном, отражающим былую ионизационную активность ядра, как в случае прототипа «затухающих» активных ядер — Hanny's Voorwerp (IC 2497 Lintott et al. 2009). Совместные наблюдения на БТА и HST выборки кандидатов в галактики с затухающими ядрами (fading AGN) доказали справедливость предложенного объяснение существования природы EELR, удаленных более чем на 10 кпк (Keel et al. 2015). Кинематические карты, построенные с ИФП, продемонстрировали, что ионизованный газ имеет низкую дисперсию скоростей и в целом следует круговому вращению. То есть имеет место ионизация межгалактического газа, часто связанного с приливными структурами, а не выброс материи из ядра. На рис. 6 показана галактика UGC 7342, в которой газ на больших расстояниях от центра вращается регулярно, и только в области центрального килопарсека наблюдаются возмущения, связанные с ядерным истечением (Keel et al. 2017).

5. НАБЛЮДАТЕЛЬНЫЕ РЕЗУЛЬТАТЫ: ВОЗДЕЙСТВИЕ ЗВЕЗДООБРАЗОВАНИЯ НА ОКРУЖАЮЩИЙ ГАЗ

5.1. Галактический ветер

Наиболее глобальным воздействием текущего звездообразования на межзвездную среду является галактический ветер (сверхветер) — конические выбросы газа из плоскости галактики под действием коллективных взрывов сверхновых в околоядерной области. Лучше всего ветровые структуры видны при большом угле наклона диска галактики к лучу зрения, но при этом в наблюдаемых лучевых скоростях доминирует круговое вращение, как в поле скоростей NGC 4460 на рис. 6. Геометрическая модель ветра в этой галактике, рассмотренная Oparin and Moiseev (2015), дает диапазон скоростей истечения 30–80 км $с^{-1}$, что меньше скорости убегания из галактики. Поэтому выметенное вещество, охладившись, вновь упадет на диск. Этот

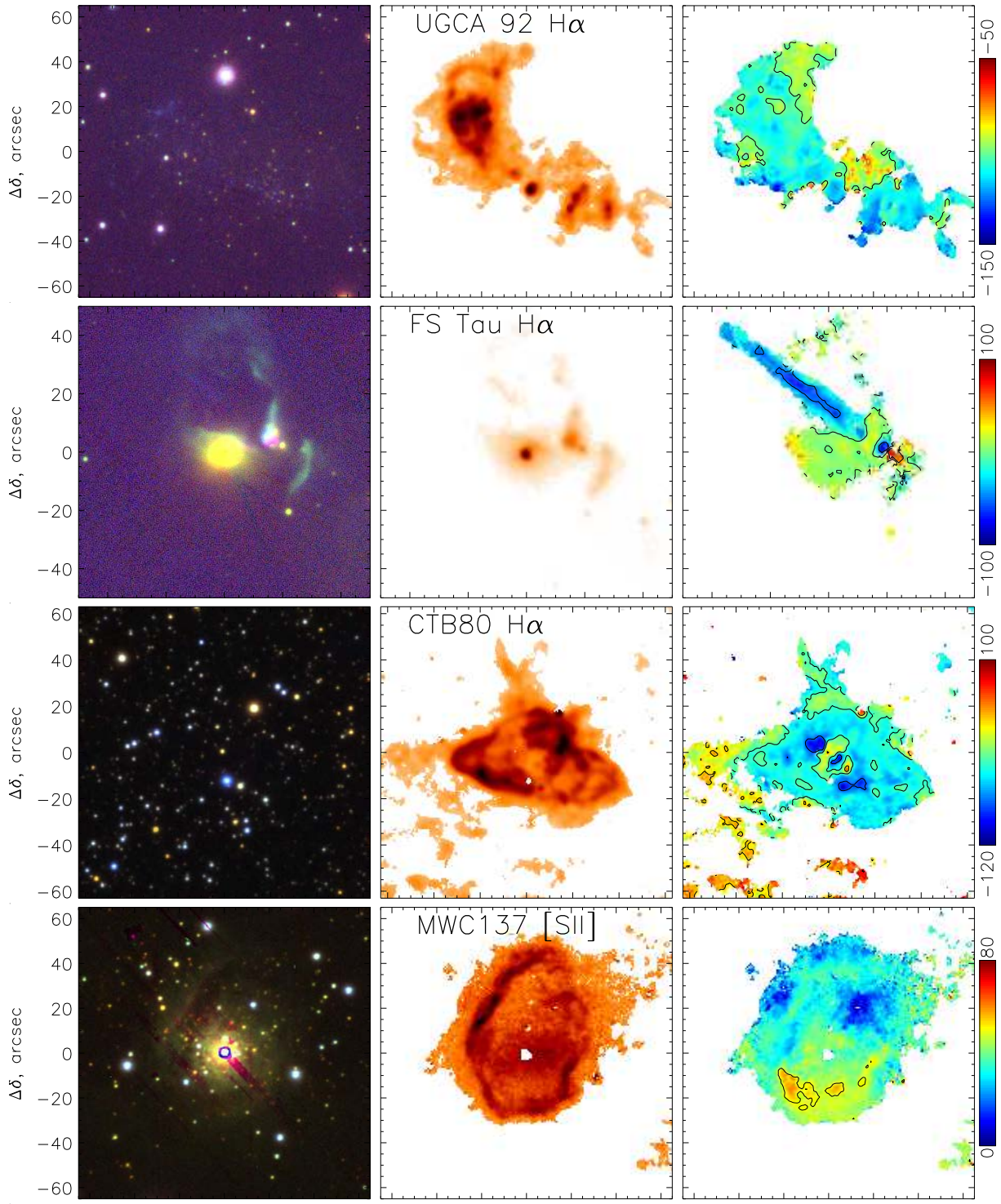

Рис. 8. Объекты с заметным воздействием звезд на газовую среду. Слева направо: изображение из Pan-STARRS DR1, распределения яркости в указанной эмиссионной линии и поле скоростей ионизованного газа, построенные из наблюдений с ИФП на БТА. Сверху вниз: карликовая галактика UGC 92 (Moiseev et al. 2015b), джет вблизи молодой звезды FS Tau (Movsessian et al. 2019), пульсарная туманность CTB 80 (Lozinskaya et al. 2005), туманность вокруг Be-звезды MWC 137 (Kraus et al. 2021).

же подход по анализу данных ИФП был применен для исследования ветра в UGC 10043 совместно со спектрофотометрическими данными IFS PPAK из обзора CALIFA (López-Cobá et al. 2017). Наша оценка скорости истечения (100–250 км $с^{-1}$) согласуется с тем, что следует из фотоионизационных моделей по отношению эмиссионных линий на BPT-диаграммах (Baldwin et al. 1981). Важной особенностью галактического ветра является высокая турбулентность газа, что проявляется в виде роста дисперсии скоростей вдоль луча зрения (σ). Спектральное разрешение наших ИФП достаточно высоко, чтобы проследить рост σ с удалением от плоскости диска. Это видно в том числе в архивных наблюдениях галактики NGC 6286, сверхветер в которой был обнаружен впервые Shalyapina et al. (2004b) и недавно подтвержден данными CALIFA (López-Cobá et al. 2019).

Ударные волны в случае галактического ветра и менее мощных «галактических фонтанов» приводят как к росту σ, так и к увеличению наблюдаемой светимости в запрещенных линиях. Поэтому одновременное использование данных о кинематики газа, полученных с ИФП высокого разрешения, и данных длиннощелевой или интегрально-полевой спектроскопии о потоках в эмиссионных линиях позволяет выполнять диагностику межзвездной среды галактик, однозначно выделяя области ударной ионизации. Эта методика, названная нами «BPT-σ» успешно опробована при анализе кубов данных галактик, наблюдавшихся с ИФП с приборами MPFS и PPAK (Опарин и Моисеев 2018).

5.2. Газ в областях звездообразования

С помощью сканирующего ИФП на БТА Moiseev et al. (2015b) построили карты распределения дисперсии лучевых скоростей ионизованного газа в большой выборке близких карликовых галактик (см. пример UGCA 92 на рис. 8). Было продемонстрировано существование глобального соотношения между текущим темпом звездообразования (SFR) и средневзвешенной по яркости дисперсии скоростей. Соотношение выполняется в широчайшем диапазоне SFR (5.5 порядков) и верно как для дисков, форма которых поддерживается вращением, так и для отдельных гигантских областей H II. Авторы интерпретировали это как аргумент в пользу того, что σ в карликовых галактиках не отражает вириальные движения, а в основном определяется энергией, впрыскиваемой в межзвездную среду в процессе звездообразования. Полученные данные о турбулентных движениях газа в близких галактиках сейчас используются для построения унифицированных моделей галактических дисков (Krumholz et al. 2018).

Yang et al. (1996) предложили использовать карты ИФП для построения диаграмм «интенсивность–дисперсия скоростей» ($I-\sigma$). Это позволяет не только изучать расширяющиеся оболочки, связанные с областями звездообразования (Martínez-Delgado et al. 2007), но и выделять уникальные объекты: остатки сверхновых, эмиссионные звезды и т.д. Подробно данная методика описана Moiseev and Lozinskaya (2012), которые обнаружили кандидат в звезду LBV в UGC 8508.

В случае dIrr-галактик Местной Вселенной угловой масштаб составляет 3–20 пк/″, поэтому с помощью ИФП можно в деталях рассмотреть динамику процессов, приводящих к росту дисперсии скоростей газа: остатки сверхновых, оболочки, связанные с ветром из областей звездообразования. Отсутствие спиральных волн плотности и большая толщина газовых дисков делают dIrr-галактики оптимальными полигонами для изучения взаимодействия звезд и межзвездной среды. Такие работы начались на БТА по инициативе Т. А. Лозинской (ГАИШ МГУ) с исследования галактики IC 1613, где оболочки ионизованного газа связаны с крупномасштабными структурами нейтрального водорода (Lozinskaya et al. 2003). Здесь одними из первых в практике анализа данных ИФП мы использовали технику PV-диаграмм (раздел 3.2) с одновременным анализом кубов данных H I в линии 21 см. Это дало возможность определить динамические возраста оболочек и сравнить их с возрастами центральных звездных скоплений. Дальнейшее развитие данное направление получило в связи с изучением гигантских (до 1 кпк диаметром) сверхоболочек H I в ряде карликовых галактик, для создания которых явно не хватало энергетики центральных звездных скоплений. Сейчас этот феномен объясняется индуцированием звездообразования в плотных стенках сверхоболочек. Наблюдения с ИФП позволяют в деталях изучить этот процесс. Подробное обсуждение приведено в обзоре Egorov et al. (2015) и недавних работах, посвященных галактикам Holmerg I и II (Egorov et al. 2017b; 2018).

5.3. Эмиссионные звезды, уникальные объекты

Переходя к исследованию туманностей, созданных отдельными звездами, прежде всего отметим измерения динамических возрастов гигантской (более 200 пк размером) биполярной оболочки вокруг уникальной звезды WO (Afanasiev et al. 2000) в IC 1613 и возможного остатка гиперновой в виде синхротронной сверхоболочки в галактике IC 10 (Lozinskaya and Moiseev 2007). В центре кандидата в остатки гиперновой находится рентгеновский источник IC10 X-1, состоящий из звезды WR в паре с массивной (23–24 $M_\odot$) черной дырой. В

последние годы интерес к таким объектам вырос в связи с детектированием гравитационных волн от сливающихся черных дыр (см. обсуждение у Bogomazov et al. 2018).

Интересные результаты были получены при изучении с ИФП туманностей, связанных с ультраяркими рентгеновскими источниками (ULX) в галактиках Holmerg IX (Abolmasov and Moiseev 2008) и Holmerg II (Egorov et al. 2017a). В последнем случае анализ полей скоростей в линиях [O III], [S II] и Hα выявил структуру, интерпетируемую как проявление головной ударной волны (bow shock), вызванной быстрым полетом ULX через межзвездную среду и воздействием его горячего ветра на туманность. Наилучшее согласие с наблюдениями получается в предположении, что ULX вылетел из центральной части близлежащего скопления со скоростью около 70 км с$^{-1}$. Это подтверждает точку зрения о том, что многие ULX являются аккрецирующими черными дырами звездных масс (Poutanen et al. 2013). Отметим также картирование сверхзвуковых течений газа в туманности, связанной с объектом SS433 (Abolmasov et al. 2010).

Аналогично случаю Holmberg II ULX данные о лучевых скоростях и распределении яркости в пульсарной туманности CTB 80 (рис. 8) послужили основой для оценки пространственной скорости пульсара (Lozinskaya et al. 2005).

Многолетние наблюдения истечений типа Хербига–Аро, связанных с молодыми звездными объектами, дают возможность измерять собственные движения отдельных деталей в кубе данных ИФП. Так, первые наблюдения со сканирующим ИФП выявили сложную кинематику в истечении от HL Tau (Movsessian et al. 2007): компактные сгустки с высокой лучевой скоростью (-150 км с$^{-1}$) и дугообразные структуры впереди них со сравнительно низкой скоростью (-50 км с$^{-1}$). Для измерения собственных движений структур с разными лучевыми скоростями использовались две эпохи наблюдений с ИФП (2001 и 2007 гг.). Тангенциальные скорости обеих структур одинаковы и составили около 160 км с$^{-1}$. Этот результат свидетельствует о том, что структуры в истечении от HL Tau образуются вследствие эпизодических выбросов материи, при которых мы видим свечение сгустка высокоскоростного газа и дугообразной ударной волны перед ним (Movsessian et al. 2012). На рис. 8 показан пример аналогичного исследования FS Tau (Movsessian et al. 2019).

Наблюдения с ИФП на БТА туманностей нашей Галактики, связанных с массивными звездами, имеют лишь эпизодический характер. В качестве примера можно привести Be-звезду Хербига S 235B (Boley et al. 2009) и туманность вокруг

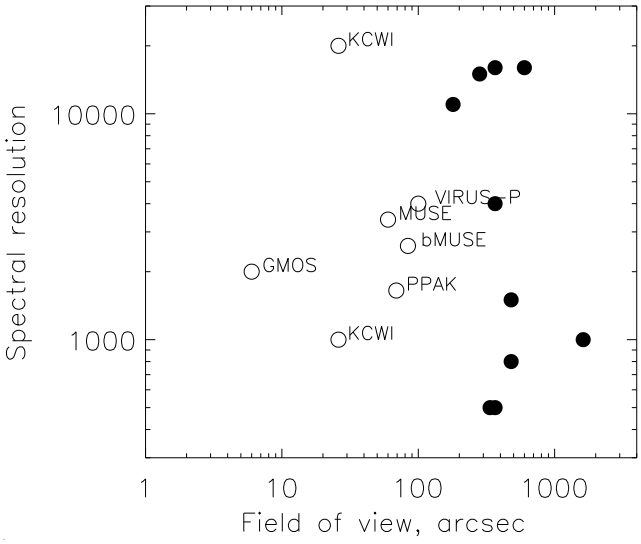

Рис. 9. Параметры приборов для 3D-спектроскопии на базе сканирующих ИФП (черные точки) и интегрально-полевых спектрографов (незаполненные кружки) на плоскости «FOV–$\mathcal{R}$». Для KCWI показаны режимы высокого и низкого спектрального разрешения.

супергиганта MWC 137 (рис. 8). В последнем случае обнаружены структуры, связанные с ударными волнами, находящиеся вне поля, ранее исследованного с MUSE на VLT (Kraus et al. 2021). Аналогичные наблюдения продолжаются, авторы надеются на интересные результаты.

6. ЗАКЛЮЧЕНИЕ

Boulesteix (2002) сравнивал приборы для панорамной спектроскопии на плоскости «поле зрения–спектральное разрешение». На рис. 9 приводится такая диаграмма, где показаны $\mathcal{R}$ и FOV для всех систем со сканирующим ИФП из таблицы 1. Для сравнения показан ряд интегрально-полевых спектрографов 3.6–10 м телескопов: MUSE (Bacon et al. 2014) и проект blueMUSE (Jeanneau et al. 2020), PPAK (Kelz et al. 2006), GMOS (Allington-Smith et al. 2002) и KCWI (Morrissey et al. 2018) в двух конфигурациях.

На приведенной диаграмме видно, что даже сейчас, в эпоху бурного развития методов 3D-спектроскопии, системы на базе сканирующего ИФП остаются непревзойденными[6] по сочетанию большого поля зрения ($FOV > 100''$) и высокого углового разрешения ($\mathcal{R} > 10\,000$). Это определяет

[6]Пример прибора, сочетающего протяженный спектральный диапазон, высокое разрешение и большое поле зрения дает фурье-спектрограф SITELLE на CFHT (Drissen et al. 2019). Но эта техника тоже имеет свои ограничения и пока не очень распространена на телескопах.

как минимум одну важную область исследований, в том числе и на 6-м телескопе САО РАН — исследование движений ионизованного газа в больших полях (туманности Млечного Пути и близкие галактики). Определенную проблему представляет вычитание фона неба в случаях, когда все поле зрения занято эмиссионным объектом, но здесь должны помочь новые алгоритмы анализа данных. В частности, уже имеется положительный опыт построения ИФП-мозаик, например, при исследовании эмиссионных оболочек в звездной ассоциации Cyg OB1 (Sitnik et al. 2019).

Опыт автора и его коллег по исследованию различных галактических и внегалактических объектов с помощью сканирующего ИФП показывает, что наиболее эффективной эта техника оказывается при сочетании ее с другими методами 3D-спектроскопии и данными интерферометрии в радиодиапазоне. Наблюдения на 6-м телескопе с ИФП в составе SCORPIO-2 показывают, что эти данные могут дополнить принципиально новой и важной информацией кубы, полученные с такими IFS, как MUSE, PPAK и MaNGA. Наша группа в САО РАН открыта для обсуждения любых новых проектов совместных исследований со сканирующими ИФП.

БЛАГОДАРНОСТИ

Автор благодарит за помощь коллег из лаборатории СФВО САО РАН, своих соавторов, учителей и учеников, вместе с которыми были написаны статьи, упомянутые в данном обзоре. Отдельное спасибо С. Н. Додонову и А. А. Смирновой за замечания, позволившие улучшить рукопись. Статья посвящается памяти В. Л. Афанасьева, благодаря энтузиазму и труду которого были созданы приборы SCORPIO и SCORPIO-2.

ФИНАНСИРОВАНИЕ

Работа выполнена в рамках государственного задания САО РАН, утвержденного Министерством науки и высшего образования Российской Федерации. Наблюдения на 6-м телескопе САО РАН выполняются при поддержке Министерства науки и высшего образования Российской Федерации (включая соглашение № 05.619.21.0016, уникальный идентификатор проекта RFMEFI61919X0016).

КОНФЛИКТ ИНТЕРЕСОВ

Автор заявляет об отсутствии конфликта интересов.

СПИСОК ЛИТЕРАТУРЫ

1. P. Abolmasov, O. Maryeva, and A. N. Burenkov, Astronomische Nachrichten **331** (4), 412 (2010).
2. P. Abolmasov and A. V. Moiseev, Revista Mexicana Astronom. Astrofis. **44**, 301 (2008).
3. V. L. Afanasiev, Y. Y. Balega, M. A. Grudzinsky, et al., Tehnika sredstv svyazi, Ser. Tehnika televidenia **5** 13 (1987).
4. V. L. Afanasiev, J. Boulesteix, F. Bonnarel, et al., in *Proc. of Int. Conf. Dynamics and Interactions of Galaxies*, ed. by R. Wielen, pp. 354–355 (1990a).
5. V. L. Afanasiev, A. N. Burenkov, A. I. Shapovalova, and V. V. Vlasyuk, ASP Conf. Ser. **91**, 218 (1996).
6. V. L. Afanasiev, A. N. Burenkov, A. V. Zasov, and O. K. Sil'chenko, Astrofizika **28**, 243 (1988).
7. V. L. Afanasiev, A. N. Burenkov, A. V. Zasov, and O. K. Silchenko, Astron. Zh. **69**, 19 (1992).
8. V. L. Afanasiev, S. N. Dodonov, S. S. Khrapov, et al., Astrophysical Bulletin **62** (1), 1 (2007a).
9. V. L. Afanasiev, S. N. Dodonov, S. S. Khrapov, et al., Astrophysical Bulletin **62** (1), 15 (2007b).
10. V. L. Afanasiev, S. N. Dodonov, and A. V. Moiseev, in *Stellar Dynamics: From Classic to Modern, Proc. Int. Conf. held in Saint Petersberg, August 21–27, 2000*, ed. by L. P. Ossipkov and I. I. Nikiforov., p. 103 (2001).
11. V. L. Afanasiev and A. M. Fridman, Astronomy Letters **19** (5), 319 (1993).
12. V. L. Afanasiev and A. I. Shapovalova, Astrofizika **17**, 403 (1981).
13. V. L. Afanasiev, T. A. Lozinskaya, A. V. Moiseev, and E. Blanton, Astronomy Letters **26**, 153 (2000).
14. V. L. Afanasiev and A. V. Moiseev, Astronomy Letters **31**, 194 (2005).
15. V. L. Afanasiev and A. V. Moiseev, Baltic Astronomy **20**, 363 (2011).
16. V. L. Afanasiev and A. I. Shapovalova, in *Mass-Transfer Induced Activity in Galaxies, Proc. Conf. held at the University of Kentucky, Lexington, April 26-30, 1993*, ed. by Isaac Shlosman, p. 95 (1994).
17. V. L. Afanasiev and O. K. Sil'chenko, Astrofiz. Issled.: Izvestiya Spets. Astrofiz. Obs. **33**, 88 (1991).
18. V. L. Afanasiev, V. V. Vlasyuk, S. N. Dodonov, and O. K. Sil'chenko, Preprint No. **54**, (SAO RAS, Nizhnii Arkhyz, 1990b).
19. J. Allington-Smith, G. Murray, R. Content, et al., Publ. Astron. Soc. Pacific **114** (798), 892 (2002).
20. P. Amram, M. Marcelin, F. Bonnarel, et al., Astron. and Astrophys. **263**, 69 (1992).
21. V. I. Ardilanov, V. A. Murzin, I. V. Afanasieva, et al., in *Ground-Based Astronomy in Russia. 21st Century, Proc. Conf. held in Nizhny Arkhyz September, 21–25, 2020*, ed. by I. I. Romanyuk, I. A. Yakunin, A. F. Valeev, and D. O. Kudryavtsev, pp. 115–118 (2020).
22. S. Arribas, E. Mediavilla, and J. L. Rasilla, Astrophys. J. **369**, 260 (1991).
23. P. D. Atherton, ASP Conf. Ser. **71**, 50 (1995).
24. R. Bacon, G. Adam, A. Baranne, et al., Astron. and Astrophys. Suppl. **113**, 347 (1995).

25. R. Bacon, J. Vernet, E. Borisova, et al., The Messenger **157**, 13 (2014).
26. J. A. Baldwin, M. M. Phillips, and R. Terlevich, Publ. Astron. Soc. Pacific **93**, 5 (1981).
27. K. G. Begeman, Astron. and Astrophys. **223**, 47 (1989).
28. G. Bekiaris, K. Glazebrook, C. J. Fluke, and R. Abraham, Monthly Notices Royal Astron. Soc. **455** (1), 754 (2016).
29. D. V. Bizyaev, A. V. Moiseev, and E. I. Vorobyov, Astrophys. J. **662** (1), 304 (2007).
30. J. Bland and R. B. Tully, Astron. J. **98**, 723 (1989).
31. A. I. Bogomazov, A. M. Cherepashchuk, V. M. Lipunov, and A. V. Tutukov, New Astronomy **58**, 33 (2018).
32. P. A. Boley, A. M. Sobolev, V. V. Krushinsky, et al., Monthly Notices Royal Astron. Soc. **399** (2), 778 (2009).
33. N. Bouché, H. Carfantan, I. Schroetter, et al., Astron. J. **150** (3), 92 (2015).
34. J. Boulesteix, ASP Conf. Ser. **282**, 374 (2002).
35. J. Boulesteix, Y. Georgelin, M. Marcelin, and J. A. Fort, Astroph. Space Science Library **92**, 223 (1982).
36. J. Boulesteix, Y. Georgelin, M. Marcelin, and G. Monnet, SPIE Conf. Ser. **445**, 37 (1984).
37. J. Boulesteix, Y. P. Georgelin, E. Lecoarer, et al., Astron. and Astrophys. **178**, 91 (1987).
38. N. Brosch, I. Finkelman, T. Oosterloo, et al., Monthly Notices Royal Astron. Soc. **435** (1), 475 (2013).
39. N. Brosch, A. Y. Kniazev, A. Moiseev, and S. A. Pustilnik, Monthly Notices Royal Astron. Soc. **401** (3), 2067 (2010).
40. H. Buisson, C. Fabry, and H. Bourget, Astrophys. J. **40** (1914).
41. D. A. Ciampa, K. A. Barger, N. Lehner, et al., Astrophys. J. **908** (1), 62 (2021).
42. S. Ciroi, V. L. Afanasiev, A. V. Moiseev, et al., Monthly Notices Royal Astron. Soc. **360** (1), 253 (2005).
43. L. Coccato, E. M. Corsini, A. Pizzella, and F. Bertola, Astron. and Astrophys. **465** (3), 777 (2007).
44. G. Courtès, Annales d'Astrophysique **23**, 115 (1960).
45. G. Courtes, Astroph. Space Science Library **92**, 123 (1982).
46. O. Daigle, C. Carignan, O. Hernandez, et al., Monthly Notices Royal Astron. Soc. **368** (3), 1016 (2006).
47. G. de Vaucouleurs and W. D. Pence, Astrophys. J. **242**, 18 (1980).
48. V. P. Debattista and T. B. Williams, Astrophys. J. **605** (2), 714 (2004).
49. E. M. Di Teodoro and F. Fraternali, Monthly Notices Royal Astron. Soc. **451** (3), 3021 (2015).
50. S. N. Dodonov, V. V. Vlasyuk, and S. V. Drabek, *Fabry–Perot interferometer. User Manual* (SAO RAS, Nizhnij Arkhyz, 1995).
51. L. Drissen, T. Martin, L. Rousseau-Nepton, et al., Monthly Notices Royal Astron. Soc. **485** (3), 3930 (2019).
52. O. V. Egorov, T. A. Lozinskaya, and A. V. Moiseev, Astronomical and Astrophysical Transactions **29** (1), 17 (2015).
53. O. V. Egorov, T. A. Lozinskaya, and A. V. Moiseev, Monthly Notices Royal Astron. Soc. **467** (1), L1 (2017a).
54. O. V. Egorov, T. A. Lozinskaya, A. V. Moiseev, and Y. A. Shchekinov, Monthly Notices Royal Astron. Soc. **464** (2), 1833 (2017b).
55. O. V. Egorov, T. A. Lozinskaya, A. V. Moiseev, and G. V. Smirnov-Pinchukov, Monthly Notices Royal Astron. Soc. **478** (3), 3386 (2018).
56. E. S. Egorova, O. V. Egorov, A. V. Moiseev, et al., Monthly Notices Royal Astron. Soc. **504** (4), 6719 (2021).
57. E. S. Egorova, A. V. Moiseev, and O. V. Egorov, Monthly Notices Royal Astron. Soc. **482** (3), 3403 (2019).
58. B. Epinat, P. Amram, and M. Marcelin, Monthly Notices Royal Astron. Soc. **390**, 466 (2008).
59. C. Fabry and A. Perot, Astrophys. J. **13**, 265 (1901).
60. K. Fathi, T. Storchi-Bergmann, R. A. Riffel, et al., Astrophys. J. **641** (1), L25 (2006).
61. K. Fathi, G. van de Ven, R. F. Peletier, et al., Monthly Notices Royal Astron. Soc. **364** (3), 773 (2005).
62. I. Finkelman, A. Moiseev, N. Brosch, and I. Katkov, Monthly Notices Royal Astron. Soc. **418** (3), 1834 (2011).
63. M. Franx, J. H. van Gorkom, and T. de Zeeuw, Astrophys. J. **436**, 642 (1994).
64. A. M. Fridman, V. L. Afanasiev, S. N. Dodonov, et al., Astron. and Astrophys. **430**, 67 (2005).
65. A. M. Fridman, O. V. Khoruzhii, V. V. Lyakhovich, et al., Astron. and Astrophys. **371**, 538 (2001a).
66. A. M. Fridman, O. V. Khoruzhii, E. V. Polyachenko, et al., Monthly Notices Royal Astron. Soc. **323** (3), 651 (2001b).
67. A. M. Fridman, O. V. Koruzhii, A. V. Zasov, et al., Astronomy Letters **24** (6), 764 (1998).
68. A. M. Fridman, A. G. Morozov, M. V. Nezlin, and E. N. Snezhkin, Physics Letters A **109** (5), 228 (1985).
69. K. Gebhardt, C. Pryor, R. D. O'Connell, et al., Astron. J. **119** (3), 1268 (2000).
70. K. Gebhardt, C. Pryor, T. B. Williams, and J. E. Hesser, Astron. J. **110**, 1699 (1995).
71. J. J. González, J. Cepa, J. I. González-Serrano, and M. Sánchez-Portal, Monthly Notices Royal Astron. Soc. **443** (4), 3289 (2014).
72. S. Gordon, B. Koribalski, S. Houghton, and K. Jones, Monthly Notices Royal Astron. Soc. **315**, 248 (2000).
73. L. M. Haffner, R. J. Reynolds, S. L. Tufte, et al., Astrophys. J. Suppl. **149** (2), 405 (2003).
74. V. A. Hagen-Thorn, L. V. Shalyapina, G. M. Karataeva, et al., Astronomy Reports **49** (12), 958 (2005).
75. O. Hernandez, K. Fathi, C. Carignan, et al., Publ. Astron. Soc. Pacific **120**, 665 (2008).
76. A. Jeanneau, J. Kosmalski, E. Muslimov, et al., SPIE Conf. Ser. **11447**, 114475M (2020).
77. G. I. G. Józsa, F. Kenn, U. Klein, and T. A. Oosterloo, Astron. and Astrophys. **468** (2), 731 (2007).
78. W. C. Keel, C. J. Lintott, W. P. Maksym, et al., Astrophys. J. **835** (2), 256 (2017).

79. W. C. Keel, W. P. Maksym, V. N. Bennert, et al., Astron. J. **149** (5), 155 (2015).
80. A. Kelz, M. A. W. Verheijen, M. M. Roth, et al., Publ. Astron. Soc. Pacific **118** (839), 129 (2006).
81. T. J. Kentischer, W. Schmidt, M. Sigwarth, and M. V. Uexkuell, Astron. and Astrophys. **340**, 569 (1998).
82. S. Khoperskov, A. Moiseev, and A. Khoperskov, Memorie della Societa Astronomica Italiana Supplementi **25**, 51 (2013).
83. S. A. Khoperskov, A. V. Moiseev, A. V. Khoperskov, and A. S. Saburova, Monthly Notices Royal Astron. Soc. **441** (3), 2650 (2014).
84. D. V. Kozlova, A. V. Moiseev, and A. A. Smirnova, Contr. Astron. Obs. Skalnate Pleso **50** (1), 309 (2020).
85. D. Krajnović, M. Cappellari, P. T. de Zeeuw, and Y. Copin, Monthly Notices Royal Astron. Soc. **366** (3), 787 (2006).
86. M. Kraus, T. Liimets, A. Moiseev, J. P. Sanchez Arias, et al., arxiv:2106.15981 (2021).
87. M. R. Krumholz, B. Burkhart, J. C. Forbes, and R. M. Crocker, Monthly Notices Royal Astron. Soc. **477** (2), 2716 (2018).
88. C. J. Lintott, K. Schawinski, W. Keel, et al., Monthly Notices Royal Astron. Soc. **399** (1), 129 (2009).
89. C. López-Cobá, S. F. Sánchez, J. Bland-Hawthorn, et al., Monthly Notices Royal Astron. Soc. **482** (3), 4032 (2019).
90. C. López-Cobá, S. F. Sánchez, A. V. Moiseev, et al., Monthly Notices Royal Astron. Soc. **467** (4), 4951 (2017).
91. T. A. Lozinskaya, Sov. Astron. **13**, 192 (1969).
92. T. A. Lozinskaya, Sov. Astron. **16**, 945 (1973).
93. T. A. Lozinskaya, V. N. Komarova, A. V. Moiseev, and S. I. Blinnikov, Astronomy Letters **31** (4), 245 (2005).
94. T. A. Lozinskaya and A. V. Moiseev, Monthly Notices Royal Astron. Soc. **381** (1), L26 (2007).
95. T. A. Lozinskaya, A. V. Moiseev, and N. Y. Podorvanyuk, Astronomy Letters **29**, 77 (2003).
96. V. V. Lyakhovich, A. M. Fridman, O. V. Khoruzhii, and A. I. Pavlov, Astronomy Reports **41** (4), 447 (1997).
97. M. Marcelin, P. Amram, P. Balard, et al., SPIE Conf. Ser. **7014**, 701455 (2008).
98. M. Marcelin, J. Boulesteix, and G. Courtes, Astron. and Astrophys. **108** (1), 134 (1982).
99. M. Marcelin, J. Boulesteix, and Y. Georgelin, Astron. and Astrophys. **128**, 140 (1983).
100. D. Martínez-Delgado, R. J. Gabany, K. Crawford, et al., Astron. J. **140** (4), 962 (2010).
101. I. Martínez-Delgado, G. Tenorio-Tagle, C. Muñoz-Tuñón, et al., Astron. J. **133** (6), 2892 (2007).
102. J. Melnick, M. Moles, R. Terlevich, and J.-M. Garcia-Pelayo, Monthly Notices Royal Astron. Soc. **226**, 849 (1987).
103. C. Mendes de Oliveira, P. Amram, B. C. Quint, et al., Monthly Notices Royal Astron. Soc. **469** (3), 3424 (2017).
104. O. A. Merkulova, G. M. Karataeva, V. A. Yakovleva, and A. N. Burenkov, Astronomy Letters **38** (5), 290 (2012).
105. O. A. Merkulova, L. V. Shalyapina, and V. A. Yakovleva, Astronomy Letters **35** (9), 587 (2009).
106. C. J. Mitchell, T. B. Williams, K. Spekkens, et al., Astron. J. **149**, 116 (2015).
107. A. V. Moiseev, Astron. and Astrophys. **363**, 843 (2000).
108. A. V. Moiseev, Bull. Spec. Astrophys. Obs. **54**, 74 (2002).
109. A. V. Moiseev, Astrophysical Bulletin **63**, 201 (2008).
110. A. Moiseev, EAS Publications Series **48**, 115 (2011).
111. A. V. Moiseev, Astrophysical Bulletin **67** (2), 147 (2012).
112. A. Moiseev, ASP Conf. Ser. **486**, 61 (2014a).
113. A. V. Moiseev, Astrophysical Bulletin **69**, 1 (2014b).
114. A. Moiseev, S. Khoperskov, A. Khoperskov, et al., Baltic Astronomy **24**, 76 (2015a).
115. A. Moiseev, A. Perepelitsyn, and D. Oparin, Experimental Astronomy **50** (2-3), 199 (2020).
116. A. V. Moiseev and D. V. Bizyaev, New Astronomy Reviews **53** (7–10), 169 (2009).
117. A. V. Moiseev and O. V. Egorov, Astrophysical Bulletin **63**, 181 (2008).
118. A. V. Moiseev and T. A. Lozinskaya, Monthly Notices Royal Astron. Soc. **423**, 1831 (2012).
119. A. V. Moiseev and V. V. Mustsevoi, Astronomy Letters **26**, 565 (2000).
120. A. V. Moiseev, S. A. Pustilnik, and A. Y. Kniazev, Monthly Notices Royal Astron. Soc. **405**, 2453 (2010).
121. A. V. Moiseev, K. I. Smirnova, A. A. Smirnova, and V. P. Reshetnikov, Monthly Notices Royal Astron. Soc. **418** (1), 244 (2011).
122. A. V. Moiseev, A. V. Tikhonov, and A. Klypin, Monthly Notices Royal Astron. Soc. **449**, 3568 (2015b).
123. A. V. Moiseev, J. R. Valdés, and V. H. Chavushyan, Astron. and Astrophys. **421**, 433 (2004).
124. G. Monnet, ASP Conf. Ser. **71**, 12 (1995).
125. J. P. Morgenthaler, W. M. Harris, F. Scherb, et al., Astrophys. J. **563** (1), 451 (2001).
126. A. G. Morozov, Astron. Zh. **56**, 498 (1979).
127. P. Morrissey, M. Matuszewski, D. C. Martin, et al., Astrophys. J. **864** (1), 93 (2018).
128. T. A. Movsessian, T. Y. Magakian, J. Bally, et al., Astron. and Astrophys. **470** (2), 605 (2007).
129. T. A. Movsessian, T. Y. Magakian, and A. N. Burenkov, Astron. and Astrophys. **627**, A94 (2019).
130. T. A. Movsessian, T. Y. Magakian, and A. V. Moiseev, Astron. and Astrophys. **541**, A16 (2012).
131. D. V. Oparin and A. V. Moiseev, Astrophysical Bulletin **70** (4), 392 (2015).
132. H. Plana and J. Boulesteix, Astron. and Astrophys. **307**, 391 (1996).
133. H. Plana, J. Boulesteix, P. Amram, et al., Astron. and Astrophys. Suppl. **128**, 75 (1998).
134. J. Poutanen, S. Fabrika, A. F. Valeev, et al., Monthly Notices Royal Astron. Soc. **432** (1), 506 (2013).
135. D. Punzo, J. M. van der Hulst, J. B. T. M. Roerdink, et al., Astronomy and Computing **12**, 86 (2015).

136. S. A. Pustilnik, L. N. Makarova, Y. A. Perepelitsyna, et al., Monthly Notices Royal Astron. Soc. **465** (4), 4985 (2017).
137. S. Ramya, D. K. Sahu, and T. P. Prabhu, Monthly Notices Royal Astron. Soc. **381** (2), 511 (2007).
138. N. Rangwala, T. B. Williams, C. Pietraszewski, and C. L. Joseph, Astron. J. **135**, 1825 (2008).
139. N. Rangwala, T. B. Williams, and K. Z. Stanek, Astrophys. J. **691** (2), 1387 (2009).
140. D. H. Rogstad, I. A. Lockhart, and M. C. H. Wright, Astrophys. J. **193**, 309 (1974).
141. M. Rosado, R. Langarica, A. Bernal, et al., Revista Mexicana de Astronomia y Astrofisica Conf. Ser. **3**, 263 (1995).
142. J. R. Roy, R. Arsenault, and G. Joncas, Astrophys. J. **300**, 624 (1986).
143. S. D. Ryder, A. V. Zasov, V. J. McIntyre, et al., Monthly Notices Royal Astron. Soc. **293** (4), 411 (1998).
144. F. K. Sakhibov and M. A. Smirnov, Sov. Astron. **33**, 476 (1989).
145. L. V. Shalyapina, O. A. Merkulova, V. A. Yakovleva, and E. V. Volkov, Astronomy Letters **33** (8), 520 (2007).
146. L. V. Shalyapina, A. V. Moiseev, V. A. Yakovleva, et al., Astronomy Letters **30**, 583 (2004a).
147. L. V. Shalyapina, A. V. Moiseev, V. A. Yakovleva, et al., Astronomy Letters **30**, 1 (2004b).
148. P. V. Sheglov, Nature **199** (4897), 990 (1963).
149. O. K. Sil'chenko and A. V. Moiseev, Astron. J. **131** (3), 1336 (2006).
150. O. K. Sil'chenko, A. V. Moiseev, and O. V. Egorov, Astrophys. J. Suppl. **244** (1), 6 (2019).
151. T. G. Sitnik, O. V. Egorov, T. A. Lozinskaya, et al., Monthly Notices Royal Astron. Soc. **486** (2), 2449 (2019).
152. A. Smirnova and A. Moiseev, Monthly Notices Royal Astron. Soc. **401** (1), 307 (2010).
153. A. A. Smirnova, N. Gavrilović, A. V. Moiseev, et al., Monthly Notices Royal Astron. Soc. **377** (2), 480 (2007).
154. A. A. Smirnova, A. V. Moiseev, and V. L. Afanasiev, Astronomy Letters **32** (8), 520 (2006).
155. A. A. Smirnova, A. V. Moiseev, and S. N. Dodonov, Monthly Notices Royal Astron. Soc. **481** (4), 4542 (2018).
156. K. T. Soto, S. J. Lilly, R. Bacon, et al., Monthly Notices Royal Astron. Soc. **458** (3), 3210 (2016).
157. O. Streicher, P. M. Weilbacher, R. Bacon, and A. Jarno, ASP Conf. Ser. **442**, 257 (2011).
158. K. Taylor and P. D. Atherton, Monthly Notices Royal Astron. Soc. **191**, 675 (1980).
159. P. J. Teuben, ASP Conf. Ser. **275**, 217 (2002).
160. R. B. Tully, Astrophys. J. Suppl. **27**, 415 (1974).
161. S. Veilleux, B. J. Weiner, D. S. N. Rupke, et al., Astron. J. **139**, 145 (2010).
162. L. Weitzel, A. Krabbe, H. Kroker, et al., Astron. and Astrophys. Suppl. **119**, 531 (1996).
163. B. C. Whitmore, R. A. Lucas, D. B. McElroy, et al., Astron. J. **100**, 1489 (1990).
164. V. A. Yakovleva, O. A. Merkulova, G. M. Karataeva, et al., Astronomy Letters **42** (4), 215 (2016).
165. H. Yang, Y.-H. Chu, E. D. Skillman, and R. Terlevich, Astron. J. **112**, 146 (1996).
166. A. V. Zasov and A. V. Moiseev, Proc. IAU Syposium **194**, 279 (1999).
167. A. V. Zasov and O. K. Sil'chenko, ASP Conf. Ser. **91**, 207 (1996).

Scanning Fabry–Perot Interferometer of the 6-m SAO RAS Telescope

A. V. Moiseev[1]

[1] Special Astrophysical Observatory, Russian Academy of Sciences, Nizhnii Arkhyz, 369167 Russia

The scanning Fabry–Perot interferometer (FPI)—is the oldest method of optical 3D spectroscopy. It is still in use because of the high spectral resolution it provides over a large field of view. The history of the application of this method for the study of extended objects (nebulae and galaxies) and the technique of data reduction and analysis are discussed. The paper focuses on the performing observations with the scanning FPI on the 6-m telescope of the Special Astrophysical Observatory of the Russian Academy of Sciences. The instrument is currently used as a part of the SCORPIO-2 multimode focal reducer. The results of studies of various galactic and extragalactic objects with the scanning FPI on the 6-m telescope—star-forming regions and young stellar objects, spiral, ring, dwarf and interacting galaxies, gas subsystems associated with the ionization cones of active galactic nuclei, galactic winds, etc. are briefly discussed. Further prospects for research with the scanning FPI of the Special Astrophysical Observatory of the Russian Academy of Sciences are discussed.

Keywords: *techniques: interferometric—techniques: image processing—techniques: imaging spectroscopy—instrumentation: interferometers*

Monthly Notices
of the
ROYAL ASTRONOMICAL SOCIETY

MNRAS **478,** 3386–3409 (2018)
Advance Access publication 2018 May 4

doi:10.1093/mnras/sty1158

Star formation complexes in the 'galaxy-sized' supergiant shell of the galaxy Holmberg I

Oleg V. Egorov,[1,2]★ Tatiana A. Lozinskaya,[1] Alexei V. Moiseev[1,2,3] and Grigorii V. Smirnov-Pinchukov[1,4]

[1]*Sternberg Astronomical Institute, Lomonosov Moscow State University, Universitetsky pr. 13, Moscow 119234, Russia*
[2]*Special Astrophysical Observatory, Russian Academy of Sciences, Nizhny Arkhyz 369167, Russia*
[3]*Space Research Institute, Russian Academy of Sciences, Profsoyuznaya ul. 84/32, Moscow 117997, Russia*
[4]*Max Planck Institute for Astronomy, Konigstuhl 17, D-69117 Heidelberg, Germany*

Accepted 2018 April 27. Received 2018 February 8; in original form 2018 April 19

ABSTRACT

We present the results of observations of the galaxy Holmberg I carried out at the Russian 6-m telescope in the narrow-band imaging, long-slit spectroscopy, and scanning Fabry–Perot interferometer modes. A detailed analysis of gas kinematics, ionization conditions, and metallicity of star-forming regions in the galaxy is presented. The aim of the paper is to analyse the propagation of star formation in the galaxy and to understand the role of the ongoing star formation in the evolution of the central 'galaxy-sized' supergiant H I shell (SGS), where all regions of star formation are observed. We show that star formation in the galaxy occurs in large unified complexes rather than in individual giant H II regions. Evidence of the triggered star formation is observed both on scales of individual complexes and of the whole galaxy. We identified two supernova-remnant candidates and one late-type WN star and analysed their spectrum and surrounding-gas kinematics. We provide arguments indicating that the SGS in Holmberg I is destructing by the influence of star formation occurring on its rims.

Key words: ISM: bubbles – ISM: kinematics and dynamics – ISM: supernova remnants – galaxies: individual: Holmberg I – galaxies: irregular – galaxies: star formation.

1 INTRODUCTION

The origin of multiple kpc-scale supergiant shells (SGSs) and holes in the H I discs of galaxies is a topic of lively discussions, yet it is now not an intriguing issue. Dwarf irregular (dIrr) galaxies served as the main testing ground to study SGSs with sizes up to 2–3 kpc and a lifetime of hundreds Myr. Today it is clear that dwarf galaxies sustain a high SF efficiency over several hundred Myr and even up to 1000 Myr in some cases (McQuinn et al. 2009, 2010a,b) with local short starbursts occurring during this period. Such a long period of intense star formation provides sufficient energy from stellar winds and supernovae from multiple generations of stars to drive formation of the observed holes and SGSs (see e.g. Weisz et al. 2009a,b; Cannon et al. 2011a,b).

Today the study of short local current starburst events usually occurring on the rims of SGSs seems to be most interesting. Such regions of star formation are observed as the extended complexes of ionized gas embedded in the walls of H I SGSs. It is important to understand what triggers these local starburst events and how the ongoing star formation affects the evolution of an H I SGS. A new burst of star formation can either help an SGS grow to larger sizes or push the neutral gas back into the central hole and/or outside the SGS destroying the giant structure. According to Warren et al. (2011), the interplay between these effects will ultimately define whether a galaxy will or will not form a large H I hole.

In order to shed light on the highlighted topic, we previously studied two well-known SGSs in the irregular galaxies IC 2574 (Egorov et al. 2014) and Holmberg II (Egorov et al. 2017). Both galaxies contain a large number of H I SGSs, while bright regions of the ongoing star formation are observed only in the walls of few of them. Such a picture of the H I distribution and star formation is typical of many irregular and spiral galaxies (see e.g. Bagetakos et al. 2011). In Egorov et al. (2017), we showed that star formation on the rims of an SGS can often be a result of its collision with other neighbouring H I SGSs. The existing models of collided superbubbles also support this possibility (e.g. Chernin, Efremov & Voinovich 1995; Ntormousi et al. 2011; Kawata et al. 2014; Vasiliev & Shchekinov 2017).

In this work, we focus on another type of galaxy with SGSs. Some dIrr galaxies contain a galaxy-sized central H I supershell that becomes the main feature of the ISM encompassing the whole optical disc. The most striking examples of such galaxy-sized SGSs might be observed in DDO 88 (Simpson, Hunter & Knezek 2005),

★ E-mail: egorov@sai.msu.ru

© 2018 The Author(s)
Published by Oxford University Press on behalf of the Royal Astronomical Society

Downloaded from https://academic.oup.com/mnras/article-abstract/478/3/3386/4992763
by Special Astrophysical Observatory of the Russian Academy of Sciences user
on 06 August 2018

Table 1. Published parameters of Holmberg I.

Parameter	Value	Reference
	DDO 63	
Alternative names	UGC 5139	
	KDG 57	
RA (2000)	$09^h40^m32.3^s$	
Dec. (2000)	$+71°11'11''$	
D (Mpc)	3.9	Dalcanton et al. (2009)
M_B (mag)	−14.8	Walter et al. (2008)
R_{25} (kpc)	1.9	Walter et al. (2008)
$R_{\rm H\,I}$ (kpc)	4.5	Bagetakos et al. (2011)
$M_{\rm H\,I}$ (10^8 $M_\odot$)	1.4	Bagetakos et al. (2011)
$V_{\rm sys}$ (km s^{-1})	140	Oh et al. (2011)
log(SFR$_{\rm H\alpha}$) ($M_\odot$ yr^{-1})	−2.21	Karachentsev, Makarov & Kaisina (2013)
12 + log(O/H)	7.9	Moustakas et al. (2010)

Sextans A (Skillman et al. 1988; van Dyk, Puche & Wong 1998), M81 dwA (Sargent, Sancisi & Lo 1983; Westpfahl & Puche 1994), SagDIG (Young & Lo 1997), Holmberg I (Tully et al. 1978; Ott et al. 2001). The latter galaxy is the object of our study in this paper.

Holmberg I is a low-mass dIrr galaxy (IAB(s)m according to the de Vaucouleurs et al. 1991 classification) belonging to the M81 group. Its main parameters are listed in Table 1.

The first H I radio observations of Holmberg I performed at the Westerbork radio telescope were presented by Tully et al. (1978). Puche & Westpfahl (1994) and Walter et al. (2008) published the data obtained at the VLA. According to these observations, the H I disc in Holmberg I shows the low velocity dispersion $\sigma_{\rm H\,I} \sim 9$ km s^{-1} and a slow rotation (Oh et al. 2011; Stilp et al. 2013). Due to the low inclination ($i = 10-14°$), the estimates of the vertical H I scale height by different authors are very uncertain: $h = 250-550$ pc according to Ott et al. (2001), 640 pc according to Bagetakos et al. (2011), and 191 ± 41 pc in Stilp et al. (2013).

The most detailed analysis of H I in Holmberg I was performed by Ott et al. (2001). The authors showed that the H I distribution in Holmberg I is dominated by the central supergiant shell; its morphological centre is offset by 0.75 kpc with respect to the dynamical centre of the galaxy. From a comparison with isochrones, as well as from dynamical modelling based on the H I data, the authors derived that the age of the central supergiant H I shell is equal to 80 ± 20 Myr. Later Bagetakos et al. (2011) have detected five other H I holes of a smaller size in the galaxy.

Vorobyov & Basu (2005) carried out numerical simulations of the ISM structure in Holmberg I. They investigated three scenarios of the central H I hole formation: multiple supernova (SN) explosions, a single gamma-ray burst, and a vertical impact of a high-velocity cloud. Multiple SN explosions were shown to reproduce the H I morphology of Holmberg I more accurately.

A comparison of optical images and the H I distribution shows that the regions of ionized gas are observed on the rims of the central H I supergiant shell in Holmberg I (see Fig. 1). The H II regions in the galaxy were catalogued by Miller & Hodge (1994). The authors identified 32 H II regions and measured their sizes and luminosities. Only a few of them were previously spectroscopically observed. The metallicity of a few bright H II regions in Holmberg I has been studied earlier by Miller & Hodge (1996), Croxall et al. (2009), and Moustakas et al. (2010). Berg et al. (2012) performed a deep spectroscopy of one H II region in the galaxy and estimated the oxygen abundance using the direct method. These studies have showed that the galaxy has a low oxygen abundance 12 + log (O/H) ∼ 7.9 that is typical of its luminosity.

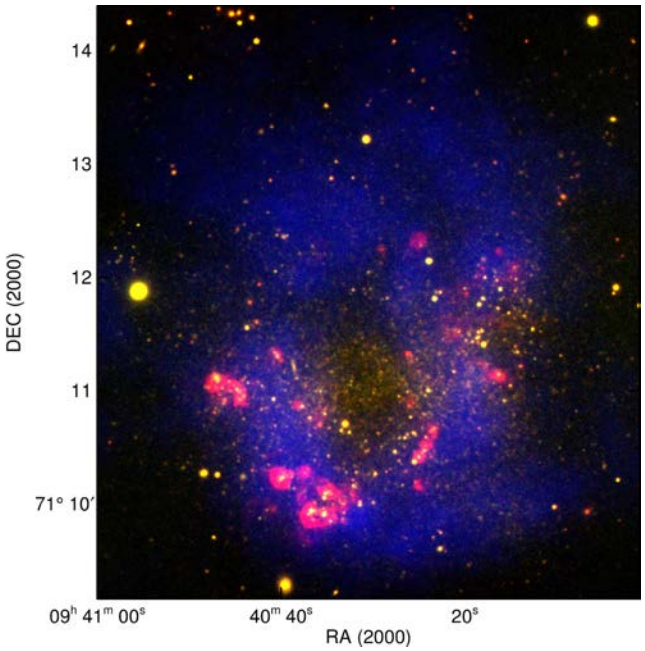

Figure 1. False-colour image of Holmberg I. Blue colour shows the H I emission in 21 cm taken from the LITTLE THINGS survey (Hunter et al. 2012); red and yellow colours show the optical images presented in this work and trace the emission in the H α line and the stellar population, respectively.

In this paper, we analyse the gas kinematics and the emission spectrum of star-forming regions in the galaxy Holmberg I and discuss the origin of these regions. Our aim is to recognize how star formation affects the evolution of H I SGSs using Holmberg I as an example. The paper is organized as follows. Section 2 presents the details of performed observations and data reduction. Section 3 describes the young stellar population in the galaxy. In Section 4, we analyse the general H I kinematics of the galaxy and perform a search for expanding shells and supershells in H I and H α. Section 5 is dedicated to the analysis of the ionized gas morphology in Holmberg I, while in Section 6 we describe the spectroscopic properties of the individual H II regions. In Section 7, we discuss the inferred results and in Section 8 summarize the main conclusions.

2 OBSERVATIONS AND DATA REDUCTION

2.1 Optical FPI observations

The observations were carried out at the prime focus of the 6-m telescope of the Special Astrophysical Observatory of the Russian Academy of Sciences (SAO RAS) using the scanning Fabry–Perot interferometer (FPI) – IFP751 – mounted inside the SCORPIO-2 multimode focal reducer (Afanasiev & Moiseev 2011). The operating spectral range around the H α emission line was cut by a bandpass filter with the FWHM ≈ 14 Å bandwidth. During the scanning process, we have consecutively obtained 40 interferograms at different distances between the FPI plates. The log of these observations and the parameters of other data sets are given in Table 2, where $T_{\rm exp}$ is the exposure time, FOV is the field of view, arcsec px^{-1} is the pixel size on the final images, θ is the final angular resolution, λ_c

Downloaded from https://academic.oup.com/mnras/article-abstract/478/3/3386/4992763
by Special Astrophysical Observatory of the Russian Academy of Sciences user
on 06 August 2018

Table 2. Log of the observations.

Data set	Date of obs.	T_{exp} (s)	FOV (arcmin)	arcsec px^{-1}	θ (arcsec)	Sp. range	λ_c (Å)	$\delta\lambda$ or FWHM (Å)
FPI #1	2014 Dec 19/20	40 × 300	6.1 × 6.1	0.71	2.1	8.8 Å around Hα	–	0.48 (22 km s^{-1})
FPI #2	2015 Nov 04/05	40 × 300			1.5			
LS PA = 142	2016 Mar 02/03	6600	1/60 × 6.1	0.36	3.5	3600–7070	–	5.2
LS PA = 150	2017 Dec 09/10	3600			1.5			4.7
LS PA = 212	2017 Dec 08/09	8100			2.2			4.7
LS PA = 259	2016 Feb 10/11	4500			2.2			4.5
LS PA = 259	2015 Nov 05/06	2700			1.0			4.5
Image FN655	2015 Apr 25/26	3600	6.1 × 6.1	0.36	1.2	Hα + [N II]	6559	97
Image FN674	2017 May 28/29	2700			1.3	[S II] 6717+ 6731	6733	60
Image FN501	2017 May 28/29	1800			1.4	[O III] 5007	5012	119
Image FN608	2015 Apr 25/26	1200			1.2	Continuum	6099	166
Image FN712	2015 Apr 25/26	1200			1.2	Continuum	7137	209
Image SED525	2017 May 28/29	900			1.6	Continuum	5271	251

is the central wavelength of the filters used, $\delta\lambda$ is the final spectral resolution, and FWHM is a bandwidth of the filters used.

The data reduction was performed using a software package running in the IDL environment. For a detailed description of the data reduction algorithms and software, see Moiseev (2002), Moiseev & Egorov (2008), and Moiseev (2015). After the initial reduction, sky line subtraction, photometric and seeing corrections made using the reference stars, and wavelength calibration, the observed data were combined into data cubes, where each pixel in the field of view contains a 40-channel spectrum. We observed the galaxy at two position angles in order to remove the parasitic ghost reflection. These data were reduced separately to get the wavelength cubes of the object. The analysis of Hα line profiles was carried out using the multicomponent Voigt fitting (Moiseev & Egorov 2008) that yields flux, line-of-sight velocity, and velocity dispersion corrected for instrumental broadening for each component as an output.

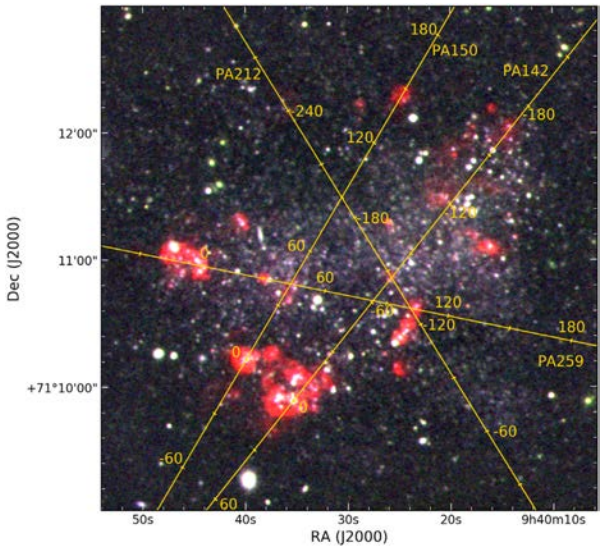

Figure 2. False-colour image of Holmberg I. Red colour corresponds to the image obtained with the narrow-band filter centred on the Hα emission line, while the blue and green channels show the emission in the continuum (see Section 2.3 for details). The slit positions used during spectroscopic observations are overlaid.

2.2 Long-slit spectroscopic observations

We observed the galaxy Holmberg I in the long-slit mode of the SCORPIO-2 focal reducer at 6-m SAO RAS telescope. Using the VPHG1200@540 grism as a disperser, we have obtained spectra with four slit positions (PA = 142, PA = 150, PA = 212, and PA = 259, see Fig. 2). The length of the used slit was 6 arcmin, while its width was 1 arcsec. The spectral resolution estimated as the FWHM of air-glow emission lines varied from 4.5 to 5.2 Å.

The data reduction was performed in a standard way using the IDL-based pipeline for reducing long-slit spectroscopic data obtained with SCORPIO-2. The data reduction includes the bias subtraction, line curvature and flat-field corrections, linearization, and air-glow lines subtraction. We linearized the spectra using the reference spectrum of the He–Ne–Ar lamp obtained during observations. In order to calibrate the spectra to the absolute intensity scale, we observed one of spectrophotometric standards (AGK 81d266 and G191B2B) at a close zenith distance immediately after or before the object.

The spectrum corresponding to the slit position PA = 259 was observed twice with different exposures and at different seeings. In order to increase the signal-to-noise ratio, we have combined the two observations into a single spectrum for a further analysis. Before that, the spectrum with a better seeing was convolved with the Gaussian kernel to achieve the same spatial resolution as for the second one.

It is worth noting that the spectrum with PA = 150 was observed in bad weather conditions. The unstable transparency due to clouds has made the flux calibration unreliable for that spectrum, yet the relative flux ratios of nearby emission lines analysed in this paper are correct.

The main purpose of the long-slit observations was to analyse the age, ionization conditions, and gas metallicity of H II regions in the galaxy. Hence, we were interested in the emission-line fluxes and equivalent width (EW). To measure the fluxes of emission lines we used our own software working in the IDL and based on the MPFIT (Markwardt 2009) routine. The Gaussian fitting was applied to measure the integrated line fluxes of each studied region. To subtract a spectrum underlying stellar population, we performed its

Downloaded from https://academic.oup.com/mnras/article-abstract/478/3/3386/4992763
by Special Astrophysical Observatory of the Russian Academy of Sciences user
on 06 August 2018

modelling using the ULYSS[1] package (Koleva et al. 2009). However, its influence on the measured emission-line fluxes of H II regions appears to be almost negligible in our case, so we decided to skip this procedure in order to not add systematic errors, which can be produced in case of an unreliable model. For estimating the final uncertainties of the measured line fluxes, we quadratically added the errors propagated through all data-reduction steps to the uncertainties returned by the MPFIT.

A reddening correction was applied to each spectrum before estimating the line-flux ratios listed in the paper. For that we derived the $E(B-V)$ colour excess from the observed Balmer decrement and then used the Cardelli, Clayton & Mathis (1989) curve parametrized by Fitzpatrick (1999) to perform a reddening correction. In this paper, we use the following abbreviations of the emission-line flux ratios: [S II]/H α is F([S II] 6717,6731 Å)/F(H α); [N II]/H α is F([N II] 6584 Å)/F(H α); [O III]/H β is F([O III] 5007 Å)/F(H β).

2.3 Narrow-band imaging

Deep optical images of Holmberg I in the H α, [S II], and [O III] emission lines were taken at the prime focus of the 6-m SAO RAS telescope with the SCORPIO (Afanasiev & Moiseev 2005) and SCORPIO-2 multimode focal reducers using the narrow-band filters FN655, FN674, and FN501, respectively. The transmission curves of each used filter can be found on the SCORPIO-2 website.[2]

We used the broader-band FN608, FN712, and SED525 filters centred on the continuum to subtract stellar contamination from the images obtained in the same night.

In order to calibrate the images to the absolute intensity scale, we observed the spectrophotometric standard AGK 81d266 with each line-centred filter immediately after the object at a close zenith distance. The obtained images were additionally corrected for the interstellar reddening using the Cardelli et al. (1989) curve parametrized by Fitzpatrick (1999) and the colour excess $E(B-V)=0.05$ derived from our spectra.

IIBecause the FWHM of the FN655 filter is broader than the distance between the H α and [N II] emission lines, the image in this filter is contaminated by the [N II] 6548, 6584 Å emission. According to our spectroscopic observations, the [N II]/H α flux ratio is 0.05−0.07 for Holmberg I (see Section 6). Since the transmission of the FN655 filter is lower in the region of [N II] emission lines than that of H α, we conclude that the [N II] contamination of H α images does not exceed 5 per cent.

A similar situation also takes place for the FN501 filter – the [O III] 5007 Å image is contaminated by the [O III] 4959 Å line that is three times fainter. Taking it into account, as well as the differences of the FN501 filter transmission at 5007 and 4959 Å, we multiplied the fluxes of the final [O III] image to 0.8 to reveal only [O III] 5007 Å emission-line contribution.

Our final narrow-band images show surface brightness value at the 3σ level corresponding to (3.3, 2.4, 3.6) $\times$ 10^{-17} erg s^{-1} cm^{-2} arcsec^{-2} in the H α, [S II], and [O III] emission lines, respectively.

In order to get the [O III]/H β flux ratio from our images, we took into account a theoretical ratio of H α/H $\beta=2.86$ for $T_e=10\,000$ K and used the reddening-corrected H α image divided to this value to estimate the H β flux. All the [O III]/H β maps and values derived from the images and used further in the paper were obtained in that way. Because of the low metallicity and hence the low dust content in Holmberg I, as well as of the small variations of $E(B-V)$ (according to our spectra, see Section 6), this procedure yields realistic values of the [O III]/H β flux ratio in our case. The performed Monte Carlo simulations showed that typical relative uncertainties of that ratio for our data are 10 per cent for the signal-to-noise ratio S/N = 30 and 30 per cent for S/N = 5. At the same time these uncertainties should be 5 and 27 per cent, respectively, if direct measurements of the H β flux were available.

2.4 Multiwavelength archival data used

We used the archival VLA data in the H I 21-cm line from the LITTLE THINGS survey (Hunter et al. 2012) for studying the H I gas distribution and kinematics. In this work, we used the natural-weighted data cube with the angular resolution beam = 14.7 × 12.7 arcsec and velocity scale 2.6 km s^{-1} per channel.

In order to analyse the stellar population, we used the images of Holmberg I obtained with the ACS/WFC camera at the *Hubble Space Telescope* (*HST*) with the *F*555*W* and *F*814*W* wide-band filters. These images were obtained as part of a larger *HST* program aimed at studying M81 Group dwarf galaxies (GO-10605; PI: Skillman; Weisz et al. 2008) and were reprocessed within the ACS Nearby Galaxy Survey Treasury (ANGST) project in Dalcanton et al. (2009). In this paper, we used their published results of stellar photometry.

The archival far-ultraviolet (FUV) images from the *GALEX* observatory were used for analysing the recent star formation activity in Holmberg I. The calibrated data published by Hunter, Elmegreen & Ludka (2010) were downloaded from the LITTLE THINGS archive.

3 YOUNG STELLAR POPULATION

The first studies of the young stellar population in Holmberg I were performed by Hoessel & Danielson (1984) with an early CCD imaging. They found that the galaxy has a small number of stars with the masses $M > 20\,M_\odot$, and that even the majority of the $16\,M_\odot$ stars appear to have evolved significantly to the red.

The abilities of *HST* images allowed one to study the resolved stellar population and star formation history in the galaxy. Weisz et al. (2008) presented the spatial density distribution of blue and red stars in Holmberg I (see their fig. 9). They found that older red stars are highly concentrated in the interior of the central H I SGS, while the blue stars location correlates with the H II regions. The authors showed that Holmberg I had two episodes of the intense star formation – the ancient one that occurred several Gyr ago and the current one that started in the last 100 Myr.

We used the available results of the *HST* photometry of individual stars in Holmberg I to identify main-sequence OB stars which could be responsible for ionization of the observed H II complexes. The selection of these stars was performed following the procedure described in Bastian et al. (2011). Analysing the colour–magnitude diagram (CMD), shown in the top panel of Fig. 3, we identified 121 objects that should be young OB stars, 40 stars among them have $M_{F555W} < -5$ and give the major contribution to ionization. Their location is shown in Fig. 4 in light blue; the size of star symbols correlates with their number of ionizing quanta on the logarithmic scale. It is worth noting, however, that since the main-sequence branch is not very clearly resolved in the CMD, some of the detected OB stars might not be OB stars actually.

[1] http://ulyss.univ-lyon1.fr
[2] https://www.sao.ru/hq/lsfvo/devices/scorpio-2/filters_eng.html

Downloaded from https://academic.oup.com/mnras/article-abstract/478/3/3386/4992763
by Special Astrophysical Observatory of the Russian Academy of Sciences user
on 06 August 2018

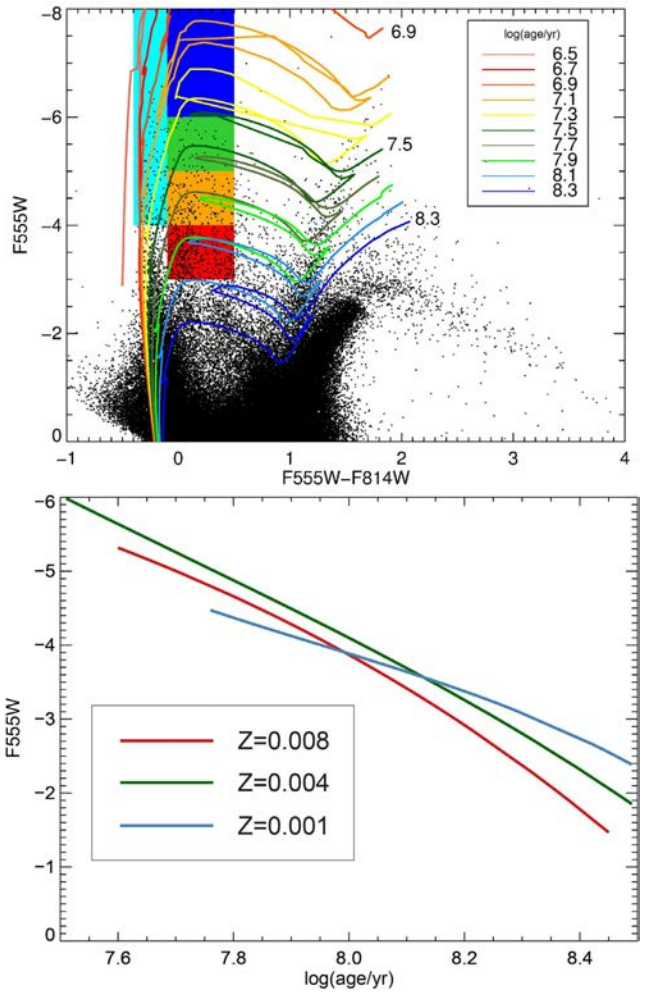

Figure 3. Top panel: observed CMD of the galaxy Holmberg I. The coloured lines correspond to the PARSEC isochrones (Bressan et al. 2012) computed with the CMD 2.9 code for different ages and for the metallicity $Z = 0.004$. The coloured rectangles show the areas filled by stars of different ages. Cyan – OB stars younger than 20 Myr; blue – BHeB (Blue Helium Burners) stars younger than 30 Myr; green – BHeB of ages from 30 to 55 Myr; orange – BHeB of ages from 55 to 115 Myr; red – BHeB of ages from 115 to 190 Myr. Bottom panel: dependence of the $F555W$ magnitude on the age of BHeB stars for different metallicities.

Many previous studies (see e.g. Dohm-Palmer et al. 1997; Weisz et al. 2008; Bastian et al. 2011) used the position of Blue Helium Burner stars (BHeB) in the CMD as a good indicator of their age. To select BHeB stars of different ages in Holmberg I, we used the PARSEC isochrones (Bressan et al. 2012; Chen et al. 2014, 2015; Tang et al. 2014) computed with the CMD 2.9 code.[3] As is shown in the bottom panel of Fig. 3, the $F555W$ luminosity of such stars almost linearly correlates with their age. We plotted the isochrones for the metallicity $Z = 0.004$ and age $\log\tau = 6.7$–9.0 over the CMD shown in the top panel of Fig. 3. The coloured regions in the CMD represent different stages of stellar evolution. The cyan region is for young main-sequence OB stars (mostly O stars) with absolute $F555W$ magnitude less than -4; their age is smaller than 20 Myr. The colours from blue to red show the location of BHeBs of different ages. The blue colour corresponds to the stars younger than 30 Myr, green – to those between 30 and 55 Myr, orange – to the stars with ages between 55 and 115 Myr, and the red area contains the stars with ages from 115 to 190 Myr. Note that stars at other evolution stages should also appear in the mentioned areas, but the BHeB stage is noticeably longer, and we can expect most of the detected stars to be at that stage. The locations of the detected OB and BHeB stars are shown in Fig. 4.

As follows from Fig. 4, the main-sequence O stars that trace the areas of the ongoing star formation are indeed located mainly in the H II regions. The distribution of BHeBs traces the location of regions of the recent star formation and as one can see from Fig. 4, most BHeBs aged between 30 and 55 Myr are located inside the central SGS and northwestern supershell. The older BHeBs are distributed more or less uniformly which agrees with the results of Bastian et al. (2011) for other galaxies.

4 IONIZED- AND NEUTRAL-GAS KINEMATICS

4.1 General neutral-gas kinematics

The previous studies (Ott et al. 2001; Oh et al. 2011) of the neutral-gas kinematics of Holmberg I have shown that this galaxy rotates slowly and demonstrates significant radial motions. The shapes of rotation curves reported by different authors look similar, yet the maximum velocity and the corresponding radius differ (see fig. 9 in Ott et al. 2001 and fig. A.10 in Oh et al. 2011). These discrepancies might be explained by a low inclination of Holmberg I and significant radial motions. All these factors make the analysis difficult and a bit controversial.

For analysing the gas kinematics, we would like to subtract the component corresponding to the regular galaxy rotation from any data cube we obtained. Such a procedure allows us to highlight the local gas motions caused by a stellar feedback or gas inflow/outflow processes. This 'derotation' method and its advantages are described in Egorov et al. (2014).

We tried to model the observed H I velocity field by tilted rings. Significant discrepancies were found towards the northwestern and southern outer parts of the galaxy, where the influence of the ram pressure or tidal interaction are probable. Because of that, we found that a simple tilted-ring model is not applicable in the case of Holmberg I, and the inclusion of warp and radial flows is necessary. However, since we are interested mostly in the inner part of the galaxy, the construction of such a detailed model is out of the scope of our paper.

In this paper for reconstruction of the velocity map corresponding to the galaxy rotation, we used the results of a more detailed modelling performed by Oh et al. (2011). The inclination $i = 14^\circ$ and the position angle PA $= 45^\circ$ were adopted. Using this model, we have found that the residual motions in the H I do not exceed 8 km s^{-1} in the area surrounded by the SGS. We subtracted the obtained model of the Holmberg I circular rotation from all H I and H α data cubes used further.

4.2 Searching for H I and H α superbubbles

Up to now, seven H I supershells in Holmberg I were known. The central galaxy-sized SGS was studied in detail by Ott et al. (2001); these authors also mentioned the existence of a smaller H I supershell (#7 in Fig. 5) in the southeastern part of the SGS which is clearly seen on the H I map. Bagetakos et al. (2011) found six H I holes and expanding supershells (including the central SGS) by

[3] http://stev.oapd.inaf.it/cmd

Downloaded from https://academic.oup.com/mnras/article-abstract/478/3/3386/4992763
by Special Astrophysical Observatory of the Russian Academy of Sciences user
on 06 August 2018

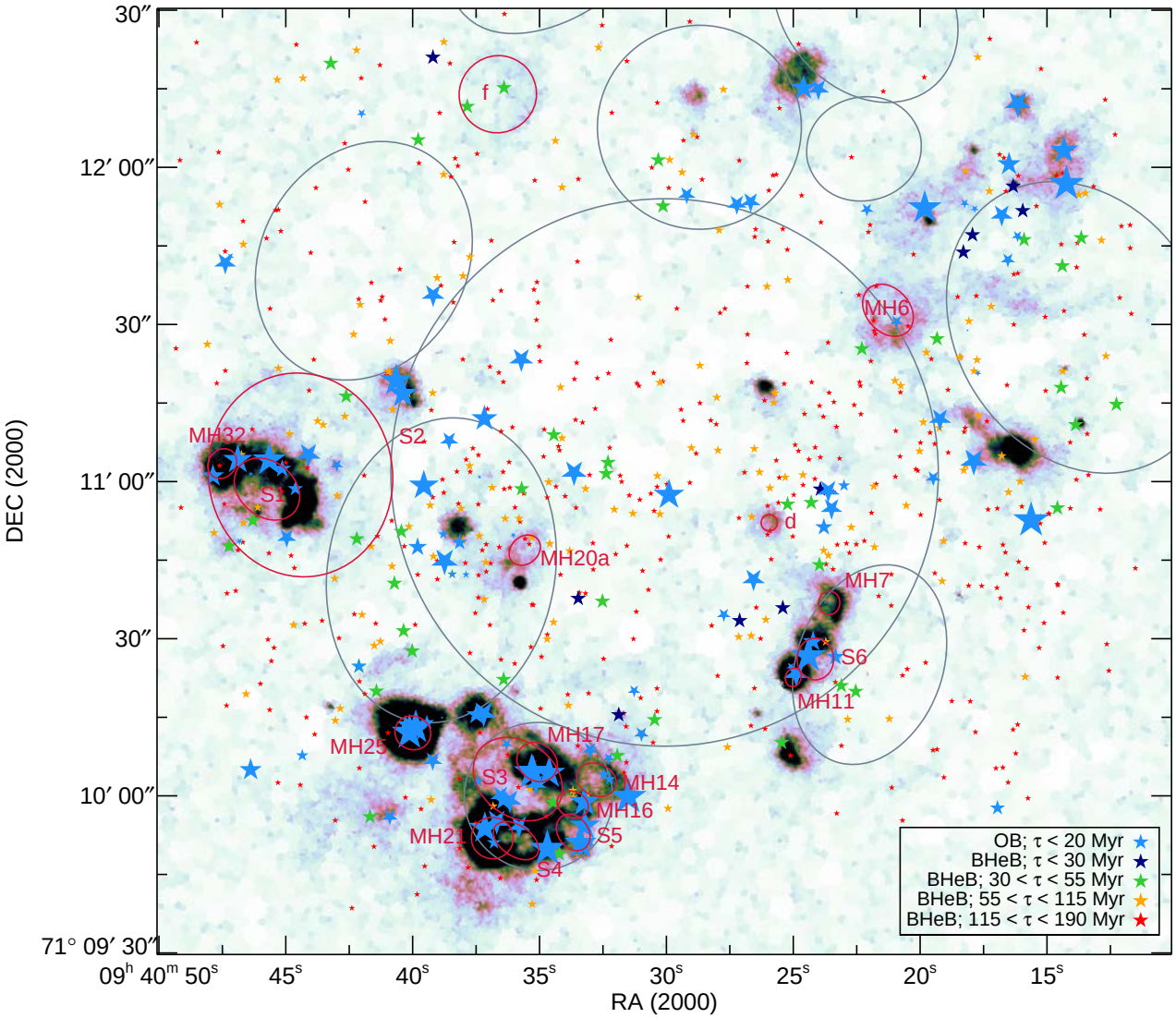

Figure 4. Distribution of young stars of different ages shown on the Hα emission-line image of Holmberg I. As well as in Fig. 3, different colours correspond to different ages: light blue – OB stars younger than 20 Myr; dark blue – BHeB stars younger than 30 Myr; green – BHeB of ages from 30 to 55 Myr; orange – BHeB of ages from 55 to 115 Myr; red – BHeB of ages from 115 to 190 Myr. Red and grey ellipses show the location of the identified Hα and H I shells, respectively (see Section 4.2).

a visual inspection of channel maps and further confirmation by analysing the position-velocity (PV) diagrams. Warren et al. (2011) derived a slightly larger size of the SGS than other authors using the reprocessed H I data. The location of all the mentioned H I shells is shown in Figs 4 and 5, and their properties are listed in Table 3. We adopt a diameter of shell #7 given by Ott et al. (2001) (recalculated for a distance of 3.9 Mpc) and that for shell #4 (SGS) given by Warren et al. (2011). For all the other H I shells, we used the parameters listed in table 7 of Bagetakos et al. (2011).[4]

In this paper, we are interested in the distribution and kinematics of the H I supershells in the context of their relation to the young stellar population and to the regions of the current star formation. We analysed the H I line profile in the vicinity of the star-forming regions in the SGS and constructed a large number of PV diagrams crossing different parts of the SGS. Fig. 5 shows several examples of them. One can see that almost all the H I supershells mentioned above exhibit approaching and/or receding sides in these PV diagrams (so-called velocity ellipse). Based on the analysis of the PV diagrams and two-component H I line fitting, we confirm previously published values of the expansion velocities for all of these supershells except for #2. For the latter, we found V_{exp} to be significantly lower than that published by Bagetakos et al. (2011). Moreover, since the largest separation between two components of the H I line profile inside shell #2 is observed at the border with shell #3, we propose that shell #2 might be just a part of larger shell #3.

As follows from the demonstrated PV diagrams, clear signs of 'velocity ellipses' are also seen outside the previously known H I supershells. Based on that, we detect four new expanding H I supershells denoted as #8–#11. Their borders were derived from a visual inspection of the PV diagrams crossing the shell in different directions. Borders of shells #8 and #11 are seen on the H I integral

[4]We corrected a misprint in their table – radii are listed instead of diameters for Holmberg I which follows from a comparison with other works and the available H I data.

Downloaded from https://academic.oup.com/mnras/article-abstract/478/3/3386/4992763
by Special Astrophysical Observatory of the Russian Academy of Sciences user
on 06 August 2018

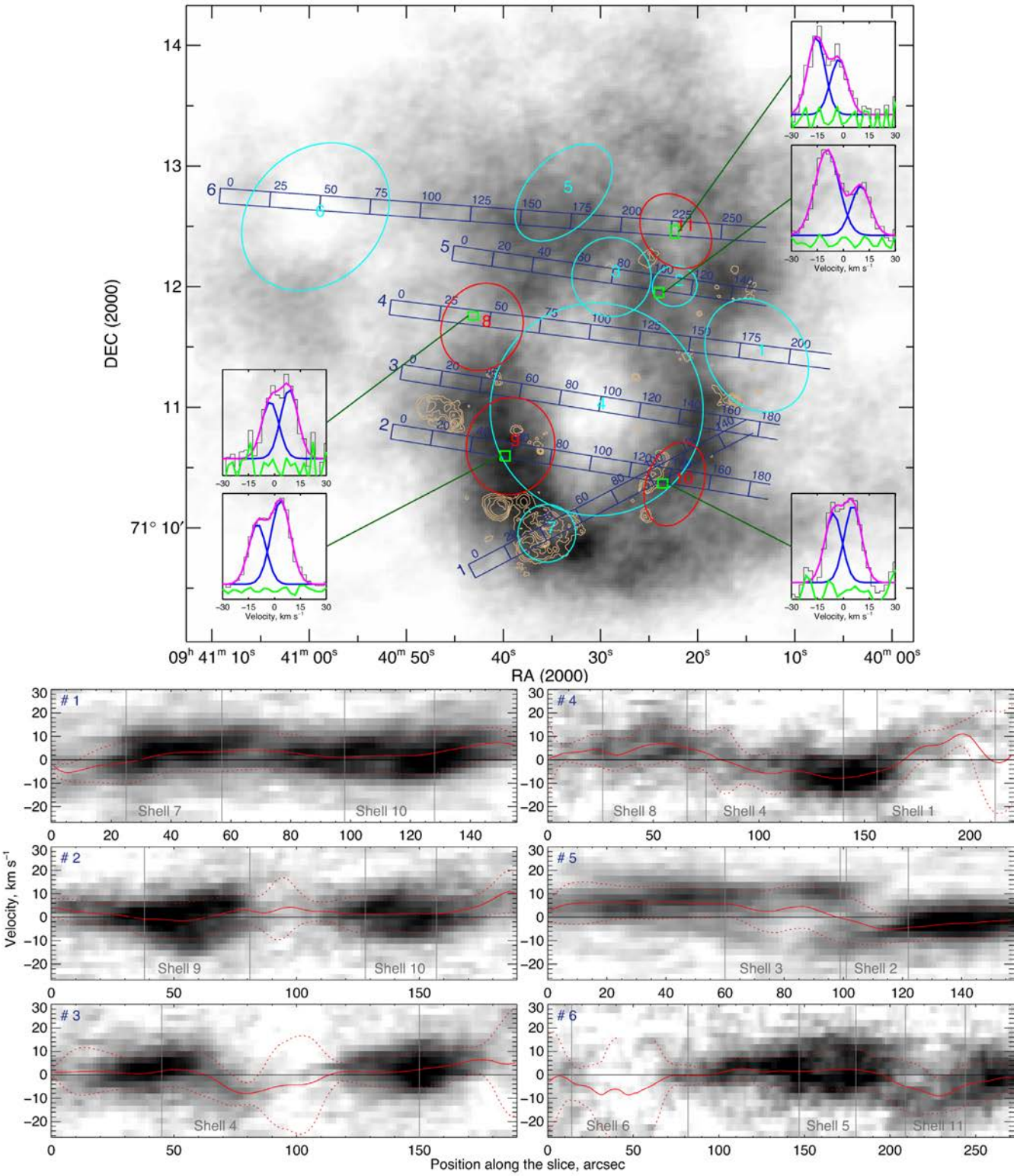

Figure 5. Location of the slices for the PV diagrams in the H I image of Holmberg I (top), which are shown as examples in the bottom panels. The contours show the H α flux distribution. Cyan ellipses denote the location of the previously known H I supershells; the red colour shows the borders of the expanding H I supershells discovered in this work. The examples of the H I line profiles integrated over the area inside green squares and the results of their multicomponent fitting are shown: black line corresponds to the observed line profile, red – to the model, blue – to individual components, and green – to residuals. Vertical grey lines in the PV diagrams show the edges of supershells. Red solid and dotted lines there trace the intensity-weighted mean velocity and its standard deviation, respectively.

Downloaded from https://academic.oup.com/mnras/article-abstract/478/3/3386/4992763
by Special Astrophysical Observatory of the Russian Academy of Sciences user
on 06 August 2018

Table 3. Parameters of the identified H I and H II shells. The expansion velocities of H II regions were measured from shifted details in the wings of the H α line profiles. The values of V_{exp} and the age in brackets were obtained using equation (1).

Name	D (pc)	V_{exp} (km s^{-1})	Age (Myr)
	H I shells		
1	1008	6	50
2	400	10	12
3	745	12	19
4	2000	6	50
5	858	12	21
6	1371	6	69
7	528	7	23
8	796	5	48
9	874	7	37
10	660	6	33
11	679	6	34
	H II shells		
S1	229	38	1.8
S2	708	<22	>9.7
S3	310	(34)	(2.7)
S4	144	(32)	(1.3)
S5	126	(35)	(1.1)
S6	143	27	1.6
MH6	184	20	2.8
MH7	82	85	0.3
MH11	63	(20)	(1.0)
MH14	132	(29)	(1.3)
MH16	106	(39)	(0.8)
MH17	145	(24)	(1.8)
MH20a	111	25(17)	1.3 (2.0)
MH21	152	(29)	(1.6)
MH25	127	(20)	(2.0)
MH32	106	31 (27)	1.0 (1.2)
d	60	74	0.2
f	282	<22	>3.8

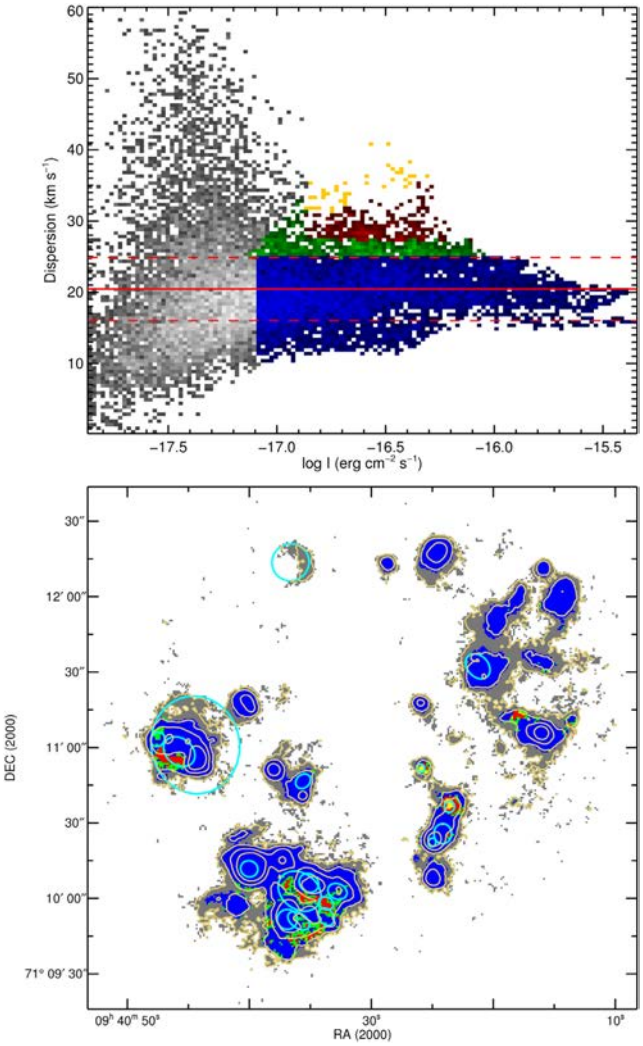

Figure 6. H α intensity–velocity dispersion diagram for Holmberg I (top). The red solid horizontal line marks the intensity-weighted mean velocity dispersion of ionized gas in the galaxy and the dashed lines – its standard deviation. The bottom plot shows the location of regions marked by different colours in the $I-\sigma$ diagram. The contours correspond to the lines of equal H α intensity. Cyan ellipses show the borders of shell-like structures appearing in the H α image (see Fig. 4).

map, while shells #9 and #10 do not appear on it. The last two are implicitly seen on the channel maps. The expansion velocities of these new detected H I shells were derived with the H I line fitting (see examples in Fig. 5); they correspond to $V_{exp} = 5-7$ km s^{-1}.

We estimated the kinematic ages of all the H I supershells in terms of the Weaver et al. (1977) model by the relation $t = 0.3D/V_{exp}$, where D is the diameter in pc, V_{exp} is the expansion velocity in km s^{-1}, and t is the age in Myr. All the values are listed in Table 3.

Thus, the central SGS exhibits a number of local expanding H I supershells of a smaller size on its rim; all H I supershells are plotted in Fig. 4.

By analysing the H α image we identified 18 shell-like emission structures. They mostly correspond to H II regions, while six of them are faint shells between several H II regions named S1–S6. We show all the identified ionized shells in Fig. 4 by the red ellipses.

It has been shown in many studies (Muñoz-Tuñon et al. 1996; Moiseev & Lozinskaya 2012; Vasiliev, Moiseev & Shchekinov 2015a, see also references therein) that the intensity–velocity dispersion ($I-\sigma$) diagrams for ionized gas can be successfully used to identify areas where the increased velocity dispersion is caused by expanding shells. We fitted a single-component Voigt profile to the H α line profile in each pixel obtained from the FPI data cube and constructed the $I-\sigma$ diagram shown in Fig. 6. The red line in the diagram marks the intensity-weighted average velocity dispersion of ionized gas in the galaxy – $\sigma_m = 20.5 \pm 4.5$ km s^{-1}. The identical colours in the diagram (top panel) and map (bottom panel) are used to highlight the characteristic areas. Thus, the horizontal strip with a relatively low velocity dispersion and high surface brightness marked in blue corresponds to bright H II regions and includes 50 per cent of galaxy's H α flux. The areas of the increased dispersion, which are most likely associated with spectroscopically unresolved expanding shells, are shown in green, whereas the red colour corresponds to shell-like structures with the expected clear separation of the line profile components. As was shown in Moiseev & Lozinskaya (2012), the diagonal yellow lane could correspond to the presence of compact objects, which highly influence the ISM (like WR, LBV stars, supernova remnants). The remaining areas of low surface brightness corresponding to the diffuse gas and to the edges of H II regions are shown in grey.

As it follows from a comparison of $I-\sigma$ with the location of the identified ionized shells, a half of them are clearly expanding. Additionally, two areas not showing the corresponding shell-like

Downloaded from https://academic.oup.com/mnras/article-abstract/478/3/3386/4992763
by Special Astrophysical Observatory of the Russian Academy of Sciences user
on 06 August 2018

nebula appear in the $I-\sigma$ diagram as expanding superbubbles. One of them is located at the southern edge of the complex of ionized shells and might represent faint expanding superbubbles without resolved morphology, while another (in the western complex of ionized nebulae in the galaxy) coincides with the relatively bright H II region – MH4.

We tried to estimate the expansion velocities of the identified ionized superbubbles applying a multicomponent Voigt fitting to the observed Hα line profile towards the inner part of each of them (see the examples of the line profiles in Figs 8–12). Unfortunately, with the current spectral and spatial resolution only two regions – MH7 and d – show clear separated components in the line profiles. These objects are marked by the yellow colour in the $I-\sigma$ diagram and identified as probably unique energy sources. In Section 6, we will show that they are good supernova remnant candidates.

Most of the remaining shells reveal the enhanced velocity dispersion inside them, and the blue- or redshifted faint components are observed in the wings of the Hα line profile in some of them. For those objects, we used a separation between the components to estimate their expansion velocity.

A small angular size of some of the observed ionized shells results in smoothing the line profiles (even for relatively fast-expanding regions) and makes impossible the direct detection of signs of their expansion from the line profile asymmetry at the given spatial resolution. At the same time, for several H II regions we observe the maximum line-of-sight velocity dispersion σ in its centre, while it slowly decreases towards the edge. As was shown in Guerrero, Villaver & Manchado (1998), in such a case, the expansion velocity correlates well with the gradient of the line-of-sight velocity dispersion, and as we will show in Smirnov-Pinchukov & Egorov (in preparation), it can be estimated as

$$V_{\rm exp} = \alpha \times \sqrt{\sigma^2_{\rm H\,II} - \sigma^2_0}, \quad (1)$$

where $\sigma_{\rm H\,II}$ is the velocity dispersion inside the nebula, σ_0 – in its unperturbed vicinity. The coefficient α depends on the spectral resolution and on σ_0; in the case of our data $\alpha = 1.59 \pm 0.04$. The results are listed in Table 3.

Using the estimated expansion velocities, we measured a kinematic age of each ionized superbubble using the same approach as for H I supershells. The obtained values do not exceed 3 Myr for all the regions except S2 and f. These older faint supershells will be discussed in Sections 5 and 6, respectively.

It is worth noting that the estimated values of the kinematic age correspond to the expansion velocities measured by faint details in the wings of the Hα line profiles for almost all regions. Since these faint components can be of origin not related to an expanding superbubble (e.g. a local gas inflow/outflow), the calculated values of $V_{\rm exp}$ can be significantly overestimated which leads to possible underestimation of the age.

5 COMPLEXES OF IONIZED GAS AND IONIZATION BALANCE

The ionized gas in Holmberg I is distributed along the walls of the central H I SGS revealing the brightest H II regions in its southeastern part and relatively faint regions in the area between this SGS and another one in the west. Our estimate of the galaxy's Hα flux corrected for reddening $F({\rm H}\alpha) = (3.60 \pm 0.04) \times 10^{-13}$ erg s^{-1} cm^{-2} is in good agreement with the previous measurements made by Karachentsev & Kaisin (2007).

Our deep Hα images, as well as FPI data, allowed us to identify several new faint H II regions and diffuse structures that were never observed before in Holmberg I. It is clearly seen from our data that the individual H II regions in the galaxy are bound together by faint filament-like structures with a surface brightness of $0.2-1.0 \times 10^{-16}$ erg s^{-1} cm^{-2} arcsec^{-2} in the Hα line.

Based on these newly discovered faint structures joining bright nebulae, we select five unified extended complexes in Holmberg I. Further, we will show that they indeed represent physically connected complexes of the ongoing star formation. The location of these H II complexes (#1, 2, 3, 4, and NW), as well as the names of bright nebulae (according to the list of Miller & Hodge 1994) inside them, are shown in Fig. 7. The faint newly identified H II regions are named by letters.

Almost all the H II regions, except for MH10, 13, 26, e, and f are part of these selected complexes. Note, however, that a diffuse emission is observed between complex #1 and the H II region MH26. Similarly, a faint bridge in Hα is also seen between the complex NW and the H II regions MH10, 13, and e. Despite that, we do not include them in the mentioned complexes because of a large relative distance and different environment in H I (e.g. the region MH10 is located in the place where three H I supershells collide, and is separated from the complex NW by H I shell #2).

In general, the morphology of ionized gas in Holmberg I in the [S II] and [O III] lines (see Fig. 8) is consistent with the Hα distribution, yet the images in [S II] and [O III] are much more noisy. Note that several H II regions appear to be brighter in [O III] than in Hα, that is especially clear in the bottom right-hand panel of Fig. 8. We will discuss these regions in Section 6. The maps of the [S II]/Hα ratio shown in the bottom right-hand panels of Figs 8–12 for each complex reveal a picture typical of other Irr galaxies: most H II regions have a low value of [S II]/Hα in their centres, while it grows towards their edges. In the majority of regions, the ratio [S II]/H$\alpha > 0.4$ is observed only in the areas of faint filaments and diffuse emission outside the bright H II regions. Most probably, we observe an emission of the diffuse ionized gas (DIG) there which is detected in many other galaxies. Its emission and enhanced line ratios in star-forming galaxies are usually explained by the leakage of hard ionizing quanta from H II regions with an additional influence of shock waves propagating through the low-density medium and turbulent mixing layers (see e.g. Hoopes & Walterbos 2003; Seon 2009; Zhang et al. 2017, and references therein).

If the H II complexes we selected are indeed unified structures, their Hα emission should be consistent with the location of the young stars inside a complex, and the age of H II regions in a complex should be more or less identical. We estimated the age of each H II region from the EW of its Hα emission line derived from the images in this line and in the nearby continuum ($\rm EW_{H\beta}$ derived from the spectra is also used in Section 6).

The possibility of using the EW of Balmer lines as an age indicator was illustrated by a number of authors (e.g. Copetti, Pastoriza & Dottori 1986; Schaerer & Vacca 1998; Leitherer et al. 1999). We use the model published by Levesque & Leitherer (2013) for the sub-solar metallicity ($Z = 0.004$). The results are listed in Table 4. Taking into account that $\rm EW_{H\alpha}$ becomes much less sensitive to ages older than $\sim$5–6 Myr, we may state that the ages of H II regions are almost identical in each H II complex, yet a few younger or older regions than median value are observed.

As follows from a comparison between Tables 3and 4, the age of the H II regions derived from $\rm EW_{H\alpha}$ is systematically higher than kinematic-age estimates for the same regions. Such a problem of inconsistency between these two methods of age estimation

Downloaded from https://academic.oup.com/mnras/article-abstract/478/3/3386/4992763
by Special Astrophysical Observatory of the Russian Academy of Sciences user
on 06 August 2018

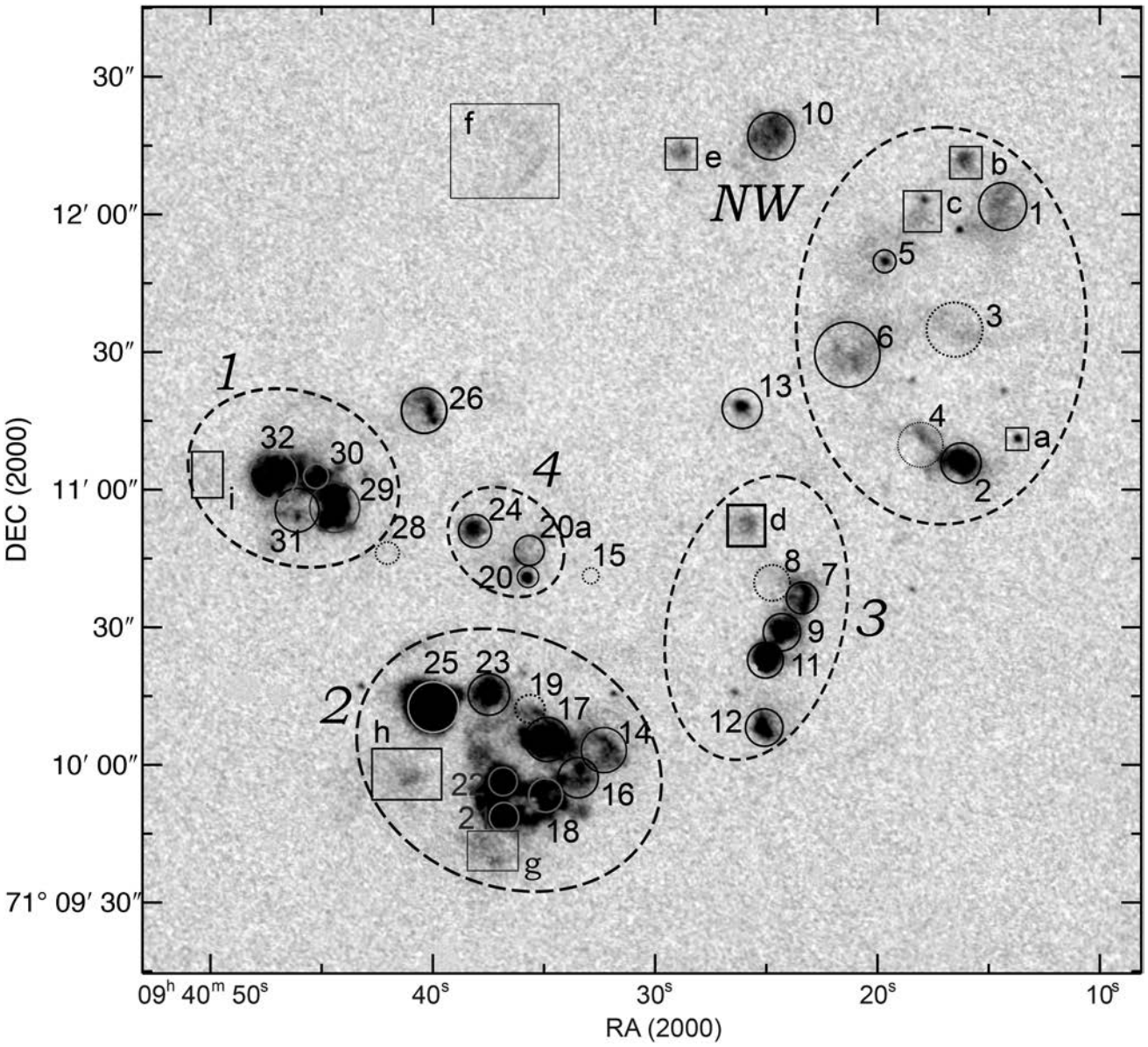

Figure 7. H α image of Holmberg I. The identification of the H II regions according to the list from Miller & Hodge (1994) is shown along with their names. Dotted circles show the objects from their list which appear not to be H II regions. The new faint H II regions identified in this paper are shown by squares and named by letters. Dashed ellipses denote the borders of the H II complexes discussed in Section 5.

was discussed previously in Wiebe et al. (2014). As we mentioned in Section 4, because of the assumption used for estimating the expansion velocity, the obtained values of kinematic ages can be underestimated. On the other hand, the relation between $EW_{H\alpha}$ and the age of H II region was obtained assuming a single stellar population and is highly dependent on the used models and initial mass function. The presence of an additional older stellar population in the region (that is very probable in Holmberg I since stars with ages of about 100 Myr are observed in the same place as OB stars, see Fig. 4) will increase the observed continuum level and decrease the age derived with this method.

We analysed the ionization balance for each complex based on the selection of O stars made in Section 3. Using the models from Martins, Schaerer & Hillier (2006), we evaluated the bolometric luminosity and the number of ionizing photons LyC$\star$ from each O star. Similar values can be inferred from the observed H α flux. We estimated the number of ionizing photons Q_0 needed for gas ionization in each H II complex with the procedure described in Osterbrock & Ferland (2006). For the case of optically thick nebulae, its H α luminosity $L_{H\alpha}$ depends on Q_0 as

$$\frac{L(\mathrm{H}\alpha)}{h\nu_{\mathrm{H}\alpha}} \simeq \frac{\alpha^{\mathrm{eff}}_{\mathrm{H}\alpha}}{\alpha_B} Q_0 \simeq 0.45 Q_0, \quad (2)$$

where the H α effective recombination coefficient $\alpha^{\mathrm{eff}}_{\mathrm{H}\alpha} \simeq 1.17 \times 10^{-13}$ cm^3 s^{-1} and the total recombination coefficient of hydrogen $\alpha_B \simeq 2.59 \times 10^{-13}$ cm^3 s^{-1} for $T = 10\,000$ K. Hereafter we refer to the estimated amount of needed ionizing photons Q_0 from (2) as $\mathrm{LyC}_{\mathrm{H\,II}}$ to note that it has been converted from the H α luminosity.

The estimated values of $\mathrm{LyC}_{\mathrm{H\,II}}$ and LyC$\star$ for each H II complex are shown in Table 4. As follows from this table, the identified

Downloaded from https://academic.oup.com/mnras/article-abstract/478/3/3386/4992763
by Special Astrophysical Observatory of the Russian Academy of Sciences user
on 06 August 2018

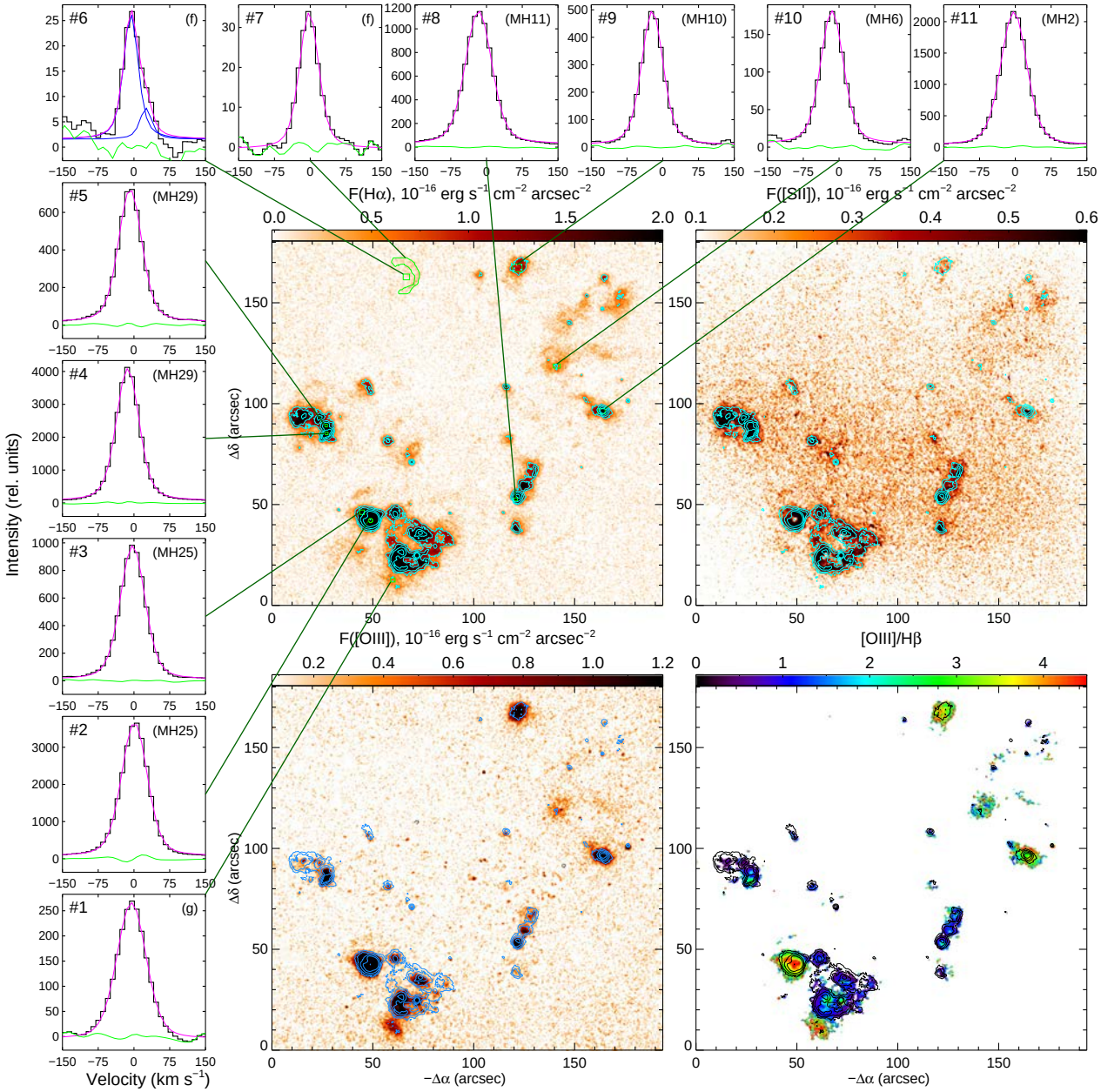

Figure 8. Images of Holmberg I in the H α, [S II], [O III] lines and a map of the [O III] /H β line ratio (constructed as [O III] /H α multiplied by 2.86). The contours on each panel correspond to the H α intensities of (0.75, 1.5, 3, 4.5) $\times$ 10^{-16} erg s^{-1} cm^{-2} arcsec^{-2}. Examples of the H α line profile averaged over the areas denoted by the green borders (in the H α image) are shown. The observed line profiles are shown by the black line, the results of its decomposition on to the individual Voigt components – by the blue line, the sum of components – by the magenta line, and the residuals – by the green line. The names of the corresponding H II region are given in parentheses.

young massive stars provide even more than enough ionizing quanta to produce the observed H α luminosity of each complex.

The excess of ionizing quanta points to their possible leakage from the H II complexes because of the porosity of the ISM. About 60 per cent of the available ionizing radiation should escape from each H II complex to provide the observed H α flux. A recent modelling of the feedback of a star cluster on to the ISM performed by Rahner et al. (2017) has shown that the escape fraction of ionizing radiation from low-metallicity (the same as for Holmberg I) massive molecular clouds might indeed be large – up to 60 per cent and even higher in some short periods of its evolution.

The large escape fraction of ionizing radiation from the H II complex should provide a large amount of the diffuse H α emission in the galaxy. Thus, Oey et al. (2007) showed that about 60 per cent of the total H α emission of a galaxy (independently on its type) is represented by its diffuse component. Our values of the escape fraction are in agreement with these estimates. Our images actually reveal a number of elongated diffuse structures towards the inner part of the SGS and on the rims of smaller H I supershells. Earlier in Egorov et al. (2014, 2017), we have identified faint ionized giant (1.5–2 kpc sized) supershells on the inner rims of H I SGS of the galaxies IC 2574 and Holmberg II. Probably, such a large

Downloaded from https://academic.oup.com/mnras/article-abstract/478/3/3386/4992763
by Special Astrophysical Observatory of the Russian Academy of Sciences user
on 06 August 2018

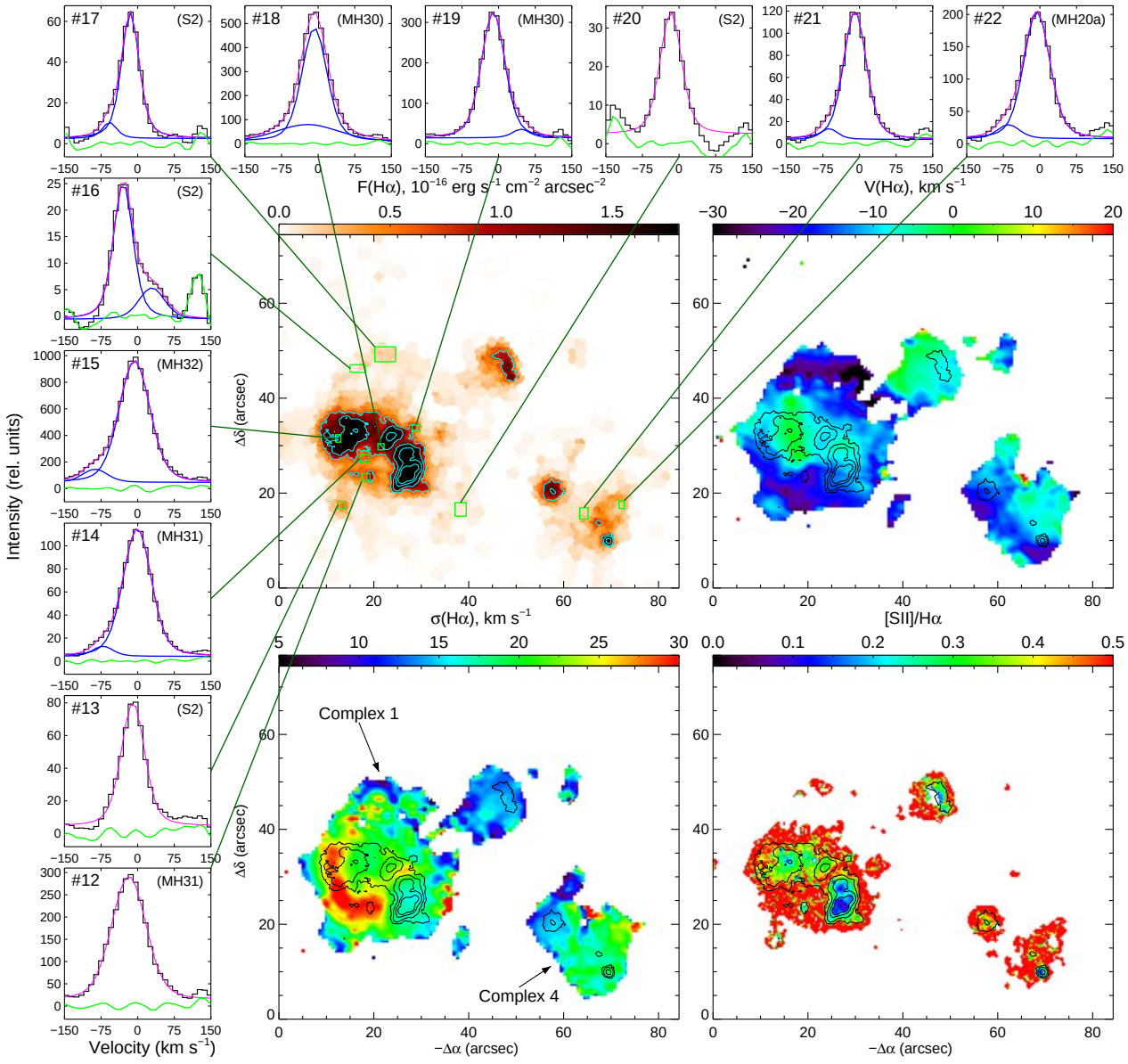

Figure 9. Complexes #1 and #4: their image in the H α line (top left), line-of-sight velocity (top right) and velocity dispersion (bottom left) maps, and the distribution of the [S II]/H α ratio (bottom right). The contours on each panel correspond to H α intensities of (0.75, 1.5, 3, 4.5) $\times$ 10^{-16} erg s^{-1} cm^{-2} arcsec^{-2}. The examples of the H α line profile averaged over the areas denoted by the green borders (in the H α image) are shown. The observed line profiles are shown with the black line, the results of its decomposition on to the individual Voigt components – with the blue line, the sum of components – with the magenta line, and the residuals – with the green line. The names of the corresponding H II region or shell (if any) are given in parentheses.

structure could also exist in Holmberg I, but its brightness is below the detection limit of our observations. Indeed, the ionized supershell in Holmberg II was observed at a surface brightness level of 3−6 $\times$ 10^{-18} erg s^{-1} cm^{-2} arcsec^{-2} that is nearly the detection limit during our observations of Holmberg II but below that for Holmberg I.

Note also that some stars identified as being of the OB type could be not OB actually (see Section 3). Some young stars classified as OB in Fig. 4 lie significantly outside the H II regions and probably are misclassified. This fact will reduce the estimated fraction of ionizing quanta especially calculated for the whole galaxy ($f_{esc} \sim 70$ per cent).

Below we describe each of the identified H II complexes and analyse their ionized-gas kinematics (see Figs 8–12).

5.1 H II complex #1

This complex contains an arc of several bright H II regions and the faint diffuse shell S1, and is limited by a faint ring with a diameter of about 700 pc (the shell S2). The brightest H II regions in the complex are located at the outer edge of the SGS.

Faint blueshifted (and even broad underlying) components in the H α line profiles are observed in the central part of the complex near the bright nebulae (see profiles #14, 18 in Fig. 9), while the faint redshifted emission is detected in the line profiles outside the bright nebulae towards the outer part of the complex (profile #19).

The most intriguing structure observed in this complex is a surrounding ring – shell S2. While it is only noticeable in other H α

Downloaded from https://academic.oup.com/mnras/article-abstract/478/3/3386/4992763
by Special Astrophysical Observatory of the Russian Academy of Sciences user
on 06 August 2018

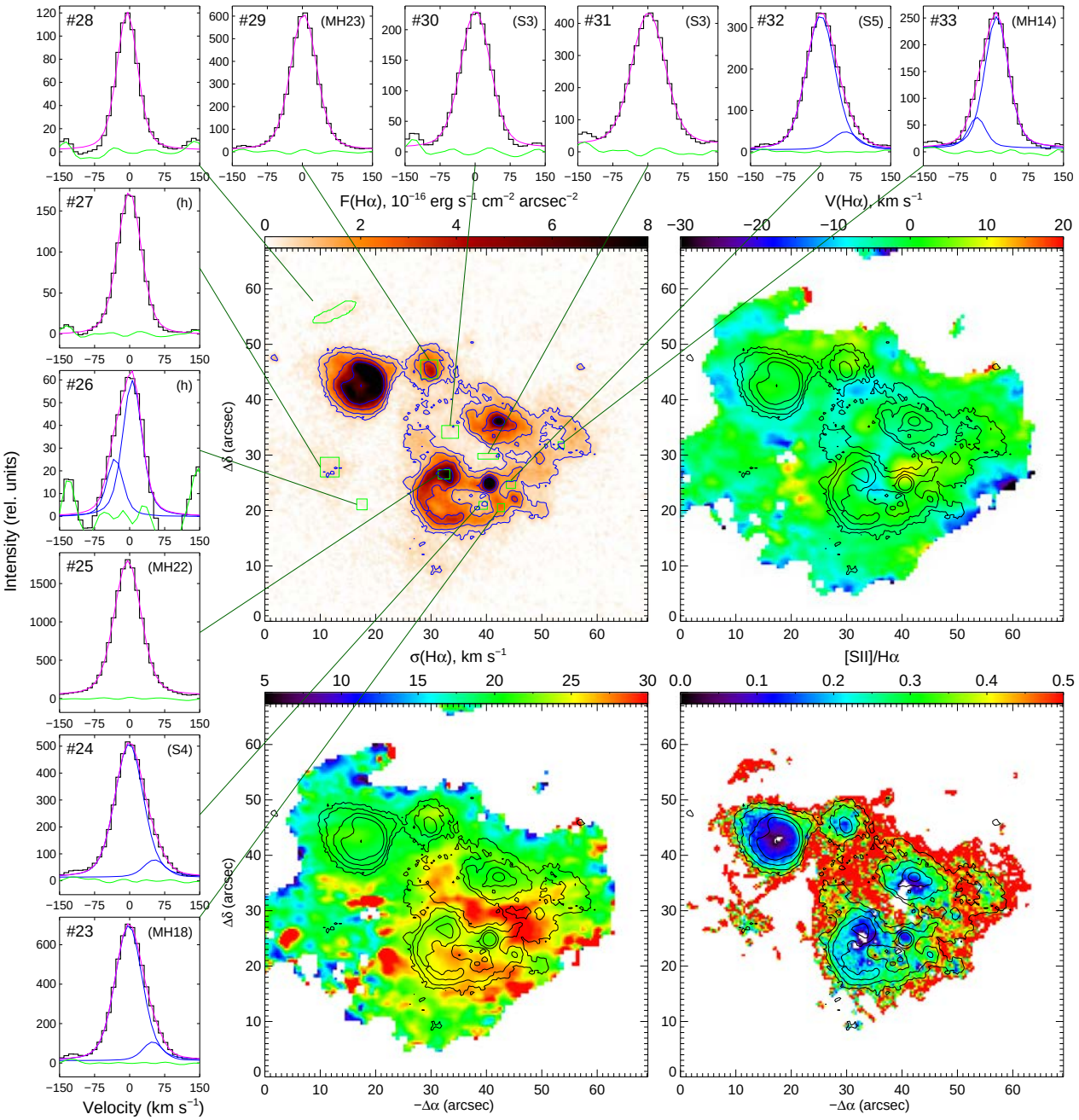

Figure 10. Same as in Fig. 9 but for complex #2.

images as a faint filament (see e.g. Fig. 4), it is much better seen in the top left-hand panel of Fig. 9, where adaptive binning was used to reach a signal-to-noise ratio better than 10 in each pixel. An analysis of the FPI data cube shows that this structure is clearly seen at blueshifted velocities and almost disappear at red channels. The top right-hand panel of Fig. 9 also shows that the shell S2 is blueshifted relative to other part of the complex and of the whole galaxy as well.

Several faint clumps in the southern part of the ring S2 demonstrate the unperturbed single component Hα line profiles (see profiles #13 and #20 in Fig. 9), while its northern part reveals the slightly asymmetrical Hα line profiles (#16 and #17) with blue- or redshifted components in their wings. Note, however, that the signal-to-noise ratio for these components is low.

Only with this information at hand, we can speculate on a possible nature of the shell S2. It might be created by the ionizing radiation of a few O stars outside bright H II regions as well as the UV photons leakage from those regions influencing surrounding neutral gas. As follows from Figs 1 and 5, complex #1 is located in the low-density medium (in comparison with the other part of the SGS) but at the edge of the relatively bright H I cloud. We propose that the complex is located at the front edge of this dense H I cloud. In that case we should observe the faint ionizing front moving towards us through the low-density H I medium even at a great distance

Downloaded from https://academic.oup.com/mnras/article-abstract/478/3/3386/4992763
by Special Astrophysical Observatory of the Russian Academy of Sciences user
on 06 August 2018

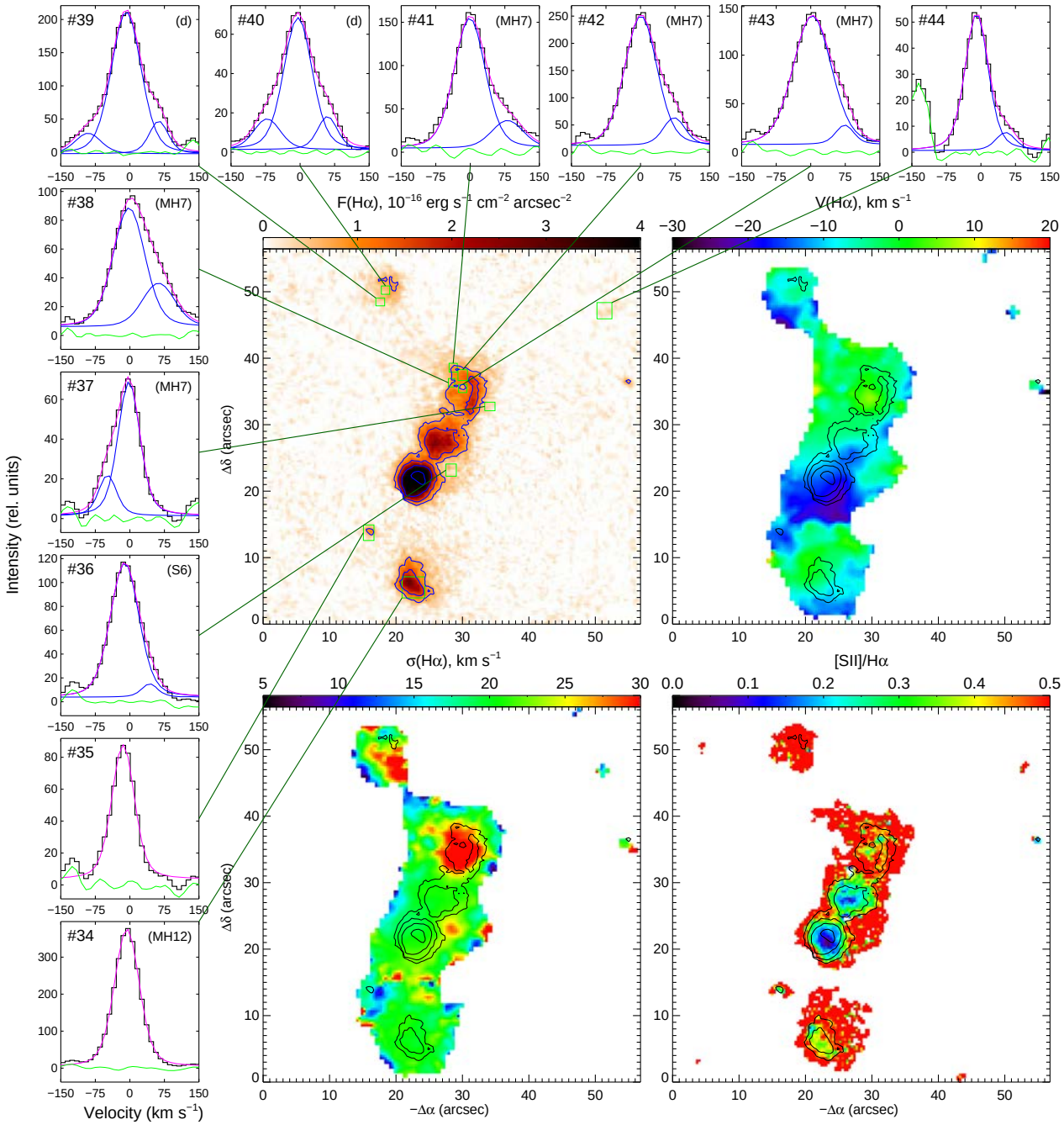

Figure 11. Same as in Fig. 9 but for complex #3.

from the complex, while its bright receding side should be much slower and will be interpreted as a non-shifted component of the line profile. Such a picture is able to explain the observed blue shift of the ring on the line-of-sight velocity map and is consistent with the observed Hα line profiles (the presence of a faint blueshifted component) from different regions of complex #1.

5.2 H II complex #2

The brightest complex of star formation is located in the southeastern part of the SGS in the area of its maximum H I density that explains a large number of O stars and H II regions there. Most H II regions are encircled by H I supershell #7, and the northeastern H II regions are located at the edge of H I supershell #9 (see Figs 4 and 5). Many H II regions there have the shell-like morphology, and their Hα line profiles (e.g. #24, 32, 33 in Fig. 10) show signs of expansion with velocities corresponding to kinematic ages of 1−2 Myr. The second largest ionized superbubble in the galaxy – S3 – is observed in the central part of the complex and joins several bright H II regions. Its kinematic age (∼3 Myr) is slightly greater than that of other shells in the complex, which can point to its relation to the previous generation of stars formed there. Most O stars found in the complex are located inside the H II regions, and none of them was found towards the centre of the S3 shell.

Downloaded from https://academic.oup.com/mnras/article-abstract/478/3/3386/4992763
by Special Astrophysical Observatory of the Russian Academy of Sciences user
on 06 August 2018

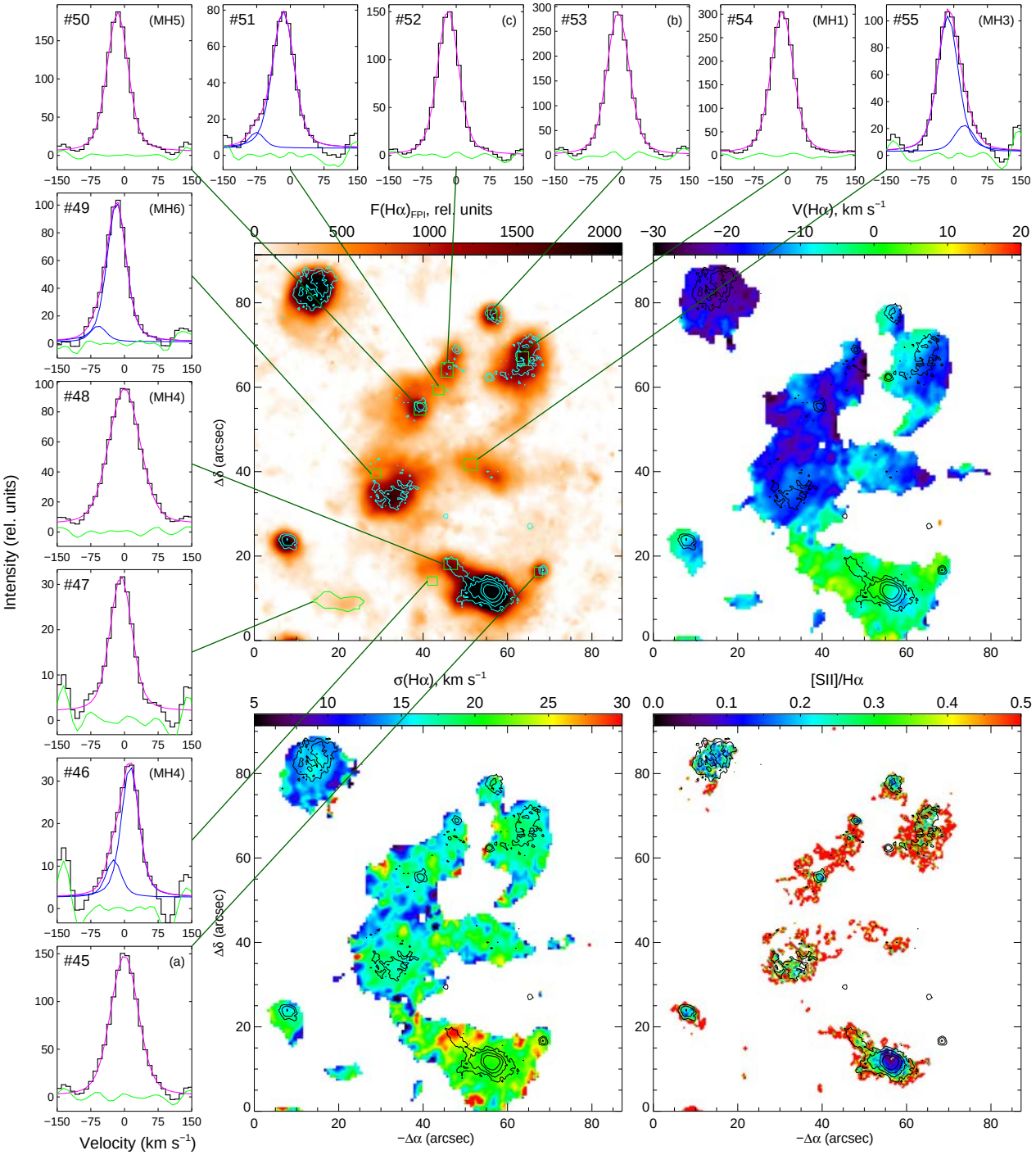

Figure 12. Same as in Fig. 9 but for the complex NW. The H α flux distribution from the FPI data is used here instead of the H α narrow-band image because of a better sensitivity to faint emission features. The contours on each panel correspond to H α intensities of (0.5, 1, 2, 4) $\times$ 10^{-16} erg s^{-1} cm^{-2} arcsec^{-2}.

An extended area of the DIG (including two faint H II regions g and h) is observed at the southeastern edge of the complex in the low-density environment showing the multicomponent Hα line profile at some places (e.g. profile #26 in Fig. 10). The faint filaments extending towards the centre of the SGS and of H I supershell #9 are also observed. All these features are probably the result of the ionizing quanta leakage from H II regions due to inhomogeneities of the ISM.

In general, all the H II regions and ionized shells are of more or less the same age (see Tables 3 and 4), that together with the detection of a large amount of diffuse filaments and the presence of surrounding H I supershell #7 indicates that complex #2 is indeed a unified structure. Probably, at a higher spatial and spectral resolution it would be worth exploring this complex as a separate H I supershell with star formation in its walls.

Downloaded from https://academic.oup.com/mnras/article-abstract/478/3/3386/4992763
by Special Astrophysical Observatory of the Russian Academy of Sciences user
on 06 August 2018

Table 4. Parameters of the H II regions of Holmberg I.

Complex	LyC⋆	LyC H II	H II reg.	Size	v_{los}	σ_v	$F(H\alpha)$	$EW_{H\alpha}$	Age	Morphology
	10^{50}	10^{50}		(pc)	($km\,s^{-1}$)	($km\,s^{-1}$)	10^{-15} erg s^{-1} cm^{-2}	(Å)	(Myr)	
Total	16.0	4.5								
			29	165	-12.2 ± 2.5	17.3 ± 1.7	25.7	629	4.6	Multiple
			30	90	-8.7 ± 0.9	21.7 ± 1.2	4.2	463	5.0	Compact
1	1.52	0.86	31	90	-18.3 ± 3.0	29.1 ± 0.8	1.2	119	7.2	Diffuse
			32	220	-6.4 ± 4.8	24.4 ± 3.6	16.7	231[a]	6.1[a]	Shell
			i	∼170	–	–	0.6	190	6.4	Diffuse
			14	230	0.0 ± 3.2	24.4 ± 2.2	10.0	290	5.5	Shell
			16	160	4.1 ± 3.4	28.9 ± 2.0	6.7	289	5.5	Multiple
			17	160	-2.2 ± 1.4	22.0 ± 1.7	14.7	325	5.4	Comp. + shell
			18	60	2.3 ± 3.3	22.3 ± 0.6	6.8	241	6.0	Compact
			19	85	-5.2 ± 1.7	21.3 ± 0.9	1.3	648	4.6	Diffuse
2	7.06	2.49	21	220	-1.4 ± 3.4	25.1 ± 1.2	20.8	769	4.4	Shell
			22	90	-4.1 ± 2.7	23.1 ± 1.1	8.6	331	5.3	Compact
			23	110	0.7 ± 4.1	20.5 ± 1.3	5.6	826	4.3	Compact
			25	200	-0.6 ± 1.8	19.9 ± 0.8	50.0	980	4.1	Shell
			g	150	-4.8 ± 2.2	22.3 ± 1.6	2.2	816	4.3	Diffuse
			h	115	-3.0 ± 2.6	19.7 ± 1.4	1.3	291	5.5	Diffuse
			7	150	-0.1 ± 2.8	28.8 ± 4.1	4.7	299	5.5	Shell
			8	130	-2.3 ± 2.4	20.8 ± 3.4	0.8	78	7.8	Diffuse
3	1.2	0.46	9	140	-7.6 ± 4.0	20.9 ± 1.1	6.0	341	5.3	Compact
			11	120	-15.5 ± 3.0	20.7 ± 1.2	10.2	422	5.0	Shell
			12	140	-5.8 ± 4.0	20.6 ± 0.6	4.2	1081	3.8	Compact
			d	130	-8.6 ± 4.2	22.8 ± 5.5	1.4	93	7.5	Shell
			20	60	-14.0 ± 3.6	18.2 ± 0.8	1.3	246	5.9	Compact
4	0.33	0.12	20a	185	-8.0 ± 1.9	18.5 ± 1.9	2.6	70	8.1	Shell
			24	130	-16.1 ± 3.0	14.6 ± 0.9	2.8	127	7.1	Compact
			1	245	-11.0 ± 3.9	18.0 ± 2.9	4.6	237	6.0	Diffuse
			2	95	-3.5 ± 3.4	21.0 ± 0.5	9.6	657	4.6	Compact
			3	110	-13.5 ± 1.8	18.7 ± 1.7	0.6	86	7.6	Diffuse
			4	110	-0.8 ± 1.7	26.2 ± 2.3	1.2	86	7.6	Diffuse
NW	1.86	0.6	5	60	-15.3 ± 1.4	16.6 ± 0.4	0.6	526	4.8	Compact
			6	290	-15.4 ± 2.5	17.7 ± 1.9	5.7	94	7.6	Shell
			a	40	-1.2 ± 2.7	23.9 ± 0.7	0.4	196	6.4	Compact
			b	115	-9.7 ± 4.6	17.2 ± 1.5	1.5	1690	2.9	Compact
			c	205	-18.8 ± 4.9	16.3 ± 3.0	2.0	99	7.4	Multiple
	0.30	0.11	10	235	-21.3 ± 1.6	14.5 ± 1.3	7.4	1610	2.9	Diffuse
	0	0.03	13	75	-10.1 ± 2.3	17.8 ± 1.3	1.2	165	6.6	Compact
Separate	0.83	0.06	26	200	-6.3 ± 2.1	14.1 ± 1.2	4.6	147	6.1	Multiple
	0.036	0.016	e	125	4.8 ± 2.6	13.2 ± 2.0	1.1	263	5.7	Compact
	0	0.03	f	310	-0.6 ± 4.5	11.3 ± 5.6	1.7	225	6.1	Shell

Notes. [a]EW(H α) value is highly contaminated by the presence of a background galaxy. Hence, the age can be overestimated.

Note that one of the brightest H II regions in the galaxy – MH25 – may not be related to H II complex #2. We consider it as a part of complex #2 because of a very close location to it, but neither obvious emission filaments nor diffuse gas connecting them are observed. In addition, it is located at the edge of H I supershell #9 and far away from supershell #7, while the latter joins all other H II regions in complex #2.

5.3 H II complex #3

We joined a chain of the H II regions in the southwestern part of the SGS to complex #3. As follows from Figs 4 and 5, most part of this complex is located at the edge of H I supershell #10.

In contrast with the previous two, this complex does not show any extended diffuse emission around the H II regions, yet a filament connecting all of them can be clearly seen. The velocity field (the top right-hand panel in Fig. 11) shows a significant difference of the line-of-sight velocity in this complex. The area surrounding the H II region MH11 is blueshifted at $\simeq 20\,km\,s^{-1}$ in comparison with the other part of the complex. Taking it into account, the physical relation of the H II regions in this complex with each other is less evident than that in other complexes.

5.4 H II complex #4

This small complex consists of two bright nebulae MH20 and MH24, the shell MH20a, and the extended diffuse emission

Downloaded from https://academic.oup.com/mnras/article-abstract/478/3/3386/4992763
by Special Astrophysical Observatory of the Russian Academy of Sciences user
on 06 August 2018

filling the area. The enhanced [S II]/Hα ratio in our long-slit spectra between these nebulae (see also Fig. 9) together with the presence of a blueshifted component in the wing of the Hα line profile (e.g. #21 in Fig. 9) indicates a major role of shocks in excitation of the diffuse emission. The complex is located towards the inner wall of the SGS and the centre of H I supershell #9. Hence, it resides in the environment of a lower density in comparison with complexes #1 and 2 which can explain a small number of H II regions and low star formation rate there.

In contrast with all other H II complexes in the galaxy, this complex is seen close to the centre of a large H I supershell. We suppose that it is actually located at the approaching side of H I supershell #9. This assumption is consistent with the H I and Hα kinematics in the region. Indeed, as follows from the PV diagrams and H I line profiles shown in Fig. 5, H I supershell #9 is clearly expanding and its approaching side has the velocity $V \simeq 10\,\mathrm{km\,s^{-1}}$ at the position of complex #4. This estimate agrees well with the line-of-sight velocity of ionized gas there: the whole complex #4 is blueshifted at $\simeq$10−18 $\mathrm{km\,s^{-1}}$ (see the top right-hand panel in Fig. 9).

As follows from fig. 9 in Weisz et al. (2008), the spatial density distribution of both red and blue stars shows a peak there. Note, however, that most of the O stars detected there lie close to, although, outside the mentioned H II regions and the whole complex as well. At the same time many of BHeB stars of ages of 50−200 Myr are observed towards this complex. Together with the age estimates of the H II regions (see Table 4), it allows one to propose that this complex is older than those previously discussed.

5.5 H II complex NW

Especially interesting is a group of nebulae located at the north-western side of the galaxy in the dense layer of H I between the SGS and supershell #1.

We classified this 'arc' of faint H II regions as a unified complex based on the presence of the diffuse emission connecting them with each other that coincides with the distribution of H I. The additional evidence is that almost all the H II regions show more or less similar ages (see Table 4). Taking into account the localization of neutral and ionized gas, we conclude that the ongoing star formation in this complex was triggered by the collision of supershell #1 with the SGS (see the discussion in Section 7).

The ionized gas in the complex NW almost does not reveal any high-velocity motions except for few diffuse areas, where the blue- or redshifted components in the wings of the Hα line profiles are observed (profiles #46, 49, 51, 55 in Fig. 12), and the region MH4 revealing a broad Hα line profile (#48 in Fig. 12). Note, however, that the northeastern part of the complex shows a significant blue shift of the line-of-sight velocity (up to $-25\,\mathrm{km\,s^{-1}}$). Moreover, the kinematics of ionized and neutral gas are different there: H I is observed even at the redshifted velocities at some places (see e.g. the PV diagram #4 in Fig. 5). The collision of two H I supershells and inhomogeneities in the H I density distribution can be a reason of such a complex gas kinematics.

6 INDIVIDUAL H II REGIONS AND ANALYSIS OF THEIR SPECTRA

In this section, we analyse the emission spectra and chemical abundance of the H II regions in the galaxy Holmberg I. Several most interesting H II regions are discussed in details.

The most complete catalogue of the H II regions in Holmberg I by Miller & Hodge (1994) contains 32 H II regions. In this paper, we reveal several new H II regions (shown with squares and denoted by letters in Fig. 7) together with the faint extended structures of ionized gas mentioned in the previous section. On the other hand, some areas of ionized gas identified by Miller & Hodge (1994) as H II regions seem to be extended filaments of ionized gas created by the stellar wind or supernovae from a nearby OB association: MH3, 4, 8, 19, and 28. The region MH15 does not reveal any emission in the Hα line and seems to be a bright star. These non-H II regions from Miller & Hodge (1994) are shown in Fig. 7 by the dotted circles.

Table 4 lists the properties of each H II region in the galaxy: its size, median line-of-sight velocity V_{LOS} and velocity dispersion σ, integrated Hα flux F(Hα), equivalent width of the Hα line EW(Hα), age derived from EW(Hα), and the type of its morphology according to our classification made by eye. Note that several H II regions are classified as multiple – they represent several compact (or compact and diffuse) nebulae instead of single as was defined earlier.

Only four brightest H II regions have been previously spectroscopically studied: MH18, 22, and 29 (Croxall et al. 2009), and MH25 (Miller & Hodge 1996). We obtained the spectra for the galaxy with slits crossing a large part of its H II regions (see Fig. 2). For every observed region, we obtained the integrated emission spectrum for a further analysis. The reddening-corrected values of most measured emission-line fluxes (normalized to the fluxes of the Hα or Hβ lines) are listed in Table 5. The adopted values of the interstellar extinction coefficient c(Hβ) calculated from the observed Balmer decrement are also shown in the table. The values of [S II]/Hα and [O III]/Hβ obtained from direct images agrees well with those measured from the long-slit spectra.

In Fig. 13, we plot the H II regions, for which we obtained spectroscopic data in the diagnostic BPT (Baldwin, Phillips & Terlevich 1981) diagrams. The right-hand panel shows also a 2D histogram corresponding to the distribution of line ratios for each pixel of our images. The emission from the regions lying above the black 'maximum starburst line' (Kewley et al. 2001) cannot be explained by photoionization from massive OB stars. Composite mechanism of excitation should work for regions lying between this line and the grey curve from Kauffmann et al. (2003) (for the solar abundance) in the left-hand panel. As follows from the right-hand diagram, some pixels in our narrow-band images fall into the area above the maximum starburst line. These pixels correspond to a faint emission outside H II regions only, and as we noted in the previous section, they most probably represent the DIG.

All the H II regions observed with the long-slit spectrograph (except for the faint diffuse region MH8) show the emission-line ratios corresponding to their positions in the BPT diagrams below the separation lines. Despite that, the shock waves should produce lower line ratios due to the low metallicity of Holmberg I. In fact, the separation lines should be shifted towards the lower [N II]/Hα and [S II]/Hα line ratios. We add a grid of shock waves ionization models in the BPT diagrams from Allen et al. (2008) which correspond to the shock velocity from 100 $\mathrm{km\,s^{-1}}$ and to the metallicity $Z = 0.004$ (SMC-like). As follows from the comparison of the [S II]/Hα ratios with these models, a shock excitation can play a significant role in ionization of the regions MH7, 8, 24, d, and i. Two of them – MH7 and d – show a high value of [S II]/H$\alpha > 0.4$ estimated from direct images and the multicomponent Hα line profile with high-velocity components (see Fig. 11). Because of this, we consider these regions as probable supernova remnants. The region MH24 lies close to MH7 in the BPT diagram but does not show any peculiarities of

Downloaded from https://academic.oup.com/mnras/article-abstract/478/3/3386/4992763
by Special Astrophysical Observatory of the Russian Academy of Sciences user
on 06 August 2018

Table 5. Results of the emission spectra analysis.

Region	1	6_3*	7	7	8	8	10
Slit	PA142	PA142	PA259	PA212	PA259	PA212	PA150
Pos. (arcsec)	−167 to −158	−138 to −116	101–107	−132 to −122	95–99	−138 to −133	141–151
$c(\mathrm{H}\beta)$	0.00 ± 0.17	0.00 ± 0.26	0.20 ± 0.04	0.25 ± 0.09	0.03 ± 0.33	0.23 ± 0.59	0.10 ± 0.21
[O II]3727, 3729/H β	2.79 ± 0.36	–	–	–	–	–	–
He II 4686/H β	–	–	–	–	–	–	–
[O III] 5007/H β	<0.16	1.87 ± 0.40	1.02 ± 0.04	1.10 ± 0.09	2.62 ± 0.69	0.49 ± 0.39	3.93 ± 0.65
[N II] 6583/H α	<0.05	<0.06	0.06 ± 0.01	0.06 ± 0.01	–	–	<0.03
[S II] 6717,6731/H α	0.33 ± 0.03	0.19 ± 0.05	0.39 ± 0.01	0.36 ± 0.01	0.48 ± 0.09	0.44 ± 0.09	0.18 ± 0.04
[Ar III] 7136/H β	–	–	–	–	–	–	–
EW(H β)	41 ± 7	18 ± 4	31 ± 1	45 ± 3	9 ± 2	13 ± 6	120 ± 34
Age (Myr)	5.4 ± 0.2	6.6 ± 0.4	5.7 ± 0.1	5.3 ± 0.1	7.6 ± 0.3	7.2 ± 0.6	4.2 ± 0.3
12 + log(O/H)	–	<8.02	7.71 ± 0.03	7.74 ± 0.05	–	–	<7.78
Region	14_17*	18	20a	20a	21*	24	25
Slit	PA142	PA142	PA259	PA150	PA142	PA259	PA150
Pos. (arcsec)	−20 to −8	−3–2	41–47	34–44	4–10	28–33	−6–4
$c(\mathrm{H}\beta)$	0.11 ± 0.12	0.14 ± 0.04	0.06 ± 0.10	0.36 ± 0.40	0.00 ± 0.06	0.00 ± 0.04	0.08 ± 0.03
[O II] 3727,3729/H β	–	–	–	–	–	–	1.42 ± 0.68
He II 4686/H β	–	–	–	–	–	–	0.07 ± 0.02
[O III] 5007/H β	0.47 ± 0.06	2.59 ± 0.07	0.16 ± 0.06	<0.62	1.06 ± 0.06	1.25 ± 0.07	4.76 ± 0.10
[N II]6583/H α	0.06 ± 0.01	0.04 ± 0.01	0.05 ± 0.02	<0.04	0.05 ± 0.01	0.07 ± 0.01	0.03 ± 0.00
[S II]6717, 6731/H α	0.31 ± 0.02	0.15 ± 0.01	0.30 ± 0.02	0.18 ± 0.08	0.23 ± 0.01	0.35 ± 0.01	0.10 ± 0.01
[Ar III]7136/H β	–	0.05 ± 0.01	–	–	–	–	0.06 ± 0.01
EW(H β)	64 ± 8	72 ± 3	11 ± 1	11 ± 3	253 ± 46	43 ± 1	99 ± 3
Age (Myr)	4.9 ± 0.1	4.8 ± 0.1	7.4 ± 0.1	7.3 ± 0.4	2.9 ± 0.4	5.3 ± 0.1	4.4 ± 0.1
12 + log(O/H)	7.40 ± 0.07	7.84 ± 0.04	–	–	7.63 ± 0.05	7.81 ± 0.03	7.94 ± 0.06
Region	25c	25se	25nw	29	31*	32*	d
Slit	PA150	PA150	PA150	PA259	PA259	PA259	PA142
Pos. (arcsec)	−2–0	−6 to −4	2–5	−3–2	−11 to −6	−19 to −14	−78 to −72
$c(\mathrm{H}\beta)$	0.02 ± 0.04	0.00 ± 0.06	0.32 ± 0.07	0.07 ± 0.02	0.00 ± 0.06	0.07 ± 0.04	0.09 ± 0.32
[O II]3727, 3729/H β	1.85 ± 1.24	–	3.07 ± 2.07	2.88 ± 0.63	–	1.74 ± 1.30	–
He II 4686/H β	0.16 ± 0.05	–	–	–	–	–	–
[O III]5007/H β	5.09 ± 0.18	4.15 ± 0.20	4.08 ± 0.21	1.21 ± 0.02	0.25 ± 0.03	0.26 ± 0.03	1.02 ± 0.34
[N II]6583/H α	0.02 ± 0.01	0.04 ± 0.01	0.04 ± 0.01	0.05 ± 0.00	0.05 ± 0.01	0.05 ± 0.00	–
[S II]6717, 6731/H α	0.06 ± 0.01	0.13 ± 0.01	0.14 ± 0.01	0.20 ± 0.00	0.38 ± 0.01	0.38 ± 0.01	0.49 ± 0.07
[Ar III]7136/H β	0.06 ± 0.02	0.10 ± 0.04	0.05 ± 0.02	0.05 ± 0.00	–	–	–
EW(H β)	65 ± 3	197 ± 21	118 ± 9	86 ± 1	26 ± 1	51 ± 2	30 ± 8
Age (Myr)	4.9 ± 0.1	3.5 ± 0.6	4.3 ± 0.1	4.6 ± 0.1	6.1 ± 0.1	5.1 ± 0.1	5.8 ± 0.6
12 + log(O/H)	–	7.99 ± 0.08	–	7.66 ± 0.02	7.15 ± 0.07	–	–
Region	d	f	g	i			
Slit	PA212	PA212	PA142	PA259			
Pos. (arcsec)	−150 to −145	−252 to −237	13–19	−37 to −26			
$c(\mathrm{H}\beta)$	0.08 ± 0.18	0.29 ± 0.57	0.00 ± 0.17	0.00 ± 0.20			
[O II]3727, 3729/H β	–	–	–	–			
He II 4686/H β	–	–	–	–			
[O III]5007/H β	0.63 ± 0.17	0.92 ± 0.50	2.97 ± 0.40	2.69 ± 0.45			
[N II]6583/H α	<0.04	<0.08	0.05 ± 0.03	–			
[S II]6717, 6731/H α	0.43 ± 0.04	0.26 ± 0.07	0.18 ± 0.04	0.28 ± 0.05			
[Ar III]7136/H β	–	–	–	–			
EW(H β)	31 ± 5	9 ± 4	162 ± 55	–			
Age (Myr)	5.7 ± 0.4	7.5 ± 0.5	3.8 ± 0.9	–			
12 + log(O/H)	<7.66	<8.21	7.96 ± 0.15	–			

Note. *The slit crossed only the edge of the region. EW, age, and oxygen abundance estimates can be unreliable.

the ionized-gas kinematics – that is why, we do not consider it as an SNR candidate. The two regions – MH8 and i – are faint diffuse areas of ionized gas.

Table 5 provides the estimates of $\mathrm{EW}_{\mathrm{H}\beta}$ and corresponding age for all the observed H II regions obtained in the way we described in the previous Section. The ages of H II regions are consistent with those obtained using $\mathrm{EW}_{\mathrm{H}\alpha}$ derived from direct images (see Table 4).

We estimated the oxygen abundance 12 + log(O/H), which is the indicator of gas metallicity for the most observed H II regions, yet for several of them we provide only the upper-limit value. The results are reported in Table 5. Since the weak [O III] 4363

Downloaded from https://academic.oup.com/mnras/article-abstract/478/3/3386/4992763
by Special Astrophysical Observatory of the Russian Academy of Sciences user
on 06 August 2018

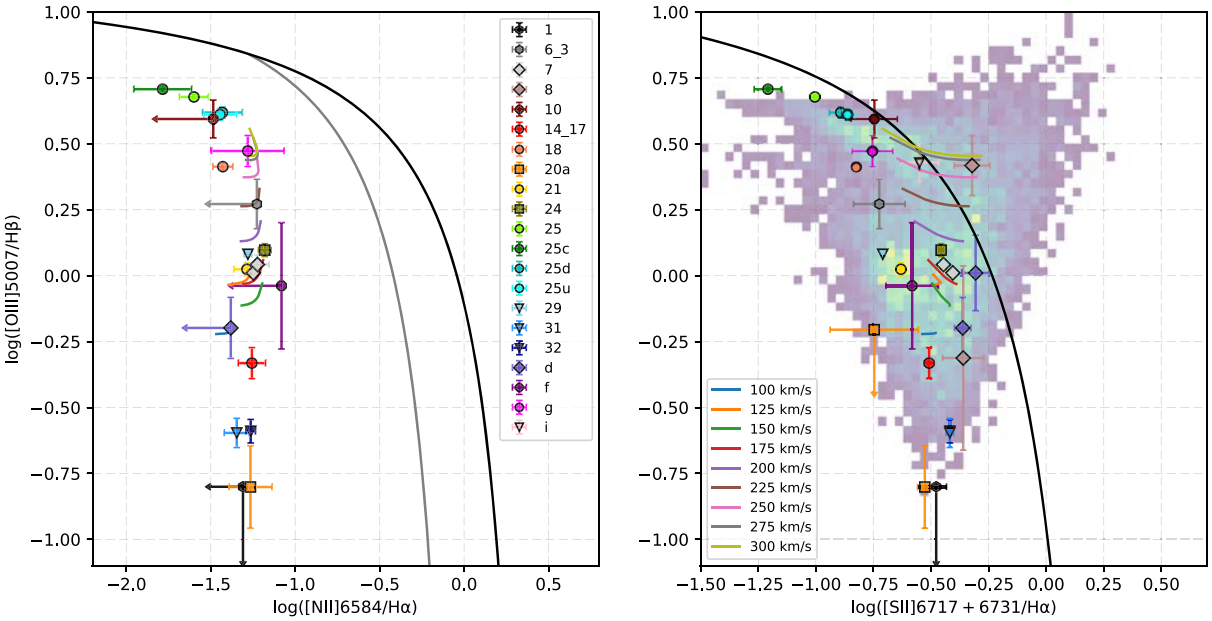

Figure 13. Diagnostic diagrams [O III] /H β versus [N II] /H α (left) and [S II] /H α (right) constructed for the individual H II regions in Holmberg I. The models of the shock + precursor emission for the metallicity $Z = 0.004$ (the SMC set of models) from Allen et al. (2008) are overplotted in both diagrams. The 2D histogramin the right-hand panel shows the distribution of [O III] /H β versus [S II] /H α derived from direct images. The black line in both panels is for the 'maximum starburst line' from Kewley et al. (2001), and the grey line from Kauffmann et al. (2003) in the left-hand panel separates pure star-forming regions from those with a composite mechanism of excitation.

Å emission line, which is sensitive to electron temperature, does not appear in our spectra, we were unable to use the 'direct' T_e method for this. We applied the empirical S method by Pilyugin & Grebel (2016), which is based on the flux ratios of the strong emission lines [S II], [N II], and [O III] to H β. This method was selected among many other developing strong-line empirical calibrations, because it is applicable for low-metallicity galaxies, is consistent with the results of the T_e method and does not demand measurements of [O II] 3727, 3729 Å which are very noisy in our data due to the poor sensitivity of the spectrograph in the blue region of the spectrum.

The oxygen abundance of only four brightest regions was measured before. We have obtained spectroscopic data for three of them – MH18, 29, and 25. Croxall et al. (2009) estimated $12 + \log(\mathrm{O/H}) = 8.04$ for the first two of these regions using the 'direct' T_e method, while their measurements with the empirical method (McGaugh 1991) gave lower values (7.71 and 7.82, respectively). Moustakas et al. (2010) used another empirical method by Pilyugin & Thuan (2005) and obtained the values $12 + \log(\mathrm{O/H}) = 7.55$ and 7.71, and 7.54 ± 0.36 for the region MH25. Because of the well-known problem of discrepancy between different methods of oxygen abundance estimation (see e.g. Kewley & Ellison 2008; López-Sánchez et al. 2012), we recalculated the metallicity of these regions with the S method (Pilyugin & Thuan 2005) using the line ratios reported by Croxall et al. (2009) to directly compare with our results. Thus, we obtained $12 + \log(\mathrm{O/H}) = 7.83 \pm 0.03$ and 7.87 ± 0.03 for MH18 and MH29, respectively. While our metallicity estimate for MH18 is in a very good agreement with the previous data, its value for MH29 is lower and is in a better agreement with a value reported by Moustakas et al. (2010). In fact, the latter region consists of four compact and one diffuse H II regions. Our oxygen-abundance estimate for this region corresponds to its northern part, while Croxall et al. (2009) performed the observations of its brightest central part which can be a reason for the discrepancy. In addition, Croxall et al. (2009) used a much larger value of the extinction coefficient, that can also influence the reported oxygen abundance. Due to the absence of reported fluxes of the [S II] lines in Miller & Hodge (1996) and Moustakas et al. (2010), we were unable to make a similar comparison for the MH25 region, yet our results do not conflict with the published estimates taking into account their large reported uncertainty. In general, our oxygen abundance estimates for Holmberg I are consistent with the previously published values, yet we observe a significant spread of metallicity between different regions.

It is worth noting that for some H II regions (denoted by an asterisk in Table 5) the obtained spectra cross only their outer part. The reported line fluxes for two such regions (6_3 and 14_17) correspond to the area of diffuse emission between the nearby H II regions mentioned in their names. In all these cases, the observed emission lines come from the outer parts of H II regions and, hence, could be highly contaminated by the DIG and biased towards a lower ionization state. Hence, these regions can show higher values of [S II]/H α and [N II]/H α as well as an incorrect value of $\mathrm{EW}_{\mathrm{H}\beta}$. The measured metallicity of them can be unreliable. Additionally, shock waves might have high contribution into the excitation of the MH7 and d regions and, hence, the empirical metallicity calibration used in our analysis is not applicable to them.

Below we consider some interesting H II regions in more details.

6.1 MH25 (complex 2)

The brightest and among the largest H II regions in Holmberg I appears as a shell-like structure around six identified O stars. Our data show a single slightly broaden H α line profile, but the observed gradient of velocity dispersion towards the centre of the region

Downloaded from https://academic.oup.com/mnras/article-abstract/478/3/3386/4992763
by Special Astrophysical Observatory of the Russian Academy of Sciences user
on 06 August 2018

points to the presence of an unresolved expanding superbubble there.

While we consider this region as a part of H II complex #2, it could not be related to it. It is located relatively far away from the majority of the nebulae in the complex and is clearly tied with H I supershell #9 instead of #7 (see Figs 4 and 5). Probably, star formation in MH25 was triggered by the influence of expanding H I supershell #9 with the ISM in the SGS.

This region was divided into MH25 and MH27 in Miller & Hodge (1994), while recent images demonstrate that it is a single object. Differences in ionization conditions of the inner and outer parts of the region are clearly seen in our observed data. The gradient of [O III]/H β ratio (Fig. 8, bottom right-hand panel) and the invert gradient of [S II]/H α (Fig. 9, bottom right-hand panel) are typical of H II regions with a central source of ionization. The central part of MH25 show the highest [O III]/H β in the galaxy. Because of that, in addition to the integrated spectrum of MH25, we also analysed separately its central (MH25c in Table 5 and Fig. 13), northwestern (MH25nw), and southeastern (MH25se) parts.

The central part of MH25 is the only place in Holmberg I, where we have detected the He II 4686 Å line. It also appears in the integrated spectrum, yet it is not observed in the outer bright areas MH25nw and MH25se, and the He II/H β ratio is two times higher in the central part MH25c. Hence, we expect to find a source of ionization in the centre of MH25 having a sufficiently hard spectrum and high temperature to explain high ratios of [O III]/H β and He II/H β.

Given the emissivities and recombination coefficients for hydrogen and helium (Osterbrock & Ferland 2006), we obtain that L(He II 4686)/L(H β) $\simeq 2.14 Q_2/Q_0$, where Q_2 and Q_0 are the amount of the emitted helium and hydrogen ionizing quanta per second. Hence, in order to explain the observed line ratio of He II/H $\beta = 0.16$ in the central part of MH25, the ionizing source should produce Q_2 no less than 7 per cent of Q_0. According to the models by Smith, Norris & Crowther (2002), all types of O stars provide less amount of Q_2 and are not available to produce the observed intensity of the He II 4686 Å line. The presence of the Wolf–Rayet (WR) star WN10–WN11 is necessary to get the observed flux ratio. Comparing the measured EW of the He II 4686 Å line ($\simeq$ 9 Å) and its FWHM ($\simeq$3.5 Å corrected for instrumental broadening) with the empirical diagnostic diagram of Crowther & Smith (1997) made for different types of WR stars (see their fig. 1b), we obtain that the MH25 central source falls into the region occupied by WN9–10 stars.

Summing up, we conclude that despite the fact that there are no observed peculiarities in the ionized-gas kinematics in the MH25 region, it represents a slowly expanding superbubble around a young star cluster with at least 6 O stars and one WN9–11 star.

6.2 MH20 and MH20a (complex 4)

We consider the region MH20 from the list of Miller & Hodge (1994) as two separate nebulae – the compact H II region MH20 and the connected faint shell MH20a because of quite a large separation between them (see Fig. 7).

A shell-like structure of MH20a is clearly seen in our H α images, while no O stars were found inside it. We obtained two spectra of different parts of this shell – they point to photoionization as a mechanism of emission-line excitation according to the BPT diagrams (Fig. 13). A single slightly asymmetric Hα line profile is observed towards the central and northern part of MH20a; its blue wing reveals a faint component at the level of about 10 per cent of the maximum and shifted by 58 km s^{-1} (profile #22, Fig. 9).

The most interesting fact is that the only bright (1.4 mJy) radio continuum point-like source in the galaxy according to the VLA observations presented in Hindson et al. (2018) (see fig. 20 there) clearly coincides with the MH20a region. The author has shown that this non-thermal radio emission dominates there, and proposed that its origin can be an SNR, yet it can also come from some background source. Our spectral analysis does not reveal any signs of shock waves there. Moreover, the broad lines corresponding to a distant quasar are clearly seen in our spectrum PA = 259. Hence, MH20a is not an SNR, and a background source is responsible for the emission in the radio continuum there.

6.3 MH 10

This bright isolated H II region is located in the area of interaction of three H I supershells – #2, 3, and 11. Probably, star formation there has been triggered by their collision.

Two O stars detected there provide a sufficient amount of ionizing quanta to create the H II regions, while the analysis of [S II]/H α and [O III]/H β line ratios point to the absence of the outer area of low-excitation ionized gas. Hence, this region seems to be density bound and should demonstrate an efficient leakage of ionizing quanta. Indeed, a faint diffuse tail of ionized gas is observed elongated towards the centre of H I supershell #3 (see Fig. 4).

6.4 Region f

This nebula at the north of the SGS was detected for the first time in our H α images. It represents a faint bubble-like nebula with irregular density around the star identified as BHeB of an age from 30 to 55 Myr (see Fig. 4).

The H α line profiles on the rim of the nebula represent a single narrow component, while some asymmetry is observed towards the centre of the nebula (see profiles #6 and 7 in Fig. 8). Note, however, that the redshifted component detected there shows a low signal-to-noise ratio and, hence, could not be considered as a confident proof of the nebula expansion.

We observed this region with the long slit in order to reveal its nature. The obtained spectrum showed that the main source of emission-line excitation should be photoionization. The estimated age of the region is about 7 Myr. Taking into account its large size (about 300 pc), the region f seems to be an ionized bubble around a poor OB association at the late stage of its evolution, yet we have no sufficient data to definitely state this.

6.5 Regions MH7 and d (complex 3): SNR candidates

The compact faint shell-like region d with a size of about 60 pc observed on the inner rim of the SGS in complex #3 draws our particular attention. Its H α line profile is significantly broad and clearly multicomponent (see profiles #39, 40 in Fig. 11). The estimated expansion velocity of the region is 74 km s^{-1} that corresponds to a kinematic age of 0.2 Myr. An analysis of the spectra crossing the region d show the enhanced flux ratio of [S II]/H $\alpha = 0.43$–0.49 indicating high contribution of shock excitation. As we noted above, despite the region falls into the area of pure photoionization in the BPT diagrams (Fig. 13), its position agrees well with the models of the shocks in the low-metallicity environment.

Another region showing similar properties – MH7 – is located close to the region d in the same complex #3. It also has a broad

Downloaded from https://academic.oup.com/mnras/article-abstract/478/3/3386/4992763
by Special Astrophysical Observatory of the Russian Academy of Sciences user
on 06 August 2018

multicomponent H α line profile (#38, 41–43 in Fig. 11) corresponding to a high expansion velocity (85 km s^{-1}) and a low kinematic age (0.3 Myr). The flux ratio of [S II]/H α = 0.36–0.39 there is a bit lower than for the region d, yet the MH7 location in the BPT diagrams still agrees with the models of ionization by shocks.

Both regions MH7 and d stand out among all other H II regions in the galaxy. They were classified according to the $I-\sigma$ diagram (Fig. 6) as the unique energetic objects. They appear to be the only regions in the galaxy with the clearly resolved multicomponent H α line profile corresponding to a high expansion velocity; they show the highest [S II]/H α ratio in the galaxy. Because of that, we consider these regions as good SNR candidates.

The emission in the region d might be wholly created by an old SNR, because there are no ionizing sources revealed inside the region (see Fig. 4). A more complicated situation is in the region MH7 – there are two O stars observed towards the centre of the region. The contribution of photoionization from them probably reduce the observed [S II]/H α as compared with the region d.

Fig. 14 presents a spatially resolved kinematics of the region MH7 in details: maps of the flux, line-of-sight velocity and, velocity dispersion of the central and shifted components are shown. It is clearly seen that the highest velocity dispersion corresponds to a non-shifted component in the centre of this shell-like region. It is interesting that while the flux distribution of the central component sets the morphology of the region, the blue- and redshifted components are clearly separated and dominate in different parts of MH7. We can explain this fact by a high inhomogeneity of the H I density in the region. Indeed, the local minimum of the H I density is observed towards the centre of MH7, while it grows up at its edges. Hence, the shifted components may correspond to the expanding bubble, whose receding side has a higher density in its northern part, while the approaching side – in the southern part.

Given the measured optical size and the expansion velocity of both SNR candidates d and MH7 (see Table 3), we can derive their energy of explosion necessary to match the observed properties of the nebulae. A high expansion velocity suggests that the SNR still undergoes adiabatic expansion. According to the self-similar solution of Sedov (1946), the evolution of an SNR at this stage can be described by the following equation:

$$R_s = 13.5(E_{51}/n_o)^{0.2}(t/10^4\ \mathrm{yr})^{0.4}\ (\mathrm{pc}),$$

where $E_{51} = E_o/10^{51}$ erg is the explosion energy, R_s is the radius, and t is the age of an SNR. The expansion velocity of an SNR evolves as $v_{exp} = 0.4R_s/t$ during this stage. The unperturbed density $n_o \simeq 0.35$ cm^{-3} is derived from the H I data (helium contribution is taken into account). Using these relations, we obtained $E_{51} \simeq 0.07$ and 0.24 for the regions d and MH7, respectively, proposing the adiabatic stage of expansion. If an SNR currently undergo the post-adiabatic snow-plough stage of evolution, we can use the analysis performed by Chevalier (1974). According to this work,

$$E_{51} = 5.3 \times 10^{-8} n_o^{1.12} v_{exp}^{1.4}(\mathrm{km\,s^{-1}}) R_s^{3.12}(\mathrm{pc}),$$

that gives us $E_{51} \simeq 0.36$ and 0.87 for the regions d and MH7.

Such low values of E_{51} derived from our analysis do not contradict the hypothesis of the SNR nature of the objects d and MH7. Indeed, according to modern understanding, supernovae having even much lower explosion energy are observed (see e.g. Benetti et al. 2016; Chugai 2016; Utrobin & Chugai 2017). In addition, high radiation loses can also be responsible for the observed values of the SNR energy much lower, than the initial explosion energy (Sharma et al. 2014; Vasiliev, Nath & Shchekinov 2015b).

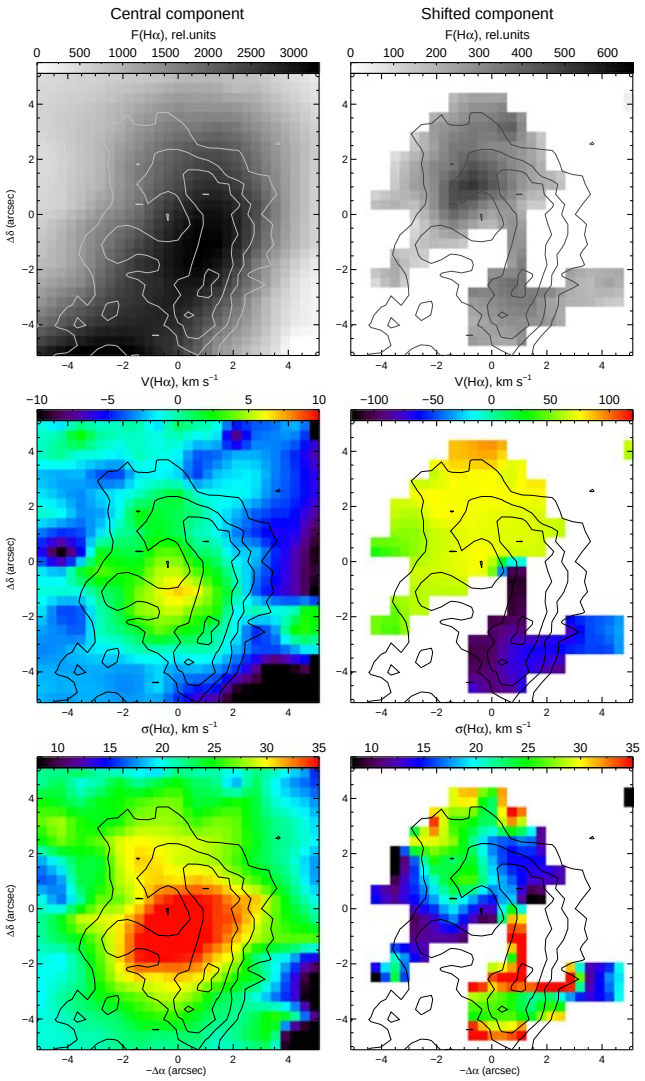

Figure 14. Region MH7: the map of the central and shifted components of the H α line profile (top panels), their line-of-sight velocities (middle panels), and velocity dispersions (bottom panel). The contours correspond to the H α intensities (0.6, 1, 1.4, 1.8) $\times$ 10^{-16} erg s^{-1} cm^{-2} arcsec^{-2}.

It is interesting that despite the fact that these two regions appear to be good SNR candidates, they do not exhibit any bright emission in the radio continuum. Only a faint source of the non-thermal radio continuum could be identified between the regions MH7 and d in the images presented by Hindson et al. (2018). This fact does not contradict their identification as SNRs. As follows from the analysis of detections of an extragalactic SNR performed by Bozzetto et al. (2017), optical SNR candidates statistically tend not to be detected in the radio or X-rays. Probably, deeper radio observations are needed to clarify the nature of the MH7 and d regions.

7 DISCUSSION

In this paper, we present the deepest Hα images of Holmberg I available to date, as well as a detailed study of the ionized-gas kinematics. These data allow us to treat star formation in the galaxy as a process taking place in large (several hundreds of pc) unified complexes presenting the same age and gas kinematics within them.

Downloaded from https://academic.oup.com/mnras/article-abstract/478/3/3386/4992763
by Special Astrophysical Observatory of the Russian Academy of Sciences user
on 06 August 2018

All the individual H II regions within a complex are tied together with faint filaments or diffuse clouds of ionized gas. We state that star formation in Holmberg I is a self-regulating process at the scales of such complexes, while the external factors like the SGS expansion influence the whole star formation in the galaxy.

All regions of the ongoing star formation in Holmberg I, similarly to other dIrr galaxies with SGSs, are located on the rim of the central H I SGS in the areas of high H I density. This is natural in the framework of the generally accepted theory of star formation, propagated within an expanding supershell. Complex #2 represents another example of the same process but on a smaller scale. The bright nebulae of this complex are located in the walls of the local H I supershell #7.

Another well-known mechanism of triggering of star formation is the collision of several expanding supershells. It was reproduced in numerical and analytical models by different authors (e.g. Chernin et al. 1995; Ntormousi et al. 2011; Kawata et al. 2014; Vasiliev & Shchekinov 2017) and observed in a number of nearby galaxies (e.g. Lozinskaya 2002; Egorov et al. 2017). Several facts point to the conclusion that the supershell collision is a mechanism that triggered the ongoing star formation in the complex NW. Its related H I supershell #1 has the same age as the SGS (see Table 3) which points to their previous independent evolution. Currently, the rims of both supershells are in contact, and the ionized gas is distributed between them. Moreover, the distribution of young stars of different ages (see Fig. 4) inside the complex NW shows a gradient from the centre of H I supershell #1 towards its northeastern part that is the evidence for its independent evolution by the influence of stellar feedback from these stars. Such a gradient is absent in the southeastern part of the complex (towards the SGS) that allows one to propose triggering of star formation there as a result of the supershell collision. Warren et al. (2012) have found several clumps of the cold low-dispersion H I gas in Holmberg I. The most extended of them are located on the rims of the NW shell (in particular, between supershell #1 and the SGS) that also points to the ongoing cooling and compression of the ISM that stimulates star formation.

Triggering of star formation by colliding shells can take place also for several other regions in the galaxy. Thus, the H II regions MH10 and MH26 are located at the intersections of several H I supershells. The first one probably formed in the collision of quite young H I supershells #2, 3 with an older one #11. A collision of two old H I supershells of almost an equal age – SGS and #8 – can stimulate star formation in the MH26 region. Young OB stars are also observed in the intersection of the SGS and H I supershell #3 (see Fig. 4).

Taking into account the old age of supershells #9 and #10 together with their location relative to the SGS, we may also propose that star formation in H II complexes #3 and #4 was also triggered by the collision of those shells with the SGS several Myr ago. However, we cannot exclude now an opposite scenario – that these supershells on the rim of the SGS were produced by feedback of supernovae and stellar winds in the mentioned complexes supposing that star formation in them was taking place at least for several tens of Myr. The last scenario is supported by a large number of BHeB stars with ages of 50–200 Myr inside supershell #9, while only few of such stars are observed inside supershell #10.

The signs of star formation propagation and triggering in Holmberg I are shown not only by the distribution of stars of different ages, but also by the comparison between Hα and FUV images. Both Hα and FUV emission trace the young stellar population in galaxies but they dominate at different ages. The Hα emission is a good tracer of the current star formation (age $<$ 10 Myr), while

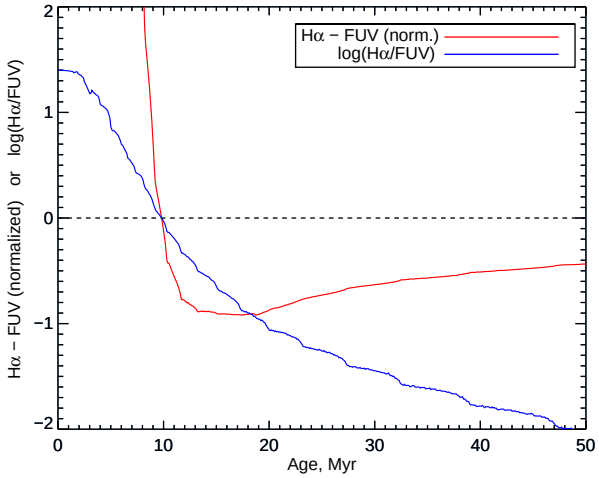

Figure 15. Evolution of the Hα and FUV fluxes logarithm ratio (blue curve) and difference (red curve) with the age of the cluster according to STARBURST99 model. The flux difference is normalized to one-third of the maximum FUV flux over the whole time-scale of the model in order to fit both curves to the same scale.

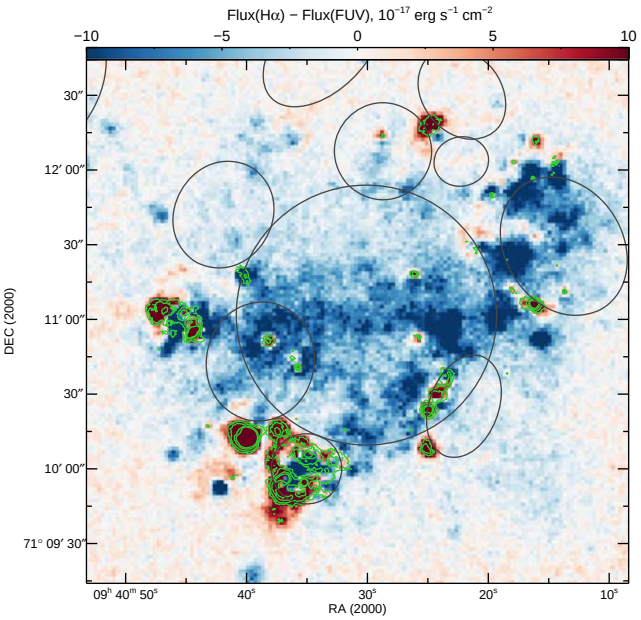

Figure 16. Map of the Hα and FUV fluxes difference for Holmberg I. The red colour denotes the regions with the dominated Hα emission, while the blue colour traces the ones with enhanced contribution of the FUV emission. Green contours correspond to the Hα intensities (0.75, 1.5, 3, 4.5) $\times$ 10^{-16} erg s^{-1} cm^{-2} arcsec^{-2}. Grey ellipses denote the location of the detected H I supershells.

the FUV emission traces the recent star formation that took place on longer time-scales (age $<$ 100 Myr). Fig. 15 shows the evolution of the Hα/FUV flux ratio as well as their difference according to the STARBURST99 simulations (Leitherer et al. 1999) for the Holmberg I metallicity $Z = 0.2$ Z$_\odot$. The red line traces the change of the normalized Hα–FUV flux difference with the age of the star cluster. This difference is positive at ages less than about 9 Myr and negative for older regions. The map of Hα–FUV (Fig. 16) exhibits the regions with a negative value (older than 9 Myr) in blue and with a positive value (younger than 9 Myr) in red. Hence, red colour in

Downloaded from https://academic.oup.com/mnras/article-abstract/478/3/3386/4992763
by Special Astrophysical Observatory of the Russian Academy of Sciences user
on 06 August 2018

this image corresponds to the regions of the ongoing star formation, while blue regions – to the areas where star formation has recently occurred. In many places, especially in complexes #1, 2, and NW, the blue area is closely bordered by a younger red area, that points to star formation propagation within the complex.

The morphology of ionized and neutral gas together with the young-star distribution allow us to make some speculative assumptions on further evolution of the SGS. Given a large number of H II regions and young massive stars, we may expect a gradual fragmentation and destruction of the SGS in the area of its interaction with supershell #1 (NW complex), where the observed H I density is lower than in other parts of the SGS. This process will form an open tunnel in the H I distribution like it is already observed in the eastern part of the galaxy (towards supershell #6).

As we have mentioned before, the origin of two expanding supershells #9 and #10 observed on the rim of the SGS is unclear now. But in any case, their presence demonstrates a current instability of the SGS there. If they were formed on the rim of the SGS during the late stages of its evolution, then these supershells could be considered as a consequence of the ongoing fragmentation of the SGS driven by stellar feedback. Or else, if they have evolved independently of the SGS, we now observe a process of dissipation of these two supershells as a result of their collision with the SGS – this process should destabilize the SGS as well.

Summing up, we observe a propagation of star formation in Holmberg I, and in some places it is triggered by the interaction of several H I supershells. In its turn, the ongoing star formation on the rims of the SGS gradually leads to its destruction.

8 SUMMARY

We present a detailed multiwavelength analysis of the regions of star formation in the nearby dIrr galaxy Holmberg I. Since all the H II regions in the galaxy are located inside the galaxy-sized H I supergiant shell, we focused on investigation of star formation triggering on the rims of the SGS, as well as on the role of star formation in the evolution of the SGS.

Our work was based on the data set obtained with the SCORPIO and SCORPIO-2 focal reducers at the 6-m SAO RAS telescope: deep Hα, [S II], and [O III] narrow-band images of the galaxy, four long-slit spectra crossing most of the H II regions, and the high spectral resolution H α data cube obtained with the scanning Fabry–Perot interferometer. These data were complemented with the archival data in HI 21-cm (VLA) and FUV (*GALEX*) from the LITTLE THINGS archive, as well as by the photometric data of individual stars observed with the *HST* (ANGST archive). Using all these data, we performed an analysis of the ionized and neutral gas morphology and kinematics; described the emission spectrum of H II regions in terms of their excitation mechanism and metallicity; identified young massive stars and compared their energetics and distribution with properties of the observed ionized gas; traced the spatial distribution of the ongoing and recent star formation in the galaxy. Below we highlight the most important results obtained.

(i) Four expanding H I supershells and nine new faint H II regions were found and analysed in addition to the previously known.

(ii) We show that star formation in the galaxy takes place in five large unified complexes rather than in the individual H II regions. The H II regions in these complexes are tied together by faint filaments of ionized gas or embedded into common clouds of DIG.

(iii) Triggering of star formation on scales of individual complexes, as well as of the whole galaxy, is observed. Most H II regions surround places of the recent star formation. In the northwestern complex, we also observed a gradient in the age distribution of individual stars. Also our observations point to the fact that the current star formation there was triggered by the collision of the SGS with other H I supershells.

(iv) The ionized gas distribution in the galaxy reveals 18 shell-like structures. Most of them appear to be expanding superbubbles (according to their enhanced velocity dispersion), yet only a half demonstrate weak high-velocity components in the H α line profile, and only two of them show a clearly multicomponent line profile.

(v) We identified two SNR candidates and one WR star in the galaxy. One object with the bright radio continuum emission previously proposed as a possible SNR candidate turned out to be a background quasar.

(vi) A large fraction of the escaping ionizing radiation from each H II complex is observed. It points to the expected large amount of DIG which appears to be only partially detected in our observations.

(vii) The presence of younger H I supershells of a smaller size on the rims of the SGS together with a large fraction of escaping ionizing quanta allows us to propose that currently we observe a process of SGS fragmentation and destruction by the influence of star formation on its rim.

ACKNOWLEDGEMENTS

We thank the anonymous referee for detailed comments that helped us to improve the clarity of this manuscript.

This work is based on the observations obtained with the 6-m telescope of the Special Astrophysical Observatory of the Russian Academy of Sciences carried out with the financial support of the Ministry of Education and Science of the Russian Federation (agreement no. 14.619.21.0004, project ID RFMEFI61914X0004). We thank A. Burenkov, D. Oparin, and R. Uklein for the assistance in 6-m telescope observations.

The study was supported by the Russian Foundation for Basic Research (RFBR), project 18-02-00976. OVE is also thankful to the European Astronomical Society for a travel grant for participation in the EWASS-2017 conference, where the first results of this work have been presented.

The study is partially based on the observations made with the NASA/ESA *Hubble Space Telescope* obtained from the Data Archive at the Space Telescope Science Institute which is operated by the Association of Universities for Research in Astronomy, Inc., under the NASA contract NAS 5-26555. These observations are associated with program # 10605.

REFERENCES

Afanasiev V. L., Moiseev A. V., 2005, Astron. Lett., 31, 194
Afanasiev V. L., Moiseev A. V., 2011, Baltic Astron., 20, 363
Allen M. G., Groves B. A., Dopita M. A., Sutherland R. S., Kewley L. J., 2008, ApJS, 178, 20
Bagetakos I., Brinks E., Walter F., de Blok W. J. G., Usero A., Leroy A. K., Rich J. W., Kennicutt R. C., 2011, AJ, 141, 23
Baldwin J. A., Phillips M. M., Terlevich R., 1981, PASP, 93, 5
Bastian N. et al., 2011, MNRAS, 412, 1539
Benetti S. et al., 2016, MNRAS, 456, 3296
Berg D. A. et al., 2012, ApJ, 754, 98
Bozzetto L. M. et al., 2017, ApJS, 230, 2
Bressan A., Marigo P., Girardi L., Salasnich B., Dal Cero C., Rubele S., Nanni A., 2012, MNRAS, 427, 127
Cannon J. M. et al., 2011a, ApJ, 735, 35
Cannon J. M. et al., 2011b, ApJ, 735, 36

Downloaded from https://academic.oup.com/mnras/article-abstract/478/3/3386/4992763
by Special Astrophysical Observatory of the Russian Academy of Sciences user
on 06 August 2018

Cardelli J. A., Clayton G. C., Mathis J. S., 1989, ApJ, 345, 245
Chen Y., Girardi L., Bressan A., Marigo P., Barbieri M., Kong X., 2014, MNRAS, 444, 2525
Chen Y., Bressan A., Girardi L., Marigo P., Kong X., Lanza A., 2015, MNRAS, 452, 1068
Chernin A. D., Efremov Y. N., Voinovich P. A., 1995, MNRAS, 275, 313
Chevalier R. A., 1974, ApJ, 188, 501
Chugai N. N., 2016, Astron. Lett., 42, 82
Copetti M. V. F., Pastoriza M. G., Dottori H. A., 1986, A&A, 156, 111
Crowther P. A., Smith L. J., 1997, A&A, 320, 500
Croxall K. V., van Zee L., Lee H., Skillman E. D., Lee J. C., Côté S., Kennicutt R. C., Miller B. W., 2009, ApJ, 705, 723
Dalcanton J. J. et al., 2009, ApJS, 183, 67
de Vaucouleurs G., de Vaucouleurs A., Corwin H. G.,, Jr, Buta R. J., Paturel G., Fouqué P., 1991, Third Reference Catalogue of Bright Galaxies. Volume I: Explanations and References. Volume II: Data for Galaxies Between 0^h and 12^h. Volume III: Data for Galaxies Between 12^h and 24^h. Springer-Verlag, New York, NY
Dohm-Palmer R. C. et al., 1997, AJ, 114, 2527
Egorov O. V., Lozinskaya T. A., Moiseev A. V., Smirnov-Pinchukov G. V., 2014, MNRAS, 444, 376
Egorov O. V., Lozinskaya T. A., Moiseev A. V., Shchekinov Y. A., 2017, MNRAS, 464, 1833
Fitzpatrick E. L., 1999, PASP, 111, 63
Guerrero M. A., Villaver E., Manchado A., 1998, ApJ, 507, 889
Hindson L. et al., 2018, ApJS, 234, 29
Hoessel J. G., Danielson G. E., 1984, ApJ, 286, 159
Hoopes C. G., Walterbos R. A. M., 2003, ApJ, 586, 902
Hunter D. A., Elmegreen B. G., Ludka B. C., 2010, AJ, 139, 447
Hunter D. A. et al., 2012, AJ, 144, 134
Karachentsev I. D., Kaisin S. S., 2007, AJ, 133, 1883
Karachentsev I. D., Makarov D. I., Kaisina E. I., 2013, AJ, 145, 101
Kauffmann G. et al., 2003, MNRAS, 346, 1055
Kawata D., Gibson B. K., Barnes D. J., Grand R. J. J., Rahimi A., 2014, MNRAS, 438, 1208
Kewley L. J., Ellison S. L., 2008, ApJ, 681, 1183
Kewley L. J., Dopita M. A., Sutherland R. S., Heisler C. A., Trevena J., 2001, ApJ, 556, 121
Koleva M., Prugniel P., Bouchard A., Wu Y., 2009, A&A, 501, 1269
Leitherer C. et al., 1999, ApJS, 123, 3
Levesque E. M., Leitherer C., 2013, ApJ, 779, 170
López-Sánchez Á. R., Dopita M. A., Kewley L. J., Zahid H. J., Nicholls D. C., Scharwächter J., 2012, MNRAS, 426, 2630
Lozinskaya T. A., 2002, Astron. Astrophys. Trans., 21, 223
Markwardt C. B., 2009, in Bohlender D. A., Durand D., Dowler P., eds, ASP Conf. Ser. Vol. 411, Astronomical Data Analysis Software and Systems XVIII. Astron. Soc. Pac., San Francisco, p. 251
Martins F., Schaerer D., Hillier D. J., 2006, A&A, 436, 1049
McGaugh S. S., 1991, ApJ, 380, 140
McQuinn K. B. W., Skillman E. D., Cannon J. M., Dalcanton J. J., Dolphin A. E., Stark D., Weisz D. R., 2009, ApJ, 695, 561
McQuinn K. B. W. et al., 2010a, ApJ, 721, 297
McQuinn K. B. W. et al., 2010b, ApJ, 724, 49
Miller B. W., Hodge P. W., 1994, ApJ, 427, 656
Miller B. W., Hodge P. W., 1996, ApJ, 458, 467
Moiseev A. V., 2002, Bull. Spec. Astrophys. Obs., 54, 74
Moiseev A. V., 2015, Astrophys. Bull., 70, 494
Moiseev A. V., Egorov O. V., 2008, Astrophys. Bull., 63, 181
Moiseev A. V., Lozinskaya T. A., 2012, MNRAS, 423, 1831
Moustakas J., Kennicutt R. C.,, Jr, Tremonti C. A., Dale D. A., Smith J.-D. T., Calzetti D., 2010, ApJS, 190, 233
Muñoz-Tuñon C., Tenorio-Tagle G., Castañeda H. O., Terlevich R., 1996, AJ, 112, 1636
Ntormousi E., Burkert A., Fierlinger K., Heitsch F., 2011, ApJ, 731, 13
Oey M. S. et al., 2007, ApJ, 661, 801
Oh S.-H., de Blok W. J. G., Brinks E., Walter F., Kennicutt R. C.,, Jr, 2011, AJ, 141, 193
Osterbrock D. E., Ferland G. J., 2006, Astrophysics of Gaseous Nebulae and Active Galactic Nuclei, 2nd edn. University Science Books, Mill Valley, CA
Ott J., Walter F., Brinks E., Van Dyk S. D., Dirsch B., Klein U., 2001, AJ, 122, 3070
Pilyugin L. S., Grebel E. K., 2016, MNRAS, 457, 3678
Pilyugin L. S., Thuan T. X., 2005, ApJ, 631, 231
Puche D., Westpfahl D., 1994, in Meylan G., Prugniel P., eds, European Southern Observatory Conference and Workshop Proceedings, Vol. 49. European Southern Observatory, Garching, p. 273
Rahner D., Pellegrini E. W., Glover S. C. O., Klessen R. S., 2017, MNRAS, 470, 4453
Sargent W. L. W., Sancisi R., Lo K. Y., 1983, ApJ, 265, 711
Schaerer D., Vacca W. D., 1998, ApJ, 497, 618
Sedov L. I., 1946, Dokl. Akad. Nauk SSSR, 52, 17
Seon K.-I., 2009, ApJ, 703, 1159
Sharma P., Roy A., Nath B. B., Shchekinov Y., 2014, MNRAS, 443, 3463
Simpson C. E., Hunter D. A., Knezek P. M., 2005, AJ, 129, 160
Skillman E. D., Terlevich R., Teuben P. J., van Woerden H., 1988, A&A, 198, 33
Smith L. J., Norris R. P. F., Crowther P. A., 2002, MNRAS, 337, 1309
Stilp A. M., Dalcanton J. J., Warren S. R., Skillman E., Ott J., Koribalski B., 2013, ApJ, 765, 136
Tang J., Bressan A., Rosenfield P., Slemer A., Marigo P., Girardi L., Bianchi L., 2014, MNRAS, 445, 4287
Tully R. B., Bottinelli L., Fisher J. R., Gougenheim L., Sancisi R., van Woerden H., 1978, A&A, 63, 37
Utrobin V. P., Chugai N. N., 2017, MNRAS, 472, 5004
van Dyk S. D., Puche D., Wong T., 1998, AJ, 116, 2341
Vasiliev E. O., Shchekinov Y. A., 2017, Open Astron., 26, 233
Vasiliev E. O., Moiseev A. V., Shchekinov Y. A., 2015a, Baltic Astron., 24, 213
Vasiliev E. O., Nath B. B., Shchekinov Y., 2015b, MNRAS, 446, 1703
Vorobyov E. I., Basu S., 2005, A&A, 431, 451
Walter F., Brinks E., de Blok W. J. G., Bigiel F., Kennicutt R. C., Thornley M. D., Leroy A. K., 2008, AJ, 136, 2563
Warren S. R. et al., 2011, ApJ, 738, 10
Warren S. R. et al., 2012, ApJ, 757, 84
Weaver R., McCray R., Castor J., Shapiro P., Moore R., 1977, ApJ, 218, 377
Weisz D. R., Skillman E. D., Cannon J. M., Dolphin A. E., Kennicutt R. C.,, Jr, Lee J. C., Walter F., 2008, ApJ, 689, 160
Weisz D. R., Skillman E. D., Cannon J. M., Walter F., Brinks E., Ott J., Dolphin A. E., 2009a, ApJ, 691, L59
Weisz D. R., Skillman E. D., Cannon J. M., Dolphin A. E., Kennicutt R. C., Lee J. C., Walter F., 2009b, ApJ, 704, 1538
Westpfahl D., Puche D., 1994, in Meylan G., Prugniel P., eds, European Southern Observatory Conference and Workshop Proceedings, Vol. 49. European Southern Observatory, Garching, p. 295
Wiebe D. S., Khramtsova M. S., Egorov O. V., Lozinskaya T. A., 2014, Astron. Lett., 40, 278
Young L. M., Lo K. Y., 1997, ApJ, 490, 710
Zhang K. et al., 2017, MNRAS, 466, 3217

This paper has been typeset from a TEX/LATEX file prepared by the author.

Downloaded from https://academic.oup.com/mnras/article-abstract/478/3/3386/4992763
by Special Astrophysical Observatory of the Russian Academy of Sciences user
on 06 August 2018

Monthly Notices
of the
ROYAL ASTRONOMICAL SOCIETY

MNRAS **467,** L1–L5 (2017) doi:10.1093/mnrasl/slw246

The ultraluminous X-ray source HoII X-1: kinematic evidence of its escape from a cluster

Oleg V. Egorov,[1⋆] Tatiana A. Lozinskaya[1] and Alexei V. Moiseev[1,2]

[1]*Sternberg Astronomical Institute, Lomonosov Moscow State University, Universitetsky pr. 13, Moscow 119234, Russia*
[2]*Special Astrophysical Observatory, Russian Academy of Sciences, Nizhnii Arkhyz 369167, Russia*

Accepted 2016 December 6. Received 2016 November 22; in original form 2016 July 5

ABSTRACT

We analyse the structure and kinematics of ionized gas in the vicinity of the ultraluminous X-ray source (ULX) HoII X-1 in the Holmberg II galaxy using observational data obtained with a scanning Fabry–Perot interferometer in the Hα, [S II] and [O III] emission lines at the Russian 6-m telescope. Decomposition of the line profiles allows us to identify the broad component of emission lines caused by the ULX action. We found evidence of an expanding superbubble around the young star cluster located in the region studied. We conclude that the blueshifted 'arc' around the ULX observed in the line-of-sight velocity field may correspond to a bow shock caused by the ULX movement from that nearby young star cluster. If this interpretation is correct, it will be the first kinematic evidence of a ULX's escape from its parent star cluster.

Key words: ISM: bubbles – H II regions – ISM: kinematics and dynamics – galaxies: individual: Holmberg II – X-rays: individual: HoII X-1.

1 INTRODUCTION

Ultraluminous X-ray sources (ULXs) are unique off-nucleus point-like objects, with luminosities (10^{39}–10^{41} erg s^{-1}) exceeding the Eddington limit. Their nature has been under debate for over 20 years. These objects are often considered as intermediate-mass black hole (IMBH) candidates (e.g. Colbert & Mushotzky 1999; Miller et al. 2003), while recent studies support the idea of supercritical accretion discs around stellar mass black holes as the source of anisotropic X-ray radiation of ULXs (e.g. Begelman 2002; Fabrika et al. 2015; Roberts et al. 2016).

Studies of extragalactic ULXs revealed their association with young star clusters (Zezas et al. 2002; Abolmasov et al. 2007; Swartz, Tennat & Soria 2009). Poutanen et al. (2013) showed that all bright X-ray sources (including 6 ULXs) in the Antennae galaxies are significantly associated with young clusters, but they are located outside these clusters. Together with similar findings by Kaaret et al. (2004b) for X-ray binaries of lower luminosities, this result allows to assume that the offset from star clusters is a common property of both ULXs and less bright X-ray binaries. Poutanen et al. concluded that the large displacements (up to 300 pc) are most probably caused by their fast (∼80 km s^{-1}) ejection from clusters due to close encounters (e.g. Mapelli et al. 2011; Goswami, Kiel & Rasio 2014). Despite the fact that observations reveal displacement of ULXs, no direct evidence of their motion outward from star clusters has been found so far.

Only a small fraction of ∼150 known ULXs reveal surrounding optical nebulae (Pakull & Mirioni 2002). Among such objects is HoII X-1 in the Holmberg II galaxy – one of the most luminous ULXs known ($L_{\rm bol} \sim 1.34 \times 10^{40}$ erg s^{-1} according to Berghea et al. 2010a). It is located in the eastern part of the H II region HSK 70 (according to the catalogue by Hodge, Strobel & Kennicutt 1994), also known as the 'Foot Nebula' owing to its geometry (see Fig. 1). The shape of the 'Foot Nebula' is most probably caused by the influence of the young star cluster (its age is ∼3.5–4.5 Myr, according to Stewart et al. 2000) located to the west from the ULX.

A nebula with a size of about 20 × 50 pc bright in the He II 4686-Å emission line surrounds the ULX HoII X-1 in the small eastern part ('heel') of the 'Foot Nebula' (Pakull & Mirioni 2002; Kaaret, Ward & Zezas 2004a; Lehmann et al. 2005). Moon et al. (2011) revealed that the He II nebula is more extended and has a size of ∼122 pc. Our long-slit observations presented in Egorov, Lozinskaya & Moiseev (2013) also revealed He II emission at such a distance from the ULX. These studies support the photoionization mechanism of He II line excitation by reprocessing of HoII X-1 X-ray emission.

Lehmann et al. (2005) performed integral-field unit (IFU) spectral observations of the nebula and investigated ionization conditions and gas kinematics in the 'heel' of the 'Foot Nebula'. They found that the velocity dispersion in the Hβ emission line is two times higher at the position of the ULX compared with the HSK 70 nebula, as well as finding significant radial velocity variations inside the He II region. The authors explained complex gas kinematics as

⋆ E-mail: egorov@sai.msu.ru

© 2016 The Authors
Published by Oxford University Press on behalf of the Royal Astronomical Society

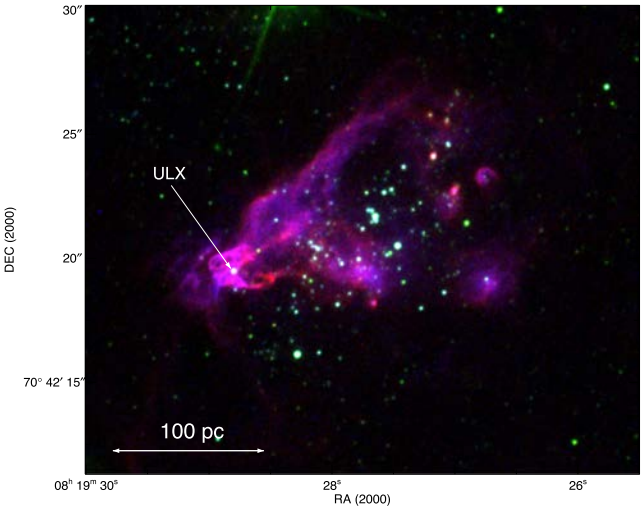

Figure 1. False–colour image of the 'Foot Nebula' HSK 70 constructed using *Hubble Space Telescope* ACS/WFC archive data, which were originally published in Hong et al. (2013). The red channel corresponds to the image obtained with filter F658N, green with F814W and blue with F502N. The ULX HoII X-1 location is shown.

arising from the influence of the ULX, which dynamically perturbs the surrounding interstellar medium (ISM) via jets or the accretion-disc wind.

An extended synchrotron radio source surrounds the ULX (Miller, Mushotzky & Neff 2005) and coincides with the He II emission-line nebula in the 'heel' (Cseh et al. 2012). Cseh et al. (2014, 2015) discovered a collimated jet structure responsible for the inflation of the surrounding radio bubble. Their results suggest that HoII X-1 is powered by a black hole with mass in the range 25–100 $M_{\odot}$ accreting at a high Eddington rate with intermittent radio activity.

Berghea et al. (2010a,b) have detected [O IV] 25.89-μm emission in the 'heel' and concluded that photoionization by soft X-ray and far-ultraviolet (FUV) radiation from the ULX is responsible for the [O IV] emission, while shocks likely contribute very little.

Heida et al. (2014) discovered the near-infrared (NIR) counterpart; its NIR luminosity far exceeds the expected jet contribution. The authors related the NIR excess to a red supergiant companion or to the nebula surrounding the ULX.

The data mentioned above suggest the influence of both the ULX and the nearby young star cluster on the surrounding ISM. The accurate separation of the ULX contribution from the totality of processes regulating the morphology and dynamics of the 'Foot Nebula' is necessary.

In our recent article (Egorov et al. 2017, hereafter Paper I), we report the results of ionized gas structure and kinematics investigations of the star formation complexes in the Holmberg II galaxy. In this article, we present a detailed study of the ULX vicinity using the data described in Paper I and some additional data sets.

2 OBSERVATIONS AND DATA REDUCTION

Observations were made at the prime focus of the 6-m telescope of the Special Astrophysical Observatory of the Russian Academy of Sciences (SAO RAS) using a scanning Fabry–Perot interferometer (FPI) IFP751 mounted inside the SCORPIO-2 multi-mode focal reducer (Afanasiev & Moiseev 2011). A detailed description of the observations performed and data reduction are presented in Paper I.

Table 1. Log of FPI observational data.

Data set	Date of obs	T_{exp}, s	θ, ″	$\Delta\lambda$, Å	$\delta\lambda$, Å
Hα #1	2011 Apr 26/27	40 × 240	1.4	8.7	0.48
Hα #2	2014 Dec 16/17	40 × 160	1.4	8.7	0.48
[S II]	2011 Oct 30/31	40 × 360	1.1	9.2	0.48
[O III]	2009 Feb 27/28	27 × 200	1.5	7.6	0.81

All the data cubes have a field of view of 6.1 × 6.1 arcmin, where each pixel of 0.71 arcsec in size contains a 36- or 40-channel spectrum of a small region $\Delta\lambda$ around the desired emission line. Table 1 summarizes the properties of the observed data: name of data set, date of observations, exposure time, final spatial resolution (θ), spectral range ($\Delta\lambda$) and spectral resolution ($\delta\lambda$ – full width at half-maximum (FWHM) of the instrumental profile).

In addition to the mosaic of two observed data cubes in the Hα line used in Paper I, we also analyse the data cubes in the [S II] λ6717-Å and [O III] λ5007-Å emission lines reduced in the same way as the Hα data cube. The [S II] data cube was obtained with the same SCORPIO-2 device, while [O III] observations taken from the SAO RAS archive were performed for a program by P. Abolmasov with the focal reducer SCORPIO (Afanasiev & Moiseev 2005) and FPI having twice as low a spectral resolution (see Table 1). The original [O III] data set was completed only by 75 per cent on 36 scanning channels because of bad weather conditions. Fortunately, our new wavelength calibration algorithms (Moiseev 2015) allow us to restore emission-line spectra in the region around the HSK 70 nebulae.

Before analysing, we have subtracted a circular rotation model for Holmberg II from the data cubes (the procedure is described in Paper I). It allowed us to analyse the local ionized gas motions, not related to the regular rotation of the galaxy disc. Due to that, the velocity scale in all figures is shown to be relative to the mean velocity.

Because of the lower signal-to-noise ratio for the [S II] and [O III] data cubes in comparison with the Hα one, we used them only for additional control of the results obtained from the Hα line. We fitted the line profiles in each pixel of the reduced data cubes with a one- or two-component Voigt function (a convolution of the Lorentzian and Gaussian functions corresponding to the FPI instrumental profile and to the broadening of the observed emission lines, respectively) to obtain information about ionized gas kinematics in the region (the procedure is described in Moiseev & Egorov 2008).

3 RESULTS AND DISCUSSION

3.1 Ionized gas kinematics of the 'Foot Nebula'

As we noted above, Lehmann et al. (2005) performed IFU observations of the nebula around HoII X-1 and revealed the complexity of the 'Foot Nebula' kinematics. While their observations provide a much larger spectral range, our data have 3–15 times better spectral resolution and slightly better spatial resolution and sampling. This allows us to decompose a line profile in the regions where it shows asymmetry or significant broadening.

Fig. 2 shows several examples of the Hα line profile, which correspond to different parts of the 'Foot Nebula', and the results of their decomposition. The top image in this figure corresponds to the Hα line intensity distribution in the nebula according to our FPI data, while the bottom image shows the line-of-sight velocity dispersion ($\sigma_{H\alpha}$) map, free from instrumental broadening.

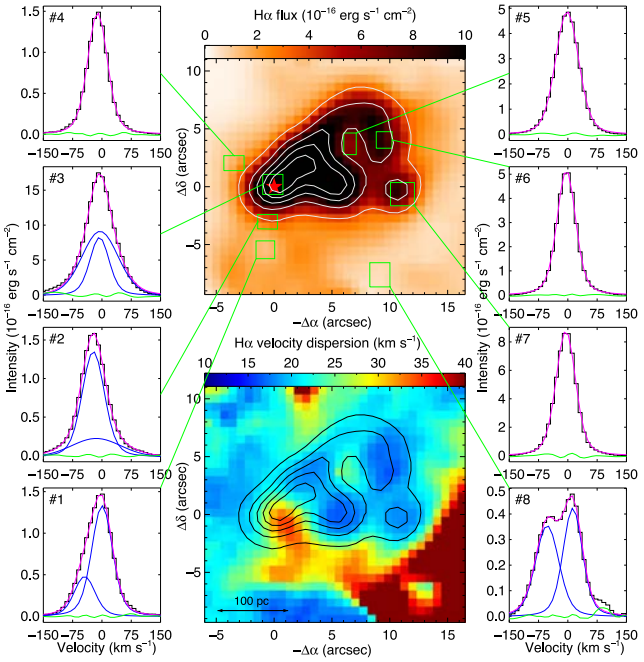

Figure 2. 'Foot Nebula' mapped with the scanning FPI in the Hα line. The line flux (top image) and line-of-sight velocity dispersion (bottom image) are shown. Isophotes of the Hα brightness are overlaid. A red star shows the position of the ULX. Green rectangles denote the area of emission-line profile integrations. Black lines denote the observed line profiles, blue lines show individual Voigt components, magenta lines the model spectrum and green lines the residuals of its subtraction.

The Hα line profile could be fitted by a single narrow component ($\sigma_{\mathrm{H}\alpha} = 13$–$18$ km s^{-1}) in most parts of the HSK 70 nebula. Our data show two regions with peaks of velocity dispersion consistent with Lehmann et al. (2005). One of them corresponds to the ULX vicinity, while another is located in the north-western part of the nebula.

The line-of-sight velocity dispersion is twice as large near the ULX, which agrees with the estimates of Lehmann et al. (2005). Broadening of the line profiles is probably caused by the contribution of the broad component from the ULX to the observed line-of-sight spectrum. Indeed, the Hα line profiles there could be fitted by narrow and broad ($\sigma_{\mathrm{H}\alpha} = 42$–$60$ km s^{-1}) components (profiles 2 and 3 in Fig. 2).

A region of significant contribution of the broad component to the emission-line profile surrounds the ULX. It coincides with the northern part of the area of elevated velocity dispersion around the ULX (in the bright part of the HSK 70 nebula), while two resolved narrow components are presented in the southern part of this area (see profiles 1 and 8). The Hα line profile broadening there, as well as its clear separation into two components, is caused by the interaction of HSK 70 with the ionized supershell southwestward of it, the origin of which is not related to the 'Foot Nebula' (see Paper I).

The Hα line profiles of the second region of increased velocity dispersion inside the HSK 70 nebula (profile 5 in Fig. 2) might be represented by a single component with $\sigma_{\mathrm{H}\alpha}$ up to 24 km s^{-1}. The Hα image reveals a shell-like structure in this area. Its comparison with the location of the stars in Fig. 1 allows us to conclude that there we observe an expanding shell around a young star cluster, but our resolution is insufficient to separate the individual components corresponding to its approaching and receding sides clearly.

Therefore, the 'Foot Nebula' is located at the north-eastern edge of the kinematically active star formation complex and is regulated by the influence of the young star cluster (which blew up the ionized superbubble around it) and the ULX. The presence of a broad component in emission-line profiles points to the significant influence of the ULX on the surrounding ISM.

3.2 Bow shock around the ULX?

We found an intriguing structure in the ionized gas line-of-sight velocity distribution constructed by pixel-by-pixel fitting of the data cubes with a single-component Voigt function. Fig. 3 shows velocity fields for the HSK 70 nebula and its surroundings in the Hα, [S II] and [O III] emission lines. These maps reveal a blueshifted 'arc' surrounding the 'Foot Nebula' from the east of the ULX. This 'arc' is better seen in Hα but is also detected in both [S II] and [O III] lines. Its line-of-sight velocities are shifted by −10 to −15 km s^{-1} from the mean velocity in the nebula. Here we try to explain this observed feature.

The 'arc' is located at the edge of the bright HSK 70 nebula and corresponds to faint emission of the ionized gas. Its mean brightness in the Hα line is about 4.6×10^{-16} erg s^{-1} cm^{-2} arcsec^{-2} (2.7×10^{-16} and 9.5×10^{-16} in the faint north-eastern and bright eastern parts, respectively). For comparison, the mean brightness of the HSK 70 nebula is 1.9×10^{-15} erg s^{-1} cm^{-2} arcsec^{-2}. Due to this fact, one may suggest that we observe some sort of edge effects at the border of the bright H II region and background or foreground diffuse emission. However, in this case it is straightforward to expect such features at the borders of other bright nebulae in the galaxy, but only HSK 70 reveals it. Moreover, the reasonable question arises: why is this feature not homogeneous or randomly distributed, but has a shape that clearly matches the shape of the nebula? Even if the 'arc' is indeed corresponds to a diffuse emission, it most probably should be regulated by something tied with the 'Foot Nebula' and the most obvious source is the ULX.

Note that the 'blue filament' at $(-\Delta\alpha, \Delta\delta) = (12, -8)$ connected to the 'arc' (see Hα velocity field in Fig. 3) has a different origin. Contrary to what observed in the 'arc', the Hα line profile there is clearly composed of two components (see profile 8 in Fig. 2 as an example), which is the reason why this structure is blueshifted in the velocity fields constructed by fitting with a single Voigt component. The complex kinematics of the ionized gas in this region located to the south of the ULX is discussed in our Paper I.

The 'arc' shape (as well as the shape of the 'heel' of the 'Foot Nebula') looks like a bow shock. We propose that it may be indeed a bow shock caused by the ULX motion. Let us check now whether the ULX escaping from the nearby young star cluster might create such a large bow shock having the shape of the observed 'arc'.

According to the analytical solution for the shape of a stellar wind bow shock in the thin-shell limit, as derived in Wilkin (1996):

$$R = R_0 \csc\theta \sqrt{3(1 - \theta \cot\theta)}, \quad (1)$$

where R is the distance from the source at which a bow shock front is observed in the direction of an azimuthal angle θ. The stand-off radius R_0 can be expressed as (Baranov, Krasnobaev & Kulikovskii 1971)

$$R_0 = \sqrt{\frac{\dot{M}_{\mathrm{w}} \upsilon_{\mathrm{w}}}{4\pi \rho_{\mathrm{AMB}} \upsilon_{\mathrm{ULX}}^2}}, \quad (2)$$

where $\dot{M}_{\mathrm{w}}$ is the wind mass-loss rate, υ_{w} is the terminal wind velocity, υ_{ULX} is the velocity of the ULX and ρ_{AMB} is the ambient gas

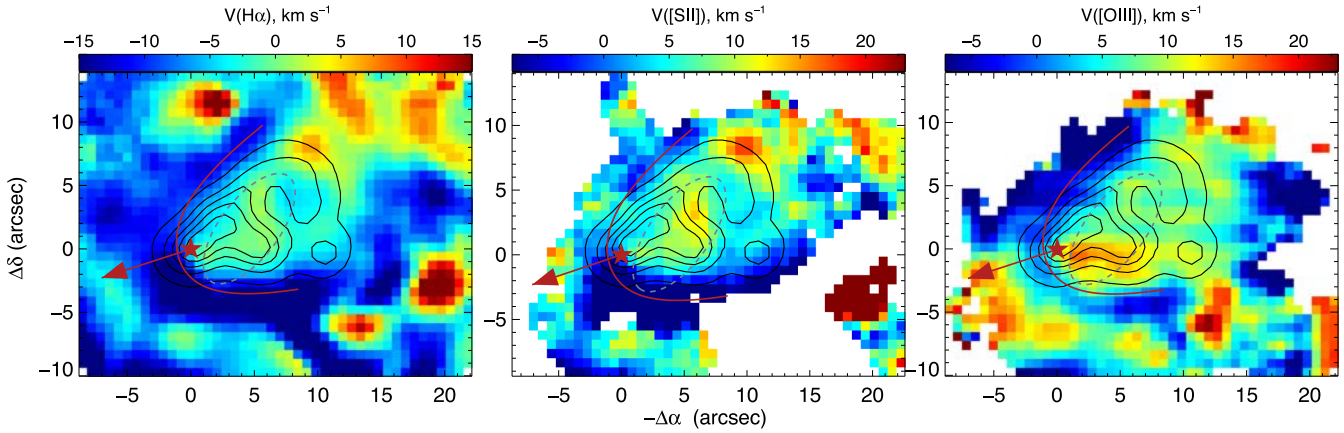

Figure 3. 'Foot Nebula' HSK 70 and its surroundings: line-of-sight velocity fields in the Hα (left), [S II] (middle) and [O III] (right) emission lines. Pixels with signal-to-noise ratio less than 5 were masked. A red star denotes the position of HoII X-1, black contours are Hα isophotes from the previous figure and a grey dashed ellipse shows the borders of a young cluster. A red curve shows the modelled shape of a bow shock that might be induced by the ULX motion in the direction shown with an arrow (see text).

density. According to Paper I, the ambient volume density in the area is $n_{\rm H} \simeq 0.7\,{\rm cm}^{-3}$, which corresponds to $\rho_{\rm AMB} \simeq 1.6 \times 10^{-24}\,{\rm g\,cm}^{-3}$, if the helium contribution in the total gas mass is taken into account.

We estimate the velocity of HoII X-1 from the following considerations. The borders of the young cluster associated with the HSK 70 nebula are shown in Fig. 3. Most probably, the ULX was ejected from that cluster. Stewart et al. (2000) have found that the age of this cluster is 3.5–4.5 Myr. For the $\upsilon_{\rm ULX}$ estimation, we assume that the ULX started to move from the cluster's centre in the direction of its current position ∼4 Myr ago. In that case, the length of the HoII X-1 path in the galactic plane is 290 pc (for the accepted disc inclination $i = 49^\circ$ according to Oh et al. 2011), which gives $\upsilon_{\rm ULX} \simeq 70\,{\rm km\,s}^{-1}$. This value agrees with typical velocities of ULXs in the Antennae galaxy ($\upsilon_{\rm ULX} = 80$–$90\,{\rm km\,s}^{-1}$) according to Poutanen et al. (2013).

Unfortunately, there are no HoII X-1 wind parameters known, but we still may estimate R_0 using the following suggestions. Fabrika et al. (2015) showed that the nature of the well-known Galactic X-ray source SS 433 is most probably the same as that of extragalactic ULXs. Hence, in our analysis we may use the values of $\dot{M}_{\rm w} = 5 \times 10^{-4}\,{\rm M}_\odot\,{\rm yr}^{-1}$ (Begelman, King & Pringle 2006) and $\upsilon_{\rm w} \sim 1500\,{\rm km\,s}^{-1}$ (Fabrika 2004) adopted for SS 433. On the other hand, Pinto, Middleton & Fabian (2016) discovered very high outflow velocities $\upsilon_{\rm w} \sim 0.2c$ from two ULXs. Due to the fact that the supersonic wind power of ULXs is often comparable to their X-ray luminosity, $\dot{M}_{\rm w} \sim 1 \times 10^{-5}\,{\rm M}_\odot\,{\rm yr}^{-1}$ for HoII X-1. Both estimates give almost the same value of $\dot{M}_{\rm w}\upsilon_{\rm w}$.

Using the parameters estimated above, we found $R_0 \simeq 27$ pc from Equation (2) and the bow shock shape in the Galactic plane computed from Equation (1). The red curves in Fig. 3 correspond to the shape of a bow shock after projection on to the sky plane using the parameters of Holmberg II galactic disc orientation from Oh et al. (2011). These curves coincide well with the 'arcs' of negative line-of-sight velocities in all three emission lines. Note that variations of galaxy inclination and ULX velocity would change these curves insignificantly. Therefore, we suppose that the observed features in the velocity field could indeed be treated as a sign of a bow shock from the moving ULX HoII X-1.

The results presented suppose that HoII X-1 was ejected from the cluster in the galactic plane, or at least with a small angle to that. We performed several calculations proposing a larger angle and found that our adopted parameters give the best agreement with observations.

The shape of the observed 'arc' is consistent with the calculated model of a bow shock from the moving ULX. However, it is still desirable to find additional signs of the bow shock origin of the 'arc'. Unfortunately, relatively low spatial resolution and strong contamination by the bright H II region make comparison with existing models (e.g. Meyer et al. 2016) of the emission from bow shocks unreliable. Optical spectroscopy might provide an additional clue but, as follows from Fig. 3, we deal with slow shocks, the contribution of which to the emission is negligible – according to Allen et al. (2008), the significant influence of shocks on the spectrum starts from velocities of about $100\,{\rm km\,s}^{-1}$. However, we still may observe local high-velocity filaments in the bow shock having an elevated ratio of sensitive to collisional excitation lines. We indeed see an increase of the I([S II])/I(Hα) ratio at the positions of the 'arc' in the spectra published in Egorov et al. (2013) (and much better in the archival spectra of HoII X-1 obtained by Fabrika et al. 2015 at the SUBARU telescope), yet its values are still too low to be interpreted as a sign of shock excitation. The elevated I([S II])/I(Hα) ratio may be explained by high velocity filaments, or by the lower ionization state at the border of the H II region. In the first case it might be revealed, for example, by high-resolution narrow-band imaging with the *Hubble Space Telescope* (*HST*). Unfortunately, Holmberg II has never been observed by *HST* in the [S II] emission line.

Summing up, the 'arc' could indeed be a bow shock caused by the ULX moving from the star cluster in HSK 70, though additional confirmation is desirable. In that case, it is the first kinematic evidence of ULX's escape from its parental star cluster. Our conclusion agrees with the results obtained by Kaaret et al. (2004b) and Poutanen et al. (2013), who showed that the majority of ULXs are associated with young ($t < 5$ Myr) star clusters, yet reside outside them.

4 SUMMARY

The HSK 70 nebula ('Foot Nebula') associated with the ULX HoII X-1 was observed in Hα, [S II] and [O III] emission lines with a scanning Fabry–Perot interferometer. Using these data, we obtained the following results.

(i) Two regions of increased line-of-sight velocity dispersion are observed inside the nebula. Relatively high velocity dispersion in one of them most probably corresponds to the expanding ionized superbubble around the young star cluster, while the second one clearly reveals the presence of a broad component caused by the ULX influence on the ISM.

(ii) The velocity fields reveal a blueshifted 'arc', the shape of which looks like a bow shock. Comparison with the analytical solution by Wilkin (1996) for the shape of a stellar wind bow shock in the thin-shell limit shows that this structure could indeed be a bow shock created by the ULX moving from the central part of the star cluster in HSK 70.

The most important result is that we found kinematic evidence of a bow shock around the ULX, which in our view strongly suggests its escape from the parental star cluster. Up to now, all conclusions about the escape of ULXs were based only on their location outside the cluster.

ACKNOWLEDGEMENTS

The authors are grateful to the anonymous referee for constructive comments and suggestions and also to S. I. Blinnikov for useful discussions. The work is based on observations obtained with the SAO RAS 6-m telescope carried out with the financial support of the Ministry of Education and Science of the Russian Federation (agreement No. 14.619.21.0004, project ID RFMEFI61914X0004). Fig. 1 in this article is based on observations made with the NASA/ESA *Hubble Space Telescope* and obtained from the *Hubble* Legacy Archive, which is a collaboration between the Space Telescope Science Institute (STScI/NASA), the European Space Agency (ST-ECF/ESAC/ESA) and the Canadian Astronomy Data Centre (CADC/NRC/CSA). The study was supported by the Russian Foundation for Basic Research (RFBR), project 14-02-00027. AVM and OVE are also grateful for financial support (grant MD3623.2015.2) from the President of the Russian Federation.

REFERENCES

Abolmasov P., Fabrika S., Sholukhova O., Afanasiev V., 2007, Astrophys. Bull., 62, 36
Afanasiev V. L., Moiseev A. V., 2005, Astron. Lett., 31, 194
Afanasiev V. L., Moiseev A. V., 2011, Baltic Astron., 20, 363
Allen M. G., Groves B. A., Dopita M. A., Sutherland R. S., Kewley L. J., 2008, ApJS, 178, 20
Baranov V. B., Krasnobaev K. V., Kulikovskii A. G., 1971, Sov. Phys. Dokl., 15, 791
Begelman M. C., 2002, ApJ, 568, L97
Begelman M. C., King A. R., Pringle J. E., 2006, MNRAS, 370, 399
Berghea C. T., Dudik R. P., Weaver K. A., Kallman T. R., 2010a, ApJ, 708, 354
Berghea C. T., Dudik R. P., Weaver K. A., Kallman T. R., 2010b, ApJ, 708, 364
Colbert E. J. M., Mushotzky R. F., 1999, ApJ, 519, 89
Cseh D. et al., 2012, ApJ, 749, 17
Cseh D. et al., 2014, MNRAS, 439, 1
Cseh D. et al., 2015, MNRAS, 452, 24
Egorov O. V., Lozinskaya T. A., Moiseev A. V., 2013, MNRAS, 429, 1450
Egorov O. V., Lozinskaya T. A., Moiseev A. V., Shchekinov Yu. A., 2017, MNRAS, 464, 1833
Fabrika S., 2004, Astrophys. Space Phys. Rev., 12, 1
Fabrika S., Ueda Y., Vinokurov A., Sholukhova O., Shidatsu M., 2015, Nature Phys., 11, 551
Goswami S., Kiel P., Rasio F. A., 2014, ApJ, 781, 81
Heida M. et al., 2014, MNRAS, 442, 1054
Hodge P., Strobel N. V., Kennicutt R. C., 1994, PASP, 106, 309
Hong S., Calzetti D., Gallagher J. S., Martin C. L., Conselice C. J., Pellerin A., 2013, ApJ, 777, 63
Kaaret P., Ward M. J., Zezas A., 2004a, MNRAS, 351, L83
Kaaret P., Alonso-Herrero A., Gallagher J. S., Fabbiano G., Zezas A., Rieke M. J., 2004b, MNRAS, 348, L28
Lehmann I. et al., 2005, A&A, 431, 847
Mapelli M., Ripamonti E., Zampieri L., Colpi M., 2011, MNRAS, 416, 1756
Meyer D. M.-A, van Marle A.-J., Kuiper R., Kley W., 2016, MNRAS, 416, 1756
Miller J. M., Fabbiano G., Miller M. C., Fabian A. C., 2003, ApJ, 585, L37
Miller N. A., Mushotzky R. F., Neff S. G., 2005, ApJ, 623, 109
Moiseev A. V., 2015, Astrophys. Bull., 70, 494
Moiseev A. V., Egorov O. V., 2008, Astrophys. Bull., 63, 181
Moon D.-S., Harrison F. A., Cenko S. B., Shariff J. A., 2011, ApJ, 731, 32
Oh S.-H., de Blok W. J. G., Brinks E., Walter F., Kennicutt R. C., Jr, 2011, AJ, 141, 193
Pakull M. W., Mirioni L., 2002, preprint (astro-ph/0202488)
Pinto C., Middleton M. J., Fabian A. C., 2016, Nature, 533, 64
Poutanen J., Fabrika S., Valeev A. F., Sholukhova O., Greiner J., 2013, MNRAS, 432, 506
Roberts T. P., Middleton M. J., Sutton A. D., Mezcua M., Walton D. J., Heil L. M., 2016, Astron. Nachr., 337, 534
Stewart S. G. et al., 2000, ApJ, 529, 201
Swartz D. A., Tennant A. F., Soria R., 2009, ApJ, 703, 159
Wilkin F. P., 1996, ApJL, 459, L31
Zezas A., Fabbiano G., Rots A. H., Murray S. S., 2002, ApJS, 142, 239

This paper has been typeset from a TEX/LATEX file prepared by the author.

Monthly Notices
of the
ROYAL ASTRONOMICAL SOCIETY

MNRAS **464,** 1833–1853 (2017)
Advance Access publication 2016 September 16

doi:10.1093/mnras/stw2367

Complexes of triggered star formation in supergiant shell of Holmberg II

Oleg V. Egorov,[1⋆] Tatiana A. Lozinskaya,[1] Alexei V. Moiseev[1,2] and Yuri A. Shchekinov[3]

[1]*Sternberg Astronomical Institute, Lomonosov Moscow State University, Universitetsky pr. 13, Moscow 119234, Russia*
[2]*Special Astrophysical Observatory, Russian Academy of Sciences, Nizhny Arkhyz 369167, Russia*
[3]*P. N. Lebedev Physical Institute, 53 Leninskiy Prospekt, Moscow 119991, Russia*

Accepted 2016 September 15. Received 2016 September 4; in original form 2016 May 11

ABSTRACT

We report a detailed analysis of all regions of current star formation in the walls of the supergiant H I shell (SGS) in the galaxy Holmberg II based on observations with a scanning Fabry–Perot interferometer at the Russian 6-m telescope. We compare the structure and kinematics of ionized gas with that of atomic hydrogen and with the stellar population of the SGS. Our deep Hα images and archival images taken by the *Hubble Space Telescope* demonstrate that current star formation episodes are larger and more complicated than previously thought: they represent unified star-forming complexes with sizes of several hundred pc rather than 'chains' of separate bright nebulae in the walls of the SGS. The fact that we are dealing with unified complexes is evidenced by identified faint shell-like structures of ionized and neutral gas which connect several distinct bright H II regions. Formation of such complexes is due to the feedback of stars with very inhomogeneous ambient gas in the walls of the SGS. The arguments supporting an idea about the triggering of star formation in SGS by the H I supershells collision are presented. We also found a faint ionized supershell inside the H I SGS expanding with a velocity of no greater than 10–15 km s^{-1}. Five OB stars located inside the inner supershell are sufficient to account for its radiation, although a possibility of leakage of ionizing photons from bright H II regions is not ruled out as well.

Key words: ISM: bubbles – ISM: kinematics and dynamics – galaxies: individual: Holmberg II – galaxies: ISM – galaxies: star formation.

1 INTRODUCTION

Irregular galaxies are widely used to study stellar feedback: radiation, stellar winds and supernovae (SNe) that regulate the structure and kinematics of the interstellar medium (ISM) and might trigger new episodes of star formation. Due to the lack of spiral waves and the fact that gaseous discs are thicker than those in spiral galaxies, irregular galaxies reveal giant H I supershells and holes with sizes as large as 1–2 kpc and lifetimes up to several hundred Myr. Giant supershells and holes in some galaxies represent the dominant feature of the ISM (see e.g. Young & Lo 1997; Ott et al. 2001; Simpson, Hunter & Knezek 2005; Cannon et al. 2011a; Warren et al. 2011, and references therein). Such large structures are usually called supergiant shells (SGS), or giant supershells.

Formation mechanisms of supergiant shells have been discussed extensively in recent decades. In the standard approach based on the Weaver et al. (1977) model, the cumulative action of multiple stellar winds and SNe explosions is responsible for H I shells formation (see e.g. McCray & Kafatos 1987; Tenorio-Tagle & Bodenheimer 1988; Ott et al. 2001). However, it has been recognized long ago (see e.g. Tenorio-Tagle & Bodenheimer 1988; Kim et al. 1999; Rhode et al. 1999; Simpson at al. 2005; Silich et al. 2006) that this scenario cannot explain the origin of giant supershells, in which the mechanical energy input from detected stellar clusters appears to be inconsistent with that required by the standard model. Several other mechanisms have been proposed: collisions of high-velocity clouds with galactic discs (Tenorio-Tagle 1981), fractal ISM (Elmegreen 1997), radiation pressure from field stars (Elmegreen & Chiang 1982), ram pressure of the intergalactic medium (Bureau & Carignan 2002), H I dissolution by UV radiation (Vorobyov & Shchekinov 2004), non-linear evolution of self-gravitating turbulent galactic discs (Wada, Spaans & Kim 2000; Dib & Burkert 2005) and even exotic mechanisms (see references in Silich et al. 2006 and Warren et al. 2011).

The Im type (Magellanic-type irregulars) non-interacting gas-rich galaxy Holmberg II (Ho II), a member of the M81 – NGC 2403 group, is one of the main 'laboratories' for studying this phenomenon. Puche et al. (1992) explained the formation of SGSs and giant H I cavities in Holmberg II by the effect of multiple SN

⋆ E-mail: egorov@sai.msu.ru

© 2016 The Authors
Published by Oxford University Press on behalf of the Royal Astronomical Society

Downloaded from http://mnras.oxfordjournals.org/ at Special Astrophysical Observatory of the Russian Academy of Sciences on November 15, 2016

explosions and stellar winds of massive stars located inside the associations. Maschenko & Silich (1995) adopted this mechanism of SGSs formation and explained the discrepancy between the computed and observed elongation of many such shells by their mutual interaction and inhomogeneity of the ambient medium. The problem of the validity of such a 'standard mechanism' in the case of Holmberg II was first considered by Rhode et al. (1999) and then discussed by Bureau & Carignan (2002) and Weisz et al. (2009b). The trouble with it was that many supershells lacked young stellar associations whose energy could be sufficient to produce the observed structures.

By now, it is well established that high star formation rates can be maintained for a much longer time period than previously believed: dwarf galaxies are characterized by the ability to sustain a high star-formation efficiency over several hundred Myr, and in some cases even up to 1 Gyr – the specific (per stellar mass unit) star formation rate is high enough to exhaust gas content in 0.4–1 Gyr (McQuinn et al. 2009, 2010a,b) with local short starbursts occurring during this period. Such long periods of intense star formation provide enough energy from stellar winds and SN explosions to drive the formation of giant cavities and supershells (see e.g. Weisz et al. 2009a; Cannon et al. 2011a,b; Warren et al. 2011). Weisz et al. (2009b) have shown that the supershells and holes in the galaxy Holmberg II contain multiple stellar generations and might have been formed from the energy input of these stars integrated over the lifetime of the H I structure. A comparison of the energy of supergiant shells with the energy inflow from SNe performed by Bagetakos et al. (2011) is also consistent with their formation as a result of multiple starbursts spanning a long period of time.

The energetics of supergiant shells, i.e. the fraction of energy deposited in them by SNe explosions and stellar winds, is a crucial issue for understanding their origin. It is commonly known since the first numerical studies of dynamics of SNe remnants Cox (1972); Chevalier (1974) that after entering the radiative expansion stage, the total energy of the remnant decreases with a radius of $\propto R^{-2}$ to $\propto R^{-3}$, so that on a time-scale of 0.1 Myr, only around 2 per cent of the SN energy is available for driving the shell (see more recent simulations with non-equilibrium cooling by Sharma et al. 2014). Tomisaka, Habe & Ikeuchi (1981) assumed that the fraction of energy radiatively lost by an SN might decrease, when an explosion occurs into a low-density bubble produced by a stellar wind and/or previously exploded SN(e). Within a simplistic model of sequential explosions of 20 to 100 SNe occurring at the same centre, they found qualitatively reasonable agreement with galactic superbubbles. The principal issues: the exact expansion law and the fraction of energy remained for a continuous support of growing superbubbles, have been none the less left beyond clear understanding. In full 3D numerical simulations of sequential SNe exploding at the same centre, Sharma et al. (2014) have found that even on a long time-scale (30–50 Myr), up to 30 per cent of the injected energy can retain into slow expansion of the supershell. This conclusion is valid though only in case of 'coherent' SNe explosions, i.e. when the remnants overlap before entering the radiative stage (Nath & Shchekinov 2013). Numerical models with scattered explosions, i.e. spread through over an active volume, confirm this result: collective action of 'coherent' SNe makes them more efficient in driving supershells, with a fraction of retained energy of $\sim$0.1 on times up to 10 Myr (Vasiliev, Nath & Shchekinov 2015; Yadav et al. 2016). In all cases, the expansion sets asymptotically into a power law close to the standard $t^{3/5}$ wind regime with mechanical luminosity reduced by a factor of approximately 10, though still depending on interrelation between gas density and SN rate (Vasiliev et al. 2015). When the origin of supergiant shells of kpc-scales are concerned, particularly in such galaxies as Ho II and IC 2574, where signs of merging of different superbubbles are clearly seen, numerical description becomes more challenging. However, in conditions typical of dwarf galaxies, the wind expansion law with energy reduced by a factor of 10 would be a reasonable conservative approach.

Short (about 10 Myr) local starbursts, which we observed as complexes of ionized gas, are located mainly inside dense walls of giant H I structures in Holmberg II. According to the modern concepts, ongoing star formation there could be triggered by the expansion and/or collision of supergiant shells. The analysis of the influence of these new sites of star formation on the evolution of supergiant shells and hence on the structure of the gaseous medium of the galaxy is of greatest interest.

This work is a third in the series of our investigations of the galaxy Holmberg II. Previously in Egorov, Lozinskaya & Moiseev (2013), we studied the ionized gas spectra of star-forming regions in Ho II using optical long-slit spectroscopic observations carried out with the 6-m Special Astrophysical Observatory of the Russian Academy of Sciences (SAO RAS) telescope. We estimated oxygen, nitrogen, sulphur, neon and argon abundances in individual H II regions and found the average metallicity in the galaxy to be either 0.1 $Z_\odot$ or 0.3 $Z_\odot$ depending on the estimation method applied.

In Wiebe et al. (2014), we performed a multiwavelength photometric study of star formation regions in Ho II using archival data of *GALEX*, *Spitzer* and *Herschel* space telescopes. We have examined for the first time how the emission of star-forming regions over a wide wavelength range evolves with time. We traced the evolution of the fraction of polycyclic aromatic hydrocarbons and of the hot-grain properties in the galaxy.

The aim of this study is to analyse the kinematics of ionized gas in all regions of star formation and of their ambient neutral gas in the most extended 2 kpc-sized supergiant shell in the galaxy. We search for shell-like structures of ionized gas that reveal signs of expansion and compare them with stellar population in star-forming regions. We also try to recognize kinematic evidences for possible SNe shocks in the eastern chain of bright emission nebulae predicted by Tongue & Westpfahl (1995).

An analysis of gas kinematics in the rim of an H I SGS is of great interest, because it may help to find out how such giant structures change when affected by new local bursts of triggered star formation. When studying the supergiant H I shell with triggered star formation located in the Irr galaxy IC 2574 (Egorov et al. 2014), we found for the first time an inner weak diffuse emission of ionized gas in Hα and [S II] 6717, 6731 lines with kinematic evidences for expansion. We showed that such an inner giant ionized supershell must have likely be formed as a result of the action of Lyman continuum photons escaping the star-forming regions on to the neutral gas in the supergiant H I shell. This is a new phenomenon hitherto unobserved in IC 2574, and the search of such inner shell-like H II structures inside H I supergiant shells in other irregular galaxies seems to be interesting. Earlier, we briefly announced the discovery of a similar giant faint ionized supershell inside the H I SGS in Holmberg II (Egorov, Lozinskaya & Moiseev 2015), which is seen on the bottom panel of Fig. 1; here we report the results of its investigation.

To avoid confusion, further we will use the SGS abbreviation to refer to the supergiant shell in Holmberg II under consideration and will use the full term 'supergiant shell' to denote the entire class of such objects.

This study is based on our observations conducted with the scanning Fabry–Perot interferometer (FPI) in Hα line and with

Downloaded from http://mnras.oxfordjournals.org/ at Special Astrophysical Observatory of the Russian Academy of Sciences on November 15, 2016

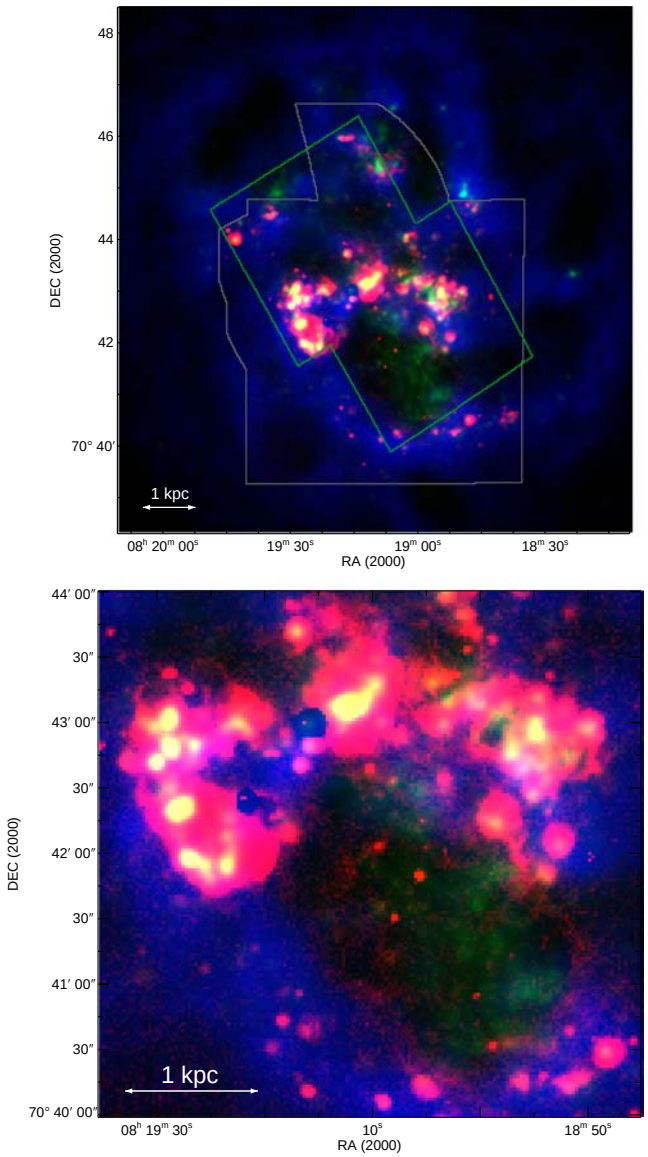

Figure 1. False-colour image of the galaxy Holmberg II: red, green and blue channels correspond to Hα, FUV (*GALEX*) and H I 21-cm (LITTLE THINGS) emission, respectively. The grey line denotes the area covered by our Hα observations (both imaging and FPI) excluding the regions with optical ghosts contamination; the green line shows the area covered by *HST* data we used to identify OB-stars. Bottom image shows the area of active star formation with the different brightness setup.

narrow-band Hα , [S II] and [O III] filters at the 6-m telescope of the SAO RAS. High spatial and spectral resolutions of FPI data allows to analyse the ionized gas kinematics in superbubbles in details. A number of such studies made using this technique were published (see e.g. Lozinskaya, Moiseev & Podorvanyuk 2003; Relaño & Beckman 2005; Egorov, Lozinskaya & Moiseev 2010; Egorov et al. 2014; Camps-Farinã et al. 2015; Sánchez-Cruces et al. 2015, and references therein).

The observations and data reduction performed are described in Section 2. In Section 3, we overview the results of previous multiwavelength studies of Holmberg II. Section 4 is devoted to the search for expanding ionized and neutral shells and supershells. In Section 5, we analyse the morphology of H II complexes in the galaxy. In Section 6, we discuss the results obtained, including the nature of the faint ionized inner supershell inside the H I SGS. Section 7 summarizes the main results of this study.

2 OBSERVATIONS AND DATA REDUCTION

2.1 Optical FPI observations

The observations were carried out at the prime focus of the 6-m SAO RAS telescope using a scanning FPI mounted inside the SCORPIO-2 multimode focal reducer (Afanasiev & Moiseev 2011). The operating spectral range around the Hα emission line was cut by a narrow bandpass filter with a full width at half-maximum, FWHM $\approx$ 14 Å bandwidth. The interferometer provides a free spectral range between the neighbouring interference orders $\Delta\lambda = 8.8$ Å with a spectral resolution (FWHM of the instrumental profile) of about 0.48 Å. During the scanning process, we have consecutively obtained 40 interferograms at different distances between the FPI plates. The log of these observations and parameters of the other data sets are given in Table 1, where $T_{\rm exp}$ is the exposure time; FOV – the field of view; $''/px$ – the pixel size; θ – the final angular resolution; $\delta\lambda$ and δv are the final spectral and velocity resolution.

The data reduction was performed using a software package running in the IDL environment. For a detailed description of the data reduction algorithms, see Moiseev (2002), Moiseev & Egorov (2008) and Moiseev (2015). After the initial reduction, sky line subtraction, photometric and seeing corrections made using the reference stars and wavelength calibration, the observational data were combined into data cubes, where each pixel in the field of view contains a 40-channel spectrum. The calibration wavelength was 6598.95 Å. We observed the galaxy in three overlapped fields (see Table 1), each field was exposed at two position angles in order to remove the parasitic ghost reflection. The regions of interest are filled less than a half of each observed field. This technique allowed us to get rid of the ghost contamination almost everywhere at the cost of reduced signal-to-noise ratio in the area of the ghosts (see details of this algorithm in Moiseev & Egorov 2008). The remaining symmetric ghosts are located in the outer regions of the total observed field. All the central regions studied in this paper are free from ghost contamination.

The data for all fields were reduced separately to obtain the wavelength cubes of the object. After the data reduction, we constructed mosaic of these three fields. We found the data for field #1 to be of poor quality (variable atmospheric conditions) compared to the data for the two other fields. That is why we included it in the mosaic only in the area of the faint inner supershell (see Section 6.3) in order to increase the signal-to-noise ratio there (the location of field #1 coincides with that of #3).

In order to get rid of the stellar continuum emission in the data cube, we performed a zero-order background fit for each pixel at the edges of line profiles and then subtracted it. The analysis of Hα line profiles was carried out using the multicomponent Voigt fitting (Moiseev & Egorov 2008).

The gas morphology and kinematics in the region of the interaction of multiple supershells are very complex and it would therefore be useful to exclude the regular component associated with the rotation of the galaxy to understand its local kinematics. We constructed a rotation model of Ho II from the H I velocity field using the tilted-ring approximation adapted to dwarf galaxy kinematics (Moiseev 2014) with initial parameters for Ho II taken from Oh et al. (2011,

Downloaded from http://mnras.oxfordjournals.org/ at Special Astrophysical Observatory of the Russian Academy of Sciences on November 15, 2016

Table 1. Log of the observed data.

Data set	Date of obs.	T_{exp}, s	FOV	$''/px$	θ, $''$	Sp. range	$\delta\lambda$ (δv)
FPI field #1	2010 Feb 07/08	40 × 150	$6.1' \times 6.1'$	0.71	1.8	8.8 Å around Hα	0.48 Å (22 km s^{-1})
FPI field #2	2011 Apr 26/27	40 × 240	$6.1' \times 6.1'$	0.71	1.4	8.8 Å around Hα	0.48 Å (22 km s^{-1})
FPI field #3	2014 Dec 16/17	40 × 160	$6.1' \times 6.1'$	0.71	1.4	8.8 Å around Hα	0.48 Å (22 km s^{-1})
FN655 image	2014 Oct 18/19	3600	$6.1' \times 6.1'$	0.36	1.9	Hα + [N II]	
FN674 image	2014 Oct 18/19	1800	$6.1' \times 6.1'$	0.36	2.0	[S II] 6717, 6731Å	
IFP502 image	2016 Mar 02/03	2400	$6.1' \times 6.1'$	0.36	1.8	[O III] 5007 Å	
FN641 image	2014 Oct 18/19	1200	$6.1' \times 6.1'$	0.36	2.0	Continuum	
FN712 image	2014 Oct 18/19	1200	$6.1' \times 6.1'$	0.36	2.0	Continuum	
SED525 image	2016 Mar 02/03	1200	$6.1' \times 6.1'$	0.36	2.0	Continuum	

Table 2. General parameters of Holmberg II.

Parameters (units)	Value
Name[a]	Holmberg II; Ho II; DDO 50; UGC 4305; PGC 23324; VII Zw 223
Centre position[b]:	
RA (J2000.0)	$08^h19^m03^s.7$
DEC (J2000.0)	$+70^\circ43'24''.6$
Morphology type[a]	Im
Holmberg radius R^c_{26}	267.3 arcsec (4.4 kpc)
Distance[c]	3.39 ± 0.20 Mpc
Spatial scale	16.4 pc arcsec^{-1}
M_B magnitude[c]	-16.71 ± 0.16
Colour $B - V^c$	0.11 ± 0.05
Gas mass[b]	1.3×10^9 M$_\odot$
Inclination	$49^{\circ b}$
	$38^{\circ d}$
	$27^{\circ e}$
Position angle[b]	176°
Systemic velocity[b, c]	157 km s^{-1}
Rotation velocity[b]	35.7 km s^{-1}

[a]NED, NASA/IPAC Extragalactic Database, (http://ned.ipac.caltech.edu/).
[b]Oh et al. (2011).
[c]Updated Local Volume galaxies data base (Karachentsev et al. 2013, http://www.sao.ru/lv/lvgdb/).
[d]Moustakas et al. (2010).
[e]Sánchez-Salcedo et al. (2014).

we list them in Table 2) and then subtracted this model from the observed data cube. As a result, we have obtained the data cube that reflects the local motions caused by stellar feedback. In the final cube, zero velocity corresponds to the regions that show no signs of the feedback influence on the kinematics of ionized gas. We described this 'derotation' method in Egorov et al. (2014).

2.2 Narrow-band imaging

Deep optical images in the Hα , [S II] and [O III] emission lines were obtained at the 6-m telescope with the same SCORPIO-2 device using the filters FN655, FN674 and IFP502 with central wavelengths of 6559 Å, 6733 Å and 5014 Å, and FWHM = 97, 60 and 18 Å, respectively. The images taken with FN674 and IFP502 represent the [S II] 6717, 6731Å and [O III] 5007 Å emission lines, respectively. As the FWHM of the FN655 filter is broader than the separation between the Hα and [N II] emission lines, the image in this filter is contaminated by [N II] 6548, 6584Å emission. However, given the mean I([N II])/I(Hα) ratio for H II regions in Ho II adopted from Egorov et al. (2013), we find that the contribution of the [N II] emission to total flux is less than 4 per cent.

We used the broad-band FN641, FN712 and SED525 filters centred on the continuum near the Hα , [S II] and [O III] emission lines to subtract the stellar contamination from the images obtained in the same night. Note that the subtraction was not ideal and residuals due to the stellar contribution can be seen in our final images in several areas, especially in those taken in the [S II] lines. In order to calibrate the emission-line images to energy fluxes, we observed the standard star AGK+81d266 (G191B2B in the case of [O III] observations) immediately after observing the galaxy.

2.3 Archival data used

In order to study the H I gas kinematics in the SGS, we analysed archival H I 21-cm line VLA data from the LITTLE THINGS survey (Hunter et al. 2012). We used the natural-weighted data cube and applied the same 'derotation' procedure to it as for the FPI data cube.

We trace the recent star formation distribution in Ho II by using the far-UV (FUV) images obtained with the *GALEX* space telescope as a part of the LITTLE THINGS survey.

To analyse the distribution of ionized gas, we use the data of the *Hubble Space Telescope* (*HST*) ACS/WFC Hα line observations carried out with the narrow-band filter *F*658*N* (programme ID 10522, data are published in Hong et al. 2013) downloaded from the Hubble Legacy Archive.[1] While our Hα image is deeper than *HST* data, the last have better spatial resolution which is essential for understanding the internal structure of bright H II regions.

We adopted stellar photometry data from the ACS Nearby Galaxy Survey Treasury catalogue (Dalcanton et al. 2008) which includes the apparent magnitudes in the *F*606*W* and *F*814*W* filters for each star in the *HST* ACS/WFC field.

3 MULTIWAVELENGTH OVERVIEW OF HOLMBERG II

The galaxy Holmberg II has been thoroughly studied in the whole wavelength range. It is included in several large surveys: SINGS (Kennicutt et al. 2003), THINGS (Walter et al. 2008), LITTLE THINGS (Hunter et al. 2012), HERACLES (Leroy et al. 2009), KINGFISH (Kennicutt et al. 2011) and Local Volume galaxies data base (Karachentsev, Makarov & Kaisina 2013). The basic parameters of the galaxy are listed in Table 2.

The morphology of atomic hydrogen in this galaxy is extremely inhomogeneous. The observed large-scale comet-like asymmetry of the H I disc is probably caused by the ram pressure stripping due to the hot intragroup medium (Bernard et al. 2012). The H I distribution

[1] http://hla.stsci.edu/

Downloaded from http://mnras.oxfordjournals.org/ at Special Astrophysical Observatory of the Russian Academy of Sciences on November 15, 2016

in the galaxy disc represents a large number of contiguous giant supershells and 'holes' (most representable of them are shown in Fig. 1). Thus Puche et al. (1992) identified 51 giant cavities and slowly expanding H I supergiant shells in Ho II, some of which required a kinetic energy as high as 10^{53} erg for their formation. The subsequent analysis by Bagetakos et al. (2011), who used more rigid criteria allowed them to identify 39 H I cavities surrounded by shells in this galaxy, the overwhelming majority of which coincide with objects from the list by Puche et al. (1992). The sizes of shells range from 0.26 to 2.11 kpc and their expansion velocities vary in the 7–20 km s^{-1} interval, which corresponds to the kinematic age of 10–150 Myr.

The Ho II rotation curve determined by Puche et al. (1992) based on H I 21-cm line observations shows rigid rotation in the central region with the radius of 2 arcmin which contains the entire optical emission of the galaxy. Oh et al. (2011) performed tilted-ring analysis of the H I line-of-sight velocity field and obtained circular rotation models of the galaxy for studying the dark matter distribution. We use hereafter the basic kinematics parameters listed in Table 2 adopted from the above paper.

Note that there is still no consensus concerning the measurement of the galaxy inclination. For instance, Oh et al. (2011) reported $i = 49^\circ$; Moustakas et al. (2010) found $i = 38^\circ$ based on the results of surface photometry; Sánchez-Salcedo, Hidalgo-Gámez & Martínez-García (2014) supposed an inclination of $i \simeq 27^\circ$ requiring to place the Ho II disc above the stability threshold.

The thickness of the gaseous disc (about 400 pc) varies insignificantly with galactocentric distance (Banerjee et al. 2011), making Ho II a preferred object among other dwarf irregular galaxies for studying the nature of supershells. Such a large vertical scaleheight allows supershells in Ho II to grow to large sizes before breaking through the H I disc.

Hodge, Strobel & Kennicutt (1994) identified 82 H II regions in the galaxy; hereafter for the sake of consistency we use the HSK numbers from the catalogue of the above authors to denote bright H II regions shown in Fig. 2. The brightest emission nebulae are mostly concentrated in the northern wall of the most extended (about 2 kpc) H I SGS (#21 in the list by Puche et al. 1992 and #17 in the list by Bagetakos et al. 2011), which is the subject of our study. Fig. 1 shows that bright H II regions form several 'chains' assembling the overall 'central arc' (this term was used by Stewart et al. 2000) in the northern wall of the SGS. The brightest of these regions are concentrated in the eastern chain. The brightest emission of heated dust is also observed in this 'central arc' (see e.g. Hunter, Hawley & Gallagher 1993; Karachentsev & Kaisin 2007; Walter et al. 2007; Wiebe et al. 2014). In general, the location of the Hα emission agrees with the distribution of the FUV emission in the galaxy, see also figs 5, 6 in Stewart et al. (2000) and fig. 29 in Weisz et al. (2009b). Bright regions of the FUV emission are also located in the northern rim of H I SGS. Apart from them the region of weak diffuse FUV emission extending to the south-west, three separate FUV regions to the north of the central arc and a compact one to the west of it are also seen in Fig. 1. The last one (furthest FUV region in Ho II) was analysed by Hunter, Elmegreen & Gehret (2016).

Stewart et al. (2000) studied 45 H II regions using *B*, Hα and FUV photometry and estimated the ages of the corresponding star-forming regions by dividing them into four age groups. Most of the star-forming regions fell into groups with ages smaller than 6.3 Myr. This is consistent with the star formation history of Ho II: according to (Weisz et al. 2008), the star-formation rate has been increasing over the last several million years.

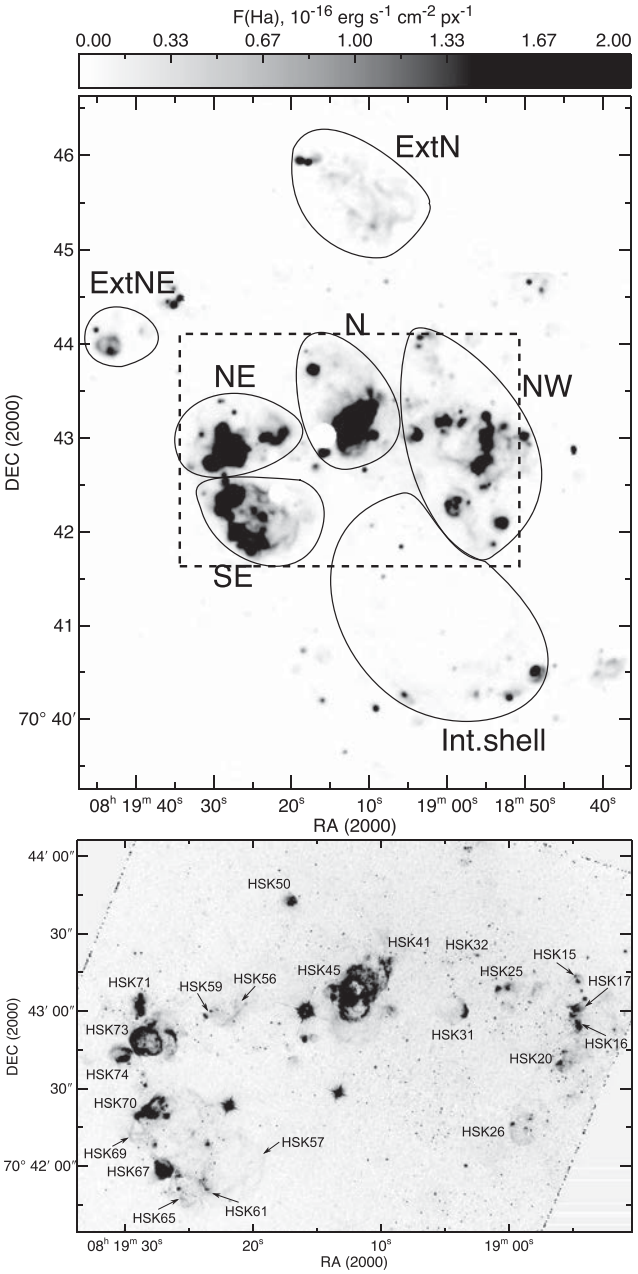

Figure 2. Top: an Hα image obtained by combining our deep narrow-band image and the sum of FPI data cube channels, with overlaid borders of the unified star formation complexes we identified (see Section 6.2) and of the internal supershell (see Section 6.3); bottom: the *HST* Hα image with HSK numbers of H II regions denoted according to Hodge et al. (1994). A dashed line on the top panel outlines the borders of the area shown on the bottom panel.

Radio observations of the galaxy (Tongue & Westpfahl 1995; Braun et al. 2007; Heald, Braun & Edmonds 2009) revealed continuous radio emission in the region of bright emission nebulae. The above authors associated this radio emission with active star formation and suspected the presence of SN remnants in the eastern chain of H II regions. We discuss this subject in Section 6.4 in more detail. According to the *Chandra* observatory data, the ultraluminous X-ray source (ULX) Ho II X-1 located in the eastern chain of star-forming regions is the only X-ray source in the galaxy and one of the sources of the observed bright synchrotron emission.

Downloaded from http://mnras.oxfordjournals.org/ at Special Astrophysical Observatory of the Russian Academy of Sciences on November 15, 2016

Earlier, the kinematics of ionized gas in Ho II was studied in detail in the neighbourhood of ULX Ho II X-1 only (Lehmann et al. 2005, see also our paper Egorov, Lozinskaya & Moiseev 2016 about this object). Tomita et al. (1998) analysed the kinematics of other bright H II regions of the galaxy based on observations made with a slit spectrograph. They combined seven obtained spectra into a broad strip covering only one third of the bright H II regions in the SGS. The resulting 'position-velocity' diagrams (PV diagrams) for the H II region that the authors denoted as the 'centre' (HSK 45) revealed the radial velocity gradient amounting to 30 km s^{-1} over 200 pc; the most blueshifted Hα velocity is smaller than the H I velocity by about 15 km s^{-1}.

Observations of Holmberg II with FPI were performed previously at the Observatoire du mont Mégantic 1.6-m telescope as a part of Hα kinematics follow-up survey of the SINGS sample (Dicaire et al. 2008). The aim of that project was to investigate the global kinematics of galaxies observed. The authors did not provide the kinematic parameters of Holmberg II due to its weak rotation and a lack of spatial coverage.

4 SEARCH FOR EXPANDING SHELLS IN STAR-FORMING REGIONS

Our deep Hα images of Holmberg II and the archival *HST* images of the galaxy (Fig. 2) reveal numerous faint extended filaments connecting several H II regions and located beyond the bright nebulae. A similar picture is observed in the [S II] and [O III] emission lines (see Fig. 3). Based on this morphology, we combined the emission features observed in the rim of the SGS into four extended areas (SE, NE, N and NW in Fig. 2) and into two areas beyond the SGS (ExtN and ExtNE).

To confirm the conclusion that the observed emission structures we identified are indeed unified physically bound complexes of ongoing star formation, we performed a detailed analysis of the kinematics of ionized and neutral gas in these areas.

The structure and kinematics of both ionized and neutral gas in the studied H I SGS are not homogeneous. Fig. 4 shows several examples of PV diagrams in the Hα and H I lines, that demonstrate how line-of-sight velocity changes with position along a chosen direction. Deviations of the line-of-sight velocity from the circular rotation model of the galaxy (zero velocity line) are clearly seen in the largest slice #1. Signs of the 'velocity ellipses' – the characteristic feature of expanding shells – are also present in this PV diagram.

Earlier, Weisz et al. (2009b) identified four local H I shells in the SGS wall with sizes of 300–400 pc expanding with velocities 7–15 km s^{-1}. These shells (# 8, 12, 14 and 27 in fig. 2 of their paper) are located in the immediate vicinity of the H II HSK 70, 16, 17 and 26 regions (see Fig. 2). In addition, shells # 16 and 23 are also seen and located north of the central chain of star-forming regions which might be connected with it.

We refined the location of the H I shells associated with star-forming regions and performed search for ionized gas shells in the galaxy. Below, we report the details and results of our kinematic analysis.

An expanding shell can be identified by a velocity ellipse (or a part of it) in PV diagrams or by splitting of an emission-line profile. In the case where the expansion velocity of a shell is small and spectral resolution is insufficient to resolve two components, the shell distinguishes itself by its higher velocity dispersion in the centre.

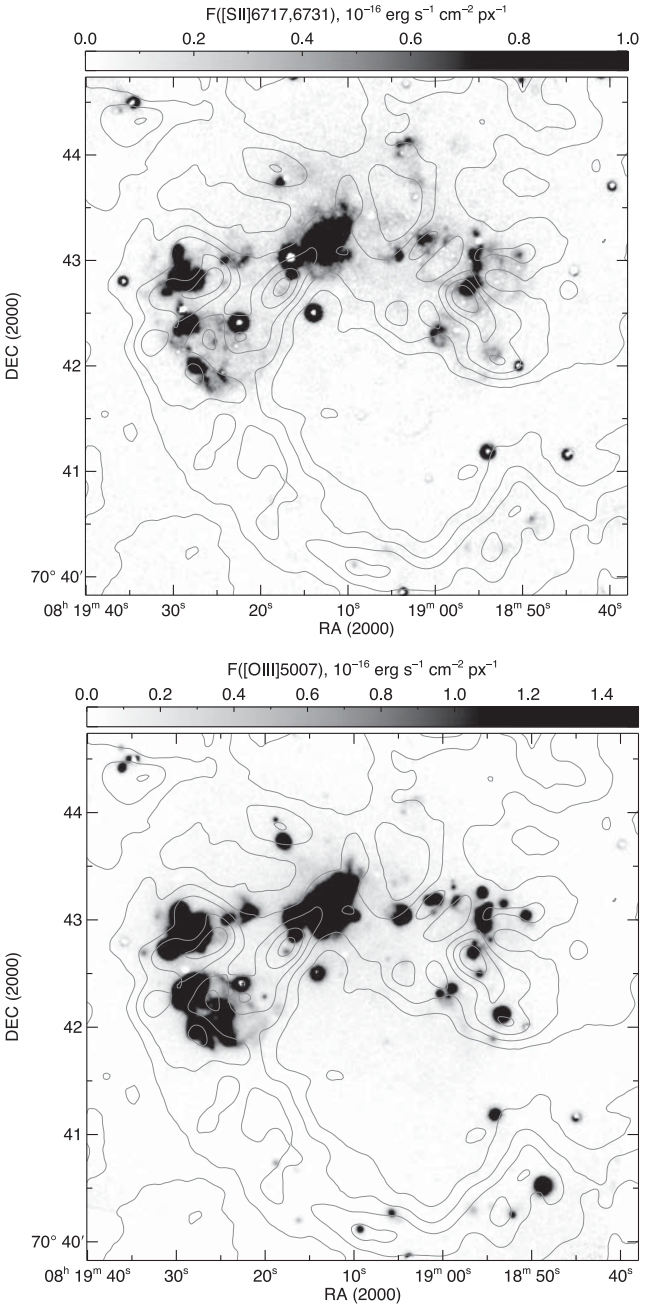

Figure 3. [S II] (top) and [O III] (bottom) images obtained with narrow-band filters after continuum subtraction. Isophotes denote the H I column density distribution.

We used all the above techniques to search for expanding shells and estimate their expansion velocities.

Fig. 5 shows the H I column density and line-of-sight velocity dispersion (second moment) maps for three areas – SE, N and NW – where we see increased H I velocity dispersion. The areas of high velocity dispersion in Fig. 5 correspond indeed to the expanding H I superbubbles. This suggestion is confirmed by our analysis of PV diagrams. For example, the 'velocity ellipse' might be seen at positions of 100–140, 170–220 arcsec along PV diagram # 1 (H I) and 15–65 arcsec along PV diagram # 2 (H I) in Fig. 4, which correspond to the regions of the increased velocity dispersion in Fig. 5 in the areas of N, NW and SE, respectively.

Downloaded from http://mnras.oxfordjournals.org/ at Special Astrophysical Observatory of the Russian Academy of Sciences on November 15, 2016

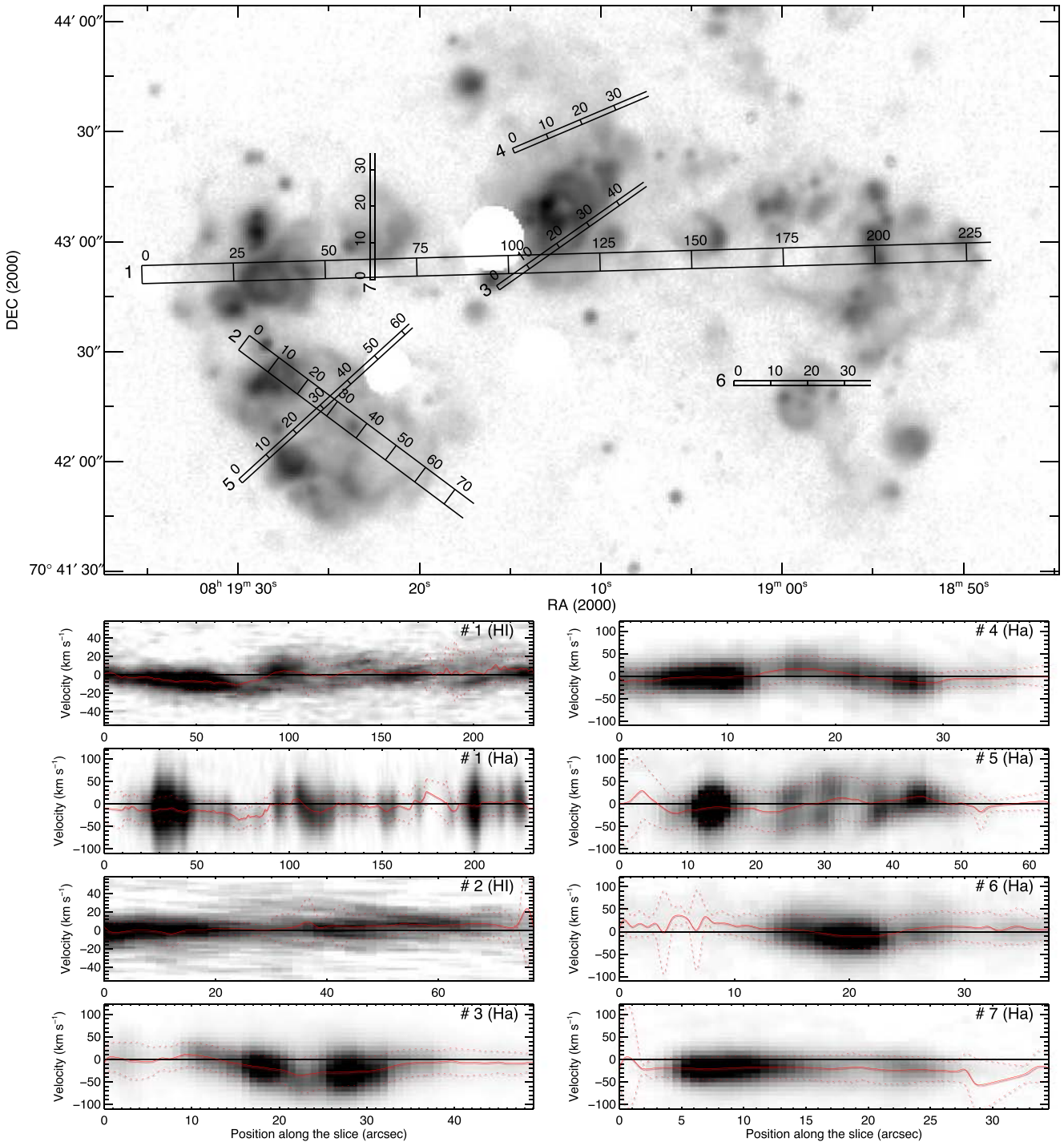

Figure 4. Examples of Hα and H I PV diagrams. Top panel: an Hα image arcsinh (intensity-scale) with the localization of the PV diagram superimposed. PV diagram names shown to the left of the bar denote their position. Bottom panels: examples of PV diagrams with the median velocity (red solid curves) and its dispersion (red dotted curves) overlaid. The zero-velocity line is shown by a black solid line.

It was shown in many studies (Muñoz-Tuñón et al. 1996; Moiseev & Lozinskaya 2012, see also references therein) that the intensity – velocity dispersion diagrams of ionized gas ($I - \sigma$) can be successfully used to identify areas, where the increased velocity dispersion is caused by expanding shells. We fitted the Hα line profile to a single-component Voigt profile in each pixel obtained from the FPI data cube and constructed the $I - \sigma$ diagram for the galaxy Holmberg II (see Fig. 6). The red line in the diagram marks the intensity-weighted average velocity dispersion of ionized gas in the galaxy $-\sigma_{\rm m} = 20.4 \pm 7.1\,{\rm km\,s^{-1}}$. Identical colours in the diagram (the top panel) and map (the bottom panel) are used to highlight the characteristic areas. Thus, the horizontal strip with relatively low velocity dispersion and high surface brightness marked in blue corresponds to bright H II regions and includes 50 per cent of the galaxy's Hα flux. Areas of increased dispersion, which are most likely associated with spectroscopically unresolved

Downloaded from http://mnras.oxfordjournals.org/ at Special Astrophysical Observatory of the Russian Academy of Sciences on November 15, 2016

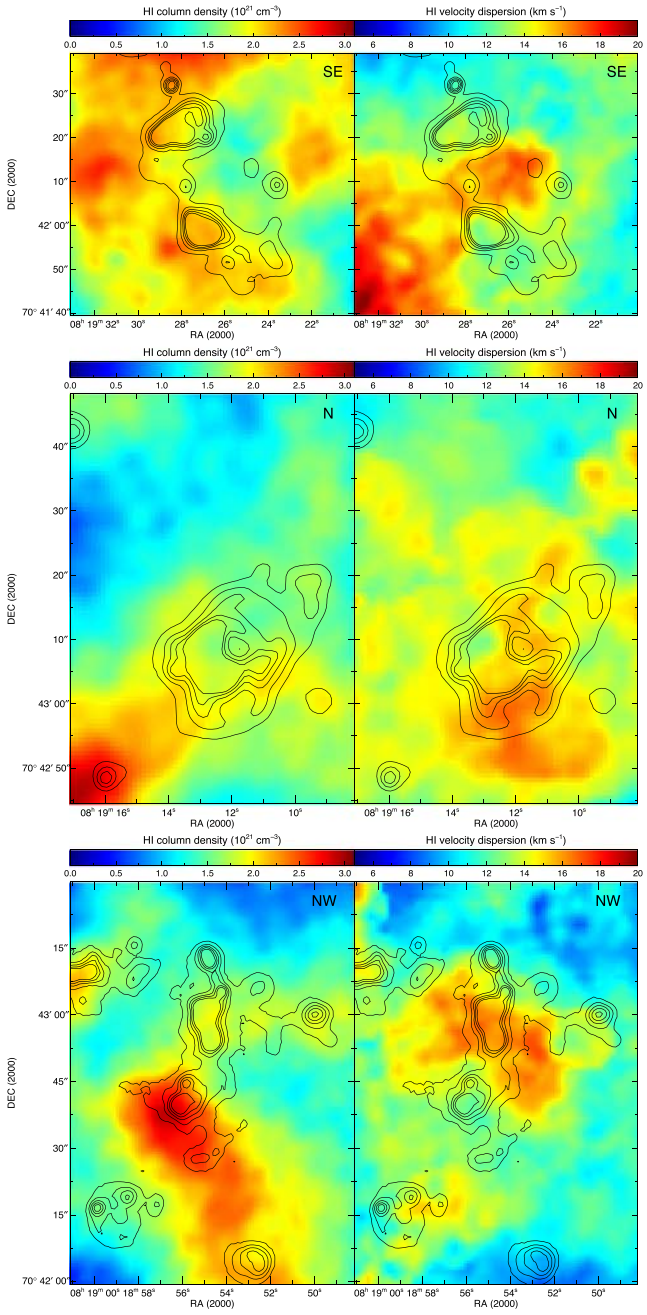

Figure 5. H I column density (left) and line-of-sight velocity dispersion (right) maps of three star-forming complexes (SE, N and NW) with local H I superbubbles detected. Hα line intensity contours are overlaid.

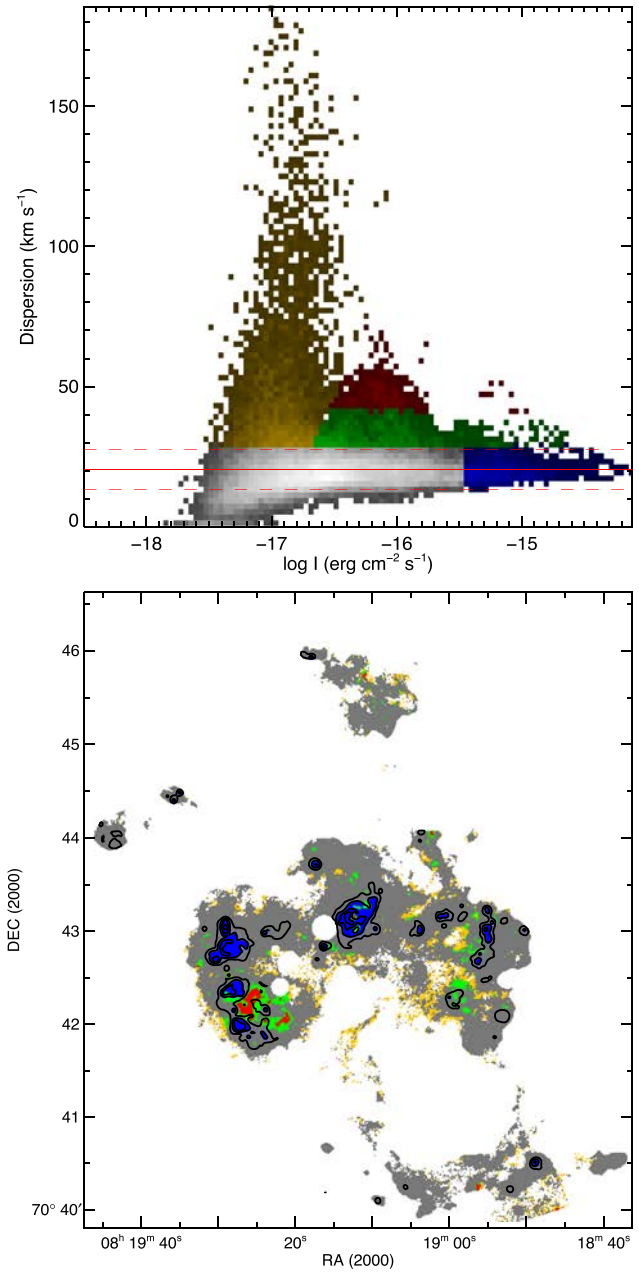

Figure 6. Hα intensity – velocity dispersion diagram for Holmberg II (top). A red solid horizontal line marks the intensity-weighted mean velocity dispersion of ionized gas in Ho II and the dashed lines – its standard deviation. The bottom plot shows the location of regions marked by different colours in the $I - \sigma$ diagram.

expanding shells, are shown in green colour, whereas the red colour corresponds to shell-like structures with clear separation of the components of the Hα line profile. The remaining areas of the increased velocity dispersion are shown in orange colour, and areas of low surface brightness, in grey colour.

We performed a more bona fide search for expanding structures of ionized gas by analysing the PV diagrams that uniformly cover each region of ongoing star formation in the galaxy. Some examples of them are shown in Fig. 4. In the areas shown in red colour in Fig. 6, we see clear evidence for gas expansion in the form of the velocity ellipse or a part of it. Subsequent fitting of the Hα profiles by one, two or three Voigt components allowed us to estimate the expansion velocities of the corresponding structures.

Our analysis of gas kinematics in the H I and Hα lines revealed three local neutral-gas shells associated with star-forming regions and 22 ionized gas shells. Their location is shown in grey and blue colours, respectively, in Figs 7–12.

We found no signs of expansion of bright H II regions. Despite a rather high spectral resolution of FPI, the expansion velocities of these regions proved to be low: it does not exceed 11 km s^{-1} (half of the instrumental FWHM of FPI used). All the expanding shells of ionized gas, which we found, represent faint filamentary features in the Hα image and possibly reside in a medium with a

Downloaded from http://mnras.oxfordjournals.org/ at Special Astrophysical Observatory of the Russian Academy of Sciences on November 15, 2016

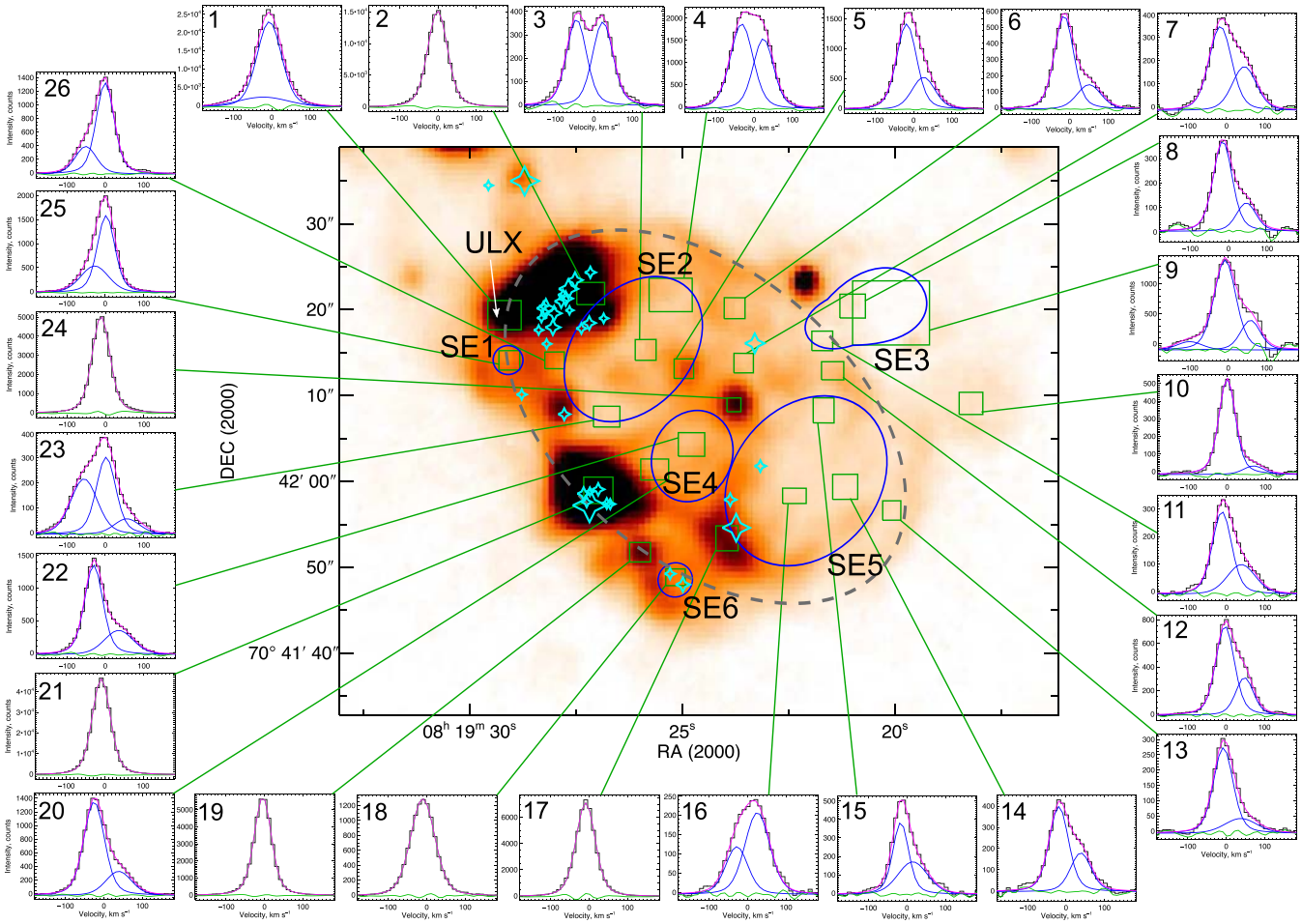

Figure 7. Hα image of the SE complex; Hα line profile examples obtained by integration inside the green borders in the image. The results of 1, 2 or 3 component Voigt fitting are shown: blue colour denotes the individual components, while the fitting model is shown in magenta colour. Green colour is used to show the residuals after subtraction of the model from the observed line profile. Blue ellipses in the image mark the positions of faint shell-like structures identified in the area. A grey-dashed ellipse shows the location of the neutral-gas shell identified as a result of the analysis of the H I PV diagrams and associated with the observed multishell complex of ionized gas. Light-blue asterisks denote the location of OB-stars identified by the analysis of *HST* colour–magnitude diagrams; their sizes are proportional to their luminosity.

relatively low density. In our earlier paper Wiebe et al. (2014), we have estimated the expansion velocity of the H II regions HSK45 and HSK73, however, it is now clear that the evidence of their expansion does not refer to bright nebulae but rather to faint shell-like ionized-gas structures around them.

We estimated the kinematic ages of the identified local H II shells in terms of Weaver et al. (1977) model by the following relation:

$$t = 0.6R/V_{\rm exp},$$

where R is the radius in pc, $V_{\rm exp}$ – the expansion velocity in km s^{-1} and t – the age in Myr.

To estimate the ages of bright H II regions that show no signs of expansion, in Wiebe et al. (2014) we used the equivalent width (EW) of the Hβ emission line which correlates rather well with the age of H II regions (see e.g. Schaerer & Vacca 1998; Leitherer et al. 1999).

The derived ages of the faint local shells found inside the H II complexes and of bright H II regions are summarized in Table 3. This table also lists the age estimates made by Stewart et al. (2000) for star-forming regions based on the results of FUV and optical observations. Because of the uncertainty in the method used for age determination, the above authors divided all H II regions studied into four age groups: 0–3.5 Myr, 3.4–4.5 Myr, 4.5–6.3 Myr and older than 6.3 Myr (see table 5 in their paper).

Given the results of the search for expanding shells and the study of their kinematics, we can conclude that the observed emission structures in the four areas in the SGS walls (SE, NE, N and NW) that we identified based on morphology and in two areas outside the SGS (ExtN and ExtNE) are indeed physically connected. This means (see also Sections 5 and 6.2 below) that the current star formation in the galaxy is represented by unified complexes with sizes of several hundred pc which combine several bright nebulae.

5 MORPHOLOGY AND IONIZATION BUDGET OF STAR FORMATION COMPLEXES

As shown above, the deep Hα images of the galaxy and the presence of local H I and H II shells suggest the existence of unified extended complexes joining several bright HSK nebulae. Hence the four extended areas (SE, NE, N and NW in Fig. 2) that we identified in the SGS studied and the areas outside this SGS (ExtN and ExtNE) are physically connected complexes of ongoing star formation.

Each of the star-forming complexes contains several young star clusters. Weisz et al. (2009b) and Bastian et al. (2011) compared

Downloaded from http://mnras.oxfordjournals.org/ at Special Astrophysical Observatory of the Russian Academy of Sciences on November 15, 2016

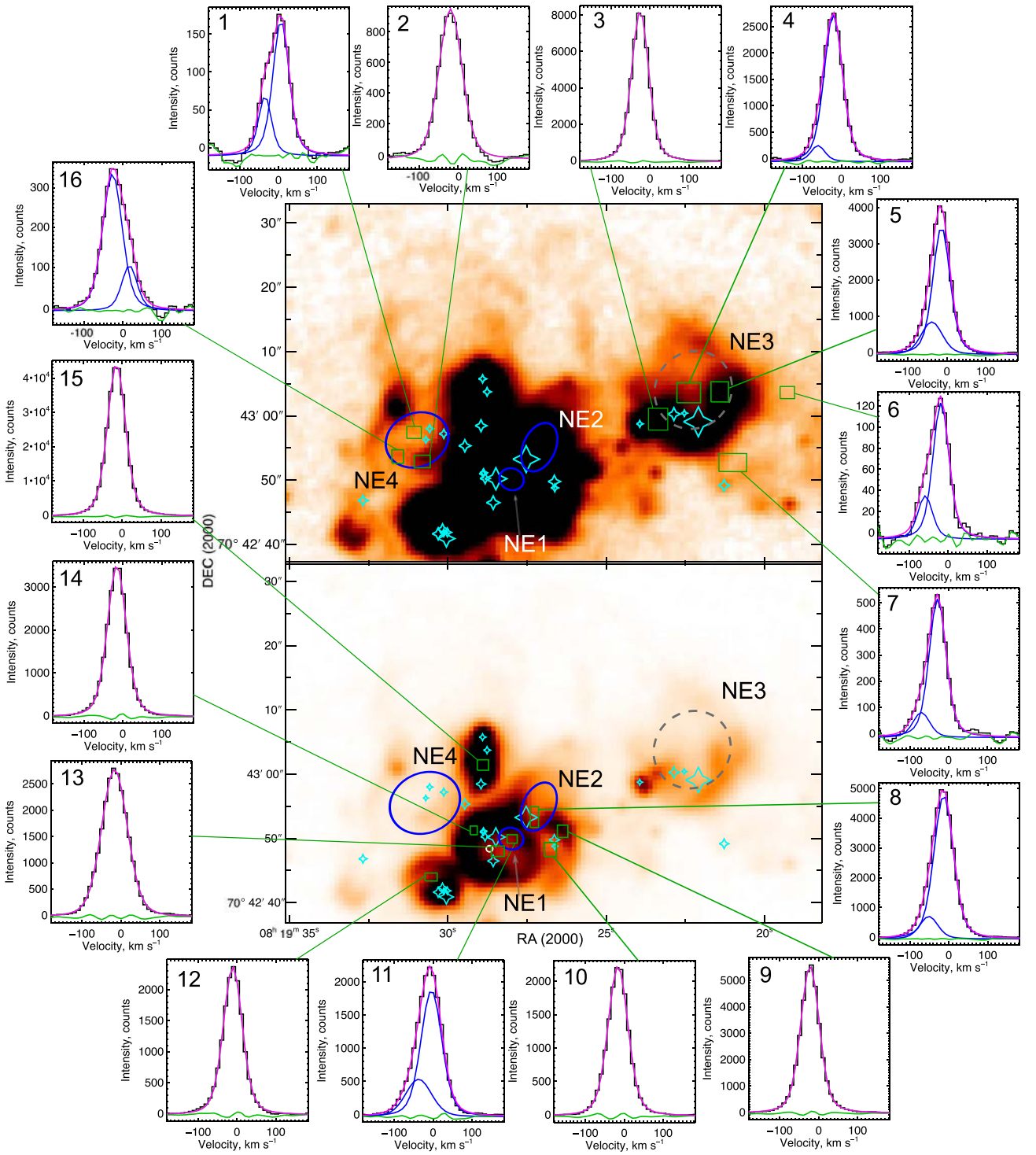

Figure 8. The same as in Fig. 7, but for the NE complex. The top and bottom images correspond to the same area with different contrast. White circle shows the area of He II 4686 Å emission detected in Egorov et al. (2013).

observed colour–magnitude diagrams based on *HST* data to stellar evolution tracks and selected objects younger than 10 Myr that should be OB stars. We used the same method as Weisz et al. (2009b) to obtain the list of OB stars with their magnitudes from the Hubble source catalogue (HSC[2]). The locations of the OB stars identified in such a way agree well with the list reported by Bastian et al. (2011). We used *F*555*W*- and *F*814*W*-band photometry to estimate the *V*-band absolute magnitude of each star. We further assume that all the selected stars are young main-sequence stars (the method used to select them should ensure this) and use O-type star models from Martins, Schaerer & Hillier (2006) to compute the bolometric luminosity and the number of ionizing photons Q_0 from each star. These stars are shown in Figs 7–12 by asterisks with the

[2] http://archive.stsci.edu/hst/hsc/

Downloaded from http://mnras.oxfordjournals.org/ at Special Astrophysical Observatory of the Russian Academy of Sciences on November 15, 2016

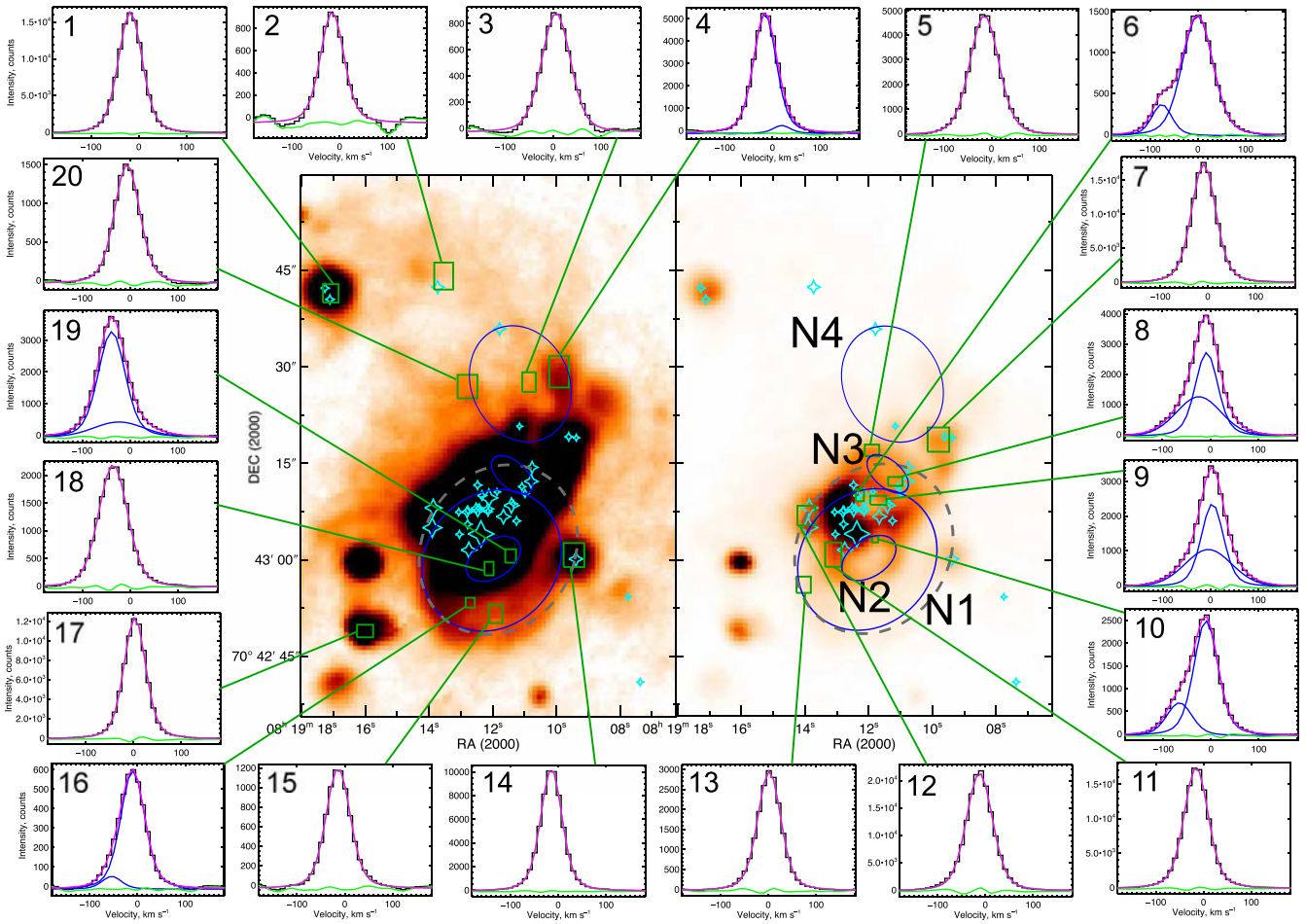

Figure 9. The same as in Fig. 7 but for the N complex. Right- and left-hand images correspond to the same area with different contrast.

size proportional to their luminosity. We used the above procedure to estimate the amount of ionizing quanta $Q_{\rm stars}$ in Table 4 from the OB stars observed in each complex.

Similar values can be readily inferred from the observed number of Hα photons. With the observed Hα flux of each complex (corrected for interstellar extinction $A_V = 0.11^m$), we estimated the equivalent number of O5V stars (N(O5V) in Table 4) and of ionizing photons Q_0 needed for gas ionization in the area with the procedure described in Osterbrock & Ferland (2006). For the case of optical thick nebulae, its Hα luminosity $L(\mathrm{H}\,\alpha)$ depends on Q_0 as

$$\frac{L(\mathrm{H}\,\alpha)}{h\nu_{\mathrm{H}\,\alpha}} \simeq \frac{\alpha^{\rm eff}_{\mathrm{H}\,\alpha}}{\alpha_B} Q_0 \simeq 0.45 Q_0, \qquad (1)$$

where the Hα effective recombination coefficient $\alpha^{\rm eff}_{\mathrm{H}\,\alpha} \simeq 1.17 \times 10^{-13}$ cm^3 s^{-1} and the total recombination coefficient of hydrogen $\alpha_B \simeq 2.59 \times 10^{-13}$ cm^3 s^{-1} for $T = 10\,000$ K. Further, we will refer the estimated amount of needed ionization photons Q_0 from (1) as $Q_{\mathrm{H}\,\alpha}$ to mention that it has been converted from the Hα luminosity.

In such a way, our measurements of the Hα flux of H II regions and of the luminosity of OB stars inside them were used to estimate both the needed and available amount of ionizing quanta in all star formation complexes studied. The results are summarized in Table 4.

Let us now consider the structure, kinematics and energy sources in each selected H II complex in more detail.

5.1 SE complex (HSK 57, 61, 65, 67, 69 and 70)

Deep Hα images of the region reveal a faint filamentary structure connecting H II regions HSK 57, 61, 65, 67, 69 and 70 (see Fig. 7). The kinematics of neutral gas shows the existence of the local H I superbubble that has a size of about 650 × 950 pc expands with the velocity of about 20 km s^{-1} and covers the whole bright part of star formation complex. The location of this H I shell coincides with that of the H I cavity #27 identified by Weisz et al. (2009b).

While the bright H II regions are located in the direction of dense parts of the H I SGS, the central part of the SE complex resides in a more exhausted medium (see the top panel of Fig. 5). Such density distribution allowed one to expect the highest expansion velocities of ionized gas in the centre of the complex. We found three faint expanding ionized superbubbles there which possibly interact with each other and three superbubbles located at the periphery of the complex (including two young compact supershells SE1 and SE6).

As is evident from the Hα line profiles decomposition (see Fig. 7), the ionized gas kinematics is inhomogeneous in the whole SE complex. This area exhibits the most clear signs of the expansion of shell-like structures of ionized gas. For example, the northern SE2 superbubble reveals clear two-component Hα line profile in its centre corresponding to the expansion velocity of about 37 km s^{-1} – one of the highest among the ionized superbubbles we found in Ho II. The 'velocity ellipse' for SE2 – another evidence of its expansion – is also clearly seen in the PV diagram constructed in the direction of its elongation (#5 in Fig. 4).

Downloaded from http://mnras.oxfordjournals.org/ at Special Astrophysical Observatory of the Russian Academy of Sciences on November 15, 2016

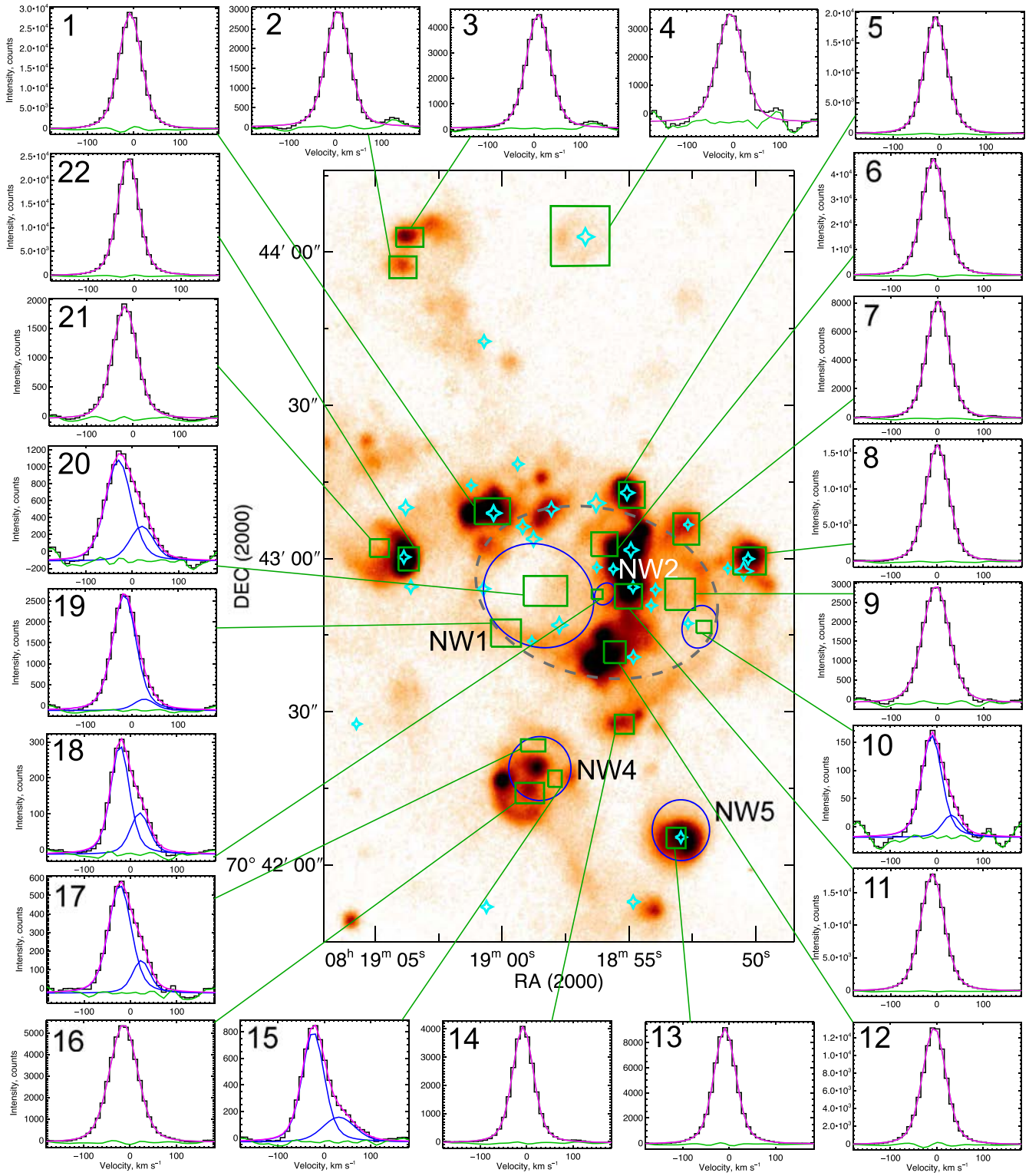

Figure 10. The same as in Fig. 7 but for the NW complex.

The bright HSK 70 region containing the ULX source Holmberg II X-1 and a young star cluster is located in the northeastern part of one of the inner shells. We will analyse the kinematics of ionized gas in its neighbourhood in our forthcoming paper (Egorov et al. 2016). The young cluster in that nebulae is the main source of ionizing photons in the complex. Another sources of the ionizing radiation are the star cluster in HSK 67 nebula (in particular, the brightest one among the selected O stars) at the south-east of the complex and 10 OB stars spread inside the complex. As it follows from Table 4, the amount of ionizing photons emitted by the observed OB stars is consistent to that needed to ionize gas in the complex.

Downloaded from http://mnras.oxfordjournals.org/ at Special Astrophysical Observatory of the Russian Academy of Sciences on November 15, 2016

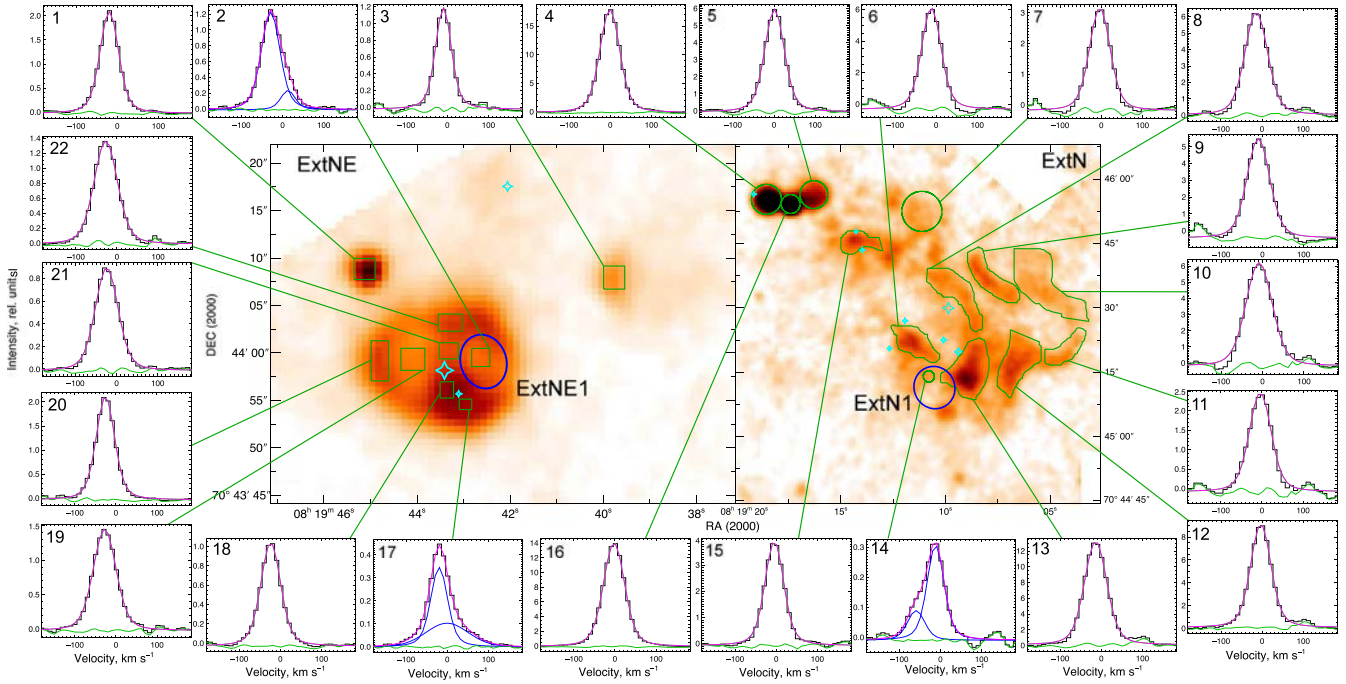

Figure 11. The same as in Fig. 7 but for the ExtN (right) and ExtNE (left) complexes.

Note that massive OB stars are absent inside all the mentioned ionized superbubbles (except the compact one SE6) or located at their rim close to the bright nebulae. It may indicate that the source of mechanical energy needed to support the expansion of these structures can stem from leakage of wind mechanical energy from the bright H II regions through their broken irregular shells. An order of magnitude supports such an assumption: the two OB stars inside the SE6 shell can give the wind energy leakage of $\dot{E}_w \sim 10^{37}\eta$ erg s^{-1} ($\eta < 1$ is the leakage efficiency), where the values $\dot{M}_w = 10^{-5} M_\odot$ yr^{-1} and $v_w = 2000$ km s^{-1} corresponding to the high end range Markova & Puls (2008) have been accepted for the mass-loss rate and wind velocity. On the other hand, the total radiation energy loss in the shell can be readily estimated as $\dot{E}_r \sim 3 \times 10^{36}$ erg s^{-1}, while the kinetic energy consumption $\dot{E}_k = \dot{M}_{sh} V_{exp}^2/2 \sim 10^{36}$ erg s^{-1} with $\dot{M}_{sh} = 4\pi\rho R^2 V_{exp}$; here we accepted the parameters for the expanding shell SE6 as shown in Table 3, and gas density is assumed $n \sim 0.3$ cm^{-3} (see estimates below); for the cooling rate, we assumed the typical value $\Lambda/(n_H n_e) \simeq 2 \times 10^{-24}$ erg cm^3 s^{-1} at $T_e \simeq 8000$ K (Draine 2011). It is seen that $\eta \simeq 0.4$ would be sufficient to replenish energy consumption in this shell.

As we pointed out above, the presence of the faint extended structures jointing the H II regions and of the H I supershell around the whole SE star-forming complex confirms that we are dealing with a single entity here.

5.2 NE complex (HSK 71, 73, 74, 56 and 59)

The filaments of ionized gas between HSK 56, 59 and 73 H II regions as well as the brighter emission between HSK 71, 73 and 74 are clearly seen in our deep Hα image (Fig. 8). It allows us to consider these structures as a single star formation complex.

The observed Hα profiles in this area are mostly single, albeit four faint compact expanding shell-like structures of ionized gas can be identified (see Fig. 8). Except them, several faint shell-like structures without any signs of expansion are observed it the north part of the complex. Broadening of the Hα profile is observed inside the ring-like H II region HSK 73, in whose centre we have earlier found (Egorov et al. 2013) an object with a rather broad He II 4686 line (the area with the observed He II emission is shown with a white circle in Fig. 8). This nebula does not reveal a clear evidence of expansion; we found signs of its expansion only at the northwestern part of the region, where the young compact shell NE1 is located. The more extended shell NE2 we found at the periphery of HSK 73 region.

The complex NE is located in a dense H I cloud on the outer side of the SGS rim. Its northern part penetrates into the adjacent H I supershell (see Fig. 1). Such distribution of the neutral gas density in the complex is consistent with the observed faint arcs of ionized gas extended to the north of bright H II regions over more than 350 pc (see Fig. 8). The faint supershell NE3 between HSK 56 and 59 nebulae is also north elongated.

In the same way as in the SE complex, the absence of massive stars in the centre of all superbubbles in the NE complex (excluding NE4) indicates the necessity of mechanical energy to escape from the bright H II regions in order to drive it.

Massive OB stars – the sources of required ionizing Lyman continuum photons, are spread in the whole NE complex and do not reveal concentration to the star clusters as it was for the SE complex. The only poor star cluster is located at the southeastern part of the complex. As it evident from Table 4, the number of identified OB stars is enough to ionize the gas in the complex.

5.3 N complex (HSK 45 and 41)

We refer to the brightest H II region in the galaxy, HSK 45, (and also adjacent compact nebula HSK 41) as an individual complex. Its Hα images and kinematics reveal a number of interacting shell-like structures inside these H II regions, see Fig. 9. The expansion velocity of the H II region HSK 45 may be as high as 35 km s^{-1},

Downloaded from http://mnras.oxfordjournals.org/ at Special Astrophysical Observatory of the Russian Academy of Sciences on November 15, 2016

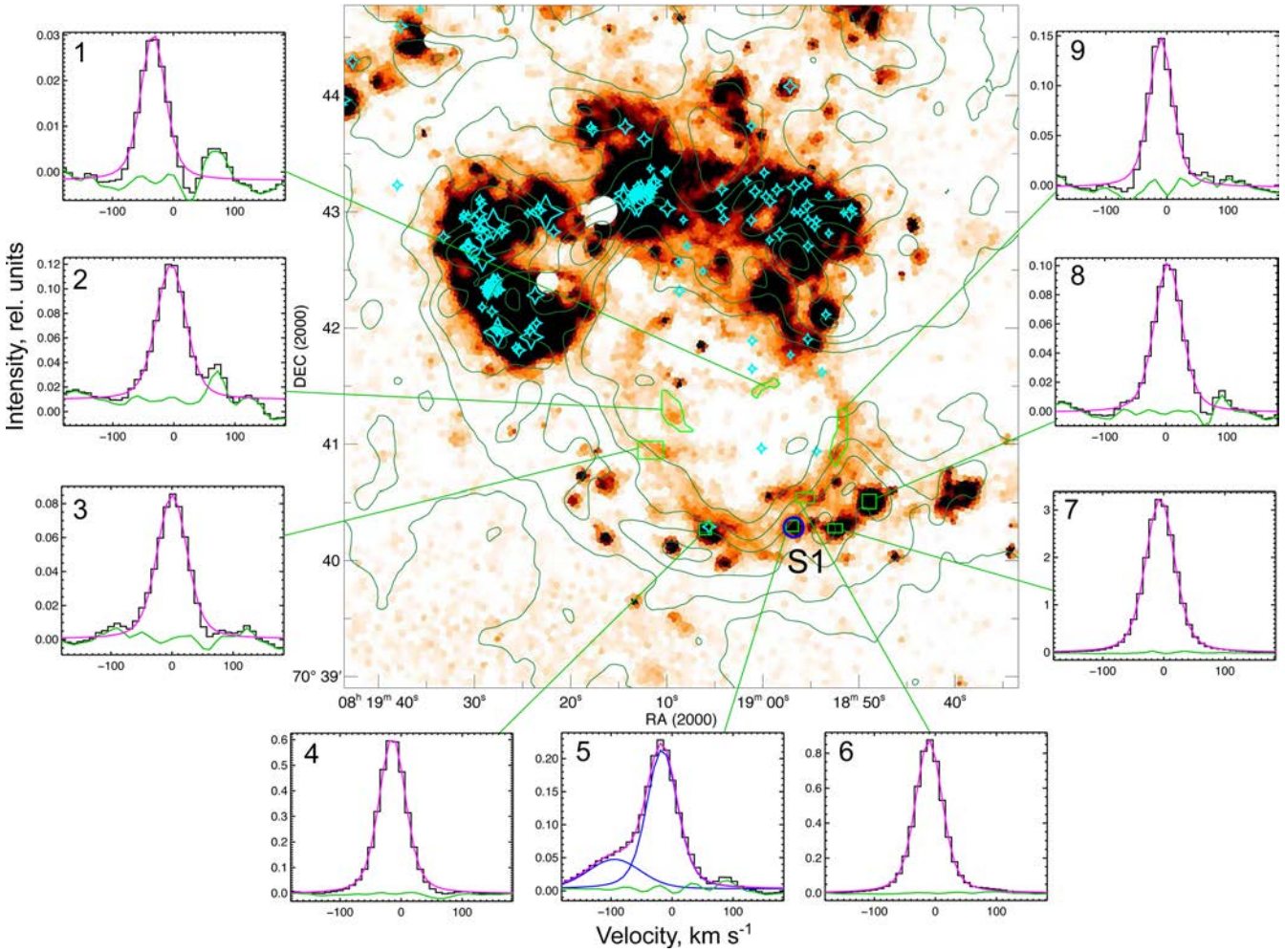

Figure 12. The same as in Fig. 7 but for the whole region of ongoing star formation in the walls of the SGS. The Hα image shown here was obtained by applying of adaptive binning with the signal-to-noise ratio equal to 30. Green contours show the lines of equal H I column density.

albeit the observed kinematic perturbations are most likely due to the interaction between three identified local shells. Based on the ionized gas kinematic analysis, we found the N2 shell to be located inside the older and more extended superbubble N1. For example, the evidence of such a structure is a more deep 'dip' at the velocity ellipse in the PV diagram constructed through the both shells (see position 23 arcsec along PV diagram #3 in Fig. 4).

The complex is located at the site of probable collision of three H I supershells – the SGS and two other to the north of it. The H I kinematics reveals the existence of expanding H I shell (previously unknown) that covers the whole complex. Signs of its expansion are clearly seen on PV diagram #1 (H I) at positions of 100–130 arcsec along the slice in Fig. 4.

Massive OB stars mostly located in the centre of the HSK 45 nebula are the sources of energy for ionization and maintaining the expansion of the observed emission structures. Our deep Hα and [S II] images of the region reveal extended arcs of ionized gas in the northern part of the complex. These structures show enhanced ratios of I([S II])/I(Hα), although their position on the diagnostic diagram I([O III]5007)/I(Hβ) versus I([S II])/I(Hα) does not indicate the clear signs of collisional ionization by shocks (see Section 6.4 for details). The relatively old faint shell N4 shows up among these structures. Evidence of its expansion follows from PV diagram #4 in Fig. 4. Most likely, the mechanical energy leakage from HSK 45 region should be a source of the necessary energy to drive its expansion.

Decomposition of the Hα profile reveals the presence of a broad component inside the bright region HSK 45 (see profiles # 8, 9 and 19 in Fig. 9). This component might be caused by the influence of the shock waves from some energetic source, e.g. the Wolf–Rayet star, to the ISM. This idea is supported by findings of Hong et al (2013), who identified signs of shocks in several areas in the central part of the HSK 45 nebula from the *HST* observations.

5.4 NW complex (HSK 15, 16, 17, 20, 25, 26)

This is a chain of relatively compact bright H II regions in the northern part of the complex of ongoing star formation in the SGS surrounded by faint shell-like structures of ionized gas with the signs of their expansion (see Fig. 10). The bright H II regions exhibit a single-component Hα profile which is broadened in some places. Their possible expansion velocities do not exceed 11 km s^{-1}.

The complex NW located in the direction of the dense part of the H I SGS rim, albeit the neutral hydrogen density varies considerably there. As it follows from the bottom panel of Fig. 5, the location of the bright nebulae basically correlates with the H I column density. Kinematics of the neutral gas reveals the existence of an H I shell

Downloaded from http://mnras.oxfordjournals.org/ at Special Astrophysical Observatory of the Russian Academy of Sciences on November 15, 2016

Table 3. Expansion velocity, size and kinematic age of faint shell-like structures of ionized gas shown in Figs 7–12. Ages of the bright H II regions tied with these shells are also shown.

Shell	V_{exp}(km s^{-1})	Size (pc)	Age (Myr)
SE1	15	86	1.7
SE2	30–37	322 × 230	2.6
SE3	25–30	282 × 188	2.8
SE4	27–32	190 × 128	1.8
SE5	27	358 × 240	4.0
SE6	$\lesssim$20	74	1.1
	Age of HSK 67, 70:		3.8–4.8[a]
			2.5–4.5[b]
NE1	26	72 × 50	0.8
NE2	15	162 × 104	3.2
NE3	17	254 × 224	4.5
NE4	24	210 × 168	2.6
	Age of HSK 59, 71, 73:		3.5–4.1[a]
			2.5–4.5[b]
N1	22	362 × 316	4.9
N2	28	142 × 96	1.5
N3	10	124 × 76	3.7
N4	18	230 × 203	7.2
	Age of HSK 45:		3.7[a]
			2.5–3.5[b]
NW1	25	392 × 312	4.7
NW2	21	112 × 70	1.6
NW3	21	163 × 102	2.3
NW4	27	216	2.4
NW5	$\simeq$ 20	226	3.4
	Age of HSK 15, 16, 17, 20, 25:		4.8–6.2[a]
			4.5–6.3[b]
ExtNE1	20	49	1.5
	Age of ExtNE:		3.5–4.5[b]
ExtN1	23	139	3.6
	Age of ExtN:		3.5–4.5[b]
S1	40	120	1.8

[a]Estimates made by Wiebe et al. (2014) using Hβ equivalent width.
[b]Estimated by Stewart et al. (2000) using Hα and FUV data.

that covers the central part of the complex. The chain of the bright H II regions is located in the central part of that H I shell.

According to Weisz et al. (2009b), the peak of star formation was in the direction of the NW complex about 20 Myr ago. Indeed, the *GALEX* images reveal bright FUV emission there (see Fig. 1) which poorly correlates with the distribution of the Hα emission. As the FUV emission indicates a recent star formation, while Hα emission corresponds to the ongoing star formation, such disagreement in their distribution might be an evidence for the triggering of the ongoing star formation by the feedback of the recent star formation episode in the chain of compact H II regions of the complex.

The distribution of massive OB stars does not show any concentration to star clusters. The expansion of only two of five ionized superbubbles could be explained by the stellar wind of OB stars located inside them. The mechanical energy leakage from the adjoint bright H II regions can provide the necessary energy to drive the expansion of another three superbubbles. As it follows from Table 4, the amount of Lyman continuum photons from the identified OB stars is enough to ionize the gas in the NW complex.

5.5 External complexes (ExtN and ExtNE)

Let us analyse now the two regions marked as ExtN and ExtNE in Fig. 2 which are not connected with the walls of the SGS discussed in this paper. As is evident from Fig. 1, both these regions are located in the rims of H I supergiant shell located next to the SGS. Note that the ExtNE region is relatively compact and bright when observed in the Hα line and surrounds the compact central source of UV radiation. Here the presence of the broad component of the Hα profile in the brightest part of the complex is immediately apparent, as well as the expanding shell ExtNE1 east of it (Fig. 11). Unfortunately, we cannot determine the boundaries of this shell and, hence, its age with certainty.

The ExtN region, in turn, appears as a complex of filamentary diffuse structures surrounding compact UV sources. It is fair to assume that Hα radiation is caused by younger regions in the area, where star formation is triggered by the previous generation of stars located in accordance with the FUV emission. We found the only ionized superbubble having signs of its expansion (ExtN1) in the southern part of the complex. Generally, the Hα profile in both northern regions can be well fitted by a single unbroadened component implying that the expansion velocity of ExtN and ExtNE does not exceed 11 km s^{-1}.

Despite the scarcity of massive OB stars inside both complexes, their energy input is enough to ionize the gas there. The low brightness of these H II complexes is consistent with a small number of sources of ionizing radiation. Note that due to the above-mentioned lack of information about stellar population of the northwestern part of the complex, in Fig. 11 and in Table 4, we indicate only a part of OB stars which probably influence the complex.

5.6 Internal ionized supershell in SGS

Our deep Hα images allowed us to identify a faint diffuse component of ionized gas inside the SGS close to its walls which is not seen in the *HST*/ACS and any previous images of the galaxy. We observed an Hα line emission inside this SGS with an average brightness level of 3–6 × 10^{-18} erg s^{-1} cm^{-2} arcsec^{-2} and [S II] line emission with an average brightness level of about 0.5–1 × 10^{-18} erg s^{-1} cm^{-2} arcsec^{-2}. The Hα profile in the inner ionized supershell is narrow and symmetric. Based on the difference of the line-of-sight velocities in different parts of this supershell, we may conclude that its expansion velocity does not exceed 10–15 km s^{-1} which corresponds to the expansion velocity of the neutral SGS.

Several filaments of ionized gas are observed in the central part of the area covered by internal ionized supershells. Probably, they correspond to the emission projected towards the supershell region. Hα line profile #1 which shows the line-of-sight velocity shifted at almost 30 km s^{-1} from the mean velocity of the supershell, supports this idea.

We denote the area that corresponds to this faint supershell as Int.shell in Table 4 and Fig. 2. Several compact H II regions projected to the Int.shell, are located in the southern part of the H I SGS. One of them (the S1 shell in Table 3 and Fig. 12) shows the clear evidence of expansion.

6 DISCUSSION

6.1 What triggered star formation in Ho II?

Detailed multicolour *HST* photometry of the stellar population inside each supergiant H I shell in the Ho II galaxy reported by

Downloaded from http://mnras.oxfordjournals.org/ at Special Astrophysical Observatory of the Russian Academy of Sciences on November 15, 2016

Table 4. Sizes and ionization budget of complexes of ongoing star formation.

Complex	Size (pc)	F(Hα), (10^{-13} erg s^{-1} cm^{-2})	N(OV5)	N(OB)	$Q_{\mathrm{H}\alpha}$ (10^{50} s^{-1})	Q_{stars} (10^{50} s^{-1})
SE	1150 × 1050	9.3	56	35	8.8	9.7
NE	1400 × 980	9.7	58	26	9.1	8.3
N	1500 × 1000	14.0	83	36	13.2	11.1
NW	2450 × 1600	8.4	50	31	7.9	7.6
Int.shell (diff)	2730 × 2280	0.7	4	5	0.7	1.0
Int.shell (all)	2730 × 2280	1.7	10	7	1.6	1.5
ExtN	1530 × 1030	1.1	7	8[a]	1.1	1.9[a]
ExtNE	960 × 700	0.5	3	3	0.5	1.1

[a]Might be underestimated because of the incomplete coverage by *HST* observations (see Fig. 1).

(Weisz et al. 2009b, see also references therein) revealed stars of several age groups rather than single coeval clusters as previously believed. It stimulated a new currently widely accepted model: neutral supergiant shells were formed from several generations of stars over several hundred Myr.

The main criterion of current starburst –g the Hα emission in the neighbourhood of a newly formed cluster of young stars – appears for 1–2 Myr and rapidly fades (in about 10 Myr – the main-sequence lifetime of OB stars and the time-scale of coherent existence of young star clusters Lada & Lada 2003). The UV radiation of massive young stars of the cluster reaches its maximum at about 5 Myr, and FUV decays over much longer time-scale limiting the time period, when the traces of star formation remain visible to $\simeq$ 100–150 Myr (O'Connell 1997; Stewart et al. 2000). That is why in terms of accepted model of supergiant shells formation, the Hα emission and 24 μm IR radiation which trace the sites of current SF in Irr galaxies and, in particular, in Ho II, do not always correlate with the location of giant H I supershells of at least several hundred Myr old.

Two questions concerning star formation processed in Irr galaxies remain to be of interest today: what actually triggers the ongoing star formation in a particular region of a galaxy? And how does the structure and kinematics of giant H I cavities and shells change under the influence of new episodes of star formation in their walls? The analysis of the structure and kinematics of H II regions in the walls of the SGS in the Ho II galaxy that we perform in this study is an attempt to shed certain light on the problem. In this section, we discuss the probable mechanism responsible for initiation of the ongoing star formation in Holmberg II.

An analysis of deep Hα images of 51 Irr and diffuse galaxies allowed Hunter et al. (1993) to discover a distinguishing feature of Ho II, which consisted of the very local disposition of H II regions. The authors formulated the question: why there are so few shell-like ionized structures despite the presence of many neutral supergiant shells which most likely have been produced by the stellar wind and SN explosions of rich OB associations? As we pointed out above, all local star-forming complexes – the brightest emission nebulae as well as the brightest UV and IR regions – are located in the northern wall of the most extended H I cavity in the galaxy (see Fig. 1). Such localization makes the question about the nature of ongoing star formation in Ho II to be more intriguing – why H II regions are observed mostly in the north part of SGS, but not spread over it?

One of possible explanation of such star formation distribution might be its occurring in the densest gaseous clouds in the galaxy. Does the locations of star-forming regions in Ho II correlate with the gas volume density in the SGS? To answer to this question, we estimated the H I volume density from the LITTLE THINGS data. We constructed the 21-cm line intensity map using the technique described by Walter et al. (2008) based on the H I 21-cm line intensity distribution. To convert column density into volume density, we assumed that the scaleheight of the H I disc and its inclination to be $h = 400$ pc (Banerjee et al. 2011) and $i = 47^{\circ}$ (Oh et al. 2011), respectively.

As a result, we establish that the distribution of H I volume density in the SGS discussed, where regions of ongoing star formation are located, is, on the whole, uniform with $n_{\mathrm{H\,I}}$ varying from 0.3 to 0.7 cm^{-3}. The inferred densities agree with the previous estimates of the density in the SGS: 0.5 cm^{-3} and 0.3 cm^{-3} according to Bagetakos et al. (2011) and Puche et al. (1992), respectively.

The 'central arc' of bright ionized nebulae in the Ho II galaxy is indeed located in the region of the highest H I column density. However, the average column density of neutral gas at this location does not substantially exceed the density in the southern wall of the SGS which contains small separate star-forming regions but with no extended Hα emission complexes similar to the regions in the 'central arc' (see Fig. 1).

Moreover, star formation in galaxies may occur in environments with sufficiently low densities. Recent studies fail to reveal the so-called gas surface density threshold above which star formation begins; at lower densities, the star-formation efficiency decreases more rapidly with the decrease of gas density but does not vanish even at $\Sigma_{\mathrm{H\,I+H_2}} < 0.5\,\mathrm{M_{\odot}\,pc^{-2}}$ (see Bigiel et al. 2008, 2010; Zasov & Abramova 2012; Abramova & Zasov 2012 and references therein) and, apparently even at lower densities (Shi et al. 2014). Summing up, we cannot explain the observed location of H II regions in Ho II by the gas density distribution.

Our study shows that the region that separates the SGS discussed and the giant irregularly shaped northern cavity consisting of several shells adjoining each other in the sky plane is characterized by a very non-uniform structure and the greatest local variations of the neutral-gas velocity in the galaxy. The distribution of H I velocity dispersion along the SGS discussed here shows insignificant variations – approximately from 7 to 16 km s^{-1}. However, it is interesting to verify whether these variations are related to ongoing star formation in the SGS rims. In order to answer this question we compared pixel-by-pixel the H I velocity dispersion and Hα flux that traces star formation rate.

The procedure had several steps. First of all, we performed a Gaussian convolution of our Hα image in order to obtain the same spatial resolution as for the H I LITTLE THINGS data. We then resized the convolved Hα image in order to obtain the same pixel scale with an H I velocity dispersion map. After that, the pixels corresponding to the bright H I rim of the SGS were selected for a further analysis. We constructed a 2D histogram of the Hα flux

Downloaded from http://mnras.oxfordjournals.org/ at Special Astrophysical Observatory of the Russian Academy of Sciences on November 15, 2016

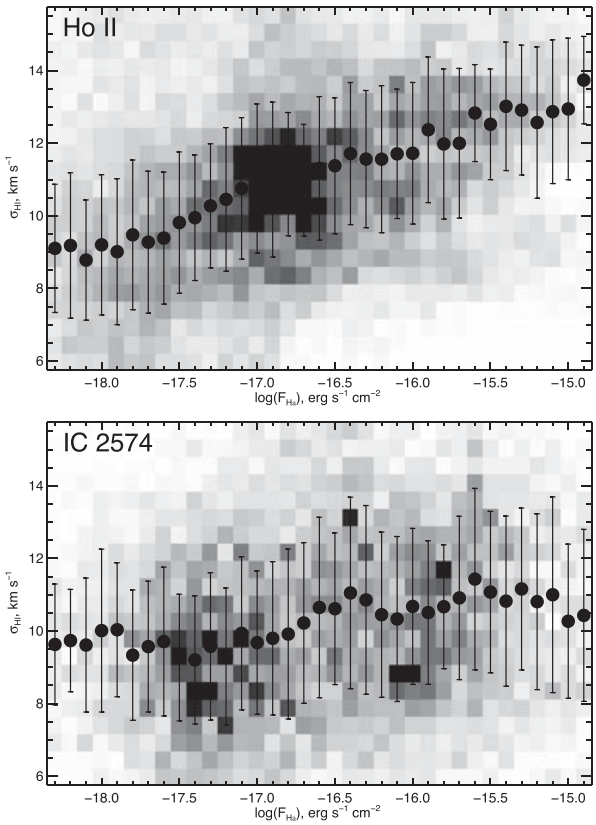

Figure 13. 2D histogram of the Hα flux and H I velocity dispersion along the SGS in Ho II (top) and IC 2574 (bottom) galaxies. Black points and bars denote the mean value and standard deviation of the H I velocity dispersion for each Hα flux bin.

and H I velocity dispersion distributions among these pixels. The resulting histogram is shown in the top panel of Fig. 13. We also show the mean H I velocity dispersion and its standard deviation for each flux bin.

As is evident from the constructed histogram, the H I velocity dispersion in the SGS does not change in the areas with a very low Hα flux. However, starting from $F(\mathrm{H}\alpha) \simeq 2 \times 10^{-18}$erg s^{-1} cm^{-2} arcsec^{-2}, velocity dispersion begins to show an increasing trend.

The observed dependence can be explained by two factors. First, the H I velocity dispersion may have become higher because of the collision of the SGS with the above northern supershells resulting in ignition of star formation in this region. Secondly, the ongoing star formation itself may have an effect on the SGS by increasing the H I turbulence level near bright H II regions. In the bottom panel of Fig. 13, we show the similar histogram for another supergiant shell we previously studied (Egorov et al. 2014) located in IC 2574 galaxy. In contrast to Ho II SGS, the morphology of a supergiant shell in IC 2574 does not reveal any signs of its interaction with neighbouring shells, and we do not see any clear correlation between the H I velocity dispersion and the Hα flux for that case. This allows us to prefer the first explanation of the dependence observed for the Ho II galaxy.

The above facts and considerations suggest that the last episode of star formation in the Ho II galaxy, which we observed as areas of bright H II regions and shells, was triggered by the collision of two above mentioned giant H I shell-like structures (or, possibly, by the collision of multiple shells that produced them).

The mechanism of star formation triggered by the collision of supergiant shells is well known (see Chernin, Efremov & Voinovich 1995); many colliding supergiant shells with star formation have been found in the LMC (see the references in the above paper).

One of the most striking examples of this process is clearly observed in the irregular Local Group galaxy IC 1613, where the region of ongoing star formation is localized at the periphery of a supergiant H I shell at the place of its collision with another supergiant shell located north of it (see Lozinskaya 2002).

Another example of this type can be found in the NGC 6946 galaxy: a complex of H II regions, which is the second largest such complex in the galaxy, is located at the interface between two neutral gas cavities #107 and #106 identified by Boomsma et al. (2008), see also Efremov, Afanasiev & Egorov (2011).

Note that the collision of supergiant shells by itself is, generally speaking, also a natural consequence of the interaction between the collective wind and SNe and the ambient gas over a more extended scalelength and time-scale.

6.2 Complexes of current star formation

Faint extended filamentary structures of ionized gas identified in this study, which connect individual bright H II regions, have changed our understanding of the regions of triggered star formation in the galaxy. It is evident that current sites of star formation are not 'chains' of bright nebulae in the walls of the H I SGS, as previously thought, but rather unified extended star-forming complexes with sizes extending up to several hundred pc, i.e. comparable to the size of the SGS. The conclusion that the structures considered are single entities is further corroborated by our discovery of faint neutral shells surrounding the complexes SE, N and NW.

The formation of such unified complexes can be understood in terms of the current view on the feedback between stars and the ambient gas given the strong inhomogeneity of gas in the SGS walls. The UV radiation of massive stars ionizes the surrounding gas and creates bright H II regions. At the outer boundary of a dense parent cloud, the ionization front penetrates further into the tenuous medium creating 'blisters' on the side of the dense cloud (a so-called champagne effect) according to the model by Tenorio-Tagle (1979). Radiation and stellar winds form faint shell-like structures in the tenuous ambient medium. These structures resemble faint filamentary structures observed in the SE, NE, N and NW complexes. As expected in terms of this model, the observed expansion velocity of faint shell-like formations exceeds the expansion velocities of the bright and more compact nebulae (see Section 4). Note that the age of faint extended structures should be close to that of bright and more compact structures if these are unified sites of star formation.

Unfortunately, the accuracy of age determination for individual objects in these unified complexes of star formation listed in Table 3 leaves a lot to be desired because of too many uncertain factors involved.

We discussed the errors of age estimations based on the EW of the Hβ line in our earlier paper Wiebe et al. (2014). The main ones are the assumption about a single starburst in a given H II complex and the internal extinction (see also Stasińska & Leitherer 1996).

The age determined by Stewart et al. (2000) should be treated as the mean age of stars in the aperture because of the fact that a single-generation model is used to interpret a flux from what is potentially a mix of populations of slightly different ages. To compensate for this uncertainty, regions are classified into four age groups. According to the authors, when comparing regions the actual age cutoffs for each group should be ignored and groups should be just thought to

Downloaded from http://mnras.oxfordjournals.org/ at Special Astrophysical Observatory of the Russian Academy of Sciences on November 15, 2016

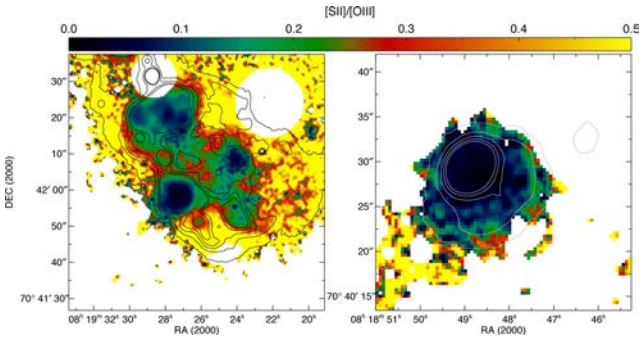

Figure 14. [S II] 6717, 6731Å to [O III] 5007 emission-line ratio maps for the SE complex (left) and the H II region at the south-west of the SGS rim (right). Isophotes correspond to the Hα flux levels (5, 15, 25, 35 and 45) $\times$ 10^{-17} erg s^{-1} cm^{-2} arcsec^{-2}. The regions contaminated by the foreground stars are masked.

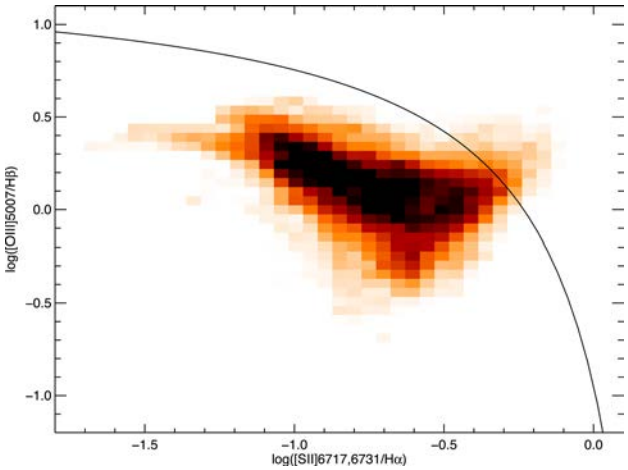

Figure 15. Diagnostic diagram log([O III]5007/H β) (computed by dividing the Hα flux by 2.86) versus log([S II]6717, 6731/H α) constructed for our narrow-band images in Hα, [S II] and [O III] lines. A separation line from Kewley et al. (2001) between regions of pure photoionization excitation and of significant contribution of the shocks is shown by a black line.

consist of relatively very young, young, intermediate-age or older star-forming regions.

In principle, the most accurate age estimate is the kinematic age if the expansion velocity and the radius of a shell are correctly determined. However, in the case of Ho II the spatial resolution is insufficient to construct the 'velocity ellipse' in each nebula. We attempted to estimate the expansion velocity from the split of the PV diagrams, however, no such evidence was revealed for bright regions. For this reason, we have estimated the expansion velocities of the nebulae from individual profiles, i.e. without any guarantee that they refer to the region of the most high-velocity motions. Furthermore, the irregular structure of the H II regions complicates a correct determination of the shell radius.

Given these uncertainties, the ages estimated by different methods (listed in Table 3) are consistent with our conclusion about single complexes of current star formation in the galaxy, which combine several bright nebulae and the associated weak shell-like structures.

In Section 5, we report the estimations of the amount of ionizing radiation from the young massive stars located inside the complexes. It follows from Table 4 that it is sufficient to account for the observed Hα flux for all the complexes. In faint external complexes the energy of stars is more than sufficient for ionizing the gas. The 'extra' photons from these complexes probably leak from these low-density and high-humidity complexes.

Pellegrini et al. (2011) proposed the method of distinguishing between density- and radiation-bounded H II regions based on the I([S II])/I([O III]) ratio map. The main idea of the method is that for an optically thick nebula one should observe the increased I([S II])/I([O III]) ratio at the edges of a region, while in the optically thin case the low ionization zone with the enhanced [S II] emission might not appear. We have applied this method to the galaxy Holmberg II and found that almost all regions of ionized gas show the ionization structure that is typical of optically thick H II regions – they exhibit the outer shell of the enhanced I([S II])/I([O III]) ratio surrounding the [O III] dominated core corresponding to the hot regions near the ionization sources. As an example of such structures, we show the I([S II])/I([O III]) map for the SE complex on the left-hand panel of Fig. 14. Note, however, the increased contribution of [O III] emission outside the border of the northern H II region probably caused by the ionizing radiation leakage towards the centre of the SE complex. The only optically thin region in the galaxy that does not represent such an [S II] shell is the compact H II region at the southwestern part of the SGS (shown in the right panel of Fig. 14). Thus, we may expect large escape fraction of ionizing radiation from this region, but also we cannot rule out the possible leakage from other H II regions due to their porosity. Strictly speaking, this method allows us to identify density-bounded regions, but the regions which look like radiation-bounded in the I([S II])/I([O III]) maps still might be optically thin.

6.3 Internal ionized supershell in SGS

We were the first to identify a faint diffuse internal supershell of ionized gas inside the SGS which was not seen in the *HST*/ACS images. The expansion velocity of the inner shell coincides with the expansion velocity of the neutral SGS.

The I([O III]5007)/I(Hβ) versus I([S II])/I(Hα) diagnostic diagram shown in Fig. 15 suggests that the increased values of these ratios corresponding to a gas glow behind the shock front is practically not observed in the galaxy including the region inside the SGS. It can be concluded from this that the nature of the ionized gas emission inside the SGS in the Ho II galaxy differs from that we have discovered inside the supergiant H I shell of the IC 2574 galaxy. Based on the observed increased I([S II])/I(Hα) and I([N II])/I(Hα) line ratios of diffuse gas in the IC 2574 SGS, we concluded (Egorov et al. 2014) that it should be similar to those of the extraplanar diffuse ionized medium (DIG) in spiral and irregular galaxies. Owing to that similarly to the DIG, we explained the faint diffuse ionized gas emission inside the SGS in IC 2574 as a result of leakage of both the ionizing photons and mechanical energy from the bright H II regions. In the case of Ho II, the location of the regions corresponding to the ionized internal superbubble on the diagnostic diagram (Fig. 15) is indicative of the photoionization mechanism of gas emission there.

The analysis of the FUV morphology of the galaxy presented by Stewart et al. (2000) shows the large region of faint diffuse FUV emission extending to the south-west of the central arc of bright H II complexes. This structure is clearly seen in Fig. 1. The relatively bright regions of FUV emission, denoted as star-forming regions 23, 35, 36 and 37 in the list of Stewart et al. (2000) and selected by the above authors as areas with FUV and no Hα emission and also fainter regions practically completely fill the inner supergiant shell (see Fig. 1). However, the observed FUV emission comes from the regions, where intensive star formation occurred 20–60 Myr ago

Downloaded from http://mnras.oxfordjournals.org/ at Special Astrophysical Observatory of the Russian Academy of Sciences on November 15, 2016

(Weisz et al. 2009b) and hence there was a lack of ionizing Lyman quanta. What is responsible for the creation of this internal ionized supershell in SGS then?

As it follows from Fig. 12, five identified OB stars are located inside the internal Hα superbubble near its northwestern edge. Their photometry shows that all of them are massive O stars. Correspondingly, these stars are most likely the main source of ionizing photons. Thus, according to Table 4, the amount of ionizing quanta from these stars is consistent with the value necessary to maintain the observed Hα flux. Note that the pure diffuse component of the ionized superbubble is denoted as 'Int.shell (diff)' in Table 4, while 'Int.shell (all)' means the whole region including the compact bright H II nebulae at the rim of the superbubble. Additional sources of ionizing radiation could be located in the southwestern chain of bright compact H II regions, for which there are no available data about their stellar population.

However, a certain contribution of energy leakage to the ionization of the superbubble cannot be ruled out. The latter is supported with the fact that the brightest nebula at the southern rim of the superbubble seems to be optically thin (see Fig. 14 and Section 6.2) that might cause the high fraction of ionizing photons escape.

Summing up, the ionized internal supershell was created most probably by the influence of ionizing radiation of 5 O stars located at its interior and of the additional energy leakage from nearby bright H II complexes to the internal walls of the H I SGS.

In addition, a continuing mechanical energy input from stellar activity, winds and SNe explosions, may also act on to the internal side of the SGS and contribute to its dynamics. For instance, speaking about the SE complex shown in Fig. 7, it can be clearly seen from rough estimates that the total mechanical energy input from the stars inside the shell $\dot{E}_{\rm wind} \sim 10^{38}$ erg s^{-1} and the shell kinetic energy consumptions $\dot{E}_{\rm k} \sim \sum 4\pi\rho R^2 v_{\rm s}^3 \sim 2 \times 10^{38}$ erg s^{-1} are marginally equal (the gas density $n \sim 0.3$ cm^{-3} is assumed, see above).

Shock waves from a stellar wind and SNe evacuate most of gas into the shell, so that the cavity remains filled mostly by wind and SNe ejecta with a very low density. For instance, when a supergiant shell is produced by multiple SNe explosions the remaining density might be as low as $\lesssim 10^{-4}$ of the ambient density (Sharma et al. 2014). Even if a much less violent energy release by ionizing radiation from underlying OB stars evacuates the gas, its density within the photoionized bubble remains as low as $\sim 10^{-2.5}$ (Henney et al. 2005; Henney 2007). One, therefore, estimates the gas density inside the bubble as $n_{\rm b} \lesssim 5 \times 10^{-5}$ cm^{-3} if the bubble is due to SNe explosions, and as $n_{\rm b} \sim 10^{-3}$ cm^{-3} otherwise.

In these conditions, the wind generated by massive stars inside the SGS acts from the interior and transfer momentum to the supershell. The free expansion phase of the wind continues until the swept-up mass equals to the wind-blown mass (see e.g. Draine 2011)

$$t_0 \simeq 10^2 n_{\rm b}^{-1/2} \dot{M}_6^{1/2} v_{\rm w,8}^{-3/2} \ {\rm yr}, \qquad (2)$$

where $\dot{M}_6$ in units $10^{-6}\,{\rm M}_\odot$ yr^{-1}, $v_{\rm w,\,8}$ is the wind velocity in 10^3 km s^{-1}. This gives $t_0 \simeq 3 \times 10^4$ yr and the corresponding radius $R_0 \simeq 30$ pc for an SNe produced the SGS and an order of magnitude lower t_0 and R_0 for the case of an SGS driven by ionization fronts. Accounting that the massive stars inside the supershell (marked in Fig. 12) are located at larger distances – 100 to 400 pc, one can estimate pressure acting on to the shell as

$$P_{\rm w} = \rho_{\rm b} \dot{R}_{\rm b}^2 \simeq 10^{-8} \left(\frac{L_{36} n_{\rm b}^2}{R_{\rm 1pc}^2} \right)^{1/3} \ {\rm dyn\,cm^{-2}}, \qquad (3)$$

where L_{36} is the wind mechanical luminosity in units 10^{36} erg s^{-1}, $R_{\rm b}$ is the radius of a wind-driven shock in the ambient medium, $R_{\rm 1pc}$ is its value in 1 pc. When the wind-driven shock acts on to the supershell it can support the expansion with the velocity

$$v_{\rm SGS} \simeq \left(\frac{P_{\rm w}}{\rho_0} \right)^{1/2} \simeq 0.8 \times 10^8 \left(\frac{L_{36}}{R_{\rm 1pc}^2} \right)^{1/6} \frac{n_{\rm b}^{1/3}}{n_0^{1/2}} \ {\rm cm\,s^{-1}}, \qquad (4)$$

so that for an SNe swept-up supershell with $n_{\rm b} \sim 5 \times 10^{-5}$ cm^{-3} a star located at $R = 100$ pc (as e.g. the brightest star in the left-hand corner of the SE5 shell in Fig. 7) would produce the velocity of the supershell of 6 km s^{-1}, while for $n_{\rm b} = 10^{-3}$ cm^{-3} it would support $v_{\rm SGS} \simeq 13$ km s^{-1}. It is worth stressing that episodic wind and SNe explosions and the respective feedback during the whole evolution of the SGS can support gas density in the bubble at a level sufficient for transferring a proper momentum on its internal surface.

In those cases, when OB stars lie closer than R_0 to the SGS edge, they act on to the supershell by the expanding wind directly without transferring momentum through the gas inside the cavity. In this case, the shell velocity supported by wind would be a factor of $(L_{36} n_0 / R_{\rm 1pc}^2 n_{\rm b}^2)^{1/6}$ higher than the above estimate in equation (3). One may expect that the similar enhancement of the action of a stellar wind on the supershell would take place, when the wind propagates through low density tunnels inside the bubble. Overall, one may think that energy release in the form of Ly-continuum photons and corpuscular winds emitted by massive stars inside the supershells does not only support their expansion, but also provides proper conditions for transferring momentum from stars to the walls and keeping them continuously expanding until star formation is exhausted.

6.4 Search for SN remnants in the SGS

Radio observations of the Ho II galaxy (Tongue & Westpfahl 1995; Braun et al. 2007; Heald et al. 2009) revealed a continuum radio emission in the region of bright emission nebulae. The synchrotron component of radio emission was identified in the eastern chain of bright nebulae by Tongue & Westpfahl (1995) and this fact led the authors to suspect that these areas may contain SN remnants. The detected polarized radio emission also coincides with this chain (Heald et al. 2009).

Hong et al (2013) identified the shock-ionized component via the line diagnostic diagram I([O III]5007)/I(Hβ) versus I([N II])/I(Hα) inside the HSK 45 nebula using the high-resolution *HST* data.

Our spectroscopic observations (Egorov et al. 2013) did not allow us to identify the optical emission of these hypothetical SN remnants and shock fronts by the I([S II])/I(Hα) line ratio.

We used our narrow-band images in the [O III] 5007Å, [S II] 6717,6731Å and Hα lines to construct the diagnostic diagram of I([O III]5007)/I(Hβ) versus I([S II])/I(Hα) ratios for each pixel of the galaxy. All the used line ratios were corrected by reddening using the mean value $E(B-V) = 0.05$ (Egorov et al. 2013). We calculated the values of Hβ fluxes from the Hα flux using the theoretical ratio I(Hα)/I(Hβ) for $T = 10\,000$ K (Osterbrock & Ferland 2006). The result is shown in Fig. 15. A black curve denotes the separation line between the regions with pure photoionization and composite (with a probably significant contribution of the shocks) excitation (Kewley et al. 2001). As follows from this diagram, almost all emission observed in the galaxy has been excited by photoionization and do not show any signs of shocks. The points lying over the separation curve in the diagram correspond to the regions of low brightness with low signal-to-noise ratio. Nevertheless, we should note a

Downloaded from http://mnras.oxfordjournals.org/ at Special Astrophysical Observatory of the Russian Academy of Sciences on November 15, 2016

limited implication of this method of construction of these diagnostic diagrams, because the inhomogeneous reddening may lead to incorrect results. Also the low metallicity should shift the separation line to the area of lower line ratios. But even proposing that all points corresponding to the right wing of the 'seagull shape' in Fig. 15 should lie under the curve, the collision excitation revealed by that way will be important only in the diffuse surrounding of the HSK 45 nebula.

If shock waves from possible SNe and/or stellar winds play an important role in the excitation of emission lines in some regions, we should be able to reveal the corresponding kinematic signatures. In bright nebulae of the eastern chain, where radio observations suggested the presence of SN remnants, we found no signs of high velocities typical of not too old SN remnants. However, high-velocity components of the Hα line (in some places having the elevated velocity dispersion) are indeed observed in the outer weakly ionized structures in the SE and NE areas and especially in the N area, where the brightest nebula, HSK 45, is located (see Figs 7–9). We currently cannot say firmly whether these high-velocity motions are associated with the inflow of kinetic energy from SN explosions or from the winds of O type stars. Note, however, that when shock waves from SNe propagate in an inhomogeneous (cloudy) medium, all typical shock manifestations – via emission, morphology or kinematics, become amorphous (Korolev et al. 2015). Hence, given that the region under study has been a subject of repeated exposure of strong perturbing factors (ionization fronts, wind flows) over long time, the absence of clear signs of SNe can be explained by the inhomogeneity of the gaseous environment.

7 SUMMARY

A detailed analysis of the structure and kinematics of all bright H II complexes of ongoing star formation in the walls of the supergiant shell of neutral gas in the Ho II galaxy is performed based on the observations carried out at the SAO RAS 6-m telescope with a scanning FPI in the Hα line combined with direct images taken in the Hα, [S II] and [O III] lines. We also used the *HST* archival images. The kinematics of ionized gas is compared to that of neutral gas based on the data of VLA observations in the 21-cm radio line taken from the LITTLE THINGS survey archive (Hunter et al. 2012) and to the stellar population of the area.

The observed data sheds certain light on the process of evolution of giant H I structures under the action by ionizing radiation and inflow of mechanical energy from local bursts of star formation in the walls of these structures.

The following results have been obtained.

(i) We found 22 faint expanding ionized superbubbles in star formation complexes of the galaxy and estimated their expansion velocities and kinematic ages using the results of the ionized gas kinematics analysis. Also three local expanding H I shells tied with star formation complexes in the SGS rim were identified.

(ii) We showed that current star formation episodes in the SGS were more extensive and complex than previously thought: they represent not 'chains' of separate individual bright nebulae in the walls of the H I SGS but rather unified star-forming complexes with sizes of several hundred pc. The formation of such unified complexes is due to the stellar feedback given the strong inhomogeneity of the gas in the SGS walls. Given the large errors of different methods, the inferred age of faint extended and bright more compact structures is consistent with the assumption that they are unified complexes of ongoing star formation.

(iii) We suggest that the last episode of star formation in the galaxy that we observe as areas of bright H II regions and shells in the northern wall of the SGS was triggered by its collision with giant shell-like H I structures located north of the SGS.

(iv) We discovered a faint ionized supershell inside the neutral SGS. The origin of this weak Hα emission somewhat differs from that of the faint inner ionized supershell that we earlier found in the SGS in IC 2574 galaxy, where the leakage of ionizing photons from bright H II regions in the walls of the SGS is proposed as a main ionization source (Egorov et al. 2014). In Ho II, five OB stars located inside the ionized supershell can explain its emission; however, we do not also rule out the leakage of ionizing photons from bright H II regions.

(v) We have not been found any clear kinematic signatures of the effect of shock waves associated with SN remnants in the eastern chain of bright nebulae earlier suspected of the synchrotron component of the radio emission.

ACKNOWLEDGEMENTS

We are thankful to the anonymous referee for the constructive comments.

This work is based on observations obtained with the 6-m telescope of the Special Astrophysical Observatory of the Russian Academy of Sciences carried out with the financial support of the Ministry of Education and Science of the Russian Federation (agreement no. 14.619.21.0004, project ID RFMEFI61914X0004).

The study was supported by the Russian Foundation for Basic Research (projects 14-02-00027, 15-32-21062, 15-02-08293 and 15-52-45114-IND). The study of gas kinematics was supported by the Russian Science Foundation grant no. 14-22-00041. YS is also thankful to the Grant of the President of the Russian Federation for Support of the Leading Scientific Schools NSh-4235.2014.2. AVM is also grateful for the financial support via the grant MD3623.2015.2 from the President of the Russian Federation, and basic research programme of the Department of Physical Sciences of the RAS OFN-17.

This research has made use of the Lyon Extragalactic Database (LEDA) and of the NASA/IPAC Extragalactic Database (NED) which is operated by the Jet Propulsion Laboratory, California Institute of Technology, under contract with the National Aeronautics and Space Administration

The study is partially based on observations made with the NASA/ESA *HST*, obtained from the Data Archive at the Space Telescope Science Institute, which is operated by the Association of Universities for Research in Astronomy, Inc., under NASA contract NAS 5-26555. These observations are associated with programmes # 10522 and # 10605.

REFERENCES

Abramova O. V., Zasov A. V., 2012, Astron. Lett., 38, 755
Afanasiev V. L., Moiseev A. V., 2011, Balt. Astron., 20, 363
Bagetakos I., Brinks E., Walter F., de Blok W. J. G., Usero A., Leroy A. K., Rich J. W., Kennicutt R. C., 2011, AJ, 141, 2011
Banerjee A., Jog C. J., Brinks E., Bagetakos I., 2011, MNRAS, 415, 687
Bastian N. et al., 2011, MNRAS, 412, 1539
Bernard E. J., Ferguson A. M. N., Barker M. K., Irwin M. J., Jablonka P., Arimoto N., 2012, MNRAS, 426, 3490
Bigiel F., Leroy A., Walter F., Brinks E., de Blok W. J. G., Madore B., Thornley M. D., 2008, AJ, 136, 2846
Bigiel F., Leroy A., Walter F., Blitz L., Brinks E., de Blok W. J. G., Madore B., 2010, AJ, 140, 1194

Downloaded from http://mnras.oxfordjournals.org/ at Special Astrophysical Observatory of the Russian Academy of Sciences on November 15, 2016

Boomsma R., Oosterloo T. A., Fraternali F., van der Hulst J., Sancisi R., 2008, A&A, 490, 555
Braun R., Oosterloo T. A., Morganti R., Klein U., Beck R., 2007, A&A, 461, 455
Bureau M., Carignan C., 2002, AJ, 123, 1316
Camps-Farinã A., Zaragoza-Cardiel J., Beckman J. E., Font J., García-Lorenzo B., Erroz-Ferrer S., Amram P., 2015, MNRAS, 447, 3840
Cannon J. M. et al., 2011a, ApJ, 735, 35
Cannon J. M. et al., 2011b, ApJ, 735, 36
Chernin A. D., Efremov Yu. N., Voinovich P. A., 1995, MNRAS, 275, 313
Chevalier R. A., 1974, ApJ, 188, 501
Cox D. P., 1972, ApJ, 178, 159
Dalcanton J. J. et al., 2008, ApJS, 183, 67
Dib S., Burkert A., 2005, ApJ, 630, 238
Dicaire I. et al., 2008, MNRAS, 385, 553
Draine B. T., 2011, Physics of the Interstellar and Intergalactic Meduim. Princeton Univ. Press, Princeton, NJ
Efremov Yu. N., Afanasiev V. L., Egorov O. V., 2011, Astron. Bull., 66, 304
Egorov O. V., Lozinskaya T. A., Moiseev A. V., 2010, Astron. Rep., 54, 277
Egorov O. V., Lozinskaya T. A., Moiseev A. V., 2013, MNRAS, 429, 1450
Egorov O. V., Lozinskaya T. A., Moiseev A. V., Smirnov-Pinchukov G. V., 2014, MNRAS, 444, 376
Egorov O. V., Lozinskaya T. A., Moiseev A. V., 2015, Astron. Astrophys. Trans., 29, 17
Egorov O. V., Lozinskaya T. A., Moiseev A. V., 2016, MNRAS, in press
Elmegreen B. G., 1997, ApJ, 477, 196
Elmegreen B. G., Chiang W.-H., 1982, ApJ, 253, 666
Heald G., Braun R., Edmonds R., 2009, A&A, 503, 409
Henney W. J., 2007, in Hartquist T. W., Pittard J. M., Falle S. A. E. G., eds., Proc. Astrophysics and Space Science, Vol. 1, Diffuse Matter from Star Forming Regions to Active Galaxies. Springer, Dordrecht, p. 103
Henney W. J., Arthur S. J., Williams R. J. R., Ferland G. J., 2005, ApJ, 621, 328
Hodge P., Strobel N. V., Kennicutt R. C., 1994, PASP, 106, 309
Hong S., Calzetti D., Gallagher J. S., Martin C. L., Conselice C. J., Pellerin A., 2013, ApJ, 777, 63
Hunter D. A., Hawley W. N., Gallagher J. S., 1993, AJ, 106, 1797
Hunter D. A. et al., 2012, AJ, 144, 134
Hunter D. A., Elmegreen B. G., Gehret E., 2016, AJ, 151, 136
Karachentsev I. D., Kaisin S. S., 2007, AJ, 133, 1883
Karachentsev I. D., Makarov D. I., Kaisina E. I., 2013, AJ, 145, 101
Kennicutt R. C., Jr et al., 2003, PASP, 115, 928
Kennicutt R. C. et al., 2011, PASP, 123, 1347
Kewley L. J., Dopita M. A., Sutherland R. S., Heisler C. A., Trevena J., 2001, ApJ, 556, 121
Kim S., Dopita M. A., Stavelet-Smith L., Bessel M., 1999, A&A, 350, 230
Korolev V. V., Vasiliev E. O., Kovalenko I. G., Shchekinov Yu. A., 2015, Astron. Rep., 59, 690
Lada C. J., Lada E. A., 2003, ARA&A, 41, 57
Lehmann I. et al., 2005, A&A, 431, 847
Leitherer C. et al., 1999, ApJ, 123, 3
Leroy A. K. et al., 2009, AJ, 137, 4670
Lozinskaya T. A., 2002, Astron. Astrophys. Trans., 21, 223
Lozinskaya T. A., Moiseev A. V., Podorvanyuk N. Yu., 2003, Rev. Mex. Astron. Astrofis. Ser. Conf., 15, 284
McCray R., Kafatos M., 1987, ApJ, 317, 190
McQuinn K. B. W., Skillman E. D., Cannon J. M., Dalcanton J. J., Dolphin A., Stark D., Weisz D., 2009, ApJ, 695, 561
McQuinn K. B. W. et al., 2010a, ApJ, 721, 297
McQuinn K. B. W. et al., 2010b, ApJ, 724, 49
Markova N., Puls J., 2008, A&A, 478, 823
Martins F., Schaerer D., Hilliier D. J., 2005, A&A, 436, 1049
Maschenko S. Ya., Silich S. A., 1995, Astron. Rep., 39, 587
Moiseev A. V., 2002, Bull. Spec. Astrophys. Obs., 54, 74
Moiseev A. V., 2014, Astrophys. Bull., 69, 1
Moiseev A. V., 2015, Astrophys. Bull., 70, 494
Moiseev A. V., Egorov O. V., 2008, Astrophys. Bull., 63, 181
Moiseev A. V., Lozinskaya T. A., 2012, MNRAS, 423, 1831
Moustakas J., Kennicutt R. C., Jr, Tremonti C. A., Dale D. A., Smith J.-D. T., Calzetti D., 2010, ApJS, 190, 233
Muñoz-Tuñón C., Tenorio-Tagle G., Castañeda H. O., Terlevich R., 1996, AJ, 112, 1636
Nath B. B., Shchekinov Yu., 2013, ApJ, 777, L12
O'Connell R. W., 1997, in Waller W. H., ed., AIP Conf. Proc. Vol. 408, The Ultraviolet Universe at Low and High Redshift. Am. Inst. Phys., New York, p. 11
Oh S.-H., de Blok W. J. G., Brinks E., Walter F., Kennicutt R. C., Jr, 2011, AJ, 141, 193
Osterbrock D. E., Ferland G. J., 2006, Astrophysics of Gaseous Nebulae and Active Galactic Nuclei, 2nd edn. University Science Books, Mill Valley, CA
Ott J., Walter F., Brinks E., Van Dyk S. D., Dirsch B., Klein U., 2001, AJ, 122, 3070
Pellegrini E. W., Oey M.S, Winkler P. F., Smith R. C., Points S., 2011, Bull. Soc. R. Sci. Liege, 80, 410
Puche D., Westpfahl D., Brinks E., Roy J.-R., 1992, AJ, 103, 184
Relaño M., Beckman J. E., 2005, A&A, 430, 911
Rhode K. L., Salzer J. J., Westpfahl D., Radice L. A., 1999, AJ, 118, 323
Sánchez-Cruces M., Rosado M., Rodríguez-González A., Reyes-Iturbide J., 2015, ApJ, 799, 231
Sánchez-Salcedo F. J., Hidalgo-Gámez A. M., Martínez-García E. E., 2014, Rev. Mex. Astron. Astrofis., 50, 225
Schaerer D., Vacca W. D., 1998, ApJ, 497, 618
Sharma P., Roy A., Nath B. B., Shchekinov Yu., 2014, MNRAS, 443, 3463
Shi Y., Armus L. Helou G., Stierwalt S., Gao Y. Wang J., Zhang Z., Gu Q., 2014, Nature, 514, 335
Silich S., Lozinskaya T., Moiseev A., Podorvanyuk N., Rosado M., Borissova J., Valdez-Gutiérrez M., 2006, A&A, 448, 123
Simpson C. E., Hunter D. A., Knezek P. M., 2005, AJ, 129, 160
Stasińska G., Leitherer C., 1996, ApJS, 107, 661
Stewart S. G. et al., 2000, ApJ, 529, 201
Tenorio-Tagle G., 1979, A&A, 71, 59
Tenorio-Tagle G., 1981, A&A, 94, 338
Tenorio-Tagle G., Bodenheimer P., 1988, ARA&A, 26, 145
Tomisaka K., Habe A., Ikeuchi S., 1981, Ap&SS, 78, 273
Tomita A., Ohta K., Nakanishi K., Takeuchi T. T., Saito M., 1998, AJ, 116, 131
Tongue T. D., Westpfahl D. J., 1995, AJ, 109, 2462
Vasiliev E. O., Nath B. B., Shchekinov Yu. A., 2015, MNRAS, 446, 1703
Vorobyov E. I., Shchekinov Y. A., 2004, A&A, 416, 499
Wada K., Spaans M., Kim S., 2000, ApJ, 540, 797
Walter F. et al., 2007, ApJ, 661, 102
Walter F., Brinks E., de Blok W. J. G., Bigiel F., Kennicutt R. C., Jr, Thornley M. D., Leroy A., 2008, AJ, 136, 2563
Warren S. R. et al., 2011, ApJ, 738, 10
Weaver R., McCray R., Castor J., Shapiro P., Moore R., 1977, ApJ, 218, 377
Weisz D. R., Skillman E. D., Cannon J. M., Dolphin A. E., Kennicutt R. C., Lee J., Walter F., 2008, ApJ, 689, 160
Weisz D. R., Skillman E. D., Cannon J. M., Walter F., Brinks E., Ott J., Dolphin A. E., 2009a, ApJ, 691, L59
Weisz D. R., Skillman E. D., Cannon J. M., Dolphin A. E., Kennicutt R. C., Lee J., Walter F., 2009b, ApJ, 704, 1538
Wiebe D. S., Khramtsova M. S., Egorov O. V., Lozinskaya T. A., 2014, Astron. Lett., 40, 278
Yadav N., Mukherjee D., Sharma P., Nath B., 2016, preprint (arXiv:1603.00815)
Young L. M., Lo K. Y., 1997, ApJ, 490, 710
Zasov A. V., Abramova O. V., 2012, Astron. Astrophys. Trans., 27, 351

This paper has been typeset from a TEX/LATEX file prepared by the author.

Downloaded from http://mnras.oxfordjournals.org/ at Special Astrophysical Observatory of the Russian Academy of Sciences on November 15, 2016

Astronomical and Astrophysical Transactions (*AApTr*), 2015, Vol. 29, Issue 1, pp. 17–24,
ISSN 1055-6796, Photocopying permitted by license only, ©Cambridge Scientific Publishers

Triggered star formation in giant HI supershells: ionized gas

O.V. Egorov[1*], T.A. Lozinskaya[1†], A.V. Moiseev[2]

[1]*Sternberg Astronomical Institute, Lomonosov Moscow University, Moscow, 119991, Russia*
[2]*Special Astrophysical Observatory, Russian Academy of Sciences, Nizhnij Arhyz, 369167, Russia*

Received 22 April, 2015

We considered the regions of triggered star formation inside kpc-sized HI supershells in three dwarf galaxies: IC 1613, IC 2574 and Holmberg II. The ionized and neutral gas morphology and kinematics were studied based on our observations with scanning Fabry–Perot interferometer at the SAO RAS 6-m telescope and 21 cm archival data of THINGS and LITTLE THINGS surveys. Qualitative analysis of the observational data was performed in order to highlight two questions: why the star formation occurred very locally in the supershells, and how the ongoing star formation in HI supershells rims influence its evolution? During the investigation we discovered the phenomenon never before observed in galaxies IC 2574 and Holmberg II: we found faint giant (kpc-sized) ionized shells in Hα and [SII]6717,6731 lines inside the supergiant HI shells.

Keywords: Interstellar medium, supershells, star formation, IC 1613, IC 2574, Holmberg II, Holmberg I

1 Introduction

Stellar feedback plays significant role in the regulation of the interstellar medium (ISM) structure and the whole galaxy evolution as well. Stellar winds and supernovae explosions create complexes of shells and supershells of ionized and neutral gas; e.g. Bagetakos et al. (2011) analysed the HI distribution in 20 nearby galaxies and revealed about 1000 cavities in their discs with sizes from 80 pc to 2.6 kpc, expansion velocities from 4 to 64 km/s (in the main 10–20 km/s) and ages from 2 to 150 Myr.

The origin of the largest kpc-sized HI holes and shell-like structures (so-called supergiant shell, SGS) has been the subject of debate for more than two decades. In the standard approach based on the Weaver et al. (1977) model, HI shells result from the cumulative action of multiple stellar winds and supernovae explosions. However

*Email: egorov@sai.msu.ru
†Email: lozinsk36@mail.ru

it was recognized long ago (see e.g. Tenorio-Tagle & Bodenheimer, 1988; Rhode et al., 1999; Kim et al., 1999; Silich et al., 2006) that this scenario cannot explain the origin of SGS since stellar cluster remnants detected are inconsistent with the input of mechanical energy required by the standard multiple winds and supernovae model. Recent studies based on Hubble Space Telescope (HST) observations have found that multiple star formation events over the age of the hole do provide enough energy to drive HI hole formation (see e.g. Weisz et al., 2009a,b; Cannon et al., 2011a,b). A number of SGS exhibit signs of expansion-triggered star formation at their periphery. A special interest consists in a detailed analysis of the interaction of stars and gas in the region of new sites of star formation in the walls of SGS, which can elucidate the process of their evolution.

Dwarf irregular galaxies provide the best environments to study the creation mechanisms of giant HI structures with star-formation episodes in their rims. Because of the slow solid-body rotation and the lack of strong spiral density waves which can destroy the giant shells, they grow to a larger size and live longer compared to such structures in spiral galaxies. The overall gravitational potential of dwarfs is much smaller than that of spiral galaxies, their HI disc scale height is larger and the gas volume density is lower than in spirals. Therefore the same amount of mechanical energy fed to the ISM of dwarf Irr galaxies creates very large long-lived holes with star formation in the walls triggered by their expansion.

During several years we performed the analysis of the ionized and neutral gas structure and kinematics in nearby irregular galaxies: VII Zw 403 (Lozinskaya et al., 2006), IC 10 (Egorov et al., 2010), IC 1613 (Lozinskaya et al., 2003), IC 2574 (Egorov et al., 2014), Holmberg II (Egorov et al. 2016, in preparation). In most of them we had a deal with the star formation ongoing in the rims of the HI supershells. In this work we briefly review the results of our study in the galaxies where the different stages of the SGS evolution are clearly seen: IC 1613, IC 2574 and Holmberg II.

2 Observational data

The observations in the Hα emission line were made at the prime focus of the 6-m telescope of Special Astrophysical Observatory of Russian Academy of Sciences with SCORPIO (Afanasiev & Moiseev, 2005) or SCORPIO-2 (Afanasiev & Moiseev, 2011) multi-mode focal reducers. The data obtained in a scanning Fabry–Perot interferometer (FPI) mode were used for the study of the ionized gas kinematics, while the narrow-band Hα direct images were used for analysis of the ionized gas morphology. Neutral gas distribution and kinematics were studied using the data of archival VLA HI 21 cm observations from THINGS (Walter et al., 2008) and LITTLE THINGS (Hunter et al., 2012) surveys. The detailed description of the observational settings are shown in the corresponding papers for each galaxy discussed there.

3 Triggered star formation in SGSs

We considered three galaxies where the difference in the evolution stage of SGS is most evident. The aim of our analysis was to highlight two questions: what triggers the star

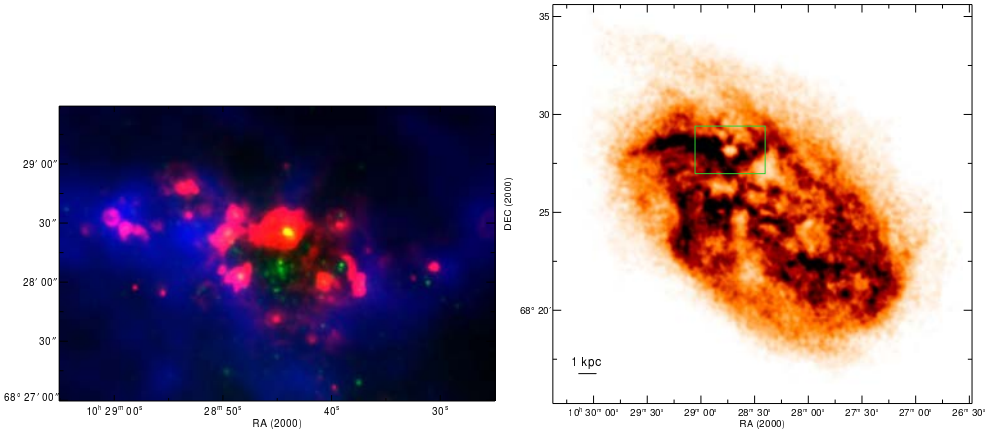

Figure 1 IC 2574. Left: False-color composite image of distribution of Hα emission (red channel) and stellar continuum (green channel) obtained with 6-m telescope of SAO RAS and HI 21 cm emission (THINGS, blue channel). Right: HI distribution according to THINGS data. Green rectangle denotes the region shown in the left panel.

formation at large scales and how the ongoing star formation influences the evolution of the "parent" SGS in a neutral gas? We describe below the most interesting results obtained during the study of each of the selected galaxies and discuss the above questions.

3.1 IC 2574

The well known "supergiant shell" (# 35 in the list of Walter & Brinks 1999) in the dwarf Irr galaxy IC 2574 is located at the north-east outskirts of its disc. This SGS surrounding a 1000×500 pc hole in the most prominent region of current and recent star-formation activity in the galaxy represents the impressive example of giant HI shells with triggered SF along rims (see Fig. 1). The analysis of resolved stars based on the HST data (Weisz et al., 2009b) shows that the last most significant episodes of star formation in SGS began $\simeq$100 Myr ago and the recent bursts of star formation along the walls of the shell are as young as 10 Myr. The ages of the younger star-formation events are consistent with those derived from broadband photometry and are younger than the estimated kinematic age of the HI SGS, 14 ± 3 Myr (Walter et al., 1998; Walter & Brinks, 1999; Egorov et al., 2014).

The analysis of the ionized and neutral gas kinematics inside the rim of SGS is presented in Egorov et al. (2014). We showed that for almost all HII complexes studied the energy input from young clusters located inside them is sufficient to drive the formation of observed ionized gas structures. The only exception we found is the shell-like region in the north-west part of the SGS that shows a high expansion velocity (65 km/s). This complex is the youngest in the region and its age is 1 Myr.

In the entire region of the SGS in IC 2574 we detected for the first time the faint diffuse emission in both Hα and [SII] lines. It seems that the source of the emission

observed is the shell-like structure that filled the internal part of the SGS.

We conclude that the observed SGS in IC 2574 is at relatively young stage where the star formation in its walls had been started recently. It is one of the most dynamically active giant HI structures among Irr galaxies. Almost the whole of the rim of the SGS shows the significant increase of star formation rate during the recent 10 Myr. The expansion of the brightest HII region in the north part of SGS rapidly disperses the local HI gas. One can see here the emission features like "horns" located beyond the northern boundary of the SGS. We can suppose that the destruction of the northern wall of the HI supergiant shell due to star formation will result in the growth of the SGS and in its merging with the neighbouring lower sized HI supershells. After several billion years there will be a system of giant adjoining and/or interacting shell-like HI structures similar to those observed in another galaxy we want to draw attention to below – Holmberg II.

3.2 IC 1613

Neutral gas distribution in IC 1613 galaxy shows a highly inhomogeneous structure with a number of HI holes, shells and arc-like structures of different sizes and expansion velocities (see Fig. 2). The only known complex of recent star formation is located in the north-eastern rim of the largest (1 to 1.5 kpc sized) HI "main supershell" in the galaxy. This supershell is older than SGS in IC 2574 – its kinematic age no less than 30 Myr (Silich et al., 2006). Three extended (300–350 pc) neutral shells with which the brightest ionized shells in the complex of star formation are associated are observed in the direction of the area of highest HI density in the galaxy. Two of H I shells were found to expand at a velocity of 15–18 km s^{-1} (Lozinskaya et al., 2003). The structure and kinematics of this complex were studied previously in a large number of papers (see, e.g., Lozinskaya et al., 2003; Silich et al., 2006, and references therein).

Figure 2 clearly demonstrates that the Hα emission in IC 1613 coincides well with the walls of three local HI shells mentioned above. The age of observed Hα bubbles are much lower (0.6–2.2 Myr) than the age of the HI shells (5.3–5.6 Myr), that may be an indirect evidence of the triggering of star formation there by the collision of these neutral gas shells. Lozinskaya (2002) proposed that the whole star formation complex in the rim of the "main supershell" is created by the collision of this largest shell with the giant HI supershell to the north.

3.3 Holmberg II

Holmberg II is another example of irregular galaxies that have a non-uniform gas structure with a large amount of shells and holes in the neutral gas distribution (see Fig. 3). Puche et al. (1992) found 51 giant holes and supershells in Holmberg II galaxy; Bagetakos et al. (2011) revealed 39 neutral gas cavities using more strong criteria. Their sizes are from 0.26 to 2.11 kpc and expansion velocity – from 7 to 20 km/s. These values correspond to kinematic age from 10 to 150 Myr. It is necessary to have energy input up to 10^{53} erg for the formation of several SGS.

The object of particular interest is the SGS #17 (according to the list of Bagetakos et al., 2011) – the largest and oldest HI supershell in the galaxy. Optical images in

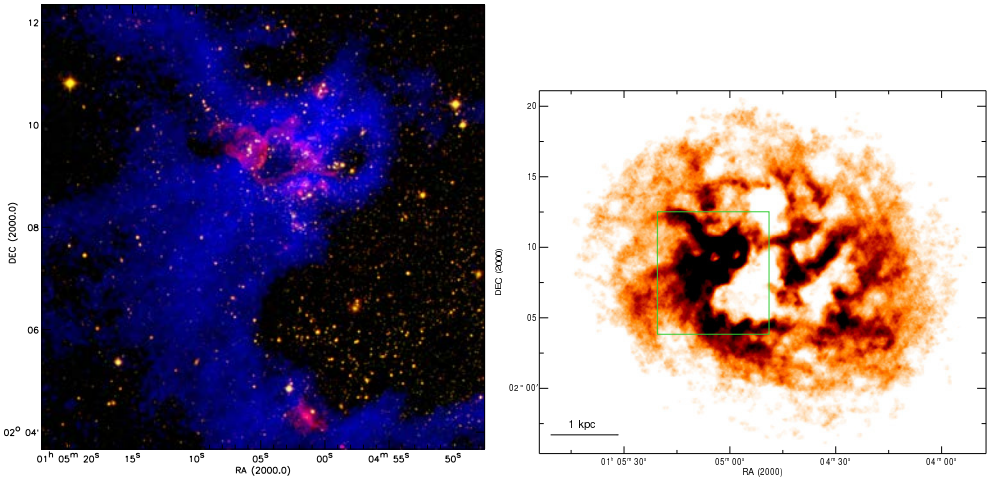

Figure 2 IC 1613. Left: False-color composite image of distribution of Hα (red color) and stellar continuum (yellow color) obtained with the SAO RAS 1-m telescope according to Lozinskaya et al. (2002), and HI 21 cm emission (LITTLE THINGS, blue color). Right: HI distribution obtained by LITTLE THINGS data. Green rectangle denotes the region shown in the left panel.

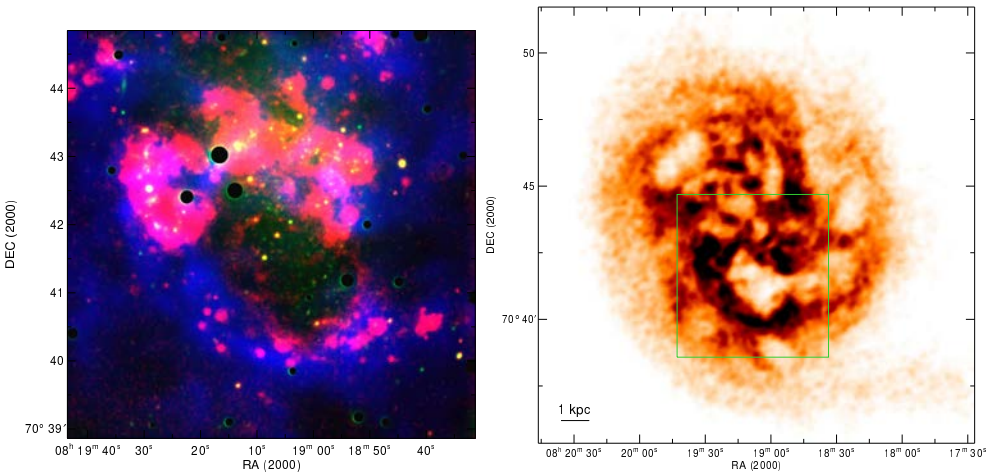

Figure 3 Similar to Fig. 1 for Holmberg II galaxy.

the Hα line reveal the brightest complexes of star formation located in the rim of this SGS. This supershell is much older than the SGS in IC 2574 described above (150 Myr against 14 Myr). Nevertheless, in both cases we observed that the triggered star formation occurred in the walls of SGS. Weisz et al. (2009a) analyzed the stellar population using the data of HST observations and showed that star formation occurs in the north rim of the SGS in Holmberg II about 40 Myr ago and during the last 15 Myr it is observed in the north-east and north-west parts of the shell.

In contrast with the case of SGS in IC 2574, in Holmberg II we observed that triggered intensive star formation occurred not along the full length of the HI supershell rim, but only in one half of them. Why is the Hα emission more intense in the northern part of HI supershell compared with its southern part? Probably, as it was in the case of IC 1613, the interaction and possible collision with two younger and smaller HI supershells to the north from the SGS considered are the reasons for triggering star formation in this region. Indeed, the age of the last starburst episode that occured in the region is in agreement with the estimations of the ages of these two supershells (#16 and #22 in the list of Bagetakos et al. 2011) – 50 and 30 Myr.

It is not surprising to detect Hα emission inside the small HI shells in galaxies (see, e.g., LITTLE THINGS survey Hunter et al., 2012), but whether giant ionized shells could be observed inside the HI SGSs? Up to date there was known only one kpc-sized Hα supershell – LMC 4 in Large Magelanic Cloud (Book et al., 2008). Also there were found several supershells with smaller size in that galaxy. We already noticed the detection of diffuse ionized kpc-scale supershell in IC 2574 located inside HI SGS, but there we proposed its shell-like morphology only by kinematics analysis. We found the unique structure in Holmberg II galaxy using the data of FPI and narrow-band imaging observation in Hα line. We clearly detected the giant ionized supershell with resolved shell-like structure that has diameter about 2 kpc and coincides with the internal wall of the examined neutral HI SGS in the galaxy. We should note that this structure has a low brightness (about 10^{-17} erg/s/cm^2/arcsec^2). Bastian et al. (2011) found 126 OB stars in Holmberg II, seven of them are located inside the Hα supershell. These seven OB stars provide enough high energy photons to ionize the internal wall of HI supershell and to create the Hα supershell observed. The detailed study of this structure as well as of the gas kinematics in the star formation regions in Holmberg II will be presented in our forthcoming paper Egorov et al. (2016, in preparation).

The observed parameters of local diffuse ionized gas in the SGS region are similar to those of the extra-planar diffuse ionized medium (DIG) in spirals and irregular galaxies. The observed [SII]/Hα and [NII]/Hα line ratios in the DIG are elevated compared to classical HII regions. The ionization of DIG in galaxies is traditionally explained by the leakage of ionizing photons from the HII regions as the main source (see, e.g., Seon, 2009; Hidalgo-Gámez, 2006, and references in these papers). Because of this similarity we may propose that faint ionized gas emission observed in the SGSs in IC 2574 and Holmberg II galaxies is the result of leakage from the bright HII regions in the SGSs walls. Indeed, all the HII complexes in the walls of studied galaxies have nonuniform, clumpy, or filamentary structure, which allows radiation to leak outside through low-density regions.

4 Conclusions

In this paper we have discussed the nature of triggered star formation complexes located in the rims of the giant (1 kpc and more) HI supershells. These structures are common in nearby irregular galaxies. Here we considered three galaxies: IC 1613, IC 2574 and Holmberg II, that might be best examples of the triggering of star formation in supergiant shells at the different evolution stages. Gas kinematics analysis

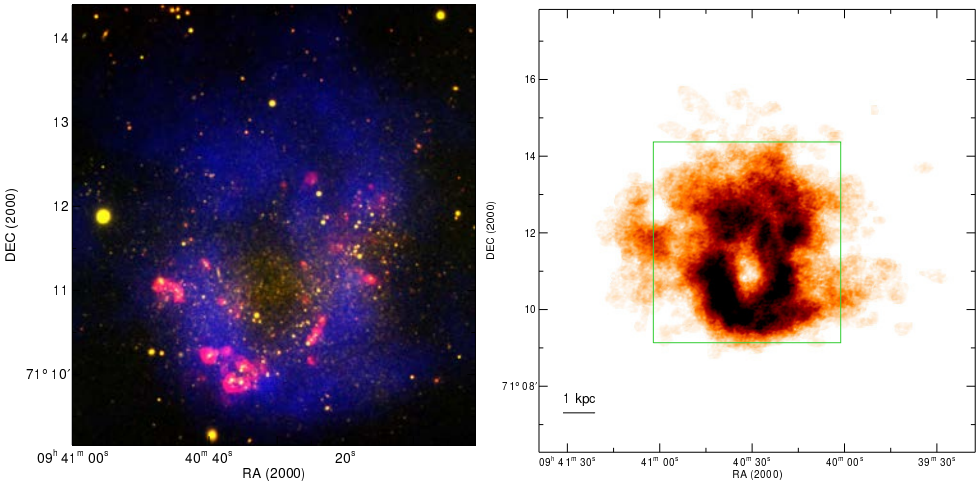

Figure 4 Holmberg I. Left: False-color composite image of distribution of Hα (red color) and stellar continuum (yellow color) obtained with the SAO RAS 6-m telescope, and HI 21 cm emission (LITTLE THINGS, blue color). Right: HI distribution obtained by LITTLE THINGS data. Green rectangle denotes the region shown in the left panel.

gave us evidence about the influence of ongoing star formation onto HI supershells. We observe weak and faint filaments of ionized gas outside HII regions that might be a consequence of the ionizing photons leakage from embedded star formation regions. This process might perturb HI shells and lead to their destruction at the later stage. In the final consequence of that process, the ISM of the irregular galaxy might represent a single neutral supershell with diameter about the disc size and the ongoing star formation in its rim. A picture resembling this is observed in Holmberg I galaxy (see Fig. 4).

Large numbers of HI supershells in galaxy discs is a common picture for nearby irregular galaxies, but the star formation is not distributed uniformly inside them. It seems that the collision of the HI supershells might be one of the main drivers of the star formation triggering on such large scales.

We found for the first time diffuse ionized gas inside the SGS in IC 2574 that shows the signs of the expansion and have size similar to diameter of the SGS. Similar and more confidently detected structures were discovered in Holmberg II galaxy. The structure of the Hα supershell in that galaxy also coincides with the inner wall of the largest HI supershell with active ongoing star formation inside. We considered two mechanisms of the formation of such structures: ionization of the inner wall of neutral supershell by the stellar population inside and/or by the leakage of the ionizing photons from the bright HII complexes.

Acknowledgements

The work was supported by the Russian Foundation for Basic Research (project 14-02-00027) and by a grant from the President of the Russian Federation (MD3623.2015.2). A. Moiseev is grateful for the financial support of the Dynasty Foundation. The observations at the 6-meter BTA telescope were carried out with the financial support of the Ministry of Education and Science of the Russian Federation (agreement No. 14.619.21.0004, project ID RFMEFI61914X0004).

References

Afanasiev V.L., Moiseev, A.V., 2005, Astron. Letters, 31, 194
Afanasiev V.L., Moiseev A.V., 2011, Baltic Astronomy, 20, 363
Bagetakos I., Brinks E., Walter F., de Blok W.J.G., Usero A., Leroy A.K., Rich J.W., Kennicutt R.C., 2011, AJ, 141, 2011
Bastian N., 2011, MNRAS, 412, 1539
Book L.G., Chu Y., Gruendl R.A., 2008, ApJSS, 175, 165
Cannon J. M. et al., 2011a, ApJ, 735, 35C
Cannon J. M. et al., 2011b, ApJ, 735, 36C
Egorov O.V., Lozinskaya T.A., Moiseev A.V., 2010, Astron. Reports, 54, 277
Egorov O.V., Lozinskaya T.A., Moiseev A.V., Smirnov-Pinchukov G.V., 2014, MNRAS, 444, 376
Hidalgo-Gámez A.M., 2006, AJ, 131, 2078
Hunter et al., 2012, AJ, 144, 134
Lozinskaya T.A., 2002, Astron.& Astrophys. Tr., 21, 223
Lozinskaya T.A., Arkhipova V. P., Moiseev A.V., Afanasiev V.L., 2002, Astron. Reports, 46, 16
Lozinskaya T.A., Moiseev A.V., Podorvanyuk N.Yu., 2003, Astron. Letters, 29, 77
Lozinskaya T.A., Moiseev A.V., Avdeev V.Yu, Egorov O.V., 2006, Astron. Letters, 32, 361
Puche D., Westpfahl D., Brinks E., Roy J.-R., 1992, AJ, 103, 184
Rhode K.L., Salzer J.J., Westpfahl D., Radice L.A., 1999, AJ, 118, 323
Seon K., 2009, ApJ, 703, 1159
Silich S., Lozinskaya T., Moiseev A., Podorvanyuk N., Rosado M., Borissova J., Valdez-Gutiérrez M., 2006, A&A, 448, 123
Tenorio-Tagle G., Bodenheimer P., 1988, ARA&A, 26, 145
Kim S., Dopita M. A., Stavelet-Smith L., Bessel M., 1999, A&A, 350, 230
Walter F., Brinks E., 1999, AJ, 118, 273
Walter F., Kerp J., Duric N., Brinks E., Klein U., 1998, ApJ, 502, L143
Walter F., Brinks E., de Blok W.J.G., Bigiel F., Kennicutt R.C. Jr, Thornley M.D., Leroy A., 2008, AJ, 136, 2563
Weaver R., McCray R., Castor J., Shapiro P., Moore R., 1977, ApJ, 218, 377
Weisz D.R., Skillman E.D., Cannon J.M., Dolphin A.E., Kennicutt R.C., Lee J., Walter F., 2009a, ApJ, 704, 1538
Weisz D.R., Skillman E.D., Cannon J.M., Walter F., Brinks E., Ott J., Dolphin A.E., 2009b, ApJ, 691, L59

Monthly Notices of the ROYAL ASTRONOMICAL SOCIETY

MNRAS **449,** 3568–3580 (2015) doi:10.1093/mnras/stv489

What controls the ionized gas turbulent motions in dwarf galaxies?

Alexei V. Moiseev,[1⋆] Anton V. Tikhonov[2†] and Anatoly Klypin[3]

[1]*Special Astrophysical Observatory, Russian Academy of Sciences[‡], 369167 Nizhnii Arkhyz, Karachaevo-Cherkesskaya Republic, Russia*
[2]*St Petersburg State University, Universitetskii pr. 28, 198504 St Petersburg, Stary Peterhof, Russia*
[3]*Astronomy Department, New Mexico State University, MSC 4500, PO Box 30001, Las Cruces, NM 880003-8001, USA*

Accepted 2015 March 4. Received 2015 February 24; in original form 2014 May 20

ABSTRACT

Using three-dimensional (3D) spectroscopy with a scanning Fabry–Perot interferometer, we study the kinematics of ionized gas in 59 nearby dwarf galaxies. Combining our results with data from the literature, we provide a global relation between the gas velocity dispersion σ and the star formation rate (SFR) and Hα luminosity for galaxies with a very broad range of star formation rates: SFR = 0.001–300 $M_\odot$ yr^{-1}. We find that the SFR–σ relation for the combined sample of dwarf galaxies, star-forming, local luminous and ultraluminous infrared galaxies can be fitted in the form $\sigma \propto \mathrm{SFR}^{5.3 \pm 0.2}$. This implies that the slope of the L–σ relation inferred from a sample of rotation-supported disc galaxies (including mergers) is similar to the L–σ relation of individual giant H II regions. We present arguments that the velocity dispersion of the ionized gas does not reflect virial motions in the gravitational potential of dwarf galaxies and instead is determined mainly by the energy injected into the interstellar medium by ongoing star formation.

Key words: ISM: bubbles – galaxies: dwarf – galaxies: ISM – galaxies: kinematics and dynamics.

1 INTRODUCTION

The nature of high-velocity turbulent motions of ionized gas in giant star-forming regions and dwarf galaxies has been studied for almost half a century, starting with Smith & Weedman (1970), who showed that the velocity dispersion σ (the root-mean-square (rms) velocity along the line of sight) in giant star-forming regions of the M33 and M101 galaxies, determined from the width of the integral Hα emission-line profiles, is about a few tens of km s^{-1}. A close correlation was later found between the rms velocity σ, the diameter and the total Balmer line luminosity (in the Hβ emission line) of the emitting nebula (Melnick 1977; Terlevich & Melnick 1981). Similar trends were found for individual H II regions and for dwarf irregular (dIrr) and blue compact dwarf galaxies (BCDG) or H II galaxies. Because of the tightness of the observed L(Hβ)–σ relation of starbursting compact galaxies, it was proposed as an independent indicator of cosmological distance (e.g. Melnick et al. 1987; Melnick, Terlevich & Terlevich 2000; Chávez et al. 2012; Koulouridis, et al. 2013; Chávez et al. 2014).

The relation between the emission-line luminosity L and ionized gas σ is also important for understanding how star formation affects the motion of gas and how star formation is regulated by different stellar feedback processes. Although the existence of a close correlation between these quantities has been known for a long time, the origin of the luminosity–velocity dispersion relation in H II galaxies and giant H II regions remains unclear (Terlevich & Melnick 1981; Chu & Kennicutt 1994; Scalo & Chappell 1999; Bordalo, Plana & Telles 2009; Moiseev & Lozinskaya 2012). The following factors may affect the width of the observed ionized hydrogen lines.

(i) Thermal broadening, which amounts to $\sigma_{\rm th} \approx 8$–$10$ km s^{-1} for typical electron temperatures in H II regions of 7000–10 000 K.

(ii) Turbulent motions determined by the combined influence of young stellar clusters on the interstellar medium (ISM).

(iii) Gravitational broadening, caused by virial motions of gas clouds in the galaxy gravitational potential.

(iv) Non-virial gravitational motions: ISM turbulence associated with tidal interactions, galaxy merging and external gas accretion (see e.g. the numerical simulations by Bournaud, Chapon & Teyssier 2011, observational constraints in Arribas et al. 2014 and references therein.)

When presenting and discussing the L–σ relation, we will always assume, except in specifically mentioned cases, that L is the total luminosity of a galaxy or a H II region in the Hα line and σ is the average (luminosity-weighted) velocity dispersion of ionized gas.

It is often assumed that gravitational effects are the dominant factor in giant H II regions and H II galaxies (e.g. Terlevich & Melnick 1981; Melnick et al. 1987; Tenorio-Tagle, Muñoz-Tuñón & Cox

⋆E-mail: moisav@sao.ru
†Deceased.
‡ The system of Russian Academy of Sciences institutes was liquidated in 2013 September.

© 2015 The Authors
Published by Oxford University Press on behalf of the Royal Astronomical Society

1993). The main argument is that the velocity dispersion of ionized gas is largely determined by the wind of stars that participate in virial motions with characteristic velocity $\sigma_{\rm stars}$. Then σ and $\sigma_{\rm stars}$ are mainly controlled by the gravitational potential of the object and the L–σ relation is similar to the Faber–Jackson relation for elliptical galaxies: $L \propto \sigma^4_{\rm stars}$. Different studies of the ionized gas kinematics in giant extragalactic H II regions give a value between ∼3 and ∼7 for the exponent in the L–σ relation (Blasco-Herrera et al. 2010, 2013). Chávez et al. (2014) present a detailed analysis of this relation for a sample of 128 local compact H II galaxies. They demonstrate that adding a second (the size of H II regions) or even a third (emission-line equivalent width *EW* or the continuum colour and metallicity) parameter significantly improves the correlation. They also argue in favour of a gravitational origin of the ionized gas velocity dispersion σ. They also emphasize that, in order for the L–σ to be tight, regions of recent bursts of star formation should be gravitationally bound, compact, massive and have strong emission lines with $EW(\rm H\beta) > 50$ Å with a pure Gaussian profile without any evidence of multiplicity or rotation.

A different view of the L–σ relation was developed beginning with Gallagher & Hunter (1983), who suggested that processes related to the energy of embedded OB stars drive the ionized gas velocity dispersion in giant H II regions on scales smaller than 0.5 kpc, while the properties of larger supergiant H II complexes agree with a gravitationally driven σ. Based on Fabry–Perot interferometric observations of nearby galaxies, Arsenault & Roy (1988) also concluded that effects of stellar wind and turbulence are more important for the kinematics of giant H II regions compared with virial motions. There are different ways in which a young stellar population affects the surrounding ISM. According to Mac Low & Klessen (2004, see also Lopez et al. 2014 and references therein), the main mechanisms are protostellar outflows, stellar winds and ionizing radiation pressure of massive stars, supernova (SN) explosions, dust-processed infrared radiation and warm and hot gas pressure. The contribution of different factors changes with spatial and density scale. For instance, Lopez et al. (2014) found that warm ionized gas dominates over the other terms of pressure in all H II regions considered in the Large and Small Magellanic Clouds. Numerical simulations also demonstrate that the radiation pressure is a very important feedback mechanism for models of of galaxy formation, compared with the hot gas contribution (heated by SNe and stellar winds, e.g. Hopkins, Quataert & Murray 2012; Ceverino et al. 2014; Trujillo-Gomez et al. 2015). Note that, together with the chaotic gas motions responsible for the Gaussian emission-line profile, effects related to individual expanding shells may lead to the appearance of non-symmetric features such as wings and peaks in the line profile (see examples in Melnick, Tenorio-Tagle & Terlevich 1999; Bordalo & Telles 2011).

Some recent observations also provide evidence that energy injected into the interstellar medium by the ongoing star formation process is the main factor affecting gas turbulent motions. For example, Green et al. (2010) show that for a wide range of galaxy luminosities the ionized gas σ is determined by the star formation rate (SFR), which is proportional to the Hα luminosity and does not correlate with the galaxy mass. Earlier, Dib, Bell & Burkert (2006) showed that σ for neutral gas also depends on the SFR. However, other numerical simulations with higher resolution in a stratified ISM suggested that this trend is absent if the gas surface density increases with the SN rate (Joung, Mac Low & Bryan 2009). On the other hand, galaxy-scale simulations that include stellar feedback (Hopkins et al. 2012) clearly demonstrate that the average velocity dispersion of the gas (in all cold, warm and hot phases) increases with total SFR. Also, Dopita (2008) argues that the kinetic energy of ionized gas in star formation regions is proportional to the local SFR, integrated over the duration of the burst. Moiseev & Lozinskaya (2012) demonstrate a close correlation between the two-dimensional distribution of the radial velocity dispersion of ionized gas and the surface brightness in the Hα line for a sample of nearby dwarf galaxies: most of the regions with the highest velocity dispersion belong to a low-brightness diffuse background surrounding large H II regions. Recent simulations of multiple SN explosions were able to reproduce the Hα intensity–velocity dispersion diagrams observed for these galaxies when a realistic spatial resolution was used (Vasiliev, Moiseev & Shchekinov 2015).

However, some other recent studies of high-redshift galaxies contradict with Green et al. (2010). For instance, integral-field data by Genzel et al. (2011) demonstrate a very weak correlation of σ and SFR density for star-forming clumps in galaxies at $z = 2.2$–2.4. Further, Wisnioski et al. (2012) and Swinbank et al. (2012), using observations with a similar technique, argue that such clumps follow the same L–σ relation as gravitational bounded local giant H II regions, according to Terlevich & Melnick (1981) and related studies.

To summarize, the question of the nature of high-velocity turbulent motions of ionized gas in dwarf galaxies still remains open. One of the problems is the lack of sufficiently uniform observational data. Recent results by Bordalo & Telles (2011) fill this gap to a certain extent. They give a uniform set of high-resolution spectroscopy observations for 118 star formation regions in H II galaxies. Chávez et al. (2014) presented similar data for 128 H II galaxies selected from the Sloan Digital Sky Survey (SDSS). They also discussed the impact of other factors (gas metallicity, ionization state, history of star formation) on the L–σ relation.

However, most of the results are based on slit spectroscopy. The distribution of ionized gas in dwarf galaxies has a complex irregular morphology and the two-dimensional velocity dispersion maps obtained using 3D spectroscopy can provide the most complete information about gas turbulence.

The second important issue is related to the fact that the luminosity-weighted velocity dispersion has become a widely used value to characterize the turbulent gas motions in samples of distant and nearby galaxies (Östlin et al. 2001; Green et al. 2010; Davies et al. 2011; Blasco-Herrera et al. 2013; Arribas et al. 2014). How does the L–σ relation work for galaxies of different types and luminosities? Do galaxies obey the same scaling relation as H II regions and star-forming clumps?

In this article, we analyse ionized gas turbulent motions in 59 galaxies observed at the 6-m Big Telescope Alt-azimuthal (BTA) of the Special Astrophysical Observatory of the Russian Academy of Sciences (SAO RAS) using a scanning Fabry–Perot interferometer (FPI). Most of our sample consists of dwarf galaxies in the local Universe. Using this unique material, we were able to extend the L–σ relation to objects much weaker than in the samples described earlier.

2 OBSERVATIONS AND DATA REDUCTION

2.1 Sample of galaxies

Our sample is based on the archive data of observations at the 6-m telescope of SAO RAS. It consists of several subsamples of galaxies studied within the framework of several observational programmes.

(i) The Local Volume (LV) subsample: 36 nearby dwarf galaxies with galactocentric distances $D < 15$ Mpc. These are mostly low-luminosity objects with average absolute magnitude $M_B \approx -14$. The ionized gas velocity dispersion maps of 10 galaxies from this subsample were already reported by Moiseev & Lozinskaya (2012).

(ii) The eXtremely Metal Deficient (XMD) subsample of 9 more distant ($D = 14$–86 Mpc) and bright ($M_B \approx -15$) dwarf galaxies with extremely low metallicity and two low-surface-brightness companion galaxies. Their internal kinematics were described and analysed in Moiseev, Pustilnik & Kniazev (2010b).

(iii) The BCDG subsample: 12 blue compact dwarf galaxies at distances $D = 10$–78 Mpc; all are brighter than $M_B = -15$. Some of them (e.g. Mrk 297 or III Zw 102) are sometimes included in BCDG samples (see Cairós et al. 2001), though they cannot be formally called dwarf galaxies, since their absolute magnitude is brighter than $M_B = -20$ and the amplitude of the rotation curve exceeds 140 km s^{-1}. The observational data for three of these galaxies were presented by Martínez-Delgado et al. (2007).

The full sample consists of 59 galaxies and covers a wide range of luminosities from $M_B = -11$ to $M_B = -21$. The overwhelming majority (51/59 = 86 per cent) of them are dwarf galaxies with absolute magnitude $M_B > -18$.

The observations were carried out in the prime focus of the 6-m telescope of SAO RAS using a scanning FPI mounted inside the Spectral Camera with Optical Reducer for Photometric and Interferometric Observations (SCORPIO) focal reducer (Afanasiev & Moiseev 2005). In 2014, its new version SCORPIO-2 (Afanasiev & Moiseev 2011) was used. The operating spectral range around the Hα line was cut using a narrow bandpass filter. About two-thirds of the observations were performed using the FPI501 interferometer, providing in the Hα emission line a free spectral range between neighbouring interference orders $\Delta\lambda = 13$ Å and a spectral resolution (full width at half-maximum (FWHM) of the instrumental profile) of about 0.8 Å (35 km s^{-1}), sampled at 0.36 Å per channel. After 2009 November, we used a new FPI751 interferometer, which has $\Delta\lambda = 8.7$ Å and a spectral resolution of 0.4 Å (18 km s^{-1}), sampled at 0.21 Å per channel. The Mrk 33 galaxy was observed in the [N II] λ6583 line, all others in the Hα line.

In 2003–2014, the detectors were CCD EEV 42-40 and E2V 42-90, given the image scale of 0.71 arcsec pixel^{-1} in the on-chip binned 4 × 4 mode. In 2002, the TK1024 CCD was used, yielding a scale of 0.56 arcsec pixel^{-1} in the 2 × 2 binning mode.

During the scanning process, we have consistently obtained 36 interferograms (40 for FPI751) at different distances between the FPI plates. The seeing on different nights varied from 1–4 arcsec. The reduction of observational data was performed using a software package running in the IDL environment (Moiseev 2002; Moiseev & Egorov 2008). Following the primary reduction, airglow line subtraction, photometric and seeing corrections using reference stars and wavelength calibration, the observational data were combined into data cubes, where each pixel in the field of view contains a 36- or 40-channel spectrum.

The log of observations is shown in Table 1, which lists the galaxy name, date of observations, interferometer type, exposure time and resulting angular resolution after smoothing the reduced data cubes with a two-dimensional Gaussian to increase the signal-to-noise ratio in areas of low surface brightness. Only the information for the Local Volume galaxies and the BCDG subsamples is shown; see the log of observations in Moiseev et al. (2010b) for the XMD subsample.

Table 1. Log of observations.

Name	Date	FPI	Exp. time time (s)	Ang. res. (arcsec)
Local Volume subsample				
CGCG 269–049	06.02.2010	FPI751	150 × 40	4.4
DDO 53	26.02.2009	FPI501	200 × 36	3.3
DDO 68	30.12.2006	FPI501	240 × 36	2.7
DDO 99	26.02.2009	FPI501	180 × 36	3.8
DDO 125	18.05.2005	FPI501	180 × 36	3.0
DDO 190	04.03.2009	FPI501	100 × 36	3.3
IC 10	08.09.2005	FPI501	300 × 36	1.2
IC 1613	12.09.2001	FPI501	200 × 36	2.2
KK 149	05.03.2009	FPI501	150 × 36	2.8
KKH 12	23.08.2004	FPI501	120 × 36	2.7
KKH 34	12.11.2009	FPI751	230 × 40	3.4
KKR 56	20.05.2010	FPI751	150 × 40	3.3
UGC 231	11.11.2009	FPI751	200 × 40	2.4
UGC 891	11.11.2009	FPI751	200 × 40	3.1
UGC 1281	14.08.2009	FPI751	110 × 40	2.7
UGC 1501	10.11.2009	FPI751	200 × 40	2.3
UGC 1924	11.11.2009	FPI751	180 × 40	2.3
UGC 3476	02.11.2010	FPI751	220 × 40	2.4
UGC 3672	12.11.2009	FPI751	160 × 40	3.1
UGC 5221	16.12.2014	FPI751	160 × 40	2.0
UGC 5423	26.02.2009	FPI501	180 × 36	3.5
UGC 5427	04.03.2009	FPI501	180 × 36	3.7
UGC 8638	24.02.2009	FPI501	150 × 36	3.9
UGC 6456	29.11.2002	FPI501	300 × 36	2.2
UGC 7611	19.05.2010	FPI751	160 × 40	3.5
UGC 8508	16.05.2005	FPI501	200 × 36	3.0
UGC 11425	14.08.2009	FPI751	140 × 40	3.0
UGC 11583	10.11.2009	FPI751	220 × 40	1.9
UGC 12713	16.05.2005	FPI501	200 × 36	3.0
UGC 2455	07.10.2010	FPI751	240 × 40	2.3
UGC 7047	17–18.03.2012	FPI751	360 × 40	2.2
UGC 7648/51	08.02.2011	FPI751	160 × 40	2.8
UGC 8313	19.03.2012	FPI751	450 × 40	2.7
UGCA 92	10.11.2009	FPI751	180 × 40	2.5
UGCA 292	07.02.2010	FPI751	120 × 40	3.6
BCDG subsample				
II Zw 40	01.12.2003	FPI501	120 × 36	1.9
II Zw 70	30.01.2004	FPI501	180 × 36	2.5
III Zw 107	01.12.2006	FPI501	100 × 36	1.9
III Zw 102	30.11.2003	FPI501	180 × 36	2.7
Mrk 5	30.01.2004	FPI501	240 × 36	2.6
Mrk 33	30.01.2004	FPI501	150 × 36	2.3
Mrk 35	01.12.2003	FPI501	150 × 36	2.1
Mrk 36	29.11.2003	FPI501	160 × 36	1.6
Mrk 297	13.08.2009	FPI751	144 × 40	3.5
Mrk 324	30.11.2003	FPI501	120 × 36	2.8
Mrk 370	30.11.2003	FPI501	120 × 36	2.6
Mrk 600	01.12.2006	FPI501	120 × 36	2.2

2.2 Construction of maps and measuring velocity dispersion

We define the velocity dispersion of ionized gas σ as the standard deviation of the Gaussian profile fitted to the Hα emission line after accounting for the FPI instrumental profile and subtracting the contribution of thermal broadening in the H II regions. The procedure to measure σ is described in detail in Moiseev & Egorov (2008). In short, the observed profiles of the Hα line were fitted by the Voigt function, which is a convolution of Lorentzian and Gaussian functions corresponding to the FPI instrumental profile and broadening of observed emission lines, respectively. The FWHM of the

instrumental profile was estimated each night from Lorentzian fitting of the He–Ne–Ar calibration lamp emission scanned with the FPI (Moiseev & Egorov 2008). The results of profile fitting were used to construct two-dimensional line-of-sight velocity fields of ionized gas, maps of line-of-sight velocity dispersion free from instrumental profile ($\sigma_{\rm obs}$) influence and also images of galaxies in the Hα emission line and the continuum.

The accuracy of velocity dispersion was estimated from measurements of the signal-to-noise ratio (S/N) using the relations given in fig. 5 of Moiseev & Egorov (2008). On the σ maps, we masked out the regions with a weak signal, where the formal error of the velocity dispersion measurements exceeded 10–12 km s^{-1} (which corresponds to $S/N \leq 5$). Emission-line intensity maps were constructed even for regions where the signal-to-noise ratio was smaller: $S/N \approx 2$–3.

The correction from the measured $\sigma_{i,\,\rm obs}$ to the final σ_i, where i corresponds to the pixel number, was made according to the relation (Rozas et al. 2000)

$$\sigma_i^2 = \sigma_{i,\rm obs}^2 - \sigma_N^2 - \sigma_{\rm tr}^2, \quad (1)$$

where $\sigma_N \approx 3$ km s^{-1} and $\sigma_{\rm tr} \approx 9.1$ km s^{-1} correspond to the natural width of the emission line and its thermal broadening at a temperature of 10^4 K.

In most of the objects, the emission-line spectrum is very well described by a single-component Voigt profile. Only a few galaxies have areas where the emission-line profile has a complex (usually two-component) structure, showing the presence of expanding shells around regions of star formation or possible supernova remnants. In addition to the previously reported cases of UGC 8508, UGCA 92 (Moiseev & Lozinskaya 2012) and SBS 0335-052E (Moiseev et al. 2010b), compact regions with a two-component Hα profile were found in UGC 260, UGC 1281, UGC 7047 and UGC 7651.

The mean velocity dispersion for the whole galaxy, weighted by intensity, was calculated as

$$\sigma = \frac{\sum \sigma_i I_i}{\sum I_i}, \quad (2)$$

where I_i is the observed emission line in the ith pixel.

Fig. 1 presents the results of our observations with the scanning FPI: the image in the Hα line, the velocity field and the velocity dispersion, corrected for thermal broadening and natural width according to equation (1). The velocity fields usually have more points than the velocity dispersion maps since, at the same S/N level, the velocity is measured with a higher accuracy than the line width.

3 L–σ RELATION

The calculated kinematic parameters of the galaxies, together with their adopted distances, absolute magnitudes in B and K_s bands and total Hα luminosity, are given in Table 2. We use the distances and luminosities in the B and K_s bands and Hα emission line for nearby galaxies provided by the Local Volume Galaxies (LVG) data base[1] (Kaisina et al. 2012). All luminosities are corrected for internal ($A_B^{\rm i}$) and Galactic ($A_B^{\rm g}$) extinction according to the values given in this data base.[2]

[1] http://www.sao.ru/lv/lvgdb/

[2] The absorption in the Hα line was assumed to be $0.538(A_B^{\rm i} + A_B^{\rm g})$ and that in the K_s band $0.085(A_B^{\rm i} + A_B^{\rm g})$.

For nearby galaxies not listed in the LVG data base (UGC 231, UGC 891, UGC 1924 and UGC 3672), the distances from Karachentsev et al. (2004) were adopted. For UGC 8313, we use data from Tully (1988). The apparent magnitudes of these galaxies from RC3 (de Vaucouleurs et al. 1991) were adopted; the m_K values were retrieved from the Two Micron All-Sky Survey (2MASS) and $A_B^{\rm i}$ was obtained according to the relation of Verheijen (2001). The flux in Hα was taken from van Zee (2000) and Kennicutt et al. (2008). Distances and luminosities for the XMD sample were taken as in Moiseev et al. (2010b) and those for BCDG from Cairós et al. (2001).

When estimating $L_{\rm H\alpha}$, we take into account the fact that, in observations with narrow-band filters, authors measure the flux in Hα+[N II]. The contribution of the nitrogen lines [N II] $\lambda\lambda$6548, 6584 was determined by an empirical correlation, linking the [N II]/Hα ratio with M_B (Kennicutt et al. 2008; Lee et al. 2009). For most galaxies considered, fainter than $M_B = -18$ this ratio is small ([N II]/Hα < 0.2).

The inclination angles i and maximal rotational velocities $V_{\rm max}$ for the XMD sample are based on the results of Moiseev et al. (2010b). For most Local Volume galaxies, the data are taken from Moiseev (2014). The kinematic parameters of III Zw 102 and UGC 8313 were presented by Moiseev (2008) and Voigtlaender, Bomans & Moiseev (2015). For other galaxies, i and $V_{\rm max}$ were derived from the ionized gas velocity field in the same manner as described in Moiseev (2014). In cases where Hα rotation curves never clearly come to a plateau or the velocity field of ionized gas is dominated by non-circular motions (objects marked by asterisks in Table 2), we use estimates from HyperLeda (Makarov et al. 2014).

The velocity fields shown in Fig. 1 reveal a component related to regular rotating discs in the majority of the sample (61 per cent). The fraction of rotation-dominated galaxies changes significantly in the different subsamples. In the LV subsample, the majority of galaxies (72 per cent or 26 objects) have disc-like ionized gas kinematics. Even among the remaining objects, in some dwarf galaxies (DDO 53, UGC 6456, UGC 8638) a component appears corresponding to circular rotation. However, in these galaxies, non-circular velocities have larger amplitude (Moiseev 2014). In these low-mass galaxies, the Hα-emitted gas is observed only in the central region, where the amplitude of the rotation curve is about 5–10 km s^{-1}. In contrast with the LV subsample, only half of XMD galaxies (55 per cent or 6 objects) demonstrate a disc-like rotation gradient, including cases of merger remains (HS 0822+3542 and UGC 772), which reveal two rotating discs with different spin orientation. This is not surprising, because analysis of Moiseev et al. (2010b) provides evidence for the crucial role of interaction-induced star formation among galaxies in this subsample. A similar situation also holds for the BCDG subsample, where only 33 per cent of objects (namely III Zw 102, Mrk 33, Mrk 35 and Mrk 370) show disc-dominated rotation in their velocity fields.

The maps of velocity dispersion σ clearly demonstrate that in the centre of star-forming regions the velocity dispersion of ionized gas has a minimum, whereas σ increases towards the periphery. Such a feature in the distribution of the ionized gas velocity dispersion was noted earlier in a number of studies (e.g. Moiseev et al. 2010b; Marino et al. 2013) and was discussed in Moiseev & Lozinskaya (2012), where such behaviour is attributed to the influence of young stellar groups on the surrounding gas.

Fig. 2 shows different variants of L–σ dependence for the galaxies in our sample. The literature most often discusses the dependence of σ on $L_{\rm H\alpha}$ (or $L_{\rm H\beta}$), shown in the upper panels. The top left figure separately shows all the three subsamples of galaxies we

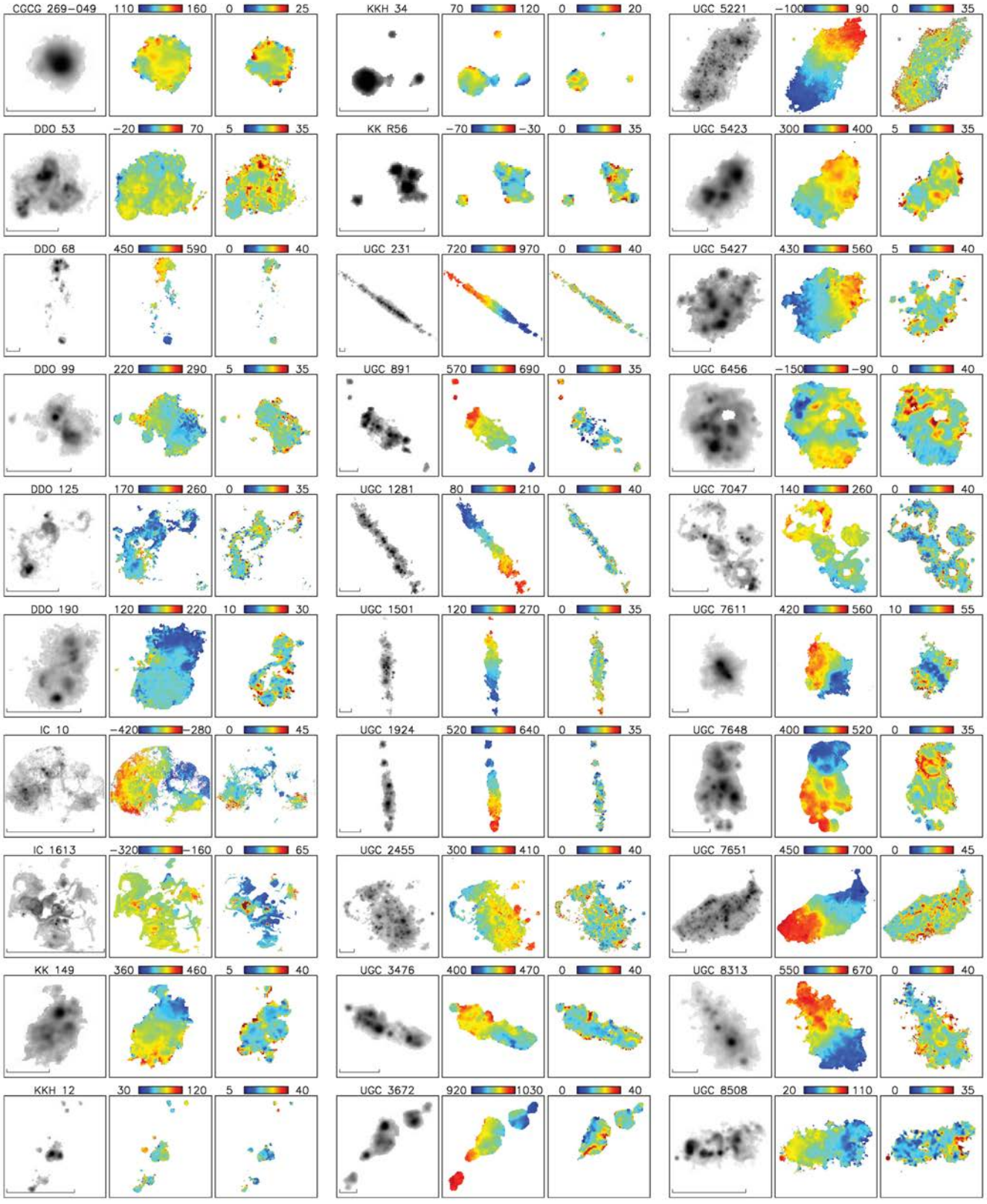

Figure 1. Results of observations with the scanning FPI at the SAO RAS 6-m telescope. The following are given for each galaxy: an image in the Hα line, maps of line-of-sight velocities and velocity dispersion, corrected for thermal line broadening. The colour scale is in $\mathrm{km\,s^{-1}}$. The horizontal bar in the first panel for each galaxy shows a linear scale of 1 kpc.

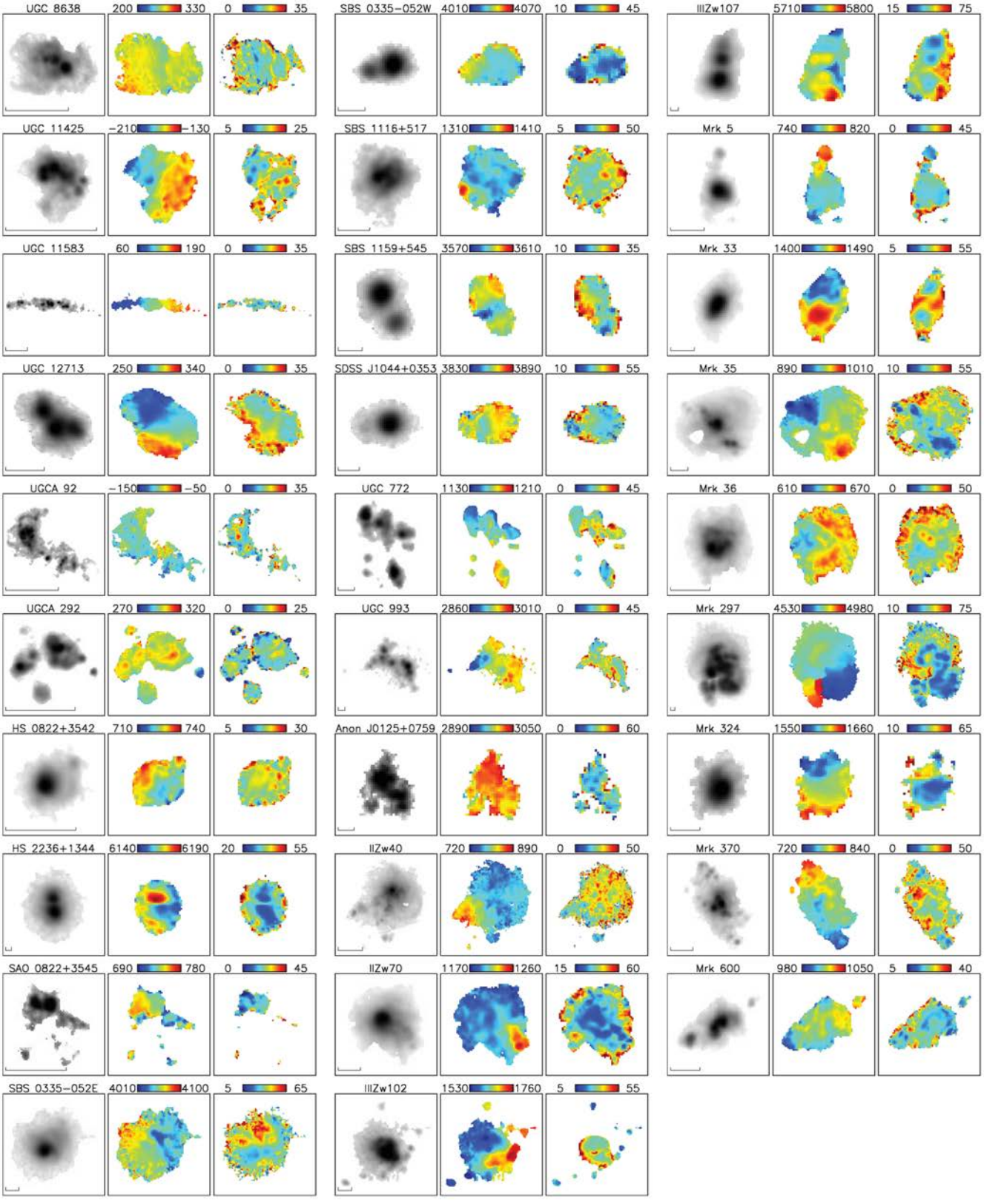

Figure 1 – *continued*

Table 2. Integral parameters of galaxies.

Name	D Mpc	M_B	M_K	log $L_{H\alpha}$ erg s^{-1}	σ km s^{-1}	i deg.	V_{max} km s^{-1}
			Local Volume subsample				
CGCG 269–049	4.59	−13.11	− 15.46	37.24	13.6 ± 1.9	43	9.8
DDO 53	3.56	−13.37	− 15.00	38.93	21.0 ± 1.8	27	16.4
DDO 68	9.80	−15.27	− 17.15	39.33	19.9 ± 3.9	65	57.2
DDO 99	2.64	−13.52	− 15.26	38.44	19.2 ± 2.4	52	11.7
DDO 125	2.74	−14.33	− 16.97	38.28	16.3 ± 2.3	63	17.8
DDO 190	2.80	−14.19	− 16.52	38.44	18.5 ± 2.9	60	24.7
IC 10	0.66	−15.99	− 17.90	40.73	17.6 ± 0.7	31	52.8*
IC 1613	0.73	−14.54	− 16.90	38.43	25.9 ± 1.3	22	26.7*
KK 149	8.90	−14.85	− 17.20	38.58	19.0 ± 4.1	58	26.2
KKH 12	3.00	−13.03	− 15.89	38.65	17.9 ± 4.5	90	19.5*
KKH 34	4.61	−12.30	− 14.65	37.18	11.6 ± 6.6	55	12.8*
KKR 56	5.90	−14.39	− 16.74	38.27	17.8 ± 6.3	–	–
UGC 231	12.82	−18.38	− 19.98	39.75	18.0 ± 3.8	90	92.8
UGC 891	9.38	−15.90	0.00	38.94	15.4 ± 5.9	65	60.0
UGC 1281	4.97	−16.07	− 15.51	39.07	16.7 ± 5.0	90	56.4
UGC 1501	4.97	−16.52	− 18.22	39.52	16.6 ± 2.4	75	47.5
UGC 1924	9.86	−15.80	− 17.41	38.66	14.5 ± 5.4	90	50.6
UGC 2455	7.80	−18.14	− 20.00	40.71	18.3 ± 2.6	51	47.9
UGC 3476	7.00	−14.27	− 16.62	39.22	16.5 ± 2.3	90	47.3*
UGC 3672	15.10	−13.89	0.00	39.30	18.3 ± 3.6	56	67.8
UGC 5221	3.56	−17.09	− 20.27	40.02	18.1 ± 1.6	61	58.5*
UGC 5423	8.71	−15.62	− 17.74	39.20	22.0 ± 2.2	56	24.8
UGC 5427	7.10	−14.48	− 15.50	38.75	21.3 ± 4.8	55	54.1
UGC 6456	4.34	−14.03	− 15.72	39.23	17.9 ± 1.3	66	15.0
UGC 7047	4.31	−15.07	− 17.42	39.25	15.3 ± 1.5	46	37.5
UGC 7611	9.59	−17.73	− 20.86	40.26	23.1 ± 2.5	77	51.5
UGC 7648	5.80	−16.72	− 18.26	40.01	18.9 ± 1.8	55	78.1*
UGC 7651	5.80	−19.42	− 21.50	40.93	22.8 ± 1.8	47	129.2
UGC 8313	9.20	−15.22	− 17.94	39.58	21.9 ± 2.0	77	45.0
UGC 8508	2.69	−13.09	− 15.58	38.43	13.3 ± 2.4	51	32.6
UGC 8638	4.27	−13.74	− 16.63	38.66	16.1 ± 1.9	49	18.2*
UGC 11425	3.60	−14.32	− 15.57	38.49	14.4 ± 0.0	35	37.1
UGC 11583	5.90	−14.32	− 16.67	38.35	14.6 ± 4.5	90	46.7
UGC 12713	12.20	−15.95	− 16.83	39.45	18.6 ± 2.2	72	44.9*
UGCA 92	3.01	−15.59	− 16.56	39.44	16.5 ± 3.1	56	39.7*
UGCA 292	3.62	−11.79	− 13.56	38.44	11.8 ± 1.7	45	21.9
			XMD subsample				
HS 0822+3542	13.50	−12.90	–	39.24	19.4 ± 0.7	31	12.3
HS 2236+1344	86.40	−17.04	–	41.02	28.0 ± 0.9	35	21.8
SAO 0822+3545	13.50	−13.26	–	37.96	17.9 ± 5.4	63	12.4
SBS 0335-052E	53.80	−16.87	− 18.44	41.02	30.6 ± 1.6	37	28.2
SBS 0335-052W	53.80	−14.68	− 16.12	39.70	20.2 ± 2.7	37	12.4
SBS 1116+517	23.10	−14.73	–	39.97	27.4 ± 1.5	50	10.4
SBS 1159+545	52.20	−14.65	–	40.24	22.9 ± 1.3	66	9.1
SDSS J1044+03	53.80	−16.19	–	40.69	28.7 ± 1.9	51	9.0
UGC 772	16.30	−14.88	–	39.33	22.0 ± 2.9	40	38.5
UGC 993	40.30	−17.72	–	40.55	22.1 ± 2.5	69	48.5
Anon J0125+07	40.30	−16.20	–	39.46	25.0 ± 5.0	64	22.9
			BCDG subsample				
II Zw 40	9.69	−18.29	− 17.89	41.14	32.5 ± 1.2	60	50.5
II Zw 70	19.12	−16.56	− 18.61	40.47	25.7 ± 1.2	76	35.0
III Zw 102	22.71	−19.24	− 22.91	40.85	31.7 ± 2.6	60	108.4
III Zw 107	78.09	−19.53	− 22.04	41.37	41.1 ± 1.4	51	25.1
Mrk 5	13.96	−15.47	− 18.04	39.55	18.0 ± 1.6	48	33.5*
Mrk 33	22.30	−18.28	− 21.31	40.98	37.7 ± 2.4	47	32.6
Mrk 35	15.60	−17.76	− 20.14	40.43	27.7 ± 1.2	27	63.6
Mrk 36	10.43	−14.71	− 16.14	39.91	23.8 ± 1.2	47	18.8
Mrk 297	65.10	−21.16	− 23.49	41.65	36.7 ± 1.7	40	121.8
Mrk 324	22.43	−16.44	− 18.95	39.68	28.8 ± 5.1	38	108.0*
Mrk 370	10.85	−16.83	− 19.51	40.12	24.9 ± 2.0	45	53.5
Mrk 600	12.81	−15.43	− 17.43	39.78	18.7 ± 1.6	59	35.5*

*V_{max} data from HyperLEDA.

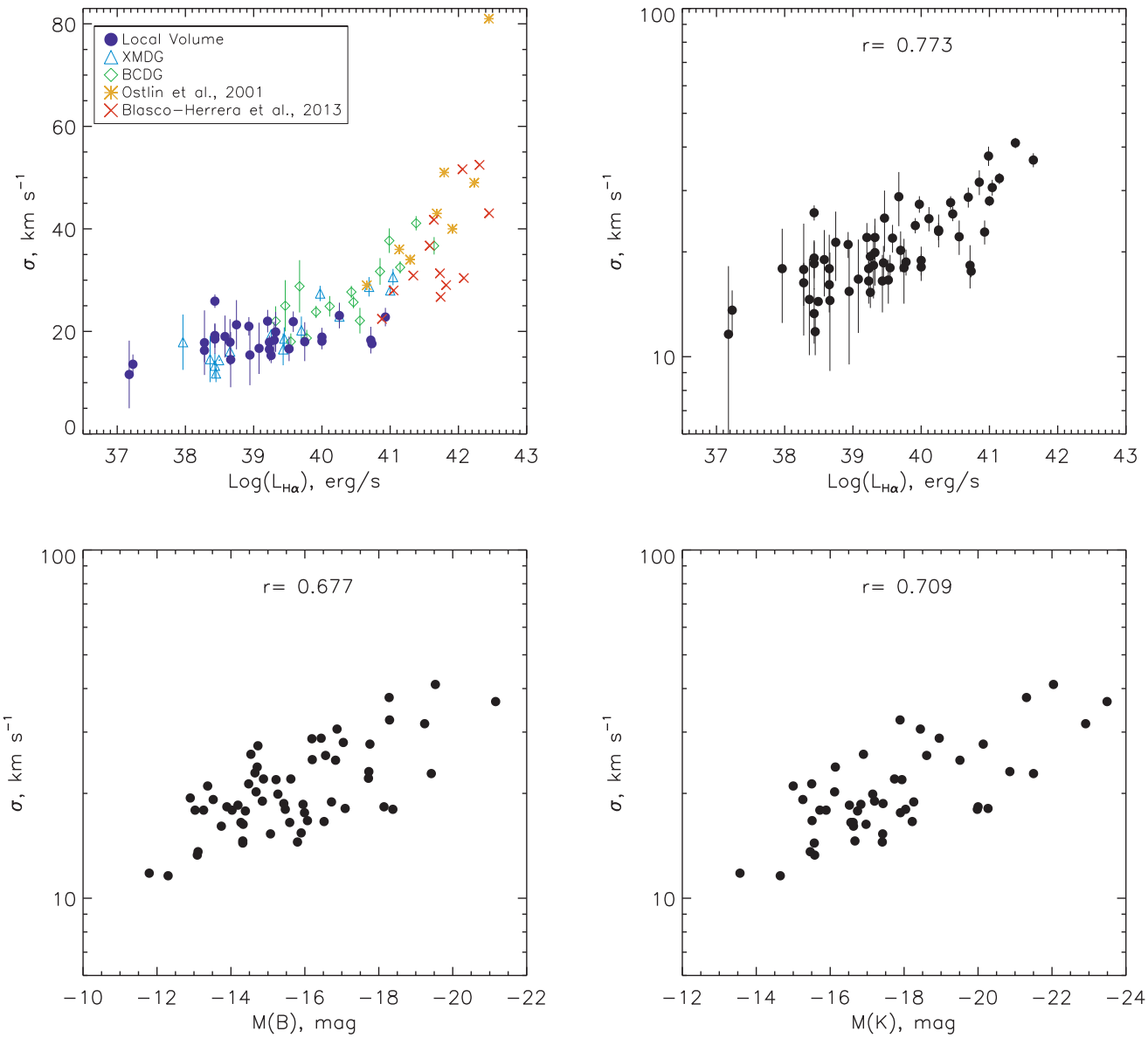

Figure 2. *Top*: the correlation of the average velocity dispersion σ with Hα luminosity. *Left*: linear scale for σ. Colours mark different subsamples and data from the literature. *Right*: the same plot on a logarithmic vertical scale. Only the 6-m telescope data are plotted. *Bottom*: dependence of σ on the absolute *B* (left) and *K* (right) magnitudes. The correlation coefficient is marked in each panel. Error bars are not shown in the bottom panels, to avoid crowding. The velocity σ correlates with the absolute magnitude, but the tightest relation is with the Hα luminosity.

have observed. It is clear that they form a common sequence without any significant systematic offsets. Given that, the galaxies from the LV in general have a lower luminosity than the XMD and BCDG. For completeness, we present the same data for the nine bright BCDGs from Östlin et al. (1999, 2001) and 12 starburst galaxies from Blasco-Herrera et al. (2013), since the measurement technique used by these authors is completely analogous to ours – averaging of the map of Hα velocity dispersion, obtained with a scanning FPI. Their measurements complement our $L_{\rm H\alpha}$–σ sequence in the direction of higher luminosities. Note that, significantly, we have been able to continue the dependence on $L_{\rm H\alpha}$–σ towards dwarf galaxies, up to $L_{\rm H\alpha} \propto 10^{37}$ erg s^{-1}, while the vast majority of articles (Terlevich & Melnick 1981; Bordalo & Telles 2011) consider H II galaxies with $L_{\rm H\alpha} > 10^{39}$ erg s^{-1} (with the exception of articles devoted to various H II regions in the interiors of large galaxies: Arsenault & Roy 1988; Wisnioski et al. 2012, and others). In order not to crowd the figures, further on we will not show subsamples separately, nor depict the error bars.

The upper right panel shows the distribution of $L_{\rm H\alpha}$–σ in a more traditional form, on a logarithmic scale along both axes. It can be clearly seen that the relation between the logarithms of luminosity and dispersion is almost exactly linear with a rather small scatter. This fact was noted in many studies, but, as already mentioned in the Introduction, in the case of giant H II regions it was usually associated with the virial ratio, i.e. by the fact that the ionized gas velocity dispersion is definitely related to the stellar velocity dispersion and is controlled by the total mass of the system. However, the luminosity in the Balmer emission lines is

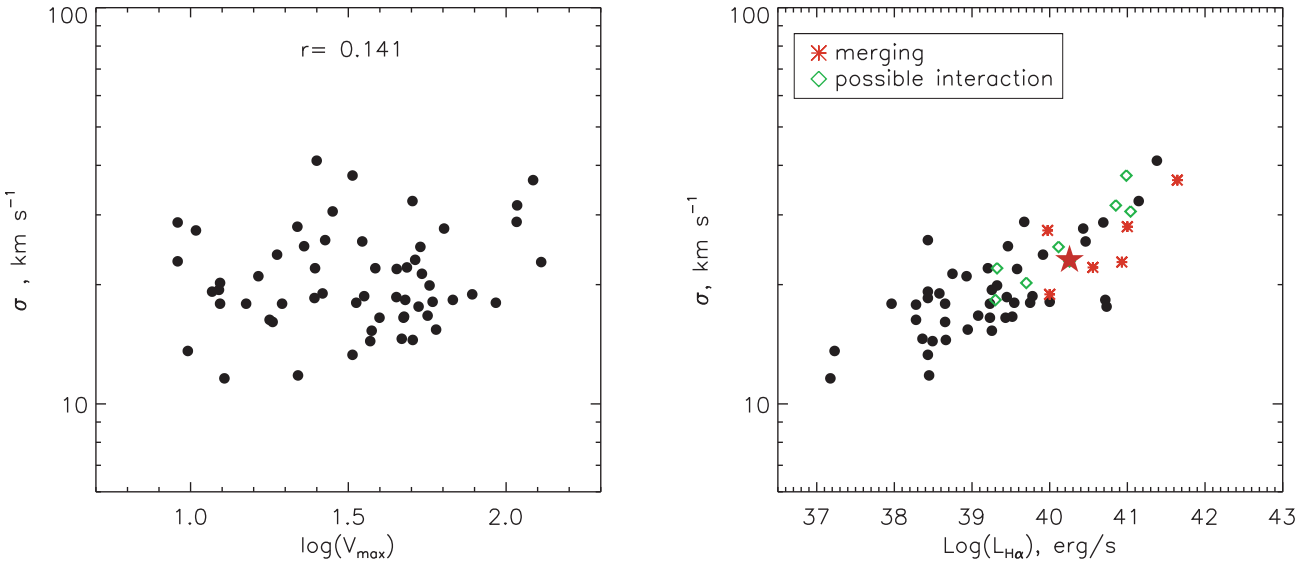

Figure 3. *Left*: dependence of σ on the amplitude of the rotation curve. *Right*: the $L_{H\alpha}$–σ diagram, where the coloured dots mark interacting galaxies. The asterisk shows the superwind galaxy UGC 7611 (NGC 4460).

not a unique function of mass; rather, it is determined by the number of young OB stars (Kennicutt 1998, and references therein). Also, for any reasonable initial stellar mass function, the total stellar mass is determined by more numerous but less massive stars that cannot ionize the surrounding gas. The mass of dark matter also correlates exactly with this stellar mass through the Tully–Fisher relation. If σ is defined by the mass of the system, it should correlate better not with $L_{H\alpha}$ but with the luminosity in broader spectral bands, or other parameters that are directly related to the mass.

However, this is not observed. Fig. 2 shows the L–σ dependence built for M_B. In the optical B band, the older stellar population has a larger contribution compared with the Hα luminosity. However, the point spread here is larger and the correlation coefficient is smaller: $r = 0.68$ versus $r = 0.77$ in the case of of $L_{H\alpha}$. The K-band luminosity is directly related to the total mass of the stellar population of the galaxy; moreover, the effect of interstellar reddening is much smaller here. However, the point spread on the M_K–σ diagram is the same with M_B ($r = 0.71$, Fig. 2 bottom right).

We also use a parameter related to the dynamical mass of the system – the amplitude of the rotation velocity, V_{max}. The left panel in Fig. 3 indicates that ionized gas velocity dispersion does not depend on the amplitude of the rotation velocity V_{max}, with the correlation coefficient being very low ($r = 0.14$). For galaxies with $V_{max} = 10$–50 km s^{-1}, the gas velocity dispersion is remarkably large. On average, $\sigma \approx 20$ km s^{-1}, with substantial galaxy-to-galaxy variations. Green et al. (2010) came to a similar conclusion that σ is not related to the total stellar mass for more distant galaxies with violent star formation.

Another argument against a direct relation of σ and galaxy mass is that a systematic departure from the general trend should be observed for galaxies in the transient unrelaxed state, such as merger and interacting. We also attribute to clear mergers systems such as Mrk 297 (two clearly kinematically decoupled components), UGC 993, HS 2236+1344 and SBS 1116+517, where two rotating discs can be identified in the velocity fields (Moiseev et al. 2010b), and the tight pair UGC 7648/7651 (NGC 4485/4490), distorted by interaction. As 'possible interaction' galaxies, we classify UGC 772, UGC 3672, SBS 0335-052W/E and SBS 1159+545 (see the arguments in Moiseev et al. 2010b) and the galaxies with kinematically decoupled polar components: Mrk 33, Mrk 370 (Moiseev 2011) and IIIZw102 (Moiseev 2008). However, in Fig. 3 all these galaxies follow a general relationship, just like isolated galaxy UGC 7611 (NGC 4460), where the ionized gas is associated with a circumnuclear starburst and galactic wind outflow (Moiseev, Karachentsev & Kaisin 2010a; Moiseev 2014).

The features of the L–σ and V_{max}–σ correlations discussed above suggest that the relation between σ and $L_{H\alpha}$ (i.e. the current SFR) is primary. In this case, the correlations of velocity dispersion with M_B, M_K and the stellar and total mass are secondary, being the consequences of other scaling relations in the galaxies. Indeed, more massive and bright galaxies with ongoing star formation tend, as a rule, to have a greater luminosity in the Balmer lines as well.

3.1 Line width σ in dense and diffuse gas

Tenorio-Tagle et al. (1993) used an analytical model to support the idea that the σ of ionized gas observed in giant star-forming regions and H II galaxies is determined by the mass of these objects. The authors conclude that σ in the regions of greatest brightness ('the kinematic cores of H II regions') is directly related to the mass and size of the star-forming region. At the same time, bright H II regions are surrounded by low-brightness coronae of ionized gas with a larger velocity dispersion. Such structures occur as a result of the influence of young stellar groups on the ISM. However, if the velocity dispersion in the centres of star-forming regions is determined by virial motions, then this value, σ(core), should be better correlated with parameters related to mass (M_B, M_K), rather than with $L_{H\alpha}$, which is controlled by the number of ionizing photons from young massive stars. On the other hand, the average velocity dispersion of a diffuse environment should show a clearer (than on average for the entire galaxy) relation with $L_{H\alpha}$, since not only the number of Lyman quanta but also the kinetic energy output of the winds of young stars and supernovae is directly scaled with the total number of OB stars (see fig. 1 of Dopita 2008), while

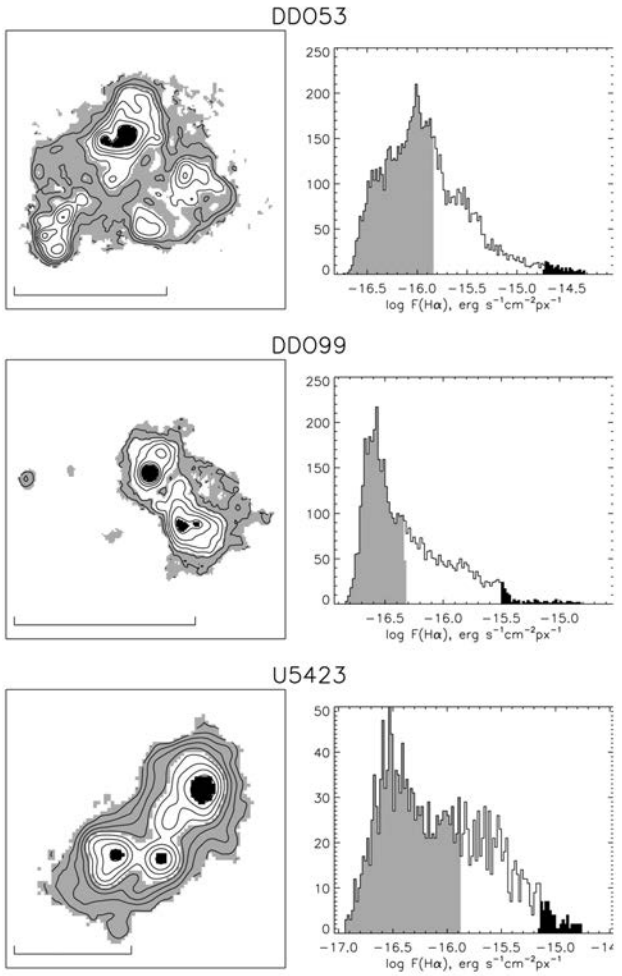

Figure 4. Examples of Hα 'cores' (regions with very large Hα fluxes, dark grey on the maps) and 'diffuse' regions (low fluxes, light grey) in galaxies DDO53, DDO99 and UGC 5423. The isophotes of the Hα images are overlaid. The horizontal bar shows a linear scale of 1 kpc. To the right of each map, we plot a histogram of the surface brightness distribution of the image pixels in Hα. The 'core' and 'diffuse' components are filled with the same shades of grey.

the gas velocity dispersion is proportional to the square root of the kinetic energy of turbulent motions.

We separate the velocity dispersion maps into cores of H II regions and a diffuse component. For that, we use a histogram of the brightness distribution in the Hα emission line for each galaxy. We consider as belonging to 'cores' all pixels that contain the top 20 per cent of the total Hα luminosity, while, likewise, 20 per cent of the total luminosity in low-flux pixels is assigned to the diffuse component. Typical examples of galaxy Hα map separation into two components are shown in Fig. 4, which also presents the corresponding histograms of the intensity of surface brightness in Hα, explaining the method of separation (the bright and faint tail of the distribution of surface brightness). We can see that 'cores' really correspond to the very centres of bright H II regions, while pixels marked as 'diffuse' correspond to the envelopes surrounding regions of star formation.

For each of the components, we calculate the flux-weighted velocity dispersion. Fig. 5 shows the corresponding relations. It is clear that the gas velocity dispersion of the core, σ(core), and diffuse component, σ(diffuse), is very similar. This is also confirmed by the correlation coefficients of the respective luminosities, which are almost the same as or even lower than those for σ of the entire disc.

Therefore, separation into central and diffuse components shows that the velocity dispersion at the centres of H II regions, as well as the diffuse component, is primarily determined by Hα luminosity, i.e. by the number of young massive stars. We have performed this analysis for various 'core/diffuse' separation criteria. The general conclusion is the same as for the 20 per cent criterion described here.

4 GLOBAL L–σ AND SFR–σ RELATIONS

As discussed in the Introduction, the L–σ relation has been extensively studied, mainly for intergalactic and extragalactic H II regions and compact H II galaxies. All the results agree that there is a power-law relation: $L \propto \sigma^{\alpha}$. However, the exponent α measured in different studies varies considerably, from $\alpha = 3.15$ (Roy, Arsenault & Joncas 1986) to 6.6 (Hippelein 1986). For discussion, see also Blasco-Herrera et al. (2010), Bordalo & Telles (2011) and Wisnioski et al. (2012). Recently, Chávez et al. (2014) obtained $\alpha = 4.65 \pm 0.14$ using a large sample of compact H II galaxies restricted by velocity dispersion ($\log \sigma < 1.8$ km s^{-1}) and equivalent width ($EW(\mathrm{H}\beta) > 50$ Å) in order to minimize the contribution of rotation-supported systems and/or objects with a complex emission-line structure. Swinbank et al. (2012) suggested $\alpha = 3.8$, which provides a common fit to both local H II regions and star-forming clumps in high-redshift galaxies. It is possible that the different flux limits used in observations to measure σ for different types of objects (e.g. individual H II regions, dwarf emission galaxies, objects at large redshift) make some contribution to the uncertainty in α. Potential biases due to selecting bright Hα regions in long-slit spectroscopy, compared with full 3D spectroscopy, may also contribute to the disagreement. Indeed, Fig. 5 shows that the velocity width σ(core) in regions with high Hα fluxes is systematically smaller than σ(diffuse) in regions with low fluxes. If one uses spectra that are not deep enough, the measured mean velocity dispersion will be underestimated. Another possible reason for the disagreement is that the slope of the $L(\sigma)$ relation changes with luminosity and with the age of the most recent burst of star formation.

Fig. 6 combines our measurements with results by other authors who used similar techniques to estimate the ionized gas σ, i.e. 3D spectroscopic observations (integral-field or scanning FPI) and calculation of the flux-weighted velocity dispersion for the whole galaxy instead of individual H II regions: 9 blue compact galaxies from Östlin et al. (2001), 11 starburst galaxies selected from the SDSS for $z < 0.03$ (Blasco-Herrera et al. 2013), 65 star-forming disc galaxies at $z \sim 0.1$ (Green et al. 2010) and 57 local luminous and ultraluminous infrared galaxies (U/LIRGs) without evidence of active galactic nuclei (Arribas et al. 2014). The published data on high-redshift systems were not included, because beam smearing of the velocity gradient can produce a bias in the estimate of the velocity dispersion (Davies et al. 2011).

The figure shows that, for a wide range of luminosities $L_{\mathrm{H}\alpha} = 10^{37}$-$10^{43.5}$ erg s^{-1}, there is a tight correlation between $L_{\mathrm{H}\alpha}$ and σ. Using a least-squares fit, we derive the slope $\alpha = 5.0 \pm 0.2$ for the present L–σ relation.[3] This is why a linear approximation of the

[3] Here, σ is considered as an independent variable, in agreement with previous studies, as discussed in Bordalo & Telles (2011). The plots show that there is a sort of kink at $\sim 10^{41}$ erg s^{-1}, corresponding to $\sigma \sim 30$ km s^{-1}.

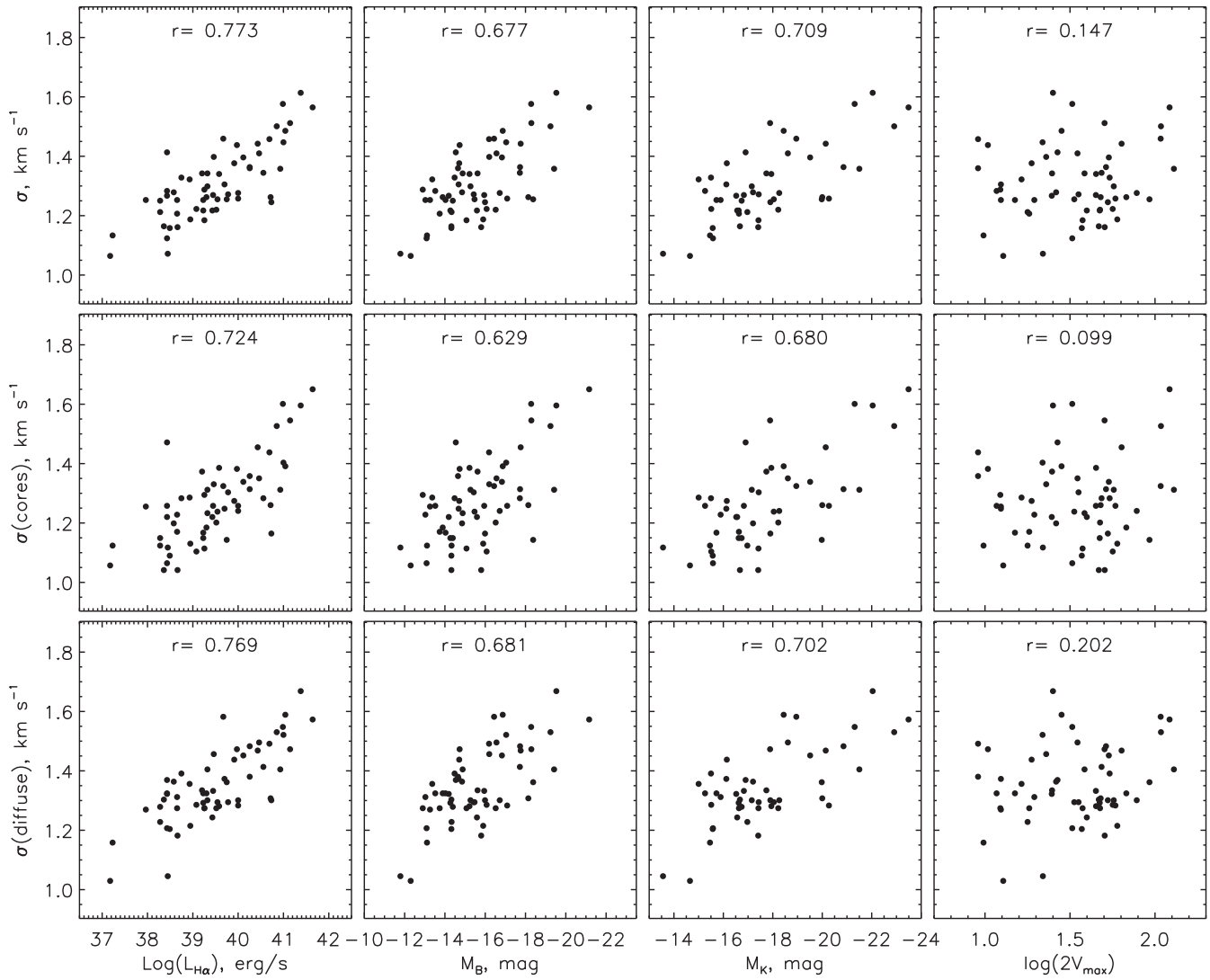

Figure 5. The σ correlations with luminosity in different ranges. Only galaxies observed with the 6-m telescope are shown. *Top*: σ calculated from all pixels of the galaxy image. *Middle*: σ computed only for the cores of star formation regions, where 20 per cent of the total Hα luminosity is concentrated. *Bottom*: the same for the diffuse component (20 per cent of the total Hα luminosity in the low-brightness 'tail' in the surface brightness distribution).

$\log L_{\rm H\alpha}$–$\log\sigma$ relation yields substantially different slopes for large and small luminosities.

Another way of presenting our results is to relate $L_{\rm H\alpha}$ luminosity to the star formation rate SFR. It is known that the $L_{\rm H\alpha}$ luminosity is almost exactly proportional to the rate of ongoing star formation (SFR) of young massive stars (Kennicutt 1998). However, a comparison of SFRs estimated separately from Hα data and *Galaxy Evolution Explorer* (*GALEX*) far-ultraviolet observations shows that for low luminosities this ratio is broken, due to the relative scarcity of massive stars in dwarf galaxies in relation to their initial mass function. Lee et al. (2009) show that SFR$\propto L_{\rm H\alpha}^{0.62}$ for $L_{\rm H\alpha} < 2.5\times10^{39}$ erg s^{-1}.

The right panel of Fig. 6 presents the SFR–σ relation when we use the Lee et al. (2009) conversion equations. The full range of SFR in the objects considered is 0.001–300 $M_\odot$ yr^{-1}. For the U/LIRGs sample, we accepted SFR calculated from the near-infrared (IR) luminosity using an equation from Kennicutt (1998), because of large uncertainties with a reddening correction of $L_{\rm H\alpha}$ in these 'dusty' systems (Arribas et al. 2014). Indeed, the resulting scatter of points corresponding to high σ for SFR seems to be smaller than for Hα luminosities. Note that the combination of the above factors (non-linearity of the SFR–$L_{\rm H\alpha}$ relation for faint dwarf galaxies and IR-based SFR for the most luminous ULIRGs) leads to a linear relation fitted as SFR $\propto\sigma^{5.3\pm0.2}$.

Using their data for the U/LIRGs sample, Arribas et al. (2014) fitted a similar relation of form $\sigma\propto$ SFR$^{0.12\pm0.03}$, which corresponds to the slope $\alpha = 8.3\pm2.1$. This value is significantly larger than our measurements derived for the full sample including both faint and ultraluminous galaxies. Arribas et al. (2014) suggested that the relatively weak dependence of σ on total SFR inferred from their fit is related to the fact that star formation is not a dominant source driving the ionized gas velocity dispersion. Instead, they present arguments in support of a scenario where gravitational energy associated with interaction and mergers has a significant contribution to gas turbulence for SFR $> 10\,M_\odot$ yr^{-1}. However, our results clearly demonstrate the same tendency in SFR–σ for dwarf galaxies with and without interactions as well as U/LIRGs, which appear to have a larger fraction of ongoing mergers. This fact may indicate that the role of interactions in driving ionized gas turbulence in U/LIRGs was overestimated.

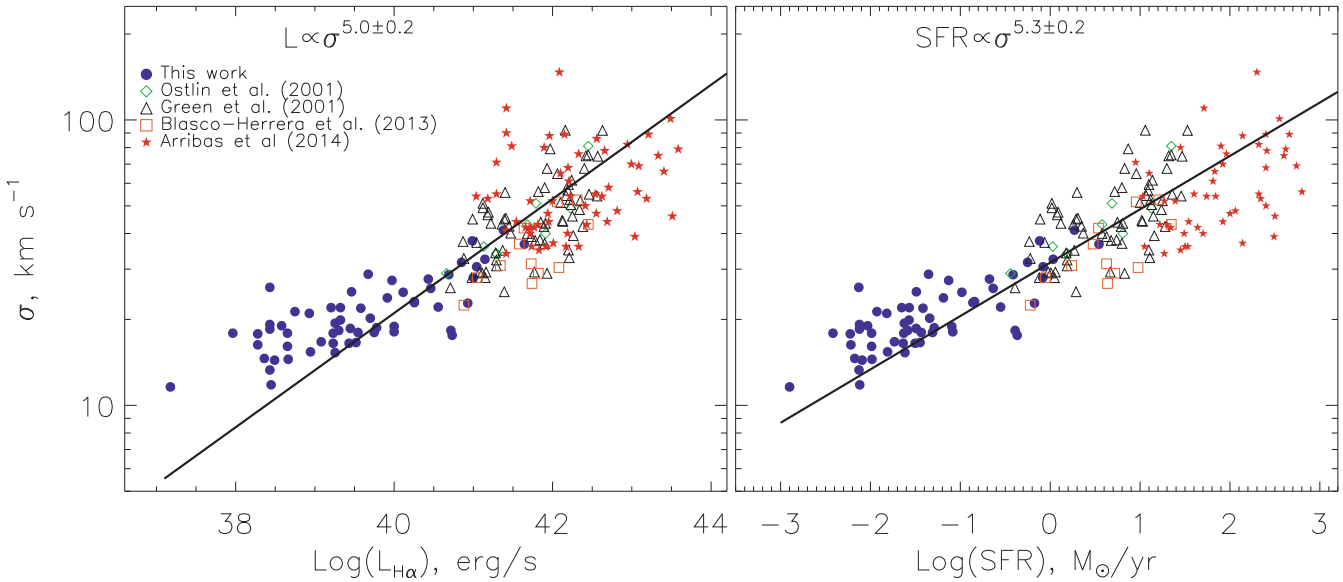

Figure 6. The σ dependence on Hα luminosity (left) and on SFR (right) for different types of galaxies. Black dots (blue in the on-line version) depict the galaxies of our sample, while other colours show the 3D spectroscopic data of other authors for nearby starburst galaxies (see the legend). Black lines show a linear fit of these relationships in different regions.

The other intriguing fact is that the slope of the L–σ relation inferred from our analysis ($\alpha \approx 5.0$–5.3) is near the value $\alpha = 4.7$ obtained by Chávez et al. (2014). On the one hand, Chávez et al. (2014) considered individual giant H II regions and avoided rotation-supported systems. On the other hand, most galaxies presented in Fig. 6 reveal a dominance of circular rotation discs in their kinematics. In previous sections, we presented arguments that ongoing star formation is a dominant driver of σ calculated for the whole galactic disc. Why do galaxies of very different types and luminosities follow a similar L–σ relation to systems where 'the main mechanism of line broadening is linked to the gravitational potential of the young massive cluster' (Chávez et al. 2014)? Note that the range of luminosities in the relation shown in Fig. 6 is twice as large compared with the L–σ for compact H II galaxies considered in previous works.

5 DISCUSSION

Green et al. (2010) show convincingly that over a wide range of galaxy luminosities, including objects at $z = 1$–3, the mean velocity dispersion σ is determined only by the star formation rate (i.e. by the Hα luminosity) and does not correlate with mass. In this case, σ is characteristic of the energy injected into the ISM by stellar winds, supernova explosions and stellar radiation. For the velocity dispersion of neutral gas, a similar conclusion – a weak correlation with galaxy mass – was previously drawn by Dib et al. (2006). Further, analysis of the shape of integrated H I profiles by Stilp et al. (2013) shows that the velocity dispersion of a broad component of the H I line in dwarf galaxies is defined by the SFR/$M_{\rm HI}$ ratio, although a dependence on galaxy mass is also present.

Previously, we found that there is a close relationship between the two-dimensional distributions of the line-of-sight velocity dispersions of ionized gas and the local Hα luminosity (Moiseev & Lozinskaya 2012). Specifically, we found that most of the areas with the highest velocity dispersion belong to diffuse low-brightness gas surrounding star-forming regions. This contradicts the idea that σ is determined mainly by the distribution of mass in a galaxy. In this case, one would have expected a different pattern: a maximum of velocity dispersion at the centre of star-forming regions and σ decreasing with distance from the centre.

In the present article, we discuss different types of correlations of σ with integral parameters of galaxies – the amplitude of the rotation curve and luminosities in different bands. We find that the relationship with the parameters characterizing the mass of the galaxy is considerably less distinct than that with ongoing star formation, determined by the Hα luminosity. Moreover, the current SFR determines the magnitude of supersonic turbulent motions of gas, not only in starburst galaxies but also in objects with a very low SFR, up to $10^{-3}\,{\rm M}_\odot\,{\rm yr}^{-1}$.

We analyse two-dimensional velocity fields of ionized gas using observations at the 6-m BTA telescope. This allows us to measure the mean σ across a galaxy confidently and study the details of its distribution inside and outside star-forming regions. Our new data significantly extend the published L–σ relations to low-mass galaxies and provide observational evidence that star formation determines the velocity dispersion of ionized gas.

(i) The ionized gas velocity dispersion, luminosity-averaged across the galaxy, is better correlated with the luminosity in the Hα line than in the broad B and K bands. There is almost no correlation of the velocity dispersion σ with the rotation velocity of a galaxy.

(ii) The gas velocity dispersion σ in the cores of star-forming regions is nearly the same as σ in the diffuse component for low Hα fluxes.

(iii) There a common SFR–σ relation for local galaxies over a very broad range of luminosities, $L_{\rm H\alpha} = 10^{37}$–$10^{43.5}$, which corresponds to SFR $= 0.001$–$300\,{\rm M}_\odot\,{\rm yr}^{-1}$. The fit of this relation $\sigma \propto {\rm SFR}^\alpha$ provides the slope $\alpha = 5.3 \pm 0.2$.

We therefore conclude that the velocity of turbulent motions of ionized gas in galaxies is defined mainly by the energy that is transferred to the interstellar medium from young stellar populations in

the form of ionizing radiation pressure and by the winds of young stars and supernova explosions. We believe that this conclusion is important for both simulations of galaxy formation and interpretation of the apparent emission-line widths in galaxies affected by various processes (e.g. star formation, merging and virial motions).

ACKNOWLEDGEMENTS

We are very grateful to the anonymous referee and to Santiago Arribas, Eduardo Telles and Roberto Terlevich for their constructive comments and suggestions, which helped us to improve and clarify our results. We also thank Sean Markert for discussions and comments. Our observations were performed with the 6-m telescope of the Special Astrophysical Observatory of the Russian Academy of Sciences. We are grateful to the staff of the Observatory and especially Victor Afanasiev for his great contribution to spectroscopy at the 6-m telescope. The observations were carried out with the financial support of the Ministry of Education and Science of the Russian Federation (agreement No. 14.619.21.0004, project ID RFMEFI61914X0004). We have used the NASA/IPAC Extragalactic Database (NED), which is operated by the Jet Propulsion Laboratory, California Institute of Technology, under contract with the National Aeronautics and Space Administration. We acknowledge the usage of the HyperLeda data base (http://leda.univ-lyon1.fr). This work was supported by the Ministry of Education and Science of the Russian Federation (project 8523) and by the Research Program OFN-17 of the Division of Physics, Russian Academy of Sciences. AM is also grateful for the financial support of the non-profit 'Dynasty' Foundation. AK acknowledges the support of NASA and NSF grants to NMSU.

REFERENCES

Afanasiev V. L., Moiseev A. V., 2005, Astron. Lett., 31, 194
Afanasiev V. L., Moiseev A. V., 2011, Baltic Astron., 20, 486
Arribas S., Colina L., Bellocchi E., Maiolino R., Villar-Martín M., 2014, A&A, 568, A14
Arsenault R., Roy J.-R., 1988, A&A, 201, 199
Blasco-Herrera J. et al., 2010, MNRAS, 407, 2519
Blasco-Herrera J., Fathi K., Östlin G., Font J., Beckman J. E., 2013, MNRAS, 435, 1958
Bordalo V., Telles E., 2011, ApJ, 735, 52
Bordalo V., Plana H., Telles E., 2009, ApJ, 696, 1668
Bournaud F., Chapon D., Teyssier R., 2011, ApJ, 730, 4
Burkert A., 2006, Comptes Rendus Physique, 7, 433
Cairós L. M., Vílchez J. M., González-Pérez J. N., Iglesias-Páramo J., Caon N., 2001, ApJS, 133, 321
Ceverino D., Klypin A., Klimek E. S., Trujillo-Gomez S., Churchill C. W., Primack J., Dekel A., 2014, MNRAS, 442, 1545
Chávez R., Terlevich E., Terlevich R., Plionis M., Bresolin F., Basilakos S., Melnick J., 2012, MNRAS, 425, L56
Chávez R., Terlevich E., Terlevich R., Bresolin F., Melnick J., Plionis M., Basilakos S., 2014, MNRAS, 442, 3565
Chu Y.-H., Kennicutt R. C., Jr, 1994, Ap&SS, 216, 253
Davies R. et al., 2011, ApJ, 741, 69
de Vaucouleurs G., de Vaucouleurs A., Corwin H. G., Buta R. J., Paturel G., Fouque P., 1991, Third Reference Catalogue of Bright Galaxies, Version 3.9. Springer, New York
Dib S., Bell E., Burkert A., 2006, ApJ, 638, 797
Dopita M. A., 2008, in Bresolin F., Crowther P. A., Puls J., eds, IAU Symp. 250, Massive Stars as Cosmic Engines. Cambridge Univ. Press, Cambridge, p. 367
Gallagher J. S., Hunter D. A., 1983, ApJ, 274, 141
Genzel R. et al., 2011, ApJ, 733, 101
Green A. W. et al., 2010, Nat, 467, 684
Hippelein H. H., 1986, A&A, 160, 374
Hopkins P. F., Quataert E., Murray N., 2012, MNRAS, 421, 3488
Joung M. R., Mac Low M.-M., Bryan G. L., 2009, ApJ, 704, 137
Kaisina E. I., Makarov D. I., Karachentsev I. D., Kaisin S. S., 2012, Astrophys. Bull., 67, 115
Karachentsev I. D., Karachentseva V. E., Huchtmeier W. K., Makarov D. I., 2004, AJ, 127, 2031
Kennicutt R. C., Jr, 1998, ARA&A, 36, 189
Kennicutt R. C., Jr, Lee J. C., Funes S. J., José G., Sakai S., Akiyama S., 2008, ApJS, 178, 247
Koulouridis E., Plionis M., Chávez R., Terlevich E., Terlevich R., Bresolin F., Basilakos S., 2013, A&A, 554, 13
Lee J. C. et al., 2009, ApJ, 706, 599
Lopez L. A., Krumholz M. R., Bolatto A. D., Prochaska J. X., Ramirez-Ruiz E., Castro D., 2014, ApJ, 795, 121
Mac Low M.-M., Klessen R. S., 2004, Rev. Mod. Phys., 76, 125
Makarov D., Prugniel P., Terekhova N., Courtois H., Vauglin I., 2014, A&A, 570, A13
Marino A. et al., 2013, MNRAS, 428, 476
Martínez-Delgado I., Tenorio-Tagle G., Muñoz-Tuñón C., Moiseev A. V., Cairós L. M., 2007, AJ, 133, 2892
Melnick J., 1977, ApJ, 213, 15
Melnick J., Moles M., Terlevich R., Garcia-Pelayo J.-M., 1987, MNRAS, 226, 849
Melnick J., Tenorio-Tagle G., Terlevich R., 1999, MNRAS, 302, 677
Melnick J., Terlevich R., Terlevich E., 2000, MNRAS, 311, 629
Moiseev A. V., 2002, Bull. Spec. Astrophys. Obs., 54, 74
Moiseev A. V., 2008, Astrophys. Bull., 63, 201
Moiseev A. V., 2011, EAS Publ. Ser., 48, 115
Moiseev A. V., 2014, Astrophys. Bull., 69, 1
Moiseev A. V., Egorov O. V., 2008, Astrophys. Bull., 63, 181
Moiseev A. V., Lozinskaya T. A., 2012, MNRAS, 423, 1831
Moiseev A. V., Karachentsev I. D., Kaisin S. S., 2010a, MNRAS, 403, 1849
Moiseev A. V., Pustilnik S. A., Kniazev A. Y., 2010b, MNRAS, 405, 2453
Muñoz-Tuñón C., Tenorio-Tagle G., Castañeda H. O., Terlevich R., 1996, AJ, 112, 1636
Östlin G., Amram P., Masegosa J., Bergvall N., Boulesteix J., 1999, A&AS, 137, 419
Östlin G., Amram P., Bergvall N., Masegosa J., Boulesteix J., Márquez I., 2001, A&A, 374, 800
Roy J.-R., Arsenault R., Joncas G., 1986, ApJ, 300, 624
Rozas M., Zurita A., Beckman J. E., Pérez D., 2000, A&AS, 142, 259
Scalo J., Chappell D., 1999, MNRAS, 310, 1
Smith M. G., Weedman D. W., 1970, ApJ 161, 33
Stilp A. M., Dalcanton J. J., Warren S. R., Skillman E., Ott J., Koribalski B., 2013, ApJ, 765, 136
Swinbank M., Smail I., Sobral D., Theuns T., Best Ph . N., Geach J. E., 2012, ApJ, 760, 130
Tenorio-Tagle G., Muñoz-Tuñón C., Cox P. D., 1993, ApJ, 418, 767
Terlevich R., Melnick J., 1981, MNRAS, 195, 839
Trujillo-Gomez S., Klypin A., Primack J., Romanowsky A. J., 2015, MNRAS, 446, 1140
Tully R. B., 1988, Nearby Galaxy Catalog. Cambridge Univ. Press, Cambridge
van Zee L., 2000, AJ, 119, 2757
Vasiliev E. O., Moiseev A. V., Shchekinov Y. A., 2015, Baltic Astron., in press (arXiv:1411.1269)
Voigtlaender P., Bomans D. J., Moiseev A. V., 2015, A&A, submitted
Wisnioski E., Glazebrook K., Blake Ch., Poole G. B., Green A. W., Wyder T., Martin Ch., 2012, MNRAS, 422, 3339

This paper has been typeset from a TEX/LATEX file prepared by the author.

Monthly Notices of the ROYAL ASTRONOMICAL SOCIETY
MNRAS **444,** 376–391 (2014) doi:10.1093/mnras/stu1369

The supergiant shell with triggered star formation in the dwarf irregular galaxy IC 2574: neutral and ionized gas kinematics

O. V. Egorov,[1⋆] T. A. Lozinskaya,[1] A. V. Moiseev[1,2] and G. V. Smirnov-Pinchukov[1]

[1]*Lomonosov Moscow State University, Sternberg Astronomical Institute, Universitetsky pr. 13, Moscow 119991, Russia*
[2]*Special Astrophysical Observatory, Russian Academy of Sciences†, Nizhnii Arkhyz 369167, Russia*

Accepted 2014 July 6. Received 2014 June 1; in original form 2014 April 5

ABSTRACT

We analyse the ionized gas kinematics in the star formation regions of the supergiant shell (SGS) of the IC 2574 galaxy using observations made with the Fabry–Perot interferometer at the 6-m telescope of the Special Astrophysical Observatory of the Russian Academy of Sciences; the data of the H I Nearby Galaxy Survey (THINGS) are used to analyse the neutral gas kinematics in the area. We perform the 'derotation' of the Hα and H I data cubes and show its efficiency in the kinematics analysis. We confirm the SGS expansion velocity of 25 km s^{-1} obtained previously and conclude that the SGS is located at the far side of the galactic disc plane. We determine the expansion velocities, kinematic ages and the required mechanical energy input rates for four star formation complexes in the walls of the SGS; for those remaining, we give the limiting values of the above parameters. A comparison with the age and energy input of the stellar population of the complexes shows that sufficient energy is fed to all H II regions except one. We discuss in detail the possible nature of this region and that of another region, which was believed to be a supernova remnant, according to radio observations. We have measured the expansion velocity of the latter and we can confirm its identification as an old supernova remnant. Our observations have allowed us to identify a faint diffuse Hα emission inside the SGS, which was not been previously observed.

Key words: ISM: bubbles – ISM: kinematics and dynamics – galaxies: individual: IC 2574 – galaxies: star formation.

1 INTRODUCTION

Extensive observations of 1–2 kpc large supergiant shells (SGS) and holes in the H I distribution in galaxies have been performed for a long time (e.g. Warren et al. 2011). Giant holes in some dwarf irregular (dIrr) galaxies represent the dominant feature of the interstellar medium (ISM; see, for example, Young & Lo 1997; Ott et al. 2001; Simpson, Hunter & Knezek 2005; Cannon et al. 2011a; Warren et al. 2011, and references therein). Their origin has been the subject of debate for more than two decades. In the standard approach based on the model of Weaver et al. (1977), H I shells result from the cumulative action of multiple stellar winds and supernova explosions (e.g. McCray & Kafatos 1987; Tenorio-Tagle & Bodenheimer 1988; Ott et al. 2001). However, it was recognized long ago that this scenario cannot explain the origin of giant supershells in which the mechanical energy input from the detected stellar clusters appears to be inconsistent with that required by the standard model (e.g. Tenorio-Tagle & Bodenheimer 1988; Rhode et al. 1999; Kim et al. 1999; Simpson at al. 2005; Silich et al. 2006). Several other mechanisms have been proposed for the formation of the observed H I distribution and kinematics in galaxies: collisions of high-velocity clouds with galactic discs (Tenorio-Tagle 1981), radiation pressure from field stars (Elmegreen & Chiang 1982), nonlinear evolution of self-gravitating turbulent galactic discs (Wada, Spaans & Kim 2000; Dib & Burkert 2005), ram pressure of the intergalactic medium (Bureau & Carignan 2002), fractal ISM (Elmegreen 1997), H I dissolution by ultraviolet (UV) radiation (Vorobyov & Shchekinov 2004) and even exotic mechanisms (see the references in Silich et al. 2006 and Warren et al. 2011).

Recent studies have found that multiple star formation events over the lifetime of the giant hole do provide enough energy to drive the hole formation. The situation has become clear as a result of *Hubble Space Telescope* (*HST*) observations. Weisz et al. (2009a) have shown that the holes in the Holmberg II galaxy contain multiple stellar generations and could indeed be formed from the energy input of these stars. Now it is clear that high star formation rates can be maintained for a much longer time period than previously believed.

⋆ E-mail: egorov@sai.msu.ru
† Note that the system of the Russian Academy of Sciences institutes was liquidated in 2013 September.

© 2014 The Authors
Published by Oxford University Press on behalf of the Royal Astronomical Society

Downloaded from http://mnras.oxfordjournals.org/ by guest on August 17, 2014

Dwarf galaxies are characterized by the ability to sustain a high star formation efficiency over several hundred Myr, and even up to 1000 Myr in some cases (McQuinn et al. 2009, 2010a, 2010b), with local short starbursts occurring during this period. Such long periods of intense star formation provide enough energy from stellar winds and supernova explosions to drive the formation of giant cavities and SGSs (e.g. Weisz et al. 2009a, 2009b; Cannon et al. 2011a, 2011b). Note that a number of SGSs exhibit conspicuous signs of expansion-triggered star formation at their periphery. Of special interest is a detailed analysis of the interaction of stars and gas in the regions of new star formation sites in the walls of giant shell-like H I structures, which can elucidate the process of their evolution.

Dwarf irregular (dIrr) galaxies provide the best environment for studying the creation mechanisms of giant H I structures with star formation episodes on their rims. Because of the slow solid-body rotation and the lack of strong spiral density waves, which can destroy the giant shells, they grow to a larger size and live longer compared to such structures in spiral galaxies. The overall gravitational potential of dwarfs is much smaller than that of spiral galaxies; their H I disc scaleheight is larger and the gas volume density is lower than in spirals. Therefore, the same amount of mechanical energy fed to the ISM of dIrr galaxies creates very large long-lived holes with star formation in the walls triggered by their expansion.

Our aim in this paper is to clarify the effect on supergiant H I shells of new bursts of star formation in their walls. For this purpose, we analyse the recent bursts of star formation in the rims of the well-known SGS in the dIrr galaxy IC 2574, based on the detailed kinematics of both neutral and ionized gas.

The IC 2574 galaxy (which has the alternative names UGC 5666, DDO 81 and VII Zw 330) is a member of the M81 group and is located at a distance $D = 4.02$ Mpc (1 arcsec = 19.5 pc) according to Karachentsev, Makarov & Kaisina (2013); the systemic velocity of IC 2574 is $V_{\rm hel} \simeq 53\,{\rm km\,s^{-1}}$. It hosts a large number of giant H I supershells and holes: 48 holes have been identified by Walter & Brinks (1999) and 27 holes have been identified by Bagetakos et al. (2011); see also Rich et al. (2008). The difference in the total number of holes is a result of the different criteria used to classify a structure as a hole or a supershell.

The SGS surrounding a 1000 × 500 pc hole in the most prominent region of current and recent star formation activity near the north-east outskirts of the IC 2574 galaxy represents an impressive example of a giant H I shell with triggered star formation along the rims (see Figs 1 and 2). It is the best candidate for a detailed study of the interplay between the recent bursts of star formation and the gas in the rims of giant supershells. This elliptical SGS, denoted as 35 in the list of Walter & Brinks (1999), has been extensively studied at radio (Walter et al. 1998; Walter & Brinks 1999), UV (Stewart & Walter 2000), optical (Tomita et al. 1998; Pasquali et al. 2008; Weisz et al. 2009b), mid-infrared (Cannon et al. 2005; Dalcanton et al. 2012) and X-ray wavelengths (see Walter et al. 1998; Yukita & Swartz 2012, and references therein).

An analysis of the resolved stars based on *HST* data (Weisz et al. 2009b) shows that the last most significant episodes of star formation in the SGS began ≃100 Myr ago and that the recent bursts of star formation along its walls are as young as ≤10 Myr. The ages of the younger star formation events are consistent with those derived from broad-band photometry (e.g. Stewart & Walter 2000; Cannon et al. 2005; Pasquali et al. 2008) and are younger than the estimated kinematic age of the H I shell, 14 ± 3 Myr (Walter et al. 1998; Walter & Brinks 1999).

In this paper, we present a new study of the morphology and kinematics of ionized and neutral gas in the SGS. Our analysis is based on observations made with the 6-m telescope of the Special Astrophysical Observatory (SAO) of the Russian Academy of Sciences (RAS). We also use the Very Large Array (VLA) 21-cm observations of H I gas in the galaxy from the H I Nearby Galaxy Survey (THINGS; Walter et al. 2008).

The paper is organized as follows. In Section 2, we describe the observations and data reduction. In Section 3, we present the results of our re-estimation of the SGS expansion velocity from the 21-cm data. In Section 4, we present an analysis of ionized gas kinematics in the star formation regions in the rims of the SGS. In Section 5, we discuss the obtained results. In Section 6, we summarize our main conclusions.

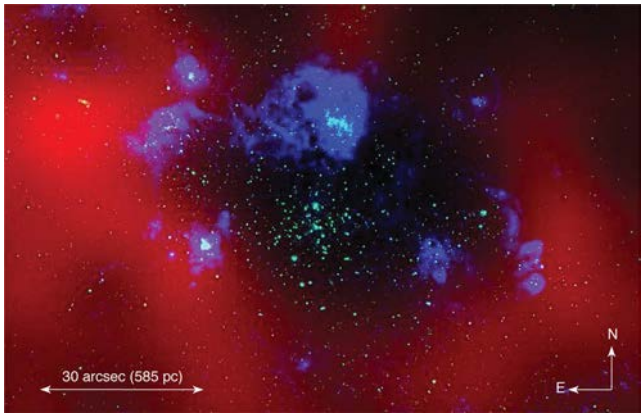

Figure 1. False-colour image of the SGS in IC 2574: red, H I column density map; blue, Hα + [N II] intensity from the *HST*/ACS F658N image; green, continuum from the *HST*/ACS F814W image. The location of the SGS on the IC 2574 H I map is shown in Fig. 2.

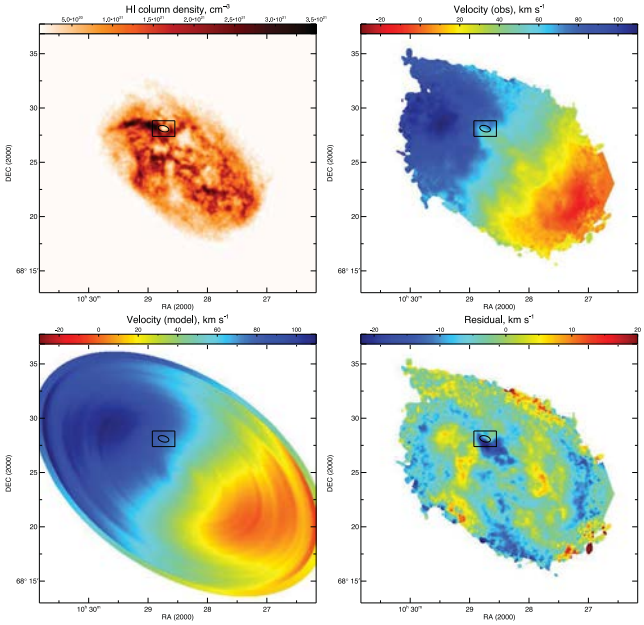

Figure 2. IC 2574 in H I 21-cm: H I column density map (top left), observed line-of-sight velocity map (top right), tilted-ring model of the velocity field (bottom left) and residuals after subtracting this model from the observed H I velocity field (bottom right). The black ellipse denotes the location of the hole inside the SGS and the black rectangle represents the SGS area shown in Fig. 1.

Downloaded from http://mnras.oxfordjournals.org/ by guest on August 17, 2014

2 OBSERVATIONS AND DATA REDUCTION

2.1 Optical Fabry–Perot interferometer observations

The observations were made at the prime focus of the 6-m telescope of the SAO RAS using a scanning Fabry–Perot interferometer (FPI) mounted inside the SCORPIO-2 multimode focal reducer (Afanasiev & Moiseev 2011). The operating spectral range around the Hα emission line was cut by a narrow bandpass filter with a FWHM $\approx$ 14 Å bandwidth. The FPI751 interferometer provides a free spectral range between the neighbouring interference orders $\Delta\lambda = 8.8$ Å, with a spectral resolution (FWHM of the instrumental profile) of about 0.48 Å. During the scanning process, we have consecutively obtained 40 interferograms at different distances between the FPI plates. The log of these observations and the parameters of other data sets are given in Table 1, where $T_{\rm exp}$ is the exposure time, FOV is the field of view, θ is the final angular resolution and $\delta\lambda$ or δv is the final spectral or velocity resolution.

The data reduction was performed using a software package running in the IDL environment. After the initial reduction, sky line subtraction and photometric and seeing corrections made using the reference stars and wavelength calibration, the observational data were combined into data cubes, where each pixel in the FOV contains a 40-channel spectrum. (For a detailed description of the data reduction algorithms and software, see Moiseev 2002 and Moiseev & Egorov 2008.) We observed the galaxy at two position angles in order to remove the parasitic ghost reflection. These data were reduced separately to obtain the wavelength cubes of the object. Both cubes were then co-added.

In order to remove the stellar continuum emission in the constructed data cube and to reveal only the gas emission details, we perform a second-order background fit in each pixel at the edges of the line profiles and subtract it. The analysis of the Hα line profiles was carried out using the multicomponent Voigt fitting (Moiseev & Egorov 2008).

2.2 Narrow-band imaging

The deep optical images in the Hα and [S II] emission lines were taken at the prime focus of the 6-m telescope of the SAO RAS with the SCORPIO-2 multimode focal reducer, using filters FN655 and FN674 with central wavelengths of 6559 and 6733 Å and FWHM of 97 and 60 Å, respectively. While the FWHM of the FN655 filter is broader than the distance between the Hα and [N II] emission lines, the image in this filter is contaminated by [N II] 6548, 6584 Å emission. The image obtained with FN674 represents the emission of the [S II] 6717, 6731 Å lines.

We used the broader-band FN608 and i-SDSS filters centred on the continuum near the two emission lines to subtract the stellar contamination from the images obtained on the same night. Note that the subtraction was not ideal and residuals resulting from the stellar contribution can be seen in our final images in several regions, especially in those taken in the [S II] lines. In order to calibrate the emission-line images to energy fluxes, we observed the standard star AGK+81d266 immediately after observing the galaxy.

2.3 Other observational data

In order to study the H I gas kinematics in the SGS, we analysed archival H I 21-cm line THINGS VLA data (Walter et al. 2008). In this work, we used the natural-weighted data cube (see the parameters in Table 1).

We performed long-slit spectroscopy of the H II regions in IC 2574 with the 6-m telescope of the SAO RAS and the SCORPIO focal reducer (Afanasiev & Moiseev 2005). An analysis of these data will be presented in our forthcoming work (Egorov et al., in preparation); here, we use the data obtained with one slit position to analyse the I([S II])/I(Hα) ratio distribution in H II Region 7 (see Section 5.1).

To study the ionized gas morphology in the SGS region, we used the archival *HST* Advanced Camera for Survey (ACS) images in the F658N filter (which contains the Hα + [N II] emission lines) and the F814W filter presented by Weisz et al. (2008, 2009b).

2.4 Construction of a circular rotation model

The structure and kinematics of gas in the region around the SGS are very complex. Therefore, it would be useful to exclude the regular component associated with the rotation of the galaxy in order to understand the SGS local kinematics. We construct a rotation model of IC 2574 from the H I velocity field (moment 1) using the tilted-ring approximation adapted to dwarf galaxy kinematics (Moiseev 2014). The coordinates of the dynamical centre, the inclination and the initial value of the major axis position angle were adapted from Oh et al. (2008), who performed a careful study of the H I kinematics of this galaxy. The model takes into account the radial variation of the position angle of the kinematic major axis in order to describe the large-scale non-circular streaming motions associated with the bar and two-armed spiral structure. The final model is based only on the data for the regions whose velocity does not deviate significantly from the initial model based on the entire field. Fig. 2 shows the model velocity map as well as the observed velocity field, the residual velocities and the H I column density map.

We correlated the observed data cubes as follows. The velocity of each spectral channel in each pixel was modified by the value of the radial velocity at a given location in the galaxy taken from the rotation model. A new velocity grid (common for all pixels) was then constructed with the same velocity sampling. The spectrum from each spatial element was then interpolated ('derotated') to the new

Table 1. Properties of the observational data.

Data set	Date of obs.	$T_{\rm exp}$	FOV	Arcsec px^{-1}	θ (arcsec)	Sp. range	$\delta\lambda$ or δv
Scanning FPI	2012 Oct 17/18	40 × 120 s	6.1′ × 6.1′	0.71	2.1	8.8 Å around Hα	0.48 Å (21 km s^{-1})
	2012 Oct 18/19	40 × 120 s					
THINGS H I	1992 Sep 03	14 h	25.6′ × 25.6′	1.5	12.8 × 11.9	261 km s^{-1} around 21 cm	2.6 km s^{-1}
FN655 image	2013 Mar 07/08	1800 s	6.1′ × 6.1′	0.36	2.0	Hα + [N II]	
FN674 image	2013 Mar 07/08	3000 s	6.1′ × 6.1′	0.36	2.0	[S II]	
Long-slit	2012 Nov 19/20	3600 s	6.1′ × 1.0″	0.35	1.7	5800–7400 Å	5.5 Å
F658N image	2008 Jan 06	1200 s	3.4′ × 3.4	0.05	0.09	Hα + [N II]	
F814W image	2008 Jan 06	6400 s	3.4′ × 3.4	0.05	0.10	Continuum	

Downloaded from http://mnras.oxfordjournals.org/ by guest on August 17, 2014

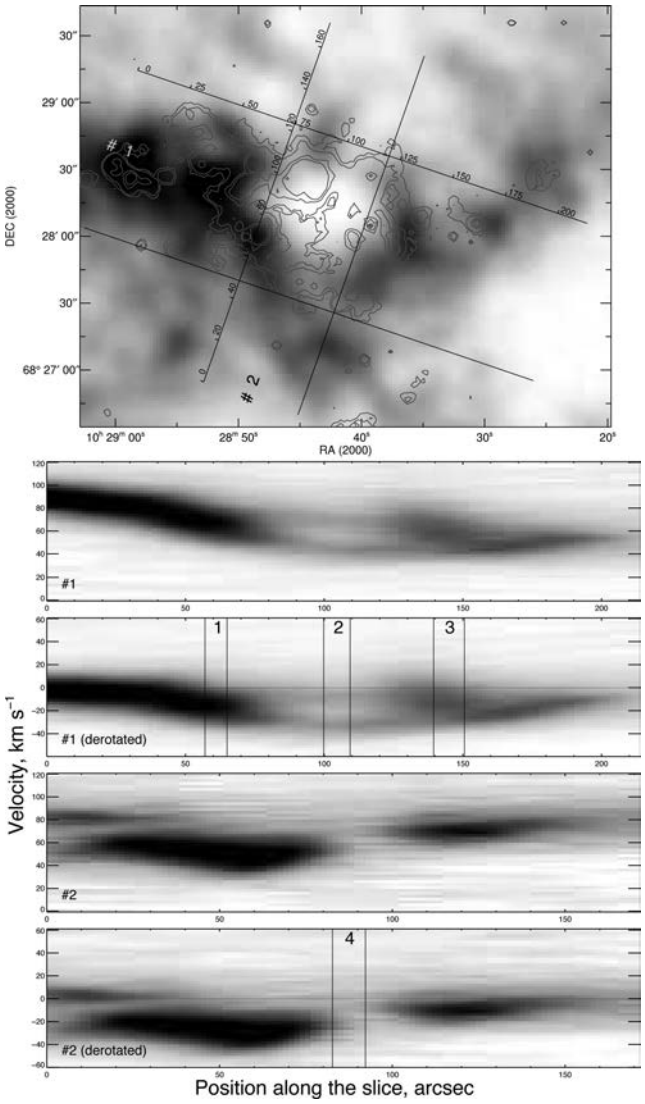

Figure 3. Location of the wide PV diagrams on the H I map of the SGS. The contours correspond to the Hα emission intensity levels of [0.5, 1.0, 5, 10] $\times$ 10^{-16} erg s^{-1} cm^{-2} (top panel). Below this image, the corresponding H I 21-cm line PV diagrams are shown, both uncorrected and corrected (derotated) for the rotation of the galaxy. The vertical lines on the PV diagrams indicate the location of the profiles shown in Fig. 4.

velocity grid and a new data cube was constructed. This procedure was carried out for the H I 21-cm and Hα line data cubes presented below. To demonstrate the result of this correction, we show two position–velocity (PV) diagrams along and across the SGS in Fig. 3, where the corrected PV diagrams are denoted as derotated. The effect of derotation is most clearly seen in PV diagram #1 because it crosses the SGS in the direction of a significant line-of-sight velocity gradient. Considering the relatively large size of the investigated area and hence a possible large contribution of galactic rotation to the PV diagrams, the derotation allowed us to eliminate the effect of the disc rotation and to emphasize the local kinematics.

3 GLOBAL GAS KINEMATICS OF THE SGS

Two reasons prompted us to re-estimate the expansion velocity $v_{\rm exp}$ of the H I SGS. First, Walter & Brinks (1999) measured $v_{\rm exp}$ = 25 km s^{-1} (see also Walter et al. 1998). However, Weisz

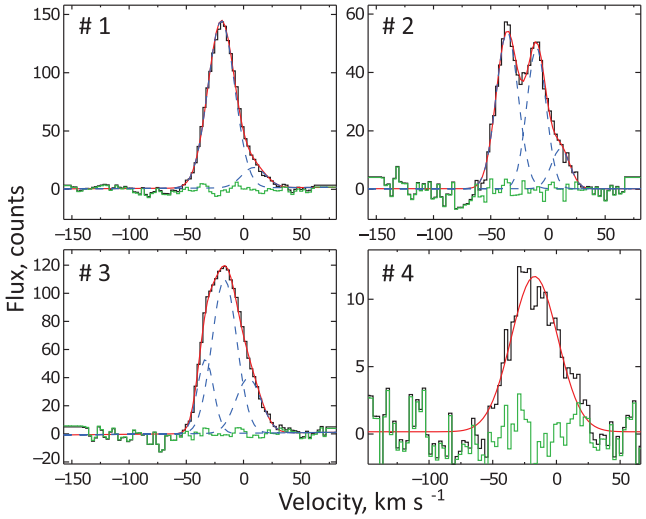

Figure 4. H I 21-cm line profiles and their Gaussian decomposition. The locations of these profiles are shown in the PV diagrams of Fig. 3. The black solid line denotes the observed data, the red solid line denotes the fitted profile, the blue dashed line denotes single Gaussian components and the green line denotes the residuals.

et al. (2009b) have pointed out that: 'Walter & Brinks (1999) measure an H I expansion velocity of 25 km s^{-1} from a break in the PV diagram, which is only an indirect measure of expansion, and in fact is consistent with stalled expansion as well.' Secondly, the neighbourhood of the SGS is a dynamically very complex region of the galaxy in the 21-cm line, making it difficult to distinguish the effect of SGS expansion.

We created two wide PV diagrams along the SGS major and minor axes (with full widths of 75 and 45 arcsec, respectively). Fig. 3 shows the location of these wide scans and the corresponding PV diagrams. A clear 'velocity ellipse' corresponding to the emission of the approaching and receding sides of the shell is seen in the derotated PV diagram 1 in Fig. 3.

To provide an accurate estimate of the expansion velocity of neutral gas in the entire SGS region, we made a Gaussian decomposition of the H I 21-cm line profile at several positions along the PV diagram. These positions are shown in Fig. 3, and the corresponding line profiles are shown in Fig. 4. All profiles show a complex structure and can be decomposed into two or three components. The maximum velocity difference between the components is observed in line profile 2 from the entire SGS region. This difference is 48 $\pm$ 4 km s^{-1}, implying that the expansion velocity[1] in this area is about 24 $\pm$ 2 km s^{-1}. Profile 4, constructed for the SGS region at the position shown in the bottom PV diagram in Fig. 3, is not separated into components, but its FWHM is the same as for profile 2. All these results confirm the value $v_{\rm exp}$ = 25 km s^{-1} estimated by Walter & Brinks (1999).

The vicinity of the SGS is a place where several contacting and, possibly, interacting shells are located. It is the only region showing significant deviations of the line-of-sight velocity field from the fitted circular rotation model (see the bottom-right panel in Fig. 2). If these peculiar velocities occur in the disc plane, they should represent the inflow of gas into the large-scale stellar bar, because in the case of a normal trailing spiral, the south-east half of the

[1] Hereafter, we give the formal uncertainties of the expansion velocity measurements obtained by fitting synthetic spectra with the same signal-to-noise ratio as the observed spectra.

Downloaded from http://mnras.oxfordjournals.org/ by guest on August 17, 2014

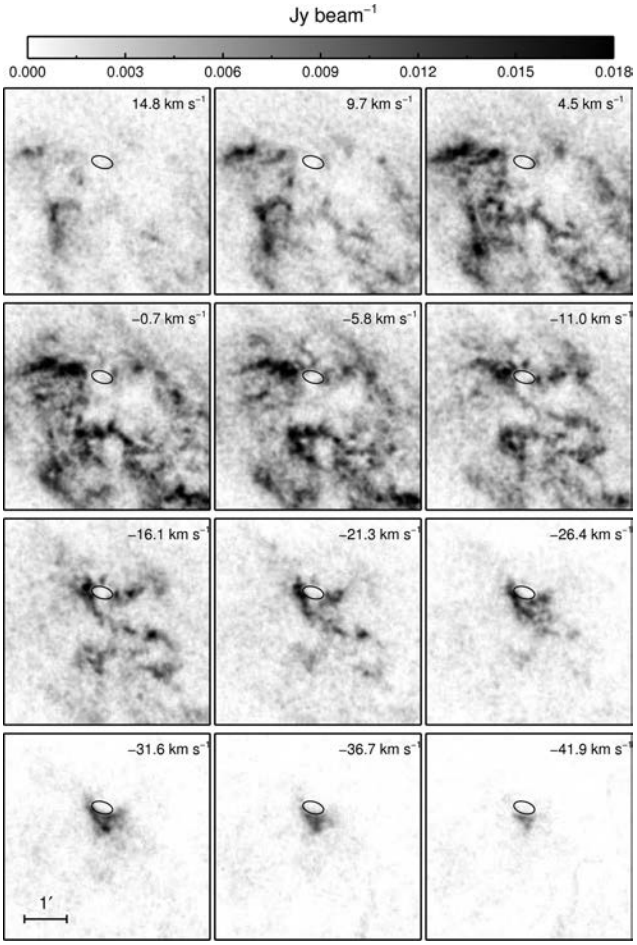

Figure 5. Channel map of the SGS region in the derotated H I data cube. The velocity of each channel is shown in the top-right corner of the panel. The black ellipse indicates the position of the hole inside the SGS.

galaxy's disc is nearest to the observer. An alternative explanation of the observed kinematics is their attribution to vertical gas motions, caused, for example, by the fall of an H I gas cloud, or vice versa, by SGS expansion. The channel map of the derotated data cube (Fig. 5) reveals that these negative residual velocities are related to the high-velocity (-25 to $-45\,\mathrm{km\,s^{-1}}$) H I cloud, which moves towards us and is located south of and adjacent to the SGS. It is the only place in the galaxy that emits in the H I 21-cm line at such high negative velocities. At smaller velocities, the channel map shows a pattern typical of expanding shells: the bright approaching south-eastern part of the SGS can be seen mostly at negative velocities, whereas the faint receding north-western part shows up at positive velocities. Note that the SGS has a non-uniform structure, which is very different from the regular elliptical shape that most authors use to describe the central hole. The observed elliptical shape of the SGS is a result of the inclination of the galaxy, $i = 53^{\circ}$ (Oh et al. 2008). In the first approximation, the shell has a round shape if seen in the plane of the galaxy. Because of the non-uniform structure and kinematics of neutral gas in the extended north-eastern region of the galaxy, we decided to analyse the H I kinematics in the region in more detail. For this aim, we created 18 PV diagrams along the SGS major axis, each with a width of 7.5 arcsec; they cover a $3.2 \times 2.3\,\mathrm{arcmin^2}$ area around the SGS. Their location is shown in the top panel of Fig. 6; the bottom panels show the most interesting PV diagrams. The approaching side of the shell shows

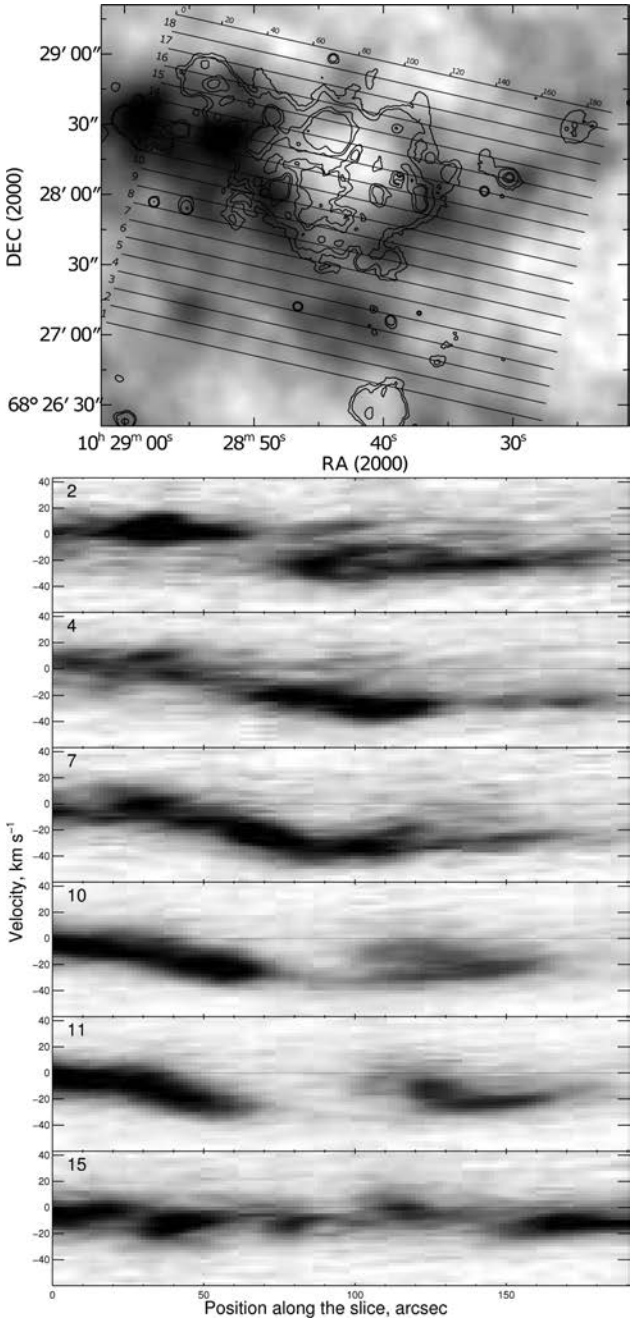

Figure 6. Location of the PV diagrams on the H I map of the SGS. The contours correspond to the Hα emission intensity levels of [0.5, 1.0, 5, 10] $\times\ 10^{-16}$ erg s^{-1} cm^{-2}. Selected PV diagrams are shown in the bottom panels.

up conspicuously in these diagrams, whereas the contribution of the receding side to the neutral hydrogen emission is barely discernible. This might be because the density of the ambient gas at the receding side of the SGS is lower than at the approaching side. Hence, the SGS must reside at the far side of the galactic disc.

4 IONIZED GAS KINEMATICS IN STAR FORMATION REGIONS

The rims of SGS contain numerous groups of triggered star formation that are observed as H II complexes. The Hα image of the region obtained with *HST*/ACS is shown in Fig. 7. The complexes of star

Downloaded from http://mnras.oxfordjournals.org/ by guest on August 17, 2014

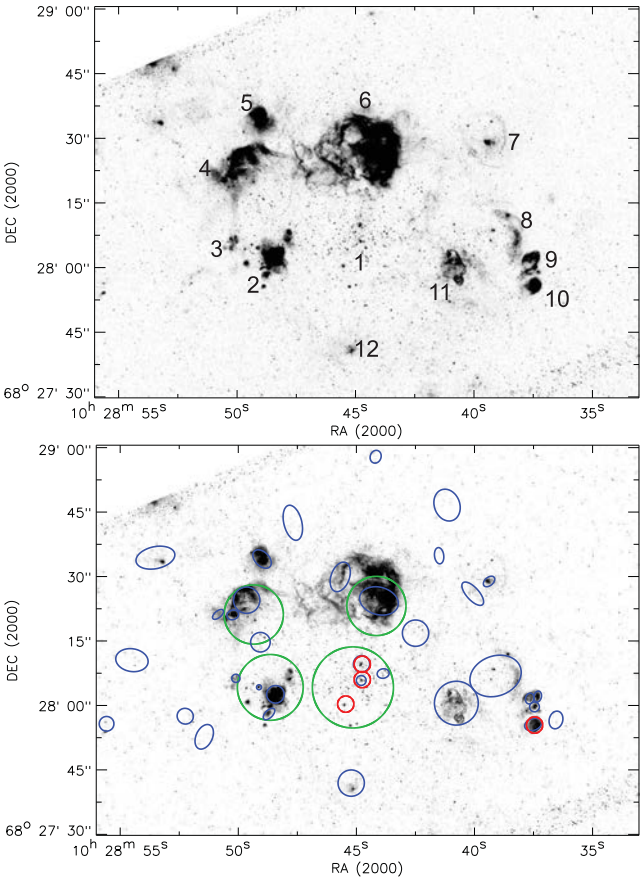

Figure 7. The top panel shows the identification of giant H II regions on the *HST*/ACS F658N image of the SGS area, according to the list of Stewart & Walter (2000). The bottom panel shows the location of the star clusters on the same image. The clusters identified by Pellerin et al. (2012) are shown in blue. The red circles denote the clusters from Cook et al. (2012). The four largest green circles show the star clusters identified by Yukita & Swartz (2012).

formation are denoted by numbers according to their identification in Stewart & Walter (2000). Note that these authors called the region of far-ultraviolet (FUV) emission around the central star cluster inside the SGS 'Region 1'. They noticed the absence of Hα emission in this region. We detected faint extended Hα emission inside the interior of the SGS. Therefore, we have designated as Region 1 not only the area near the central cluster, but also the entire interior of the SGS.

To study the nature of the H II complexes in the wall of the SGS, we evaluated their expansion velocities. Given the size R_s and expansion velocity v_{exp} of the H II shell, we can estimate its kinematic age t and the energy input rate L_w needed for its formation, using the relations that describe the evolution of the supershell driven by supernovae and stellar wind (Mac Low & McCray 1988):

$$R_s(t) = \left(\frac{125 L_w}{154\pi\rho_0}\right)^{1/5} t^{3/5} = 67 \left(\frac{L_{38}}{n_0}\right)^{1/5} t_6^{3/5} \text{ pc} \quad (1)$$

$$v_{exp}(t) = \frac{0.6 R_s}{t} = 39.4 \left(\frac{L_{38}}{n_0}\right)^{1/5} t_6^{-2/5} \text{ km s}^{-1}. \quad (2)$$

Here, $L_{38} = L_w/10^{38}$ erg s^{-1}, $t_6 = t/10^6$ yr and n_0 is the ambient gas volume density (in our case, the ambient H I density $n_{H\,I}$). According to Walter et al. (1998), the mean value in the SGS is $n_{H\,I} = 2$–3 cm^{-3}.

The density distribution in the SGS walls is highly non-uniform and therefore, for our analysis of H II complexes, we estimate the local unperturbed H I density in their neighbourhood. We use two methods to convert the observed H I surface density into H I volume density.

The first method consists of the use of the relation between the column density $N_{H\,I}$ and the volume density $n_{H\,I}$,

$$N_{H\,I} = \int_{-\infty}^{+\infty} n_{H\,I} \exp\left(\frac{-z^2}{2h^2}\right) dz = \sqrt{2\pi} h n_{H\,I}, \quad (3)$$

where we adopt the scaleheight of the H I disc of the galaxy $h = 350$ pc (Walter & Brinks 1999). The inclination of the galactic disc increases the scaleheight along the line of sight as $h/\cos i$. We adopted $i = 53^\circ$ from Oh et al. (2008). Note that this method might underestimate the density, because the line-of-sight H I distribution is non-uniform and can be dominated by the contribution of small dense clouds.

The second method is a modification of the method suggested by Walter & Brinks (1999), who defined areas with an effective radius r_{eff} around each of the H II regions and assumed that H I emission comes mostly from the volume of the sphere of radius r_{eff}. We believe that it is more correct to compute the volume where the H I emission emerges as the area of the cloud in the SGS wall multiplied by the wall thickness. We assume a uniform gas distribution and we assume that the size of the gas layer in the wall is the same along the line of sight and in the sky plane. We found this size to be equal to 360 pc, based on an analysis of several H I clouds in the southern and western parts of the SGS. Unlike the first method, this method might overestimate the volume density H I, because it does not take into account the fact that H I emission is integrated along the line of sight outside the volume considered.

The volume density estimates H I obtained for all the H II regions studied are listed in Table 2. The densities obtained using the first and second methods are marked by [1] and [2] in columns (5) and (6), respectively. The densities obtained by Walter & Brinks (1999) are given in parentheses.

The other columns of Table 2 give the following: column (1), the number of the complex according to Stewart & Walter (2000) (shown in Fig. 7) and Yukita & Swartz (2012) (in parentheses); column (2), the size estimated from the *HST*/ACS F658N image; column (3), v_{exp} obtained from our ionized gas kinematics analysis; column (4), the kinematic age calculated from equation (2); column (7), the kinetic energy input rate required to drive the formation of the complex computed from its size and expansion velocity; column (8), the age of the complex reported by Stewart & Walter (2000) and Yukita & Swartz (2012) (in parentheses); column (9), the kinetic energy input rate provided by the stellar population of the complex according to the estimates of Stewart & Walter (2000) and Yukita & Swartz (2012) (in parentheses).

To reveal the effect of the expansion of H II complexes using the data of FPI observations in the Hα line, we covered each of the H II regions in the SGS walls by a series of PV diagrams. We use these, together with the results of multicomponent fitting of Hα line profiles, to estimate v_{exp}, kinematic age t and the required energy input rate L_{38}. In this way, we measure the expansion velocities for four star formation complexes in the SGS and the upper limits of v_{exp} for the other regions. As an example of our analysis, we discuss in detail the largest region, Region 6. Fig. 8 shows the Hα PV diagrams and their locations for this region. To avoid overloading the figures, for the other H II complexes (except for the special case of Region 11), we have marked in Fig. 9 the locations of the most distinctive PV diagrams shown in Fig. 10. Examples of Hα line profiles from

Downloaded from http://mnras.oxfordjournals.org/ by guest on August 17, 2014

Table 2. Parameters of the star-forming regions.

Region no. SW[b] (YS[c]) (1)	Size (pc) *HST*[d] (2)	v_{exp} [a] (km s^{-1}) FPI[e] (3)	t (Myr) FPI (4)	$n_{H\,I}$ (cm^{-3}) [1] (5)	[2] (6)	L_{38} (10^{38} erg s^{-1}) FPI (7)	Age (Myr) SW (YS) (8)	E/Age (10^{38} erg s^{-1}) SW (YS) (9)
1 (C2)	800[f]	25[f]	9.6[f]	0.05	0.3	0.5 − 2.7[f]	8.5 (17)	1.50 (29)
2 (C3)	90 × 150	≤19	≥1.9	0.63	2.6 (2.93)	≤(0.05 − 0.23)	3.5 (17)	0.80 (16)
3	80 × 55	≤18	≥1.1	0.70	3.0 (2.93)	≤(0.02 − 0.06)	4.0	0.24
4 (C4)	150 × 250	27	2.4	0.56	2.5 (2.7)	0.5 − 2.2	4.2 (7)	0.90 (4.7)
5	65 × 95	≤18	≥1.5	0.53	2.0 (2.7)	≤(0.02 − 0.09)	3.5	0.22
6 (C1)	450 × 320	30	4.0	0.20	0.9 (1.03)	0.8 − 3.5	4.1 (7)	2.40 (27)
7	210	65	1.0	0.23	0.9 (3.02)	2.5–9.9	4.2	0.11
8	260	45	1.7	0.33	1.5 (2.54)	1.9 − 8.4	4.5	0.23
9	90	≤20	≥1.3	0.55	2.3 (2.54)	≤(0.03 − 0.14)	3.4	0.04
10	65	≤20	≥1.0	0.55	2.0 (2.54)	≤(0.02 − 0.06)	3.4	0.03
11 SNR	110 × 175	70–80	0.3[g]	0.20	0.8 (3.52)	See text	4.3	0.32
12	40	≤20	≥0.6	0.40	1.5 (2.75)	≤(0.005 − 0.017)	4.1	0.07

Notes: [a]The typical uncertainty of v_{exp} is 2 km s^{-1}. [b] SW denotes data derived by Stewart & Walter (2000). [c] YS denotes results obtained by Yukita & Swartz (2012) for complexes C1, C2, C3 and C4 (in parentheses). [d] *HST* means that the results are estimated based on the *HST*/ACS F658N image. [e] FPI denotes data obtained from our FPI observations in the Hα line. [f] Estimates based on the H I data. [g] Data obtained using the Sedov (1946) solution for the SNR (see Section 4.3).

all regions and the results of their Voigt decomposition are shown in Fig. 11.

4.1 H II complexes with measured expansion velocities

Region 6 (C1)

The star-forming complex 6 (C1) – an extended (∼450 × 320 pc) fine-filamentary H II region – is located in the northern wall of the SGS. Yukita & Swartz (2012) identified the young star cluster C1 inside Region 6. The C1 cluster includes PI 13z from the list of Pellerin et al. (2012); cluster PI 07c is located in the eastern part of the region (Fig. 7). Drissen, Roy & Moffat (1993) found three Wolf–Rayet (WR) star candidates in Region 6.

The PV diagrams (Fig. 8) reveal several expanding shell-like structures inside the complex. In the brightest western part of the complex, the profile does not resolve into two components, but has a large FWHM of up to 70 km s^{-1} compared to FWHM = 45–55 km s^{-1} in the neighbouring positions. The expansion effect shows up conspicuously east of this bright region in the fainter filamentary part of the complex (see the positions from 7 to 20 arcsec in Fig. 8). The corresponding profiles (6-1, 6-3 and 6-5 in Fig. 11) can be fitted confidently by two components. The distance between the components is about 60 km s^{-1}, while their FWHM is 45–50 km s^{-1}. These data yield a characteristic expansion velocity of $v_{exp} \simeq 30$ km s^{-1} for Region 6 (C1).

The eastern shell-like structure, which appears at 0–7 arcsec in the PV diagrams 7–12 of Fig. 8, is probably not a part of Region 6 but belongs to Region 4, and the interaction of these two structures produces the faint details in the Hα line profile 6-2 in Fig. 11.

The average radius $R_s \simeq 200$ pc combined with $v_{exp} = 30$ km s^{-1} yields $t = 4$ Myr and $L_{38}/n_{H\,I} \simeq 3.9$ according to relations (1) and (2).

We estimate the ambient gas volume density H I for Region 6 to be 0.2 and 0.9 cm^{-3} using the first and second methods, respectively. The corresponding energy input rates are 0.8 × 10^{38} and 3.5 × 10^{38} erg s^{-1}.

Yukita & Swartz (2012) determined the age $t = 7$ Myr and the current mechanical energy produced by the central star cluster C1, $L_w \simeq 27 \times 10^{38}$ erg s^{-1}; according to Stewart & Walter (2000), the age of the cluster is 4.1 Myr and the mechanical energy input rate is $L_w \simeq 2.5 \times 10^{38}$ erg s^{-1} (see Table 2). As is evident from the above, this energy is definitely sufficient to drive the formation of the shell-like complex, given the inferred expansion velocity.

Region 4

This region has the form of a bright 'half-shell' whose eastern part adjoins the dense wall of the SGS (see Fig. 1), with a fainter filamentary inner part. The full size of the region is about 250 × 150 pc, and the accepted characteristic radius is $R_s = 110$ pc. The faint filaments in the north-west extend out to the faint eastern filaments of Region 6. This region hosts the clusters PI 21z, 22z and 23z (see Fig. 7). In the PV diagrams (Fig. 10), the intensity of the line decreases and its width increases in the direction from the bright edge of the half-shell towards its inner parts. The characteristic velocity of the region is about −15 km s^{-1}. Inside the region, the line profiles (Fig. 11) reveal a two-component structure with the peak velocities equal to 25 and −30 km s^{-1}, respectively, implying an expansion velocity of $v_{exp} \simeq 27$ km s^{-1}.

Region 7

This region has a well-defined structure of a thin ring with a diameter of 210 pc surrounding the cluster PI 01b, with the cluster P3 01d located in the south-eastern part of the ring. Inside the ring, there is a small (∼40 pc) bright emission region coincident with the cluster.

The PV diagrams and the line profiles show a well-defined three-component structure in the ring nebula. The peak velocities of the components are equal to −80, 0 and 50 km s^{-1}. The FWHM of the shifted components is equal to about 60 km s^{-1} and that of the central component is equal to 45 km s^{-1}, which corresponds to the half-width of the single line observed outside the ring (see profile 'diff-2' in Fig. 11). This leads us to conclude that the central component is associated with the emission of the background gas in this region, and that the shifted components are associated with the approaching and receding sides of the expanding shell. The

Downloaded from http://mnras.oxfordjournals.org/ by guest on August 17, 2014

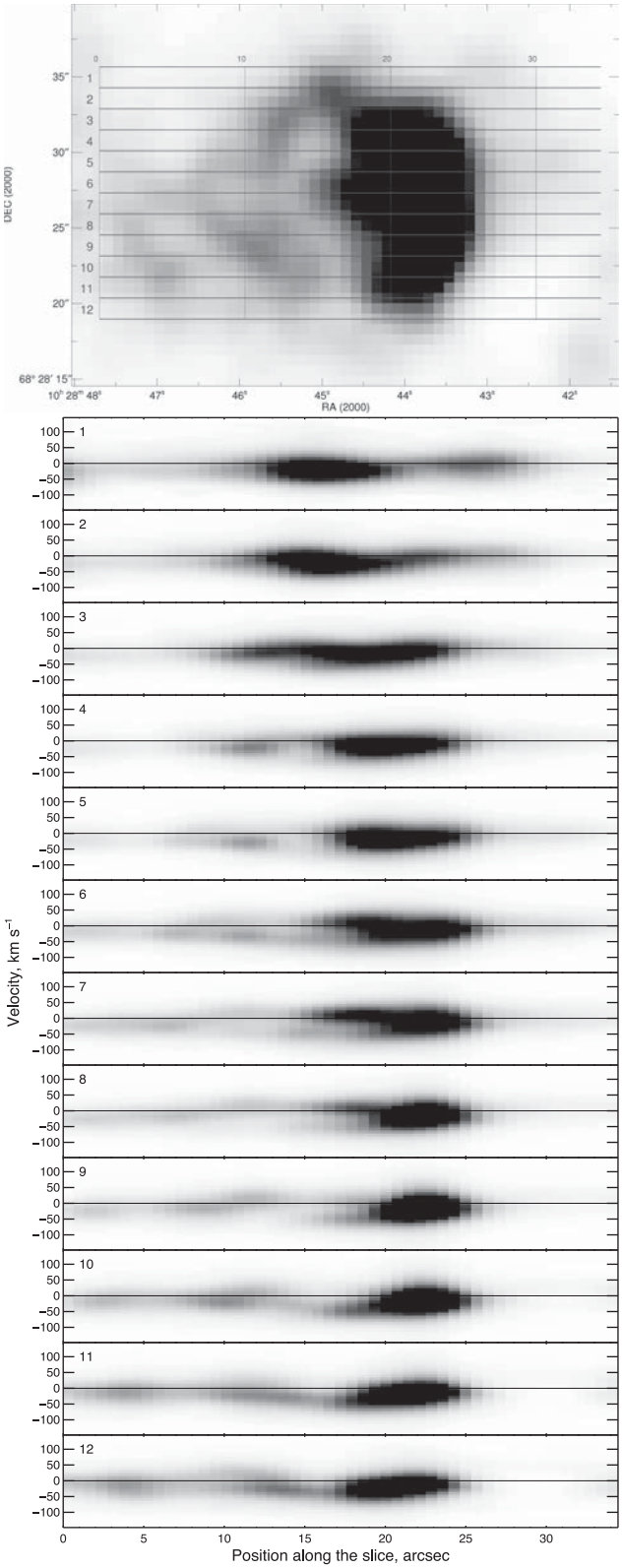

Figure 8. Region 6: PV diagrams in Hα and their location on the Hα image obtained from the FPI data cube as a sum of the channel maps.

corresponding expansion velocity is $v_{\rm exp} = 65\,{\rm km\,s^{-1}}$. The inferred expansion velocity implies an age of $t = 1.0\,{\rm Myr}$ for the ring-shaped H II region, which is substantially smaller than the ages of other star-forming complexes.

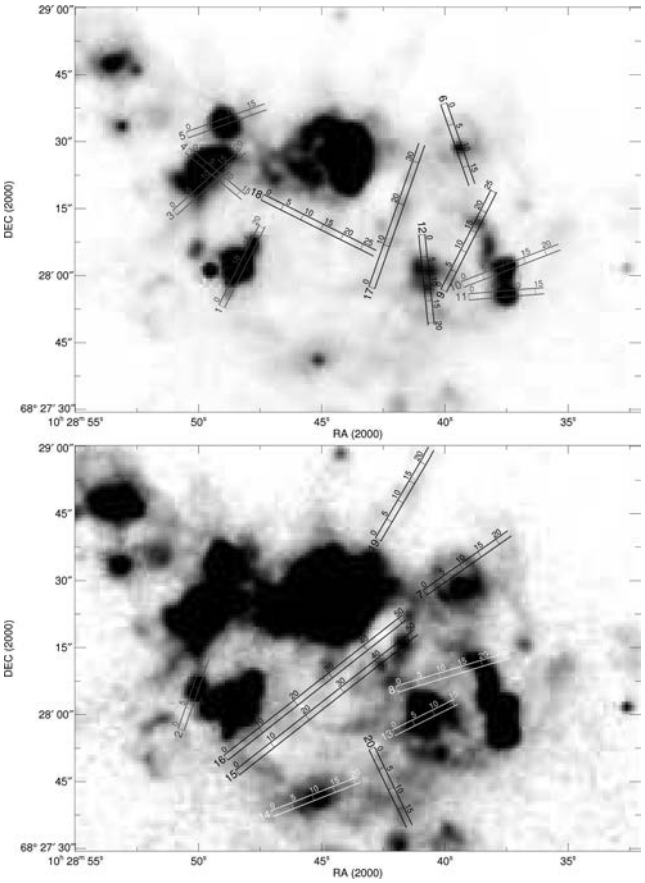

Figure 9. The locations of our PV diagrams that are shown as an example in Fig. 10. The images are the sum of the channel maps of the Hα FPI data cube; they are shown at different intensity levels.

We discuss the possible nature of this unique ring nebula in Section 5.

Region 8

In the *HST*/ACS image (Fig. 7), a very faint broad ring can be seen whose western part is Region 8 itself and the eastern part reaches Region 11. The curvature of the eastern region indicates that these two parts can be considered as a single ring structure. Region 8 itself appears as an arc with a chord length and curvature radius of about 220 and 130 pc, respectively. Its bright western edge has a single-component line profile (see profile 8-1 in Fig. 11) and the line profile of the inner part has a two-component structure (profile 8-2 in Fig. 11). The velocity of one component varies little and is equal to about $30\,{\rm km\,s^{-1}}$, whereas that of the other component varies from $-45\,{\rm km\,s^{-1}}$ in the east to $-65\,{\rm km\,s^{-1}}$ at the centre, implying an expansion velocity of about $45\,{\rm km\,s^{-1}}$ at the centre. The half-width of all the line components is 40–45 $\,{\rm km\,s^{-1}}$. In the PV diagrams shown in Fig. 10, Region 11 borders with Region 8 in its left part. As is evident from these diagrams, the extended ring expands as a whole. The radius $R_{\rm s} = 130$ pc and expansion velocity $v_{\rm exp} = 45\,{\rm km\,s^{-1}}$ of this 'combined' region imply an age of $t = 1.7\,{\rm Myr}$ and a required energy input rate of (1.9–8.4) $\times\,10^{38}$ erg s^{-1}.

Downloaded from http://mnras.oxfordjournals.org/ by guest on August 17, 2014

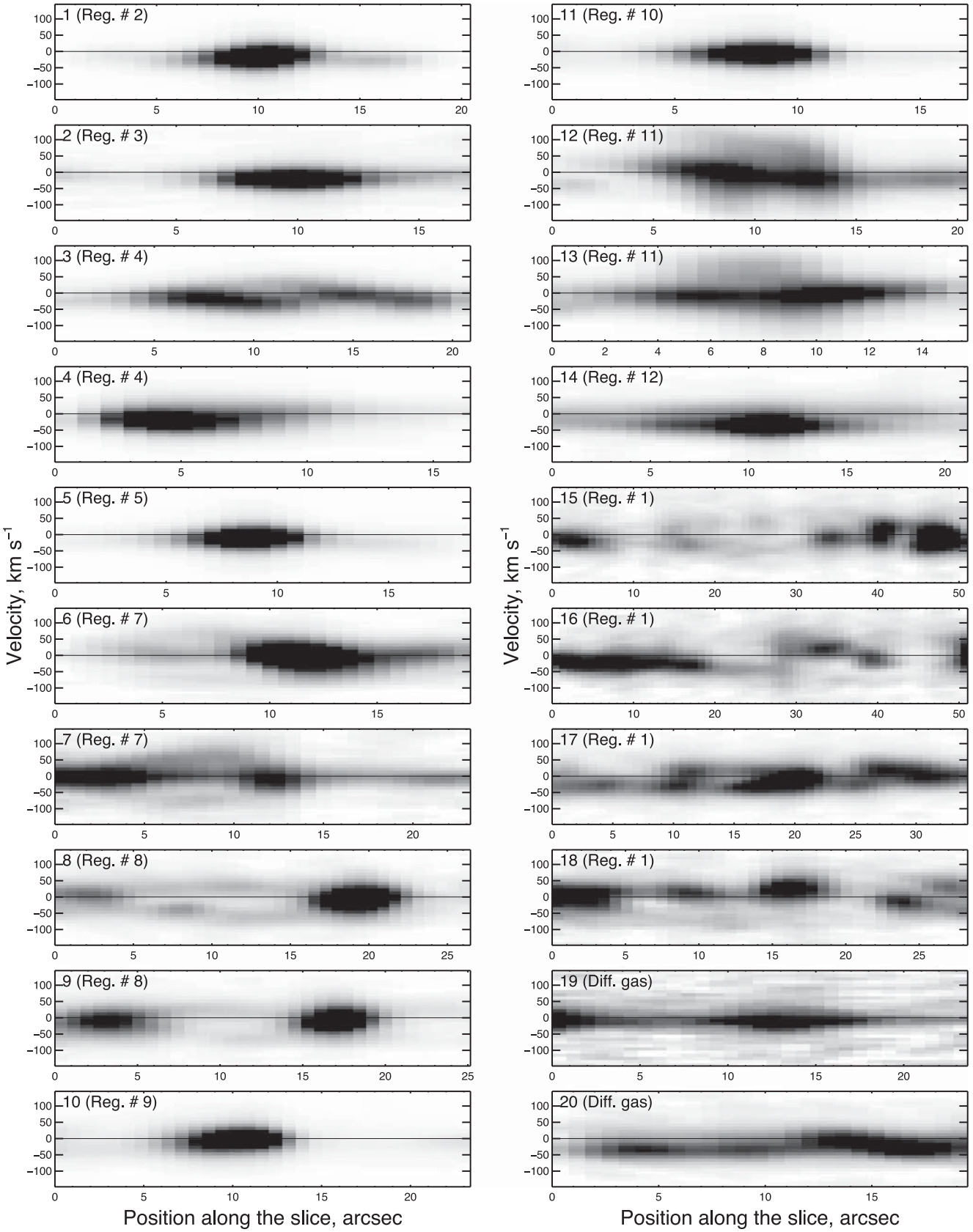

Figure 10. Examples of PV diagrams in the Hα passing through the observed H II regions. Their locations are shown in Fig. 9.

Downloaded from http://mnras.oxfordjournals.org/ by guest on August 17, 2014

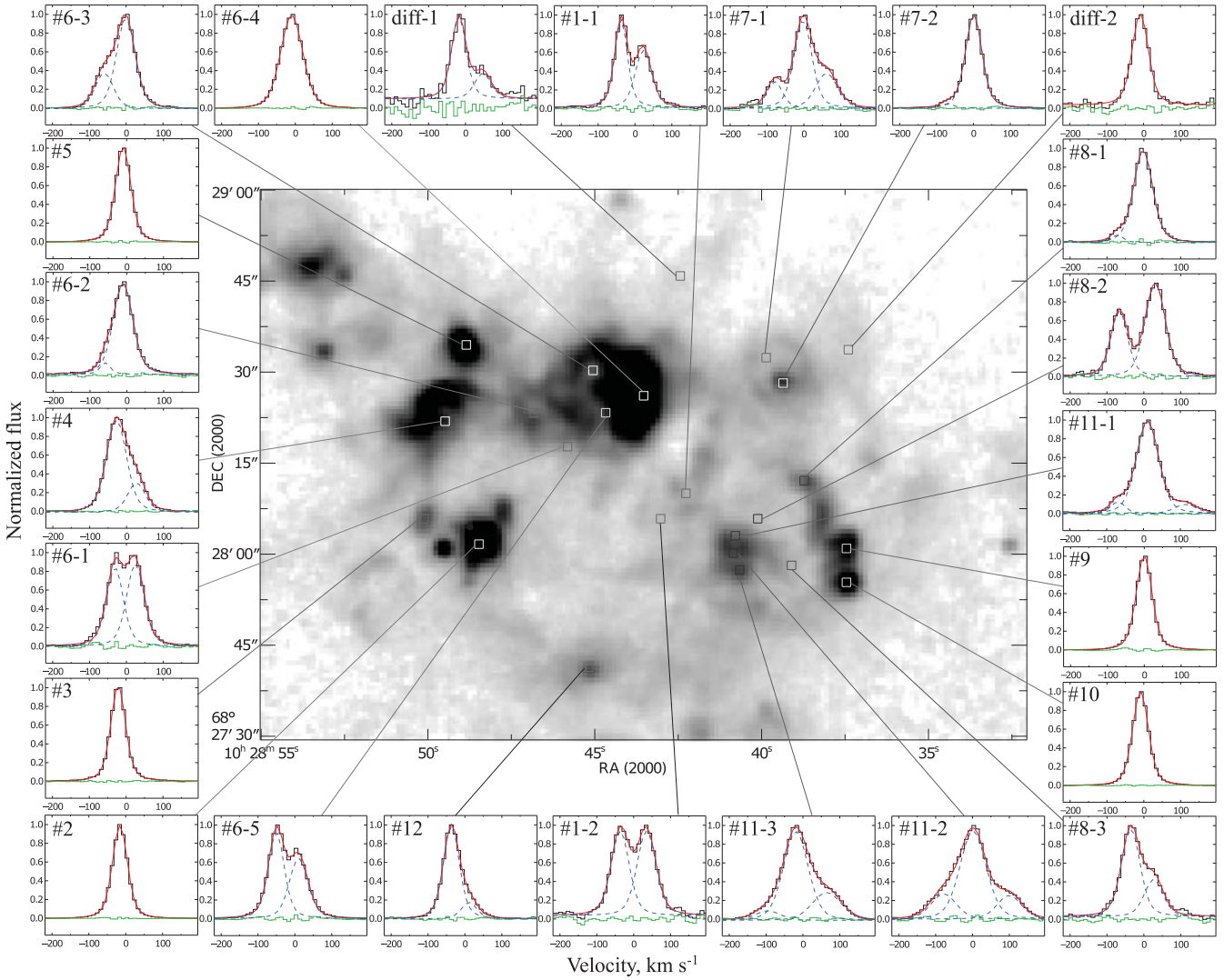

Figure 11. Examples of Hα line profiles obtained with the FPI. The black solid line denotes the observed data, the red solid line denotes the fitted profile, the blue dashed line denotes single Voigt components and the green dashed line denotes the residuals.

4.2 H II complexes with estimates of the upper limit of the expansion velocity

Region 2

The brightest nebula in the SGS, Region 2 is non-uniform and consists of a central nebula $\simeq$ 120 pc wide, several more compact ($\simeq$ 10–20 pc) clumps that surround it and two faint external shells south-east and north-west of the region, with the sizes of $\simeq$ 20 and 35 pc (see Fig. 7). The PV diagrams passing through the central nebula (see PV diagram 1 in Fig. 10) show no clear signs of expansion. The velocity of the peak of the single-component line profile (Fig. 11) varies slightly over the -15 to $-25\,\mathrm{km\,s^{-1}}$ interval; the FWHM of the line profile corrected for the instrumental contour is $\simeq 38\,\mathrm{km\,s^{-1}}$. We can estimate only the upper limit for the expansion velocity of the region as half of its FWHM, $v_{\rm exp} \leq 19\,\mathrm{km\,s^{-1}}$. Hence, the kinematic age of the complex is $t \geq 1.9$ Myr and, given the inferred density of the ambient neutral gas $n_{\rm H\,I} = 0.6$ cm^{-3} (method 1) and $n_{\rm H\,I} = 2.6$ cm^{-3} (method 2), the required mechanical energy input rate does not exceed 0.05×10^{38} and 0.23×10^{38} erg s^{-1}, respectively.

Region 3

A faint 80 $\times$ 55 pc diffuse region, Region 3 consists of several smaller ($\simeq$ 20 pc) nebulae (see Fig. 7). The PV diagrams and the line profiles show no expansion effect; the line half-width and peak velocity are equal to FWHM $\simeq 35\,\mathrm{km\,s^{-1}}$ and $v \simeq -25\,\mathrm{km\,s^{-1}}$, respectively.

Region 5

This region consists of a relatively bright 40–50 pc compact core located in the southern part and a fainter, irregularly structured extended region about 70 pc to the north. The region hosts the PI 24z cluster at its centre (see Fig. 7). The PV diagrams (Fig. 10) show no noticeable features; the line profile has a single-component structure with an FWHM of about $38\,\mathrm{km\,s^{-1}}$; the mean line peak velocity is equal to $-10\,\mathrm{km\,s^{-1}}$.

Region 9

This region is a lenticular shell with a size of about 90 pc. The line profiles do not resolve into two components and the PV

Downloaded from http://mnras.oxfordjournals.org/ by guest on August 17, 2014

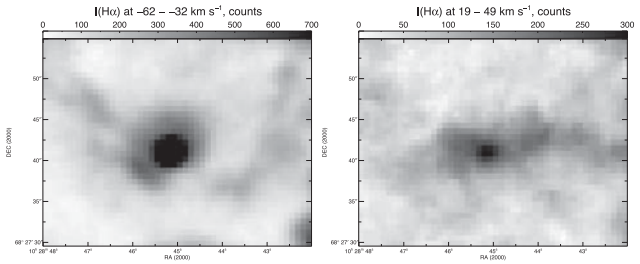

Figure 12. Region 12: Hα emission-line maps at velocities ranging from -62 to $-32\,\mathrm{km\,s^{-1}}$ (left) and from 19 to $47\,\mathrm{km\,s^{-1}}$ (right) based on the FPI observations.

diagram shows no clear signs of expansion. The average velocity of the region is about $-5\,\mathrm{km\,s^{-1}}$. The FWHM of the line is 40 and $55\,\mathrm{km\,s^{-1}}$ at the centre and periphery of the shell, respectively. The region hosts the clusters PI 25e, 25g and PII 25h.

Region 10

This region has a round shape and a size of about 65 pc. It shows no signs of expansion, either in the PV diagrams or in the line profiles; the peak velocity and FWHM of the line are equal to about -10 and $40\,\mathrm{km\,s^{-1}}$, respectively. The region hosts the cluster PI 25c.

Region 12

This region has a compact structure with a size of about 40 pc and a small bright core at its centre. It hosts the cluster PI 28b. The Hα profile is asymmetric throughout the entire region (Fig. 11). A bright component is observed at a velocity of about $-35\,\mathrm{km\,s^{-1}}$, and a second, weaker component is observed at $5\,\mathrm{km\,s^{-1}}$. The FWHM of both components is $\sim$40 $\mathrm{km\,s^{-1}}$. The shape of this region in the Hα images at different velocities (Fig. 12) reveals two regions: a bright compact region corresponding to the first profile and a faint extended region responsible for the second profile. Such a complex structure might be a result of the object being located in the non-uniform region at the north-eastern boundary of the high-velocity H I cloud mentioned in Section 3. This is why, for this region, we list only the limiting values of $v_{\rm exp}$, t and L_{38} in Table 2.

4.3 Region 11: an old supernova remnant

VLA radio observations by Walter et al. (1998) have shown that the three brightest optical star-forming regions in the SGS are the main sources of thermal radio continuum emission (see their fig. 1). The fourth source located in the area of shell 11 is non-thermal and its radio emission is much stronger than we would expect from an H II region with weak Hα emission. Walter et al. (1998) concluded that it is most likely a supernova remnant (SNR).

To verify this conclusion, we map the distribution of the I([S II])/I(Hα) line intensity ratio based on the SCORPIO narrow-band direct images (see Fig. 13). The strong [S II] 6717, 6731 Å feature in the SNR area (I([S II])/I(Hα) = 0.36–0.67) is typical for cooling gas emission behind a shock front, which confirms the SNR identification (see Allen et al. 2008; Millar, White & Filipović 2012, and references therein).

The *HST*/ACS image of the region (see Fig. 14) reveals its filamentary central shell ($D_{\rm horiz} = 5.7$ arcsec $\simeq$ 110 pc) and two $\sim$40 pc 'lobes' north and south of it (the full size is $D_{\rm vert} = 9$ arcsec = 175 pc). The region also hosts the PI 02z cluster (see Fig. 7).

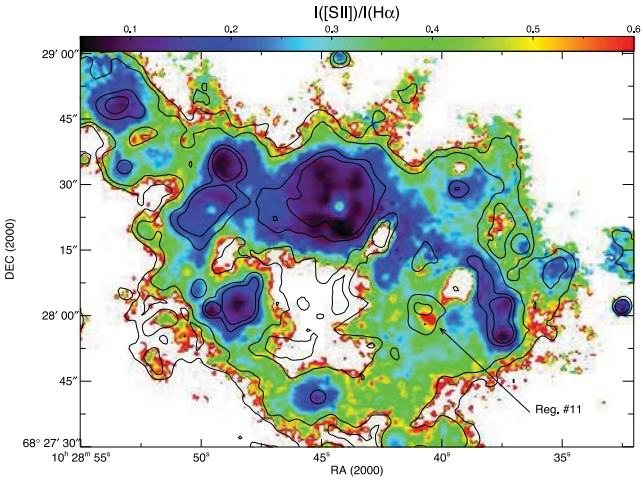

Figure 13. Map of the I([S II])/I(Hα) flux ratio with the [0.5, 1.0, 5, 10] $\times\ 10^{-16}$ erg s^{-1} cm^{-2} Hα intensity contours overlaid. The arrow indicates the position of Region 11 (SNR).

The SNR is characterized by high-velocity motions. The PV diagrams based on our FPI observations (Fig. 14) reveal the presence of high-velocity gas in the SNR; the Hα line profiles (11-1, 11-2 and 11-3 in Fig. 11) show a well-defined three-component structure of the line profile in the central part of the SNR.

All three components of the line profile are better seen in the northern part, whereas the negative velocity component disappears towards the south. The central component has a velocity of about $-30\,\mathrm{km\,s^{-1}}$. The FWHM of the central component is about $60\,\mathrm{km\,s^{-1}}$, and that of the shifted components amounts to 80–90 $\mathrm{km\,s^{-1}}$. The central component of the line probably corresponds to the background emission of gas in the SNR region.

The peak velocities of the shifted components are about 60–70 and $-80\,\mathrm{km\,s^{-1}}$ and yield an expansion velocity of $v_{\rm exp} \simeq$ 70–80 $\mathrm{km\,s^{-1}}$. This high expansion velocity provides further support for the identification of the nebula as an SNR.

The high expansion velocity suggests that the SNR still undergoes adiabatic expansion. According to the self-similar solution of Sedov (1946), the evolution of an SNR at the adiabatic stage can be described by

$$R_{\rm s} = 13.5(E_{51}/n_0)^{0.2}(t/10^4\ \mathrm{yr})^{0.4}\ (\mathrm{pc}) \quad (4)$$

and

$$v_{\rm exp} = 0.4R_{\rm s}/t, \quad (5)$$

where $E_{51} = E_0/10^{51}$ erg is the explosion energy.

Given the radius $R_{\rm s} = 55$ pc and the expansion velocity $v_{\rm exp} =$ 70–80 $\mathrm{km\,s^{-1}}$, we infer the SNR age of $t = (2.8\text{–}3.1) \times 10^5$ yr and $E_{51}/n_0 = 1.1\text{–}1.5$. Our estimates of the unperturbed ambient density 0.2 cm^{-3} (method 1) and 0.8 cm^{-3} (method 2) yield an initial explosion energy of $E_0 = (0.2\text{–}0.3) \times 10^{51}$ erg and $E_0 = (0.9\text{–}1.2) \times 10^{51}$ erg, respectively.

If the SNR currently undergoes the post-adiabatic snow-plough stage of evolution, we can use the analysis performed by Chevalier (1974). According to this work,

$$E_{50} = 5.3 \times 10^{-7} n_0^{1.12} v_{\rm exp}^{1.4}\ (\mathrm{km\ s^{-1}}) R_{\rm s}^{3.12}\ (\mathrm{pc}), \quad (6)$$

where $E_{50} = E_0/10^{50}$ erg.

In this case, the same SNR radius and expansion velocity yield the $E_{51}/n_0^{1.12}$ ratio of 5.5–6.6; the two ambient density estimates yield $E_0 \simeq 1.0 \times 10^{51}$ and $E_0 \simeq 4.7 \times 10^{51}$ erg, respectively.

Downloaded from http://mnras.oxfordjournals.org/ by guest on August 17, 2014

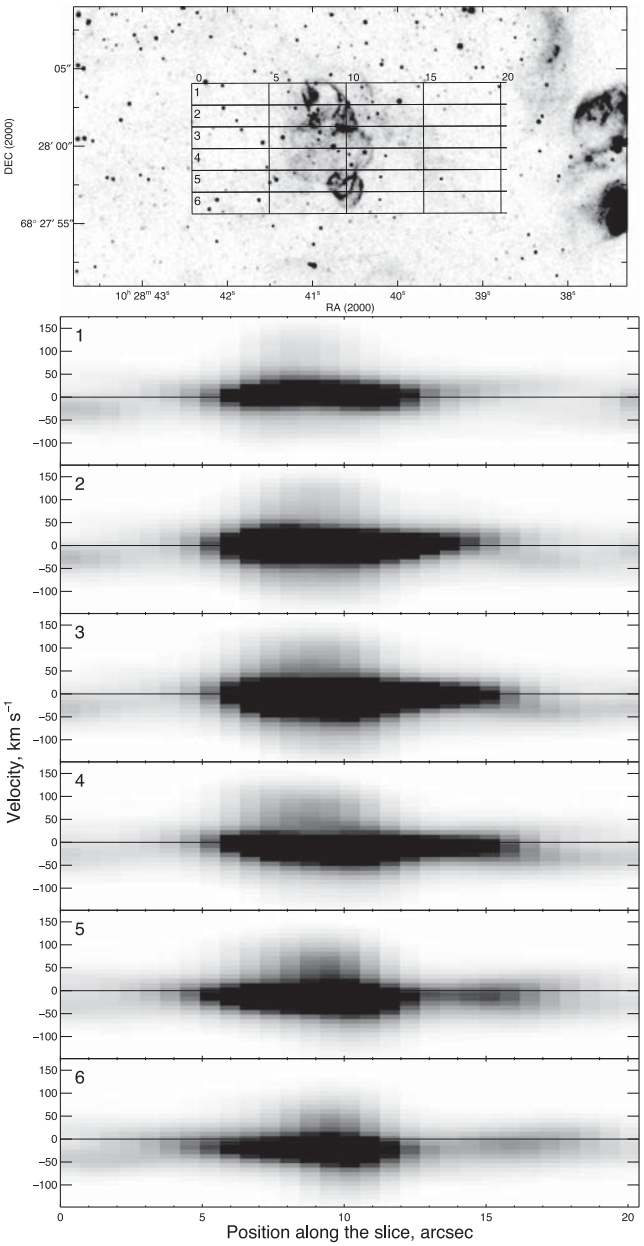

Figure 14. PV diagrams in Hα passing through Region 11 and their locations on the *HST*/ACS F658N image of the region.

Thus, our analysis of SNR kinematics confirms that Region 11 can be viewed as an old remnant of a standard SN explosion.

We can speculate that the Hα morphology of the SNR in IC 2574 considered here (a central shell and two symmetrical 'lobes' north and south of it) resembles very much the structure of the well-known Galactic SNR W50 with two symmetric eastern and western 'lobes' due to jets emerging from the central SS 433 microquasar (see Goodall, Alouani-Bibi & Blundell 2011, for a recent analysis).

There is a noticeable asymmetry in the extent of the northern and southern lobes of the SNR in IC 2574: [R(N)/R(S) $\simeq$ 1.35], which is similar to the asymmetry of the eastern and western lobes of W50 [R(E)/R(W) = 1.4]. According to Goodall et al. (2011), the asymmetry of W50 is due to the exponential density profile of the Milky Way disc. We can similarly explain the asymmetry in the extent of the lobes of the SNR in IC 2574 by the density gradient in the wall of the SGS.

A discovery of an X-ray binary in the SNR could provide evidence for the similar nature of the two objects. *Chandra* observations of the SGS by Yukita & Swartz (2012) reveal a luminous, $L_X \simeq 6.5 \times 10^{38}$ erg s^{-1} (in the 0.3–8.0 keV band), point-like source inside the hole of the SGS, but the separation between the source and the SNR is about 15 arcsec.

To sum up, we can confidently conclude that Region 11 really is an old SNR.

5 DISCUSSION

5.1 Expansion of the H II shells and their energy budget

We have measured bona fide expansion velocities of four H II complexes (4, 6, 7 and 8) from the splitting of the line profile. Thus, we can use equations (1) and (2) for the supershell produced by supernovae and stellar winds to estimate the kinematic ages and mechanical energy input rates required to drive the formation of each H II complex. For the remaining H II regions, we estimate only the upper limits for the expansion velocity and the corresponding lower age limit and upper L_w limit.

Stewart & Walter (2000) have reported the results of FUV and optical observations of the SGS, providing an independent measure of the ages, masses and total mechanical energy deposited by the central stellar association and by the clusters in giant H II regions on the rim of the SGS based on the FUV, B-band and Hα fluxes (see table 2 in their paper).

Yukita & Swartz (2012) have analysed *Chandra* X-ray observations of the SGS. They performed a multiwavelength (*GALEX* and *Spitzer*) analysis of the stellar population in the SGS area and identified four star-forming regions – young star clusters inside and at the edges of the SGS (C1, C2, C3, C4 in their table 1 and fig. 2); C2 coincides with the central star-forming region studied by Dalcanton et al. (2012). Their positions are indicated in Fig. 7 by the large green circles. These largest clusters include the small stellar groups from Pellerin et al. (2012); see Fig. 7. Yukita & Swartz (2012) determined the mass, age and mechanical energy produced by massive stars and supernovae in these four massive star clusters. They estimated the rate of mechanical energy input from the X-ray fluxes in accordance with the best-fitting STARBURST99 model.

When comparing our study of H II regions with the analysis of their stellar populations, we must bear in mind the uncertainty of our velocity estimates, on the one hand, and the fact that the reported parameters of star clusters are model-dependent, on the other hand. The uncertainty of our estimates is primarily because of the non-uniform density of neutral gas in the walls of the SGS and the irregular morphology and kinematics of H II complexes.

However, Table 2 shows that the mechanical energy input rate for the overwhelming majority of the complexes of triggered star formation associated with the SGS is sufficient to drive the formation of expanding shell-like H II regions. The only exceptions are Regions 7 and 8.

The fact that our inferred energy input rate required to drive the formation of Region 8 significantly exceeds the energy input rate estimated by Stewart & Walter (2000) is quite understandable. We significantly increased the size of this H II region (and consequently the required energy) by incorporating into it the faint extended arc-shaped nebula that adjoins the SNR from the west (i.e. by combining two faint nebulae into a single shell-like structure).

Downloaded from http://mnras.oxfordjournals.org/ by guest on August 17, 2014

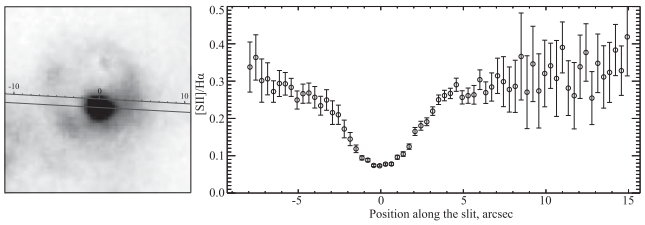

Figure 15. The position of the slit crossing Region 7 in the Hα image mapped from our FPI observations (left) and the [S II] 6717,6731 Å to Hα flux ratio along the slit (right).

The situation with Region 7 is very interesting. We estimate $v_{\rm exp} \approx 65\,{\rm km\,s^{-1}}$ and the corresponding $t = 1$ Myr (it is the youngest of the complexes discussed here). The high expansion velocity estimated in this study is indicative of a shock effect. To verify this hypothesis, we constructed the distribution of the I([S II] 6717,6731)/I(Hα) line ratio based on the SCORPIO long-slit data (Section 2.3). Fig. 15 shows the distribution of this ratio along the slit passing through the ring centre.

As is evident from Fig. 15, the ratio I([S II])/I(Hα) = 0.1–0.2 in the central bright nebula corresponds to the recombination radiation of the H II region. However, at the same time, it increases outwards and reaches I([S II])/I(Hα) = 0.35 at the edges of the ring nebula, which suggests a possible shock wave effect.

The required kinetic energy input rate of (2.5–9.9) $\times\ 10^{38}$ erg s^{-1} determined above can be provided by winds from several WR or Of stars. Note that the ring nebula is observed not inside the H I cloud, but against a background of tenuous diffuse gas. This suggests that the ambient density of unperturbed gas calculated in both methods is highly overestimated. Given the uncertainty of the estimated H I in the neighbourhood of Region 7, even a single star with a strong wind would be enough. The search for WR stars conducted by Drissen et al. (1993) produced no possible candidates in this region. Nevertheless, we consider it very interesting to perform a detailed analysis of the stellar content of the PI 01b cluster at the centre of the ring nebula.

We cannot rule out the possibility that the large ring in Region 7 might be an old SNR. At least, with the ambient density of $n_{\rm H\,I} \simeq 0.3$ cm^{-3} the ring nebula fits well the empirical evolutionary sequence of SNRs on the log ($v_{\rm exp}$) versus log[$R_{\rm s}(n_{\rm H\,I})^{1/3}$] plot suggested by Lozinskaya (1980a,b). The expected radio surface brightness of an SNR with a diameter of 210 pc is about $\Sigma_{1\,\rm GHz} = 10^{-22}$–$10^{-21}$ W m^{-2} Hz^{-1} sr^{-1} (see the Σ–D relation in Lozinskaya 1981; Berezhko & Volk 2004; Asvarov 2006). This surface brightness is less than the limiting brightness at $\lambda = 6$ cm in the observations by Walter et al. (1998), which were the basis for the identification of the SNR in Region 11.

Therefore, the nature of the youngest star-forming complex in the SGS remains an open issue.

5.2 Diffuse ionized medium inside and around the SGS

Deep ground-based images have allowed us to identify a faint diffuse component of ionized gas in the SGS region, which is not shown in the *HST*/ACS images.

Inside the SGS in the central Region 1 and also outside the SGS, we observed Hα line emission with an average brightness level of (6–8) $\times\ 10^{-17}$ erg s^{-1} cm^{-2} and [S II] line emission with an average brightness level of (2.5–3.5) $\times\ 10^{-17}$ erg s^{-1} cm^{-2}.

As is evident from Fig. 13, the I([S II])/I(Hα) intensity ratio is enhanced both in the border regions outside the SGS and in the outer layers of Region 1 inside the SGS.

To analyse the kinematics of this faint diffuse emission, we constructed the Hα line PV diagrams for several regions outside the H II complexes and several PV diagrams at the centre of Region 1 (Fig. 10, plots 15 – 20).

As is evident from Fig. 11 (diff-2), the Hα line of the faint diffuse emission in the outer SGS regions has a single-component profile with an FWHM and peak velocity of 40–45 and -10 km s^{-1}, respectively. These are typical parameters for the SGS region. However, there are several faint regions observed with kinematic evidence of local perturbations or the presence of an expanding shell (see, for example, profile diff-1 in Fig. 11).

The line profile of the central Region 1 shows a well-defined two-component structure corresponding to the expansion of very faint diffuse structures at a velocity of $v_{\rm exp} \simeq 33 \pm 2\,{\rm km\,s^{-1}}$. The kinematic age of the central cluster in Region 1, which is responsible for the formation of the SGS, is equal to 14 Myr (Walter et al. 1998; Walter & Brinks 1999). Therefore, the bright H II nebula is not observed at this location (Hα arises from the recombination of gas ionized by the radiation of massive stars and is observed over their typical lifetimes $\leq$10 Myr). However, we can still see the effect of shocks from stellar winds and SN explosions originating from the central stellar complex in Region 1. Yukita & Swartz (2012) have revealed a bright point-like source CXOU J102843.0+682816 in the SGS in the 0.3–8.0 keV band and have detected an excess of diffuse low-surface-brightness X-ray emission within and around the H I hole after removing the point source from the image (see their fig. 1). According to Sharma et al. (2014), superbubbles can retain a large fraction (up to 35–40 per cent for $n_{\rm H\,I} = 1$ cm^{-3}) of the initial energy obtained from SN explosions as bubble thermal energy and kinetic energy of the shell. This reserve of mechanical energy powers the observed diffuse X-ray emission of the hot gas that fills the central hole and drives the expansion of the neutral SGS at a velocity of 25 km s^{-1}. It might also be responsible for the observed expansion of the faint ionized gas structures inside the SGS at a velocity of $\sim$33 km s^{-1}.

The observed parameters of local diffuse gas in the SGS region are similar to those of the extraplanar diffuse ionized gas (DIG) in spiral and Irr galaxies.

The observed I([S II])/I(Hα) and I([N II])/I(Hα) line ratios in the DIG are higher than those in the classical H II regions. The ionization of the DIG is traditionally explained by the leakage of ionizing photons from the H II regions (see Hidalgo-Gámez 2006; Seon 2009, and references therein). To explain the increase of I([N II])/I(Hα), I([S II])/I(Hα) and I([O III]5007)/I(Hβ) with galactic height, additional sources of ionization were considered; ionization by shocks or turbulent mixing layers might be responsible for some of the DIG emission. Note that the photoionization simulations of a multicomponent ISM by Wood & Mathis (2004) do not require as much additional heating as the previous studies.

We can similarly explain the faint DIG emission observed in the SGS as a result of leakage from the bright H II regions of both the ionizing photons and the mechanical energy of stellar winds and supernovae. All the H II complexes studied here have a non-uniform, clumpy or filamentary structure, which allows the radiation and shocks to leak outside through low-density regions. In a number of cases, the results of such a leakage are actually observed. One striking example are the 'horns': two faint emission structures observed beyond the northern boundary of Region 6 around a dense H I cloud

Downloaded from http://mnras.oxfordjournals.org/ by guest on August 17, 2014

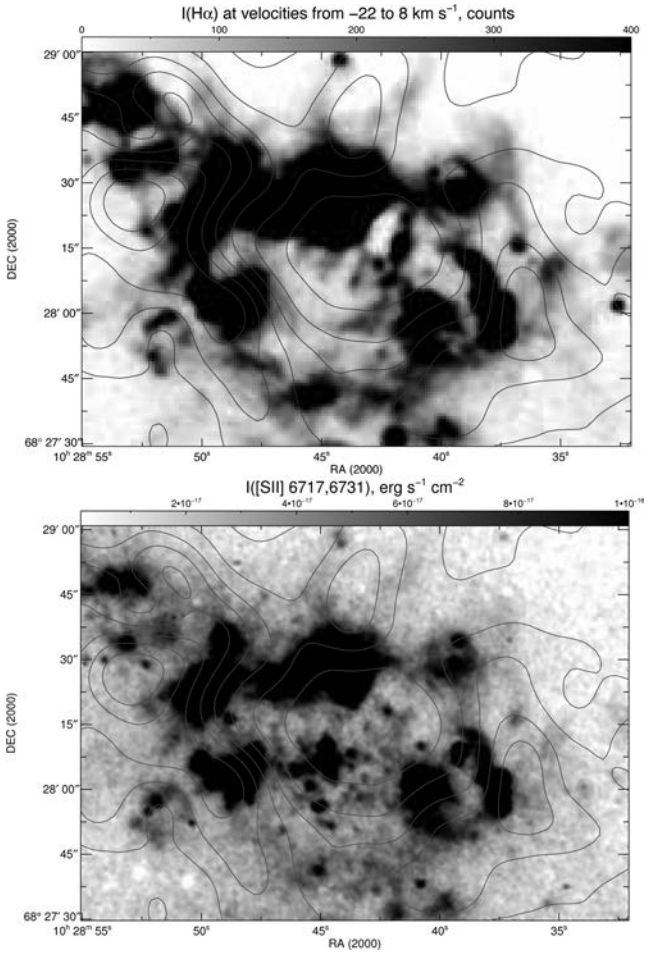

Figure 16. Hα map of the SGS region at velocities ranging from -22 to 8 km s^{-1} based on FPI observations (top) and the narrow-band filter image in the [S II] 6717, 6731 Å lines (bottom) with the [0.5, 1.0, 1.5, 2.0, 2.5, 3.0, 3.5, 4.0] $\times$ 10^{21} cm^{-2} H I column density contours overlaid.

(see Fig. 16). These structures are observed in both the Hα and [S II] lines.

5.3 Subsequent evolution of the H I structure

The SGS in IC 2574 is one of the most dynamically active H I structures among Irr galaxies, because we observe it during a period of violent star formation in its walls triggered by the expansion of the SGS. What future awaits this structure?

The most dynamically active shell-like H II complexes exhibiting the expansion effect are Regions 4, 6 and 7, which are located in the northern wall of the SGS. The expansion of Region 6 rapidly disperses the local H I gas in the northern wall of the SGS. This is, in particular, clearly demonstrated by the emission features mentioned above: the 'horns' located beyond the northern boundary of Region 6 (see Fig. 16).

The destruction of the northern wall of the H I SGS due to H II complexes will result in the growth of the SGS and, ultimately, in its merging with the neighbouring H I structures. We must primarily expect the SGS to merge with the supergiant H I shells 31 in the west and 37 in the north (see figs 9 and 14 in Walter & Brinks 1999). As a result, after several billion years there will be a system of giant adjoining and/or interacting shell-like H I structures similar to those observed in the Irr galaxy, Holmberg II (see Walter et al. 1998).

6 CONCLUSIONS

(i) To study the kinematics of ionized gas in the regions of triggered star formation in the walls of the SGS, we performed observations with the SAO RAS 6-m telescope using the SCORPIO and SCORPIO-2 multimode focal reducers operated in the scanning FPI, long-slit and direct imaging modes.

(ii) Using THINGS data to analyse the kinematics of neutral gas, we derotated both (21-cm and Hα) data cubes with a circular rotation model of IC 2574 constructed by fitting the H I velocity field.

(iii) The consideration of global H I kinematics confirms the SGS expansion velocity obtained earlier by Walter & Brinks (1999). A more detailed analysis of the H I kinematics revealed the non-uniform structure and kinematics of the SGS; it is shown to be located at the far side of the galactic disc plane.

(iv) We perform a detailed analysis of the kinematics of all extended H II complexes in the SGS. We have estimated the expansion velocities for four regions, which have allowed us to determine their kinematic ages and the kinetic energy input rate required to drive their formation. For the remaining Hα complexes, we estimated the upper limit of the expansion velocity and the corresponding limiting age and kinetic energy input. A comparison with the age and energy input from the stellar population of the complexes, based on the data of Stewart & Walter (2000) and Yukita & Swartz (2012), shows that the energy input is sufficient in all complexes except for Region 7.

(v) We discuss in detail the nature of Region 7, which is a regular faint thin ring with a bright inner region in its southern part. The obtained expansion velocity of 65 km s^{-1} shows that Region 7 is the youngest Hα complex in the SGS (t = 1.0 Myr). The high expansion velocity is indicative of a shock. The significant role of shock waves in the gas ionization process is evident from the analysis of the I([S II])/I(Hα) line ratio.

(vi) Region 11 was considered as a possible SNR based on radio observations (Walter et al. 1998). We measured its expansion velocity and estimated the age of the SNR and the initial SN explosion energy E_0 under two assumptions: the adiabatic stage or intense radiative cooling. In both cases, the results confirm that Region 11 is an old remnant of a standard SN. Therefore, the inferred high expansion velocity and the high relative [S II] line intensities provide further evidence that Region 11 is indeed an SNR.

(vii) Our observations reveal a faint diffuse component of ionized gas in the SGS area, which did not show up previously in *HST*/ACS images. In the central Region 1, as well as outside the SGS, we observe Hα and [S II] line emission with an average surface brightness of (6–8) and (2.5–3.5) $\times$ 10^{-17} erg s^{-1} cm^{-2}, respectively. The I([S II])/I(Hα) intensity ratio is higher both in the border regions outside the SGS and in the outer layers of Region 1. The observed parameters of local diffuse gas in the SGS region are similar to those of extraplanar DIG in Sp and Irr galaxies. An analysis of the kinematics of this faint diffuse emission shows a single-component line profile in the outer regions of the SGS, but reveals some structures that show perturbed kinematics with a multicomponent Hα line profile. The central Region 1 shows well-defined two-component line profiles corresponding to the expansion of faint diffuse inner structures with a velocity of $\simeq$ 33 km s^{-1}. This expansion velocity and the soft X-ray diffuse emission within the H I hole (and extending slightly beyond it) are extant traces of the initial effect of shock waves from stellar winds and SN explosions in the central stellar complex of Region 1.

Downloaded from http://mnras.oxfordjournals.org/ by guest on August 17, 2014

(viii) Based on the results of the SGS gas kinematics analysis, we have made speculative conclusions about the future of this structure: it will probably merge with the neighbouring supershells. The vicinity of the SGS will possibly look like the ISM in Holmberg II – a typical example of an object with multiple interacting SGSs with triggered star formation at their rims.

ACKNOWLEDGEMENTS

We thank the anonymous referee for valuable comments that have improved the clarity of this paper. This work was supported by the Russian Foundation for Basic Research (project nos 12-02-31356 and 14-02-00027) and partly supported by the 'Active Processes in Galactic and Extragalactic Objects' basic research programme of the Department of Physical Sciences of RAS OFN-17. AVM acknowledges support from the 'Dynasty' Foundation. We also thank Victor Afanasiev and Alexander Burenkov, who performed the imaging and long-slit observations at the 6-m telescope, and Fabian Walter for providing us with the H I data cube of IC 2574 and the corrected version of their age estimates of H II complexes. This work is based on observations obtained with the 6-m telescope of the SAO RAS. The observations were carried out with the financial support of the Ministry of Education and Science of the Russian Federation (contract nos 16.518.11.7073 and 14.518.11.7070). We used observations made with the NASA/ESA *Hubble Space Telescope* and obtained from the *Hubble* Legacy Archive, which is a collaboration between the Space Telescope Science Institute (STScI/NASA), the Space Telescope European Coordinating Facility (ST-ECF/ESA) and the Canadian Astronomy Data Centre (CADC/NRC/CSA). This work has made use of THINGS, the H I Nearby Galaxy Survey.

REFERENCES

Afanasiev V. L., Moiseev A. V., 2005, Astron. Lett., 31, 194
Afanasiev V. L., Moiseev A. V., 2011, Baltic Astron., 20, 363
Allen M. G., Groves B. A., Dopita M. A., Sutherland R. S., Kewley L. J., 2008, ApJS, 178, 20
Asvarov A. I., 2006, A&A, 459, 519
Bagetakos I., Brinks E., Walter F., de Blok W. J. G., Usero A., Leroy A. K., Rich J. W., Kennicutt R. C., 2011, AJ, 141, 2011
Berezhko E. G., Volk H. J., 2004, AJ, 427, 525
Bureau M., Carignan C., 2002, AJ, 123, 1316
Cannon J. M. et al., 2005, ApJ, 630, L37
Cannon J. M. et al., 2011a, ApJ, 735, 35
Cannon J. M. et al., 2011b, ApJ, 735, 36
Chevalier R. A., 1974, ApJ, 188, 501
Cook D. O. et al., 2012, ApJ, 751, 100
Dalcanton J. J. et al., 2012 ApJS, 198, 6
Dib S., Burkert A., 2005, ApJ, 630, 238
Drissen L., Roy J.-R., Moffat A. F. J., 1993, AJ, 106, 1460
Elmegreen B. G., 1997, ApJ, 477, 196
Elmegreen B. G., Chiang W-H., 1982, ApJ, 253, 666
Goodall P. T., Alouani-Bibi F., Blundell K. M., 2011, MNRAS, 414, 2838
Hidalgo-Gámez A. M., 2006, AJ, 131, 2078
Karachentsev I. D., Makarov D. I., Kaisina E. I., 2013, AJ, 145, 101
Kim S., Dopita M. A., Stavelet-Smith L., Bessel M., 1999, A&A, 350, 230
Lozinskaya T. A., 1980a, A&A, 84, 26
Lozinskaya T. A., 1980b, Astron.Zh., 57, 707
Lozinskaya T. A., 1981, Astron.Letters, 7, 29
McCray R., Kafatos M., 1987, ApJ, 317, 190
Mac Low M., McCray R., 1988, ApJ, 324, 776
McQuinn K. B. W., Skillman E. D., Cannon J. M., Dalcanton J. J., Dolphin A., Stark D., Weisz D., 2009, ApJ, 695, 561
McQuinn K. B. W. et al., 2010a, ApJ, 721, 297
McQuinn K. B. W. et al., 2010b, ApJ, 724, 49
Millar W. C., White G. L., Filipović M. D., 2012, Serbian Astron. J., 184, 19
Moiseev A. V., 2002, Bull. Spec. Astrophys. Obs., 54, 74
Moiseev A. V., 2014, Astrophys. Bull., 69, 1
Moiseev A. V., Egorov O. V., 2008, Astrophys. Bull., 63, 181
Oh S-H., de Blok W. J. G., Walter F., Brinks E., Kennicutt R. C. J., 2008, AJ, 136, 2761
Ott J., Walter F., Brinks E., Van Dyk S. D., Dirsch B., Klein U., 2001, AJ, 122, 3070
Pasquali A. et al., 2008, ApJ, 687, 1004
Pellerin A., Meyer M. M., Calzetti D., Harris J., 2012, AJ, 144, 182
Rhode K. L., Salzer J. J., Westpfahl D., Radice L. A., 1999, AJ, 118, 323
Rich J. W., de Block W. J. G., Cornwell T. J., Brinks E., Walter F., Bagetakos I., Kennicutt R. C. Jr, 2008, AJ, 136, 2897
Sedov L. I., 1946, Dokl. Akad. Nauk SSSR, 52, 17
Seon K., 2009, ApJ, 703, 1159
Sharma P., Roy A., Nath B. B., Shchekinov Yu., 2014, MNRAS, preprint (arXiv:1402.6695)
Silich S., Lozinskaya T., Moiseev A., Podorvanyuk N., Rosado M., Borissova J., Valdez-Gutiérrez M., 2006, A&A, 448, 123
Simpson C. E., Hunter D. A., Knezek P. M., 2005, AJ, 129, 160
Stewart S. G., Walter F., 2000, AJ, 120, 1794
Tenorio-Tagle G., 1981, A&A, 94, 338
Tenorio-Tagle G., Bodenheimer P., 1988, ARA&A, 26, 145
Tomita A., Ohta K., Nakanishi K., Takeuchi T. T., Saito M., 1998, AJ, 116, 131
Vorobyov E. I., Shchekinov Y. A., 2004, A&A, 416, 499
Wada K., Spaans M., Kim S., 2000, ApJ, 540, 797
Walter F., Brinks E., 1999, AJ, 118, 273
Walter F., Kerp J., Duric N., Brinks E., Klein U., 1998, ApJ, 502, L143
Walter F., Brinks E., de Blok W. J. G., Bigiel F., Kennicutt R. C., Jr, Thornley M. D., Leroy A., 2008, AJ, 136, 2563
Warren S. R. et al., 2011, ApJ, 738, 10
Weaver R., McCray R., Castor J., Shapiro P., Moore R., 1977, ApJ, 218, 377
Weisz D. R., Skillman E. D., Cannon J. M., Dolphin A. E., Kennicutt R. C., Lee J., Walter F., 2008, ApJ, 689, 160
Weisz D. R., Skillman E. D., Cannon J. M., Dolphin A. E., Kennicutt R. C., Lee J., Walter F., 2009a, ApJ, 704, 1538
Weisz D. R., Skillman E. D., Cannon J. M., Walter F., Brinks E., Ott J., Dolphin A. E., 2009b, ApJ, 691, L59
Wood K., Mathis J. S., 2004, MNRAS, 353, 1126
Young L. M., Lo K. Y., 1997, ApJ, 490, 710
Yukita M., Swartz D. A., 2012, ApJ, 750, L16

APPENDIX A: CHANNEL MAP FROM FPI Hα DATA CUBE

In this appendix, we present a channel map of the derotated Hα data cube of the SGS in IC 2574. During the observations, we obtained a 40-channel data cube. We present in Fig. A1 the image of a 32-channel map with noticeable Hα intensity.

Downloaded from http://mnras.oxfordjournals.org/ by guest on August 17, 2014

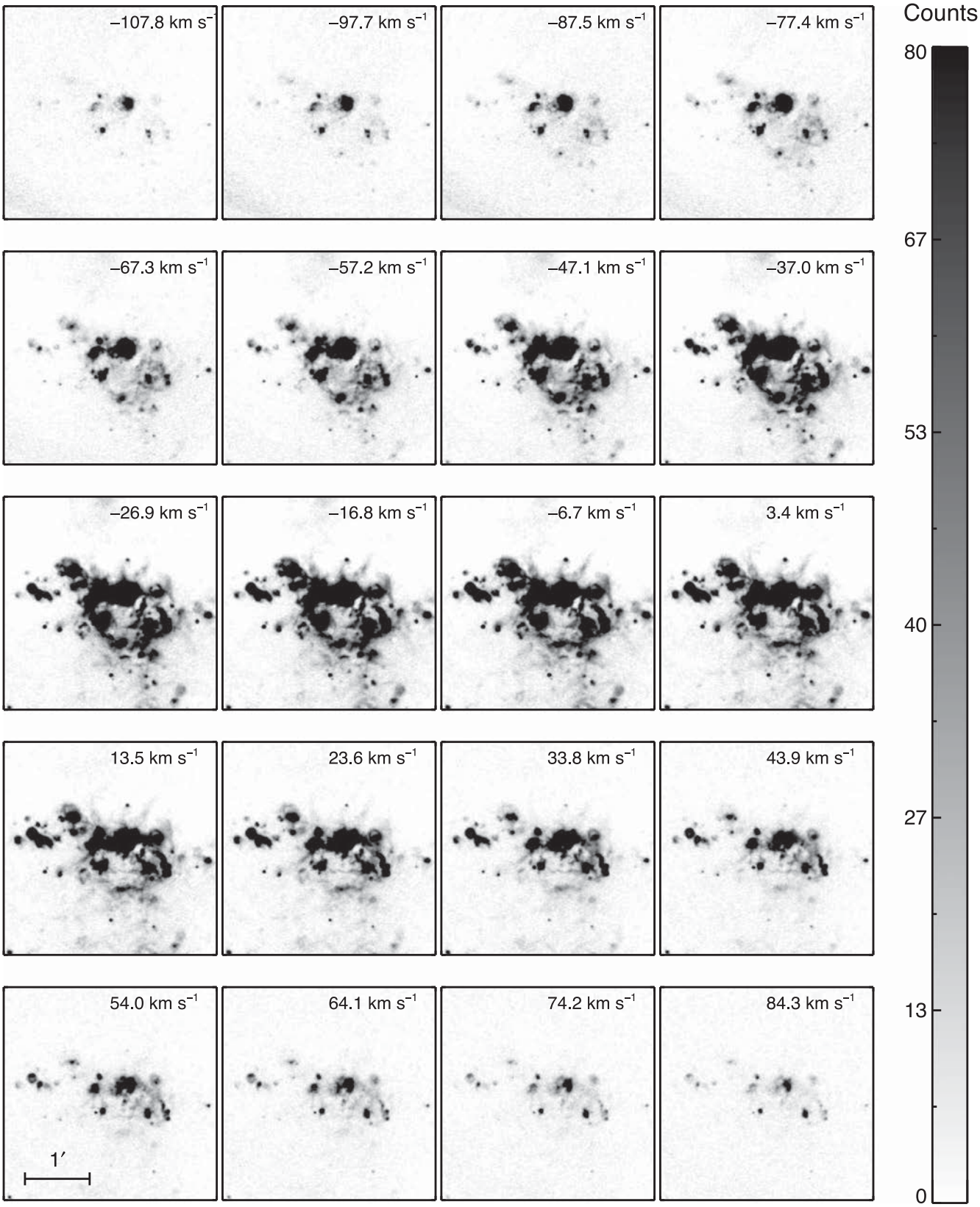

Figure A1. Channel map from the FPI Hα data cube. The velocity of each channel is shown in the top-right corner of the panel.

This paper has been typeset from a TEX/LATEX file prepared by the author.

Downloaded from http://mnras.oxfordjournals.org/ by guest on August 17, 2014

Monthly Notices of the ROYAL ASTRONOMICAL SOCIETY

MNRAS **429,** 1450–1465 (2013) doi:10.1093/mnras/sts428

Emission spectrum of ionized gas in the irregular galaxy Holmberg II

O. V. Egorov,[1⋆] T. A. Lozinskaya[1] and A. V. Moiseev[1,2]

[1]*Lomonosov Moscow State University, Sternberg Astronomical Institute, 13 Universitetskij prospekt, Moscow 119234, Russia*
[2]*Special Astrophysical Observatory, Russian Academy of Sciences, Nizhnii Arkhyz 369167, Russia*

Accepted 2012 November 16. Received 2012 November 13; in original form 2012 August 6

ABSTRACT

We studied the ionized gas spectra of star-forming regions in the Holmberg II galaxy using optical long-slit spectroscopic observations made with the 6-m telescope of the Special Astrophysical Observatory of the Russian Academy of Sciences (SAO RAS). We estimated the oxygen, nitrogen, sulphur, neon and argon abundances in individual H II regions and found the average metallicity in the galaxy to be $Z \simeq 0.1$ or $0.3\,Z_{\odot}$, depending on the estimation method employed. We used these observations combined with the results of our earlier studies of the irregular galaxy IC 10 and the blue compact dwarf galaxy VII Zw 403 to compare the currently most popular methods of gas metallicity estimation in order to select from among them the techniques that are most reliable for analysing irregular galaxies. To this end, we used the 'direct' $T_{\rm e}$ method and six empirical and theoretical methods. The results of our observations mostly confirmed the conclusions of López-Sánchez et al. based on the analysis of systematic deviations of metallicity estimates derived by applying different methods to 'model' H II regions.

Key words: techniques: spectroscopic – ISM: abundances – H II regions – galaxies: individual: Holmberg II – galaxies: ISM – galaxies: irregular.

1 INTRODUCTION

The irregular galaxy Holmberg II (Ho II, DDO 50, UGC4305, PGC 23324, VII Zw 223) currently serves as an ideal target for the study of the entire range of phenomena associated with the effects of radiation, stellar winds, and supernova explosion feedback, which determine the structure, kinematics and chemical composition of the interstellar medium as well as the process of star formation in irregular galaxies.

This gas-rich, non-interacting and rigidly rotating galaxy is a member of the M81 group and is located at a distance of $D = 3.39 \pm 0.20$ Mpc (Karachentsev et al. 2003). It is an Im (i.e. Magellanic-type irregular) galaxy with parameters $M_B = -16.71 \pm 0.16$ mag, $B - V = 0.11 \pm 0.05$, $E(B - V) = 0.032$, and an inclination angle of $i = 38^{\circ}$ (Moustakas et al. 2010).

The large-scale structure of the galaxy has been well studied in the optical, radio, infrared (IR), ultraviolet (UV) and X-ray bands. A total of about 40 giant cavities and slowly expanding H I supershells have been found (see Bagetakos et al. 2011 and references therein). The stellar population of Ho II has been thoroughly studied using *Hubble Space Telescope* (*HST*) data (see, for example, Weisz et al. 2009 and Cook et al. 2012).

A total of 82 H II regions have been found in Ho II (Hodge, Strobel & Kennicutt 1994), and for the sake of consistency we use HSK numbers to identify them throughout this paper.

Bright emission nebulae reside mostly in the 'walls' of giant H I supershells and are concentrated in several 'chains' of complexes of ongoing star formation, with the brightest nebulae located in the eastern chain (see Fig. 1 and figures in Hunter, Hawley & Gallagher 1993 and Karachentsev & Kaisin 2007). Stewart et al. (2000) estimate these star-forming regions to be between 2.4 and more than 6.3 Myr old. The large-scale distribution of the Hα emission of ionized gas is consistent with that of far ultraviolet (FUV) emission in the galaxy (see, for example, fig. 6 of Stewart et al. 2000 and fig. 29 of Weisz et al. 2009). The brightest emission of heated dust is observed in the eastern chain of the brightest nebulae (Walter et al. 2007).

Radio observations of the galaxy (Tonque & Westphal 1995; Braun et al. 2007; Heald, Braun & Edmonds 2009) revealed continuum radio emission from the region of bright emission nebulae and, in particular, from the brightest eastern chain. The polarized radio emission is also coincident with this chain (Heald et al. 2009). Tonque & Westphal (1995) identified a synchrotron component of radio emission in the eastern chain of bright nebulae, and this led them to suspect that the region may contain supernova remnants.

The main goal of this work was to perform a detailed study of the emission spectrum and estimate the metallicity of ionized gas in Ho II by analysing the spectroscopic observations made with the 6-m telescope of the Special Astrophysical Observatory of

⋆ E-mail: egorov@sai.msu.ru

© 2012 The Authors
Published by Oxford University Press on behalf of the Royal Astronomical Society

Downloaded from http://mnras.oxfordjournals.org/ by guest on January 25, 2013

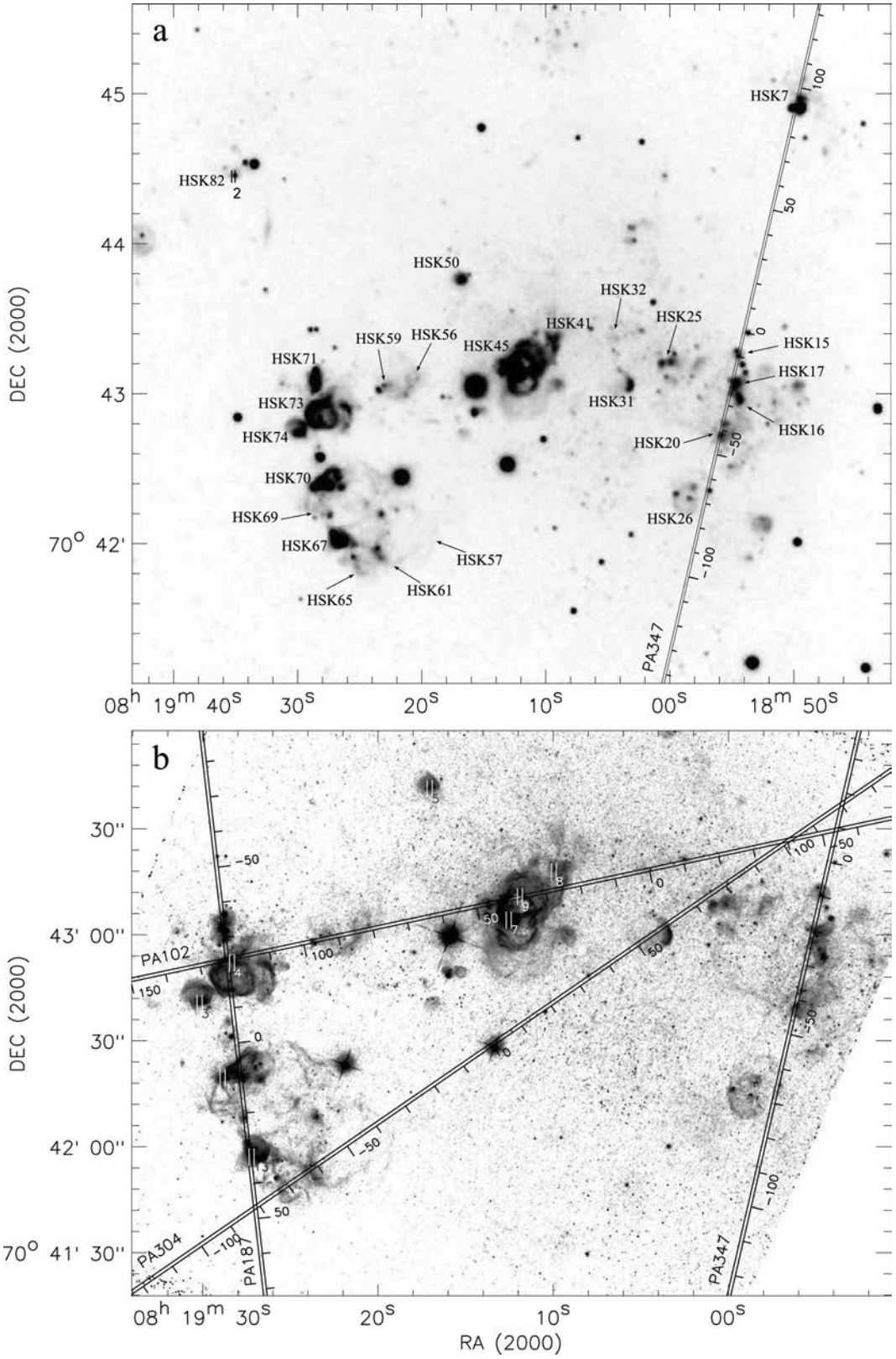

Figure 1. The Hα+continuum images of Ho II: (a) shows the image taken with the 2.1-m KPNO telescope; (b) shows an archival *HST* image (F658N/ACS WFC)). Panel (a) gives the designations of all H II regions discussed in this paper (denoted by the HSK numbers from the catalogue of Hodge et al. 1994) and shows the position of the spectrograph slit PA347 used in our observations and the position of slit no. 2 in observations of Croxall et al. (2009). Panel (b) shows the positions of the spectrograph slits in our observations; the short white line segments indicate the locations of the Croxall et al. (2009) spectrograms marked by their numbers in accordance with the above paper.

Downloaded from http://mnras.oxfordjournals.org/ by guest on January 25, 2013

the Russian Academy of Sciences (SAO RAS). We also used the available results of earlier spectroscopic observations of the galaxy made by Lee et al. (2003) and Croxall et al. (2009) combined with *HST* archival imaging data to estimate the metallicity in the same way.

We used the seven currently most popular methods to estimate the oxygen abundance, which determines the metallicity of the interstellar medium. Our aim was to compare different techniques by applying them to the observations of a large number of H II regions in the Ho II, IC 10 and VII Zw 403 galaxies in order to choose the optimal method for analysing the metallicity of gas in irregular galaxies.

We also attempted to detect the optical emission from the above-mentioned hypothetical supernova remnants using the $I([\mathrm{S\,II}])/I(\mathrm{H}\alpha)$ line intensity ratio in the spectrum.

The following section describes our observations and the data reduction technique; we then present the results, a discussion, and the main conclusions.

We defer a comparison of the results of spectroscopic observations with a detailed analysis of the kinematics of ionized and neutral gas and with IR emission of the dust component of the galaxy to our forthcoming paper.

2 OBSERVATIONS AND DATA REDUCTION

The observations were made at the prime focus of the SAO RAS 6-m telescope using the SCORPIO multi-mode focal reducer (Afanasiev & Moiseev 2005) and its new version SCORPIO-2 (Afanasiev & Moiseev 2011). When operated in the long-slit mode, both devices have the same slit size (6 arcmin × 1 arcsec) with a scale of 0.36 arcsec per pixel. However, for a similar spectral resolution, SCORPIO-2 provides a twice larger spectral range: the VPHG940@600 grism covers the wavelength interval from 3700 to 8500 Å, whereas with SCORPIO we used two grisms, namely VPHG1200B and VPHG1200R for the green and red spectral regions, respectively. The CCDs employed were an EEV 42-40 in SCORPIO and an E2V 42-90 (with the sensitivity peak at redder wavelengths) in SCORPIO-2.

Table 1 gives the log of observations: for each spectrum, designated by the position angle of the spectrograph slit, it lists the observing date, grism employed, spectral range $\Delta\lambda$, spectral resolution $\delta\lambda$ [estimated by the full width at half-maximum (FWHM) of air glow lines], total exposure T_{exp}, and seeing.

Data reduction was performed in a standard way using the IDL software package developed at the SAO RAS for reducing the long-slit spectroscopic data obtained with SCORPIO and SCORPIO-2.

To increase the signal-to-noise ratio for weak emission nebulae, we binned spectrograms into 5–6 pixel bins along the slit prior to reduction. The binning size was chosen to make the resulting spatial resolution for a single slit position consistent with the maximum 'seeing'. To compute the correction for the spectral sensitivity of each grism and convert the spectra to the absolute intensity scale, we observed the spectrophotometric standards Hz 44, Feige 34 and AGK+81d266 immediately after the object at a close zenith distance.

We used single- or two-component Gaussian fitting to measure the integrated fluxes of emission lines. We estimated the errors of the measured fluxes by analysing the synthetic spectra with the given signal-to-noise ratio. In this paper we use only spectral lines with a signal-to-noise ratio greater than 3. The error intervals listed in the tables and indicated in the figures below correspond to the 3σ confidence level.

3 RESULTS OF OBSERVATIONS

Fig. 1 shows the locations of six spectrograms taken at four slit positions, designated PA102, PA187, PA304 and PA347 in accordance with their position angles. The two panels of the figure show the Hα images of the star-forming regions of the galaxy. The upper image was taken with the 2.1-m KPNO telescope within the framework of the SINGS survey (Kennicutt et al. 2003), and the lower image was taken by the *HST* (application number 10522) and extracted from the *Hubble* Legacy Archive .[1]

In the north–south direction, the PA187 spectrogram crosses the following H II regions (named according to the catalogue of Hodge et al. 1994): HSK 71, HSK 73, HSK 70 (the nebula surrounding an ultraluminous X-ray source – ULX Holmberg II X-1), HSK 69 and HSK 67. The PA102 slit crosses the H II regions HSK 32, HSK 41, HSK 45, HSK 56, HSK 59 and HSK 73. The PA347 slit covers the western chain of H II regions: HSK 7, HSK 15, HSK 17, HSK 16, HSK 20 and HSK 26. The PA304 spectrogram is least informative, because it crosses faint H II regions, namely HSK 65, HSK 61, HSK 57, HSK 31 and HSK 25.

Fig. 2 shows examples of spectrograms taken with different grisms. The top panel shows the integrated spectrum of the part of the HSK73 H II region crossed by the PA187 slit (positions ranging from −21.4 to −17.3 arcsec along the slit) taken with the VPHG1200B grism. It is the region where we found the brightest He II λ4686 emission line (see Section 4). The middle panel shows the integrated spectrum of the eastern boundary of HSK45, which is the brightest nebula in the galaxy, taken with the VPHG1200R grism (the PA102 spectrogram, positions ranging from 40.7 to 45.0 arcsec). The bottom panel shows the integrated spectrum of the HSK7 region taken with the VPHG940@600 grism (the PA347 spectrogram, positions ranging from 94.6 to 98.2 arcsec). The spectrum of this region has the highest quality among all the spectra taken with this grism within the framework of this study (in the vicinity of the [O II] λ3727 and [O III] λ4363 lines its signal-to-noise ratio is as high as 6–7).

Owing to the wide spectral range of the VPHG940@600 grism there is possible second-order contamination on the spectra obtained with this grism at wavelengths redder than 7000 Å. However, consideration of the continuum at this range (see, for example, the bottom panel of Fig. 2) shows that possible systematic errors of emission-line intensity measurements are no more than 12 per cent and lie within the uncertainties reported below.

To ensure the homogeneity of the inferred gas metallicities in the galaxy, we also use the relative line intensities reported by Lee et al. (2003) and Croxall et al. (2009). Lee et al. (2003) do not specify the locations of the spectra and only give the names of the H II regions studied. Fig. 1 shows the locations of the spectra taken by Croxall et al. (2009) (we adopt the coordinates from the author-corrected astro-ph electronic version of the paper). The spectrograms are numbered in accordance with Croxall et al. (2009).

Table 2 lists our estimated relative emission-line intensities in the individual H II regions. We determined these intensities by integrating the spectrum along the part of the nebula crossed by the slit. The intensities are measured relative to the Hβ line intensity assuming that $I(\mathrm{H}\beta) = 100$.

We obtained two spectrograms for the PA187 slit. One of them, as in the cases of PA304 and PA347, covers the entire spectral range from the blue to the red, whereas the other contains only

[1] http://hla.stsci.edu/

Downloaded from http://mnras.oxfordjournals.org/ by guest on January 25, 2013

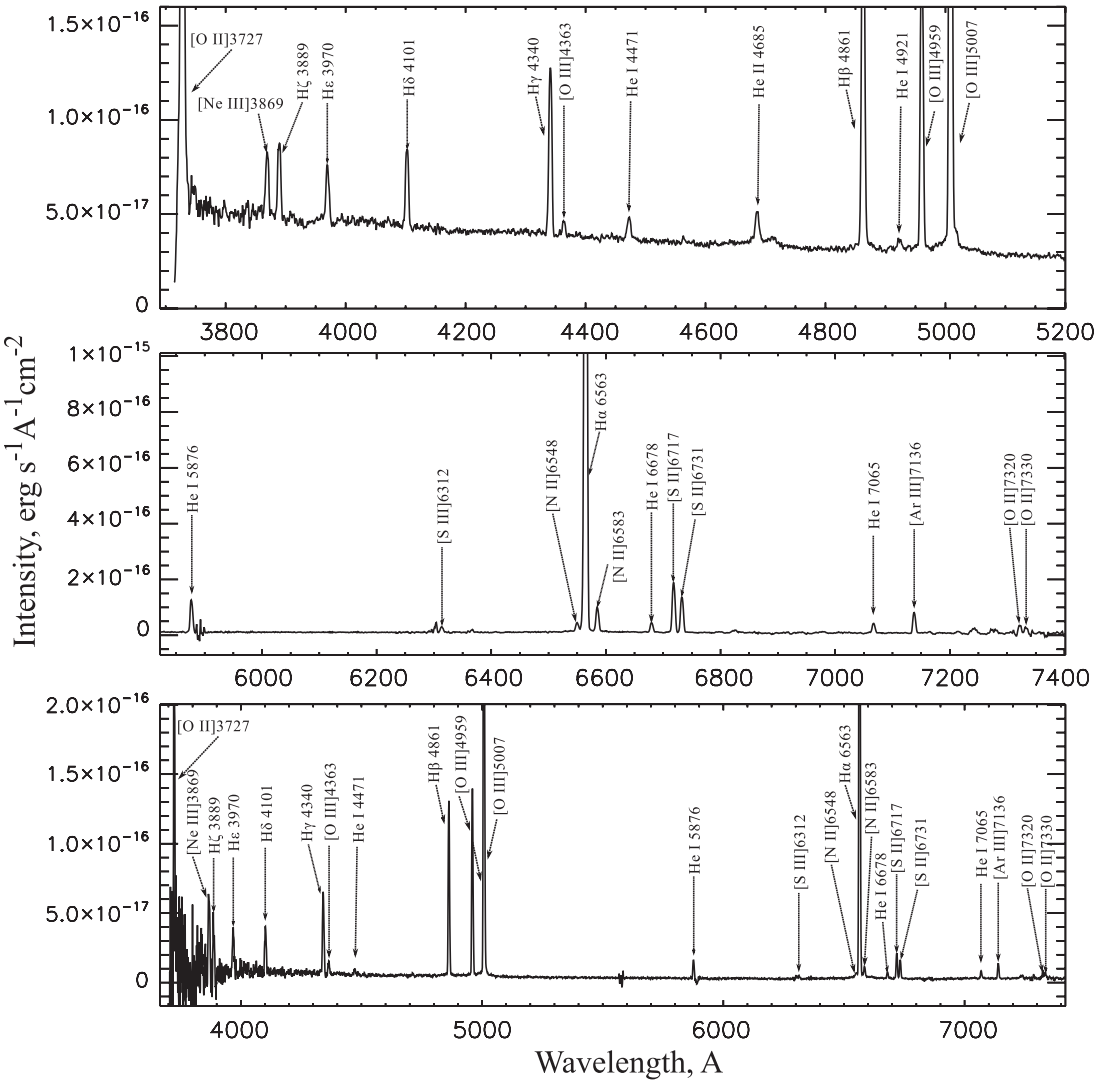

Figure 2. Examples of spectra taken with different SCORPIO/SCORPIO-2 grisms. The top panel shows the region between −21.4 and −17.3 arcsec along the PA187 slit (the central part of the HSK73 nebula, which exhibits bright emission in the He II λ4686 line) observed with the VPHG1200B grism; the middle panel shows the region between 40.7 and 45.0 arcsec along the PA102 slit (the HSK45 nebula) observed with the VPHG1200R grism; and the bottom panel shows the region between 94.6 and 98.2 arcsec along the PA347 slit (the HSK7 nebula) observed with the VPHG940@600 grism.

Table 1. Log of observations.

Spectrum (PA)	Date	Grism	Δλ (Å)	δλ (Å)	T_{exp} (s)	Seeing (arcsec)
PA102	31.10/01.11.11	VPHG1200B	3700–5500	5.5	4500	0.9
PA102	01/02.11.11	VPHG1200R	5750–7500	5.5	4800	2.2–2.7
PA187	28/29.03.11	VPHG940@600	3700–8500	6.5	2700	2.2
PA187	31.10/01.11.11	VPHG1200R	3700–5300	5.5	1800	0.9
PA304	22/23.12.11	VPHG940@600	3600–8400	6.5	3600	1.8–2.4
PA347	22/23.12.11	VPHG940@600	3700–8500	6.5	5400	1.6–2.0

the blue part of the spectrum (see Table 1). The two spectrograms were taken on different nights with varying seeing using different instruments equipped with different CCDs. Hence it is natural to ask whether the two spectra have the same intensity scale. We compared the line intensities in the blue part of the spectrum for each H II region as estimated from both spectrograms and found their intensity scales to be proportional to each other. Hence, although the line intensities measured by different spectrograms differ from each other, the ratios of the emission-line intensities to the Hβ flux are the same for both spectra within observational errors. That is why in the case of PA187 Table 2 lists relative line intensities measured either from the 'wide-range' spectrogram taken with the VPHG940@600 grism or from the spectrogram taken with the VPHG1200B grism, depending on the line wavelength. The intensities measured from spectra taken with the 'wide-range' VPHG940@600 grism are used for lines located on the red side of [O III] λ5007, and those measured from the spectra taken with the VPHG1200B grism are used for lines in the blue part of

Downloaded from http://mnras.oxfordjournals.org/ by guest on January 25, 2013

Table 2. Relative intensities of emission lines [$I(\mathrm{H}\beta) = 100$].

H II region	HSK7	HSK15	HSK16	HSK17	HSK20	HSK25	HSK26	HSK31	HSK32	HSK41	HSK45
[O II] λ3727 + λ3729	–	–	–	–	–	–	–	–	924.2 ± 68.7	360.5 ± 6.9	217.6 ± 0.6
[Ne III] λ3869	–	–	–	–	–	–	–	–	–	16.5 ± 4.2	26.8 ± 1.1
Hϵ λ3970	–	–	–	–	–	–	–	–	–	16.4 ± 3.1	21.6 ± 2.6
Hδ λ4104	20.5 ± 5.6	–	–	–	–	–	–	–	–	22.9 ± 0.9	24.0 ± 1.1
Hγ λ4340	38.1 ± 0.9	51.1 ± 27.3	42.6 ± 6.0	38.7 ± 4.2	38.6 ± 14.5	–	–	40.6 ± 5.1	35.7 ± 18.3	47.5 ± 1.3	46.3 ± 1.6
[O III] λ4363	8.5 ± 1.0	–	–	–	–	–	–	–	–	3.7 ± 0.6	6.5 ± 0.5
He I λ4471	3.2 ± 0.7	–	–	–	–	–	–	–	–	3.0 ± 0.7	3.5 ± 0.2
He II λ4686	–	–	–	–	–	–	–	–	–	–	–
He I λ4921	–	–	–	–	–	–	–	–	–	0.86 ± 0.22	0.88 ± 0.47
[O III] λ5007	425.4 ± 17.8	160.4 ± 8.4	205.9 ± 7.2	220.69 ± 16.9	101.4 ± 10.5	113.5 ± 2.2	48.5 ± 106.2	329.3 ± 4.1	86.3 ± 6.9	174.9 ± 2.0	357.8 ± 2.1
[O III] λ4959	139.8 ± 6.8	53.0 ± 3.5	69.3 ± 3.0	74.4 ± 6.7	33.2 ± 4.2	35.4 ± 1.4	14.5 ± 41.0	109.0 ± 1.8	29.1 ± 3.0	58.5 ± 0.9	124.2 ± 0.9
He I λ5876	11.0 ± 0.2	–	–	13.2 ± 1.3	15.1 ± 1.0	20.8 ± 0.7	–	22.9 ± 0.6	20.4 ± 1.8	10.9 ± 0.9	11.1 ± 0.5
[S III] λ6312	1.6 ± 0.4	3.9 ± 0.8	2.6 ± 0.4	1.8 ± 1.0	2.1 ± 0.4	–	–	–	–	–	1.5 ± 0.1
[N II] λ6548	2.0 ± 0.3	3.5 ± 1.9	2.8 ± 0.7	3.0 ± 0.3	3.6 ± 0.5	5.2 ± 0.6	9.6 ± 3.5	5.3 ± 3.6	4.1 ± 3.1	4.0 ± 0.6	3.0 ± 0.1
Hα λ6563	280.9 ± 7.4	249.0 ± 10.7	282.3 ± 6.9	279.6 ± 5.6	280.1 ± 9.6	279.8 ± 3.7	281.5 ± 8.9	280.5 ± 4.2	280.9 ± 22.0	280.9 ± 9.1	280.9 ± 13.6
[N II] λ6583	3.7 ± 0.4	10.9 ± 4.7	9.1 ± 1.7	8.1 ± 0.5	11.3 ± 1.0	11.9 ± 0.5	19.8 ± 2.5	11.9 ± 6.4	12.1 ± 7.2	12.5 ± 1.4	8.2 ± 0.2
He I λ6678	2.6 ± 0.1	–	–	2.4 ± 2.1	–	–	–	2.6 ± 0.8	–	2.5 ± 0.8	3.0 ± 0.1
[S II] λ6717	7.0 ± 0.1	16.5 ± 2.3	20.0 ± 1.0	14.8 ± 0.4	30.1 ± 2.4	33.7 ± 1.3	39.3 ± 6.8	25.8 ± 1.3	33.7 ± 4.6	34.3 ± 1.0	17.8 ± 0.2
[S II] λ6731	5.2 ± 0.1	11.4 ± 2.1	13.9 ± 1.0	10.9 ± 0.5	20.9 ± 2.1	23.8 ± 1.5	28.2 ± 6.9	18.4 ± 1.2	27.9 ± 5.1	24.2 ± 0.9	12.7 ± 0.2
He I λ7065	–	–	–	1.5 ± 0.5	–	–	–	1.8 ± 0.4	–	2.2 ± 0.2	2.8 ± 0.2
[Ar III] λ7136	4.6 ± 0.4	2.8 ± 1.6	4.1 ± 0.6	4.3 ± 2.4	2.5 ± 4.2	3.7 ± 0.6	–	7.0 ± 1.3	–	3.7 ± 0.7	5.5 ± 0.1
[O II] λ7320	1.5 ± 0.1	–	3.6 ± 0.2	3.2 ± 0.2	4.3 ± 0.2	–	–	–	–	3.4 ± 0.2	2.8 ± 0.1
[O II] λ7330	1.2 ± 0.1	–	2.8 ± 0.5	2.1 ± 0.3	2.9 ± 0.4	–	–	–	–	3.0 ± 0.4	2.2 ± 0.1

H II region	HSK56	HSK57	HSK59	HSK61	HSK65	HSK67	HSK69	HSK70	HSK71	HSK73 (PA187)	HSK73 (PA102)
[O II] λ3727 + λ3729	252.0 ± 8.2	–	267.5 ± 6.1	–	–	171.05 ± 4.1	272.1 ± 5.1	239.9 ± 6.7	205.6 ± 2.3	282.9 ± 2.4	204.1 ± 1.8
[Ne III] λ3869	28.5 ± 8.4	–	14.4 ± 1.0	–	–	19.3 ± 4.3	7.5 ± 4.6	24.7 ± 2.1	21.9 ± 3.7	19.2 ± 5.0	23.0 ± 3.0
Hϵ λ3970	16.3 ± 10.6	–	14.8 ± 9.8	–	–	20.5 ± 0.3	16.7 ± 2.9	21.4 ± 8.6	21.0 ± 2.3	20.3 ± 6.0	20.1 ± 1.9
Hδ λ4104	20.3 ± 1.5	–	20.5 ± 0.5	–	–	23.9 ± 1.8	25.3 ± 1.7	24.7 ± 1.6	23.8 ± 0.9	24.9 ± 1.3	23.1 ± 1.0
Hγ λ4340	47.4 ± 3.1	–	47.4 ± 1.7	31.6 ± 8.9	42.3 ± 47.3	45.9 ± 2.1	50.1 ± 3.7	47.5 ± 1.9	46.9 ± 2.3	49.1 ± 2.5	47.4 ± 1.3
[O III] λ4363	5.9 ± 0.4	–	–	–	–	5.2 ± 1.4	1.5 ± 0.3	5.6 ± 0.7	5.7 ± 0.6	4.0 ± 3.5	6.3 ± 0.9
He I λ4471	–	–	2.3 ± 3.4	–	–	3.5 ± 0.6	3.8 ± 0.8	3.3 ± 0.5	3.3 ± 0.3	5.4 ± 0.8	3.8 ± 0.2
He II λ4686	–	–	–	–	–	–	–	1.8 ± 0.3	–	4.3 ± 1.1	–
He I λ4921	2.71 ± 0.43	–	–	–	–	0.81 ± 0.72	–	–	0.69 ± 0.36	1.45 ± 0.62	1.37 ± 0.70
[O III] λ5007	292.9 ± 1.9	90.6 ± 6.4	182.5 ± 1.9	206.1 ± 2.7	126.3 ± 2.2	297.1 ± 2.2	119.1 ± 2.5	293.4 ± 1.6	332.4 ± 3.8	223.1 ± 1.9	263.4 ± 2.1
[O III] λ4959	98.7 ± 0.8	40.2 ± 5.6	61.2 ± 0.8	67.7 ± 1.8	42.1 ± 1.1	99.3 ± 0.9	39.4 ± 1.0	97.9 ± 0.7	107.6 ± 1.5	73.0 ± 0.8	89.2 ± 0.9
He I λ5876	13.1 ± 0.8	93.0 ± 1.9	9.8 ± 1.5	33.5 ± 0.9	20.1 ± 1.0	10.1 ± 0.3	13.4 ± 1.5	9.7 ± 1.0	10.4 ± 1.3	14.2 ± 1.1	11.4 ± 0.8
[S III] λ6312	–	–	–	–	5.8 ± 4.9	1.6 ± 1.3	–	1.3 ± 0.2	1.2 ± 0.1	1.8 ± 2.0	–
[N II] λ6548	2.7 ± 0.9	9.5 ± 2.6	2.1 ± 0.3	3.7 ± 0.9	2.0 ± 0.3	1.7 ± 0.2	4.0 ± 2.0	2.0 ± 0.2	2.6 ± 0.2	3.9 ± 0.3	2.2 ± 0.2
Hα λ6563	280.9 ± 10.7	279.5 ± 25.3	280.9 ± 9.6	282.4 ± 12.4	279.7 ± 4.3	275.7 ± 8.0	335.3 ± 9.1	280.5 ± 3.4	279.5 ± 6.6	293.7 ± 3.7	280.9 ± 10.0
[N II] λ6583	8.7 ± 2.1	13.6 ± 1.3	8.9 ± 1.0	7.5 ± 0.7	6.5 ± 0.4	3.9 ± 0.3	6.4 ± 1.7	6.1 ± 0.4	5.9 ± 0.2	8.5 ± 0.5	6.4 ± 0.4
He I λ6678	–	–	–	–	2.4 ± 0.5	2.5 ± 1.4	–	2.3 ± 0.2	2.7 ± 0.6	4.1 ± 1.5	2.3 ± 0.3
[S II] λ6717	23.6 ± 1.3	27.9 ± 30.2	21.3 ± 1.3	17.3 ± 12.0	19.7 ± 0.6	8.3 ± 0.3	19.0 ± 1.8	15.6 ± 0.4	11.0 ± 0.2	18.8 ± 1.1	19.0 ± 0.4
[S II] λ6731	14.9 ± 1.0	21.4 ± 29.6	15.1 ± 1.2	13.1 ± 11.5	14.4 ± 0.9	5.8 ± 0.3	12.9 ± 2.0	10.7 ± 0.4	8.0 ± 0.2	13.0 ± 0.9	12.8 ± 0.3
He I λ7065	–	–	–	–	1.3 ± 0.5	2.0 ± 0.7	–	1.6 ± 0.3	2.5 ± 0.9	4.1 ± 1.3	–
[Ar III] λ7136	4.5 ± 1.4	–	3.6 ± 0.4	4.6 ± 1.0	3.5 ± 0.6	3.9 ± 0.4	–	3.7 ± 0.4	4.5 ± 0.9	4.6 ± 3.3	3.8 ± 0.6
[O II] λ7320	–	–	6.9 ± 0.3	–	–	1.9 ± 0.1	–	2.1 ± 0.1	2.3 ± 2.1	2.7 ± 0.2	3.4 ± 0.1
[O II] λ7330	–	–	5.3 ± 0.6	–	–	1.5 ± 0.2	–	1.6 ± 0.3	1.9 ± 2.3	2.3 ± 0.4	1.6 ± 0.1

Downloaded from http://mnras.oxfordjournals.org/ by guest on January 25, 2013

the spectrum, where the sensitivity of the VPHG940@600 grism decreases.

The situation with PA102 is more complicated, because in this case two spectrograms were taken for the blue and red parts of the spectrum and their spectral ranges do not overlap, preventing a similar comparison. Therefore in order to correctly estimate the ratios of line intensities on the red side of [O III] λ5007 to Hβ, we calculated the ratios of the corresponding line intensities to Hα and used the 'theoretical' $I(\mathrm{H}\alpha)/I(\mathrm{H}\beta) = 2.809$ ratio for the average electron temperature $T_\mathrm{e} = 13000$ K (Osterbrock & Ferland 2006).

The line intensity ratios listed in Table 2 are reddening-corrected. We determined the $E(B-V)$ colour index from the Balmer decrement using the theoretical intensity ratios $I(\mathrm{H}\alpha)/I(\mathrm{H}\beta) = 2.809$ and $I(\mathrm{H}\gamma)/I(\mathrm{H}\beta) = 0.4745$ for the electron temperature $T_\mathrm{e} = 13\,000$ K (Osterbrock & Ferland 2006) and the extinction curve of Cardelli, Clayton & Mathis (1989) as parametrized by Fitzpatrick (1999). For the PA102 slit we used only the $I(\mathrm{H}\gamma)/I(\mathrm{H}\beta)$ ratio. The resulting $E(B-V)$ extinction values are listed in Table 3.

Our inferred colour excesses $E(B-V)$ are greater than the $E(B-V) = 0.06 \pm 0.04$ estimate reported by Croxall et al. (2009). We obtained a similar extinction value $E(B-V) = 0.03$ towards Ho II from the extinction map based on the data of the IR sky survey (Schlegel, Finkbeiner & Davis 1998).

The mean colour index averaged over all our spectrograms is $E(B-V) = 0.17 \pm 0.08$. It differs from the estimate of Croxall et al. (2009), possibly because of the use of different extinction laws. Our inferred $E(B-V)$ value possibly corresponds to the stronger local extinction, because all the bright H II regions studied are located in the direction of the maximum H I column density in the 'walls' of a giant cavity, and, most likely, are partially embedded in this dense supershell.

3.1 Estimation of electron density and temperature

Our electron density n_e and electron temperature T_e estimates for a number of H II regions in Ho II have large uncertainties.

Table 3 lists the electron densities n_e for each H II region derived from the [S II] λ6717/λ6731 line intensity ratio. This line intensity ratio proved to be very close to the limiting value for low densities, and therefore in a number of H II regions we could determine n_e only very approximately.

We determined the electron temperatures in H II regions in terms of the so-called two-zone model, assuming that T_e in the low- and high-ionization zones is the same for all ions whose radiation emerges from these regions. Correspondingly, we assume that the temperature in the high-ionization region (for the O^{2+} and Ne^{2+} ions) is equal to T_e(O III), and that the temperature in the low-ionization region (for the O^+, N^+ and S^+ ions) is equal to T_e(O II). We also adopt the common extension of the model proposed by Garnett (1992), which assumes that the temperature inside the region of the S^{2+} and Ar^{2+} emission is equal to the temperature T_e(S III).

We calculate the T_e(O III) temperature from the [O III] (λ4959 + λ5007)/[O III] λ4363 line intensity ratio (Osterbrock & Ferland 2006). However, because of the low intensity of the [O III] λ4363 line we could determine T_e(O III) accurately enough only for 10 H II regions (including two different parts of the HSK73 nebula) using the relation of Pilyugin, Vílchez & Thuan (2010):

$$t = \frac{1.467}{\log Q_3 - 0.867 - 0.193 \log t + 0.033t},$$

where $Q_3 = I_{[\mathrm{O\,III}](\lambda4959+\lambda5007)}/I_{[\mathrm{O\,III}]\lambda4363}$ and $t = 10^{-4}T_\mathrm{e}(\mathrm{O\,III})$.

We estimate the T_e(O II) temperature in low-ionization regions with the [O II] (λ3727 + λ3729)/[O II] (λ7320 + λ7330) line intensity ratio using the following relation of Pilyugin et al. (2009):

$$t_2 = \frac{0.96}{\log Q_2 - 0.86 - 0.38 \log t_2 + 0.053t_2 + \log(1 + 14.9x)},$$

where $x = 10^{-4} n_\mathrm{e} t_2^{-1/2}$, $t_2 = 10^{-4}T_\mathrm{e}(\mathrm{O\,II})$, and $Q_2 = I_{[\mathrm{O\,II}](\lambda3727+\lambda3729)}/I_{[\mathrm{O\,II}](\lambda7320+\lambda7330)}$.

While determining T_e(O II) we had to address a number of problems. First, in observations of nearby objects, such as Ho II, the [O II] λ7320 + λ7330 emission feature falls within the domain of strong atmospheric hydroxyl absorption lines, which reduces the accuracy of the intensity measurements for these lines and hence that of the inferred T_e(O II). Our failure to properly subtract the contribution of the air glow lines in the spectra of some H II regions makes the corresponding [O II] λ7320 + λ7330 intensity estimates less reliable.

Second, the sensitivity of the CCD used in half of the observations decreases sharply in the blue part of the spectrum. This prevented us from measuring the [O II] λ3727 + λ3729 lines accurately enough in the PA304 and PA347 spectra, making it impossible to calculate T_e(O II). In the case of the PA102 and PA187 spectra we derived the temperature in the low-ionization regions in only four H II regions, where the signal-to-noise ratio in the [O II] λ7320 + λ7330 lines was greater than 4.

We thus could 'directly' determine the electron temperatures in both the low- and high-ionization regions only in HSK45, HSK67, HSK71 and HSK73. However, even in these nebulae the inferred T_e(O II) estimates are not accurate and probably represent the upper temperature limits for the corresponding regions. We therefore used empirical methods to infer the temperatures in low-ionization regions in the cases where we could determine T_e(O III).

Many methods are known for the empirical determination of electron temperature in low-ionization regions from the known T_e(O III) temperature. Hägele et al. (2008) compared some of the methods used to estimate the temperature in the O^+ emission region. Pérez-Montero & Díaz (2003) pointed out that this temperature is strongly dependent not only on T_e(O III) but also on the electron density n_e. This imposes strong constraints on the applicability of the empirical dependence of the T_e(O II) on T_e(O III). In particular, we did not use the dependence of T_e(O II) on T_e(O III) found by Pérez-Montero & Díaz (2003) for three electron density values, $n_\mathrm{e} = 10$, 100 and 500 cm^{-3}, because of the above-mentioned low accuracy of the estimated n_e.

Stasińska (1980, 1990) proposed a method that gained widespread popularity. Izotov et al. (2006) proposed determining the temperature in regions with ionization higher and lower than in the O^{2+} emission region using a technique depending on the gas metallicity. Furthermore, Pilyugin et al. (2009) proposed an empirical formula for estimating T_e(O II) and T_e(N II) from T_e(O III). These authors pointed out that the T_e(N II) value should be preferred for the low-ionization regions because of its lower dispersion. López-Sánchez et al. (2012) proposed a calibration based on the model spectra of H II regions.

We used all the above-mentioned methods to determine the temperatures in the low-ionization regions. We found the calibration of López-Sánchez et al. (2012) to be the most consistent with the estimate determined from the spectra of four H II regions, which represents an upper limit for the T_e(O II) temperature in these

Downloaded from http://mnras.oxfordjournals.org/ by guest on January 25, 2013

Table 3. Physical properties of ionized gas and elemental abundances in H II regions.

H II region	HSK7	HSK15	HSK16	HSK17	HSK20	HSK25	HSK26	HSK31	HSK32	HSK41	HSK41	HSK45
Reference	PA347	PA347	PA347	PA347	PA347	PA304	PA347	PA304	PA102	PA102	Cr8	PA102
$E(B-V)$, mag	0.19 ± 0.04	–	0.10 ± 0.03	0.25 ± 0.03	0.19 ± 0.05	0.34 ± 0.11	0.13 ± 0.03	0.16 ± 0.02	0.41 ± 0.10	0.15 ± 0.06	–	0.18 ± 0.06
n_e, cm^{-3}	80 ± 10	–	10 ± 40	70 ± 30	10 ± 80	20 ± 40	40 ± 190	40 ± 50	220 ± 200	20 ± 30	180 ± 140	30 ± 10
T_e([O III]), K	15200 ± 900	–	–	–	–	–	–	–	–	15600 ± 1100	–	14600 ± 400
T_e([O II]), K	12300 ± 600	–	–	–	–	–	–	–	–	12200 ± 700	–	12200 ± 300
T_e([S III]), K	15400 ± 1100	–	–	–	–	–	–	–	–	15100 ± 1100	–	14700 ± 500
$12+\log(O^+/H^+)$	–	–	–	–	–	–	–	–	–	7.75 ± 0.08	–	7.53 ± 0.03
$12+\log(O^{2+}/H^+)$	7.66 ± 0.06	–	–	–	–	–	–	–	–	7.25 ± 0.07	–	7.64 ± 0.03
$12+\log(O/H)$ (T_e)	–	–	–	–	–	–	–	–	–	7.87 ± 0.07	–	7.89 ± 0.02
$12+\log(O/H)$ (PT05)	–	–	–	–	–	–	–	–	–	–	–	7.90 ± 0.01
$12+\log(O/H)$ (ONS)	–	–	–	–	–	–	–	–	7.71 ± 0.08	7.91 ± 0.01	7.88 ± 0.04	7.83 ± 0.01
$12+\log(O/H)$ (ON)	–	–	–	–	–	–	–	–	7.33 ± 0.16	7.68 ± 0.03	7.71 ± 0.04	7.87 ± 0.01
$12+\log(O/H)$ (NS)	7.76 ± 0.03	7.63 ± 0.10	7.68 ± 0.05	7.69 ± 0.03	7.45 ± 0.04	7.53 ± 0.02	7.34 ± 0.73	7.97 ± 0.12	7.41 ± 0.14	7.70 ± 0.03	7.72 ± 0.03	7.89 ± 0.02
$12+\log(O/H)$ (PP04)	–	8.23 ± 0.06	8.15 ± 0.03	8.13 ± 0.01	8.28 ± 0.02	8.27 ± 0.01	8.46 ± 0.30	8.12 ± 0.07	8.31 ± 0.08	8.22 ± 0.02	8.23 ± 0.02	–
$12+\log(O/H)$ (KK04)	–	–	–	–	–	–	–	–	–	8.26 ± 0.09	8.16 ± 0.27	8.23 ± 0.04
$12+\log(N^+/H^+)$	5.66 ± 0.06	–	–	–	–	–	–	–	–	6.12 ± 0.06	–	5.95 ± 0.02
$12+\log(N/H)$ (T_e)	6.29 ± 0.07	–	–	–	–	–	–	–	–	6.29 ± 0.07	–	6.36 ± 0.03
$12+\log(N/H)$ (ONS)	–	–	–	–	–	–	–	–	5.78 ± 0.27	6.31 ± 0.05	6.40 ± 0.06	6.36 ± 0.01
$12+\log(N/H)$ (ON)	–	–	–	–	–	–	–	–	5.46 ± 0.23	6.13 ± 0.04	6.28 ± 0.05	6.36 ± 0.01
$12+\log(N/H)$ (NS)	6.32 ± 0.03	6.23 ± 0.12	6.21 ± 0.09	6.25 ± 0.03	5.96 ± 0.08	6.05 ± 0.02	5.93 ± 0.70	6.51 ± 0.14	5.92 ± 0.16	6.20 ± 0.03	6.25 ± 0.03	6.41 ± 0.01
$\log(N/O)$ (T_e)	–	–	–	–	–	–	–	–	–	−1.63 ± 0.10	–	−1.56 ± 0.03
$\log(N/O)$ (ONS)	–	–	–	–	–	–	–	–	−1.93 ± 0.28	−1.60 ± 0.05	−1.48 ± 0.08	−1.47 ± 0.01
$\log(N/O)$ (ON)	–	–	–	–	–	–	–	–	−1.87 ± 0.28	−1.55 ± 0.05	−1.44 ± 0.06	−1.51 ± 0.01
$\log(N/O)$ (NS)	−1.44 ± 0.04	−1.41 ± 0.16	−1.47 ± 0.07	−1.44 ± 0.04	−1.48 ± 0.06	−1.48 ± 0.02	−1.41 ± 1.01	−1.46 ± 0.19	−1.50 ± 0.21	−1.50 ± 0.04	−1.48 ± 0.04	−1.47 ± 0.01
$12+\log(S^+/H^+)$	5.24 ± 0.04	–	–	–	–	–	–	–	–	5.92 ± 0.05	–	5.64 ± 0.02
$12+\log(S^{2+}/H^+)$	5.88 ± 0.13	–	–	–	–	–	–	–	–	–	–	5.91 ± 0.06
$12+\log(S/H)$	6.03 ± 0.11	–	–	–	–	–	–	–	–	–	–	6.11 ± 0.04
$12+\log(Ar^{2+}/H^+)$	5.25 ± 0.06	–	–	–	–	–	–	–	–	5.17 ± 0.09	–	5.36 ± 0.03
$12+\log(Ar/H)$	5.28 ± 0.06	–	–	–	–	–	–	–	–	5.23 ± 0.10	–	5.39 ± 0.03
$12+\log(Ne^+/H^+)$	6.98 ± 0.75	–	–	–	–	–	–	–	–	6.60 ± 0.14	–	6.89 ± 0.04
$12+\log(Ne/H)$	7.04 ± 0.75	–	–	–	–	–	–	–	–	6.93 ± 0.14	–	7.05 ± 0.04

H II region	HSK45	HSK45	HSK50	HSK56	HSK57	HSK59	HSK61	HSK65	HSK67	HSK67	HSK67	HSK69
Reference	Cr7	Cr9	Cr5	PA102	PA304	PA102	PA304	PA304	PA187	Cr13	Lee	PA187
$E(B-V)$, mag	–	–	–	0.15 ± 0.14	0.12 ± 0.12	0.10 ± 0.08	0.07 ± 0.06	0.06 ± 0.02	0.09 ± 0.07	–	–	0.15 ± 0.10
n_e, cm^{-3}	70 ± 100	40 ± 100	110 ± 120	–	120 ± 1320	20 ± 60	100 ± 820	60 ± 30	20 ± 40	–	–	–
T_e([O III]), K	13300 ± 600	14500 ± 1200	13400 ± 800	15200 ± 400	–	–	–	–	14300 ± 1500	13300 ± 500	22600 ± 5700	12600 ± 1100
T_e([O II]), K	11800 ± 400	12200 ± 800	11900 ± 600	12300 ± 300	–	–	–	–	12200 ± 1100	11900 ± 400	–	11500 ± 800
T_e([S III]), K	13500 ± 800	14700 ± 1500	13600 ± 1100	14800 ± 400	–	–	–	–	14100 ± 1700	13300 ± 400	20200 ± 2400	12200 ± 1400
$12+\log(O^+/H^+)$	7.46 ± 0.06	7.56 ± 0.11	7.54 ± 0.08	7.59 ± 0.04	–	–	–	–	7.43 ± 0.13	7.13 ± 0.05	–	7.72 ± 0.11
$12+\log(O^{2+}/H^+)$	7.75 ± 0.05	7.61 ± 0.09	7.72 ± 0.07	7.50 ± 0.03	–	–	–	–	7.57 ± 0.12	7.72 ± 0.04	6.96 ± 0.21	7.33 ± 0.10
$12+\log(O/H)$ (T_e)	7.93 ± 0.04	7.89 ± 0.07	7.94 ± 0.05	7.85 ± 0.02	–	–	–	–	7.81 ± 0.09	7.82 ± 0.04	–	7.87 ± 0.09
$12+\log(O/H)$ (PT05)	7.76 ± 0.02	7.91 ± 0.03	7.84 ± 0.03	7.89 ± 0.01	–	–	–	–	7.71 ± 0.01	7.47 ± 0.02	–	–
$12+\log(O/H)$ (ONS)	7.80 ± 0.03	7.82 ± 0.04	7.72 ± 0.04	7.84 ± 0.03	–	7.74 ± 0.02	–	–	7.55 ± 0.01	7.47 ± 0.03	–	7.63 ± 0.04
$12+\log(O/H)$ (ON)	7.89 ± 0.03	7.85 ± 0.03	7.74 ± 0.04	7.78 ± 0.07	–	7.58 ± 0.03	–	–	7.58 ± 0.03	7.57 ± 0.03	–	7.39 ± 0.08
$12+\log(O/H)$ (NS)	7.89 ± 0.02	7.87 ± 0.02	7.77 ± 0.03	7.80 ± 0.06	7.57 ± 0.05	7.60 ± 0.03	7.66 ± 0.03	7.38 ± 0.02	7.61 ± 0.02	7.57 ± 0.02	–	7.42 ± 0.07
$12+\log(O/H)$ (PP04)	–	–	–	–	8.32 ± 0.02	8.17 ± 0.02	8.13 ± 0.01	8.18 ± 0.01	–	–	–	8.16 ± 0.04
$12+\log(O/H)$ (KK04)	8.15 ± 0.38	8.23 ± 0.39	8.19 ± 0.38	8.21 ± 0.11	–	8.13 ± 0.06	–	–	8.09 ± 0.06	7.94 ± 0.38	8.13 ± 0.49	8.08 ± 0.06
$12+\log(N^+/H^+)$	5.99 ± 0.04	5.98 ± 0.07	5.83 ± 0.06	5.96 ± 0.09	–	–	–	–	5.65 ± 0.09	5.53 ± 0.04	–	5.98 ± 0.13

Downloaded from http://mnras.oxfordjournals.org/ by guest on January 25, 2013

Table 3 – *continued*

H II region	HSK45	HSK45	HSK50	HSK56	HSK57	HSK59	HSK61	HSK65	HSK67	HSK67	HSK67	HSK69
Reference	Cr7	Cr9	Cr5	PA102	PA304	PA102	PA304	PA304	PA187	Cr13	Lee	PA187
$12+\log(N/H)$ (T_e)	6.49 ± 0.05	6.35 ± 0.08	6.27 ± 0.07	6.26 ± 0.09	–	–	–	–	6.08 ± 0.11	6.19 ± 0.05	–	6.17 ± 0.13
$12+\log(N/H)$ (ONS)	6.44 ± 0.05	6.35 ± 0.05	6.17 ± 0.06	6.28 ± 0.11	–	6.15 ± 0.05	–	–	5.98 ± 0.04	6.07 ± 0.05	–	6.02 ± 0.14
$12+\log(N/H)$ (ON)	6.49 ± 0.03	6.34 ± 0.04	6.15 ± 0.05	6.23 ± 0.10	–	6.02 ± 0.05	–	–	5.95 ± 0.03	6.11 ± 0.04	–	5.82 ± 0.12
$12+\log(N/H)$ (NS)	6.42 ± 0.02	6.42 ± 0.02	6.29 ± 0.03	6.30 ± 0.07	6.16 ± 0.15	6.12 ± 0.03	6.20 ± 0.09	5.87 ± 0.02	6.15 ± 0.02	6.09 ± 0.03	–	5.94 ± 0.08
$\log(N/O)$ (T_e)	-1.46 ± 0.06	-1.57 ± 0.11	-1.70 ± 0.08	-1.62 ± 0.09	–	–	–	–	-1.75 ± 0.14	-1.63 ± 0.06	–	-1.74 ± 0.16
$\log(N/O)$ (ONS)	-1.37 ± 0.06	-1.47 ± 0.07	-1.54 ± 0.07	-1.55 ± 0.11	–	-1.59 ± 0.06	–	–	-1.57 ± 0.04	-1.40 ± 0.06	–	-1.61 ± 0.14
$\log(N/O)$ (ON)	-1.40 ± 0.04	-1.51 ± 0.05	-1.58 ± 0.06	-1.55 ± 0.12	–	-1.57 ± 0.06	–	–	-1.63 ± 0.04	-1.46 ± 0.05	–	-1.58 ± 0.14
$\log(N/O)$ (NS)	-1.47 ± 0.03	-1.45 ± 0.03	-1.48 ± 0.04	-1.50 ± 0.09	-1.41 ± 0.15	-1.49 ± 0.04	-1.46 ± 0.10	-1.51 ± 0.03	-1.46 ± 0.03	-1.47 ± 0.04	–	-1.47 ± 0.11
$12+\log(S^+/H^+)$	5.66 ± 0.04	5.61 ± 0.06	5.53 ± 0.05	5.73 ± 0.03	–	–	–	–	5.31 ± 0.08	5.19 ± 0.03	–	5.71 ± 0.07
$12+\log(S^{2+}/H^+)$	6.06 ± 0.10	5.97 ± 0.17	6.15 ± 0.15	–	–	–	–	–	5.99 ± 0.41	5.88 ± 0.11	–	–
$12+\log(S/H)$	6.24 ± 0.07	6.14 ± 0.12	6.26 ± 0.12	–	–	–	–	–	6.09 ± 0.34	6.04 ± 0.09	–	–
$12+\log(Ar^{2+}/H^+)$	5.48 ± 0.06	5.30 ± 0.09	5.47 ± 0.08	5.27 ± 0.14	–	–	–	–	5.25 ± 0.10	5.28 ± 0.05	–	–
$12+\log(Ar/H)$	5.51 ± 0.06	5.34 ± 0.09	5.51 ± 0.08	5.31 ± 0.14	–	–	–	–	5.28 ± 0.10	5.32 ± 0.05	–	–
$12+\log(Ne^+/H^+)$	7.00 ± 0.06	–	–	6.86 ± 0.13	–	–	–	–	6.77 ± 0.17	6.80 ± 0.05	6.52 ± 0.24	6.54 ± 0.29
$12+\log(Ne/H)$	7.12 ± 0.06	–	–	7.07 ± 0.13	–	–	–	–	6.89 ± 0.17	6.86 ± 0.05	6.64 ± 0.24	6.88 ± 0.29
HII region	HSK69	HSK70	HSK70	HSK70	HSK71	HSK71	HSK73	HSK73	HSK73	HSK73	HSK74	HSK82
Reference	Lee	PA187	Lee	Cr11	PA187	Lee	PA187	PA102	Lee	Cr4	Cr3	Cr2
$E(B-V)$, mag	–	0.21 ± 0.09	–	–	0.27 ± 0.08	–	0.16 ± 0.09	0.16 ± 0.06	–	–	–	–
n_e, cm^{-3}	–	–	–	50 ± 90	40 ± 20	–	–	–	–	40 ± 110	60 ± 100	10 ± 120
T_e([O III]), K	17400 ± 8100	14800 ± 800	15900 ± 1600	15600 ± 1000	14200 ± 600	14800 ± 1400	14500 ± 3400	16600 ± 1100	13400 ± 2700	13400 ± 1000	14000 ± 400	12500 ± 1000
T_e([O II]), K	11000 ± 3600	12300 ± 500	12100 ± 900	12200 ± 700	12200 ± 400	12200 ± 900	12200 ± 2400	11800 ± 600	11900 ± 2000	11900 ± 700	12100 ± 300	11500 ± 800
T_e([S III]), K	16800 ± 7000	14500 ± 800	15500 ± 1500	15200 ± 1000	14300 ± 700	14400 ± 1400	14100 ± 3600	16100 ± 900	13200 ± 3400	13300 ± 1300	14400 ± 600	12600 ± 1500
$12+\log(O^+/H^+)$	7.76 ± 0.56	7.57 ± 0.06	7.48 ± 0.12	7.44 ± 0.08	7.51 ± 0.05	7.35 ± 0.12	7.64 ± 0.30	7.56 ± 0.07	7.60 ± 0.27	7.51 ± 0.10	7.10 ± 0.04	7.14 ± 0.11
$12+\log(O^{2+}/H^+)$	7.02 ± 0.46	7.53 ± 0.05	7.41 ± 0.11	7.50 ± 0.07	7.63 ± 0.04	7.54 ± 0.10	7.43 ± 0.26	7.36 ± 0.06	7.50 ± 0.23	7.62 ± 0.08	7.75 ± 0.03	7.86 ± 0.09
$12+\log(O/H)$ (T_e)	7.83 ± 0.48	7.85 ± 0.04	7.75 ± 0.08	7.77 ± 0.05	7.87 ± 0.03	7.76 ± 0.08	7.85 ± 0.21	7.78 ± 0.05	7.86 ± 0.18	7.87 ± 0.06	7.84 ± 0.03	7.93 ± 0.08
$12+\log(O/H)$ (PT05)	–	7.87 ± 0.01	7.72 ± 0.05	7.74 ± 0.02	7.83 ± 0.01	7.63 ± 0.05	–	7.75 ± 0.01	–	7.72 ± 0.02	7.57 ± 0.02	7.51 ± 0.02
$12+\log(O/H)$ (ONS)	–	7.74 ± 0.01	–	7.78 ± 0.03	7.69 ± 0.01	–	7.79 ± 0.01	7.72 ± 0.01	–	7.71 ± 0.04	7.61 ± 0.03	7.67 ± 0.03
$12+\log(O/H)$ (ON)	–	7.69 ± 0.02	–	7.83 ± 0.03	7.74 ± 0.01	–	7.69 ± 0.02	7.66 ± 0.02	–	7.72 ± 0.04	7.66 ± 0.04	7.78 ± 0.04
$12+\log(O/H)$ (NS)	–	7.72 ± 0.01	–	7.83 ± 0.02	7.77 ± 0.01	–	7.72 ± 0.01	7.68 ± 0.02	–	7.73 ± 0.03	7.66 ± 0.03	7.76 ± 0.03
$12+\log(O/H)$ (PP04)	–	–	–	–	–	–	8.13 ± 0.01	–	–	–	–	–
$12+\log(O/H)$ (KK04)	8.05 ± 0.42	8.20 ± 0.08	8.09 ± 0.53	8.12 ± 0.33	8.18 ± 0.07	8.04 ± 0.60	8.19 ± 0.04	8.11 ± 0.04	8.11 ± 0.43	8.09 ± 0.31	8.03 ± 0.45	7.99 ± 0.50
$12+\log(N^+/H^+)$	–	5.83 ± 0.04	–	5.96 ± 0.05	5.84 ± 0.03	–	6.00 ± 0.18	5.88 ± 0.05	–	5.91 ± 0.07	5.52 ± 0.04	5.76 ± 0.08
$12+\log(N/H)$ (T_e)	–	6.19 ± 0.05	–	6.32 ± 0.06	6.25 ± 0.04	–	6.27 ± 0.22	6.12 ± 0.06	–	6.31 ± 0.08	6.22 ± 0.05	6.52 ± 0.10
$12+\log(N/H)$ (ONS)	–	6.13 ± 0.03	–	6.37 ± 0.05	6.19 ± 0.02	–	6.24 ± 0.03	6.15 ± 0.03	–	6.23 ± 0.06	6.17 ± 0.06	6.43 ± 0.07
$12+\log(N/H)$ (ON)	–	6.06 ± 0.03	–	6.40 ± 0.03	6.17 ± 0.02	–	6.13 ± 0.02	6.10 ± 0.03	–	6.23 ± 0.05	6.20 ± 0.05	6.50 ± 0.06
$12+\log(N/H)$ (NS)	–	6.23 ± 0.02	–	6.35 ± 0.02	6.33 ± 0.01	–	6.26 ± 0.02	6.17 ± 0.02	–	6.25 ± 0.03	6.14 ± 0.03	6.30 ± 0.04
$\log(N/O)$ (T_e)	–	-1.69 ± 0.07	–	-1.48 ± 0.08	-1.65 ± 0.05	–	-1.62 ± 0.31	-1.70 ± 0.08	–	-1.58 ± 0.10	-1.62 ± 0.06	-1.42 ± 0.13
$\log(N/O)$ (ONS)	–	-1.61 ± 0.03	–	-1.41 ± 0.06	-1.50 ± 0.02	–	-1.54 ± 0.03	-1.57 ± 0.03	–	-1.48 ± 0.07	-1.44 ± 0.07	-1.24 ± 0.08
$\log(N/O)$ (ON)	–	-1.62 ± 0.03	–	-1.42 ± 0.05	-1.57 ± 0.02	–	-1.56 ± 0.03	-1.56 ± 0.03	–	-1.49 ± 0.06	-1.46 ± 0.06	-1.29 ± 0.07
$\log(N/O)$ (NS)	–	-1.49 ± 0.02	–	-1.48 ± 0.03	-1.44 ± 0.02	–	-1.46 ± 0.02	-1.52 ± 0.02	–	-1.48 ± 0.04	-1.52 ± 0.04	-1.46 ± 0.05
$12+\log(S^+/H^+)$	–	5.57 ± 0.04	–	5.68 ± 0.05	5.44 ± 0.03	–	5.65 ± 0.17	5.69 ± 0.04	–	5.64 ± 0.06	5.30 ± 0.03	5.39 ± 0.07
$12+\log(S^{2+}/H^+)$	–	5.87 ± 0.09	–	5.80 ± 0.11	5.85 ± 0.08	–	6.05 ± 0.59	–	–	–	6.02 ± 0.07	6.19 ± 0.20
$12+\log(S/H)$	–	6.06 ± 0.06	–	6.06 ± 0.06	6.01 ± 0.05	–	6.20 ± 0.42	–	–	–	6.20 ± 0.06	6.39 ± 0.18
$12+\log(Ar^{2+}/H^+)$	–	5.19 ± 0.06	–	5.10 ± 0.06	5.29 ± 0.10	–	5.31 ± 0.37	5.13 ± 0.08	–	5.25 ± 0.10	5.32 ± 0.05	5.45 ± 0.11
$12+\log(Ar/H)$	–	5.23 ± 0.06	–	5.13 ± 0.06	5.33 ± 0.10	–	5.36 ± 0.37	5.18 ± 0.08	–	5.29 ± 0.10	5.36 ± 0.05	5.50 ± 0.11
$12+\log(Ne^+/H^+)$	–	6.83 ± 0.07	6.77 ± 0.12	6.61 ± 0.08	6.84 ± 0.09	6.72 ± 0.13	6.75 ± 0.32	6.66 ± 0.09	6.93 ± 0.28	–	6.92 ± 0.04	–
$12+\log(Ne/H)$	–	6.99 ± 0.07	6.94 ± 0.13	6.76 ± 0.08	6.98 ± 0.09	6.83 ± 0.13	6.97 ± 0.33	6.89 ± 0.09	7.15 ± 0.29	–	6.97 ± 0.04	–

Note. References PA102, PA187, PA304 and PA331 denote our observational data according to the position angle of the slit. Reference 'Lee' denotes regions investigated using Lee et al. (2003) observational data. References 'Cr' denote regions investigated using Croxall et al. (2009) observational data according to slit names in that paper.

Downloaded from http://mnras.oxfordjournals.org/ by guest on January 25, 2013

nebulae. Hereafter we adopt the estimates obtained using the above technique from the relationship

$$T_e(\mathrm{O\,II}) = T_e(\mathrm{O\,III}) + 450 - 70\exp[(T_e(\mathrm{O\,III})/5000)^{1.22}].$$

The temperatures T_e(O II) estimated by other methods are much higher than our inferred upper constraints for four H II regions.

The dependence of the temperature in the S^{2+} emission region on T_e(O III) has a much lower scatter than the corresponding dependence for low-ionization regions (see, for example, Hägele et al. 2008). We estimated T_e(S III) using the equation proposed by Izotov et al. (2006) for various H II region metallicities:

$$\begin{aligned} t_3 &= -1.085 + t\,(2.320 - 0.420t), \quad \text{for } 12 + \log(\mathrm{O/H}) \simeq 7.2,\\ &= -1.276 + t\,(2.645 - 0.546t), \quad \text{for } 12 + \log(\mathrm{O/H}) \simeq 7.6,\\ &= 2.967 + t\,(-2.261 + 1.605t), \quad \text{for } 12 + \log(\mathrm{O/H}) \simeq 8.2, \end{aligned}$$

where $t_3 = 10^{-4}T_e$(S III) and $t = 10^{-4}T_e$(O III). Table 3 lists the adopted electron temperatures in the various ionization regions.

3.2 Estimation of gas metallicity

Currently, many methods are used to estimate the abundances of chemical elements and primarily that of oxygen, which determines the metallicity of the interstellar medium. The most popular is the so-called 'direct', or T_e, method, which allows elemental abundances to be estimated from the forbidden-line intensity ratios, provided that the electron temperature T_e is known in the region where the corresponding emission line forms. However, we cannot always use this method, as we have direct spectrum-based electron temperature estimates in the zones of different ionization for only four H II regions. Only in 10 regions were the temperatures in low-ionization zones estimated using empirical methods. We therefore used the T_e method to estimate the relative abundances of the O^+, O^{2+}, N^+, S^+, S^{2+}, Ar^{2+} and Ne^{2+} ions in these regions wherever the signal-to-noise ratio for the corresponding ion lines was greater than 3.

We estimated the relative ion abundances using the relations from studies based on modern atomic data: we used the equations from Pilyugin et al. (2010) to obtain the abundances of O^+ and O^{2+} ions, and those from Izotov et al. (2006) to obtain the N^+, S^+, S^{2+}, Ar^{2+} and Ne^{2+} ionic abundances. For the unobserved ionization stages we calculated the ionization correction factors (*ICF*) using the relationships adopted from Izotov et al. (2006), which allowed us to determine the abundances of oxygen, sulphur, argon and neon.

Among the popular methods to determine metallicity are those based on the intensity ratios of bright emission lines. These include the so-called 'empirical' methods calibrated by H II regions with bona fide oxygen abundance estimates and methods based on theoretical photoionization models. In this paper we use six such methods, as follows.

(i) The PT05 method (Pilyugin & Thuan 2005), where the oxygen abundance is fitted by a function of $R_2 = I_{[\mathrm{O\,II}]\lambda3727+\lambda3729}/I_{\mathrm{H}\beta}$, $R_3 = I_{[\mathrm{O\,III}]\lambda4959+\lambda5007}/I_{\mathrm{H}\beta}$, $R_{23} = R_2 + R_3$, and the excitation parameter $P = R_3/(R_3 + R_2)$. This is one of the most widely used empirical methods, with the applicability domain confined to the interval $0.55 < P < 1$.

(ii) The ONS method (Pilyugin et al. 2010), which allows the oxygen and nitrogen abundances to be determined as a function of the parameters R_2, R_3, $N_2 = I_{[\mathrm{N\,II}]\lambda6548+\lambda6583}/I_{\mathrm{H}\beta}$, $S_2 = I_{[\mathrm{S\,II}]\lambda6717+\lambda6731}/I_{\mathrm{H}\beta}$ and P.

(iii) The ON method (Pilyugin et al. 2010), which is similar to the ONS method, but does not require knowledge of S_2.

(iv) The NS method (Pilyugin & Mattsson 2011), which does not require [O II] $\lambda3727 + \lambda3729$ intensity measurements and allows the oxygen and nitrogen abundances to be determined as functions of the parameters R_3, N_2 and S_2.

(v) The PP04 method (Pettini & Pagel 2004), which allows the relative oxygen abundance to be determined from the parameter $O_3N_2 = \log[(I_{[\mathrm{O\,III}]\lambda5007}/I_{\mathrm{H}\beta})/(I_{[\mathrm{N\,II}]\lambda6583}/I_{\mathrm{H}\alpha})]$. This method is practically extinction-independent; it works in the interval $-1 < O_3N_2 < 1.9$.

(vi) The KK04 method (Kewley & Dopita 2002 with the new parametrization by Kobulnicky & Kewley 2004), based on theoretical photoionization models, which can be used to determine the oxygen abundance as a function of the parameter R_{23} and the ionization parameter q, which, in turn, can be obtained from the $O_{32} = I_{[\mathrm{O\,III}]\lambda4959+\lambda5007}/I_{[\mathrm{O\,II}]\lambda3727+\lambda3729}$ line intensity ratio.

All the above methods can be used to determine the oxygen abundances, $12 + \log(\mathrm{O/H})$, in the H II regions. According to the authors of the original publications, these methods are accurate to about 0.1 dex (the PP04 method is less accurate – its error is about 0.2–0.25 dex; the ON, NS and ONS methods have smaller errors of about 0.075 dex). The ON, NS and ONS methods can also be used to determine the nitrogen abundance and hence the log (N/O) abundance ratio, which is important for chemical evolution models of galaxies.

The chemical abundances of the Ho II H II regions were earlier estimated by Masegosa, Moles & del Olmo (1991), Lee et al. (2003) and Croxall et al. (2009). Moustakas et al. (2010) summarized these results and reported the galaxy-averaged abundances and average abundances at various galactocentric distances. We compare all these data with our results.

Croxall et al. (2009) and Lee et al. (2003) report relative line intensities, which we used to determine the elemental abundances by applying all the methods employed in this paper.

Table 3 lists the resulting estimates of abundances of chemical elements and individual ions for the H II regions based on our observations and line intensities reported by Croxall et al. (2009) and Lee et al. (2003). Table 3 gives only the formal measurement errors, which do not include the uncertainties of each method itself.

Abundances obtained for similar slit positions based on our observations and those reported in previous studies mostly agree well with each other within the quoted observational errors. The oxygen abundances reported by Croxall et al. (2009) and Lee et al. (2003) differ slightly from those calculated in this study using the fluxes reported by the above authors. This discrepancy is caused by the use of different atomic data. For some H II regions, the abundances determined in this paper do not match those obtained by Croxall et al. (2009) and Lee et al. (2003) because we observed different parts of the nebulae, which show significant abundance variations (see Section 4.1).

4 DISCUSSION

4.1 Emission spectra of individual H II regions

We analysed the variations of the emission-line intensity and physical conditions inside the H II regions in the brightest nebulae, namely HSK45, HSK73, HSK70 and HSK67. Note that the detailed distribution of metallicity along an individual nebula could be determined only using the 'direct' method. Empirical methods can be applied only to the nebula as a whole – when they are used to determine the

Downloaded from http://mnras.oxfordjournals.org/ by guest on January 25, 2013

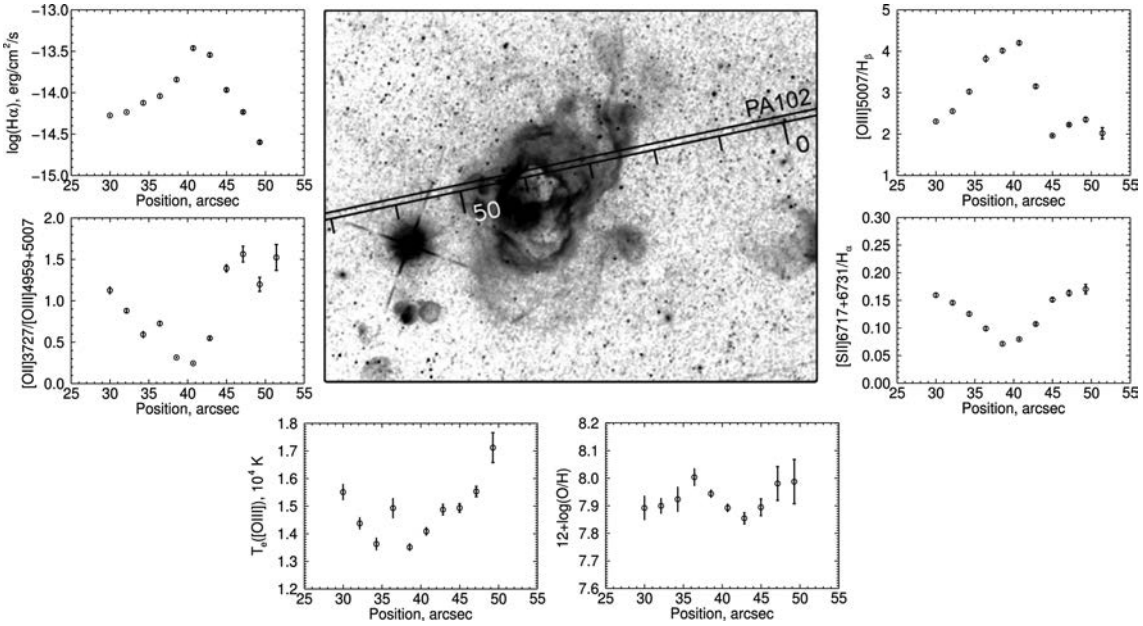

Figure 3. The H II region HSK45. The central part of the figure shows the *HST* Hα image together with the position of the PA102 slit. The left, right and bottom panels show the distributions of relative emission-line intensities, electron temperature and oxygen abundance, respectively, along the portion of the slit crossing the HSK45 region.

local chemical composition, the results are seriously affected by the emission stratification inside the region.

HSK45. This is the largest H II complex seen in the Hα images of the galaxy. Its angular size is about 25–30 arcsec, corresponding to a linear size of 410–490 pc. According to the estimates of Stewart et al. (2000), it is a young region with an age of 2.5–3.5 Myr. Its composite multishell structure shows up clearly in the images.

Fig. 3 shows the image of the HSK45 H II region and the distribution of diagnostic line ratios along the part of the PA102 slit crossing the nebula. The [O III] λ4959 + λ5007/Hβ intensity ratio in the crossed parts of the shells is equal to about 2 and reaches 4.5 in the faint central area. The degree of gas ionization at the centre is higher than at the edges of the complex. The decrease of the [O III] λ4959 + λ5007/Hβ ratio at the periphery can be explained by the fact that the oxygen emission there is dominated by O^+, and the decrease of the [S II] λ6717 + λ6731/Hα towards the centre of the region could be caused by the high-ionization stage of sulphur represented by S^{2+} (possibly in the vicinity of an ionizing cluster).

The HSK45 region exhibits a non-uniform distribution of T_e along the slit. The relative oxygen abundance also varies along the region; however, these variations are not so strong, and metallicity is more or less constant and consistent with the region-averaged value listed in Table 3.

HSK 73. This region, like HSK45, is one of the brightest and most extended among those seen in the Hα image of the galaxy (see Fig. 1). The complex has an angular size of about 15–20 arcsec (linear size 250–330 pc). It is also a young region, with an age of about t = 2.5–3.5 Myr (Stewart et al. 2000), characterized by a composite shell structure. The centre of the region hosts the most massive stellar cluster of those studied by Cook et al. (2012) in Ho II.

Fig. 4 shows the image of the HSK73 region and the distribution of relative emission-line intensities, the electron temperature and oxygen abundance along the parts of the PA102 and PA187 slits crossing the complex from west to east and from north to south, respectively.

The [O III] λ4959 + λ5007/Hβ intensity ratio is constant in the north-eastern part of the region and increases significantly in its north-western part; this ratio can also be seen to increase from north to south. The [O II] λ3727/[O III] λ4959 + λ5007 ratio, which characterizes the degree of gas ionization, decreases with increasing [O III] λ4959 + λ5007/Hβ. This behaviour indicates that gas ionization is higher in the north-western and southern parts of the region and that the cause is photoionization.

We found a bright He II λ4686 line emission in the central part of the region (positions ranging from −17 to −20 arcsec on the PA187 slit). Note that the helium line emission region is compact, and no such emission is present in the spectrum of the outer shell. The He II line emission may be caused by the fact that here the slit crosses a compact nebula ionized by a Wolf–Rayet star or by another source of intense ultraviolet radiation.

The distribution of oxygen abundance along the portions of the PA102 and PA187 slits crossing HSK73 demonstrates a constant gas metallicity in the north-western outskirts of the region and a possible north-to-south metallicity gradient. Oxygen abundance increases sharply near the north-eastern part of the shell.

HSK 70 and HSK 67. These two H II regions are more compact than HSK45 and HSK73: the size of HSK70 is about 10–15 arcsec (160–250 pc) and that of HSK67, about 8 arcsec (130 pc). Stewart et al. (2000) estimated the ages of these regions to be 3.5–4.5 and 2.5–3.5 Myr, respectively.

Fig. 5 shows the *HST* Hα images of HSK70 and HSK67, the position of the PA187 spectrograph slit, and the distribution of relative line intensities, electron temperature, and oxygen abundance along the slit.

The image of the extended surroundings of HSK70 and HSK67 reveals a faint shell-like structure with a size of 40–50 arcsec (650–820 pc), which includes the two bright nebulae.

The only known ultraluminous X-ray source (ULX) in the galaxy, Holmberg II X-1, is located at the eastern boundary of the HSK70 region. This source completely determines the kinematics and emission spectrum of the region (for a detailed study of the nebula

Downloaded from http://mnras.oxfordjournals.org/ by guest on January 25, 2013

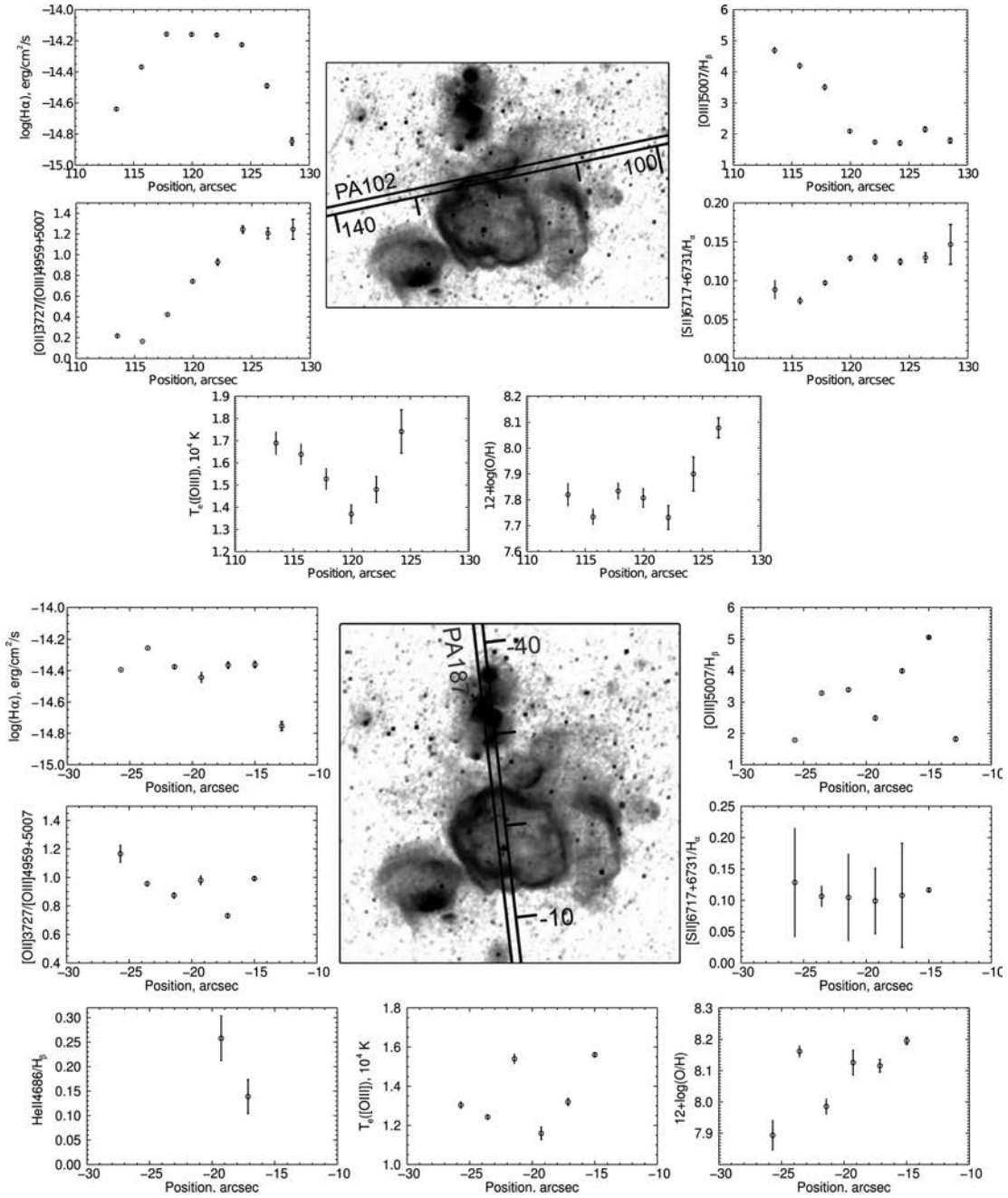

Figure 4. The H II region HSK73. The top and bottom panels show the results obtained along the PA102 and PA187 slits, respectively. The central part of each figure shows the *HST* Hα image and the corresponding slit position. The surrounding panels show the distributions of relative emission-line intensities, electron temperature and oxygen abundance along the part of the slit crossing this region.

surrounding the source see Lehmann et al. 2005). The spectrograph slit in our observations crosses the region 5 arcsec west of the source, but even at this distance (80 pc) a strong He II λ4686 line emission of the nebula surrounding the ULX is observed (see Fig. 5).

The [O III] λ4959 + λ5007/Hβ intensity ratio is high inside the two bright H II regions and decreases in the space between them. The [O II] λ3727/[O III] λ4959 + λ5007 ratio, in contrast, is low inside the regions and higher in the space between. This fact indicates that gas ionization inside HSK70 and HSK67 is higher than in the outskirts of the two bright nebulae.

Gas metallicity in HSK70 and in its outskirts is more or less the same and coincides with the region-averaged value. The HSK67 nebula exhibits a sharp decrease of oxygen abundance in the north-to-south direction.

The [S II] λ6717 + λ6731/Hα line intensity ratio does not exceed 0.2 in all the regions described above, thereby supporting the photoionization mechanism of gas excitation.

4.2 Comparison of methods of oxygen abundance determination

In recent years several authors have performed detailed comparisons of different methods of elemental abundance estimation in order to determine the bona fide applicability domain of each method (see,

Downloaded from http://mnras.oxfordjournals.org/ by guest on January 25, 2013

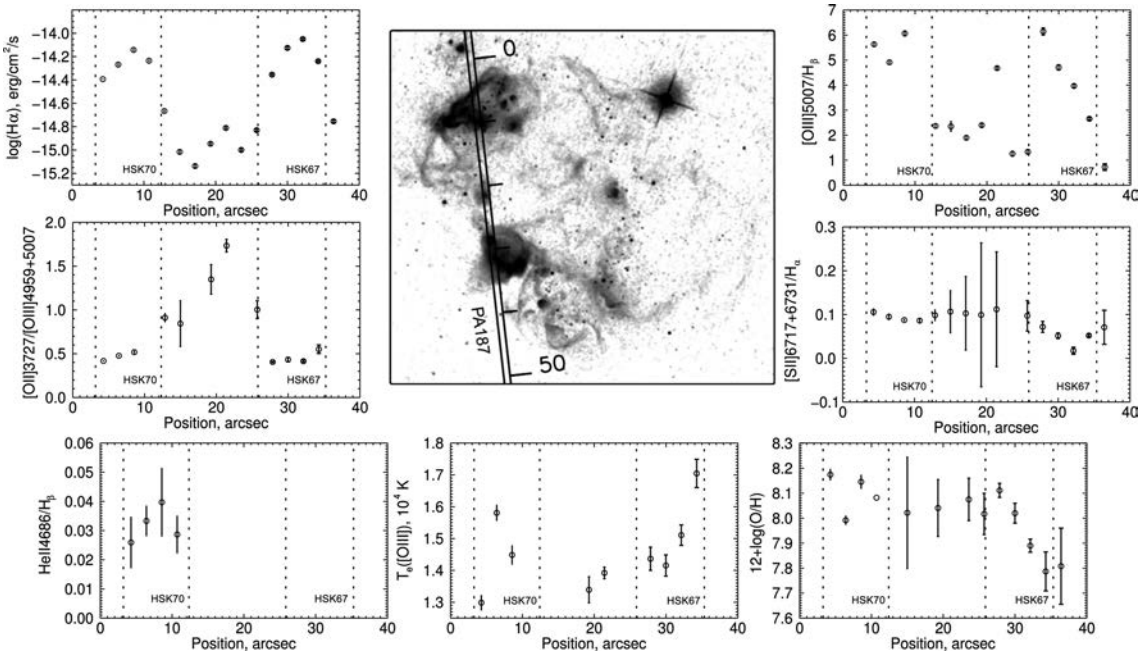

Figure 5. The H II regions HSK70 and HSK67. The central part of the figure shows the Hα image (taken from the *HST* archive). Also shown is the position of the PA187 slit. The other panels show the distributions of relative emission-line intensities, electron temperature and oxygen abundance along the slit.

for example, Kewley & Ellison 2008; López-Sánchez et al. 2012, and references therein).

Thus researchers have long questioned the correctness of results obtained even by the 'direct' T_e method. This method may yield underestimated abundances in the case of small-scale temperature fluctuations inside the H II region (Piembert 1967) or significant temperature variations across the nebula (Stasińska 1978, 2005). A similar effect can be observed if the nebula studied is not a single Stroemgren zone but a composite H II region containing several ionization sources.[2]

Pilyugin et al. (2012) showed that the T_e method can yield overestimated N/O abundance ratios for composite nebulae, whereas the empirical ON and NS methods analysed by the above authors are free from this drawback.

López-Sánchez et al. (2012) used model spectra of H II regions to perform a detailed comparison of the currently most popular methods for estimating the chemical composition. They showed that the T_e method somewhat overestimates the oxygen, neon and argon abundances compared with the input model values. They also showed that the results of the ON, NS and ONS methods are in excellent agreement with those of the T_e method when applied to the spectra of real objects. However, they yield underestimated results compared with the input values when applied to model spectra. Another conclusion of López-Sánchez et al. (2012) is that the KK04 method based on photoionization models yields results that are most consistent with the chemical composition of the stellar population. The results of this method also agree very well with those based on recombination lines. The abundances determined using the KK04 method are systematically greater than those given by the T_e method.

The Holmberg II galaxy is an excellent test ground for comparing methods of estimating the chemical composition under the conditions of inhomogeneous and extended H II regions, where effects such as temperature variation are obviously present (see Figs 3, 4, 5). Indeed, most of the bright H II regions observed have angular sizes of 10 arcsec or more, implying that their linear sizes exceed 160 pc, which is evidently greater than the size of a classical Stroemgren zone around a single O-type star, and their ionization sources are young star clusters. Furthermore, Hα images of the galaxy reveal the shell-like structure of many of the H II regions that we observed (see Figs 1, 3, 4 and 5).

Our estimates of oxygen abundance in Ho II H II regions based on the T_e method and six empirical methods fall into two groups (see Table 3). The first group contains the results obtained using the T_e, ON, NS, ONS and PT05 methods (with a median value of $12 + \log(O/H) = 7.73 \pm 0.13$), and the second group those obtained using the PP04 and KK04 methods (with a median value of $12 + \log(O/H) = 8.18 \pm 0.09$). López-Sánchez et al. (2012) analysed model spectra and showed that the PP04 method overestimates abundances at $12 + \log(O/H) < 8.7$, and therefore the results based on this method may be incorrect.

Our metallicity estimates obtained by applying different methods to the gas emission spectrum in Ho II can also be compared with the results of our earlier study of the irregular galaxy IC 10 (Lozinskaya et al. 2009; Arkhipova et al. 2011) and the blue compact dwarf (BCD) galaxy VII Zw 403 (Arkhipova et al. 2007; Egorov & Lozinskaya 2011). Both galaxies were observed with the 6-m telescope of the SAO RAS using the SCORPIO focal reducer, operating in the long-slit spectrograph mode, and the MPFS multipupil fibre spectrograph. We used these observations to measure the relative line intensities in 26 parts of 18 H II regions in IC 10 and in five extended H II complexes (giant H II regions) in VII Zw 403.

In the above studies we estimated the gas metallicity using the PT05, PP04 and T_e methods for the objects in IC 10 (Lozinskaya et al. 2009; Arkhipova et al. 2011); and the ON, ONS, NS and T_e methods for the objects in VII Zw 403 (Arkhipova et al. 2007; Egorov & Lozinskaya 2011). To correctly compare the three galaxies, we re-estimate in this paper the oxygen abundances for IC 10 and VII Zw 403 by applying all the methods that we used for Ho II. Note that in the original papers we made certain assumptions

[2] This is the case with all the H II regions we studied in Ho II.

Downloaded from http://mnras.oxfordjournals.org/ by guest on January 25, 2013

Table 4. Oxygen abundances in the IC 10 and VII Zw 403 galaxies estimated using the methods detailed in the text.

Galaxy	H II region and slit PA	12 + log (O/H) estimated using the various methods						
		T_e	PT05	ONS	ON	NS	PP04	KK04
IC 10	HL111a PA0	8.28 ± 0.04	8.34 ± 0.24	8.14 ± 0.06	8.05 ± 0.05	8.16 ± 0.02	8.36 ± 0.01	8.27 ± 0.28
IC 10	HL111b PA0	8.29 ± 0.04	8.27 ± 0.22	8.18 ± 0.06	8.11 ± 0.05	8.22 ± 0.03	8.41 ± 0.01	8.23 ± 0.29
IC 10	HL111c PA0	8.24 ± 0.02	8.24 ± 0.15	8.03 ± 0.03	7.92 ± 0.03	8.07 ± 0.01	8.18 ± 0.04	8.38 ± 0.11
IC 10	HL111e PA0	8.24 ± 0.07	8.29 ± 0.38	8.12 ± 0.12	8.05 ± 0.09	8.15 ± 0.04	8.29 ± 0.01	8.28 ± 0.45
IC 10	HL111d PA268	8.05 ± 0.05	8.28 ± 0.11	8.12 ± 0.05	8.07 ± 0.04	8.16 ± 0.03	8.26 ± 0.05	8.33 ± 0.08
IC 10	HL111c PA268	8.15 ± 0.03	7.94 ± 0.10	7.86 ± 0.03	7.71 ± 0.03	7.70 ± 0.03	8.18 ± 0.01	8.32 ± 0.02
IC 10	HL111a PA331	8.20 ± 0.04	8.05 ± 0.34	8.14 ± 0.09	8.17 ± 0.07	8.19 ± 0.03	8.13 ± 0.01	8.35 ± 0.23
IC 10	HL50 PA331	8.19 ± 0.20	8.30 ± 0.16	8.07 ± 0.34	8.04 ± 0.31	8.01 ± 0.13	8.42 ± 0.01	–
IC 10	HL45 PA45	8.15 ± 0.05	7.92 ± 0.17	7.79 ± 0.10	7.84 ± 0.08	7.84 ± 0.04	8.31 ± 0.01	8.16 ± 0.20
IC 10	HL50 PA45	8.25 ± 0.02	8.10 ± 0.16	8.24 ± 0.03	8.27 ± 0.02	8.29 ± 0.01	8.23 ± 0.01	8.35 ± 0.10
VII Zw 403	#1	7.71 ± 0.01	7.43 ± 0.03	7.72 ± 0.02	7.80 ± 0.02	7.77 ± 0.01	7.96 ± 0.03	7.90 ± 0.18
VII Zw 403	#3	7.73 ± 0.01	7.61 ± 0.09	7.68 ± 0.02	7.61 ± 0.02	7.62 ± 0.01	8.06 ± 0.02	8.02 ± 0.19
VII Zw 403	#4	7.75 ± 0.02	7.71 ± 0.05	7.71 ± 0.03	7.65 ± 0.04	7.67 ± 0.03	8.05 ± 0.02	8.09 ± 0.14

Note. The H II regions in IC 10 are designated in accordance with the list of Hodge & Lee (1990) and by the position angle of the spectrograph slit in our observations of this galaxy (Lozinskaya et al. 2009; Arkhipova et al. 2011). The H II regions of VII Zw 403 are identified by their numbers used in our previous studies (Arkhipova et al. 2007; Egorov & Lozinskaya 2011).

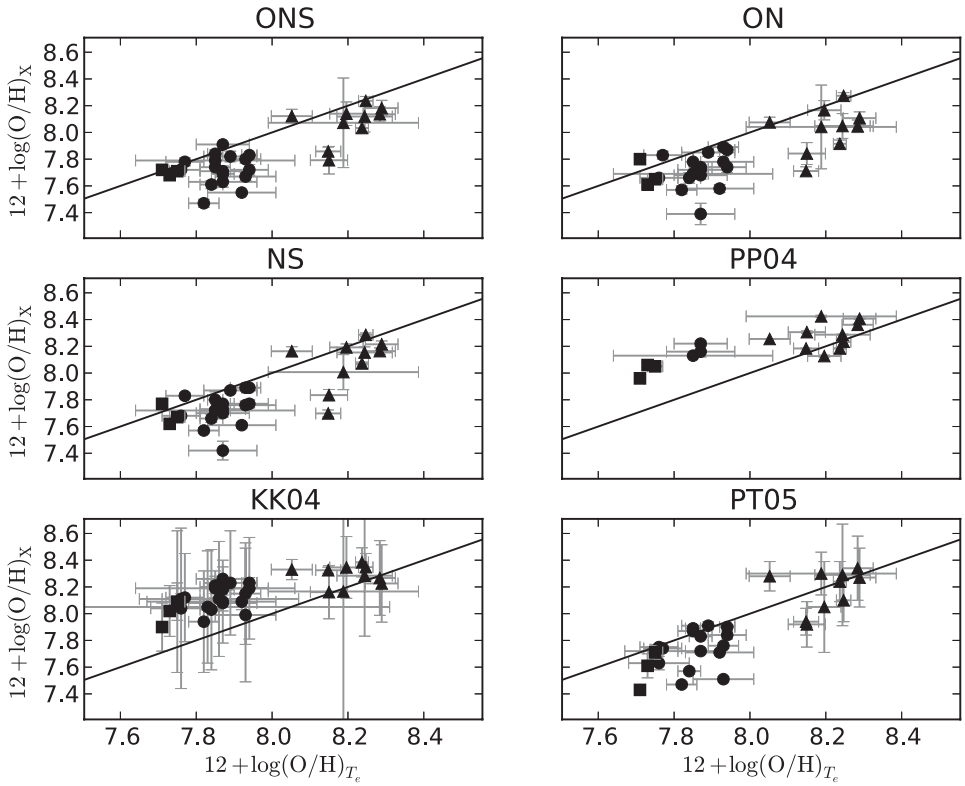

Figure 6. Comparison of various methods for oxygen abundance estimation with the 'direct' T_e method. The methods are designated by the following symbols: PP04, Pettini & Pagel (2004); KK04, Kobulnicky & Kewley (2004); PT05, Pilyugin & Thuan (2005); ONS and ON, Pilyugin et al. (2010); NS, Pilyugin & Mattsson (2011). The circles, triangles and squares show the results of these methods applied to the Holmberg II, IC 10 and VII Zw 403 galaxies, respectively. The solid lines show the $y = x$ relations for the various methods.

about T_e in the H II regions when estimating the abundances in IC 10 and VII Zw 403, as described in Lozinskaya et al. (2009) and Egorov & Lozinskaya (2011) respectively. Our spectroscopic data allowed us to measure the intensity of the [O III] λ4363 line and hence the electron temperature only in one H II region, HL 111, in IC 10. We adopted the T_e measurements for another two nebulae (HL 45 and HL 50) from the literature. We obtained T_e estimations from our spectra and from the literature for three H II regions in VII Zw 403. We used abundance measurements performed only for those regions with available T_e estimations. The oxygen abundances for these regions of IC 10 and VII Zw 403 obtained using all the methods considered are listed in Table 4.

We have thus analysed a total of 34 H II regions in three galaxies using the 'direct' T_e method and the six empirical and theoretical methods mentioned above. The results are presented in Fig. 6.

Fig. 7 shows the differences between the results obtained using these six methods as a function of the abundance determined using the direct T_e method.

Downloaded from http://mnras.oxfordjournals.org/ by guest on January 25, 2013

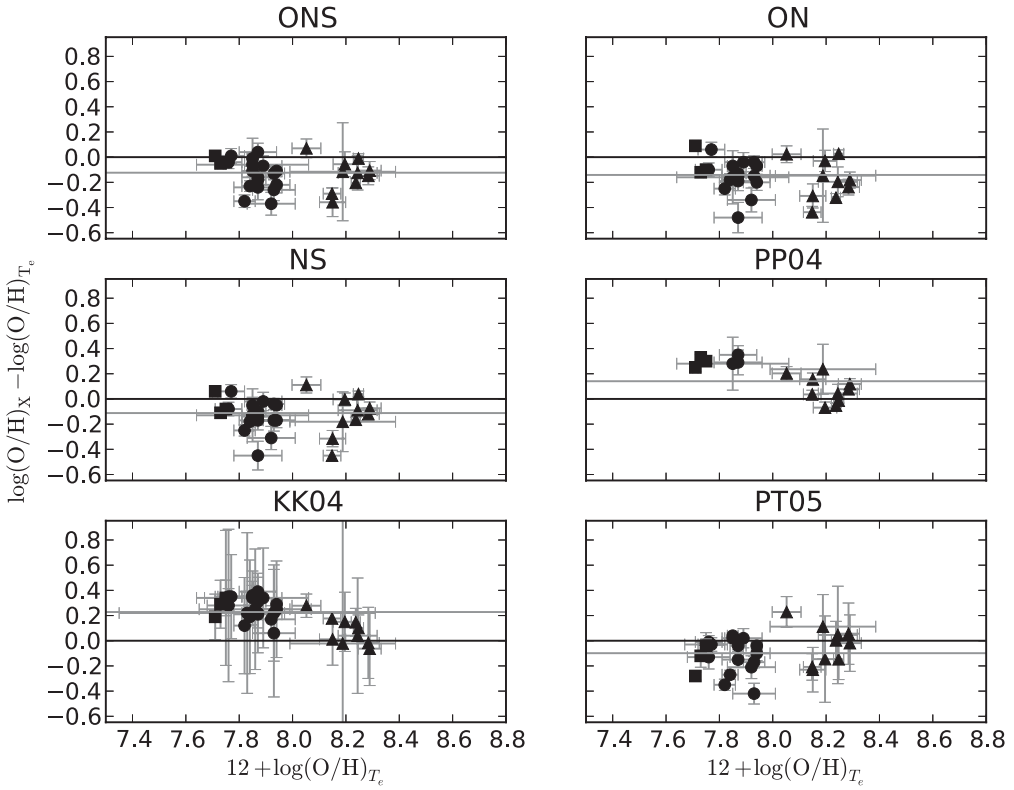

Figure 7. Difference between the oxygen abundance estimates obtained using the 'direct' T_e method and the six methods described in the text. The methods employed are designated by the following symbols: PP04, Pettini & Pagel (2004); KK04, Kobulnicky & Kewley (2004); PT05, Pilyugin & Thuan (2005); ONS and ON, Pilyugin et al. (2010); NS, Pilyugin & Mattsson (2011). The circles, triangles and squares show the results of the application of these methods to the Holmberg II, IC 10 and VII Zw 403 galaxies, respectively. The horizontal lines indicate the level of zero difference between the abundances given by the methods (black line) and the median deviation from the results of the T_e method (grey line).

It follows from Table 3 and Figs 6 and 7 that metallicities determined using different methods indeed differ systematically, and the corresponding deviations agree well with the results of simulated 'model' computations by López-Sánchez et al. (2012). The estimates based on the empirical PT05, ON, NS and ONS methods on average agree well (although for some H II regions, the ONS method yields overestimated abundances compared with the values determined using the other two methods). Note that the PT05, ON, NS and ONS methods somewhat underestimate the metallicities compared with the T_e method. The KK04 method, in contrast, systematically overestimates metallicities compared with those determined using the 'direct' method. The PP04 method yields similar results. We applied these methods to the model data of López-Sánchez et al. (2012) and found that the abundances determined using these techniques agree well with the metallicity estimates based on recombination lines and with the metallicity of the stellar population.

The observed variations of the estimated oxygen abundances of H II regions obtained by different methods may be a result of the complex shell-like and clumpy structure of these regions. Indeed, it follows from Figs 3, 4 and 5 that such regions exhibit appreciable, and in some cases quite important, electron-temperature and metallicity variations from the centre towards the periphery. When averaged over the entire region, the results of the 'direct' method are more sensitive to the dense high-temperature 'inclusions' than to the regions with 'average' density and temperature; this may explain why the direct method yields underestimated metallicities.

4.3 Comparison of diagnostic diagrams with theoretical photoionization models

Fig. 8 shows the diagnostic diagrams of relative line intensities – I([O III] λ5007)/I(Hβ) – as a function of I([N II] λ6583)/I(Hα) and I([S II] λ6717 + λ6731)/I(Hα). They are based on our observations of Ho II and on the data of Croxall et al. (2009). These diagrams are traditionally used to compare the observations with photoionization models. The curves show the theoretical diagnostic diagrams of Levesque, Kewley & Larson (2010) computed for various metallicities assuming continuous star formation over 5 Myr.

It is evident from Fig. 8 that the results of observations of H II regions in the galaxy agree well with models in the metallicity interval $Z = 0.004$–0.008. Given the current estimates of the solar metallicity, $Z_\odot = 0.0134$ (Asplund et al. 2009), this corresponds to $Z = (0.3$–$0.6)Z_\odot$. However, the mean oxygen abundance in the galaxy estimated using the T_e, ON, NS, ONS and PT05 methods is $12 + \log(\mathrm{O/H}) = 7.73 \pm 0.13$, which yields $Z \simeq 0.1Z_\odot$ (assuming $12 + \log(\mathrm{O/H})_\odot = 8.69$; see Asplund et al. 2009). If we adopt the mean oxygen abundance estimate $12 + \log(\mathrm{O/H}) = 8.18 \pm 0.09$ given by the PP04 and KK04 methods, the resulting metallicity becomes $Z \simeq 0.3Z_\odot$ and agrees well with photoionization models. This is not surprising, given that both methods have been calibrated by such models .

The [S II] λ6717 + λ6731/Hα line intensity ratio is a commonly used indicator of the shock excitation of gas. We tried to spectroscopically confirm the presence of the shock excitation mechanism in the eastern chain of H II regions, where Tonque & Westphal (1995)

Downloaded from http://mnras.oxfordjournals.org/ by guest on January 25, 2013

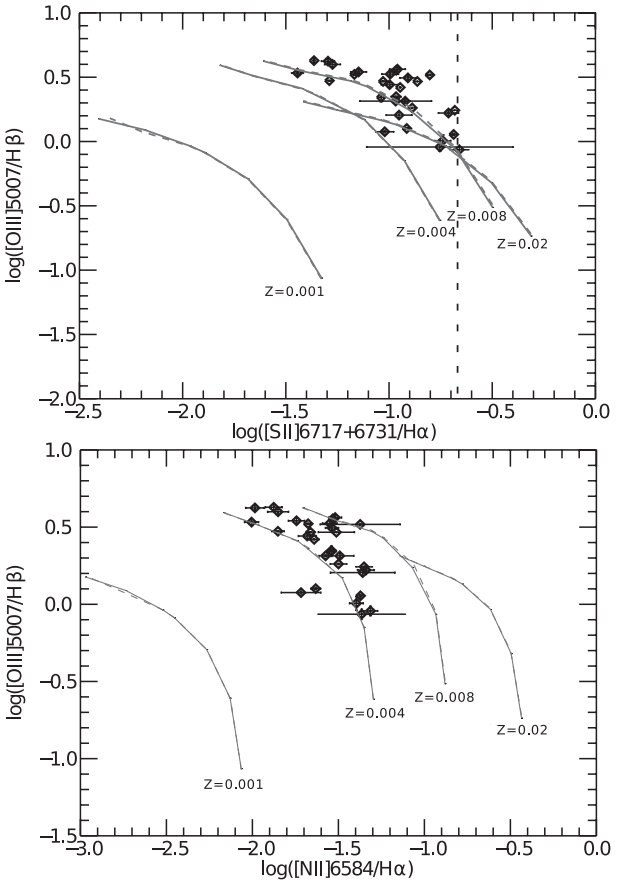

Figure 8. Diagnostic diagrams based on the results of our observations of Ho II and on the data of Croxall et al. (2009). Also shown are the theoretical photoionization models by Levesque et al. (2010) for various metallicities computed assuming continuous star formation over 5 Myr. The dashed line in the upper panel is the ratio $I([\mathrm{S\,II}]\,\lambda6717 + \lambda6731)/I(\mathrm{H}\alpha) = 0.2$.

identified the synchrotron component of the radio emission, possibly indicative of the presence of supernova remnants. However, it is evident from Fig. 8 that the [S II] $\lambda6717 + \lambda6731/\mathrm{H}\alpha$ line intensity ratio does not exceed 0.2 in any region, indicating the predominance of photoionization excitation in the areas considered. It is not surprising that no evidence for the shock excitation of gas could be found in the optical spectra. In the relatively distant galaxy we considered, the nebulae we analysed are large complexes of gas ionized by many stars, and optical emission of supernova remnants, if any, is hard to distinguish with the present spatial and spectral resolution. A detailed investigation of the kinematics of the nebulae using Fabry–Perot interferometer observations in Hα and [S II] lines, which we defer to our forthcoming paper, may be helpful in case we find evidence of supersonic gas velocities.

5 CONCLUSIONS

We report relative oxygen, nitrogen, sulphur, neon and argon abundance estimates in the Holmberg II galaxy based on long-slit spectra taken with the 6-m telescope of the SAO RAS.

The oxygen, nitrogen, sulphur, argon and neon abundances in Ho II H II regions that we report in this paper are the most detailed estimates obtained for the galaxy to date. According to our observations, the relative abundances of these elements in individual H II regions (excluding regions with high uncertainties) lie within the following intervals: $12 + \log(\mathrm{O/H}) = 7.38$–$7.89$ (or 8.08–8.32, depending on the method applied), $12 + \log(\mathrm{N/H}) = 5.92$–$6.51$, $12 + \log(\mathrm{S/H}) = 6.01$–$6.20$, $12 + \log(\mathrm{Ne/H}) = 6.89$–$7.07$, and $12 + \log(\mathrm{Ar/H}) = 5.18$–$5.39$. The average gas metallicity in the galaxy is $Z \simeq 0.1\,\mathrm{Z}_\odot$ (if computed using the T_e, PT05, ONS, ON or NS method) or $Z \simeq 0.3\,\mathrm{Z}_\odot$ (if computed using the PP04 or KK04 method).

We used our observations, which cover most of the H II regions in the galaxy, the data reported by Lee et al. (2003) and Croxall et al. (2009), as well as the results of our earlier observations of the irregular galaxy IC 10 and the BCD galaxy VII Zw 403 to compare the currently most popular methods of gas metallicity estimation in galaxies.

The results of this study, on the whole, confirm the conclusions of López-Sánchez et al. (2012) based on the analysis of 'model' H II regions. On average, the estimates made using the so-called PT05, ON, NS and ONS methods agree well with each other (although the ONS method yields overestimated abundances in some H II regions, compared with the results of other two methods). The PT05, ON, NS and ONS methods yield lower metallicities than the 'direct' T_e method. The PP04 and KK04 methods, which were used in this paper, in contrast, yield systematically overestimated metallicities compared with the T_e method.

The PP04 method yields overestimated oxygen abundances for $12 + \log(\mathrm{O/H}) < 8.7$, which are similar to those obtained by the KK04 method, leading us to conclude that the two methods yield less reliable estimates for the objects considered than those given by the T_e, PT05, ON, NS and ONS methods.

We show the metallicity estimates based on the comparison of diagnostic diagrams with the photoionization models to be less reliable than those determined from bright oxygen lines.

We tried to confirm the supernova remnants in the eastern chain of H II regions suspected by Tonque & Westphal (1995). However, we did not find any excessive $I([\mathrm{S\,II}]\,\lambda6717 + \lambda6731)/I(\mathrm{H}\alpha)$ line intensity ratio that would be indicative of gas emission behind the shock.

The distributions of relative line intensities along the slits crossing the brightest and most extended H II regions proved to be non-uniform from the viewpoint of the structure and those of metallicity, temperature and state of ionization. This fact may play a key part in the determination of metallicities of the entire regions and cause discrepancies between the estimates obtained using different methods.

We found a bright He II $\lambda4686$ line emission in the central part of the shell nebula HSK73. This emission may be indicative of the presence of a Wolf–Rayet star or another energetic source of intense UV emission.

We will study the structure and kinematics of the gas and dust structure of Ho II in our forthcoming paper.

ACKNOWLEDGMENTS

This work was supported by the Russian Foundation for Basic Research (project nos 10-02-00091 and 12-02-31356). O.V. Egorov and A.V. Moiseev acknowledge support from the Dynasty Foundation of Non-commercial Programs and the Federal Target Program 'Research and Pedagogical Cadre for Innovative Russia' (state contract no. 14.740.11.0800). This research was partly supported by the RAS program of the fundamental investigation OFN-17 'Active processes in galactic and extragalactic objects'.

We are grateful to Kevin Croxall for verifying and sharing the corrected spectrograph slit coordinates for the observations

Downloaded from http://mnras.oxfordjournals.org/ by guest on January 25, 2013

performed by his team, which we used in this work. We also thank Vera Arkhipova for helpful discussions, and Victor Afanasiev for his major contribution in the development of the spectroscopic technique at the 6-m telescope. We thank the anonymous referee for the constructive comments that improved the quality of the paper.

This work is based on observations obtained with the 6-m telescope of the Special Astrophysical Observatory of the Russian Academy of Sciences. The observations were carried out with financial support of the Ministry of Education and Science of the Russian Federation (contract nos 16.518.11.7073 and 14.518.11.7070). This research has made use of the NASA/IPAC Extragalactic Data base (NED), which is operated by the Jet Propulsion Laboratory, California Institute of Technology, under contract with the National Aeronautics and Space Administration (USA). We used observations made with the NASA/ESA Hubble Space Telescope, and obtained from the Hubble Legacy Archive, which is a collaboration between the Space Telescope Science Institute (STScI/NASA), the Space Telescope European Coordinating Facility (ST-ECF/ESA) and the Canadian Astronomy Data Centre (CADC/NRC/CSA).

REFERENCES

Afanasiev V. L., Moiseev A. V., 2005, Astron. Lett., 31, 194
Afanasiev V. L., Moiseev A. V., 2011, Baltic Astron., 20, 363
Arkhipova V. P., Lozinskaya T. A., Moiseev A. V., Egorov O. V., 2007, Astron. Rep., 51, 871
Arkhipova V. P., Egorov O. V., Lozinskaya T. A., Moiseev A. V., 2011, Astron. Lett., 37, 65
Asplund M., Grevesse N., Sauval A. J., Scott P., 2009, ARA&A, 47, 481
Bagetakos I., Brinks E., Walter F., de Blok W. J. G., Usero A., Leroy A. K., Rich J. W., Kennicutt R. C., Jr, 2011, AJ, 141, 23
Braun R., Oosterloo T. A., Morganti R., Klein U., Beck R., 2007, A&A, 461, 455
Cardelli J. A., Clayton G. C., Mathis J. S., 1989, ApJ, 345, 245
Cook D. O. et al., 2012, ApJ, 751, 100
Croxall K. V., van Zee L., Lee H., Skillman E. D., Lee J. C., Côté S., Kennicutt R. C., Miller B. W., 2009, ApJ, 705, 723
Egorov O. V., Lozinskaya T. A., 2011, Astrophys. Bull., 66, 293
Fitzpatrick E. L., 1999, PASP, 111, 63
Garnett D. R., 1992, AJ, 103, 1330
Hägele G. F., Díaz Á. I., Terlevich E., Terlevich R., Pérez-Montero E., Cardaci M. V., 2008, MNRAS, 383, 209
Heald G., Braun R., Edmonds R., 2009, A&A, 503, 409
Hodge P., Lee M. G., 1990, PASP, 102, 26
Hodge P., Strobel N. V., Kennicutt R. C., 1994, PASP, 106, 309
Hunter D. A., Hawley W. N., Gallagher J. S., 1993, AJ, 106, 1797
Izotov Y. I., Stasińska G., Meynet G., Guseva N. G., Thuan T. X., 2006, A&A, 448, 955
Karachentsev I. D., Kaisin S. S., 2007, AJ, 133, 1883
Karachentsev I. D. et al., 2003, A&A, 398, 479
Kennicutt R. C. Jr et al., 2003, PASP, 115, 928
Kewley L. J., Dopita M. A., 2002, ApJS, 142, 35
Kewley L. J., Ellison S. L., 2008, ApJ, 681, 1183
Kobulnicky H. A., Kewley L. J., 2004, ApJ, 617, 240
Lee H., McCall M. L., Kingsburgh R. L., Ross R., Stevenson C. C., 2003, AJ, 125, 146
Lehmann I. et al., 2005, A&A, 431, 847
Levesque E. M., Kewley L. J., Larson K. L., 2010, AJ, 139, 712
López-Sánchez Á. R., Dopita M. A., Kewley L. J., Zahid H. J., Nicholls D. C., Scharwächter J., 2012, MNRAS, 426, 2630
Lozinskaya T. A., Egorov O. V., Moiseev A. V., Bizyaev D. V., 2009, Astron. Lett., 35, 730
Masegosa J., Moles M., del Olmo A., 1991, A&A, 249, 505
Moustakas J., Kennicutt R. C., Tremonti C. A., Dale D. A., Smith J.-D. T., Calzetti D., 2010, ApJS, 190, 233
Osterbrock D. E., Ferland G. J., 2006, Astrophysics of Gaseous Nebulae and Active Galactic Nuclei, 2nd edn. Univ. Science Book, Sausalito, CA
Pérez-Montero E., Díaz Á.I., 2003, MNRAS, 346, 105
Pettini M., Pagel B., 2004, MNRAS, 348, L59
Piembert M., 1967, ApJ, 150, 825
Pilyugin L. S., Mattsson L., 2011, MNRAS, 412, 1145
Pilyugin L. S., Thuan T. X., 2005, ApJ, 631, 231
Pilyugin L. S., Mattsson L., Vílchez J. M., Cedrés B., 2009, MNRAS, 398, 485
Pilyugin L. S., Vílchez J. M., Thuan T. X., 2010, ApJ, 720, 1738
Pilyugin L. S., Vílchez J. M., Mattsson L., Thuan T. X., 2012, MNRAS, 421, 1624
Schlegel D. J., Finkbeiner D. P., Davis M., 1998, ApJ, 500, 525
Stasińska G., 1978, A&A, 66, 257
Stasińska G., 1980, A&A, 84, 320
Stasińska G., 1990, A&AS, 83, 501
Stasińska G., 2005, A&A, 434, 507
Stewart S. G. et al., 2000, ApJ, 529, 201
Tongue T. D., Westphal D. J., 1995, AJ, 109, 2462
Walter F. et al., 2007, ApJ, 661, 102
Weisz D. R., Skillman E. D., Cannon J. M., Dolphin A. E., Kennicutt R. C. Jr, Lee J., Walter F., 2009, ApJ, 704, 1538

This paper has been typeset from a TEX/LATEX file prepared by the author.

Downloaded from http://mnras.oxfordjournals.org/ by guest on January 25, 2013

Monthly Notices
of the
ROYAL ASTRONOMICAL SOCIETY

Mon. Not. R. Astron. Soc. **423,** 1831–1844 (2012) doi:10.1111/j.1365-2966.2012.21005.x

Ionized gas velocity dispersion in nearby dwarf galaxies: looking at supersonic turbulent motions⋆

Alexei V. Moiseev[1]† and Tatiana A. Lozinskaya[2]

[1]*Special Astrophysical Observatory, Russian Academy of Sciences, Nizhnii Arkhyz 369167, Russia*
[2]*Sternberg Astronomical Institute of Lomonosov Moscow State University, Moscow 119992, Russia*

Accepted 2012 March 28. Received 2012 March 27; in original form 2011 November 24

ABSTRACT

We present the results of an ionized gas turbulent motions study in several nearby dwarf galaxies using a scanning Fabry–Perot interferometer with the 6-m telescope of the Special Astrophysical Observatory of the Russian Academy of Sciences (SAO RAS). Combining the 'intensity–velocity dispersion' diagrams ($I-\sigma$) with two-dimensional maps of radial velocity dispersion, we found a number of common patterns pointing to the relation between the value of chaotic ionized gas motions and processes of current star formation. In five out of the seven analysed galaxies, we identified expanding shells of ionized gas with diameters of 80–350 pc and kinematic ages of 1–4 Myr. We also demonstrate that the $I-\sigma$ diagrams may be useful for the search of supernova remnants, other small expanding shells or unique stars in nearby galaxies. As an example, a candidate luminous blue variable (LBV) was found in UGC 8508. We propose some additions to the interpretation, previously used by Muñoz-Tuñón et al. to explain the $I-\sigma$ diagrams for giant star formation regions. In the case of dwarf galaxies, a major part of the regions with high velocity dispersion belongs to the diffuse low surface brightness emission, surrounding the star-forming regions. We attribute this to the presence of perturbed low-density gas with high values of turbulent velocities around the giant H II regions.

Key words: ISM: bubbles – H II regions – galaxies: dwarf – galaxies: ISM – galaxies: kinematics and dynamics.

1 INTRODUCTION

The study of the gas component of dwarf galaxies is important and challenging for several reasons. First, due to the shallow potential well and a lack of spiral density waves, such galaxies provide a good opportunity for studying the interaction of young stellar groups with the interstellar medium. The ionizing radiation of OB stars, as well as the kinetic energy of stellar winds and supernova explosions are heating the gas, forming the cavities, bubbles, shells, ordered outflows and chaotic turbulent motions in the gaseous disc. Secondly, it is important to be able to properly account for the influence of these effects on the gaseous medium in order to estimate the circular rotation curve from the observed distribution of radial velocities. The information about an accurate rotation curve is critical to study the distribution of dark matter and the mass function of dwarf galaxies within various cosmological tests.

Two-dimensional (2D) distributions of the parameters of neutral and ionized hydrogen yield the most complete and detailed data on the structure and kinematics of the interstellar medium. We managed to compare the kinematics of neutral and ionized gas for several dwarf galaxies of the Local Group using the 'position–velocity' diagram, allowing us to identify expanding shells (Lozinskaya, Moiseev & Podorvanyuk 2003; Lozinskaya et al. 2008). For more distant objects, the analysis of the velocity field and the shapes of Hα and 21-cm line profiles (van Eymeren et al. 2009a,b) allows us to identify gas outflows above the galactic plane. The advantage of the radio interferometry method in the 21-cm line is the capability to map the H I distribution far beyond the optical discs of galaxies, see e.g. the results of the Faint Irregular Galaxies GMRT Survey (FIGGS) (Begum et al. 2008) and THINGS (Oh et al. 2011) surveys. However, the typical angular resolution of such observations (beam = 10–30 arcsec) often provides an excessively smooth picture and does not allow us to study the motions of gas on small spatial scales. In contrast to radio observations, using 3D spectroscopy in the optical emission lines we can study the kinematics of ionized gas with a much higher resolution 1–3 arcsec. However, it is limited only to the regions having enough ultraviolet (UV) photons to ionize the gas.

Until recently, most of the 2D data on the kinematics of gas in dwarf galaxies were obtained from the radio observations in the

⋆Based on observations obtained with the 6-m telescope of the Special Astrophysical Observatory of the Russian Academy of Sciences. The observations were carried out with the financial support of the Ministry of Education and Science of Russian Federation (contracts no. 16.518.11.7073 and 16.552.11.7028).
†E-mail: moisav@gmail.com

© 2012 The Authors
Monthly Notices of the Royal Astronomical Society © 2012 RAS

H I line. Lately though, the situation is changing. The results of optical studies of the kinematics not only for individual objects but also for small samples of galaxies are published (Ostlin et al. 1999; Moiseev, Pustilnik & Kniazev 2010). Velocity fields of ionized gas in 200 galaxies of different morphological types, 23 of which belong to the dwarf irregular (dIrr) galaxy type, were constructed within the Gassendi Halpha Survey of SPirals (GHASP) (Epinat, Amram & Marcelin 2008) with the scanning Fabry–Perot interferometer (FPI). The growing accuracy of measurements allowed us to build and analyse not only the radial velocity fields, but also the 2D maps of ionized gas velocity dispersion (σ) in some dwarf galaxies with violent star formation. The σ maps of such galaxies were published, resulting from the observations using the methods of integral field spectroscopy (see e.g. Bordalo, Plana & Telles 2009; Lagos et al. 2009; Monreal-Ibero et al. 2010) or interferometry with the scanning FPI (Lozinskaya et al. 2006; Martínez-Delgado et al. 2007; Moiseev et al. 2010). Although such data as yet exist for less than two dozen objects, the number of constructed σ maps will be growing. That way, we are preparing to publish the results of observations of another few dozen of dwarf galaxies (Moiseev, Tikhonov & Klypin, in preparation).

The nature of the supersonic ($\sigma > 10$–$20\,\mathrm{km\,s^{-1}}$) turbulent motions of ionized gas observed in dwarf galaxies is the subject of a long-standing debate (see discussion and references in Bordalo & Telles 2011). Thus, a number of authors (Terlevich & Melnick 1981; Melnick, Terlevich & Terlevich 2000) believe that the intensity-weighted mean velocity dispersion of ionized gas (σ_m) in dwarf galaxies and in giant H II regions is determined by virial motions, i.e. by the total mass of the system. On the other hand, in their recent paper Green et al. (2010) show that in a wide range of galaxy luminosities σ_m is determined only by the current star formation rate (estimated from the flux in the Hα emission line) and does not correlate with the mass of the galaxy. In this case, σ_m is a characteristic of mechanical energy, inferred to the gas by the stellar winds and supernova explosions in the process of current star formation. For neutral gas velocity dispersion, a similar conclusion was earlier made by Dib, Bell & Burkert (2006).

To address this and other problems, related to the interaction of stellar populations and interstellar medium, we must be able to correctly interpret the structures observed in the ionized gas velocity dispersion maps. Among the few studies on this subject, let us mention the papers by Yang et al. (1996) and Muñoz-Tuñón et al. (1996), who thoroughly examined two giant star formation regions NGC 604 and NGC 588 in the disc of the M33 galaxy. They proposed a method for interpreting the observed distributions of points on the 'line intensity–velocity dispersion' diagram ($I-\sigma$) in terms of evolution of ionized shells in stellar groups. Later, with the aid of these and other similar diagrams, Martínez-Delgado et al. (2007) examined the behaviour of ionized gas in three more distant blue compact dwarf (BCD) galaxies.

How universal is this method? This paper is a subsequent attempt to thoroughly consider the nature of the structures, observed in the ionized gas velocity dispersion maps. The observational data presented here were obtained at the 6-m telescope of the Special Astrophysical Observatory of the Russian Academy of Sciences (SAO RAS) within the project devoted to the internal kinematics of ionized gas in dwarf galaxies of the Local Volume ($D < 10$ Mpc). To correctly interpret the results of this project, it seems to be necessary to consider the most typical features observed in the σ maps. In order to make a detailed analysis, we have selected seven most nearby galaxies ($D = 1.8$–4.3 Mpc) from the total sample, where we managed to study fairly well both the bright H II regions, and faint diffuse Hα emission between them. It is important that there are H I distribution maps published for all the selected galaxies, which allows us to compare the distributions of ionized and neutral fractions of the interstellar medium. In order to better understand the features of the σ distribution, we employ the data on two more nearby dIrr galaxies, IC 10 and IC 1613, we previously studied in detail.

2 OBSERVATIONS AND DATA REDUCTION

2.1 Observations with the scanning FPI

The observations were made at the prime focus of the 6-m telescope of SAO RAS using a scanning FPI, installed inside the SCORPIO focal reducer (Afanasiev & Moiseev 2005). The operating spectral range around the Hα line was cut by a narrow-band filter with a bandwidth of a full width at half-maximum (FWHM)of15−21 Å. Most of the observations were made with the FPI501 interferometer, providing in the Hα line a free spectral range between the neighbouring interference orders $\Delta\lambda = 13$ Å and spectral resolution (FWHM of the instrumental profile) of about 0.8 Å ($35\,\mathrm{km\,s^{-1}}$), with the scale of 0.36 Å channel^{-1}. In 2009 November, a new interferometer FPI751 was used, having $\Delta\lambda = 8.7$ Å and a spectral resolution of 0.4 Å ($18\,\mathrm{km\,s^{-1}}$) at the scale of 0.21 Å channel^{-1}.

Between 2005 and 2009 we used the EEV 42-40 and E2V 42-90 CCD detectors, providing the image scale of 0.71 arcsec pixel^{-1} in 4×4 on-chip binned mode. In 2002, a TK1024 CCD detector was used operating in on-chip binned 2×2 pixel mode, yielding the image scale of 0.56 arcsec pixel^{-1}.

During the scanning process, we have consistently obtained 36 interferograms of a given object (40 for FPI751) at different distances between the FPI plates. The seeing at different nights ranged from 1 to 3 arcsec. The data reduction was performed using the software package running in the IDL environment. Following the primary reduction, airglow lines subtraction, photometric and seeing corrections using the reference stars and wavelength calibration, the observational data were combined into the data cubes, where each pixel in the field of view contains a 36- (or a 40-) channel spectrum. The detailed description of data reduction algorithms and software is presented in Moiseev (2002) and Moiseev & Egorov (2008). All galaxies except VII Zw 403 were observed in two scanned cycles in order to remove parasitic ghost reflection, as described by Moiseev & Egorov (2008).

The log of observations is given in Table 1, listing the following data: the name of the galaxy; the distance, scale (pc arcsec^{-1}) and absolute stellar magnitude M_B according to Karachentsev et al. (2004); the epoch of observations; the type of interferometer; total exposure time; resulting angular resolution (ω) after the smoothing by a 2D Gaussian (typical FWHM = 1.0–2.0 pixels) in order to increase the signal-to-noise ratio (S/N) in the regions of low surface brightness. This value was estimated from foreground stars' images in the final data cube.

2.2 Velocity dispersion measurements

Referring to the velocity dispersion of ionized gas (σ) in the present paper, we mean the standard deviation of the Gaussian, describing the profile of the Hα emission line after accounting for the FPI instrumental profile and subtracting the contribution of thermal broadening in the H II regions. We used the method described in detail in Moiseev & Egorov (2008).

Table 1. Log of the observations.

Name	D (Mpc)	Scale (pc arcsec^{-1})	M_B	Date	FPI	Exp. time (s)	ω (arcsec)	(pc)
DDO 53	3.56	17	−13.21	26.2.2009	FPI501	200 × 36	3.3	57
DDO 99	2.64	13	−13.41	26.2.2009	FPI501	180 × 36	3.8	49
DDO 125	2.54	12	−14.07	18.5.2005	FPI501	180 × 36	3.0	37
DDO 190	2.79	14	−14.13	04.3.2009	FPI501	100 × 36	3.3	45
UGC 8508	2.56	12	−12.92	16.5.2005	FPI501	200 × 36	3.0	37
UGCA 92	1.80	9	−14.48	10.11.2009	FPI751	180 × 40	2.5	22
VII Zw 403	4.34	21	−13.87	29.11.2002	FPI501	300 × 36	2.2	46

The width of the instrumental profile of the FPI was measured from the calibration lamp line spectrum. The observed Hα line profiles were fitted by the Voigt function, which gives a good description of the observed profile. From the results of profile fitting, we constructed 2D radial velocity fields of ionized gas, radial velocity dispersion maps free from the effects of the instrumental profile ($\sigma_{\rm real}$), as well as the galaxy images in the Hα emission line and in the continuum. The flux maps were calibrated to the absolute scale of surface brightness (erg s^{-1} cm^{-2} arcsec^{-2}) by normalizing to the total flux of the galaxy in the Hα line, known from the literature (Moiseev et al., in preparation).

The accuracy of velocity dispersion was estimated from the measurements of the S/N using the relations given in fig. 5 of Moiseev & Egorov (2008). On the σ maps, we masked the regions with a weak signal, where the formal error of velocity dispersion measurements exceeded 6–9 km s^{-1} (which corresponds to the S/N $\leq$ 7). Meanwhile the line flux maps were constructed confidently enough even for weaker lines, down to S/N $\approx$ 2–3.

The transition from the measured $\sigma_{\rm real}$ to the needed σ was done according to the relation from Rozas et al. (2000):

$$\sigma^2 = \sigma_{\rm real}^2 - \sigma_{\rm N}^2 - \sigma_{\rm tr}^2, \quad (1)$$

where $\sigma_{\rm N} \approx 3$ km s^{-1} and $\sigma_{\rm tr} \approx 9.1$ km s^{-1} correspond to the natural width of the emission line and its thermal broadening at 10^4 K.

In the case of UGC 8508, using the formula (1) we get to $\sigma^2 < 0$ in the centre of several H II regions. This is most likely caused by a smaller value of thermal broadening there due to $T_e < 10^4$ K. For this galaxy we adopted $\sigma_{\rm tr} = 7.5$ km s^{-1} that corresponds to $T_e \approx$ 6800 K.

In most of the objects, the observed line profile is very well described by a single-component Voigt profile.

Of all the galaxies considered, only UGC 8508 and UGCA 92 have regions in which the Hα profile reveals two components with their velocity separation larger than or comparable to the spectral resolution limit (35 and 18 km s^{-1}, respectively).

3 $I-\sigma$ DIAGRAMS

Fig. 1 shows the monochromatic images in the Hα line, the σ maps, as well as the $I-\sigma$ diagrams for all the galaxies. Our diagrams differ from those built earlier (Muñoz-Tuñón et al. 1996; Yang et al. 1996; Martínez-Delgado et al. 2007): instead of the peak line intensity ($I_{\rm peak}$), we use the total flux in the line (I), having a clearer physical meaning (the luminosity per area unit). Since the σ maps were masked by the fixed S/N level, and the noise level in the outer regions is mainly determined by the sky background, the left-hand side boundary of the point cloud in the diagrams is an inclined line $I \sim \sigma I_{\rm peak}$, where $I_{\rm peak}$ = constant. The main advantage of using I against $I_{\rm peak}$ is that the total flux obviously does not depend on spectral resolution. In order to understand the difference of result using I instead of $I_{\rm peak}$, we have created both types of diagrams for the sample galaxies and we conclude that all the shell-like features are preserved on the diagrams. We also abandoned the linear scale of intensities and use the log I, since the observed surface brightness difference is 2–3 orders of magnitude, which is significantly larger than the brightness range inside the giant H II regions in Muñoz-Tuñón et al. (1996).

The characteristic features, commented on below, are illustrated with different colours in the diagrams. The horizontal lane in dark blue has a relatively low velocity dispersion σ and high surface brightness. The boundaries of brightness are chosen so that the highlighted regions contain 50 per cent of the total luminosity of the galaxy in the Hα emission line. By red, yellow and green colours we show the regions with increased σ, trying to wherever possible identify the shell structures. The red line in the diagrams marks the level of mean velocity dispersion across the galaxy, intensity-weighted in the ith pixel: $\sigma_{\rm m} = \sum \sigma_i I_i / \sum I_i$. When we further refer to 'high' or 'low' velocity dispersion, we have in mind $\sigma > \sigma_{\rm m}$ and $\sigma \leq \sigma_{\rm m}$, respectively. For instance, other regions with $\sigma > \sigma_{\rm m}$ are shown by orange, whereas low-luminosity regions with low σ are marked in grey.

Fig. 1 also contains maps indicating the locations of regions, marked on the corresponding $I-\sigma$ diagrams.

3.1 DDO 53

The kinematics of ionized gas in this galaxy was previously investigated with the scanning FPI by Dicaire et al. (2008), but the authors were only able to measure the distribution of radial velocities in the bright H II regions, whereas our data include the regions of faint diffuse emission. The σ map clearly reveals a pattern, typical of all galaxies we observed: the minimum value of velocity dispersion is seen in the centres of bright H II regions, while in the space between the star formation regions and in the outer parts of the galaxy, σ reaches its maximal values up to 40–50 km s^{-1}, which clearly points to the supersonic nature of motions.

The shape of the $I-\sigma$ diagram resembles the scheme given by Muñoz-Tuñón et al. (1996) – a horizontal lane (marked in dark blue in Fig. 1) with $\sigma \approx \sigma_{\rm m}$ and several inclined lanes with much larger σ values. According to the interpretation of Muñoz-Tuñón et al. (1996), such lanes must correspond to individual thin expanding shells: the maximal velocity dispersion (or even a double profile) and the minimal surface brightness at the centre of the shell; increasing I and decreasing σ with the growing distance from the centre until the inner edge of the shell is reached. The best example of such a

© 2012 The Authors, MNRAS **423,** 1831–1844
Monthly Notices of the Royal Astronomical Society © 2012 RAS

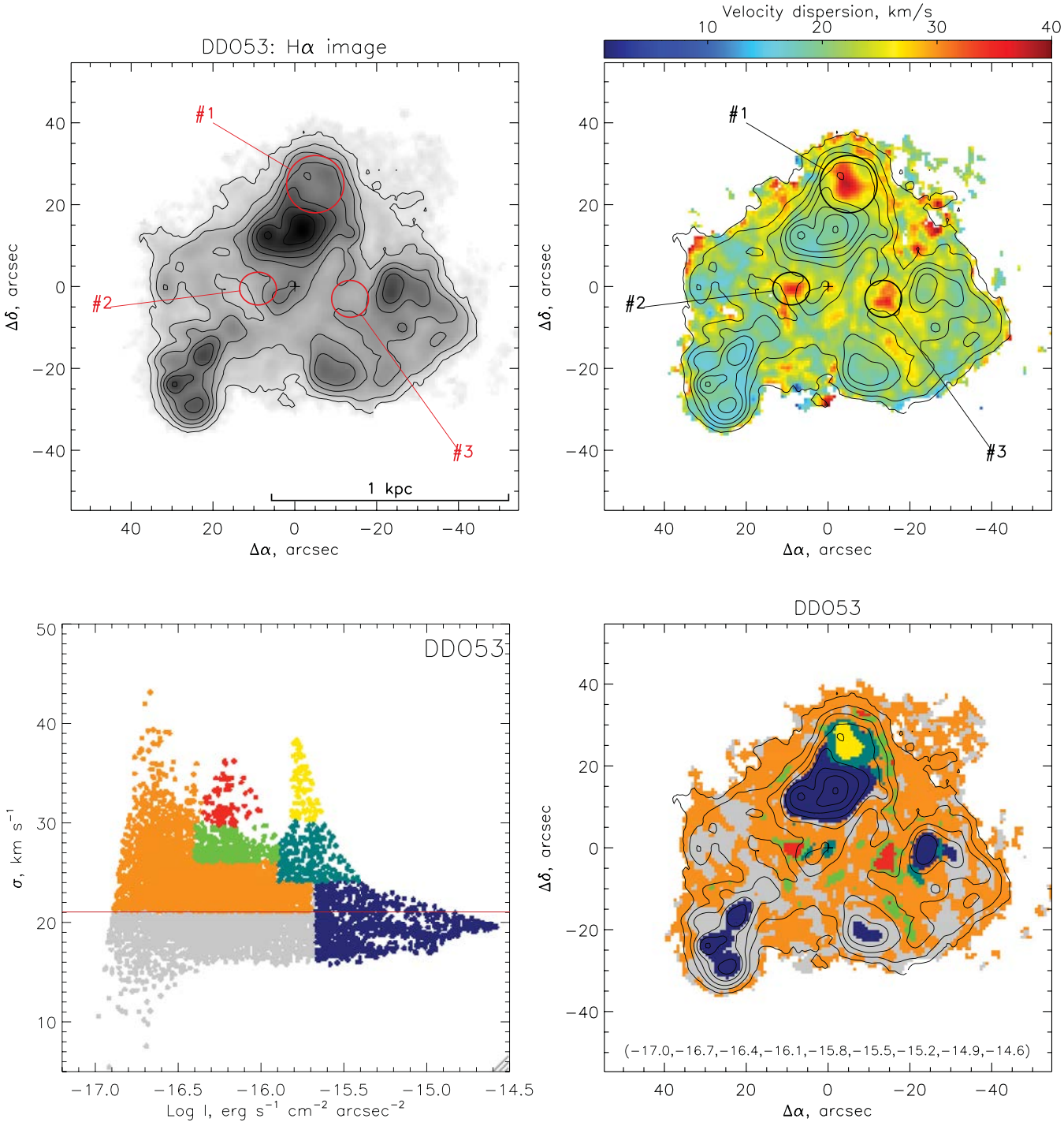

Figure 1. Results of observations with the FPI for each galaxy. The top row: the image in the Hα line in logarithmic values of intensity (left) and the velocity dispersion map with superimposed contours of the Hα image (right). The ellipses with numbers mark the shell-like structures, the parameters of which are given in Table 2. For DDO 125 and UGC 8508 the ellipses without numbers show large-scale cavern, discussed in the text. The cross marks the centre of the image in the continuum. The bottom row: the intensity–velocity dispersion diagram (left). The red horizontal line marks the intensity-weighted mean velocity dispersion σ_m. The right-hand plot shows the location of regions, marked by different colours on the $I-\sigma$ diagram. The contours correspond to the isophotes in the Hα line, their values (in log of erg s^{-1} cm^{-2} arcsec^{-2}) are given in brackets on the right-hand bottom figures. (The full version of this figure for all galaxies is published in the electronic edition of the Journal).

shell is given by a structure adjacent to the north of the brightest H II region; in the diagram it is coloured yellow (centre) and dark green (periphery). This shell-like structure is also evident in the Hα surface brightness distribution. In the figure we marked it as #1, its diameter is approximately $d \approx 14$ arcsec (240 pc). For all the shells we identified, Table 2 gives the estimates of the sizes along the major and minor axes (d_1, d_2), the maximal velocity dispersion σ_{max} and the kinematic ages $t_{kin} = 0.5 d_1/\sigma_{max}$.

Table 2. Shell parameters.

Name	Size (pc)	$\sigma_{\max}$ ($\mathrm{km\,s^{-1}}$)	$t_{\rm kin}$ (Myr)
DDO 53 #1	240 × 240	39	3.0
DDO 53 #2	150 × 140	37	2.0
DDO 53 #3	150 × 150	37	2.0
DDO 125 #1	200 × 200	27	3.6
DDO 125 #2	160 × 120	25	3.1
UGC 8508 #1	350 × 350	40	4.2
UGCA 92 #1	180 × 130	39	2.2
UGCA 92 #2	190 × 110	31	3.1
UGCA 92 #3	90 × 90	31	1.4
UGCA 92 #4	170 × 170	40	2.1
VII Zw 403 #1	190 × 190	33	2.8

The points from the second, less contrast peak in the diagram (marked in red and green) have to correspond to a younger shell according to the model by Muñoz-Tuñón et al. (1996). On our maps the points of this peak mainly lie in two shells, designated nos. #2 and #3. According to Table 2, their kinematic age is in fact about 1.5 times shorter than that of the shell #1. On the other hand, the points from the most apparent peak on the diagram (orange colour, high σ and relatively low surface brightness) do not belong to any individual knots or shells, but form a common diffuse envelope which surrounds bright H II regions.

3.2 DDO 99

Unlike the previous case, the $I-\sigma$ diagram for DDO 99 has a simpler shape – there are no pronounced features, except for the horizontal lane and a broad triangular region with a high σ. Some kind of a hint for a possible shell is a tiny cloud of points in the diagram with $\log I > -15.7, \sigma > 21\,\mathrm{km\,s^{-1}}$ (marked in green). On the map of the galaxy, these points are grouped mainly on the edge of the southern star formation region; the size of this possible shell is comparable to the spatial resolution of ∼50 pc. The remaining regions of increased σ (plotted in orange in the figure) are distributed on the periphery of H II regions.

3.3 DDO 125

The distribution of ionized gas here reveals several shells and loops, associated with two bright star formation regions to the north and south of the galactic centre. These two H II regions are located diametrically on the edge of a giant cavity, sized around 600 pc (denoted in Fig. 1 as 'cavern'), inside of which there are almost no sources of gas ionization. In the centre of the cavity the H I density is also reduced (see Section 5), indicating that the gas was depleted or swept out during the previous burst of star formation. The size of the cavity and the features of mutual distribution of H I and H II are very similar to the complex of giant shells and arcs in the galaxy IC 1613 (Lozinskaya et al. 2003; Silich et al. 2006), with a diameter from 300 pc to 1 kpc. We were unable to find any kinematic evidence for the expansion of shell DDO 125 #1, as it is not identified on the $I-\sigma$ diagram. At once the σ distribution easily reveals more compact shells DDO 125 #1 and #2, which coincides with the northern and southern H II regions (coloured red and green in the figure). Our estimate of its age is $t_{\rm kin} = 3.1$–3.6 Myr. Other regions with high σ, marked in the map with orange, are embordering the bright star-forming regions.

3.4 DDO 190

The distribution of the ionized gas velocity dispersion and the $I-\sigma$ diagram here resemble the picture observed in DDO 99. Namely, the points with high σ surround bright H II regions; velocity dispersion in H II regions is comparable to $\sigma_{\rm m}$. Only a few low-contrast peaks of the velocity dispersion around the elongated H II region in the northern part of the galaxy can be regarded here as a vague hint to the shell (in terms of the model by Muñoz-Tuñón et al. 1996). These possible shells with sizes comparable to the spatial resolution of our observations are coloured green in the diagram.

3.5 UGC 8508

The observed distribution of σ is very similar to previous objects: a minimal velocity dispersion inside the H II regions surrounded by the diffuse gas with increased σ. In addition, the $I-\sigma$ diagram reveals an inclined lane, which should correspond to a shell according to Muñoz-Tuñón et al. (1996).

Indeed, most of the points of this lane (marked in Fig. 1 with red and green) are concentrated within a huge arch of H II regions on the edge of the western part of the disc of ionized gas. Morphologically and kinematically this resembles a half of an unclosed expanding shell with a diameter of approximately 350 pc. The kinematic age of this shell, we designated as UGC 8508 #1, is about 4 Myr (Table 2).

In a recent paper, Warren et al. (2011) showed that the eastern half of the galaxy has a cavity in the H I distribution with a diameter of about 550 pc, so that the bright H II regions are located along its borders. However, this region (denoted as 'cavern' in our figure) is not distinguishable by the kinematics of ionized gas – velocity dispersion is small, except for several spots with increased σ in the heart of this cavity, where almost no Hα emission is present. They are difficult to be interpreted as a separate shell, most likely we are dealing with an increase of turbulent velocities on the border of H II regions.

A group of points, forming a 'horizontal sequence' in the upper right part of the $I-\sigma$ diagram, caught our eye, since the surface brightness here is considerably greater than that for the other points with a large velocity dispersion ($\sigma = 35$–$40\,\mathrm{km\,s^{-1}}$). All the points, marked brick-red in our scheme, are grouped within the single Hα knot on the eastern edge of the disc. Its FWHM in the image is equal to the size of stellar images, i.e. it cannot be spatially resolved. The Hα line profile has a distinct two-peak structure here with the distance between peaks of about $80\,\mathrm{km\,s^{-1}}$. The examples of emission line profiles are shown in Fig. 2. The mean systemic velocity of the knot is about $100\,\mathrm{km\,s^{-1}}$, in agreement with line-of-sight velocities of the nearest side of the galaxy disc (∼$80\,\mathrm{km\,s^{-1}}$), i.e. it seems to belong to UGC 8508. Our first explanation based on the Hα double component profiles was that we observe a single remnant of the supernova explosion (similar to the SNR S8 in IC1613, see below). However, our new spectroscopic observations revealed that it is a good candidate to unique emission star – luminous blue variable (see Appendix A).

3.6 UGCA 92

We observe here the most significant asymmetry in the distribution of ionized gas relative to the centre among all the galaxies of our sample. In the Hα line image, several shells and arcs are seen, most of which are related to the bright star formation region in the eastern part of the galaxy. There, five H II regions form a closed elongated loop in the centre of which a maximum in the σ distribution is observed. One can discern a broad inclined lane on the $I-\sigma$ diagram

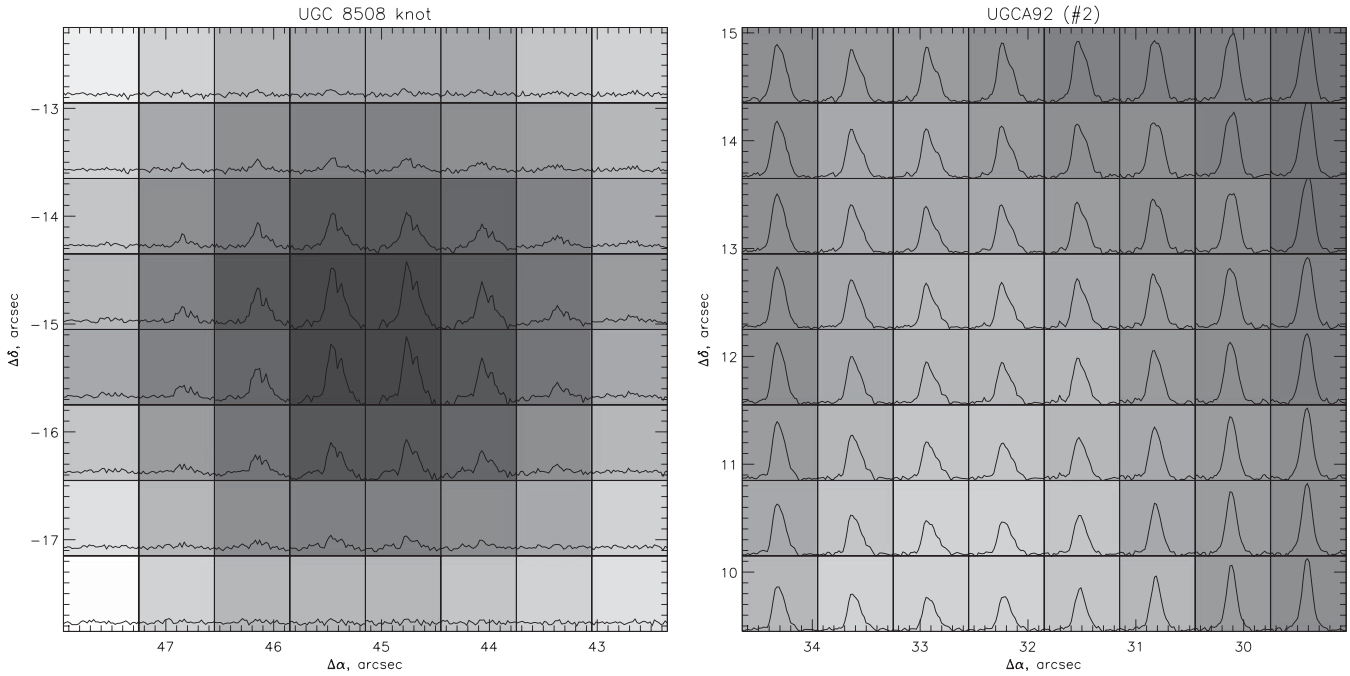

Figure 2. The regions possessing emission line profiles with a two-component structure, overlapped on the Hα images: UGC 8508 (left) and UGCA 92 (right).

(coloured green and orange), the corresponding points lying inside the above-mentioned loop of H II regions. Meanwhile, in the centre of the loop, where the velocity dispersion is maximal and intensity is minimal, the Hα line profiles have a noticeable right wing, so that they can be decomposed into two components – a more intense blue one and a 1.5–2 times fainter red one (see Fig. 2). The separation between the components is $\Delta V = 45$–57 km s^{-1}, decreasing from the centre to edges. This multicomponent profile structure could not be a result of spatial smoothing procedures ('beam smearing'), because the peak velocity in the H II regions that formed this loop is constant ± 10 km s^{-1}. The observed features indicate that we are dealing with a shell (designated as UGCA 92 #2), expanding at a rate of $v_{\rm exp} = \frac{1}{2}\Delta V \approx 30$ km s^{-1}; this value coincides with the maximal velocity dispersion in this region (see Table 2). The velocity dispersion distribution easily reveals three more expanding shells of similar size and age. It is possible that the external arch structures in the western and eastern parts of the galaxy have the same nature; however, we failed to measure their expansion velocity.

3.7 VII Zw 403

We present here the re-analysed data first described in Lozinskaya et al. (2006). An empty spot near the centre is caused by masking the trace of a bright parasitic reflex (see Moiseev & Egorov 2008 for details on the ghost reflex). Galaxy VII Zw 403 is one of the most well described in the literature objects of our sample. According to Lynds et al. (1998) the age of the latest burst of star formation here is 4–10 Myr, which closely coincides with the estimates of the kinematic age of shells, associated with bright regions of star formation (at least 3–4 Myr old, according to Lozinskaya et al. 2006). On the other hand, the velocity dispersion of ionized gas in the H II regions themselves is small: $\sigma < (\sigma_{\rm m} = 18$ km s$^{-1})$. The $I-\sigma$ diagram confidently reveals an inclined lane (marked with green and orange) which, according to the model by Muñoz-Tuñón et al. (1996), must point to the presence of an expanding shell.

The distribution of points on the map of the galaxy shows that this shell (VII Zw 403 #1) is located between the bright H II regions in the centre of the galaxy and is adjacent to region 4 according to the numbering of Lynds et al. (1998). The kinematic age of the shell coincides with the estimates by Lozinskaya et al. (2006) given above.[1] Other regions of increased velocity dispersion are located at the periphery of the H II regions and in the outer parts of the disc of ionized gas. The local gas kinematics is difficult to explain in terms of individual shells. Thus, several spots with high velocity dispersion in the northern part of the galaxy are more likely associated with the emission arcs of relatively low surface brightness, detected by Silich et al. (2002) and Lozinskaya et al. (2006). According to the cited authors, these arcs were caused by the feedback of the stellar population aged $t \approx 10$ Myr, formed at the early stages of the last burst of star formation.

4 THE EFFECT OF SPATIAL RESOLUTION

Yang et al. (1996) and Muñoz-Tuñón et al. (1996) have discussed and interpreted the $I-\sigma$ diagrams, constructed for the giant complexes of star formation in the nearby galaxy M33. The spatial resolution of their observations was $\omega \approx 3.5$ pc. In this work we study more distant galaxies with a much rougher resolution (see the last column in Table 1). It is hence clear that we are losing the data on the small-scale kinematics of gas. How seriously may this affect the shape of the $I-\sigma$ diagrams and the distribution of velocity dispersion? In order to analyse the effects of spatial resolution on the observed kinematics, we examined two nearby and well-studied dIrr galaxies of the Local Group: IC 10 and IC 1613. We have earlier observed both galaxies at the 6-m telescope with the same equipment as described in Section 2. The spatial size of regions,

[1] Note that the use of the approximation by the Voigt profile in our work allows making more accurate estimates of the expansion rate than the Gaussian approximation in Lozinskaya et al. (2006).

Table 3. Smoothing of the observational data on galaxies of the Local Group.

Name	D	ω		$\omega_{\rm smo}$	
	(Mpc)	(arcsec)	(pc)	(arcsec)	(pc)
IC 10	0.73	1.5	5.3	11	40
IC 1613	0.80	2.2	8.5	11	43

encompassed by current star formation, is about 1 kpc, just like in the galaxies described above (hereinafter the 'main sample'). A detailed description of the distributions of ionized and neutral gas, the identification of the expanding H I and H II bubbles and a discussion of the relation between these bubbles and young stellar groups are given in Lozinskaya et al. (2008) and Egorov, Lozinskaya & Moiseev (2010) for IC 10, and in Lozinskaya et al. (2003) for IC 1613. The spatial resolution of our observations of ionized hydrogen in the Hα emission line was 5 and 8 pc, correspondingly.

To imitate the effect of low resolution, the original data cubes for IC 10 and IC 1613 in the Hα line were first smoothed by the 2D Gaussians, and then binned, so that the resulting pixel size amounted to ∼5.6 arcsec. Table 3 lists the distance to the galaxy, and the initial (ω) and smoothed ($\omega_{\rm smo}$) spatial resolution. The smoothed data show how these two galaxies would look like when observed with a resolution of $\omega_{\rm smo} \approx 40$ pc, i.e. under the same conditions as the objects of the main sample. The velocity dispersion maps and the diagrams for the original and smoothed cubes were constructed using the method described in Section 2. Fig. 3 shows the original and smoothed images of both galaxies in the Hα line, and the corresponding $I-\sigma$ diagrams are shown in Figs 4 and 5.

The $I-\sigma$ diagrams, constructed from the non-smoothed data, reveal a fine structure that reflects the data on gas motions on the scales of a few tens of parsecs. It is obviously lost in the smoothed data, since the construction of the corresponding diagrams involves a significantly smaller (by 100–200 times) number of points. A detailed review of the diagrams and the σ distribution maps allows us to make the following conclusions.

(i) Smoothing significantly (by 5–10 times) decreases the observed range of surface brightness I by 'smearing' the compact bright H II regions. This is particularly notable in the case of IC 10 (Fig. 4).

(ii) Similarly, the observed spread of σ values decreases almost twice due to the averaging of small-scale perturbations. On the other hand, smoothing has almost no effect on the weighted average value of the velocity dispersion $\sigma_{\rm m}$, since the variations of radial velocity inside a sampled element ('beam-smearing effect') are small, compared with the magnitude of turbulent velocities.

(iii) The shape of the distribution of points on the $I-\sigma$ diagram preserves its old 'triangular' form – a horizontal lane with $\sigma \leq \sigma_{\rm m}$ (coloured dark blue) and the regions of low surface brightness with high velocity dispersion. It is also well seen how the deteriorating resolution results in the merger of separate regions with high σ, located on the periphery of H II regions, into a common structure, embordering the star formation regions. That is exactly the picture we often see in the main sample galaxies.

Large-scale kinematically isolated structures remain visible in the smoothed images as well. In IC 10 this is primarily the so-called synchrotron superbubble, located on the southern boundary of the brightest (eastern) star formation region, and prominent by its increased velocity dispersion. We have previously shown (Lozinskaya & Moiseev 2007) that this shell centring in the X-ray source IC 10 X-1 is probably a remnant of a hypernova explosion. IC 1613 data reveal a complex of multiple shells, located in the eastern part of the star-forming region (coloured red and orange in Fig. 5). Here, the Hα line profiles have a clear two-peak structure with the velocity difference between the components of $\Delta V \approx 100\,{\rm km\,s^{-1}}$. In Lozinskaya et al. (2003) we thoroughly examined the $P-V$ diagrams for this region and showed that the observed kinematic features are associated with the effect of expanding and possibly colliding shells of ionized gas. Among the galaxies from the main sample, similar kinematic components at congruent spatial scales were detected only in UGCA 92. The second interesting feature that attracts attention in the $I-\sigma$ diagrams in IC 1613 is the brightest in the Hα line compact region at the centre of the field [with coordinates ($\Delta x = 150$ arcsec, $\Delta y = 90$ arcsec)], also characterized by a high velocity dispersion ($\sigma \approx 50-60\,{\rm km\,s^{-1}}$). In Fig. 5 it is marked in green. This is the supernova remnant S8, which stands out by its unusually high luminosity simultaneously in the X-ray (a marker of a young remnant) and optical (a marker of an old remnant) ranges (Lozinskaya et al. 1998). The emission line profile has a multicomponent structure here. An object with a similar position in the $I-\sigma$ diagram and also with a multicomponent profile from the main sample of galaxies is an LBV candidate in UGC 8508.

5 DISCUSSION

In all of the above galaxies there exists a clear link between the flux in the Hα line and velocity dispersion of ionized gas. The brightest H II regions reveal small line widths ($\sigma \leq \sigma_{\rm m}$); the scatter of observed values increases with decreasing surface brightness, so that in most regions of low brightness the velocity dispersion significantly exceeds the mean ($\sigma \gg \sigma_{\rm m}$), although individual points may still show a low velocity dispersion ($\sigma \approx 3-7\,{\rm km\,s^{-1}}$). In general, the shape of the $I-\sigma$ diagram for dIrr galaxies bears resemblance to the diagram constructed by Muñoz-Tuñón et al. (1996) for the star formation regions NGC 588 and NGC 604. Such a resemblance is not surprising in objects of different scales, since in both cases the kinematics of gas must be primarily determined by the input of mechanical energy of the wind of massive young stars and multiple supernovae explosions, the interaction of which with the circumambient interstellar medium depends on its density.

However, there is a number of differences between the kinematic properties of giant H II regions and Irr galaxies; the sketch presented in Fig. 6 illustrates the difference.

The full scale of the regions in NGC 588 and NGC 604 emitting in the Hα line is not larger than 130–150 pc; hence, at the corresponding $I-\sigma$ diagrams the entire region of increased velocity dispersion splits into several inclined lanes, which Muñoz-Tuñón et al. (1996) identify with expanding ionized shells that differ by age. In the scheme they propose, which is illustrated in our Fig. 6 (inset b), the centre of the expanding thin shell when projected on to the sky plane has a low surface brightness and a large velocity dispersion determined by the expansion velocity. With increasing distance from the centre of the shell, the Balmer emission lines intensity increases (the line of sight intersects an even thicker layer), and σ declines, since the projection of expansion velocity on to the line of sight decreases.

In the galaxies considered above, the pattern is more complex. Here the total spatial size of the regions where we examine the motions of ionized gas is significantly (8–10 times) larger. In five out of seven galaxies of the main sample (DDO 53, DDO 125, UGC 8508, UGCA 92 and VII Zw 403), we were able to identify the expanding shells of about 80–350 pc in size. The points belonging

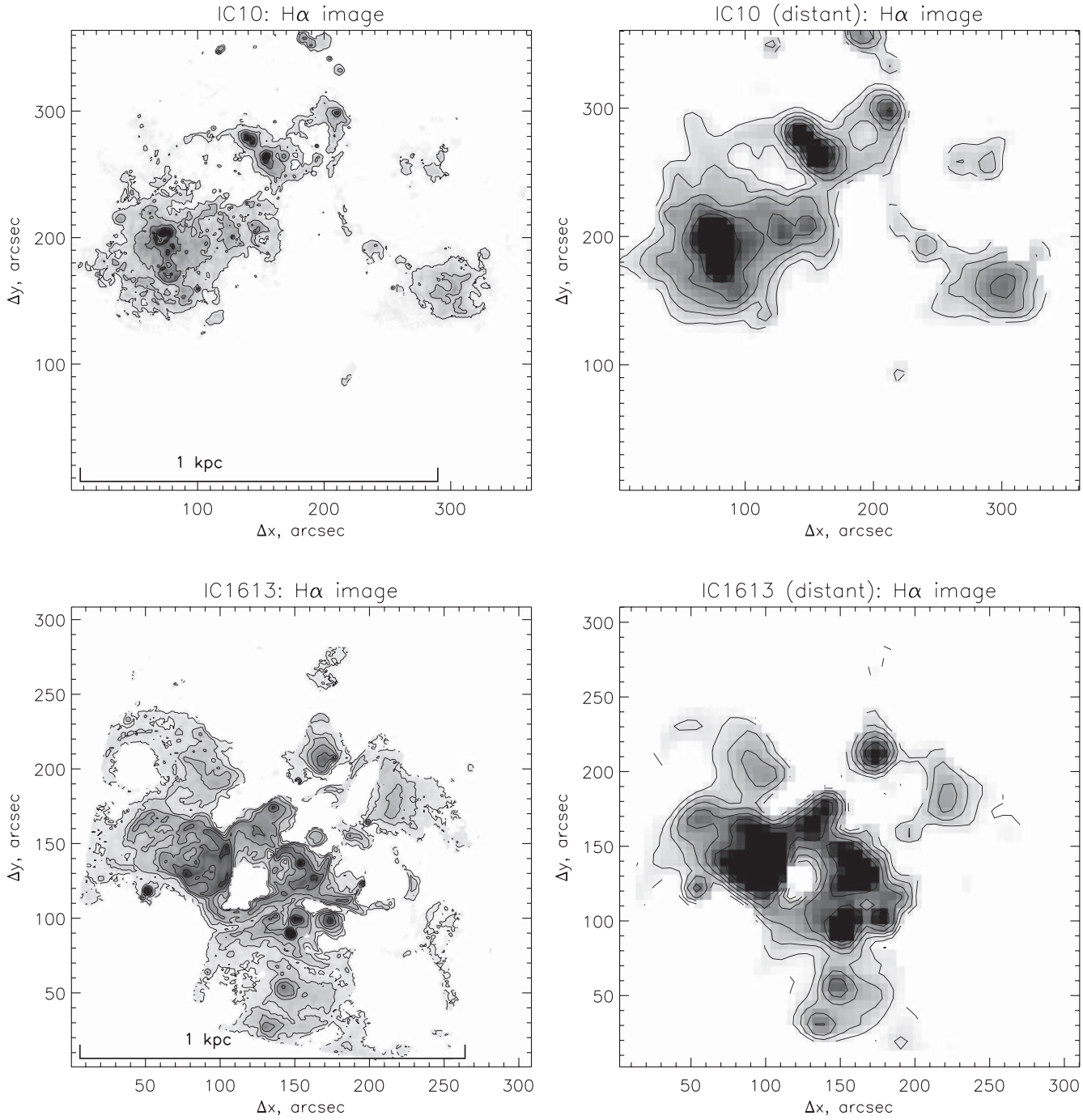

Figure 3. The Hα images of the galaxies IC 10 (top) and IC 1613 (bottom). Left-hand column: the original results of observations with the scanning FPI; right-hand column: the same data smoothed to the spatial resolution of $\sim$40 pc.

to these shells are forming inclined lanes on the diagrams as well. However, we were unable to associate the bulk of points having a high velocity dispersion with such structures. This is not surprising, since the formation of giant shells in itself requires a number of specific conditions (a sufficient initial gas density, a simultaneous onset of starburst), and in most cases, it can be the result of the influence of several generations of star groups on the interstellar medium (McQuinn et al. 2010; Warren et al. 2011).

Perhaps we simply do not notice small shells sized 5–50 pc due to the low spatial resolution. The analysis of the original and smoothed data provided for the nearby galaxies IC 10 and IC 1613 shows that an insufficient spatial resolution cannot explain the fact that most of the regions with high σ are not related to the expanding shells. A more important fact is that the points with high σ, occupying the top left part of the $I-\sigma$ diagram, belong to the diffuse emission of low surface brightness and are spatially clustered around the star formation regions and on the periphery of the disc of ionized gas in the galaxies. Note that despite the low surface brightness, the S/N here is sufficient for reliable measurements of σ.

It seems that the observed distribution of points with a high velocity dispersion of ionized gas is not bound to specific shells, but rather to the integrated effect of young stellar groups feedback.

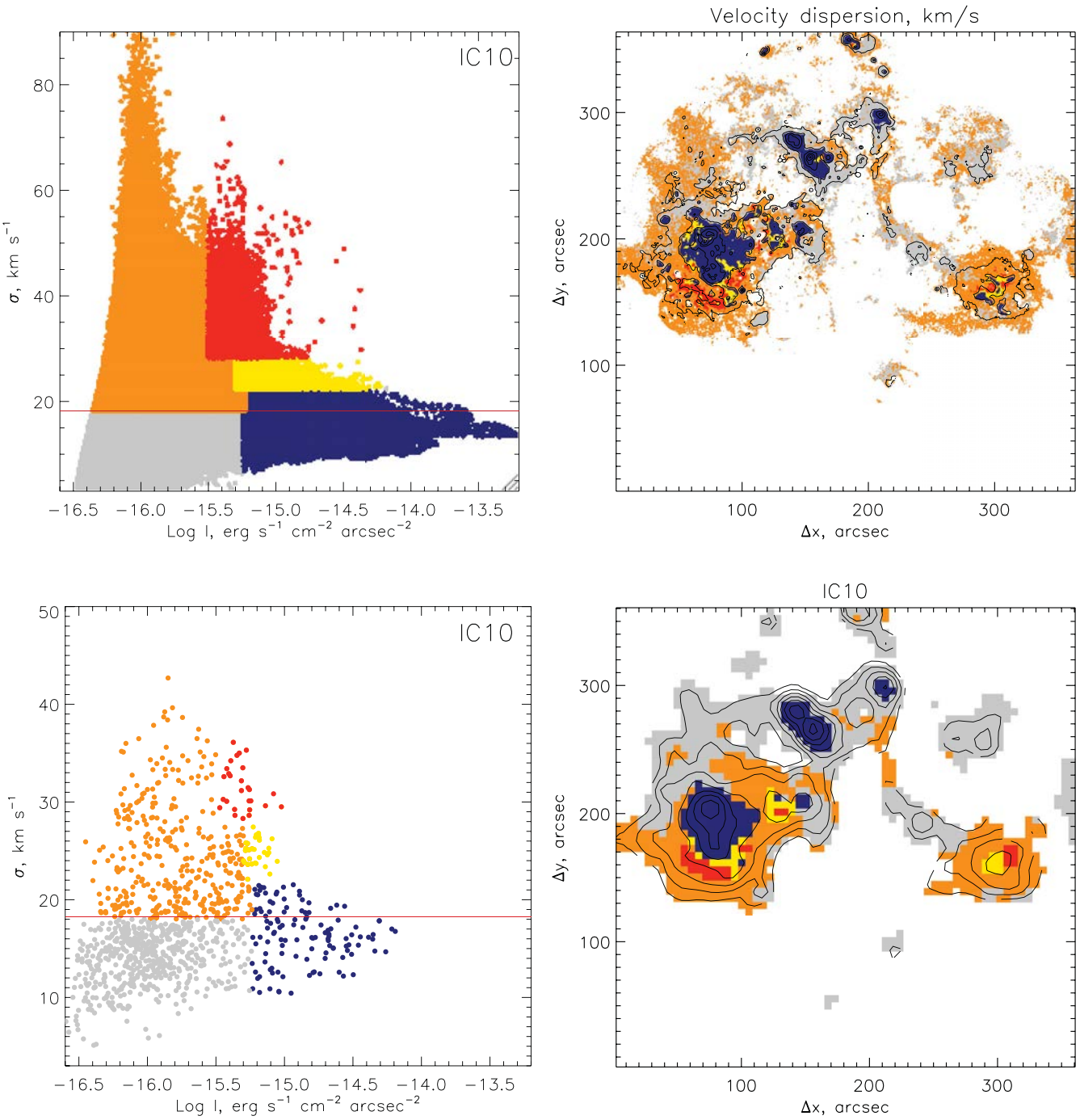

Figure 4. IC 10: the original (top) and smoothed (bottom) data. The left-hand plot shows the $I-\sigma$ diagrams. The red horizontal line marks the value of the intensity-weighted mean velocity dispersion $\sigma_{\rm m}$. The right-hand plot shows the location of regions identified by different colours on the $I-\sigma$ diagram. The contours correspond to the isophotes in the Hα line.

Meanwhile, both the photoionization radiation of OB stars, and kinetic energy of the supernova explosions and winds of young stars lead to an increase of chaotic, turbulent velocities of ionized gas. At the same time, a less dense gas has a larger amplitude of velocities than the gas in denser clouds. The same input of energy in the low-density medium provides higher gas motion velocities due to the dependence of the shock wave velocity on the density of the surrounding gas. And we have to take into account that the gas, shock-heated by stellar winds and supernovae, is only partially confined and must be leaking out of the pores in the H II shells (Lopez et al. 2011).

Given the above, to be able to interpret the observed $I-\sigma$ diagrams of dwarf galaxies, in addition to the thin shells considered by Muñoz-Tuñón et al. (1996), we have to bring in some more extended structures: the H II regions, surrounded by the coronae of perturbed gas of low density, with low surface brightness in the Balmer emission lines. This is schematically shown in Fig. 6(a). When we look at the centres of bright H II regions, there prevails

© 2012 The Authors, MNRAS **423,** 1831–1844
Monthly Notices of the Royal Astronomical Society © 2012 RAS

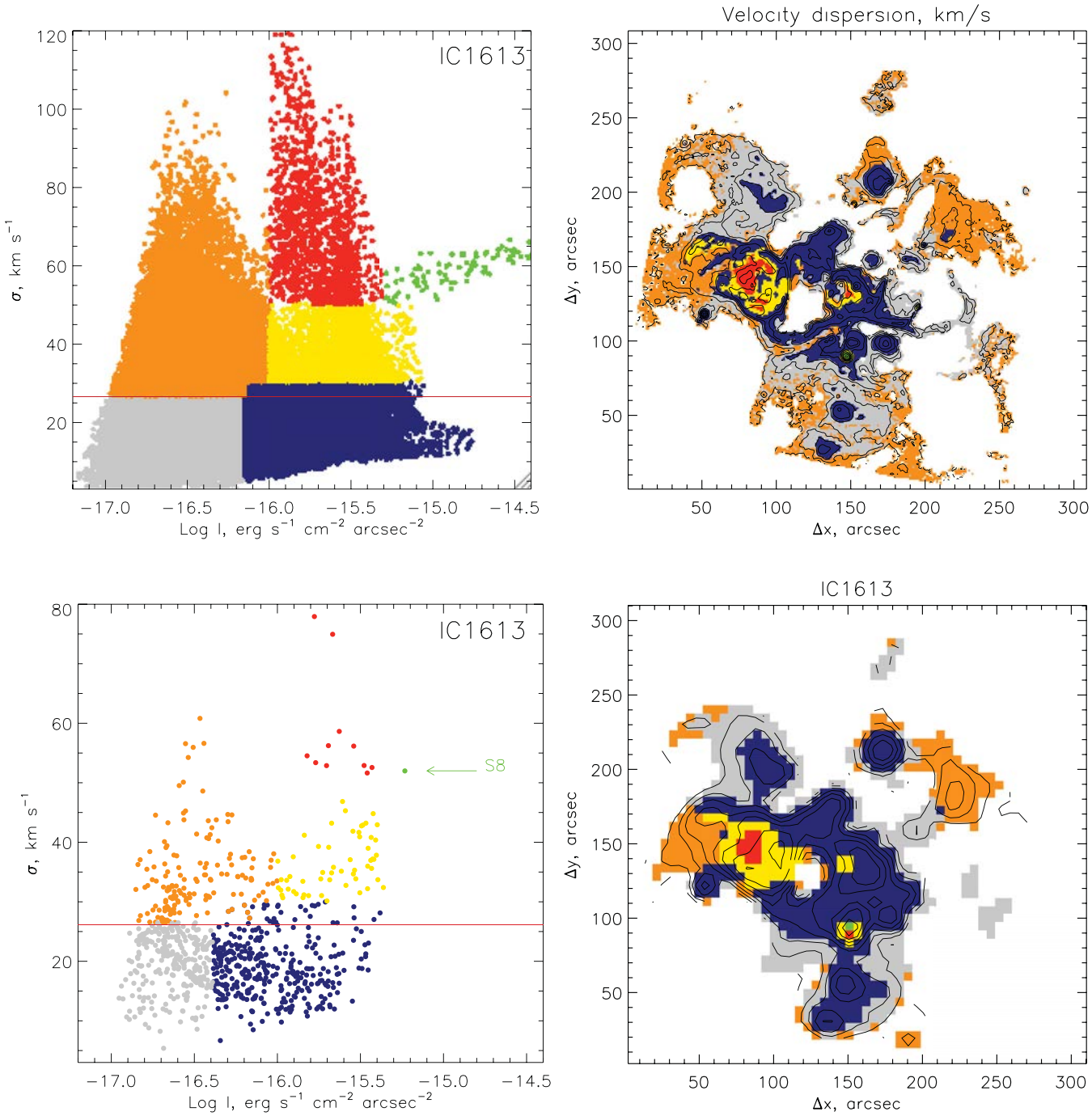

Figure 5. IC1613: the original (top) and smoothed (bottom) data. The left-hand plot shows the $I-\sigma$ diagrams. The red horizontal line marks the value of the intensity-weighted mean velocity dispersion σ_m. The arrow with a marking directs to the point, corresponding to the known supernova remnant. The right-hand plot shows the localization of regions, marked by different colours on the $I-\sigma$ diagram. The contours correspond to the isophotes in the Hα line.

a contribution of the inner regions both into Hα line intensity and into the velocity dispersion. On the periphery, however, we mainly observe high-velocity turbulent motions of the interstellar medium with low density and, consequently, with high velocity dispersion. The region of the diagram occupied by these points has a characteristic triangular shape because its right border is determined by the effect of declining observed velocity spread with increasing surface brightness.

It is clear that talking about density, we should bear in mind the total density of gas, including not only ionized but also the molecular and neutral species. First of all, because the main part of the gas in dwarf galaxies disc is in the H I state. Fig. 7 gives a comparison of the distributions of H I and H II in several galaxies of our sample, for which Begum et al. (2008) and Oh et al. (2011) have published maps of the distribution of neutral hydrogen. It can be clearly seen that the bright H II regions locate in places with high density of neutral hydrogen. Really, there are some small-scale deviations; in particular the peaks in the distribution of H I are often offset by a few hundred parsecs from the centres of current star formation. This effect is well known and associated both with

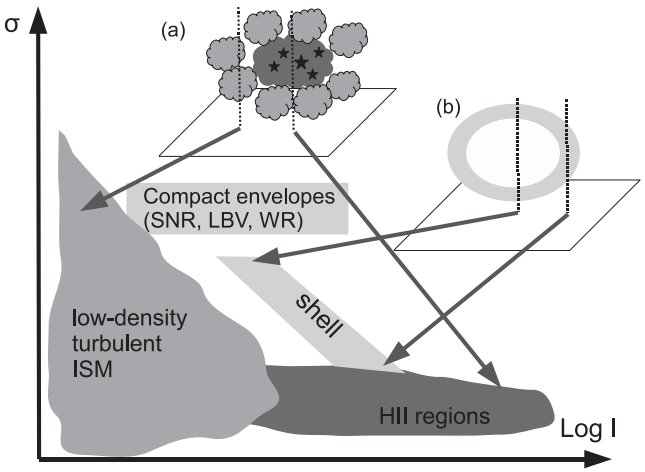

Figure 6. The scheme illustrating the location of points on the $I-\sigma$ diagram. The insets show how we projected on to the sky plane the surface brightness distribution and velocity dispersion (a) from dense H II regions, surrounded by low-density gas with considerable turbulent motions, and (b) from the expanding shell within the model by Muñoz-Tuñón et al. (1996). The dotted line shows the lines of sight passing through different spatial regions.

the depletion of gas the stars form from, and with the mechanical impact of young stellar groups on the interstellar medium. See for example the discussions in Thuan, Hibbard & Lévrier (2004) and Simpson et al. (2011), where the H I maps for another galaxy from our sample, VII Zw 403, are presented. In some cases the bright shell structures, visible in the Hα, lie at the inner boundary of the 'holes' in the H I distribution, which is caused by the sweep-out and depletion of neutral gas (see examples in Lozinskaya et al. 2003; Begum et al. 2006). Note that now the idea of formation of giant neutral supershells by several generations of stars during hundreds of millions of years becomes generally accepted. In this case, local sites of star formation occur in the dense walls of giant H I supershells formed by multiple generations of stars (see McQuinn et al. 2010; Warren et al. 2011, and references therein).

Therefore, a comparison of the H I distribution with our H II maps confirms that the gas (including both neutral and ionized states) in the regions with high σ has a low surface (and hence volume) density. Thuan et al. (2004) explain the observed features of the distribution of surface density and H I dispersion velocity in dwarf galaxies within the supposition that the neutral component of the interstellar medium has two phases in an approximate pressure balance. A 'cooler' phase is characterized by a relatively small spatial scale, higher density and low velocity dispersion, while the diffuse 'warm' phase is distinguished by increased velocity dispersion. Such ideas on *neutral* gas are consistent with our explanation of the state of the *ionized* medium of dwarf galaxies. In this case, the ionized gas of low density, characterized by high-velocity turbulent motions, is a kind of an 'energy reservoir', maintaining a high velocity dispersion of the warm phase of H I. However, speaking about the pressure balance of different phases of gas, it should be borne in mind that the early ideas of the dominant role of thermal pressure are in fact simplistic views at the state of the interstellar medium, in which an important role is played by the turbulent pressure (Burkert 2006).

The question of what determines the velocity dispersion for the points of the 'horizontal branch' in the $I-\sigma$ diagram requires a further detailed consideration. This 'branch' corresponds to the bright H II regions, for which $\sigma \leq \sigma_{\rm m}$. Muñoz-Tuñón et al. (1996) refer to these areas as the 'kinematic core', in agreement with the model proposed by Tenorio-Tagle, Muñoz-Tuñón & Cox (1993) to explain the nature of the supersonic turbulence of ionized gas in star-forming regions. These authors believe that the mean velocity dispersion of ionized gas in the 'kinematic core' is directly related to the virial motions, i.e. is approximately equal to the velocity dispersion of stellar population. The latter, in turn, is determined mainly by the mass and size of the star-forming regions. Later, this model was used by Melnick et al. (2000) to explain the physical nature of the correlation of mean gas velocity dispersion $\sigma_{\rm m}$ with the total luminosity in the Hβ line. It should however be noted that the model by Tenorio-Tagle et al. (1993) describes the evolution of isolated relaxed spheroidal stellar systems. It is hence not applicable to the behaviour of gas in an entire dwarf galaxy, the star formation regions of which are in the gravitational potential of the disc and the dark halo. An alternative view on the nature of the Hβ (or Hα) luminosity–$\sigma_{\rm m}$ correlation is given by the authors, arguing that the main contribution in the observed velocity dispersion of ionized gas in different types of galaxies is provided by the current star formation (Dib et al. 2006; Green et al. 2010). A detailed analysis of the nature of the 'luminosity–ionized gas velocity dispersion' correlation is considered in our next paper (Moiseev et al., in preparation).

Finally, note another interesting feature we detected on the $I-\sigma$ diagrams for the IC 1613 and UGC 8508 galaxies. These points are grouped in a horizontal lane with a relatively large velocity dispersion of $\sigma > 30$–$50\,{\rm km\,s^{-1}}$. These points are very well detached from the other diagram areas and belong to the isolated remnants of supernova explosions or other expanding nebulae around the young massive objects, such as the Wolf–Rayet stars, ultra-bright X-ray sources and LBV stars (see Fig. 6). Therefore, the $I-\sigma$ diagrams can also be used to search for unique and interesting objects in the emission galaxies.

6 CONCLUSION

Using a scanning Fabry–Perot interferometer mounted at the 6-m telescope of the SAO RAS, we have carried out the Hα line observations of seven nearby ($D = 1.8$–4.3 Mpc) irregular dwarf galaxies of the Local Volume. To study the features of the distribution of radial velocity dispersion over the discs of galaxies, characterizing the magnitude of chaotic turbulent motions of ionized gas, we used the $I-\sigma$ diagrams. A combination of these diagrams and 2D maps of radial velocity dispersion has allowed us to identify some common patterns, pointing to the relation between the magnitude of chaotic motions of gas and the ongoing processes of star formation.

Since the spatial resolution of these observations amounted to several tens of parsecs, we tested our results using the previously obtained high-resolution data for two galaxies of the Local Group, IC 10 and IC 1613, smoothed to the resolution of 40 pc. The main conclusions of our work are as follows.

(i) There is a clear link between the surface brightness in the Hα line and the dispersion of line-of-sight velocities: with decreasing surface brightness the range of σ values is growing, the maximum velocity dispersion is always observed in the regions of low surface brightness.

(ii) In five galaxies (DDO 53, DDO 125, UGC 8508, UGCA 92 and VII Zw 403) we have identified expanding shells of ionized gas, sized 80–350 pc, formed as a result of collective action of stellar groups on the gaseous medium of galaxies. The characteristic

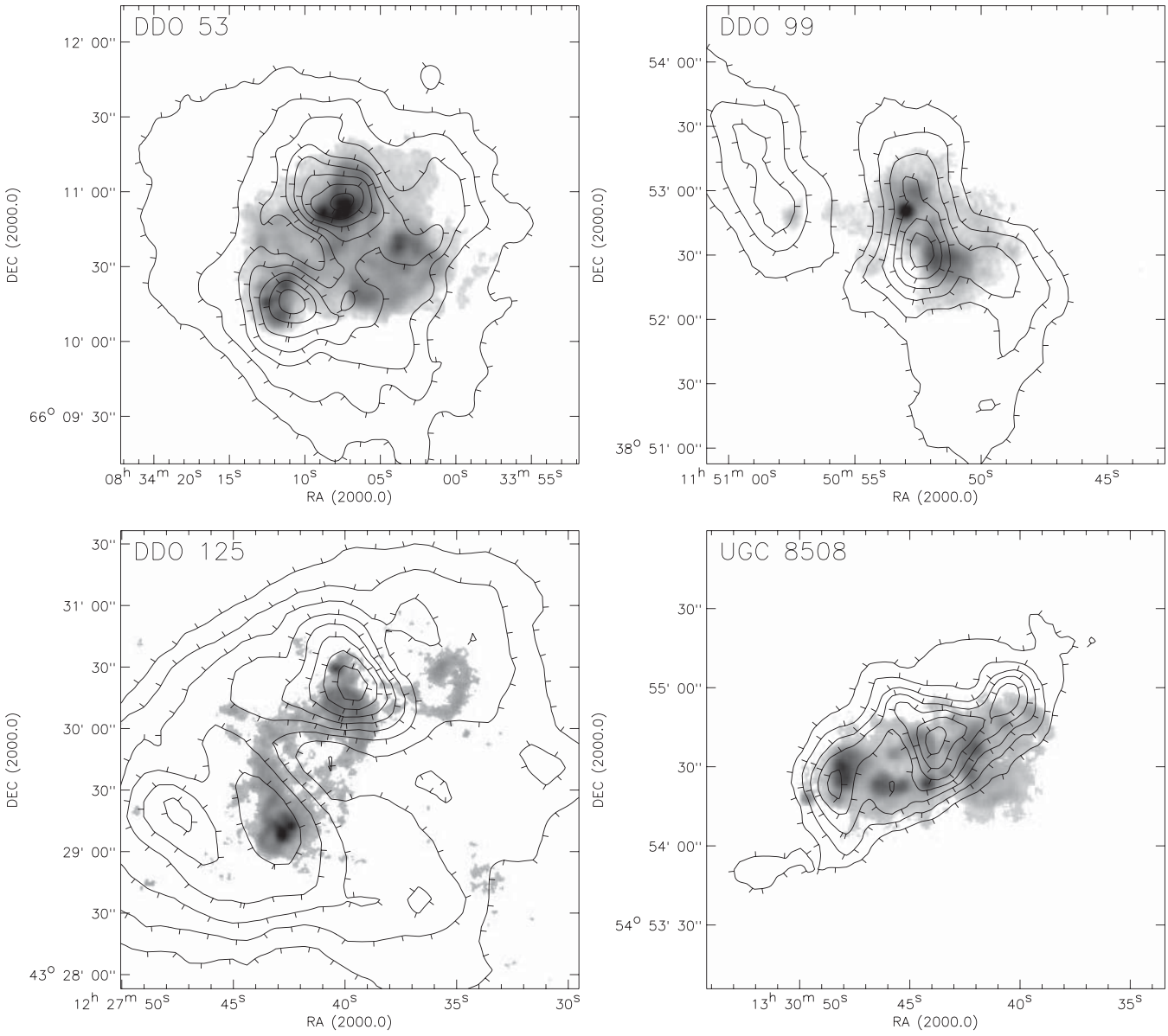

Figure 7. A comparison of surface brightness distributions in Hα (shades of grey) and H I density (contours). The data on the neutral hydrogen for DDO 53 are adopted from the THING survey (Oh et al. 2011), for the other of galaxies – from the FIGGS survey (Begum et al. 2008).

kinematic age of the shells is 1–4 Myr, indicating a relation with current star formation.

(iii) We demonstrate that the $I-\sigma$ diagrams may be useful for the search of supernova remnants or other compact expanding shells (nebulae around WR stars, etc.) in nearby galaxies. Based on $I-\sigma$ diagnostic we have found an LBV candidate in the UGC 8508 galaxy.

(iv) The model, previously proposed by Muñoz-Tuñón et al. (1996) to explain the shapes of the $I-\sigma$ diagram of individual star formation regions, requires substantial additions in the case of dwarf galaxies, where the spatial scales are substantially larger. The most important addition here is that most of regions with high velocity dispersion are not related to specific expanding shells, but rather belong to the diffuse low brightness emission, surrounding the star formation regions. We explain this behaviour of the observed σ distributions by the presence around H II regions of the coronae of perturbed gas with low density and high turbulent velocities. This supposition is consistent with current knowledge of turbulence in the interstellar medium.

We hope that our results will be useful in the interpretation of the ionized gas velocity dispersion maps in dwarf galaxies. All the more so, since an increase in the number of such observations is expected in the coming years. We consider a direct comparison of velocity dispersion distributions for neutral and ionized hydrogen as a challenging here, although the difference in spatial resolution would present a certain problem.

ACKNOWLEDGMENTS

We have made use of the NASA/IPAC Extragalactic Database (NED) which is operated by the Jet Propulsion Laboratory, California Institute of Technology, under the contract with the National Aeronautics and Space Administration. This work was supported by

the Federal Target Programme Scientific and Scientific-Pedagogical Cadre of Innovative Russia (contract no. 14.740.11.0800) and by the Russian Foundation for Basic Research (project no. 10-02-00091). AVM is also grateful for the financial support of the 'Dynasty' Foundation. We thank Professor Jayaram Chengalur who provided us the digital maps of the FIGGS galaxies and an anonymous reviewer for constructive advice, which has helped us to improve the paper. Also, we thank Sergei Fabrika, Olga Sholukhova and Vera Arkhipova for their discussion on LBV candidate spectrum.

Funding for the SDSS has been provided by the Alfred P. Sloan Foundation, the Participating Institutions, the National Science Foundation, the U.S. Department of Energy, the National Aeronautics and Space Administration, the Japanese Monbukagakusho, the Max Planck Society and the Higher Education Funding Council for England. The SDSS website is http://www.sdss.org/.

The SDSS is managed by the Astrophysical Research Consortium (ARC) for the Participating Institutions. The Participating Institutions are The University of Chicago, Fermilab, the Institute for Advanced Study, the Japan Participation Group, The Johns Hopkins University, Los Alamos National Laboratory, the Max-Planck-Institute for Astronomy (MPIA), the Max-Planck-Institute for Astrophysics (MPA), New Mexico State University, University of Pittsburgh, Princeton University, the United States Naval Observatory and the University of Washington.

REFERENCES

Afanasiev V. L., Moiseev A. V., 2005, Astron. Lett., 31, 194
Afanasiev V. L., Moiseev A. V., 2011, Baltic Astron., 20, 363
Begum A., Chengalur J. N., Karachentsev I. D., Kaisin S. S., Sharina M. E., 2006, MNRAS, 365, 1220
Begum A., Chengalur J. N., Karachentsev I. D., Sharina M. E., Kaisin S. S., 2008, MNRAS, 386, 2008
Bordalo V., Telles E., 2011, ApJ, 735, 52
Bordalo V., Plana H., Telles E., 2009, ApJ, 696, 1668
Burkert A., 2006, C. R. Phys., 7, 433
Dib S., Bell E., Burkert A., 2006, ApJ, 638, 797
Dicaire I., Carignan C., Amram P., Marcelin M., Hlavacek-Larrondo J., de Denus-Baillargeon M.-M., Daigle O., Hernandez O., 2008, MNRAS, 385, 553
Egorov O. V., Lozinskaya T. A., Moiseev A., 2010, Astron. Rep., 54, 277
Epinat B., Amram P., Marcelin M., 2008, MNRAS, 390, 466
Green A. W. et al., 2010, Nat, 467, 684
Karachentsev I. D., Karachentseva V. E., Huchtmeier W. K., Makarov D. I., 2004, AJ, 127, 2031
Lagos P., Telles E., Muñoz-Tuñón C., Carrasco E. R., Cuisinier F., Tenorio-Tagle G., 2009, AJ, 137, 5068
Lopez L. A., Krumholz M. R., Bolatto A. D., Prochaska J. X., Ramirez-Ruiz E., 2011, ApJ, 731, 91
Lozinskaya T. A., Moiseev A. V., 2007, MNRAS, 381, 26L
Lozinskaya T. A., Silchenko O. K., Helfand D. J., Goss W. M., 1998, AJ, 116, 2328
Lozinskaya T. A., Moiseev A. V., Podorvanyuk N. Yu., 2003, Astron. Lett., 29, 77
Lozinskaya T. A., Moiseev A. V., Avdeev V. Yu., Egorov O. V., 2006, Astron. Lett., 32, 361
Lozinskaya T. A., Moiseev A. V., Podorvanyuk N. Yu., Burenkov A. N., 2008, Astron. Lett., 34, 217
Lynds R., Tolstoy E., O'Neil E. J., Hunter D. A., 1998, AJ, 116, 146
McQuinn K. B. W. et al., 2010, ApJ, 724, 49
Martínez-Delgado I., Tenorio-Tagle G., Muñoz-Tuñón C., Moiseev A. V., Cairós L. M., 2007, AJ, 133, 2892
Massey P., McNeill R. T., Olsen K. A. G., Hodge P. W., Blaha C., Jacoby G. H., Smith R. C., Strong S. B., 2007, AJ, 134, 2474
Melnick J., Terlevich R., Terlevich E., 2000, MNRAS, 311, 629
Moiseev A. V., 2002, Bull. Spec. Astrophys. Obs. 54, 74
Moiseev A. V., Egorov O. V., 2008, Astrophys. Bull., 63, 181
Moiseev A. V., Pustilnik S. A., Kniazev A. Y., 2010, MNRAS, 405, 2453
Monreal Ibero A., Vílches J. M., Walsh J. R., Muñoz-Tuñón C., 2010, A&A, 517, 27
Muñoz-Tuñón C., Tenorio-Tagle G., Castañeda H. O., Terlevich R., 1996, AJ, 112, 1636
Oh S-H., de Blok W. J. G., Brinks E., Walter F., Kennicutt R. C., Jr, 2011, AJ, 141, 193
Ostlin G., Amram P., Masegosa J., Bergvall N., Boulesteix J., 1999, A&AS, 137, 419
Rozas M., Zurita A., Beckman J. E., Pérez D., 2000, A&AS, 142, 259
Silich S., Tenorio-Tagle G., Muñoz-Tuñón C., Cairós L. M., 2002, AJ, 123, 2438
Silich S., Lozinskaya T., Moiseev A., Podorvanuk N., Rosado M., Borissova J., Valdez-Gutierrez M., 2006, A&A, 448, 123
Simpson C. E. et al., 2011, AJ, 142, 82
Tenorio-Tagle G., Muñoz-Tuñón C., Cox P. D., 1993, ApJ, 418, 767
Terlevich R., Melnick J., 1981, MNRAS, 195, 839
Thuan T. X., Hibbard J. E., Lévrier G. E., 2004, AJ, 128, 617
van Eymeren J., Marcelin M., Koribalski B. S., Dettmar R.-J., Bomans D. J., Gach J.-L., Balard P., 2009a, A&A, 493, 511
van Eymeren J., Marcelin M., Koribalski B. S., Dettmar R.-J., Bomans D. J., Gach J.-L., Balard P., 2009b, A&A, 505, 105
Warren S. R. et al., 2011, ApJ, 738, 10
Yang H., Chu Y.-H., Skillman E. D., Terlevich R., 1996, AJ, 112, 146

APPENDIX A: THE LBV CANDIDATE IN UGC 8508

After the first version of the paper was submitted we have performed new spectral observations of the emission knot with a double-horned Hα emission line profile in UGC 8508. On the Sloan Digital Sky Survey Data Release 8 (SDSS DR8) image which partly resolved the galaxy on individual stars, this knot corresponds to one of the brightest stars on the UGC 8508 periphery (Fig. A1, left). In SDSS DR8, it is named J133049.80+545419.2. The spectroscopic observations were carried out on 2012 February 20 at the 6-m telescope of the SAO RAS with the SCORPIO-2 (Afanasiev & Moiseev 2011) focal reducer working in the long-slit mode. We have collected 3000-s total exposure time with slit width of 1 arcsec under seeing conditions of 0.9 arcsec. The scale along the slit amounted to 0.35 arcsec pixel^{-1}, the spectral resolution was about FWHM = 6.5 Å in the spectral range of 3800–8500 Å. The integrated spectrum of J133049.80+545419.2 is shown in Fig. A1 (right).

Unfortunately, the signal at the wavelength shorter than ∼4500 Å seems very noisy, since we used the CCD detector E2V 42-90 optimized for a 'red' spectral range. Nevertheless, the spectrum reveals a number of emission lines: strong hydrogen Balmer series with prominent He I and He II lines and weak Fe II lines are also detected. All these features are characteristic of an emission-line star, not of an H II region or supernova remnant as we initially supposed from the FPI data. This star has a huge equivalent widths of the Balmer lines [EW(Hα) = 770 Å]; moreover, the Hα line profile reveals multicomponent structure with broad wings. We fitted this profile with three Gaussians having similar central velocities and with FWHM $\approx$ 80, 640 and 2030 km s^{-1} (the spectral resolution was taken into account). Recall that the narrower component has also double-peak structure according FPI observations with high spectral resolution (Section 3.5). The emission nebula around the star is very compact, with diameter smaller than 12–15 pc, because it was not spatially resolved in the long-slit data.

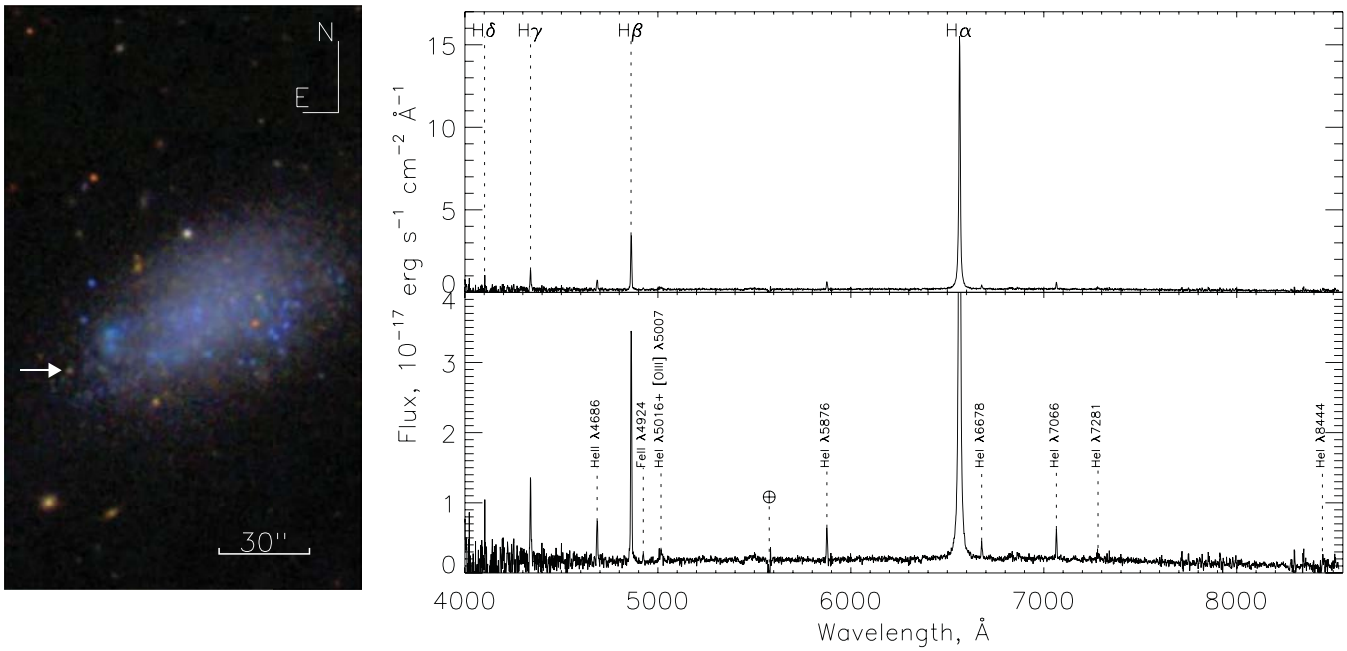

Figure A1. UGC 8508. Colour *gri* image provided by the SDSS DR8; arrow marks the LBV candidate J133049.80+545419.2 (left-hand panel). Right-hand panels show the spectra of this star in two intensity scales. The main emission lines are labelled. A colour version of this figure is available in the online version of this paper.

Based on these spectral properties we suppose that J133049.80+545419.2 is a massive star with strong stellar wind like LBVs. The observed spectrum is similar to some known LBV candidates, for example J013332.64+304127.2 in the M33 and J002020.35+591837.6 in the IC 10 galaxies (Massey et al. 2007). The SDSS DR8 photometric catalogue provides for J133049.80+545419.2 visible magnitudes $g = 22.37 \pm 0.13$, $r = 21.14 \pm 0.06$ and $i = 20.63 \pm 0.05$ mag corresponding to absolute magnitudes $M_g = -4.78$, $M_r = -6.01$ and $M_i = -6.52$. The real luminosity of the star can be significantly larger, if the possible extinction in the circumstellar envelope is taken into account (the Galaxy interstellar extinction according NED is inessential in this direction – $A_V = 0.05$). The strong Balmer decrement ($I_{H\alpha}/I_{H\beta} = 7.2$) can be connected with dust extinction as well as with shock origin of the emission line spectrum.

A discussion about the origin of this star lies outside the framework of our paper; new detailed observations are needed. However, the presented results provide a very good illustration of the power of the $I-\sigma$ diagram method that allows us to found a new LBV candidate outside the Local Group.

SUPPORTING INFORMATION

Additional Supporting Information may be found in the online version of this article:

Figure 1. Results of observations with the FPI for each galaxy.

Please note: Wiley-Blackwell are not responsible for the content or functionality of any supporting materials supplied by the authors. Any queries (other than missing material) should be directed to the corresponding author for the article.

This paper has been typeset from a TEX/LATEX file prepared by the author.

АСТРОНОМИЧЕСКИЙ ЖУРНАЛ, 2010, том 87, № 4, с. 316–334

УДК 524.5

ОБЛАСТЬ БУРНОГО ЗВЕЗДООБРАЗОВАНИЯ В Irr ГАЛАКТИКЕ IC 10: СТРУКТУРА И КИНЕМАТИКА ИОНИЗОВАННОГО И НЕЙТРАЛЬНОГО ГАЗА

© 2010 г. О. В. Егоров[1], Т. А. Лозинская[1], А. В. Моисеев[2]

[1] *Государственный астрономический институт им. П.К. Штернберга МГУ им. М.В. Ломоносова, Москва, Россия*

[2] *Учреждение Российской академии наук Специальная астрофизическая обсерватория РАН, Нижний Архыз Карачаево-Черкесской Республики, Россия*

Поступила в редакцию 02.11.2009 г.; принята в печать 19.10.2009 г.

По результатам наблюдений галактики IC 10 на 6-м телескопе САО РАН с фокальным редуктором SCORPIO в режиме интерферометра Фабри-Перо, а также с панорамным спектрографом MPFS исследованы структура и кинематика ионизованного газа в центральной области интенсивного современного звездообразования. По архивным данным наблюдений в линии 21 см на VLA рассмотрена структура и кинематика нейтрального газа в данной области. Выявлены высокоскоростные крылья эмиссионных линий Hα и [SII] во внутренней каверне туманности HL 111 и в других областях комплекса бурного звездообразования. Обнаружены локальные расширяющиеся оболочки нейтрального газа вокруг туманностей HL 111 и HL 106.

1. ВВЕДЕНИЕ

Карликовая Irr галактика IC 10 – ближайшая к нам галактика с бурным звездообразованием; на основании высоких Hα- и ИК-светимостей ее часто относят к типу BCD [1]. Звездное население IC 10 выявляет две вспышки звездообразования: возраст первой не менее 350 млн. лет, вторая произошла 4–10 млн. лет назад [2–5] (см. также ссылки в этих работах). Следствием последней вспышки звездообразования является многооболочечная тонковолокнистая структура межзвездной среды в IC 10: изображения галактики в линиях Hα и [SII] выглядят как гигантский комплекс множественных оболочек и сверхоболочек, дуговых и кольцевых структур размером от 50 пк до 800–1000 пк [6–11] (см. также ссылки в этих работах). Аномально высокое число звезд WR – их пространственная плотность в IC 10 самая высокая среди карликовых галактик и сопоставима с плотностью в массивных спиральных галактиках – является следствием короткой, но охватившей большую часть галактики вспышки современного звездообразования [1, 4, 5, 12–14] (см. также ссылки в этих работах). Столь высокая плотность звезд WR говорит о том, что фактически мы являемся "свидетелями" короткого периода, завершающего последний эпизод звездообразования.

Центральная, наиболее яркая область этого последнего эпизода звездообразования находится в юго-восточном секторе галактики и включает самое плотное облако HI, молекулярное облако CO и комплекс эмиссионных туманностей размером около 300–400 пк, в числе которых две оболочечные туманности HL 111 и HL 106 (по номинации каталога [15], а также самые молодые звездные скопления и десяток звезд WR [7–9, 16] (см. также ссылки в этих работах).

Изображения области в линиях Hα и [SII] (λ6717 + 6731 Å) показаны на рис. 1.

Согласно [5], центр последнего эпизода звездообразования локализован вблизи объекта, ранее идентифицированного как звезда WR M24. (Здесь и далее звезды WR по списку [17] обозначены буквой R, по списку [13] – буквой M). Окружающая M24 туманность HL 111c представляет собой наиболее яркую часть оболочки HL 111 (рис. 1; размер оболочки, определяемый тремя ее дуговыми частями HL 111c, HL 111d и HL 111e, составляет около 10″ или 35 пк при расстоянии 800 кпк). Хантер [2] выделила в области HL 111 три скопления: в наиболее яркой части HL 111c находится скопление 4-1, к которому принадлежит M24, в центре внутренней каверны – скопление 4-2. Это самые молодые скопления в галактике, их возраст составляет 3–4 млн. лет [2]. Третье скопление 4-7 – сравнительно бедное, его возраст и размер не определены.

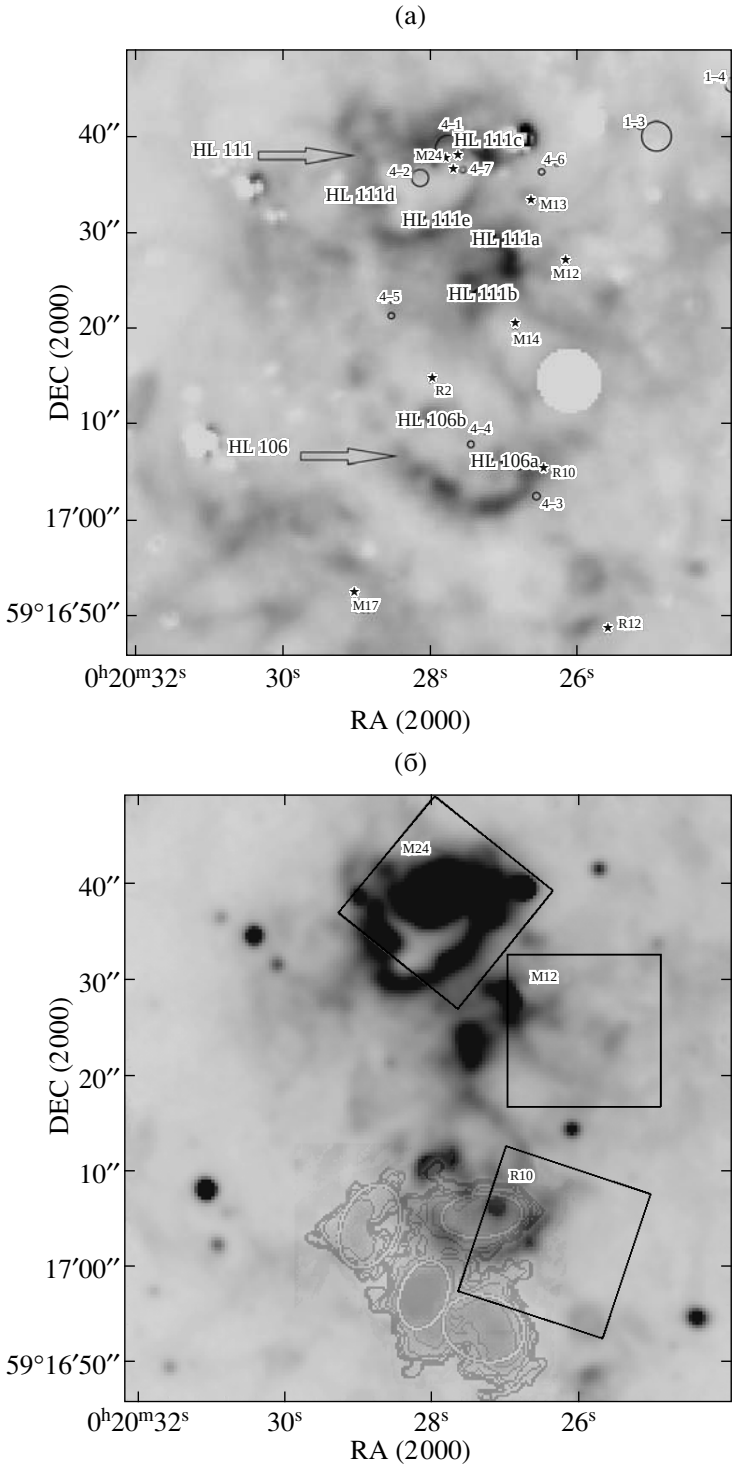

Рис. 1. (а) — Изображение исследуемой области интенсивного звездообразования в линиях [SII] $\lambda(6717+6731)$ Å (фильтровой снимок). Отмечены две протяженные оболочечные туманности HL 111, HL 106 и их отдельные составляющие. Звездочками показаны спектрально подтвержденные звезды WR по спискам [17] (отмечены буквой R) и [13] (отмечены буквой M). Кружками показаны звездные скопления из списка [2], диаметр кружков соответствует размеру скоплений, название скоплений даны двумя цифрами. (б) — Изображение области в линии Hα (по результатам ИФП-наблюдений), совмещенное с распределением интенсивности CO-излучения молекулярного облака (изофоты) по данным работы [9] (см. текст). Квадратами показана локализация использованных в данной работе трех полей MPFS (названы по центральной звезде WR).

Ранее уже отмечалось, что звезда WR M24 на самом деле состоит из трех расположенных на расстоянии $1''-2''$ друг от друга голубых звезд M24-A, M24-B и M24-C; один из компонентов был заподозрен как звезда O3If, звезда WR или скопление, содержащее звезда WR [14]. Вакка и др. [5] показали, что M24 фактически представляет собой тесную группу звезд, состоящую по крайней мере из 6 голубых звезд (в M24A выявлены 3 голубые звезды, в M24B — две). Четыре из этих 6 звезд — возможные WR-кандидаты.

В южной части упомянутого наиболее плотного в галактике облака HI и CO расположена оболочечная туманность HL 106; источниками ионизующей радиации здесь, по всей вероятности, являются звезда WR R2 и R10, а также скопления 4-3 и 4-4 (рис. 1). Возраст этих скоплений по оценке [2] в несколько раз превышает возраст молодых скоплений 4-1 и 4-2 в области HL 111.

Цель настоящей работы — детальное исследование структуры и кинематики ионизованного и нейтрального газа в области бурного звездообразования. Работа основана на наблюдениях, проведенных на 6-м телескопе САО РАН с фокальным редуктором SCORPIO, работающим в режиме интерферометра Фабри–Перо (ИФП). Использованы также результаты наших наблюдений с панорамным спектрографом MPFS и со SCORPIO в режиме щелевой спектроскопии (последние детально обсуждаются в статье [16]).

В последующих разделах описаны проведенные наблюдения, представлены полученные результаты и дано их обсуждение, в заключение суммируются основные выводы работы.

Все значения лучевых скоростей в работе являются гелиоцентрическими; расстояние до галактики принято равным 800 кпк (угловой масштаб $\simeq$3.6 пк/сек. дуги; см. раздел 4).

2. НАБЛЮДЕНИЯ И ОБРАБОТКА ДАННЫХ

Журнал наблюдений, проведенных на 6-м телескопе САО РАН с фокальным редуктором SCORPIO в режиме ИПФ, а также с MPFS, представлен в таблице. Здесь даны соответственно по столбцам: прибор; линия в которой работал ИФП или обозначение поля MPFS (по центральной звезде WR); дата наблюдений; спектральный диапазон; спектральное разрешение; время экспозиции и качество изображения (“seeing”).

2.1. Наблюдения со сканирующим интерферометром Фабри–Перо

Наблюдения на 6-м телескопе с прибором SCORPIO и сканирующим ИФП были проведены в двух линиях Hα и [SII] λ6717 Å; возможности SCORPIO в интерферометрических наблюдениях детально описаны Моисеевым [18]. Использовался сканирующий ИФП, работающий в 501 порядке интерференции на длине волны λ6562.78 Å. При этом расстояние между соседними порядками интерференции $\Delta\lambda = 13$ Å в линии Hα и $\Delta\lambda = 13.7$Å в линии [SII] λ6717 Å соответствовало свободной от перекрытия порядков области $\sim$600 км/с в шкале лучевых скоростей. Ширина инструментального контура (FWHM) составляла около 0.8 Å, или $\sim$35 км/с. Предварительная монохроматизация осуществлялась с помощью интерференционных фильтров с полушириной FWHM $\sim$15 Å, центрированных на линии Hα и [SII] λ6717 Å, соответственно. В качестве приемника излучения использовалась ПЗС-матрица EEV 42-40 размером 2048×2048 пикселей. С целью уменьшения времени считывания наблюдения проводились с аппаратным биннингом 2×2 пикселя в линии Hα и 4×4 пикселя в линии [SII] λ6717 Å. При этом в каждом спектральном канале получались изображения размером 1024×1024 пикселей в случае Hα и 512×512 пикселей в случае [SII] при масштабах $0.36''$/пикс. и $0.71''$/пикс., соответственно; полное поле зрения составляло $6.1'$.

В процессе наблюдений было последовательно получено 36 интерферометрических изображений объекта при различных расстояниях между пластинами ИФП, так что ширина спектрального канала соответствовала 0.36 Å в линии Hα и 0.38 Å в линии [SII] λ6717 Å, т.е. около 17 км/с в шкале лучевых скоростей. С целью корректного вычитания паразитных бликов от многочисленных эмиссионных областей галактики, наблюдения проводились при двух различных ориентациях поля зрения прибора. Суммарная экспозиция составляла 10 800 с при наблюдениях в линии Hα и 12 960 с — в линии [SII] λ6717 Å.

Обработка наблюдений выполнялась с помощью программного обеспечения, работающего в среде IDL [18]. После первичной редукции наблюдательные данные были представлены как “кубы данных” размером $1024 \times 1024 \times 36$ и $512 \times 512 \times 36$ элементов; здесь каждому элементу изображения соответствует 36-канальный спектр. Изображения паразитных бликов удалялись согласно алгоритмам, описанным Моисеевым и Егоровым [19]. Наблюдения выполнялись каждый раз при

Журнал наблюдений

Режим	Поле	Дата	Диапазон	$\delta\lambda$, Å	T_{exp}, с	Качество изображения
ИФП	Вся галактика	08/09.09.05	H_α	0.8	10 800	$0.8''-1.3''$
ИФП	Вся галактика	23/24.10.08	[SII] λ6717	0.8	12 960	1.4–2.0
MPFS	M24	08/09.08.04	3990–6940	6.5	2700	1.7–2.0
MPFS	R10	08/09.08.04	3990–6940	6.5	1800	1.4
MPFS	M12	28/29.09.05	3990–6940	6.5	3600	2.0

двух разворотах поля зрения, полученные промежуточные кубы затем совмещались. Такая методика давала возможность гарантированно удалить остатки бликов от ярких звезд, что важно при последующем изучении формы спектральных линий. Итоговое пространственное угловое разрешение (после сглаживания в процессе редукции данных) составляло $1.3''$ и $2.2''$ в линиях Hα и [SII] λ6717 Å, соответственно. Точность построения шкалы длин волн соответствовала 3–5 км/с.

Использование узких фильтров для предварительной монохроматизации излучения существенно уменьшало паразитный поток от близких спектральных линий из соседних порядков интерференции. Возможный остаточный вклад второй компоненты линии серы [SII] λ6731 Å при наблюдениях в линии [SII] λ6717 Å может проявляться на скорости около -300 км/с для системной скорости -330 км/с (соответственно на скорости $+30$ км/с относительно максимума основной компоненты линии). Вклад линии азота [NII] (λ6584 Å) при Hα-наблюдениях возможен на скоростях около -587 км/с и $+12$ км/с (соответственно -260 и $+340$ км/с относительно основной компоненты), вклад линии [NII] λ6548 Å – на скорости около -405 км/с (-75 км/с относительно основной компоненты); вклад линии ночного неба λ6553.62 Å в случае ее неполного вычитания возможен на скорости -420 км/с.

2.2. Наблюдения с MPFS

Наблюдения избранных областей галактики проведены с панорамным мультизрачковым волоконным спектрографом MPFS, установленным в главном фокусе 6-м телескопа (см. [20] и в Интернете (http://www.sao.ru/hq/lsfvo/devices.html). В качестве приемника использовалась ПЗС-матрица EEV 42-20 размером 2048×2048 элементов. Спектрограф позволяет одновременно регистрировать спектры от 256 пространственных элементов (конструктивно выполненных в виде квадратных линз), составляющих в картинной плоскости матрицу размером 16×16 элементов. Угловой размер элемента изображения составлял $1''$.

В этой работе частично использованы спектры с разрешением около 6.5 Å в диапазоне 3990 – – 6940 Å для 3 из 6 полей, полученных для IC 10; их локализация показана на рис. 1б.

Обработка наблюдений проводилась с помощью разработанного в лаборатории СФВО САО РАН математического обеспечения, работающего в среде IDL. Результатом обработки является “куб данных”, в котором каждому пикселю изображения размером $16'' \times 16''$ соответствует спектр из 2048 элементов.

В работе использованы также полученные нами ранее [11] изображения галактики в линиях [SII] и Hα. Показанное на рис. 1а изображение в линиях [SII] λ(6717+6731) Å получено по фильтровым снимкам со SCORPIO; монохроматическое изображение в линии Hα на рис. 1б построено путем интегрирования потока в спектрах по наблюдениям с ИФП.

3. РЕЗУЛЬТАТЫ НАБЛЮДЕНИЙ

3.1. Кинематика ионизованного газа

Исследования кинематики ионизованного газа в области бурного звездообразования, включающей HL 111 и HL 106, мы провели по наблюдениям со сканирующим ИФП в двух линиях: Hα и [SII] λ6717 Å. Для сравнения использованы также наблюдения с MPFS.

Учитывая сложную многооболочечную тонковолокнистую структуру изучаемой области и наличие упомянутых во Введении множественных источников звездного ветра, этот регион потребовал предельно детального анализа поля лучевых скоростей.

Первый этап работы состоял в систематическом поиске областей с высокими (сверхзвуковыми?)

(а)

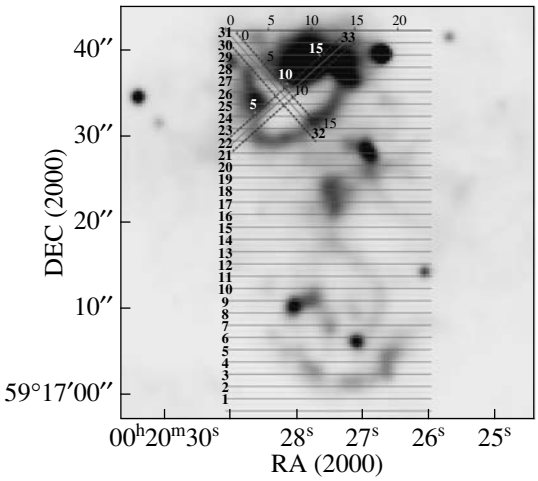
40″
30″
20″
10″
59°17′00″
DEC (2000)
00h20m30s
28s
27s
26s
25s
RA (2000)

(б)

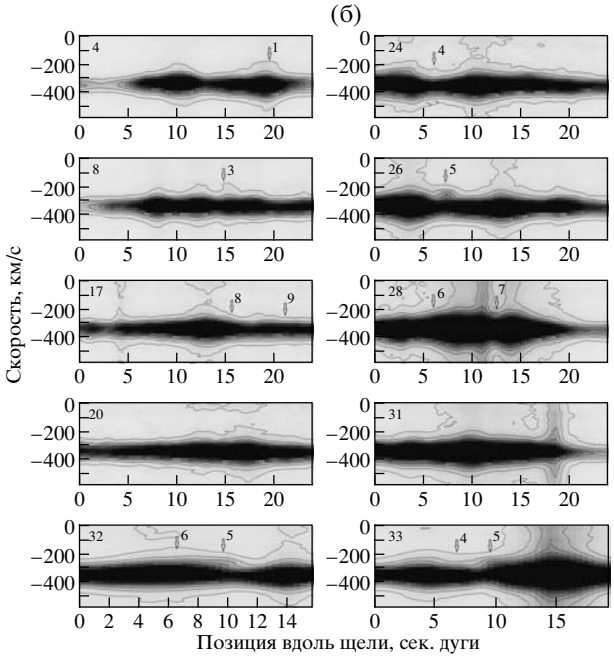
Скорость, км/с
Позиция вдоль щели, сек. дуги

(в)

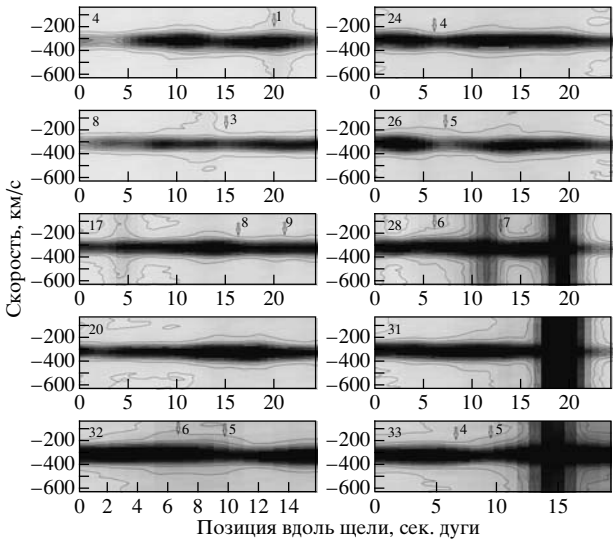
Скорость, км/с
Позиция вдоль щели, сек. дуги

Рис. 2. (а) – Локализация разрезов, вдоль которых строились P/V-диаграммы в линиях Hα и [SII] λ6717 Å по наблюдениям с ИФП. На верхней шкале данной карты и на всех последующих рисунках цифрами дана "разметка" разрезов в сек.дуги; разметка двух разрезов № 32 и № 33 показана непосредственно на них. (б) – Примеры P/V-диаграмм в линии Hα. (в) – Примеры P/V-диаграмм в линии [SII] λ6717 Å. Стрелками на рис. 2б и рис. 2в отмечены области, для которых на рис. 4 построены профили линий Hα и [SII]λ6717Å.

скоростями или другими возможными кинематическими особенностями. Для этого по наблюдениям со сканирующим ИФП вся исследуемая область была полностью перекрыта в двух перпендикулярных направлениях системой примыкающих друг к другу разрезов, вдоль которых построены диаграммы распределения лучевой скорости газа (так называемые P/V-диаграммы). Такой "поисковый" анализ был проведен по наблюдениям в обеих линиях Hα и [SII] λ6717 Å.

На рис. 2 на изображении в линии Hα показаны локализация разрезов в направлении восток–запад, вдоль которых строились P/V-диаграммы в обеих линиях, и, в качестве примера, наиболее интересные диаграммы в линиях Hα (10 средних разрезов) и [SII] λ6717 Å (10 нижних разрезов). Для удобства ориентации на рисунке дана "разметка" разрезов в сек. дуги; стрелками на рис. 2б, 2в отмечены участки, для которых построены профили обеих линий, представленные далее на рис. 4.

Второй этап работы заключался в более детальном анализе кинематики тех областей, в которых проведенный систематический поиск выявил смещенные по скорости детали линии. С этой целью были построены P/V-диаграммы для отдельных туманностей с большим пространственным масштабом, а также рассмотрены профили обеих линий.

Две такие PV-диаграммы и их локализация на изображении туманности HL 111 показаны на рис. 2 (разрезы № 32 и № 33). Здесь хорошо заметны слабые высокоскоростные детали линии внутри каверны (отмечены стрелками).

Локализация профилей линий Hα и [SII] λ6717 Å, построенных по наблюдениям с ИФП, показана на рис. 3; на рис. 4 представлены соответствующие профили Hα (верхний) и [SII] (нижний) в условных единицах.

При построении профилей основная компонента линии аппроксимировалась функцией Фойгта. Слабые высокоскоростные компоненты выделялись как превышение над фойгтовскими крыльями; при этом остаточные после вычитания фойгтовского профиля детали линии аппроксимировались гауссианой. Соответственно для каждой линии на рисунке показаны: наблюдаемый профиль и его представление функцией Фойгта, высокоскоростные компоненты, выделенные как превышение над фойгтовскими крыльями (аппроксимированы функцией Гаусса) и сумма всех выделенных компонент (практически совпадает с наблюдаемым профилем).

Суммируя результаты анализа кинематики ионизованного газа в области бурного звездообразования, можно заключить следующее.

Скорость газа в регионе, включающем туманности HL 111 и HL I06, по данным наших наблюдений с ИФП заключена в пределах $-315 \div -355$ км/с. В линии [SII] заметны вариации скорости от -318 до -335 км/с. Средняя скорость ионизованного газа в области бурного звездообразования составляет -330 км/с.

Это согласуется с измерениями Туроу и Вилкотса [21] в линии Hα (наблюдения этих авторов покрывают треть исследованной нами яркой области звездообразования в ее западной части; см. рис 5 в цитированной работе). Такую же среднюю скорость имеет и нейтральный газ в регионе [7] (см. далее).

Классический "эллипс лучевых скоростей" (лучевые скорости передней и дальней сторон расширяющейся оболочки уменьшаются по абсолютной величине вдоль радиуса в картинной плоскости) P/V-диаграммы, построенные по ИФП-наблюдениям в линиях Hα и [SII], не выявили. На отдельных разрезах, представленных на рис. 2, наблюдаются небольшие отклонения скорости максимума линии от найденной средней скорости "невозмущенного" газа в области, но во всех случаях эти отклонения не превышают 15–20 км/с. Данные скорости, определенные по максимуму линии, т.е. характеризующие наиболее яркую эмиссию, дают возможную скорость расширения оболочки HL 111 не более 10–15 км/с. В то же время в отдельных областях туманности HL 111 обнаружены асимметрия профиля или слабые детали в красном крыле линии на уровне около 2%–6% максимальной интенсивности в интервале скоростей от -280 км/с до -240 км/с.

В синем крыле линии высокоскоростные детали видны в интервале от -450 км/с до -410 км/с.

Как следует из рис. 3 и 4, наиболее заметные высокоскоростные детали наблюдаются в красном крыле линии Hα в каверне неправильной формы внутри HL 111.

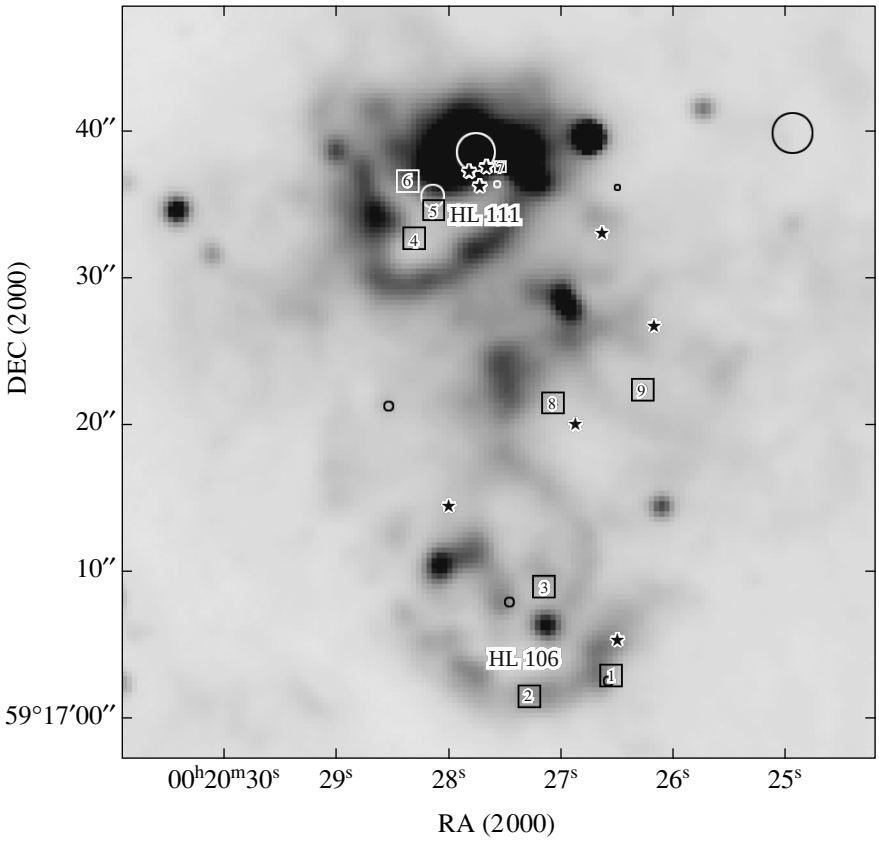

Рис. 3. Локализация профилей линий Hα и [SII] λ6717 Å, представленных далее на рис. 4, показаны квадратиками с цифрами внутри них, которые соответствуют номеру области. Кружками и звездочками, как и на рис. 1, отмечены звездные скопления и звезды WR. (Те участки P/V-диаграмм, для которых построены профили, отмечены стрелками на рис. 2б и 2в.)

В туманности HL 106 наблюдается сходная картина. Скорости, определенные по максимуму линии Hα и характеризующие наиболее яркие сгустки оболочки, обнаруживают небольшие вариации и дают возможную среднюю скорость расширения не более 10–15 км/с. Слабые детали в крыльях в линии Hα на уровне около 2%–10% максимальной интенсивности видны в HL 106 в интервале скоростей от -260 км/с до -250 км/с и от -450 км/с до -420 км/с.

В линии [SII] λ6717 Å также выделяются заметные детали в красных крыльях во внутренней каверне туманности HL 111, причем на тех же скоростях, что и в Hα (рис. 4). Хорошее совпадение скорости слабых деталей в крыльях обеих линий наблюдается и в других областях исследуемого комплекса, что является сильным аргументом в пользу их реальности. Тот факт, что в ряде областей комплекса видны слабые крылья линии Hα, но наблюдения в линии [SII] λ6717 Å не позволяют их выделить, объясняется низкой интенсивностью последней (на порядок ниже интенсивности Hα).

Наблюдения трех полей области с MPFS использованы для проверки этих результатов, полученных с ИФП. По наблюдениям с MPFS были построенные усредненные профили линий Hα, [SII] λ6717 Å и [NII] λ6584 Å для трех площадок, локализация которых показана на рис. 1б.

Мы не приводим здесь соответствующие профили линий, поскольку наблюдения с MPFS имеют по сравнению с ИФП существенно более низкое спектальное разрешение. Тем не менее MPFS-наблюдения полностью подтвердили наличие слабых крыльев линиий Hα и [SII] λ6717 Å, выявленных с ИФП. При этом из-за низкого спектрального разрешения скорости слабой компоненты линии иногда существенно (до 50–100 км/с) отличаются от данных наблюдений с ИФП. Поэтому мы используем здесь данные MPFS лишь с целью проверки самого факта наличия красных крыльев линии в этих областях, но все оценки скорости сделаны по наблюдениям с ИФП.

В заключение подчеркнем, что слабые детали в крыльях линий можно выделить в ряде областей

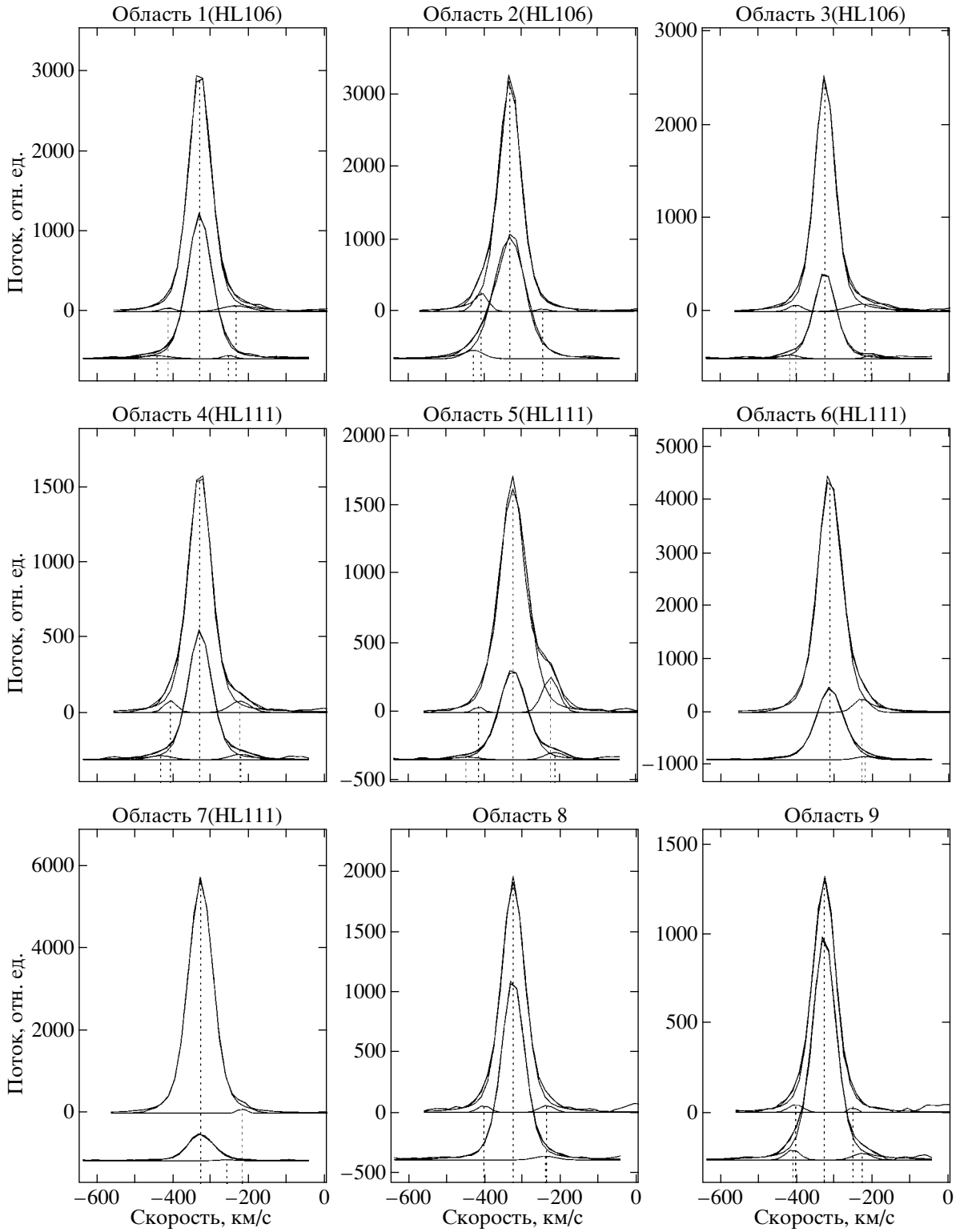

Рис. 4. Примеры профилей линии Hα (верхний профиль) и линии [SII]λ6717Å (нижний профиль) по наблюдениям с ИФП (в условных единицах). Показаны наблюдаемый профиль, аппроксимация его главной компоненты функцией Фойгта, высокоскоростные компоненты, выделенные как превышение над фойгтовскими крыльями (аппроксимированы функцией Гаусса) и сумма всех выделенных компонент (практически совпадает с наблюдаемым профилем). Указанные сверху номера областей соответствуют номерам квадратных значков на рис. 3.

исследуемого комплекса бурного звездообразования, но интенсивность их не превышает 2%–10% интенсивности в максимуме линии. В линии [SII] λ6717 Å профиль линии выглядит более симметричным, слабые детали наблюдаются и в синих, и в красных крыльях, однако интегральная яркость этой линии составляет от 4% до 12% яркости линии Hα, и выделение слабых крыльев здесь менее надежно.

Самые заметные высокоскоростные детали в красных крыльях линии Hα наблюдаются в каверне неправильной формы внутри оболочки HL 111, в частности вблизи скопления 4-2.

Упомянутые в работе [21] красные крылья линии Hα авторы заметили на западе области между HL 111 и HL 106. Однако приведенные в табл. 4 упомянутой работы скорости детали, оставшейся после вычитания главной компоненты линии ($-282 \div -256$ км/с), отличаются от результатов наших измерений в тех же участках.

3.2. Кинематика нейтрального газа

Крупномасштабная кинематика нейтрального водорода в IC 10 исследована в работе [7]. Дисперсия скоростей HI в комплексе бурного звездообразования и, в частности, в протяженных окрестностях M24, не самая высокая в галактике [7, рис. 14]. Средние скорости в максимуме линии 21 см дают возможную скорость расширения выявленных в этой работе крупномасштабных дуговых структур в регионе не более 10–15 км/с.

Мы провели повторный анализ предоставленного в наше распоряжение куба данных наблюдений IC 10 в линии 21 см на VLA с целью более детального исследования "локальной" структуры и кинематики HI в близких окрестностях комплекса звездообразования и ярчайших туманностей HL 111, HL 106. Для этого использовались данные с угловым разрешением $4.7'' \times 5''$ или около 20 пк при расстоянии 800 кпк.

Результаты проведенного анализа представлены на рис. 5 и 6. На рис. 5а показано Hα-изображение яркой области бурного звездообразования, полученное по нашим ИФП-наблюдениям, совмещенное с распределением интегральной яркости области в линии 21 см. На рис. 5б это же Hα-изображение совмещено с распределением нейтрального водорода, излучающего на скорости -336 км/с, близкой к скорости ионизованного газа в HL 111 и в HL 106. Первый рисунок свидетельствует о наличии полосы максимальной лучевой плотности нейтрального водорода в направлении северо-восток – юго-запад между HL 106 и Синхротронной сверхоболочкой, совпадающей с полосой поглощающей пыли на оптических изображениях области. (Уникальная Синхротронная сверхоболочка в IC 10, образование которой ранее объясняли множественными вспышками десятка сверхновых [21, 22], согласно нашей работе [23] является остатком вспышки гиперновой.)

Из рис. 5б следует, что в окрестности яркой области звездообразования, включающей HL 111 и HL 106, наблюдается "локальное" протяженное облако HI, излучающее на той же лучевой скорости, что и ионизованный газ.

На рис. 6а–6в представлены некоторые из P/V-диаграмм, построенных нами по излучению ионизованного и нейтрального газа в одном и том же направлении. Локализация соответствующих направлений показана на совмещенных изображениях области в линиях 21 см и Hα (изофоты).

Как следует из приведенных P/V-диаграмм, непосредственно к ионизованной оболочечной туманности HL 111 снаружи примыкает окружающая ее расширяющаяся оболочка нейтрального газа (см. участки 37–57 на рис. 6а, участки 35–56 на рис. 6б, участки 35–56 на рис. 6в). Средняя лучевая скорость этой внешней нейтральной оболочки составляет $-333 \div -336$ км/с, т.е. совпадает со средней скоростью оптической туманности. Средняя скорость расширения оболочки HI, окружающей HL 111, составляет 10–15 км/с, при этом удаляющаяся сторона нейтральной оболочки движется со средней скоростью около 10 км/с, приближающаяся – со средней скоростью около 15 км/с. Более слабые детали расширяющейся оболочки нейтрального газа наблюдаются на скоростях, отличающихся на величину до $\simeq$30 км/с от средней "несмещенной" скорости.

Таким образом, кроме протяженных оболочек нейтрального газа размером около $1'$–$1.5'$, заметных по всему полю галактики на рис. 9 работы [7], проведенный нами детальный анализ данных наблюдений в линии 21 см позволил выделить вокруг оптической туманности HL 111 нейтральную оболочку размером около $25''$–$30''$. Средняя скорость расширения этой оболочки составляет 10–15 км/с, слабые детали линии 21 см соответствуют скорости разлета около 30 км/с. Эта расширяющаяся нейтральная оболочка может быть сформирована под действием ветра группы звезд WR, принадлежащих M24, а также упомянутых выше скоплений 4-1 и 4-2 (см. разд. 4).

Как следует из рис. 6, такая же "локальная" оболочка, расширяющаяся со средней скоростью 15–20 км/с, наблюдается и вокруг туманности HL 106 в южной части области бурного звездообразования (участки 4–29 на рис. 6а, участки 4–28 на рис. 6б, участки 8–27 на рис. 6в). Здесь

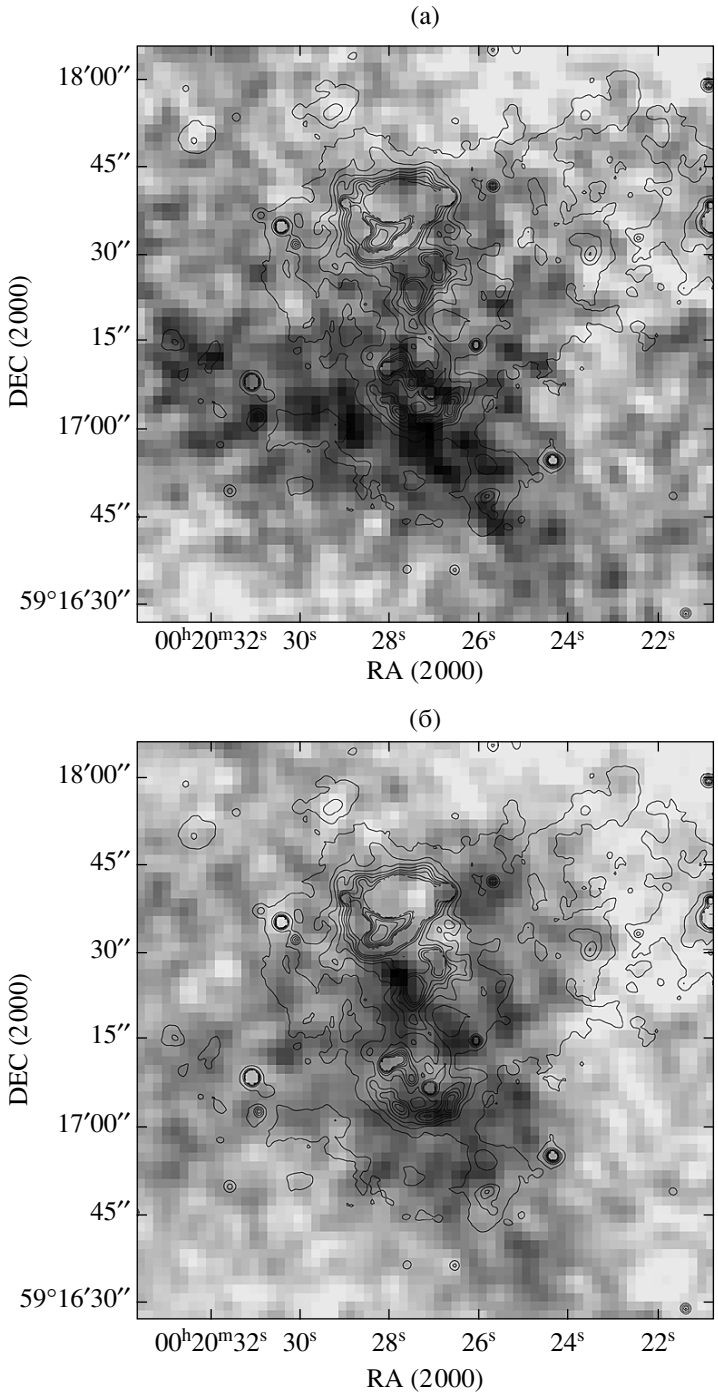

Рис. 5. (а) — Hα-изображение яркой области звездообразования (показано изофотами), совмещенное с распределением интегральной яркости области в линии 21 см. (б) — Hα-изображение, совмещенное с распределением нейтрального водорода, излучающего на скорости −336 км/с.

также наблюдаются более слабые детали, соответствующие разлету со скоростью до 25 км/с. Источниками механической энергии, ответственными за формирование оболочки HI вокруг HL 106, по всей вероятности, являются звезды WR R2 и R10, а также скопления 4-4 и 4-3.

Отметим, что обе обнаруженные нейтральные оболочки характеризуются неравномерным распределением яркости и клочковатой структурой. При этом удаляющаяся сторона оболочки HI вокруг HL 111 имеет меньшую яркость, чем приближающаяся, практически на всех пересекающих ее

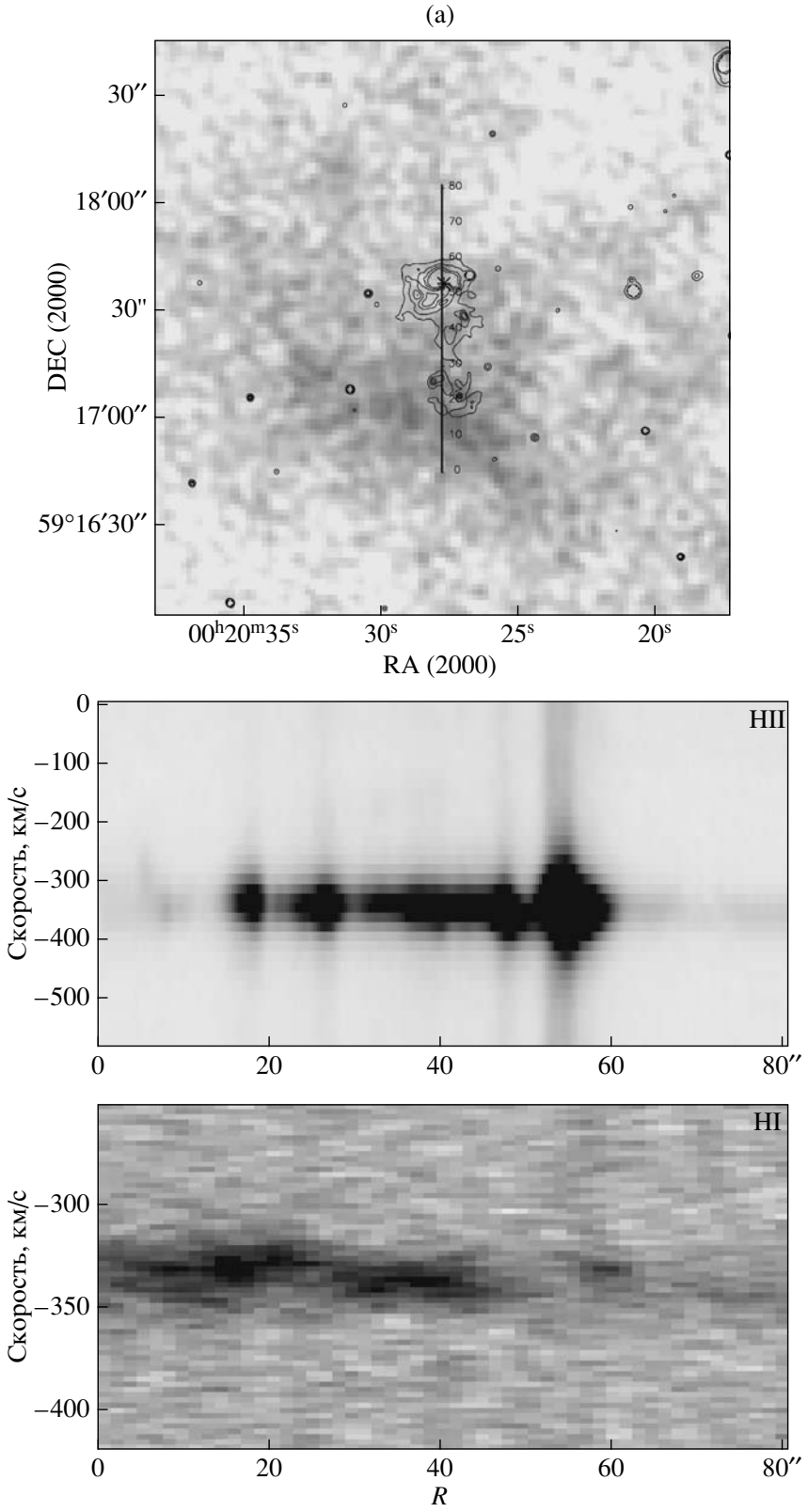

Рис. 6. P/V-диаграммы, построенные по излучению ионизованного и нейтрального газа в одном и том же направлении. На трех картах вверху показана локализация разрезов на совмещенных изображениях области в линиях 21 см и Hα (изофоты), на трех диаграммах в центре — соответствующие P/V-диаграммы в линии Hα, на трех диаграммах внизу — P/V-диаграммы в линии 21 см.

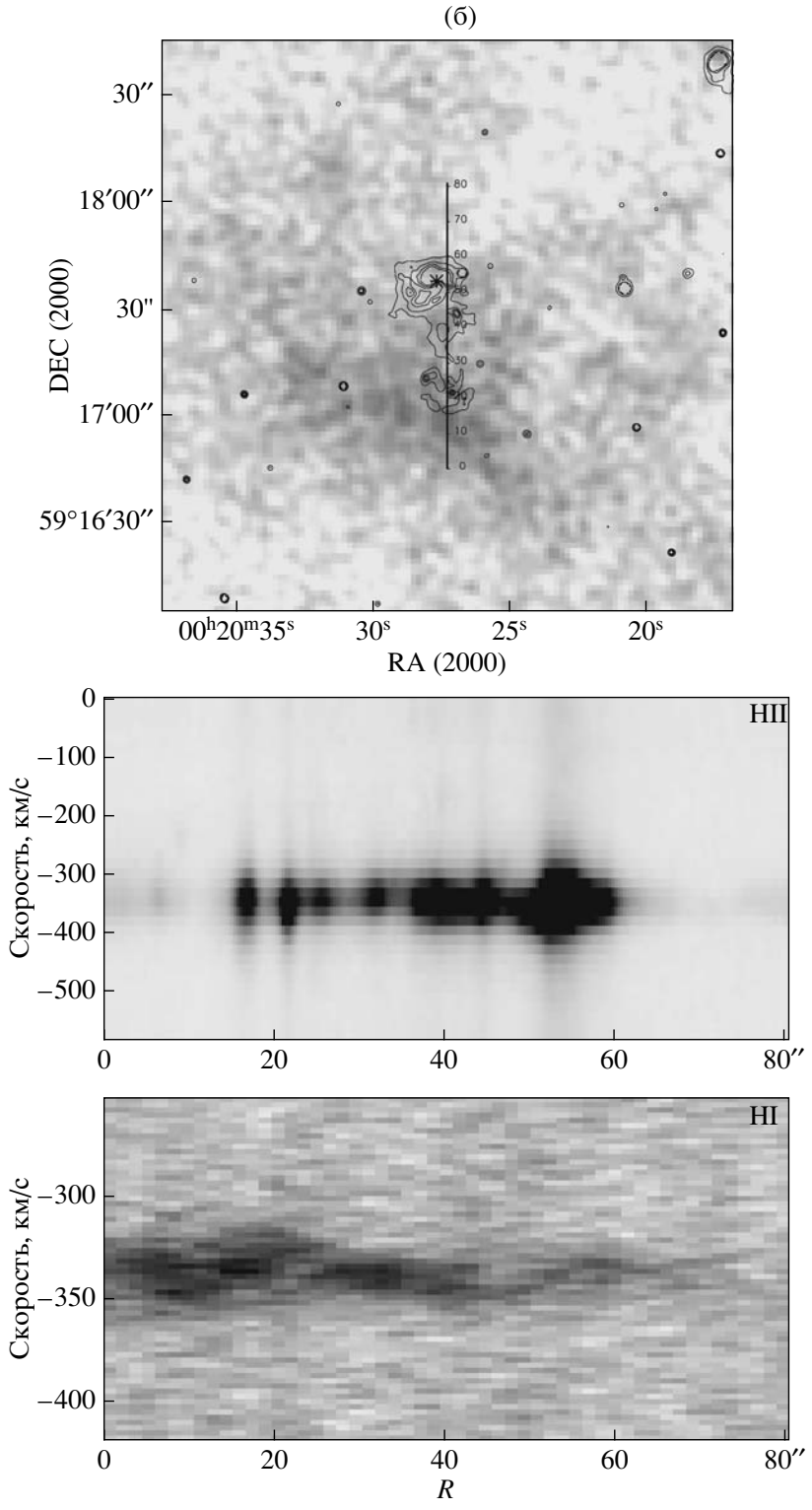

Рис. 6. (Продолжение).

в разных направлениях разрезах. В нейтральной оболочке вокруг HL 106 наоборот более яркой, как правило, является ее удаляющаяся сторона.

Третьим звеном в цепочке расширяющихся оболочек, расположенных в плотном облаке нейтрального газа, является оболочка HI вокруг Син-

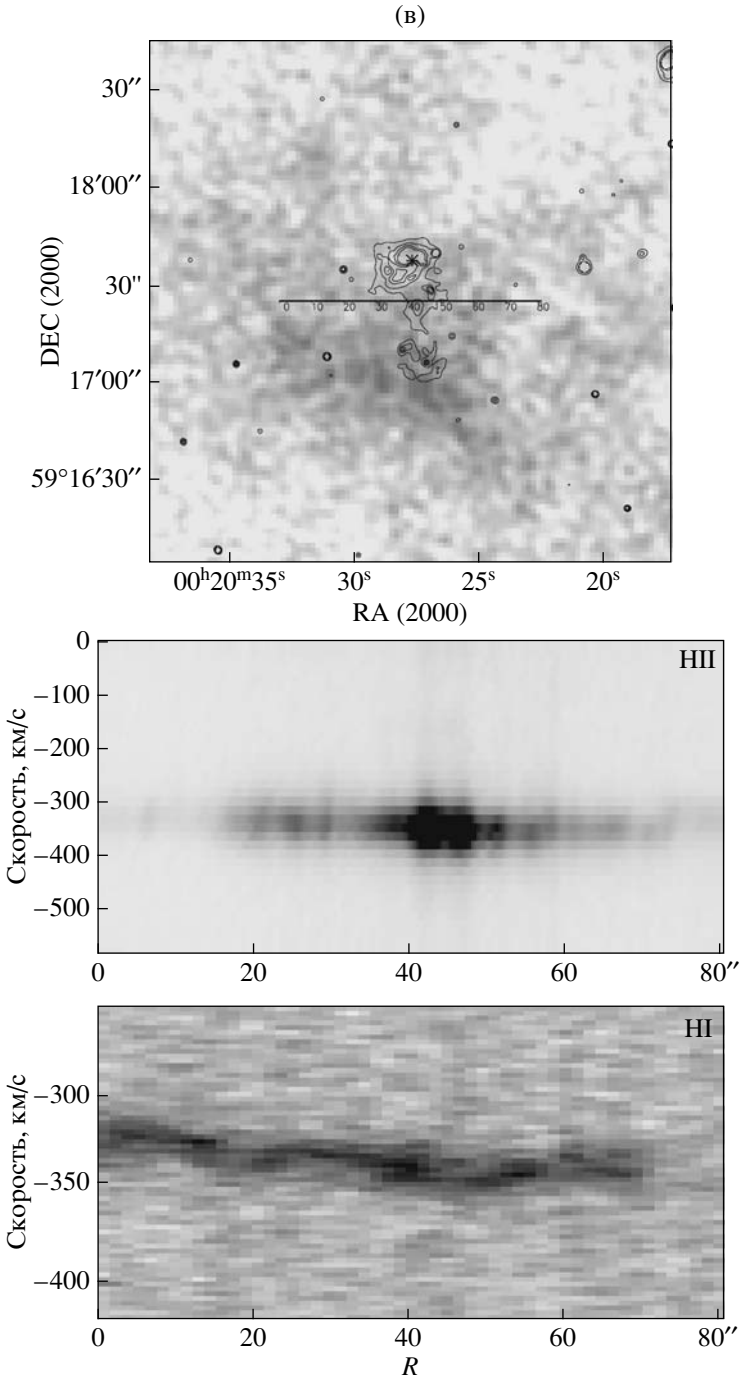

Рис. 6 (Окончание).

хротронной сверхоболочки [11]. Эта третья оболочка расположена по другую сторону плотного газо-пылевого слоя и расширяется с наибольшей средней скоростью 25–30 км/с, что естественно объясняется более мощным источником энергии — вспышкой гиперновой [23].

Разрез, показанный на рис. 6в, проходит по слабым областям ионизованного газа между HL 111 и HL 106. Здесь на фоне плавного изменения средней скорости HI в направлении с востока на запад видны также локальные "возмущения" нейтрального газа. Максимальные скорости нейтрального газа меняются в пределах от ∼30 км/с до ∼−30 км/с относительно средней скорости на соответствующих участках. Сходные локальные "возмущения" нейтрального газа видны и на других P/V-диаграммах на востоке и на западе от яркой области бурного

звездообразования (мы не приводим их здесь для экономии места).

4. ОБСУЖДЕНИЕ

Галактика IC 10 представляется наиболее перспективным объектом для исследования взаимодействия звездного ветра и сверхновых с межзвездным газом в области интенсивного звездообразования. Во-первых, это ближайшая к нам Irr-галактика с бурным звездообразованием; во-вторых, как следует из приведенных во Введении аргументов, здесь мы ближе всего по времени к этому последнему эпизоду звездообразования. В настоящей работе детально исследована структура и кинематика ионизованного и нейтрального газа в области последней вспышки звездообразования. Эта яркая область, включающая туманности HL 111 и HL 106, расположена в северной части самого плотного облака HI в галактике [7], с которым связано наиболее плотное облако молекулярного газа [9, 24] и самое яркое ИК-излучение нагретой пыли [24]. Лучевая плотность этого облака составляет $N(\mathrm{HI}) > 2.5 \times 10^{21}$ см$^{-2}$, лучевая плотность в направлении M24 по данным [7, 9] составляет $N(\mathrm{HI} + \mathrm{H_2}) = 2.2 \times 10^{21}$ см$^{-2}$. Это превышает порог звездообразования в карликовых галактиках ($N(\mathrm{HI}) > (0.4 - 1.7) \times 10^{21}$ см$^{-2}$), согласно [26], и естественно объясняет локализацию здесь центра последнего эпизода бурного звездообразования в IC 10.

Ранние *оценки поглощения и расстояния до IC 10* сильно варьировались из-за низкой галактической широты IC 10, современные дают близкие друг к другу значения.

По нашим оценкам [16], избыток цвета для HII-областей в галактике заключен в пределах 0.8^m–1.1^m; по популяции старых звезд Вакка и др. [7] определили $E(B-V) = 0.95^m$, $(m-M) = 24.48^m \pm 0.08^m$. Сходное значение $(m-M) = 24.30^{+0.18}_{-0.10}$ найдено Князевым и др. [26] по планетарным туманностям; Санна и др. [27, 28] тремя разными методами получили модуль расстояния $24.51^m \pm 0.08^m$, $24.56^m \pm 0.08^m$ и $24.60^m \pm 0.15^m$. На основании перечисленных оценок в настоящей работе использовано расстояние до IC 10 $d = 800$ кпк. (Последняя оценка Ким и др. [29] $d = 715$ кпк несущественно меняет результаты.)

Избыток цвета в области HL 111 несколько меньше среднего по галактике значения, найденного по старым звездам, и меньше оценок покраснения в других HII-областях [2, 5, 16] (см. также ссылки в этих работах).

По наблюдениям со щелевым спектрографом мы нашли $E(B-V) = 0.54^m \pm 0.15^m$ в туманности HL 111 и $E(B-V) = 1.10^m \pm 0.15^m$ в HL 106. В настоящей работе по наблюдениям с MPFS (поле M24 на рис. 1б) в яркой области HL 111 найдено среднее значение $E(B-V) = 0.84^m \pm \pm 0.14^m$, внутри каверны – $E(B-V) = 0.73^m \pm \pm 0.12^m$. Здесь можно выделить два локальных максимума: на северо-западе центральной яркой части HL 111с избыток цвета достигает значения 0.9^m, на юго-востоке – 1.0^m.

По молодым голубым звездам Вакка и др. [5] дают для области HL 111 $E(B-V) = 0.6^m$, что согласуется с нашими оценками. В ближайшей к HL 111 центральной области галактики (поле S4) в работе [28] найдено $E(B-V) = 0.60^m \pm \pm 0.14^m$ и выявлено уменьшение покраснения от центральной области звездообразования к периферии галактики. Оба эти факта легко объяснимы. С одной стороны, центральная область звездообразования примыкает к наиболее плотному облаку нейтрального и молекулярного газа в галактике и отдельные ее области по всей вероятности частично погружены в него. С другой стороны, локальное понижение поглощения может быть обусловлено тем, что ветер молодых звезд последнего эпизода звездообразования вымел окружающий газ.

Оболочка HL 111 вокруг M24 – самый яркий и наиболее интересный объект комплекса звездообразования. Как отмечено во Введении, ярчайшая звезда M24, ранее уже разделенная на три компоненты, фактически представляет собой тесную группу звезд, состоящую по крайней мере из 6 голубых звезд; четыре из них – возможные WR-кандидаты [5]. Скопление 4-1, выделенное [2] вблизи самой яркой северной части оболочечной туманности HL 111, является наиболее богатым и молодым в галактике; к нему принадлежит и тесная группа звезд WR M24. В центре каверны внутри оболочки HL 111 находится скопление 4-2. Радиус 4-1 по половине яркости равен 5 пк, радиус 4-2 – 3 пк; возраст обоих скоплений составляет 3–4 млн. лет [2]. (Термин скопление мы употребляем, следуя этой работе, на самом деле, как показала Хантер [2], большинство выделенных в IC 10 звездных групп представляют собой OB-ассоциации, сопоставимые по числу и концентрации звезд со средними ассоциациями в Галактике и в Магеллановых облаках.)

Плотность звезд в поле вокруг M24 очень высока; Вакка и др. [5] выявили в этой центральной области населения двух вспышек звездообразования: одна – моложе 10 млн лет, вторая – более старая, $t = 150 - 500$ млн. лет. Согласно [5], молодые голубые звезды образуют в области M24 ассоциацию размером около 6 пк по половине яркости. На самом деле это – упомянутое выше скопление 4-1, открытое Хантер [2]: из-за ошибки

привязки координат звезды M24-A в работе [5] на величину около 2.4″ [30], взаимное положение ассоциации и скопления 4-1 на рис. 13 работы [5] показано неправильно — практически эти объекты совпадают. Старые красные звезды распределены в поле равномерно. Локализация двух населений разного возраста различается и по лучу зрения: на основании избытков цвета Вакка и др. [5] заключили, что образующие ассоциацию голубые звезды расположены на передней границе плотного облака перед населением старых звезд. Как показано ниже, результаты проведенных нами исследований кинематики не дают однозначного подтверждения такой локализации молодых звезд.

Согласно оценкам Вакка и др. [5], выявленные в центральном скоплении вокруг M24 19 голубых звезд класса O8 или более ранние, в числе которых 4 звезды WR, обеспечивают поток ионизующих квантов около 10^{51} фот./с. При измеренной нами электронной плотности в области около 60–100 $см^{-3}$ этого достаточно для объяснения наблюдаемой яркой оптической эмиссии газа в HL 111. Дополнительными источниками ионизующей радиации являются молодые звезды скопления 4-2.

Взаимодействие ветра звезд M24 и двух скоплений 4-1 и 4-2 с окружающим газом позволяет объяснить и наблюдаемые небольшие отклонения средней скорости максимума линий Hα и [SII], и слабые высокоскоростные детали в крыльях. Судя по построенным нами P/V-диаграммам (на рис. 2 в качестве примера показаны лишь некоторые из них), наблюдаемые смещения средней скорости максимума линий Hα и [SII] дают возможную систематическую скорость расширения яркой оболочки HL 111 не более 10–15 км/с. В то же время мы впервые выявили в каверне внутри HL 111 слабые высокоскоростные детали в крыльях линии Hα, смещенные в сторону положительных скоростей на величину до 100–120 км/с относительно скорости максимума. Детали в синих крыльях линии Hα здесь несколько слабее. В линии [SII] λ6717 Å также наблюдаются слабые детали, смещенные в сторону положительных и отрицательных скоростей (рис. 4). Локализация этих высокоскоростных движений на изображении HL 111 позволяет сопоставить их с ветром звезд M24, принадлежащих скоплению 4-1, а также звезд скопления 4-2. Отметим, что именно вблизи скопления 4-2 мы обнаружили самые заметные детали в красных крыльях линии.

Вообще говоря, слабые высокоскоростные детали, смещенные в сторону положительных скоростей, которые мы наиболее отчетливо наблюдаем в каверне внутри HL 111, должны соответствовать удаляющейся стороне выметенной ветром оболочки типа блистера на дальней границе плотного облака. Однако если, как считают Вакка и др. [5], молодые голубые звезды M24 и окружающего скопления расположены на передней границе плотного облака, удаляющаяся сторона оболочки должна была бы иметь более высокую яркость и меньшую скорость, чем приближающаяся. Вывод о такой локализации сделан Вакка и др. [5] на основании меньшего покраснения молодых звезд M24 и скопления по сравнению со старыми звездами поля. Однако в принципе нельзя исключить, что M24 и родительское молодое скопление звезд локализованы на задней стороне слоя HI, а их низкое покраснение обусловлено мощным ветром нескольких звезд WR, который вымел окружающий газ, существенно уменьшив локальное поглощение.

Если звезды M24 расположены ближе к дальней стороне плотного слоя газа, наблюдаемая картина скоростей объясняется тривиально. В этом случае яркие малосмещенные детали линий ионизованного газа соответствуют яркой стороне оболочки типа блистера в плотной среде, а слабые высокоскоростные детали соответствуют удаляющейся стороне блистера в среде низкой плотности. В пользу такой модели свидетельствуют результаты наших исследований кинематики нейтрального газа. Тот факт, что приближающаяся сторона оболочки HI вокруг HL 111 ярче, чем удаляющаяся, практически на всех построенных нами P/V-диаграммах в линии 21 см, свидетельствует о меньшей плотности окружающего нейтрального газа на дальней стороне оболочки.

Если же предложенная Вакка и др. [5] пространственная локализация верна, остается предположить, что наблюдаемые высокие скорости в красных крыльях линии характеризуют инициированную звездным ветром ударную волну, распространяющуюся в разреженной среде между плотными сгустками газа в облаке. Показанное на рис. 5 распределение лучевой плотности HI действительно свидетельствует о неоднородной “клочковатой” структуре окружающего нейтрального водорода; о том же говорят и приведенные на рис. 6 P/V-диаграммы. Слабые высокоскоростные детали в синих крыльях линии в этом случае могут быть связаны с инициированной звездным ветром ударной волной, распространяющейся в среде низкой плотности на приближающейся стороне выметенной оболочки.

В обеих упомянутых схемах взаимной локализации слоя HI и молодых звезд, кинетической энергии ветра четырех выявленных здесь звезд WR и двух молодых скоплений 4-1 и 4-2 с запасом хватает для формирования яркой оболочечной туманности HL 111 размером 35 пк и окружающей ее расширяющейся оболочки HI, даже с учетом пониженного

темпа потери массы в галактиках с низкой металличностью. (Согласно Бурэ и др. [31], темп потери массы зависит от металличности как $\dot{M} \propto Z^m$, где $0.5 < m < 1.0$. При $Z \simeq 0.2$ в галактике IC 10 [16] (см. также ссылки в этой работе) мощность ветра звезд уменьшается в 2–5 раз.)

По отношению интенсивностей линий дублета [SII] из наблюдений с MPFS мы нашли электронную плотность в туманности HL 111: в самой яркой части оболочки HL 111c плотность достигает $N_e \simeq 60$–100 см$^{-3}$, в более слабых областях она падает до $N_e \simeq 20$–50 см$^{-3}$. Полученные значения согласуются с оценками, сделанными по наблюдениям со щелевым спектрографом в работе [16].

В рамках классической теории Кастора и др. [32] и Уивера и др. [33] время действия звездного ветра, необходимое для выметания оболочки HL 111 размером 35 пк, расширяющейся со скоростью 15–20 км/с, составляет $t = (0.5$–$0.7) \times 10^6$ лет, что согласуется с продолжительностью стадии WR. Необходимая мощность звездного ветра в невозмущенной среде с плотностью $n_0 \simeq 10$ см$^{-3}$ достигает при этом $L_w = (0.4$–$1) \times 10^{37}$ эрг/с. При металличности $Z \simeq 0.2$ такая мощность соответствует ветру четырех звезд WR, принадлежащих M24. Дополнительным источником механической энергии служит ветер звезд двух скоплений 4-1 и 4-2. При этом в обеих упомянутых выше пространственных схемах яркие детали профиля линии на низких скоростях связаны с газом за фронтом ударной волны, распространяющейся в плотной среде, а слабые детали в крыльях на больших скоростях около 100–120 км/с обусловлены излучением газа за фронтом ударной волны в среде низкой плотности.

Структуру и кинематику ионизованного и нейтрального газа в окрестности центра современного звездообразования M24 и HL 111 можно сопоставить с детально изученной изолированной областью звездообразования в крыле Малого Магелланова облака — молодым скоплением NGC 602 и связанной с ним туманностью N90. Данные наблюдений в линии 21 см и в оптическом диапазоне свидетельствуют о том, что скопление NGC 602 образовалось на периферии облака HI и туманность N90 представляет собой блистер на его границе [34]. При этом блистер и граница облака здесь, в отличие от области M24–HL 111 в IC 10, ориентированы в картинной плоскости, что значительно облегчает интерпретацию наблюдений. Возраст NGC 602 составляет около 4–5 млн. лет [35, 36], т.е совпадает с возрастом скоплений 4-1 и 4-2. Выделенные здесь две вытянутые группы молодых звезд, вероятно, свидетельствуют о распространяющемся звездообразовании [37]. Параметры облака HI также очень похожи на рассматриваемую нами область звездообразования в IC 10: лучевая плотность $N(\mathrm{HI}) = (3-4) \times$ $\times\, 10^{21}$ см$^{-2}$, диаметр — 220 пк, $n(\mathrm{HI}) = 1.3$ см$^{-3}$, масса — около $2.7 \times 10^5\ M_\odot$. Ионизованные оболочки N90 и HL 111 в IC 10 тоже похожи: размер N90 в линии Hα составляет 40–50 пк, скорости ионизованного газа заключены в пределах от 175 до 184 км/с. Таким образом, туманность N90, также как и яркая оболочка HL 111, является очень "спокойной" кинематически, если судить по скоростям максимума линии. В отличие от HL 111, в области N90 не выявлено слабых высокоскоростных деталей профиля линии, что может объясняться пространственной ориентацией "блистера".

Туманность HL 106 расположена в направлении самого яркого в линии CO молекулярного облака. На рис. 1б показана структура этого облака по данным совмещенная с Hα изображением области. (Мы построили единую карту облака, объединив карты его отдельных компонент B11a, B11b, B11c и B11d на рис. 7 цитированной работы.)

Распределение межзвездного поглощения в области может прояснить взаимное расположение плотного облака и туманности HL 106 на луче зрения. По щелевой спектрограмме PA 331 (участки $-19 \div -10$ на рис. 1 в работе [16]) находим избыток цвета на восточной границе HL 106 и CO-облака B11b из сравнения наблюдаемого отношения потоков в линиях Hα : Hβ : Hγ с теоретическим отношением Hα : Hβ : Hγ = 2.86 : 1.00 : 0.47 [38]. Только здесь избыток цвета достигает максимального значения $E(B-V) = 1.3^m \pm$ $\pm\, 0.15^m$, однако в центре пересекаемой щелью области наблюдаются средние для региона значения $E(B-V) = 0.8^m$–0.9^m.

В настоящей работе по наблюдениям с MPFS мы оценили по тем же линиям избыток цвета в западной части HL 106 и облака B11b (рис. 1б). На яркой дуге вблизи звезды WR R10 избыток цвета составляет $E(B-V) = 0.9^m$–1.0^m, затем уменьшается в направлении к центру оболочки до значений $E(B-V) = 0.7^m$ и возрастает до $E(B-V) =$ $= 1.1^m$ вблизи компактной HII-области HL 106a, расположенной в центральной части CO-облака.

В работе [39] определено поглощение для шести ярчайших компактных HII-областей по наблюдениям в линии Brγ. В компактной области Br5, совпадающей с HL 106a, найдено $E(B-V) =$ $= 2.18^m$, в трех других Brγ-источниках комплекса звездообразования избыток цвета заключен в пределах 1.45^m–1.88^m. Найденные в этой работе значения $E(B-V)$ переоценены по сравнению с данными других авторов, но выявляют более высокое поглощение в центральной части CO-облака B11b. (Следует отметить систематический сдвиг

координат Brγ-источников в табл. 2 работы [39]; из-за этого их локализация на рис. 16 работы [2] показана неправильно. Мы независимо определили локализацию этих компактных источников по изофотам Brγ, отождествив их на Hα-изображении галактики.)

Таким образом, имеющиеся оценки свидетельствуют о небольшом росте поглощения в области CO-облака B11b на величину около 0.1^m–0.3^m, что при солнечном обилии соответствует увеличению лучевой плотности на величину $\Delta N(\mathrm{HI}) \simeq$ $\simeq (0.5\text{–}1.5) \times 10^{21}$ см$^{-2}$. Даже с учетом низкой металличности IC 10 это лишь небольшая часть полной лучевой плотности в направлении обсуждаемого плотного облака, которая достигает $N(\mathrm{HI}) \simeq$ $\simeq 10^{22}$ см$^{-2}$ [7]. По наблюдениям CO-излучения в области полная плотность нейтрального и молекулярного водорода здесь составляет $N(\mathrm{H}) \simeq 2.8 \times$ $\times\, 10^{22}$ см$^{-2}$ [9, 24]. Соответственно можно думать, что оптическая туманность HL 106 расположена не за плотным слоем облаков, а частично погружена в него. В пользу такой взаимной локализации HL 106 и молекулярного облака говорит и тот факт, что дальняя сторона обнаруженной нами оболочки HI вокруг HL 106 ярче передней (рис. 6а, 6б).

При этом облако B11b, по всей вероятности, физически связано с оптической туманностью. Прежде всего, лучевая скорость CO-облака B11b ($V = -331$ км/с по измерениям [9] полностью совпадает со скоростью ионизованного газа в оболочке HL 106 (рис. 3, 4). Однако главное, из рис. 1б следует, что самая яркая южная дуга HL 106 в точности описывает границы облака B11b. Столь идеальное совпадение не может быть случайным, оно свидетельствует о физической связи тонкой ионизованной оболочки и молекулярного облака B11b. Возможно, оболочка HL 106, в точности ограничивающая CO-облако B11b, образована в результате фотодиссоциации молекулярного газа на границе этого облака и ионизации УФ-радиацией звезд WR R2 и R10, а также двух скоплений 4-3 и 4-4 (рис. 1). Возраст этих скоплений по оценке [2] составляет около 20–30 млн. лет.

Наши исследования кинематики ионизованного и нейтрального газа в туманности HL 106 показали, что здесь наблюдается сходная с HL 111 картина. Скорости, определенные по максимуму обеих линий Hα и [SII] и характеризующие наиболее яркие сгустки туманности, обнаруживают небольшие вариации и дают среднюю скорость расширения оболочки не более 10–15 км/с. Слабые детали в крыльях линии на уровне около 2%–10% максимальной интенсивности видны в HL 106 в интервале скоростей от -260 до -250 км/с и от -450 до -420 км/с.

Внешняя оболочка нейтрального газа, окружающая HL 106, также имеет размер и скорость расширения, сходные с оболочкой HI вокруг HL 111.

Как и в случае HL 111, легко убедиться, что ветер звезд WR R2 и R10, а также скоплений 4-3 и 4-4 поставляет механическую энергию, достаточную для формирования оболочки.

Кинематика газа в комплексе звездообразования является следствием сложной структуры окружающего нейтрального газа в регионе, наличия молекулярных облаков и множественных источников звездного ветра. В этой ситуации трудно ожидать регулярную морфологию и кинематику ионизованного газа в области бурного звездообразования.

Как показано на примере двух оболочек HL 111 и HL 106, взаимодействие звезд WR и массивных голубых звезд расположенных здесь скоплений с окружающим облаком HI, возможно подверженным влиянию предыдущего поколения звезд, позволяет объяснить и наблюдаемые небольшие отклонения средней скорости максимума линий Hα и [SII], и слабые высокоскоростные детали в крыльях.

В западной части области между HL 111 и HL 106 лучевая плотность нейтрального водорода понижена (рис. 5). Здесь, как показано в подразделе 3.1, высокоскоростные детали профиля линий Hα и [SII] λ6717 Å также наблюдаются. Действие ветра трех расположенных здесь звезд WR M13, M12 и M14 объясняет наличие высокоскоростных крыльев в данном регионе. Ветер этих звезд формирует четкую картину взаимодействия с окружающей средой: здесь наблюдаются слабые дуговые и кольцевые структуры (рис. 1). Две яркие более компактные HII-области HL 111a и HL 111b, по всей вероятности, представляют собой самые плотные сгустки облака HI, ионизованные этими звездами. На этой западной границе облака из-за пониженной плотности нейтрального газа действие ветра звезд WR наиболее эффективно разрушает “родительское” облако HI.

Как показано выше в подразделе 3.1, слабые высокоскоростные детали в крыльях обеих линий наблюдаются и в других участки комплекса звездообразования. Широкое распространение высокоскоростных движений в комплексе легко понять, учитывая высокую плотность источников звездного ветра и неоднородность окружающей межзвездной среды.

Исследования крупномасштабной кинематики нейтрального водорода в IC 10, проведенные в работе [7], выявили протяженные оболочки нейтрального газа размером около $1'$–$1.5'$ (см. рис. 9 цитированной работы). Целью проведенного нами повторного анализа данных наблюдений IC 10 в

линии 21 см на VLA было более детальное исследование "локальной" структуры и кинематики HI в комплексе звездообразования. В результате нам действительно удалось выделить вокруг двух ярчайших оптических туманностей HL 111 и HL 106 две окружающие их локальные нейтральные оболочки размером около 20″–30″, измерить скорости их расширения и предложить возможные источники кинетической энергии, необходимой для их формирования.

Восточнее и западнее комплекса ярких туманностей мы также обнаружили движения нейтрального газа со скоростью до 30 км/с на масштабах 20″ – 40″. Здесь расположены звезды WR и молодые скопления, которые могут инициировать эти движения.

5. ЗАКЛЮЧЕНИЕ

По результатам наблюдений галактики IC 10 на 6-м телескопе САО РАН с фокальным редуктором SCORPIO в режиме интерферометра Фабри–Перо, а также с панорамным спектрографом MPFS исследованы структура и кинематика ионизованного газа в центральной области интенсивного современного звездообразования. По архивным данным наблюдений в линии 21 см на VLA рассмотрены структура и кинематика нейтрального газа в регионе. Показано, что скорость ионизованного газа в области бурного звездообразования, включающей наиболее яркие туманности HL 111 и HL I06, меняется в пределах от −315 до −350 км/с, средняя скорость составляет −330 км/с. Такую же скорость имеет и нейтральный газ в регионе. Это согласуется с измерениями Туроу и Вилкотса [21] в линии Hα (наблюдения этих авторов покрывают треть исследованной нами яркой области звездообразования) и с оценками Вилкотса и Миллера [7] по линии 21 см.

Показано, что средняя скорость расширения ярких оболочек HL 111 и HL 106 не превышает 10–15 км/с. Впервые выявлены высокоскоростные крылья эмиссионных линий Hα и [SII] в интервале скоростей от −280 до −240 км/с и от −450 до −410 км/с во внутренней каверне туманности HL 111, а также в других областях комплекса бурного звездообразования.

По архивным данным наблюдений в линии 21 см на VLA обнаружены две нейтральные оболочки размером около 20″–30″, окружающие туманности HL 111 и HL 106. Средняя скорость расширения обеих оболочек HI составляет 15–20 км/с, максимальная скорость разлета сгустков нейтрального газа достигает 25–30 км/с. Предложены возможные источники кинетической энергии, необходимой для формирования оболочек HII и окружающих их оболочек HI.

Восточнее и западнее комплекса ярких туманностей также обнаружены движения нейтрального газа со скоростью до 30 км/с на масштабах 20″–40″. Локализованные здесь звезды WR и молодые скопления могут инициировать эти движения.

Обсуждается пространственная схема взаимодействия звездного и газового населений центрального комплекса бурного звездообразования в галактике.

Работа проводилась при финансовой поддержке гранта РФФИ (проект 07-02-00227). Работа основана на наблюдательном материале, полученном на 6-м телескопе САО РАН, финансируемом Минобрнауки РФ (регистрационный номер 01-43). Авторы благодарят В.Д. Вакка (W.D. Vacca) за обсуждение привязки координат звезды M24-A в его работе, Э. Вилкотса (E. Wilcots) за предоставление куба данных наблюдений HI и Н.Ю. Подорванюка за предоставление одной из программ обработки этих данных. В процессе работы над статьей мы использовали базу внегалактических данных НАСА/ИПАК (NED), функционирующей под управлением Лаборатории реактивного движения Калифорнийского технологического института по контракту с Национальным управлением по аэронавтике и исследованию космического пространства (США).

СПИСОК ЛИТЕРАТУРЫ

1. M. G. Richer, A. Bullejos, J. Borissova, *et al.*, Astron. and Astrophys. **370**, 34 (2001).
2. D. A. Hunter, Astrophys. J. **559**, 225 (2001).
3. D. B. Zucker, Bull. Amer. Astron. Soc. **34**, 1147 (2002).
4. P. Massey, K. Olsen, P. Hodge, *et al.*, Astron. J. **133**, 2393 (2007).
5. W. D. Vacca, C. D. Sheehy, and J. R. Graham, Astrophys. J. **662**, 272 (2007).
6. D. B. Zucker, Bull. Amer. Astron. Soc. **32**, 1456 (2000).
7. E. M. Wilcots and B. W. Miller, Astron. J. **116**, 2363 (1998).
8. A. Gil de Paz, B. F. Madore, and O. Pevunova, Astrophys. J. Suppl. Ser. **147**, 29 (2003).
9. A. Leroy, A. Bolatto, F. Walter, and L. Blitz, Astrophys. J. **643**, 825 (2006).
10. K. T. Chyzy, J. Knapik, D. J. Bomans, *et al.*, Astron. and Astrophys. **405**, 513 (2003).
11. Т. А. Лозинская, А. В. Моисеев, Н. Ю. Подорванюк, А. Н. Буренков, Письма в "Астрон. журн." **34**, 243 (2008).
12. P. Massey, T. E. Armandroff, and P. S. Conti, Astron. J. **103**, 1159 (1992).

13. P. Massey and S. Holmes, Astrophys. J. (Letters) **580**, L35 (2002).
14. P. A. Crowther, L. Drissen, J. B. Abbott, *et al.*, Astron. and Astrophys. **404**, 483 (2003).
15. P. Hodge and M. G. Lee, Publs Astron. Soc. Pacif. **102**, 26 (1990).
16. Т. А. Лозинская, О. В. Егоров, А. В. Моисеев, Д. В. Бизяев, Письма в "Астрон. журн." **35**, 811 (2009).
17. P. Royer, S. J. Smartt, J. Manfroid, and J. Vreux, Astron. and Astrophys. **366**, L1 (2001).
18. A. V. Moiseev, Bull. Spec. Astophys. Observ. **54**, 74 (2002); e-Print arXiv:astro-ph/0211104.
19. А. В. Моисеев, О. В. Егоров, Астрофиз. бюлл. **63**, 193 (2008).
20. V. L. Afanasiev, S. N. Dodonov, and A. V. Moiseev, in: *Stellar dynamics: from classic to modern*, eds L. P. Osipkov, I. I. Nikiforov (Saint-Petersburg: Saint-Petersburg Univ. Press, 2001), p. 103.
21. J. C. Thurow and E. M. Wilcots, Astron. J. **129**, 745 (2005).
22. H. Yang and E. D. Skillman, Astron. J. **106**, 1448 (1993).
23. T. A. Lozinskaya and A. V. Moiseev, Monthly Not. Roy. Astron. Soc. **381**, 26L (2007).
24. A. D. Bolatto, J. M. Jackson, C. D. Wilson, and G. Moriarty-Schieven, Astrophys. J. **532**, 909 (2000).
25. A. Begum, J. N. Chengalur, I. D. Karachentsev, *et al.*, Monthly Not. Roy. Astron. Soc. **365**, 1220 (2006).
26. A. Y. Kniazev, S. A. Pustilnik, and D. B. Zucker, Monthly Not. Roy. Astron. Soc. **384**, 1045 (2008).
27. N. Sanna, G. Bono, P. B. Stetson, *et al.*, Astrophys. J. (Letters) **688**, L69 (2008).
28. N. Sanna, G. Bono, M. Monelli, *et al.*, Mem. Soc. Astron. Ital. **79**, 747 (2008).
29. M. Kim, E. Kim, N. Hwang, *et al.*, Astrophys. J. **703**, 816 (2009); e-Print arXiv:astro-ph/0907.4844.
30. W. D. Vacca, Частн. сообщ. (2009).
31. J. C. Bouret, T. Lanz, D. J. Hillier, *et al.*, Astrophys. J. **595**, 1182 (2003).
32. J. Castor, R. McCray, and H. Weaver, Astrophys. J. (Letters) **200**, L107 (1975).
33. H. Weaver, R. McCray, P. Shapiro, and R. Moore, Astrophys. J. **218**, 377 (1977).
34. L. Nigra, J. S. Gallagher, L. J. Smith, *et al.*, Publs Astron. Soc. Pacif. **120**, 972 (2008); e-Print arXiv:astro-ph/0808.1033.
35. J. B. Hutchings, S. Cartledge, J. Pazder, and I. B. Thompson, Astron. J. **101**, 933 (1991).
36. L. R. Carlson, E. Sabbi, M. Sirianni, *et al.*, Astrophys. J. (Letters) **665**, L109 (2007).
37. D. A. Gouliermis, S. P. Quanz, and T. Henning, Astrophys. J. **665**, 306 (2007).
38. L. H. Aller, *Physics of thermal gaseous nebulae* (D. Reidel Publ. Comp., 1984).
39. J. Borissova, L. Georgiev, M. Rosado, *et al.*, Astron. and Astrophys. **363**, 130 (2000).

ПИСЬМА В АСТРОНОМИЧЕСКИЙ ЖУРНАЛ, 2009, том 35, № 11, с. 811–828

УДК 524.7

СПЕКТР СВЕЧЕНИЯ ГАЗА В Irr ГАЛАКТИКЕ IC 10

© 2009 г. Т. А. Лозинская[1*], О. В. Егоров[1], А. В. Моисеев[2], Д. В. Бизяев[1,3]

[1] *Государственный астрономический институт им. П.К. Штернберга, Москва*

[2] *Специальная астрофизическая обсерватория РАН, пос. Нижний Архыз*

[3] *Обсерватория Апачи Пойнт, Санспот, США*

Поступила в редакцию 17.02.2009 г.

Проведены наблюдения карликовой Irr галактики IC 10 на 6-м телескопе САО РАН с фокальным редуктором SCORPIO в режиме щелевого спектрографа. Исследован спектр свечения ионизованного газа в области интенсивного современного звездообразования. Оценено относительное содержание кислорода, а также ионов азота N^+ и серы S^+ в двух десятках областей HII и в Синхротронной Сверхоболочке. Среднее по галактике обилие кислорода составляет $12 + \lg(O/H) = 8.17 \pm 0.35$, металличность – $Z = 0.18 \pm 0.14 Z_\odot$. Показано, что металличность, найденная из сопоставления диагностических диаграмм с фотоионизационными моделями, менее надежна, чем оценки по ярким линиям кислорода.

Ключевые слова: Irr-галактики, IC 10, межзвездная среда, химический состав.

GAS EMISSION SPECTRUM IN THE Irr GALAXY IC 10, *by T. A. Lozinskaya, O. V. Egorov, A. V. Moiseev, and D. V. Bizyaev*. Observations of the dwarf Irr galaxy IC 10 have been performed with the SCORPIO focal reducer at the 6-m Special Astrophysical Observatory Telescope, Russian Academy of Sciences, in the mode of a slit spectrograph. The ionized-gas emission spectrum in the region of intense current star formation has been investigated. The relative oxygen, N^+, and S^+ abundances in two dozen HII regions and the Synchrotron Superbubble have been estimated. The galaxy-averaged oxygen abundance is $12 + \lg(O/H) = 8.17 \pm 0.35$ and the metallicity is $Z = 0.18 \pm 0.14 Z_\odot$. The metallicity found by comparing diagnostic diagrams with photoionization models is shown to be less reliable than its estimate based on intense oxygen lines.

PACS numbers : 98.52.Wz; 98.56.Si; 98.58.Ay; 98.58.Hf; 98.58.Mj; 98.62.Bj

Key words: Irr galaxies, IC 10, interstellar medium, chemical composition.

ВВЕДЕНИЕ

Карликовая Irr галактика IC 10 представляется уникальным полигоном для исследований межзвездной среды в областях бурного звездообразования. Изображения галактики в линиях Hα и [SII] выглядят как единый гигантский комплекс множественных оболочек и сверхоболочек размером от 50 пк до 800–1000 пк (Зуккер, 2000; Вилкотс, Миллер, 1998; Гил де Паз и др., 2003; Лерой и др., 2006; Чизи и др., 2003; Лозинская и др., 2008). Звездное население свидетельствует о недавней вспышке звездообразования ($t = 4$–10 млн. лет) и о более старой ($t > 350$ млн. лет) (Хантер, 2001; Зуккер, 2002; Масси и др., 2007; Вакка и др., 2007, и ссылки в этих работах). Высокие Hα- и ИК-светимости и аномально большое число звезд WR в IC 10 (пространственная плотность WR – самая высокая среди карликовых галактик, сопоставимая с массивными спиральными галактиками (Масси и др., 1992, 2007; Ричер и др., 2001; Масси, Холмс, 2002; Краутер и др., 2003; Вакка и др., 2007)) говорят о короткой вспышке современного звездообразования, охватившей большую часть галактики.

Лозинская и Моисеев (2007) объяснили вспышкой гиперновой формирование уникальной Синхротронной Сверхоболочки, которую до этого связывали с множественными вспышками десятка сверхновых (Янг, Скиллман, 1993; Буйехос, Розадо, 2002; Розадо и др., 2002; Туроу, Вилкотс, 2005).

В настоящей работе проведено исследование спектра свечения ионизованного газа в области

[*] Электронный адрес: lozinsk@sai.msu.ru

Таблица 1. Журнал наблюдений

Спектрограмма	дата	$\Delta\lambda$, Å	$\delta\lambda$, Å	$T_{\rm exp}$, с	Качество изображений, сек. дуги
PA0	17/18.08.06	3620–5370	5	6000	2.5
PA0	02/03.09.08	5650–7340	5	3600	2.1
PA132	17/18.08.06	3620–5370	5	4800	1.4
PA132	18/19.08.06	5650–7340	5	3600	1.4
PA268	14/15.02.07	6060–7060	2.5	1200	1.4
PA268	15/16.01.08	3620–5370	5	4800	1.5
PA45	29/30.10.08	3650–7350	9	3600	1.0
PA331	28/29.10.08	3650–7350	9	6000	0.9

современного звездообразования IC 10 по наблюдениям на 6-м телескопе САО РАН с фокальным редуктором SCORPIO, работающим в режиме щелевого спектрографа. Основная цель наблюдений – оценка металличности для большого числа эмиссионных областей. Ранее в работах Леке и др. (1979), Гарнетта (1990), Ричера и др. (2001) и Ли и др. (2003) металличность была определена лишь для трех самых ярких областей HII галактики.

В последующих разделах описаны методика наблюдений и обработки данных; представлены полученные результаты и их обсуждение; в заключении суммируются основные выводы работы.

НАБЛЮДЕНИЯ И ОБРАБОТКА ДАННЫХ

Наблюдения IC 10 проводились с прибором SCORPIO (Афанасьев, Моисеев, 2005), работающим в режиме щелевого спектрографа, со щелью длиной около $6'$ и шириной $1''$. Масштаб вдоль щели составлял $0''.36$/пиксель.

Для пяти положений щели были получены спектры с разрешением от 2.5 до 10 Å. Спектрограммы в соответствии с их позиционными углами далее в статье обозначены как PA0, PA45, PA132, PA268 и PA331. Соответствующий спектральный диапазон $\Delta\lambda$, спектральное разрешение $\delta\lambda$, суммарная экспозиция $T_{\rm exp}$ и среднее качество изображений (seeing) указаны в табл. 1.

Обработка данных выполнялась обычным способом; для привязки к энергетической шкале использовались спектры звезд BD+25d4655, GRW+70d5824 и GD 71, наблюдавшихся сразу после объекта практически на том же зенитном расстоянии.

В анализируемых спектрах уровень континуума от подстилающего звездного населения определялся на основании сплайн-аппроксимации. Интегральный поток в эмиссионных линиях измерялся с помощью однокомпонентной гаусс-аппроксимации. С целью увеличения отношения сигнал/шум для слабых эмиссионных областей при обработке спектрограмм проводилось усреднение по отдельным областям HII, при этом размер области интегрирования составлял от $2''$ до $20''$. Погрешности определения потоков в линиях оценивались по синтетическим спектрам, имитировавшим наблюдения с нужным отношением сигнал/шум. Приведенные далее в таблицах и на рисунках диапазоны ошибок соответствуют уровню 3σ.

РЕЗУЛЬТАТЫ НАБЛЮДЕНИЙ

Спектр свечения ионизованного газа

Локализация пяти щелей, проходящих через Синхротронную Сверхоболочку, яркую область современного звездообразования, и более слабые оболочечные структуры, показана на рис. 1а,б. Здесь же отмечены спектрально подтвержденные звезды WR по спискам Ройера и др. (2001) и Масси, Холмса (2002). Для удобства отождествления на рисунках дана разметка щелевых спектрограмм в секундах дуги.

Измерения, выполненные в точках пересечения щелей спектрографа, позволили оценить реальную точность наших наблюдений. В табл. 2 приведены значения относительных интенсивностей линий, измеренных по паре щелевых спектрограмм в местах их пересечений. Как видим, в пределах ошибок согласие в основном хорошее. Различия, превышающие формальные ошибки наблюдений, могут быть связаны с разной областью интегрирования потоков для двух положений щели на туманности, характеризующейся тонкой структурой.

Результаты обработки спектрограмм представлены на рис. 2 и в табл. 3. На рисунке в качестве примера показаны распределения вдоль щели PA132 относительных интенсивностей линий $I([\mathrm{OII}]\lambda3727+3729\text{Å})/I([\mathrm{OIII}]\lambda5007\text{Å})$, $I([\mathrm{SII}]\lambda6717+6731\text{Å})/I(\mathrm{H}\alpha)$, $I([\mathrm{NII}]\lambda6583\text{Å})/$

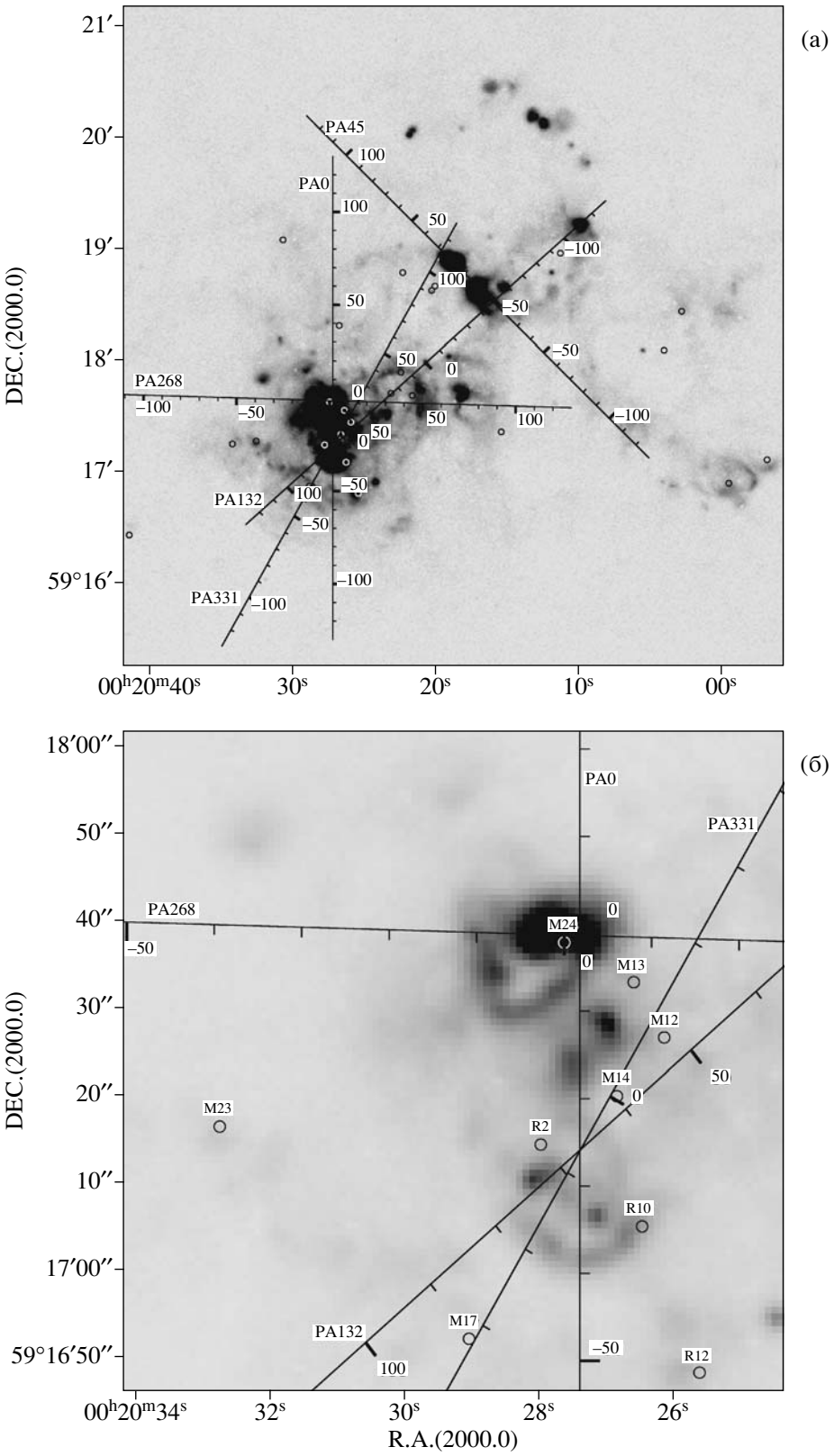

Рис. 1. Локализация пяти щелевых спектрограмм на изображении галактики в линии Hα: (а) — вся галактика, (б) — яркая область современного звездообразования. Дана разметка щелевых спектрограмм в секундах дуги, кружками отмечены спектрально подтвержденные звезды WR по спискам Ройер и др. (2001) и Масси, Холмс (2002).

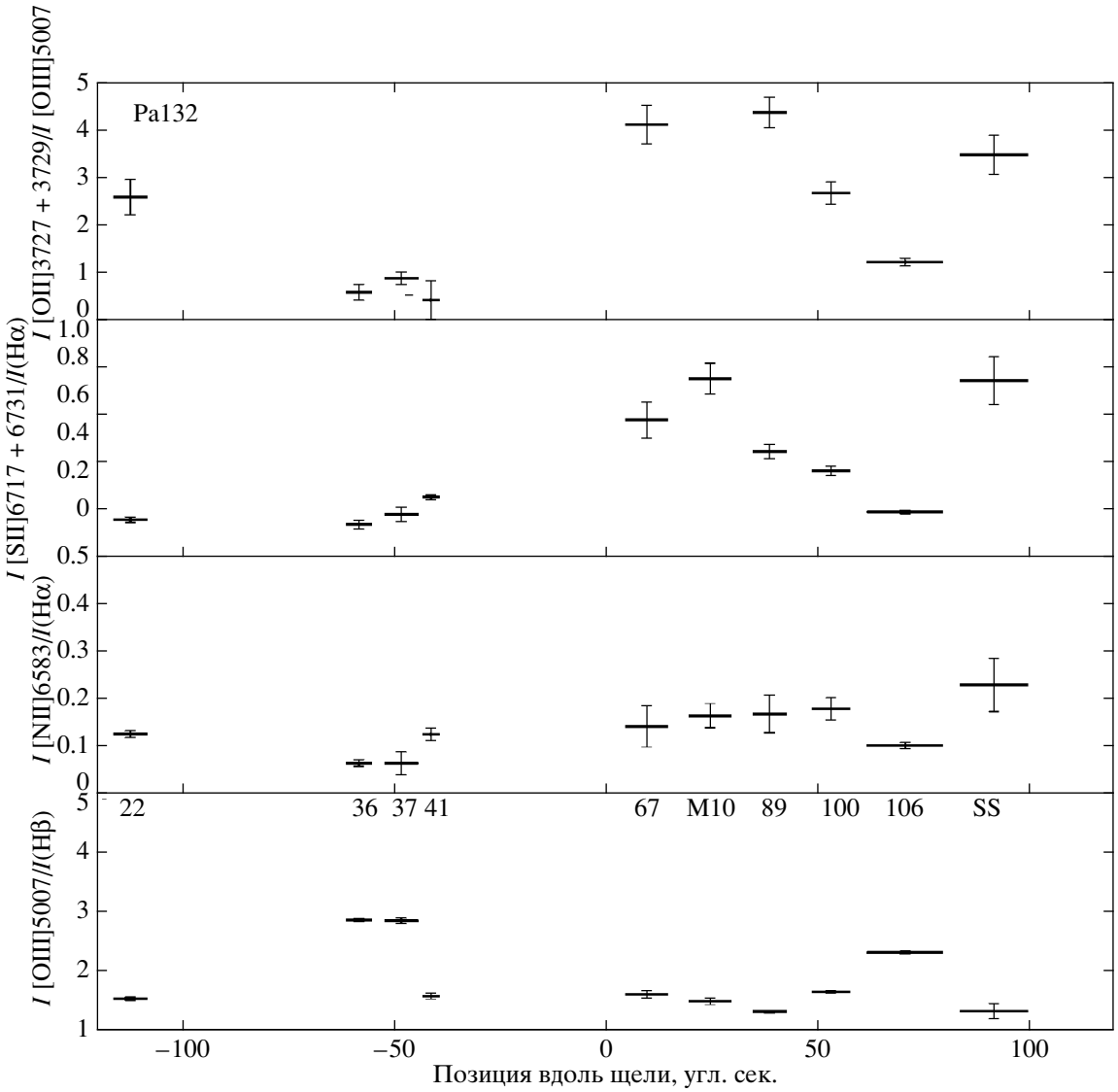

Рис. 2. Распределения вдоль щели PA132 относительных интенсивностей линий $I([\mathrm{OII}]\lambda3727 + 3729\text{Å})/I([\mathrm{OIII}]\lambda5007\text{Å})$, $I([\mathrm{SII}]\lambda6717 + 6731\text{Å})/I(\mathrm{H}\alpha)$, $I([\mathrm{NII}]\lambda6583\text{Å})/I(\mathrm{H}\alpha)$ и $I([\mathrm{OIII}]\lambda5007\text{Å})/I(\mathrm{H}\beta)$. По горизонтальной оси нижней панели дана разметка щелей в сек. дуги, номерами вверху обозначены области HII из каталога Ходжа и Ли (1990), индекс M10 отмечает слабую область вокруг звезды WR M10, SS – Синхротронную Сверхоболочку.

$I(\mathrm{H}\alpha)$ и $I([\mathrm{OIII}]\lambda5007\text{Å})/I(\mathrm{H}\beta)$. По горизонтальной оси нижней панели внизу дана разметка щели в сек. дуги, вверху номерами обозначены области HII из каталога Ходжа и Ли (1990). Обозначение M10 отмечает незарегистрированную в каталоге слабую область вокруг звезды WR M10, обозначение SS соответствует Синхротронной Сверхоболочке. Как следует из рис. 1, щель PA331 (позиции 4–11) проходит по слабой области вблизи HL111a на юго-востоке, а позиции 108–115 соответствуют северной периферии области HL50. Чтобы не загромождать рисунки и таблицы, обе эти области на щели PA331 в табл. 3 и 4 и на всех рисунках обозначены просто как HL111a и HL50 соответственно. Щель PA268 (позиции 68–71) проходит между яркими туманностями HL46 и HL48; эта область обозначена далее как HL46,48.

В табл. 3 даны соответственно по столбцам: название области HII по каталогу Ходжа и Ли (1990), использованная для оценки спектрограмма и позиции на ней, найденные средние значения относительных интенсивностей упомянутых выше линий и отношения интенсивностей линий дублета [SII]λ6717/6731 Å.

Межзвездное поглощение в табл. 3 и на рис. 2 учтено. Всюду в работе мы по-возможности определяли избыток цвета $E(B-V)$ индивидуально для каждой из областей HII. Наиболее до-

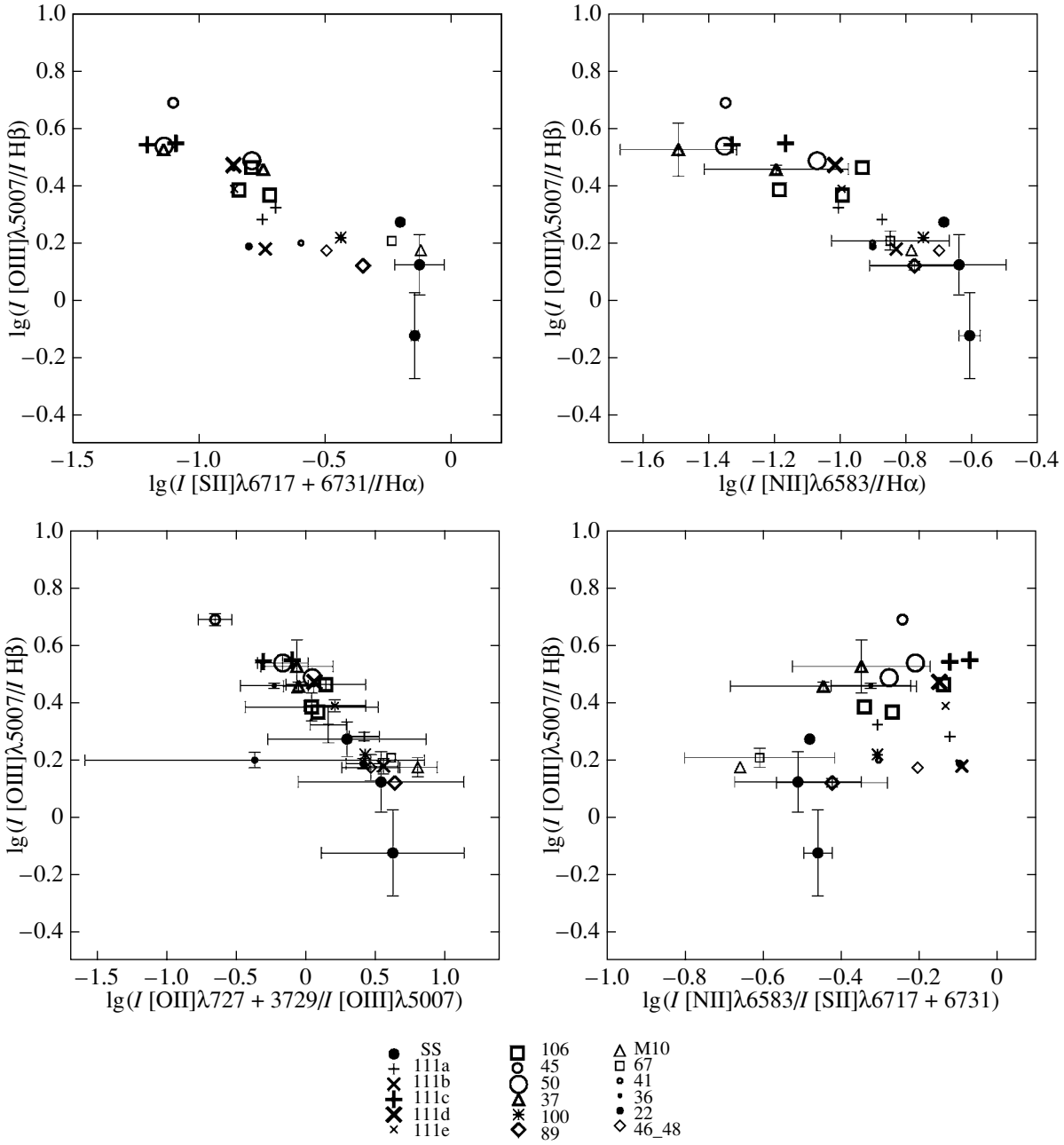

Рис. 3. Диагностические диаграммы относительных интенсивностей линий: $I([\mathrm{OIII}]\lambda5007\text{Å})/I(\mathrm{H}\beta)$ в зависимости от $I([\mathrm{SII}]\lambda6717+6731\text{Å})/I(\mathrm{H}\alpha)$, от $I([\mathrm{NII}]\lambda6583\text{Å})/I(\mathrm{H}\alpha)$, от $I([\mathrm{OII}]\lambda3727+3729\text{Å})/I([\mathrm{OIII}]\lambda5007\text{Å})$, и от $I([\mathrm{NII}]\lambda6583\text{Å})/I([\mathrm{SII}]\lambda6717+6731\text{Å})$. Разными значками, указанными внизу, даны относительные интенсивности, усредненные по индивидуальным областям HII из каталога Ходжа и Ли (1990), по области вокруг WR M10 и по Синхротронной Сверхоболочке (SS). Чтобы не загромождать рисунки, показаны только те ошибки измерений, которые превышают ±0.1.

стоверные результаты получены по спектрограммам с низким спектральным разрешением PA45 и PA331. Для этих спектрограмм оценки сделаны из сравнения наблюдаемого отношения потоков в линиях $\mathrm{H}\alpha$:$\mathrm{H}\beta$:$\mathrm{H}\gamma$ с теоретическим отношением $\mathrm{H}\alpha$:$\mathrm{H}\beta$:$\mathrm{H}\gamma = 2.86{:}1.00{:}0.47$, справедливым, согласно Аллеру (1984), для характерных значений электронной плотности в области звездообразования 30–300 см$^{-3}$ и принятой температуре 11000 K (см. ниже). Для областей, не попавших на данные щели, было принято либо среднее значение $E(B-V) = 0\overset{m}{.}95$, либо значение избытка цвета для близкой области, попавшей на одну из двух указанных щелей.

Наши оценки $E(B-V)$ для разных областей галактики варьируются в пределах $0\overset{m}{.}8$–$1\overset{m}{.}1$.

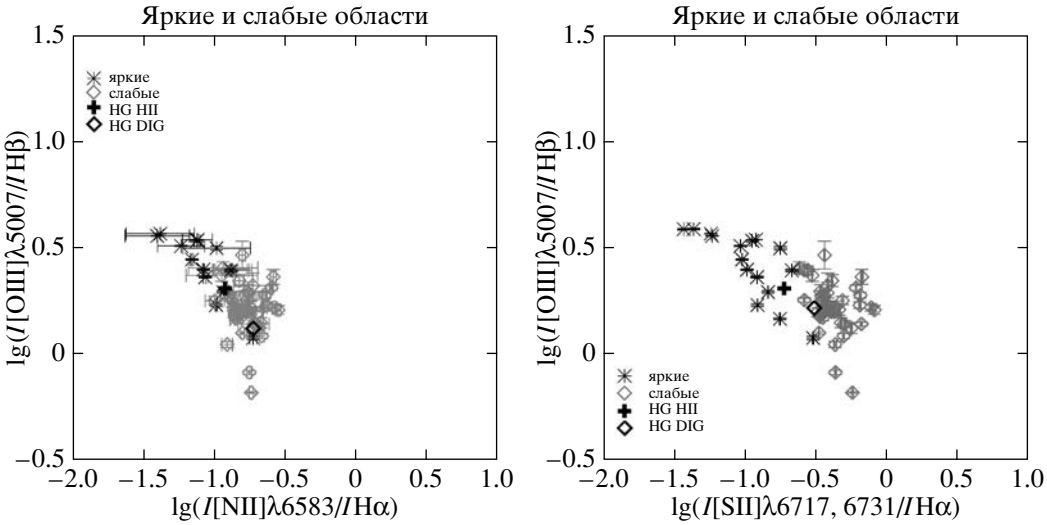

Рис. 4. Диагностические диаграммы, объединенные по ярким областям: $F_{\mathrm{H}\alpha} \geq 1.0 \times 10^{-15}$ эрг с$^{-1}$ см$^{-2}$ (показаны черными звездочками) и по слабым: $F_{\mathrm{H}\alpha} \leq 1.0 \times 10^{-15}$ эрг с$^{-1}$ см$^{-2}$ (показаны серыми ромбами). Представлены измерения в площадках размером 5 пикселей (1.″8) вдоль щелей PA0, PA132 и PA268. Яркими крестиком и ромбом даны найденные Хидалго-Гамес (2005) средние по галактике значения для ярких областей HII и для "диффузного ионизованного газа" (DIG).

Диагностические диаграммы относительных интенсивностей линий

На рис. 3 показаны построенные для IC 10 диагностические диаграммы относительных интенсивностей линий, которые традиционно используются для сопоставления наблюдений с расчетными ионизационными моделями: $I([\mathrm{OIII}]\lambda 5007\text{Å})/I(\mathrm{H}\beta)$ в зависимости от $I([\mathrm{SII}]\lambda 6717+6731\text{Å})/I(\mathrm{H}\alpha)$, от $I([\mathrm{NII}]\lambda 6583\text{Å})/I(\mathrm{H}\alpha)$, от $I([\mathrm{OII}]\lambda 3727+3729\text{Å})/I([\mathrm{OIII}]\lambda 5007\text{Å})$ и от $I([\mathrm{NII}]\lambda 6583\text{Å})/I([\mathrm{SII}]\lambda 6717+6731\text{Å})$.

Разными значками показаны значения относительных интенсивностей, усредненные по отдельным областям HII из каталога Ходжа и Ли (1990), по области вокруг WR M10 и по Синхротронной Сверхоболочке (SS). Чтобы не загромождать рисунки, показаны только те ошибки измерений, которые превышают ± 0.1.

На рис. 4 а,б объединены данные отдельно по ярким эмиссионным областям ($F_{\mathrm{H}\alpha} \geq 1.0 \times \times 10^{-15}$ эрг с$^{-1}$ см$^{-2}$) и по слабым ($F_{\mathrm{H}\alpha} \leq 1.0 \times \times 10^{-15}$ эрг с$^{-1}$ см$^{-2}$). Здесь представлены не усредненные по туманностям значения, а измерения в площадках размером 5 пикселей (1.″8) вдоль щелей PA0, PA132 и PA268. Крестиками и ромбами на этих рисунках показаны также найденные Хидалго-Гамесом (2005) средние по галактике IC 10 значения для ярких областей HII и слабых областей "диффузного ионизованного газа" (DIG), см. раздел "Обсуждение".

Оценки относительного содержания кислорода, азота и серы

Полученные спектры позволяют оценить относительное обилие кислорода в большом числе HII областей галактики, как ярких, так и слабых. Ранее такие оценки были сделаны для трех ярчайших областей HL111, HL45 и компактного сгустка HL106a внутри HL106 (Леке и др., 1979; Гарнетт, 1990; Ричер и др., 2001; Ли и др., 2003).

С этой целью мы использовали соотношения, найденные в работе Пилюгина, Туана (2005) по ревизованной этими авторами калибровочной зависимости содержания кислорода $12+\lg(\mathrm{O/H})$ от относительных интенсивностей наиболее ярких линий [OII] и [OIII]. Классический метод оценки по так называемому индикатору кислородного обилия R_{23}, предложенный Пейджелом и др. (1979) и широко используемый ранее, был модифицирован в серии работ Пилюгина (см. ссылки в статье Пилюгина, Туана, 2005) и базируется на двух параметрах: R_{23} и параметре возбуждения P. Относительное содержание кислорода определяется соотношением:

$$12+\lg(\mathrm{O/H}) = (R_{23}+106.4+106.8P-3.40P^2)/(17.72+6.60P+6.95P^2-0.302R_{23}),$$

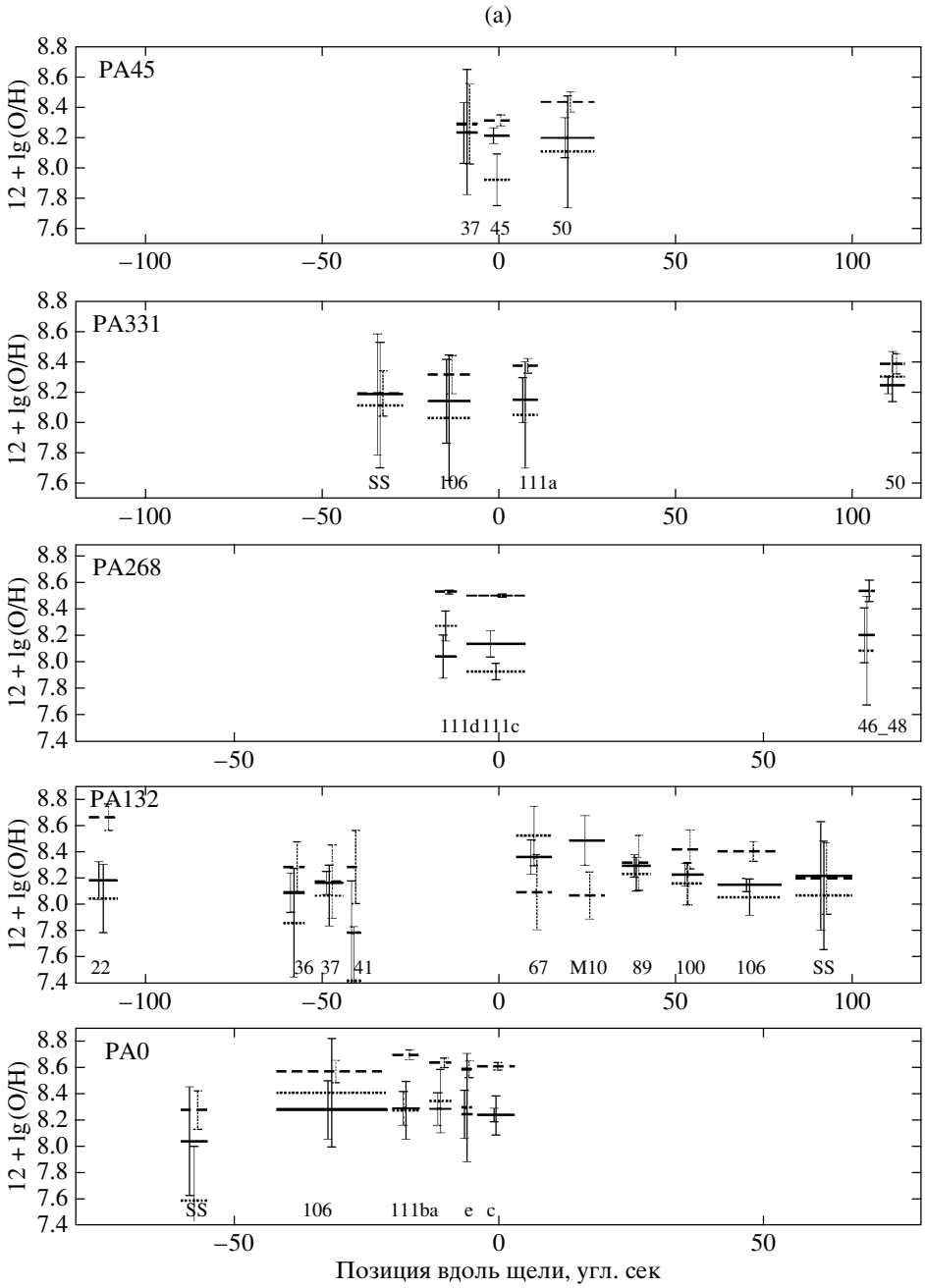

Рис. 5. Полученные из наших наблюдений распределения величин $12 + \lg(\mathrm{O/H})$ (а), $\lg(\mathrm{N}^+/\mathrm{O})$ (б) и $\lg(\mathrm{S}^+/\mathrm{O})$ (в) вдоль щели для пяти спектрограмм. На горизонтальной оси рисунков отмечены области HII. Значения кислородного обилия $12 + \lg(\mathrm{O/H})$ на рис. 5а, найденные методом Изотова и др. (2006), показаны сплошной линией, методом Пилюгина, Туана (2005) — пунктирной линией, методом, предложенным в работе Чарлота, Лонгетти (2001) — штриховой линией. Теми же линиями показаны соответствующие ошибки.

где $R_{23} = R_2 + R_3$,

$$P = R_3/(R_2 + R_3),$$

$$R_2 = (I[\mathrm{OII}]\lambda 3727 + \lambda 3729)/I(\mathrm{H}\beta),$$

$$R_3 = (I[\mathrm{OIII}]\lambda 4959 + \lambda 5007)/I(\mathrm{H}\beta).$$

Полученные из наших наблюдений распределения величин $12 + \lg(\mathrm{O/H})$ вдоль щели для пяти спектрограмм показаны на рис. 5а и приведены в табл. 4. На рисунке дана разметка щелей и отмечены области HII, для которых проведено

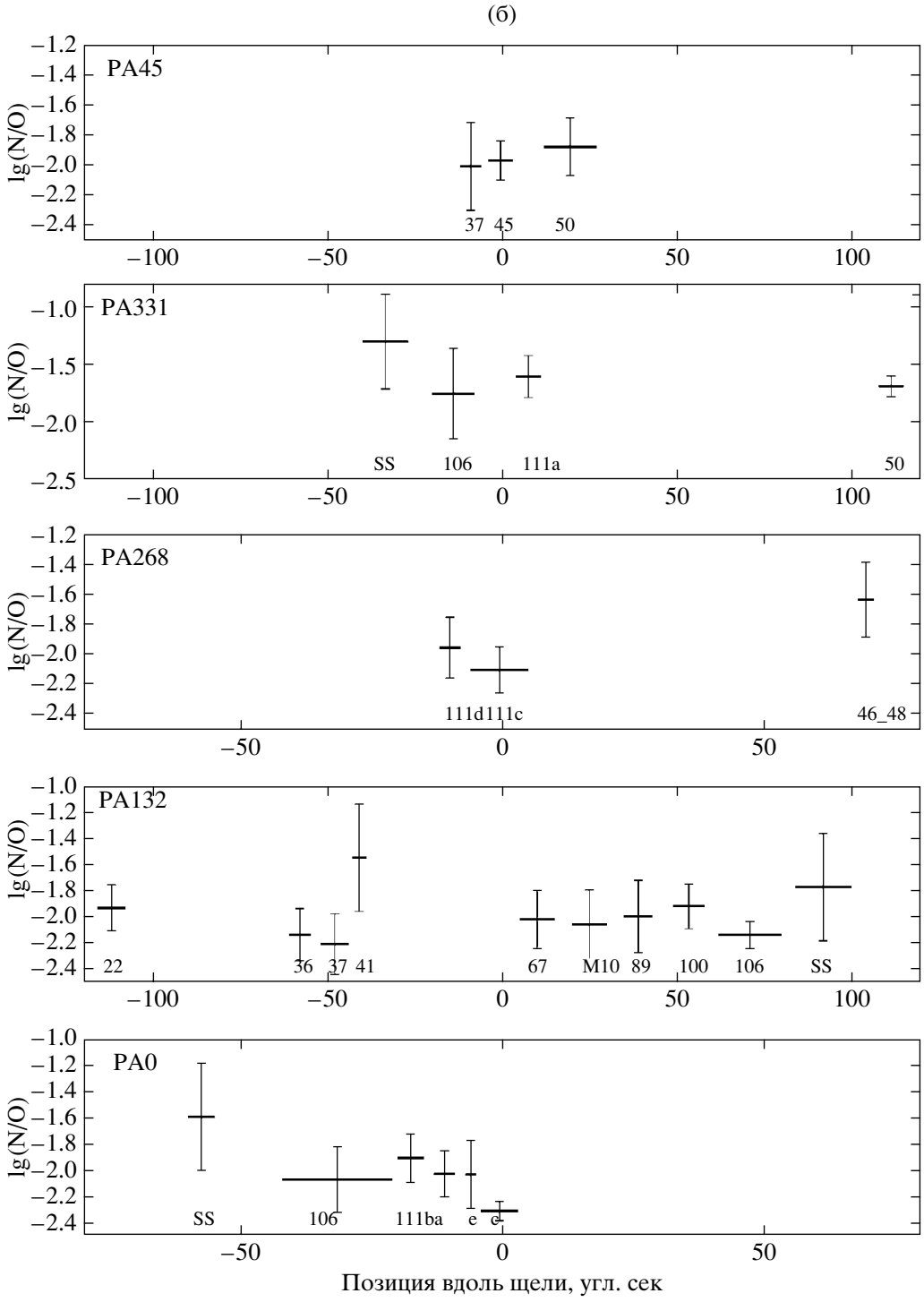

Рис. 5. (Продолжение)

усреднение потоков в линиях. Найденные для них средние значения кислородного обилия показаны горизонтальными отрезками. Здесь же приведены наши результаты оценки величины $12 + \lg(\mathrm{O/H})$ по методике других авторов, см. ниже.

Как отмечено в работе Пилюгина, Туана (2005), приведенное соотношение наиболее надежно для значений P в интервале от $\simeq 0.55$ до $\simeq 1$. Исключив точки, соответствующие $P < 0.55$, мы убедились, что в пределах ошибок это не меняет существенно полученные усредненные оценки содержания кислорода, но лишь несколько повышает точность измерений.

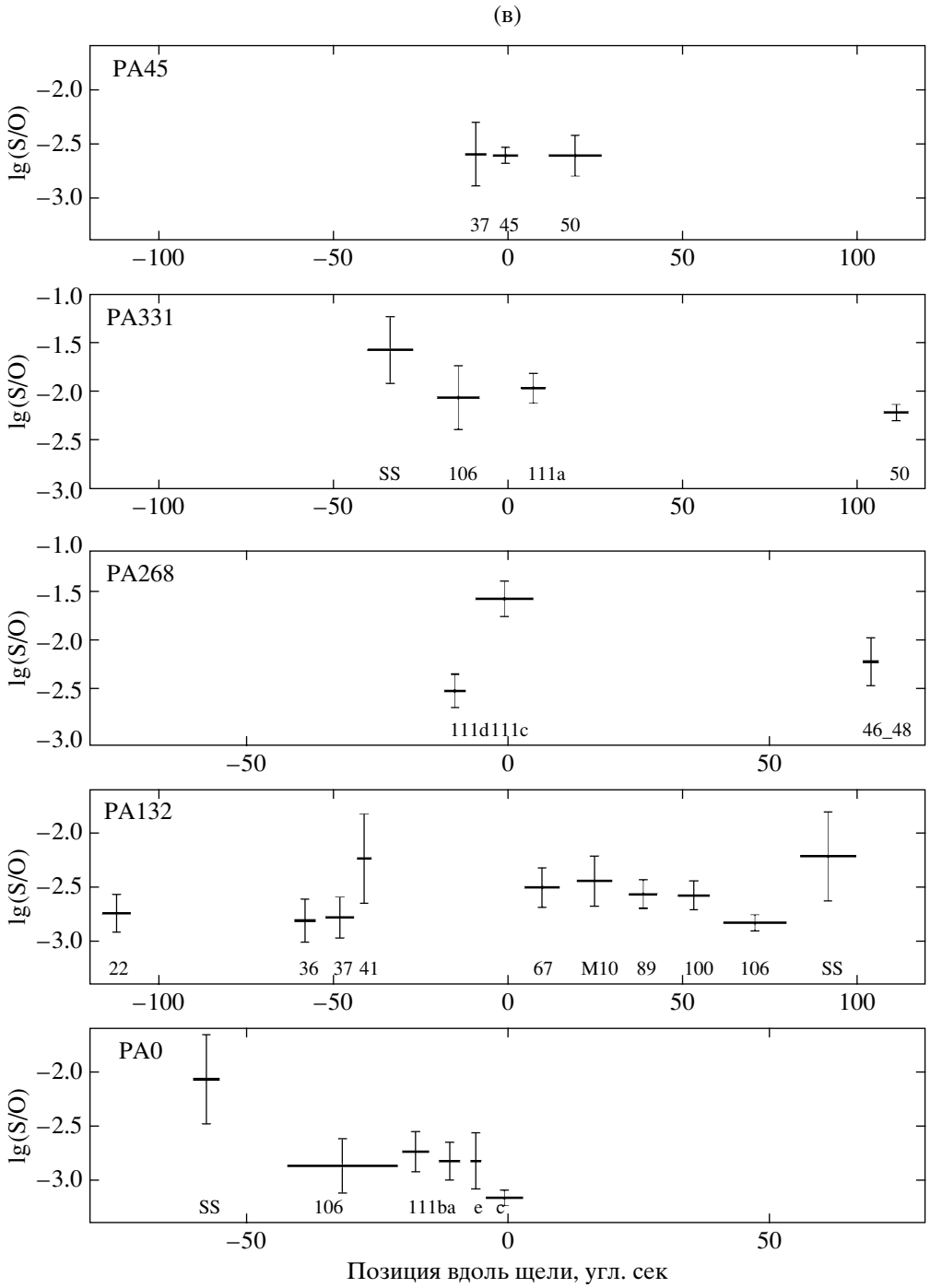

Рис. 5. (Окончание)

Для оценки относительного содержания азота и серы в разных областях HII мы использовали соотношения (6) и (8) из работы Изотова и др. (2006):

$$12+\lg(\mathrm{N}^+/\mathrm{H})=\lg\frac{\lambda6584+\lambda6548}{\mathrm{H}\beta}+$$
$$+6.234+\frac{0.950}{t}-0.42\cdot\lg t-$$
$$-0.027t+\lg(1+0.116x),$$

$$12+\lg(\mathrm{S}^+/\mathrm{H})=\lg\frac{\lambda6717+\lambda6731}{\mathrm{H}\beta}+$$
$$+5.439+\frac{0.929}{t}-$$
$$-0.28\cdot\lg t-0.018t+\lg(1+1.39x).$$

Таблица 2. Относительные интенсивности в точках пересечения щелевых спектрограмм

Спектрограмма	$\lg(I([\mathrm{OIII}]\lambda5007\ \text{Å})/I(\mathrm{H}\beta))$	$\lg(I([\mathrm{SII}]\lambda6717+6731\ \text{Å})/I(\mathrm{H}\alpha))$
1. Пересечение PA0, PA132, PA331		
PA0	0.32 ± 0.03	-0.86 ± 0.02
PA132	0.30 ± 0.03	-0.68 ± 0.04
PA331	0.31 ± 0.03	-0.84 ± 0.03
2. Пересечение PA0, PA268		
PA0	0.55 ± 0.03	-1.10 ± 0.04
PA268	0.55 ± 0.02	-1.25 ± 0.03
3. Пересечение PA268, PA331		
PA268	0.22 ± 0.04	-0.45 ± 0.03
PA331	0.18 ± 0.05	-0.47 ± 0.04
4. Пересечение PA132, PA268		
PA132	0.02 ± 0.04	-0.18 ± 0.08
PA268	0.13 ± 0.05	-0.33 ± 0.04
5. Пересечение PA45, PA331		
PA45	0.44 ± 0.11	-0.79 ± 0.04
PA331	0.48 ± 0.04	-0.85 ± 0.03
6. Пересечение PA45, PA132		
PA45	0.61 ± 0.21	-1.06 ± 0.11
PA132	0.48 ± 0.07	-0.81 ± 0.23

Здесь $t = 10^{-4}T_e(\mathrm{OIII})$, $x = 10^{-4}N_e t^{-0.5}$.

Оценка обилия серы фактически является оценкой обилия иона S^+, так как мы не принимали во внимание излучение иона S^{2+} в линии $[\mathrm{SIII}]\lambda6312$, которую удалось измерить только для области HL111c. Это же относится и к оценке обилия азота.

Для корректной оценки отношений N/O и S/O мы нашли также относительное содержание кислорода $12 + \lg(\mathrm{O/H})$ из соотношений (3) и (5) работы Изотова и др. (2006):

$$12 + \lg(\mathrm{O^+/H}) = \lg\frac{\lambda3727}{\mathrm{H}\beta} + 5.961 + \\ + \frac{1.676}{t} - 0.40\lg t - 0.034t + \lg(1 + 1.35x),$$

$$12 + \lg(\mathrm{O^{2+}/H}) = \lg\frac{\lambda4959 + \lambda5007}{\mathrm{H}\beta} + \\ + 6.200 + \frac{1.251}{t} - 0.55\lg t - 0.014t.$$

Характерная электронная плотность в областях ионизованного газа галактики, найденная нами по отношению интенсивностей линий [SII], меняется в пределах от 30 до 300–400 см^{-3} и эти изменения практически не влияют на оценки обилия.

Для всех областей HII была принята электронная температура $T_e(\mathrm{OIII}) = 11\,000$ K. Выбор этого значения основан на трех соображениях. Во-первых, оно близко к определенной нами температуре около 11 600 K по отношению интенсивностей линий кислорода для области HL111c, в которой наблюдалась линия $[\mathrm{OIII}]\lambda4363$Å. К сожалению, прямым методом мы определили электронную температуру только для этой самой яркой области, но и здесь оценка имеет низкую точность из-за слабости линии $[\mathrm{OIII}]\lambda4363$Å. Во-вторых, принятое значение лежит между оценками, найденными Леке и др. (1979) и Ли и др. (2003) для трех ярчайших областей HII в галактике. В-третьих, при данной электронной температуре удается добиться наилучшего согласия значений обилия кислорода, полученных двумя указанными выше способами. Значение температуры в области излучения [OII] было найдено из соотношения (Изотов и др., 2006):

$$t(\mathrm{OII}) = -0.744 + t(\mathrm{OIII})(2.338 - 0.610t(\mathrm{OIII})).$$

Таблица 3. Относительные интенсивности линий

Область	Щель/позиция	$\frac{I([\mathrm{OIII}]5007)}{I(\mathrm{H}\beta)}$	$\frac{I([\mathrm{SII}]6717+6731)}{I(\mathrm{H}\alpha)}$	$\frac{I([\mathrm{NII}]6583)}{I(\mathrm{H}\alpha)}$	$\frac{I([\mathrm{SII}]6717)}{I([\mathrm{SII}]6731)}$	$\frac{I([\mathrm{OIII}]3727+29)}{I([\mathrm{OIII}]5007)}$
HL111a	PA0 [−13, −9]	1.90 ± 0.03	0.178 ± 0.002	0.134 ± 0.003	1.39 ± 0.03	2.64 ± 0.33
	PA331 [4, 11]	2.09 ± 0.12	0.201 ± 0.003	0.099 ± 0.003	1.10 ± 0.01	1.44 ± 0.22
HL111b	PA0 [−20, −15]	1.51 ± 0.05	0.183 ± 0.03	0.148 ± 0.003	1.47 ± 0.05	3.63 ± 0.41
HL111c	PA0 [−4, 3]	3.52 ± 0.02	0.081 ± 0.001	0.069 ± 0.001	1.41 ± 0.03	0.80 ± 0.10
	PA268 [−6, 5]	3.47 ± 0.01	0.063 ± 0.001	0.047 ± 0.001	1.40 ± 0.01	0.50 ± 0.02
HL111d	PA268 [−12, −8]	2.95 ± 0.01	0.137 ± 0.001	0.097 ± 0.001	1.41 ± 0.02	1.16 ± 0.08
HL111e	PA0 [−7, −5]	2.44 ± 0.06	0.138 ± 0.002	0.101 ± 0.002	1.50 ± 0.05	1.62 ± 0.41
HL106	PA0 [−42, −21]	2.89 ± 0.07	0.161 ± 0.004	0.117 ± 0.004	1.46 ± 0.08	1.40 ± 0.41
	PA132 [62, 80]	2.31 ± 0.03	0.191 ± 0.007	0.102 ± 0.006	1.26 ± 0.09	1.23 ± 0.08
	PA331 [−20, −8]	2.42 ± 0.11	0.144 ± 0.002	0.066 ± 0.02	1.02 ± 0.01	1.11 ± 0.41
SS	PA0 [−60, −55]	0.75 ± 0.10	0.713 ± 0.017	0.247 ± 0.013	1.58 ± 0.08	4.24 ± 0.44
	PA132 [84, 100]	1.33 ± 0.13	0.745 ± 0.100	0.230 ± 0.056	1.24 ± 0.26	3.49 ± 0.42
	PA331 [−40, −27]	1.87 ± 0.10	0.625 ± 0.006	0.207 ± 0.04	1.63 ± 0.09	1.99 ± 0.43
HL37	PA45 [−12, −6]	3.34 ± 0.24	0.073 ± 0.002	0.033 ± 0.012	1.55 ± 0.05	0.87 ± 0.26
	PA132 [−52, −44]	2.85 ± 0.05	0.180 ± 0.030	0.064 ± 0.024	0.99 ± 0.22	0.89 ± 0.13
HL45	PA45 [−4, 3]	4.86 ± 0.09	0.079 ± 0.005	0.045 ± 0.002	1.12 ± 0.03	0.22 ± 0.05
HL50	PA45 [12, 27]	3.44 ± 0.08	0.073 ± 0.005	0.045 ± 0.002	1.35 ± 0.05	0.69 ± 0.14
	PA331 [108, 115]	3.05 ± 0.08	0.162 ± 0.009	0.086 ± 0.002	1.49 ± 0.14	1.11 ± 0.10
HL100	PA132 [49, 58]	1.65 ± 0.02	0.364 ± 0.020	0.179 ± 0.023	1.24 ± 0.11	2.69 ± 0.23
HL89	PA132 [35, 43]	1.32 ± 0.2	0.446 ± 0.029	0.168 ± 0.039	1.19 ± 0.12	4.39 ± 0.32
M10	PA132 [20, 30]	1.49 ± 0.06	0.753 ± 0.065	0.165 ± 0.026	1.03 ± 0.13	6.41 ± 0.53
HL67	PA132 [5, 15]	1.61 ± 0.06	0.578 ± 0.076	0.142 ± 0.044	0.89 ± 0.15	4.13 ± 0.48
HL41	PA132 [−43, −39]	1.58 ± 0.05	0.254 ± 0.011	0.126 ± 0.013	1.07 ± 0.09	0.43 ± 0.41
HL36	PA132 [−61, −55]	2.86 ± 0.03	0.137 ± 0.019	0.065 ± 0.007	0.94 ± 0.22	0.60 ± 0.17
HL22	PA132 [−116, −108]	1.53 ± 0.03	0.158 ± 0.011	0.126 ± 0.007	1.17 ± 0.13	2.60 ± 0.37
HL46,48	PA268 [68, 71]	1.49 ± 0.08	0.320 ± 0.011	0.200 ± 0.010	1.66 ± 0.09	2.94 ± 0.43

Такую же температуру мы приняли для области излучения линий [SII] и [NII].

Полученные результаты собраны в табл. 4. Здесь даны соответственно по столбцам: название области HII по каталогу Ходжа и Ли (1990), использованная для оценки спектрограмма и позиции на ней, найденные средние значения относительного содержания кислорода, а также ионов азота и серы. Оценки обилия кислорода по формуле (24) из работы Пилюгина, Туана (2005) обозначены в таблице индексом (1), по формулам (3), (5) из работы Изотова и др. (2006) — индексом (2).

Мы не усредняли найденные по разным спектрам обилия для одной и той же области HII, поскольку они соответствуют разным позициям щели на туманности и могут различаться из-за разных физических условий: плотности и скважности среды, локализации источника радиации и т.п.

В нижних строках табл. 4 даны обилия для двух областей № 1 и № 2 (см. рис. 1 в работе Леке и др., 1979), которые соответствуют объектам HL111 и HL45, полученные нами из приведенных выше соотношений по относительным интенсивностям линий, измеренным Леке и др. (1979). В обоих случаях направление щели в этой работе было восток-запад; размер, по которому усреднялись относительные обилия, соответствовал $3''.8 \times 12''.4$. Локализация спектрограмм на упомянутом рисунке

Таблица 4. Относительные обилия O, N^+, S^+

Область	Щель/позиция	$12+\lg(O/H)$ (1)	$12+\lg(O/H)$ (2)	$12+\lg(N^+/H)$	$12+\lg(S^+/H)$
HL111a	PA0 [−13, −9]	8.34 ± 0.24	8.28 ± 0.12	6.26 ± 0.13	5.46 ± 0.12
	PA331 [4, 11]	8.05 ± 0.34	8.15 ± 0.15	6.54 ± 0.16	6.00 ± 0.16
HL111b	PA0 [−20, −15]	8.27 ± 0.22	8.29 ± 0.13	6.38 ± 0.13	5.55 ± 0.13
HL111c	PA0 [−4, 3]	8.24 ± 0.15	8.24 ± 0.10	5.92 ± 0.10	5.07 ± 0.10
	PA268 [−6, 5]	7.94 ± 0.10	8.15 ± 0.10	6.05 ± 0.12	6.56 ± 0.22
HL111d	PA268 [−12, −8]	8.28 ± 0.11	8.05 ± 0.16	6.10 ± 0.18	5.33 ± 0.19
HL111e	PA0 [4−7, −5]	8.29 ± 0.38	8.24 ± 0.18	6.21 ± 0.19	5.42 ± 0.18
HL106	PA0 [−42, −21]	8.41 ± 0.42	8.28 ± 0.22	6.21 ± 0.22	5.41 ± 0.22
	PA132 [62, 80]	8.06 ± 0.14	8.15 ± 0.10	6.01 ± 0.10	5.32 ± 0.10
	PA331 [−20, −8]	8.03 ± 0.42	8.14 ± 0.27	6.39 ± 0.27	5.88 ± 0.28
SS	PA0 [−60, −55]	7.59 ± 0.42	8.04 ± 0.43	6.44 ± 0.41	5.97 ± 0.43
	PA132 [84, 100]	8.07 ± 0.18	8.22 ± 0.21	6.45 ± 0.38	6.00 ± 0.41
	PA331 [−40, −27]	8.12 ± 0.42	8.19 ± 0.39	6.88 ± 0.39	6.50 ± 0.39
HL37	PA45 [−12, −6]	8.23 ± 0.42	8.23 ± 0.20	6.23 ± 0.24	5.63 ± 0.21
	PA132 [−52, −44]	8.07 ± 0.23	8.17 ± 0.10	5.96 ± 0.22	5.39 ± 0.17
HL45	PA45 [−4, 3]	7.92 ± 0.17	8.21 ± 0.10	6.24 ± 0.12	5.60 ± 0.10
HL50	PA45 [12, 27]	8.10 ± 0.36	8.20 ± 0.13	6.32 ± 0.14	5.58 ± 0.13
	PA331 [108, 115]	8.30 ± 0.16	8.25 ± 0.10	6.56 ± 0.10	5.80 ± 0.10
HL100	PA132 [49, 58]	8.16 ± 0.16	8.23 ± 0.10	6.31 ± 0.15	5.65 ± 0.10
HL89	PA132 [35, 43]	8.23 ± 0.13	8.29 ± 0.10	6.30 ± 0.27	5.72 ± 0.10
M10	PA132 [20, 30]	8.74 ± 0.36	8.49 ± 0.19	6.43 ± 0.29	6.04 ± 0.20
HL67	PA132 [5, 15]	8.52 ± 0.23	8.36 ± 0.13	6.34 ± 0.20	5.86 ± 0.17
HL41	PA132 [−43, −39]	7.73 ± 0.42	7.79 ± 0.39	6.24 ± 0.39	5.55 ± 0.39
HL36	PA132 [−61, −55]	7.86 ± 0.42	8.09 ± 0.15	5.96 ± 0.19	5.28 ± 0.19
HL22	PA132 [−116, −108]	8.28 ± 0.12	8.18 ± 0.14	6.25 ± 0.16	5.44 ± 0.16
HL46,48	PA268 [68, 71]	8.10 ± 0.40	8.21 ± 0.21	6.58 ± 0.23	5.85 ± 0.21
По наблюдениям Леке и др. (1979)					
HL111		7.74	8.17	6.23	5.48
HL45		7.92	8.31	6.24	5.40

не показана, поэтому возможно лишь ориентировочное сравнение наших измерений с данными этой работы.

ОБСУЖДЕНИЕ

Межзвездное поглощение

Выявленные в настоящей работе вариации избытка цвета для разных областей галактики в пределах $0\overset{m}{.}8-1\overset{m}{.}1$ значительно меньше различия ранних оценок разных авторов от $E(B-V)=0\overset{m}{.}47$ до $E(B-V)=2\overset{m}{.}0$ (см. Сакаи и др., 1999; Демерс и др., 2004 и ссылки в этих работах). В трех ярчайших HII областях Ли и др. (2003) нашли сходное с нашей оценкой значение $E(B-V)=0\overset{m}{.}79-1\overset{m}{.}2$. Наблюдаемые нами вариации $E(B-V)$ естественно объясняются двумя факторами. Во-первых, возможно локальное более высокое поглощение,

поскольку ярчайшая область звездообразования расположена в направлении самого плотного облака нейтрального водорода и молекулярного газа в галактике и может быть частично погружена в него. Аналогичный эффект наблюдался и другими авторами. В частности, в работе Бориссовой и др. (2000) оценка поглощения по отношению интенсивностей линий Brγ и Hα в двух самых ярких туманностях HL111 и HL45 значительно превышает эту величину, найденную по звездам. Во-вторых, возможно локальное более низкое поглощение, если звездный ветер и вспышки СН в молодой группировке выметают окружающий плотный газ. В частности, в центральной области звездообразования Вакка и др. (2007) нашли по массивным голубым звездам $E(B-V) = 0\overset{m}{.}6$ и заключили, что молодые звезды последнего эпизода звездообразования находятся на передней границе упомянутого выше плотного облака впереди населения старых звезд.

Представленные в настоящей работе оценки **относительного содержания кислорода, азота и серы** в IC 10 являются сегодня наиболее детальными. Ранее Леке и др. (1979) нашли $12 + \lg(\mathrm{O/H}) = 8.17$ для HL111 и $12 + \lg(\mathrm{O/H}) = 8.45$ для HL45 (в нижних строках табл. 4 даны наши оценки по измерениям Леке и др., 1979); согласно Гарнетт (1990), $12 + \lg(\mathrm{O/H}) = 8.19$ для HL45. Согласно Ричеру и др. (2001), в самой яркой туманности HL111c $12 + \lg(\mathrm{O/H}) = 8.23 \pm 0.09$. Для ярчайших объектов с измеренной линией [OIII]λ4363 Å в работе Ли и др. (2003) найдено соответственно $12 + \lg(O/H) = 8.32 \pm 0.14$ в HL111c, $12 + \lg(\mathrm{O/H}) = 8.05 \pm 0.18$ в HL111e, а также $12 + \lg(\mathrm{O/H}) \geq 7.96$ в HL111b и $12 + \lg(\mathrm{O/H}) \geq 7.60$ в сгустке HL106a внутри HL106 (в двух последних объектах оценен лишь верхний предел температуры). Как видим, все перечисленные результаты хорошо согласуются с нашими наблюдениями упомянутых ярких туманностей.

Как показали наши измерения, относительные интенсивности кислородных линий и соответственно найденные значения относительного содержания кислорода меняются как от точки к точке, так и от области к области в широких пределах от 7.6 до 8.5. Чтобы понять, связано ли это с ошибками наблюдений или с реальными различиями областей HII, мы привели выше на рис. 4а,б значения относительных интенсивностей, найденные соответственно для ярких и для слабых объектов. Как следует из рисунка, ошибки измерений, разумеется, несколько больше для слабых областей, чем для ярких, однако разброс значений в слабых областях не превышает существенно разброс для ярких объектов. Поэтому вариации обилия кислорода в галактике, по всей вероятности, реальны. При этом наблюдается систематическая разница относительных интенсивностей в ярких и слабых областях, см. ниже.

Среднее по всем исследованным в нашей работе областям галактики значение относительного обилия кислорода составляет $12 + \lg(\mathrm{O/H}) = 8.17 \pm 0.35$, что соответствует металличности $Z = 0.18 \pm 0.14 Z_{\odot}$.

Диагностические диаграммы относительных интенсивностей линий

Средние по галактике и по четырем ее полям относительные интенсивности диагностических линий в ярких туманностях и в слабых областях диффузного ионизованного газа (DIG) были получены ранее Хидалго-Гамезом (2005) по девяти сложенным в одну широкую полосу спектрограммам. Согласно этой работе, усредненные по галактике относительные интенсивности равны

$$I([\mathrm{OIII}]5007\text{Å})/I(\mathrm{H}\beta) = 1.86,$$

$$I([\mathrm{NII}]\lambda6583\text{Å})/I(\mathrm{H}\alpha) = 0.16,$$

и

$$I([\mathrm{SII}]\lambda6717\text{Å})/I(\mathrm{H}\alpha) = 0.28.$$

Средние по ярким туманностям значения составляют:

$$I([\mathrm{OIII}]\lambda5007\text{Å})/I(\mathrm{H}\beta) = 2.05,$$

$$I([\mathrm{NII}]\lambda6583\text{Å})/I(\mathrm{H}\alpha) = 0.12,$$

$$I([\mathrm{SII}]\lambda6717\text{Å})/I(\mathrm{H}\alpha) = 0.19;$$

средние по слабому диффузному ионизованному газу (DIG) —

$$I([\mathrm{OIII}]\lambda5007\text{Å})/I(\mathrm{H}\beta) = 1.66,$$

$$I([\mathrm{NII}]\lambda6583\text{Å})/I(\mathrm{H}\alpha) = 0.19,$$

$$I([\mathrm{SII}]\lambda6717\text{Å})/I(\mathrm{H}\alpha) = 0.31.$$

Результаты наших измерений для индивидуальных областей HII на представленных выше диагностических диаграммах хорошо согласуются с этими средними значениями, учитывая ошибки наблюдений.

Как следует из рис. 4а,б, подобно другим детально исследованным Irr галактикам, диагностические диаграммы несколько различаются для ярких и слабых областей IC 10: относительные интенсивности линий [SII] заметно выше в слабых областях, линий [NII] — также несколько выше, при этом $I([\mathrm{OIII}]\lambda5007\text{ Å})/I(\mathrm{H}\beta)$ здесь ослабевает. Сходная картина наблюдается и в спиральных

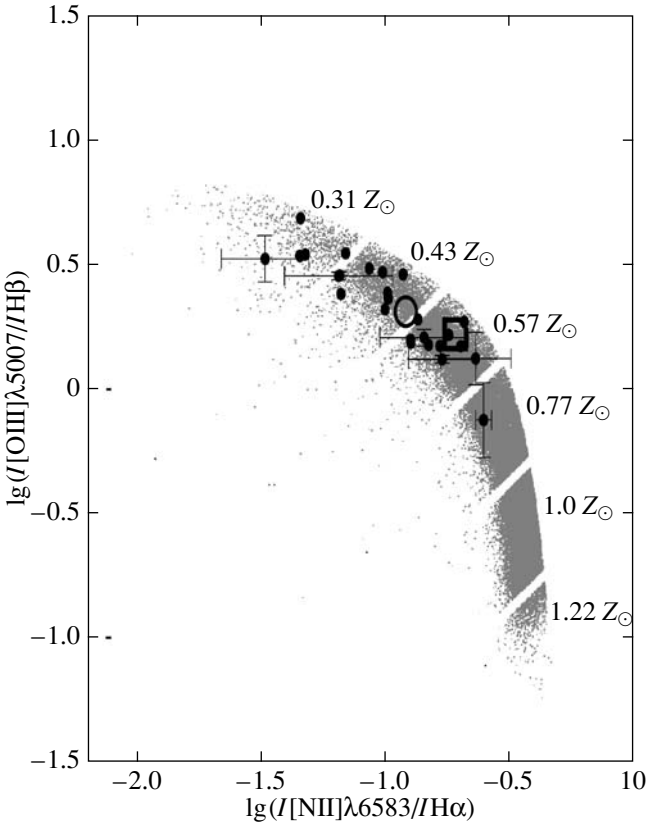

Рис. 6. Сопоставление наших результатов с данными работ Сид Фернандеса и др. (2007) и Азари и др. (2007). Справа от полосы локализации 85 000 starburst-галактик обозначена средняя металличность в каждом из секторов. Кружком и квадратом показаны найденные Хидалго-Гамес (2005) средние по IC 10 значения для ярких областей HII и для "диффузного ионизованного газа" (DIG).

галактиках, например, в M31 (см. Галарза и др., 1999). Яркие компактные области HII характеризуются более низким значением $I([\mathrm{SII}])/I(\mathrm{H}\alpha)$, чем слабые диффузные и кольцевые туманности, и тем более, чем DIG. Отмеченные различия объясняются уменьшением ионизационного параметра при переходе от компактных к слабым диффузным областям и предсказываются фотоионизационными моделями. К такому же эффекту усиления относительной интенсивности $I([\mathrm{SII}])/I(\mathrm{H}\alpha)$ приводит и вклад излучения газа за фронтом ударных волн, инициированных вспышками сверхновых и звездным ветром. О заметной роли ударных волн в IC 10 свидетельствует тонковолокнистая структура всей области $\mathrm{H}\alpha$ — эмиссии в галактике.

Следует отметить, что построенные диаграммы диагностических линий плохо согласуются с современными фотоионизационными моделями для найденной выше по ярким линиям кислорода металличности $Z = 0.2Z_\odot$.

В частности, наблюдаемые диагностические диаграммы согласуются с семействами теоретических диагностических кривых (Допита и др., 2006) только при металличности от $Z = 0.4Z_\odot$ до $Z = (1{-}2)Z_\odot$.

На рис. 6 наши данные сопоставлены с результатами работ Сид Фернандеса и др. (2007) и Азари и др. (2007), в которых суммированы оценки металличности газа для $\simeq 85\,000$ starburst-галактик. На диаграмме $I([\mathrm{OIII}]\lambda 5007\text{Å})/I(\mathrm{H}\beta)$ в зависимости от $I([\mathrm{NII}]\lambda 6583\text{Å})/I(\mathrm{H}\alpha)$ авторы этих работ приводят число галактик, попавших в каждый сектор полосы локализации галактик, и соответствующую сектору среднюю металличность. Как видим, области HII в IC 10 очень хорошо ложатся на полосу локализации галактик, но попадают в диапазон металличностей от $Z = 0.3Z_\odot$ до $Z = 0.6Z_\odot$. Одна область, а именно Синхротронная Сверхоболочка, попадает в область $Z = 0.8Z_\odot$; этот объект обсуждается ниже. Отметим, впрочем, что Азари и др. (2007) зафиксировали систематический сдвиг на 0.2 dex между своими оценками металличности и оценками Пилюгина и Туана (2005) и Изотова и др. (2006) для 177 "общих" объектов, сделанными из тех соотношений, которыми мы здесь пользовались. При этом сдвиг оказывается тем больше, чем

меньше металличность. По этой причине Азари и др. принимают для сектора А металличность $Z = 0.2Z_\odot$ вместо $Z = 0.3Z_\odot$ и соответственно значение $Z = 0.2Z_\odot$ является нижней границей интервала, в который попадают исследованные нами объекты в IC 10.

Интересно также сравнить наблюдаемые диагностические диаграммы с теоретическими фотоионизационными моделями Чарлота и Лонгетти (2001), поскольку эти авторы по отдельности учитывают изменения каждого из параметров, определяющих модельные расчеты, таких как возраст скопления, начальная функция масс, ионизационный параметр, плотность среды, металличность.

Сравнение диагностических диаграмм для галактики IC 10 с построенными Чарлотом, Лонгетти (2001) распределениями величин $I([\mathrm{OIII}])/I(\mathrm{H}\beta)$ в зависимости от $I([\mathrm{OII}])/I([\mathrm{OIII}])$, $I([\mathrm{SII}])/I(\mathrm{H}\alpha)$ и $I([\mathrm{NII}])/I([\mathrm{SII}])$ для галактик разного типа и областей HII показало, что наблюдательные данные согласуются очень хорошо. На рис. 7 наши наблюдения сопоставлены с расчетными моделями Чарлота, Лонгетти (2001) для разной металличности и для разного эффективного ионизационного параметра. Большими квадратом, кружком и треугольником на наших диагностических диаграммах (левые панели) отмечены области пониженной ($Z = 0.2Z_\odot$), солнечной ($Z = Z_\odot$) и повышенной ($Z = 2Z_\odot$) металличности соответственно согласно расчетам Чарлота, Лонгетти (2001) (см рис. 1, 2 и 3 этой работы). На правых панелях рис. 7 большими квадратом, кружком и треугольником показаны три значения эффективного ионизационного параметра $\lg U_0$: -3.0, -2.5 и -2.0 соответственно по расчетам Чарлота, Лонгетти (2001). Как видим, в полном согласии с модельными расчетами для оценки металличности газовой среды галактики наиболее перспективны диагностические диаграммы $I([\mathrm{OIII}]\lambda 5007\text{Å})/I(\mathrm{H}\beta)$ в зависимости от $I([\mathrm{NII}]\lambda 6583\text{Å})/I([\mathrm{SII}]\lambda 6717 + 6731\text{Å})$. При этом диагностические диаграммы для областей HII галактики IC 10 соответствуют вариациям металличности в пределах $Z = (0.2{-}1)Z_\odot$. Зависимости $I([\mathrm{OIII}]\lambda 5007\text{Å})/I(\mathrm{H}\beta)$ от $I([\mathrm{OII}])/I([\mathrm{OIII}])$ и $I([\mathrm{OIII}]\lambda 5007\text{Å})/I(\mathrm{H}\beta)$ от $I([\mathrm{SII}]\lambda 6717 + +6731\text{Å})/I(\mathrm{H}\alpha)$ хорошо объясняются вариациями параметра ионизации.

Отличия найденной в нашей работе металличности индивидуальных областей HII в галактике от металличности, определяемой из сопоставления диагностических диаграмм с теоретическими фотоионизационными моделями, может объясняться рядом факторов. Прежде всего, фотоионизационные модели рассчитываются для богатых звездных скоплений. В частности, в работе Допиты и др. (2006) принята масса скопления $M \geq 10^3 M_\odot$, IMF Миллера и Скало от 1 до $100M_\odot$, в то время как звездные скопления в галактике IC 10 сравнительно небогатые (см. Хантер, 2001).

Кроме того, в IC 10 может быть значительным вклад излучения газа за фронтом ударных волн, о чем свидетельствует тонковолокнистая структура всей области звездообразования в галактике. Собственно говоря, термин "диффузный ионизованный газ" (DIG) может быть применен к галактике IC 10 лишь условно, поскольку области слабой эмиссии отнюдь не являются диффузными, а характеризуются тонковолокнистой оболочечной и/или дуговой структурой. Поэтому самые слабые области внутри ряда оболочек, которые выглядят диффузными, скорее всего представляют переднюю или заднюю стороны оболочек.

Синхротронная Сверхоболочка в IC 10 является уникальным объектом и требует более подробного обсуждения. Согласно работам Лозинской, Моисеева (2007) и Лозинской и др. (2008), изображение в линиях [SII] лучше, чем в Hα, выявляет оптическую оболочку, которая отождествляется с Синхротронной Сверхоболочкой. Найденная в этих работах скорость разлета ярких сгустков и волокон оптической оболочки 50–80 км/с подтвердила оценку Рамсея и др. (2006); масса газа составляет $M \simeq 4 \times 10^5 M_\odot$, кинетическая энергия – $E_{\mathrm{kin}} \simeq (1 - 3) \times 10^{52}$ эрг. Такая энергия соответствует вспышке десятка сверхновых плюс звездный ветер их родительской ассоциации, как предполагалось ранее, или вспышке Гиперновой, как предложено Лозинской и Моисеевым (2007). Кинематический возраст Сверхоболочки $t \simeq (3{-}7) \times \times 10^5$ лет является сильным аргументом в пользу Гиперновой, поскольку для вспышки десятка сверхновых в локальной области галактики требуется более $t \simeq 10^7$ лет.

Согласно рис. 1, Синхротронной Сверхоболочке соответствует область от $85''$ до $120''$ на спектрограмме PA132, область от $-60''$ до $-25''$ на спектрограмме PA331 и область от $-50''$ до $-80''$ на спектрограмме PA0 (последняя проходит по самому краю Сверхоболочки).

Как показали наши измерения, относительная интенсивность $I([\mathrm{SII}]\lambda 6717 + 6731\text{Å})/I(\mathrm{H}\alpha)$ в области Синхротронной Сверхоболочки достигает значений 0.7–0.75, что несомненно свидетельствует об излучении газа за фронтом ударной волны (Допита, Сузерланд, 1995, 1996). О том же говорят более высокие, чем в близлежащей яркой

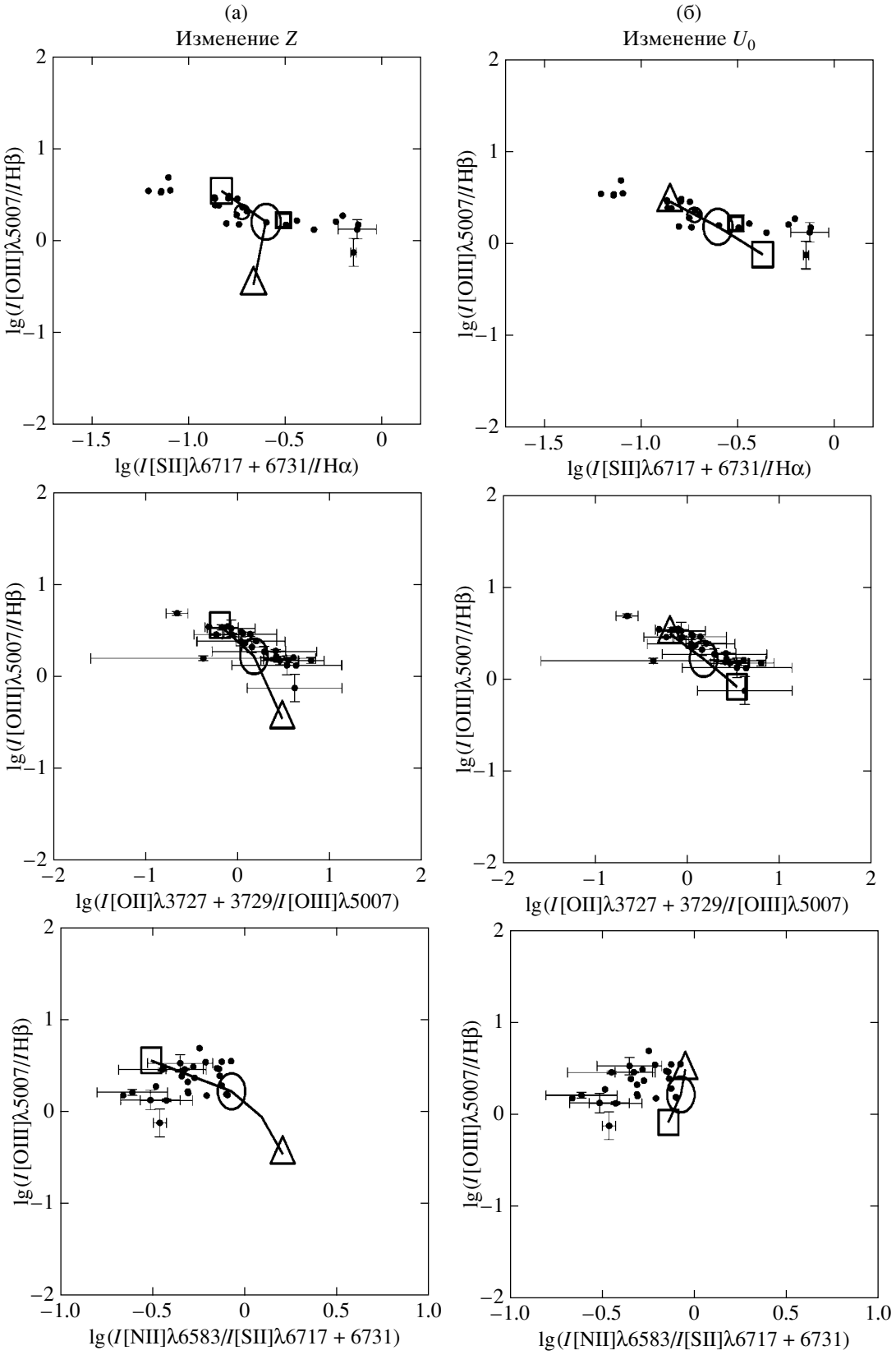

Рис. 7. Сопоставление диагностических диаграмм, построенных для галактики IC 10, с модельными расчетами Чарлота, Лонгетти (2001). Большими квадратами, кружками и треугольниками на рис. (а) отмечены области пониженной ($Z = 0.2Z_\odot$), солнечной ($Z = Z_\odot$) и повышенной ($Z = 2Z_\odot$) металличности согласно расчетам; на рис. (б) теми же значками показаны расчетные значения эффективного ионизационного параметра $\lg U_0 - 3.0$, -2.5 и -2.0 соответственно.

области HL106, значения $I([\mathrm{NII}]\lambda6583\text{Å})/I(\mathrm{H}\alpha) \simeq$ $\simeq 0.25$ и $I([\mathrm{OII}]\lambda3727+3729\text{Å})/I([\mathrm{OIII}]\lambda5007\text{Å}) \simeq$ $\simeq 2$–4, и более низкая относительная интенсивность $I([\mathrm{OIII}]\lambda5007\text{Å})/I(\mathrm{H}\beta)$.

Соответственно на представленных диагностических диаграммах область Синхротронной Сверхоболочки также отличается от областей HII более низким отношением $I([\mathrm{OIII}]\lambda5007\text{Å})/I(\mathrm{H}\beta)$ и высокими $I([\mathrm{SII}]\lambda6717+6731\text{Å})/I(\mathrm{H}\alpha)$, $I([\mathrm{NII}]\lambda6583\text{Å})/I(\mathrm{H}\alpha)$, $I([\mathrm{OII}]\lambda3727+$ $+3729\text{Å})/I([\mathrm{OIII}]\lambda5007\text{Å})$, что свидетельствует о преобладании ударного возбуждения и типично для старых остатков вспышек сверхновых.

В работе Лозинской, Моисеева (2007) по интенсивности линий [SII] ($\lambda6717/6731$Å) найдено среднее значение $n_e \simeq 20$–30 см$^{-3}$ для более яркой северной части Сверхоболочки (область $90''$–$105''$ на PA132), где ошибки сравнительно невелики. Для области $-50''$–$60''$ на спектрограмме PA0 мы находим сходное значение средней плотности $n_e \simeq$ $\simeq 30$–40 см$^{-3}$. В южной слабой части Сверхоболочки по спектрограмме PA132 можно выделить отдельные сгустки, в которых плотность достигает $n_e \simeq 200$–300 см$^{-3}$, но точность этих оценок мала. Плотность газа севернее Синхротронной Сверхоболочки (позиции $80''$–$90''$ на PA132) соответствует $n_e \simeq 200$ см$^{-3}$.

Оценка обилия кислорода в области Синхротронной Сверхоболочки неоднозначна. Вообще говоря, современные модели спектра свечения газа за фронтом ударной волны, разработанные Алленом и соавторами (2008), позволяют определить содержание тяжелых элементов, в частности, кислорода, по имеющимся диагностическим относительным интенсивностям линий, зная невозмущенную плотность окружающего газа и скорость ударной волны. Однако в нашем случае задача усложняется наличием в центральной области Синхротронной Сверхоболочки звезды WR M17, ионизующая радиация которой может оказаться существенной или даже преобладающей в близких окрестностях. С другой стороны, мы не можем корректно использовать методику, примененную выше к областям HII, не учитывая излучение газа за фронтом ударной волны.

Аккуратный расчет, учитывающий оба механизма излучения, выходит за рамки настоящей работы. Здесь мы формально оценим содержание кислорода в Синхротронной Сверхоболочке независимо двумя методами, отдавая себе отчет в некорректности обоих.

В модели области HII выше найдено $12+$ $+\lg(\mathrm{O/H}) = 8.07 \pm 0.18$ по спектрограмме PA132, 7.59 ± 0.42 по PA0 и 8.12 ± 0.42 по PA331 по методике Пилюгина, Туана (2005) или соответственно 8.22 ± 0.21 по спектрограмме PA132, 8.04 ± 0.43 по PA0 и 8.19 ± 0.39 по PA331 по методике Изотова и др. (2006), см. табл. 4. С учетом того, что измерения сделаны для трех разных областей очень слабого протяженного объекта, эти независимые оценки содержания кислорода хорошо согласуются.

Детальное исследование кинематики Синхротронной Сверхоболочки (Лозинская и др., 2008) уверенно выявило слабые крылья линии Hα в интервале скоростей от -200 км/с до -450 км/с. Эти высокоскоростные детали линии соответствуют скорости ударной волны, инициированной вспышкой Гиперновой, около 100–200 км/с. Сравнение с моделями свечения газа за фронтом ударной волны (Аллен и др., 2008), распространяющейся с такой скоростью, дает наилучшее согласие при обилии $12+\lg(\mathrm{O/H}) \simeq 8.15$ для моделей чисто ударного возбуждения или $12+\lg(\mathrm{O/H}) \simeq 8.35$ для моделей, учитывающих предионизацию газа ударной волной.

ЗАКЛЮЧЕНИЕ

Представлены результаты оценки относительного содержания кислорода, а также ионов N^+ и S^+ в карликовой Irr галактике IC 10 по пяти спектрограммам, полученным с прибором SCORPIO и щелевым спектрографом 6-м телескопа САО РАН. Наши оценки для индивидуальных областей HII и Синхротронной Свехоболочки являются сегодня наиболее детальными, прежние были сделаны лишь для трех ярчайших HII областей или давали среднее значение для большого сектора галактики.

По нашим измерениям относительные обилия O, N^+, S^+ в индивидуальных областях HII галактики IC 10 заключены в следующих пределах: $12+\lg(\mathrm{O/H}) = 7.59$–$8.52$, $12+\lg(\mathrm{N}^+/\mathrm{H}) =$ $= 5.92$–6.58 и $12+\lg(\mathrm{S}^+/\mathrm{H}) = 5.00$–$6.00$. Средняя металличность газовой среды галактики составляет $Z = 0.18 \pm 0.14 Z_\odot$. Показано, что оценки металличности из сопоставления диагностических диаграмм с фотоионизационными моделями менее надежны, чем значения, найденные по ярким линиям кислорода.

Оценки содержания кислорода в Синхротронной Сверхоболочке по измеренным относительным интенсивностям линий должны базироваться на модели совместного действия ударной волны (результат вспышки Гиперновой) и ионизующей радиации (наличие звезды WR в центральной области). Пока оценки сделаны отдельно в рамках этих двух моделей. В модели области HII найдено $12+\lg(\mathrm{O/H}) = 7.59$–$8.34$. Сравнение

с моделями свечения газа за фронтом ударной волны, распространяющейся со скоростью около 100–200 км/с, дает наилучшее согласие при обилии $12 + \lg(\mathrm{O/H}) \simeq 8.15$ для моделей чисто ударного возбуждения или $12 + \lg(\mathrm{O/H}) \simeq 8.35$ для моделей, учитывающих предионизацию газа ударной волной.

Работа проводилась при финансовой поддержке Российского фонда фундаментальных исследований (грант № 07-02-00227). Работа основана на наблюдательном материале, полученном на 6-м телескопе САО РАН, финансируемом Миннауки РФ (регистрационный номер 01-43). В процессе работы над статьей мы использовали базу внегалактических данных НАСА/ИПАК (NED), управляемую Лабораторией реактивного движения Калифорнийского технологического института по контракту с Национальным Управлением аэронавтики и космонавтики (США). Авторы благодарны анонимному рецензенту за полезные замечания.

СПИСОК ЛИТЕРАТУРЫ

1. Азари и др. (N.V. Asari, R. Cid Fernandes, G. Stasinska, et al.), MNRAS **381**, 263 (2007).
2. Аллен и др. (M.G. Allen, B.A. Groves, M.A. Dopita, et al.), Astrophys. J. Suppl. Ser. **178**, 20 (2008).
3. Аллер (L.H. Aller), *Physics of thermal gaseous nebulae* (Dordrecht: D. Reidel Publ. Co., 1984).
4. Афанасьев В.Л., Моисеев А.В., Письма в Астрон. журн. **31**, 269 (2005).
5. Бориссова и др.(J. Borissova, L. Georgiev, M. Rosado, et al.), Astron. Astrophys. **363**, 130 (2000).
6. Буйехос, Розадо (A. Bullejos and M. Rozado), Rev. Mex. Astron. Astrophys. **12**, 254 (2002).
7. Вакка и др. (W.D. Vacca, C.D. Sheehy, and J.R. Graham), Astrophys. J. **662**, 272 (2007).
8. Вилкотс, Миллер (E.M. Wilcots and B.W. Miller), Astron. J. **116**, 2363 (1998).
9. Галарза и др. (V.C. Galarza, R.A.M. Walterbos, and R. Braun), Astron. J. **118**, 2775 (1999).
10. Гарнетт (D.R. Garnett), Astrophys. J. **363**, 142 (1990).
11. Гил де Паз и др. (A. Gil de Paz, B.F. Madore, and O. Pevunova), Astrophys. J. Suppl. Ser. **147**, 29 (2003).
12. Демерс и др. (S. Demers, P. Battinelli, and B. Letarte), Astron. Astrophys. **424**, 125 (2004).
13. Допита, Сузерланд (M.A. Dopita and R.S. Sutherland), Astrophys. J. **455**, 468 (1995).
14. Допита, Сузерланд (M.A. Dopita and R.S. Sutherland), Astrophys. J. Suppl. Ser. **102**, 161 (1996).
15. Допита и др. (M.A. Dopita, J. Fischera, R.S. Sutherland, et al.), Astrophys. J. Suppl. Ser. **167**, 177 (2006).
16. Зуккер (D.B. Zucker), Bull. Am. Astron. Soc. **32**, 1456 (2000).
17. Зуккер (D.B. Zucker), Bull. Am. Astron. Soc. **34**, 1147 (2002).
18. Изотов и др. (Y.I. Izotov, G. Stasinska, G. Meynet, et al.), Astron. Astrophys. **448**, 955 (2006).
19. Краутер и др. (P.A. Crowther, L. Drissen, J.B. Abbott, et al.), Astron. Astrophys. **404**, 483 (2003).
20. Леке и др., (J. Lequeux, M. Peimbert, J.F. Rayo, et al.), Astron. Astrophys. **80**, 155 (1979).
21. Лерой и др. (A. Leroy, A. Bolatto, F. Walter, and L. Blitz), Astrophys. J. **643**, 825 (2006).
22. Ли и др. (H. Lee, M.L. McCall, R.L. Kingsburgh, et al.), Astron. J. **125**, 146 (2003).
23. Лозинская, Моисеев (T.A. Lozinskaya and A.V. Moiseev), MNRAS **381**, 26L (2007).
24. Лозинская Т.А., Моисеев А.В., Подорванюк Н.Ю., Буренков А.Н., Письма в Астрон. журн. **34**, 243 (2008).
25. Масси, Холмс (P. Massey and S. Holmes), Astrophys. J. Lett. **580**, L35 (2002).
26. Масси и др. (P. Massey, T.E. Armandroff, and P.S. Conti), Astron. J. **103**, 1159 (1992).
27. Масси и др. (P. Massey, K. Olsen, P. Hodge, et al.), Astron. J. **133**, 2393 (2007).
28. Пейджел и др. (B.E.J. Pagel, M.G. Edmunds, D.E. Blackwell, et al.), MNRAS **189**, 95 (1979).
29. Пилюгин, Туан (L.S. Pilyugin and T.X. Thuan), Astrophys. J. **631**, 231 (2005).
30. Рамсей и др. (C.J. Ramsey, R.M. Williams, R.A. Gruendl, et al.), Astrophys. J. **641**, 241 (2006).
31. Ричер и др. (M.G. Richer, A. Bullejos, J. Borissova, et al.), Astron. Astrophys. **370**, 34 (2001).
32. Розадо и др. (M. Rosado, M. Valdez-Gutierrez, A. Bullejos, et al.), ASP Conf. Ser. **282**, 50 (2002).
33. Ройер и др. (P. Royer, S.J. Smartt, J. Manfroid, and J. Vreux), Astron. Astrophys. **366**, L1 (2001).
34. Сакаи и др. (S. Sakai, B.F. Madore, and W.L. Freedman), Astrophys. J. **511**, 671 (1999).
35. Сид Фернандес и др. (R. Cid Fernandes, N.V. Asari, L. Sodre, et al.), MNRAS **375**, 16 (2007).
36. Турой, Вилкотс (J.C. Thurow and E.M. Wilcots), Astron. J. **129**, 745 (2005).
37. Хантер (D.A. Hunter), Astrophys. J. **559**, 225 (2001).
38. Хидалго-Гамез (A.M. Hidalgo-Gamez), Astron. Astrophys. **442**, 443 (2005).
39. Ходж, Ли (P. Hodge and M.G. Lee), Publ. Astron. Soc. Pacific **102**, 26 (1990).
40. Чарлот, Лонгетти (S. Charlot and M. Longhetti), MNRAS **323**, 887 (2001).
41. Чизи и др., (K.T. Chyzy, J. Knapik, D.J. Bomans, et al.), Astron. Astrophys. **405**, 513 (2003).
42. Янг, Скиллман (H. Yang and E.D. Skillman), Astron. J. **106**, 1448 (1993).

ПИСЬМА В АСТРОНОМИЧЕСКИЙ ЖУРНАЛ, 2006, том 32, № 6, с. 403–418

УДК 524.3-52; 524.7-8

СТРУКТУРА И КИНЕМАТИКА МЕЖЗВЕЗДНОЙ СРЕДЫ В ОБЛАСТИ ЗВЕЗДООБРАЗОВАНИЯ В BCD-ГАЛАКТИКЕ VII Zw 403 (UGC 6456)

© 2006 г. Т. А. Лозинская[1*], А. В. Моисеев[2], В. Ю. Авдеев[1], О. В. Егоров[1]

[1] Государственный астрономический институт им. П.К. Штернберга, Москва

[2] Специальная Астрофизическая Обсерватория РАН, Нижний Архыз

Поступила в редакцию 08.11.2005 г.

Проведено исследование структуры и кинематики ионизованных сверхоболочек в области звездообразования в BCD-галактике VII Zw 403 (UGC 6456). Использованы наблюдения на 6-м телескопе САО РАН с фокальным редуктором SCORPIO в трех режимах: прямые снимки (в линиях Hα, [OIII] и [SII]), спектроскопия с длинной щелью и со сканирующим интерферометром Фабри–Перо. Кроме известных ранее ярких HII областей и слабого гигантского кольца, окружающего всю область звездообразования, обнаружено много новых слабых диффузных и дуговых структур. Выявлена "тонкая структура" гигантского кольца. Не подтверждено обнаруженное ранее расширение ярких сверхоболочек вокруг ассоциаций молодых звезд со скоростью 50–70 км/с. Их скорости расширения, по нашей оценке, не превышают 15–20 км/с, соответствующий кинематический возраст не менее 3–4 млн. лет хорошо согласуется с возрастом связанных с ними компактных OB-ассоциаций. Слабые протяженные волокнистые и диффузные области ионизованного газа, выделенные практически во всей центральной области галактики, и гигантское кольцо HII сопоставлено с более старым (10 млн. лет) звездным населением последней вспышки звездообразования. В самой яркой HII области обнаружены слабые высокоскоростные крылья линий [OIII] и Hα (до 300 км/с от центра линии). Такие скорости наблюдаются в галактике впервые. Уточнены опубликованные ранее измерения Hα светимости галактики.

Ключевые слова: галактики, звездообразование.

STRUCTURE AND KINEMATICS OF THE INTERSTELLAR MEDIUM IN THE REGION OF STAR FORMATION IN THE BCD GALAXY VII Zw 403 (UGC 6456), *by T. A. Lozinskaya, A. V. Moiseev, V. Yu. Avdeev, and O. V. Egorov*. We analyzed the structure and kinematics of ionized superbubbles in the region of star formation in the BCD galaxy VII Zw 403 (UGC 6456). We used observations with the SCORPIO focal reducer on the 6-m Special Astrophysical Observatory telescope in three modes: direct imaging (in the Hα, [OIII], and [SII] lines), long-slit spectroscopy, and spectroscopy with a scanning Fabry–Perot interferometer. In addition to the previously known bright HII regions and the faint giant ring that surrounds the entire region of star formation, we discovered many new faint diffuse and arc structures. We found a fine structure of the giant ring. We do not confirm the previously detected expansion of the bright superbubbles around the associations of young stars with a velocity of 50–70 km s^{-1}. Their expansion velocities were estimated to be no higher than 15–20 km s^{-1}; the corresponding kinematic age, no younger than 3–4 Myr, agrees well with the ages of the associated compact OB associations. We correlate the faint extended filamentary and diffuse regions of ionized gas identified almost in the entire central region of the galaxy and the giant HII ring with the older (10 Myr) stellar population of the last starburst. Weak high-velocity [OIII] and Hα line wings (up to 300 km s^{-1} from the line center) were detected in the brightest HII region. Such velocities have been observed in the galaxy for the first time. We refined the previously published Hα luminosity measurements for the galaxy.

PACS numbers : 98.58.-w; 98.58.Kh

Key words: galaxies, star formation.

ВВЕДЕНИЕ

Наблюдения гигантских оболочек и сверхоболочек вокруг скоплений звезд разного возраста в

[*] Электронный адрес: lozinsk@sai.msu.ru

Irr и BCD-галактиках представляют уникальную возможность изучения межзвездной среды в областях звездообразования в разные эпохи. Многочисленные наблюдения ряда ближайших объектов свидетельствуют, что эпизоды бурного звездообразования в галактиках локализованы в пространстве и во времени и проявляются как гигантские комплексы, где сосредоточено основное население молодых звезд, яркие HII области, оболочки и сверхоболочки разного масштаба. В таких комплексах наиболее отчетливо проявляется "локальное" взаимодействие отдельных OB-ассоциаций с окружающим межзвездным газом.

В настоящей работе проведено детальное исследование структуры и кинематики оболочек и сверхоболочек, представляющих следы нескольких очагов последнего эпизода звездообразования в BCD-галактике VII Zw 403 (UGC 6456). Это достаточно близкая, изолированная, медленно вращающаяся и хорошо исследованная в оптическом, ИК- и рентгеновском диапазонах галактика. Звездное население VII Zw 403 изучено с помощью Космического телескопа Хаббла (HST), что позволило Линдс и др. (1998) провести многоцветную фотометрию отдельных звезд и выявить несколько эпизодов звездообразования разной интенсивности в галактике. Согласно указанной работе самая мощная вспышка звездообразования произошла в период от 800 млн. до 600 млн. лет назад. Звезды этого поколения преобладают в галактике, так что если бы не последняя (4–10 млн. лет назад) сравнительно слабая вспышка звездообразования, которая охватила центральную область размером около 1 кпк, галактика была бы классифицирована как карликовая эллиптическая (dE). Луз и Туан (1985) отнесли VII Zw 403 к наиболее многочисленному классу BCD-галактик iE, который характеризуется нерегулярной яркой областью звездообразования вблизи центра протяженного эллиптического гало, состоящего из старых звезд. Действительно, фотометрия звездного населения VII Zw 403 в ближнем ИК-диапазоне подтверждает, что область современного звездообразования окружена протяженным "старым" звездным гало (Шулте-Ладбек и др., 1999б).

Область звездообразования наблюдается в направлении гигантского облака нейтрального водорода с самой высокой лучевой плотностью HI в галактике и окружена протяженным HI-гало размером $3'.6 \times 2'.9$ или 4.7×3.8 кпк (Туан и др., 2004). Самые молодые и самые массивные звезды образуют в центральной области отчетливые ассоциации № 1, 2, 3, 4, 5, 6 (для единообразия мы будем придерживаться обозначений, принятых Линдс и др., 1998). Более проэволюционировавшие звезды, в том числе и красные сверхгиганты самой высокой светимости, распределены во внешней протяженной области и концентрации к молодым скоплениям не показывают. Вся эмиссия ионизованного газа также сосредоточена в центральной области галактики и выявляет следы нескольких очагов последнего эпизода звездообразования: 8 ярких областей HII, связанных с ассоциациями молодых звезд, и окружающее их очень слабое диффузное излучение (Туан и др., 1987). По наблюдениям с HST Линдс и др. (1998) выявили оболочечную структуру ряда ярких областей HII размером 70–150 пк. Силич и др. (2002) нашли следы слабого гигантского ($D \simeq 500$ пк) кольца в Hα-излучении диффузного газа. Сообщалось о протяженной области диффузного рентгеновского излучения внутри гигантского кольца, но эти данные пока не получили подтверждения (Пападерос и др., 1994; Лира и др., 2000; Боманс, 2001). Вопрос остается открытым: наблюдения Отт и др. (2005а,б) позволили оценить лишь верхнюю границу диффузной рентгеновской светимости $L_X \leq 2.8 \times 10^{38}$ эрг/с.

Результаты наблюдений ионизованного газа в галактике неоднозначны. Так, измерения полной Hα-светимости галактики, которая используется как основной критерий темпа звездообразования, различаются в работах Линдс и др. (1998) и Силича и др. (2002) более чем в 20 раз. По щелевым спектрам с 4-м телескопом KPNO в работе Линдс и др. (1998) обнаружен эффект расширения ярких сверхоболочек со скоростью $V_{\rm exp} = 50$–70 км/с, однако наблюдения Туан и др. (1987) и Мартин (1998) с лучшим спектральным разрешением столь высоких скоростей в галактике не выявили. Все это свидетельствует о необходимости дальнейших наблюдений ионизованного газа в области звездообразования.

Нами проведены наблюдения галактики на 6-м телескопе САО РАН с фокальным редуктором SCORPIO в трех режимах: прямые снимки в среднеполосных фильтрах, спектроскопия с длинной щелью и со сканирующим интерферометром Фабри–Перо (ИФП). Проведенные наблюдения галактики с панорамным спектрографом MPFS будут использованы для детального исследования спектра свечения газа в нашей следующей статье (Лозинская и др., 2006). В настоящей работе представлены результаты исследований структуры и кинематики ионизованного газа в области звездообразования. Во Введении собраны основные данные о галактике и сформулированы цели наших исследований; далее описаны методики наблюдений и обработки данных; представлены полученные результаты и их обсуждение. В Заключении суммируются краткие выводы работы.

В данной статье нами принято расстояние до галактики $d = 4.5$ Мпк (Линдс и др., 1998; Шулте-Ладбек и др., 1999а), что соответствует угловому масштабу 22 пк/″.

НАБЛЮДЕНИЯ И ОБРАБОТКА ДАННЫХ

Интерферометрические наблюдения

Интерферометрические наблюдения VII Zw 403 были проведены 30.11.2002 г. в первичном фокусе 6-м телескопа с использованием укорачивающей фокус системы (фокального редуктора) SCORPIO, при этом эквивалентная светосила системы составляла $F/2.9$. Описание SCORPIO представлено в работе Афанасьева и Моисеева (2005) и в Интернете (http://www.sao.ru/hq/moisav/scorpio/scorpio.html), возможности SCOPRIO в интерферометрических наблюдениях описаны также Моисеевым (2002).

Качество изображений при наблюдениях менялось в пределах 1.″5–2.″1. Использовался сканирующий ИФП, работающий в 501 порядке на длине волны линии Hα. При этом расстояние между соседними порядками интерференции $\Delta\lambda = 13$ Å соответствовало свободной от перекрытия порядков области, равной в шкале лучевых скоростей $\sim$600 км/с. Ширина инструментального контура ИФП составляла около 0.8 Å, или $\sim$35 км/с. Предварительная монохроматизация осуществлялась с помощью интерференционного фильтра с полушириной $\Delta\lambda = 15$ Å, центрированного на линию Hα. В качестве приемника излучения использовалась ПЗС-матрица TK1024 размером 1024×1024 пикселей. Наблюдения проводились с аппаратным биннингом 2×2 пикселя с целью уменьшения времени считывания. В каждом спектральном канале получались изображения размером 512×512 пикселей, при масштабе 0.55″/пиксель, полное поле зрения составляло 4.′8. Всего получено 36 интерференционных изображений при различных расстояниях между пластинами ИФП, так что размер спектрального канала соответствовал $\delta\lambda = 0.36$ Å, или 17 км/с в области Hα. Время одной экспозиции составляло 300 с.

Обработка наблюдений выполнялась с помощью программного обеспечения, работающего в среде IDL (Моисеев, 2002). После первичной редукции наблюдательные данные были представлены как “куб данных” размером $512 \times 512 \times 36$ элемента; здесь каждому элементу изображения соответствует 36-канальный спектр. Итоговое пространственное угловое разрешение (после сглаживания в процессе редукции данных) составило около 2.″2. Операция сглаживания проводилась с помощью программного пакета ADHOC[1].

Поля лучевых скоростей, карты интенсивности и полуширины (FWHM) линии Hα строились на основании результатов однокомпонентной гаусс-аппроксимации профиля эмиссионной линии в кубе данных. Карта FWHM исправлялась за ширину инструментального контура прибора согласно “стандартному” соотношению (корень из разности квадратов полуширин). Формальная точность измерения лучевых скоростей для симметричных профилей линий составляла около 3–5 км/с.

Все значения лучевых скоростей в данной работе являются гелиоцентрическими.

Изображения в эмиссионных линиях

Изображения VII Zw 403 в эмиссионных линиях и в континууме были получены на 6-м телескопе с редуктором светосилы SCORPIO. Журнал фотометрических наблюдений приведен в табл. 1, где указаны дата наблюдений, центральная длина волны (λ_c) и ширина полосы используемого фильтра (FWHM), суммарная длительность экспозиции T_{exp}, среднее качество изображений. В таблицу включены фильтры, полоса пропускания которых включала эмиссионные линии Hα, (Hα+[NII] λ6548, 6583) Å, [OIII] λ4959, 5007 Å, [SII] λ6717 Å, а также фильтры, центрированные на континуум вблизи указанных линий.

Отметим, что наблюдения в 2002 г. проводились в узком фильтре, центрированном на линию Hα галактики (этот же фильтр использовался для наблюдения с ИФП), в то время как более глубокое изображение 2003 г. получено в фильтре, полоса которого кроме Hα пропускала и две соседние линии [NII].

В качестве детектора в 2002 г. применялась ПЗС-матрица TK1024, дающая масштаб 0.28″/пиксель, а в 2003 г. – матрица EEV42–40, обеспечивающая масштаб 0.31″/пиксель (в режиме считывания 2×2). Редукция данных проводилась по стандартной методике, для калибровки изображений в шкале энергетических единиц в ту же ночь и практически на том же зенитном расстоянии, что и объект, наблюдались звезды – спектрофотометрические стандарты AGK+81 266 и Grw+70 5824.

При построении карт “чистой” эмиссии в линиях из изображений в фильтрах, содержащих эмиссионные линии, вычитались изображения в соответствующем континууме. Нормировочный коэффициент при вычитании подбирался таким образом,

[1]Пакет программ ADHOC разработан Ж. Булестексом (Марсельская обсерватория).

Таблица 1. Журнал фотометрических наблюдений

Диапазон	Дата	λ_c, Å	FWHM, Å	T_{exp}, с	Качество изображений
Hα	29/30.11.02	6560	15	600	$1\farcs2$
Hα-континуум	29/30.11.02	6608	15	240	1.2
Hα + [NII]	25/26.05.03	6552	75	3000	1.4
Hα-континуум	25/26.05.03	6608	15	1500	1.5
[OIII]	23/24.07.03	4995	220	3600	1.8
[OIII]-континуум	23/24.07.03	5310	170	1800	1.8
[SII]	22/23.07.03	6720	15	3000	1.9
[SII]-континуум	23/24.07.03	6604	21	1200	1.6

чтобы на результирующем кадре взаимно вычитались изображения звезд поля. Заметим, что поскольку VIIZw 403 — галактика с "голубым" континуумом (во всяком случае, в области звездообразования), а звезды поля в основном "красные", то такая (вообще говоря, общепринятая) методика могла привести к некоторому недоучету реального континуума в случае линий [OIII] и Hα (здесь фильтр для континуума взят более красный) и, наоборот, к переучету вклада от континуума для изображения в [SII]. Этот эффект очень трудно корректно учесть (мы не знаем наклон спектрального континуума в разных областях галактики и в звездах поля), об этом необходимо помнить при рассмотрении карт отношения интенсивности линий. Для дополнительного контроля мы использовали предварительные данные спектрофотометрии центральной области галактики с панорамным спектрографом MPFS, поскольку в этих наблюдениях континуум вычитается без проблем. К сожалению, данные MPFS имеются только для центральной области галактики.

Наблюдения с щелевым спектрографом

Спектральные наблюдения VII Zw 403 проводились с тем же прибором SCORPIO, работающим в режиме щелевого спектрографа, с щелью длиной около $6'$ и шириной $1''$. Масштаб вдоль щели составлял $0.36''$/пиксель. Использовались объемные фазовые голографические решетки (VPHG), обеспечивающие спектральное разрешение вблизи линий [OIII] и Hα 130–140 км/с. Поскольку основная задача наблюдений со щелевым спектрографом состояла в проверке факта раздвоения эмиссионной линии Hβ в ярких оболочках, обнаруженного в работе Линдс и др. (1998), то были получены два спектра со сходной локализацией щели: разрез 1 — через области N2, N3, N4 и разрез 2 — через HII-области N1 и N5 (в обозначениях Линдс и др., 1998). Позиционный угол щели спектрографа составлял в обоих случаях 88°. В журнале наблюдений (табл. 2) кроме длительности экспозиции T_{exp} и среднего качества изображений указан спектральный диапазон $\Delta\lambda$.

Таблица 2. Журнал спектральных наблюдений

Разрез	Дата	$\Delta\lambda$, Å	T_{exp}, с	Качество изображений
1	21/22.12.03	6270–7300	1200	$2\farcs2$
1	05/06.12.04	4800–5600	1200	2.0
2	21/22.12.03	6270–7300	1800	2.2
2	05/06.12.04	4800–5600	800	2.0

Отметим, что мы получили спектры не только в "зеленом" спектральном диапазоне, содержащем линии Hβ и [OIII] λ4959, 5007 Å, как в работе Линдс и др. (1998), но и в "красном" диапазоне, включающем линии Hα, [NII] λ6548, 6583 Å и [SII] λ6717, 6731 Å. Обработка данных проводилась стандартным образом, для привязки к энергетической шкале использовался спектрофотометрический стандарт AGK+81 266, наблюдавшийся сразу после объекта на близком зенитном расстоянии.

Лучевые скорости и FHWM эмиссионных линий определялись с помощью однокомпонентной гаусс-аппроксимации профилей, наблюдаемые ширины линий исправлялись за инструментальный контур аналогично данным, полученным с ИФП. Точность измерения абсолютных скоростей контролировалась по линиям ночного неба и составляла около 5 км/с.

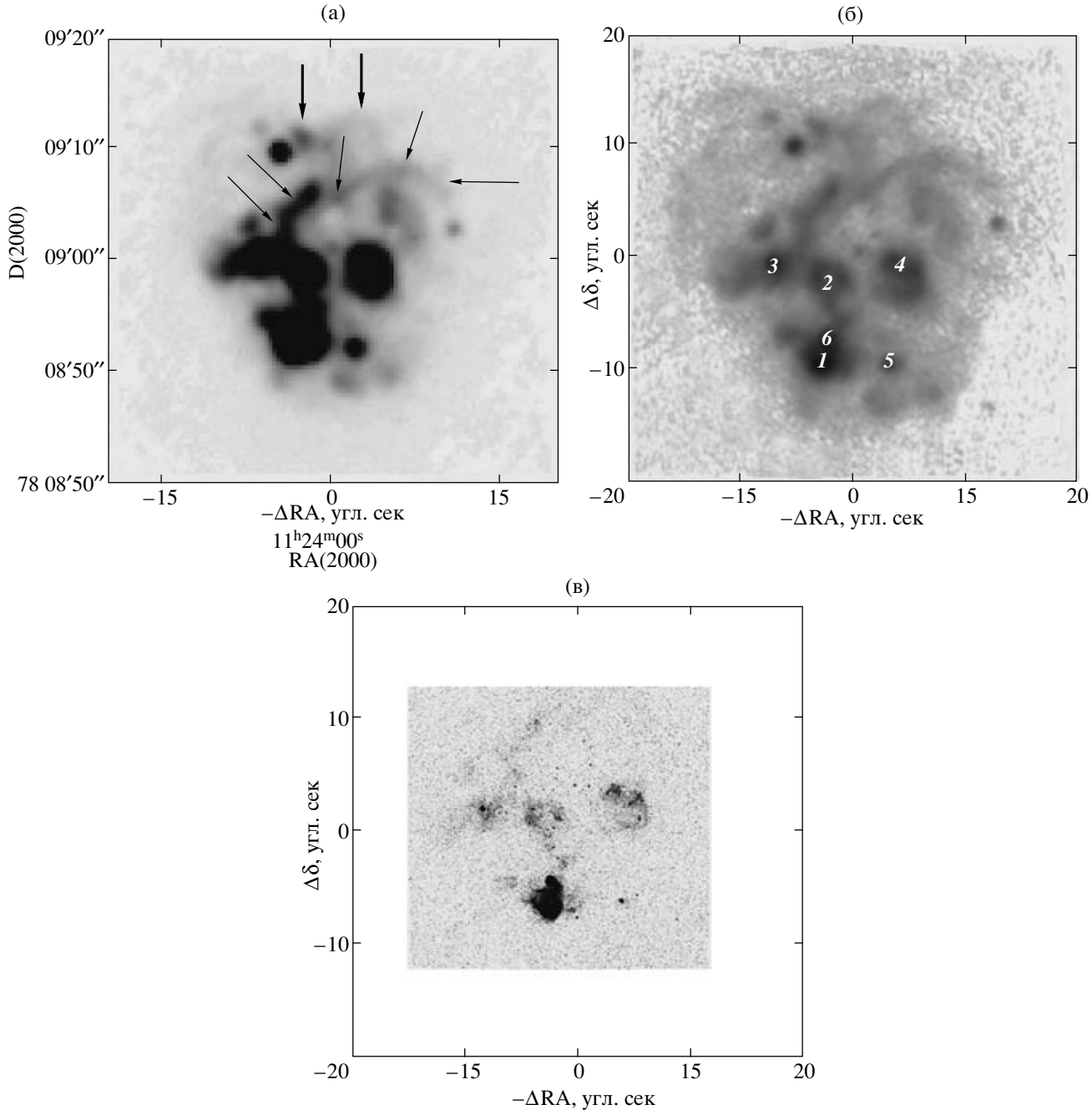

Рис. 1. Hα-изображение области звездообразования: снимок с редуктором SCORPIO 6-м телескопа САО РАН в линейной (а) и логарифмической шкале (б), а также снимок из архива HST, полученный с помощью прибора WFPC2 в фильтре F656N (в). Тонкими стрелками показаны отдельные дуги, из которых состоит "гигантское кольцо", выделенное в работе Силича и др. (2002); толстыми стрелками показана "внешняя дуга" за его пределами. Цифрами отмечены области HII согласно работе Линдс и др. (1998).

РЕЗУЛЬТАТЫ

Общая структура области звездообразования в галактике

По прямым снимкам в среднеполосных фильтрах с фокальным редуктором SCORPIO 6-м телескопа получены изображения центральной области галактики в линиях (Hα + [NII]), [SII] 6717Å и [OIII] 5007Å.

На рис. 1 показаны изображения области звездообразования в линии Hα в линейной и логариф-

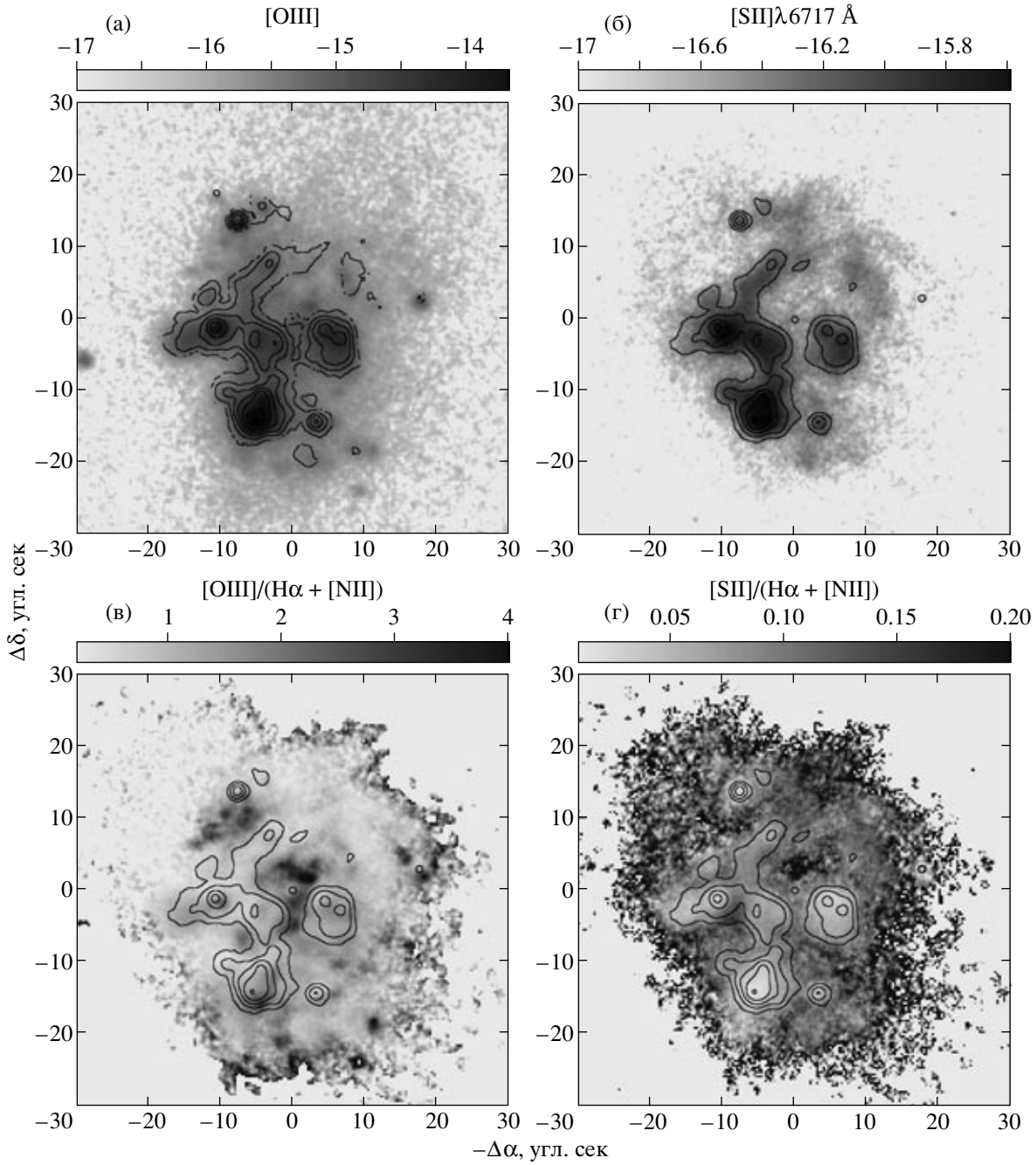

Рис. 2. Изображения области звездообразования в линиях [OIII] (а) и [SII] (б) в логарифмической шкале, совмещенные с контурами линий Hα + [NII], и карты отношения яркостей в линиях [OIII]/(Hα + [NII]) (в) и [SII]/(Hα + [NII]) (г), совмещенные с теми же контурами.

мической шкале, полученные на БТА, и снимок в фильтре, содержащем линию Hα, взятый из архива HST. Цифрами на рис. 1б отмечены области HII согласно нумерации Линдс и др. (1998). Как следует из рисунка, все выделенные с помощью HST сверхоболочки HII N1–N6 видны как самые яркие эмиссионные области и на нашем снимке (разумеется, с более низким угловым разрешением, не позволяющим выявить их оболочечную структуру). Кроме этих известных ранее ярких областей HII наши снимки обнаруживают большое число новых более слабых эмиссионных деталей. Среди них сферически-симметричные области размером 2–5″, протяженные дуговые и линейные структуры, а также область слабой диффузной эмиссии большего размера.

Наши наблюдения показали, что выделенное

Таблица 3. Оценка потока и светимости VII Zw 403 в линии Нα

Ссылка	Поток, эрг/с/см	L, эрг/с, $D = 4.5$ Мпк
Линдс и др. (1998)	–	1.80×10^{39}(Нα)
Мартин (1998)	6.5×10^{-13}	1.58×10^{39} (Нα + [NII])
Силич и др. (2002)	1.95×10^{-11}	4.70×10^{40} (Нα)
БТА (фильтр 15А)	6.14×10^{-13}	1.49×10^{39} (Нα)
БТА (фильтр 70А)	7.96×10^{-13}	1.93×10^{39} (Нα + [NII])

в работе Силича и др. (2002) "гигантское разорванное на юго-западе оболочечное образование радиусом 250 пк" (далее "гигантское кольцо") состоит из нескольких отдельных дуговых структур разной яркости и с разным радиусом кривизны (см. рис. 1а). За его пределами на севере можно выделить еще одну внешнюю дугу и три HII области размером около 2″.

Рисунок 2 позволяет сопоставить крупномасштабную структуру центральной области звездообразования в разных линиях. Здесь показаны: изображения в линиях [OIII] и [SII] в логарифмической шкале, совмещенные с контурами линий Нα+[NII] и карты отношения яркостей в линиях [OIII]/Нα и [SII]/Нα, совмещенные с теми же контурами.

Как следует из рис. 1 и 2, в целом крупномасштабная структура области звездообразования в линиях Нα + [NII], [SII] и [OIII] практически одинакова. Тем не менее можно выделить две протяженные очень слабые области диффузной эмиссии, в которых повышена относительная яркость [OIII]/Нα. Одна из этих областей расположена внутри гигантского кольца между яркими областями N2 и N4 и к северу от них, а вторая – вне гигантского кольца, между ним и внешней дугой на севере (см. рис. 2в).

В первой области повышена также относительная яркость [SII]/Нα (см. рис. 2г).

Полный размер области диффузного ионизованного газа в галактике, на фоне которого наблюдаются все яркие области HII, составляет 35–40″ или около 900 пк по уровню яркости 5×10^{-17} эрг с$^{-1}$ см$^{-2}$ (угл. сек)$^{-2}$.

Мы оценили суммарный поток Нα-излучения центральной области VII Zw 403 путем интегрирования внутри круглой диафрагмы диаметром 40″. Потоки и соответствующая им светимость галактики приведены в табл. 3. Поправка за поглощение сделана для среднего значения $E(B-V) = 0.04$ (и $R_v = A_v/E(B-V) = 3.1$), найденного Линдс и др. (1998) по всем звездам галактики. Данные работы Мартин (1998) скорректированы нами таким же образом; светимость дана для расстояния 4.5 кпк. В работе Силича и др. (2002) учтено только фоновое поглощение $E(B-V) = 0.02$ согласно Бурстейн, Хейлес (1984); учет внутреннего поглощения в VII Zw 403 еще больше увеличивает найденные этими авторами поток и светимость.

Как следует из табл. 3, измеренная нами Нα светимость галактики оказалась значительно ниже значения, полученного Силичем и др. (2002), и хорошо согласуется с более ранними оценками Линдс и др. (1998) и Мартин (1998).

Кинематика газа в области звездообразования

Наблюдения с ИФП. По данным наблюдений с ИФП построены карты распределения лучевой скорости максимума и полуширины линии Нα в центральной области галактики, показанные на рис. 3.

Найденная скорость максимума линии в области звездообразования меняется в пределах от –120 км/с до –90 км/с (в области слабой эмиссии на краю поля достигает значений –130– – 140 км/с). Эти скорости хорошо согласуются со скоростью нейтрального газа от –120 км/с до –80 км/с в протяженной окружающей области галактики и от –110 км/с до –90 км/с в самом плотном облаке HI в галактике, с которым совпадает область звездообразования (Туан и др., 2004).

Исправленная за инструментальный контур полуширина линии Нα заключена в пределах от 60–70 км/с до 100–120 км/с.

С целью поиска эффекта расширения ярких сферически-симметричных областей HII были построены так называемые диаграммы "позиция–скорость" (P/V) и "позиция–полуширина линии" ($P/\Delta V$). Ориентация разрезов была выбрана так, что они в двух-трех разных направлениях пересекали каждую область HII, в том числе и те, которые на снимках с HST выявляют четкую оболочечную

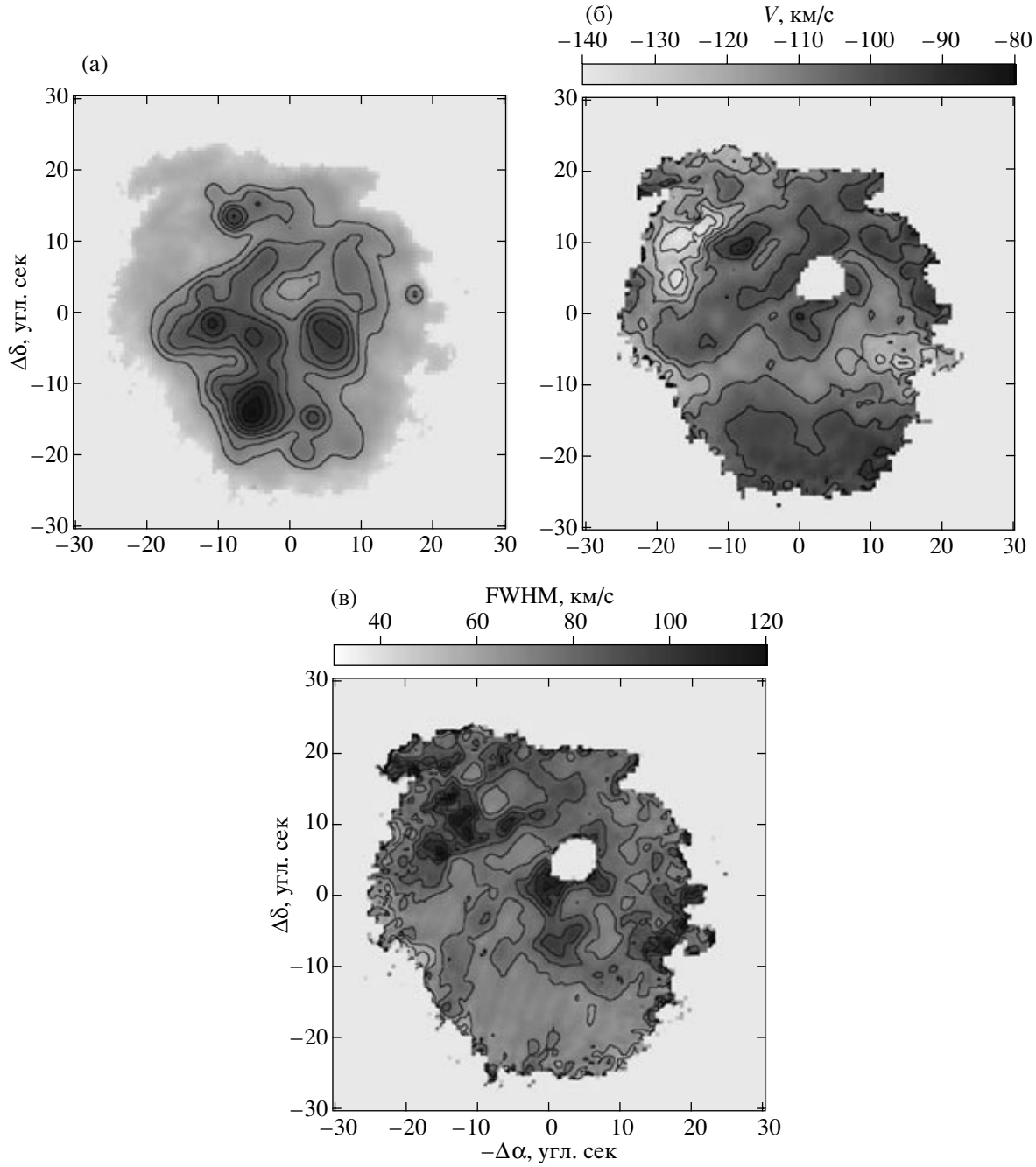

Рис. 3. Распределение яркости (а), лучевой скорости максимума (б) и полуширины линии Hα (в) по наблюдениям с ИФП. "Дыра" в центральной области вызвана паразитным бликом внутри прибора.

структуру (области HII N1, N3 и N4) и о расширении которых со скоростью 50–70 км/с сообщается в работе Линдс и др. (1998).

В качестве примера на рис. 4 показаны четыре из построенных нами более трех десятков разрезов.

Самая протяженная сверхоболочка N4 размером 6.5–8′ (140–180 пк) показала увеличение полуширины линии к центру до $\Delta V = 90$ км/с по сравнению с $\Delta V = 65$–70 км/с в ярких северной и южной периферийных частях, что может быть следствием ее расширения со скоростью 15–20 км/с (см. разрез 4 на рис. 4).

По результатам проведенных наблюдений с ИФП ни одна из ярких областей HII, кроме области N4, не выявила характерной для расширяющейся тонкой оболочки структуры "эллипса скоростей"

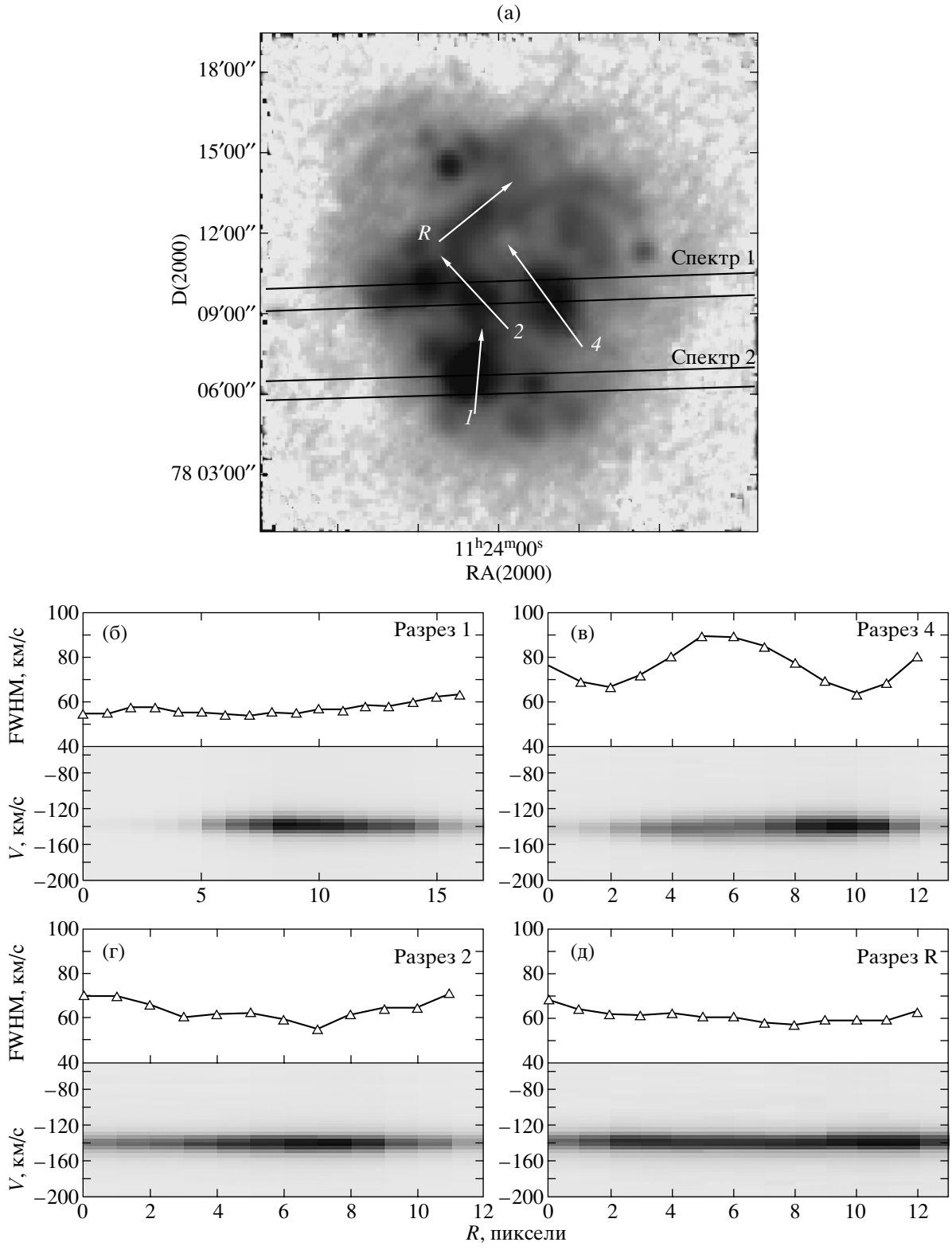

Рис. 4. (а) – Ориентация выбранных в качестве примера разрезов вместе с локализацией щели спектрографа для двух полученных спектров. (б), (в) – Примеры диаграмм “позиция–скорость”, (P/V) и ”позиция–полуширина линии” ($P/\Delta V$), полученные по наблюдениям с ИФП.

на P/V-диаграммах или уширения линии в центре на $P/\Delta V$-диаграммах.

В области самой богатой OB-ассоциации и наиболее яркой оболочки HII N1 на снимке с HST видна цепочка ассоциаций и связанных с ними областей HII: сверхоболочка N1 (вокруг ассоциации № 1), HII область N6 (вокруг ассоциации № 3) и между ними еще одна, связанная с ассоциацией № 2. (Во избежание дополнительной путаницы мы сохранили здесь все обозначения Линдс и др., 1998.) Разрез 1 на рис. 4 проходит вдоль этой цепочки; никаких изменений скорости или полуширины линии в этой цепочке областей HII наши наблюдения не выявили.

Полуширина линии в ярких сверхоболочках, не обнаруживших признаков расширения, составляет 60 км/с, что превосходит вклад тепловых и турбулентных скоростей в областях HII. Разумеется, при итоговом угловом разрешении $2''.2$ мы усредняем все вариации лучевой скорости по области, сопоставимой с радиусом оболочки. Но в любом случае гипотетическая скорость расширения этих оболочек, которая могла бы объяснить наблюдаемую ширину линии, не превышает 15–20 км/с.

По результатам наблюдений с ИФП мы определили средние скорости и полуширины линии во всех слабых областях $H\alpha$-эмиссии, впервые выделенных на наших снимках. Ни в одной из них также не найдено заметных вариаций скорости и полуширины линии, свидетельствующих о расширении со скоростью более 20 км/с.

Суммируя результаты проведенных исследований кинематики с ИФП, можно заключить, что во всей области звездообразования на масштабах, превышающих 45–50 пк, что соответствует реальному итоговому угловому разрешению $2''.2$ наших наблюдений с ИФП, не наблюдается резких изменений скоростей максимума и полуширины линии $H\alpha$. Наблюдаемые изменения скорости заключены в пределах ± 10–20 км/с, полуширина линии меняется от 60 км/с до 100–120 км/с.

Отметим, что точность наших измерений достаточно высока, чтобы обнаружить отмеченное Линдс и др. (1998) быстрое расширение оболочек. Так, к примеру, на построенных с ИФП картах четко прослеживается связь между HII-областями и вариациями лучевых скоростей и дисперсией скоростей газовых облаков (полушириной линии).

Наблюдения со щелевым спектрографом. Для выяснения причины разногласий в оценках скорости расширения ярких оболочек по спектральным наблюдениям Линдс и др. (1998) и по нашим наблюдениям с ИФП мы провели спектральные наблюдения с длинной щелью в красной ($H\alpha$, [NII], [SII]) и зеленой ($H\beta$, [OIII]) областях спектра. Спектральные наблюдения были проведены при условиях, максимально приближенных к наблюдениям Линдс и др. (1998). Реальное спектральное разрешение (оценка по линиям неба) составляло FWHM = 120 км/с, что сопоставимо с указанной работой. Угловое разрешение также было сходным $-2''$; в нашей работе оно лимитировалось качеством изображений, в работе Линдс и др. (1998) такой была ширина щели спектрографа.

В обоих диапазонах нами сделаны два разреза через те же области оболочек, спектры которых представлены в работе Линдс и др. (1998). Локализация щели спектрографа показана на рис. 4а.

На рис. 5 показаны вид линий $H\alpha$ и [OIII] в каждом из двух разрезов при разных уровнях интенсивности и результат представления профиля линии гауссианами.

Ни в одной из линий в спектре ионизованных сверхоболочек не обнаружено отчетливого раздвоения профилей, которое свидетельствовало бы об их расширении со скоростью 50–70 км/с. Однокомпонентная гауссиана хорошо описывает профиль линий $H\beta$, $H\alpha$ и запрещенных линий в ярких сверхоболочках N2, N3, N4, N5, остаточные отклонения малы.

В наиболее яркой сверхоболочке N1 вокруг самой богатой и молодой ассоциации № 1 наблюдаются очень слабые высокоскоростные крылья линий [OIII] и $H\alpha$. Как видно на рис. 5в,г, линия [OIII] здесь не симметрична и выявляет слабый синий компонент со скоростями -200– -300 км/с от центра линии по уровню около 5% максимальной интенсивности. В линии $H\alpha$ наблюдается слабая широкая подложка, которая может быть описана гауссианой с FWHM = 630 км/с, при этом полный поток в широком компоненте составляет около 4% от полного потока в линии.

Столь высокие скорости обнаружены в галактике впервые и, по всей вероятности, свидетельствуют об ускорении газа на фронте ударной волны. Разумеется, учитывая очень низкую яркость высокоскоростных деталей, эти результаты должны быть подтверждены независимыми наблюдениями. Отметим, что мы провели несколько тестов, чтобы проверить, не являются ли указанные спектральные особенности аппаратным эффектом (сложная структура инструментального контура спектрографа, особенности фокусировки и т.п.). В частности, мы контролировали форму инструментального контура как по ярким линиям ночного неба, так и по калибровочному спектру сравнения и убедились в том, что инструментальный контур не содержит широких крыльев, во всяком случае на уровне выше 0.5–1% от максимума. Отметим также, что относительная интенсивность широкой подложки

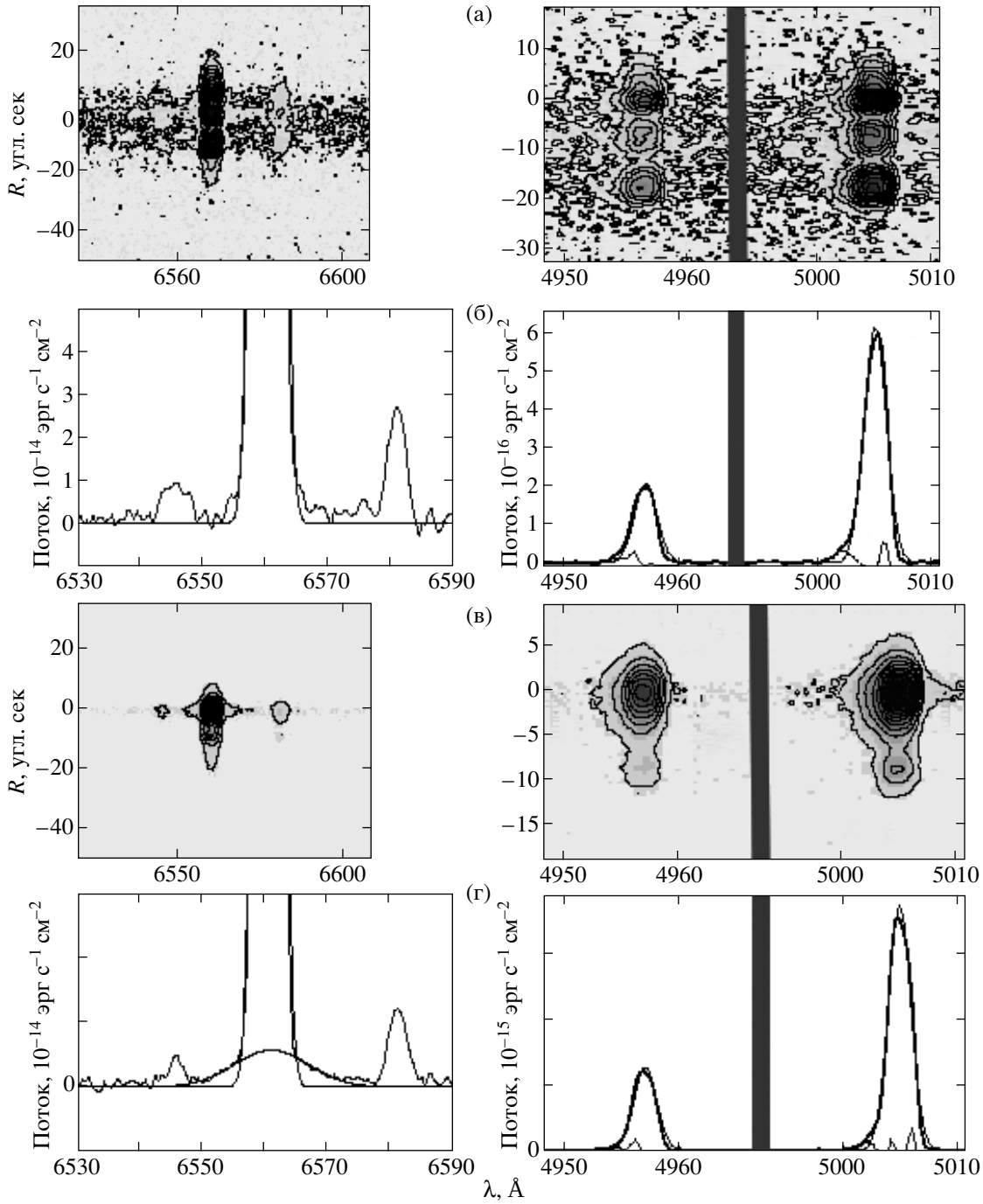

Рис. 5. Спектральная область вблизи линии Hα (слева) и линии [OIII] (справа) при разных уровнях интенсивности и их представление гауссовыми кривыми для двух спектров: спектр 1 (а,б) и спектр 2 (в,г). Локализация спектрограмм на изображении галактики показана на рис. 4а.

превосходит величину рассеянного света в спектрографе SCORPIO с VPHG-решетками (менее 1% согласно нашим оценкам).

На рис. 6 показано сравнение результатов наших спектральных и интерференционных наблюдений: изменение интенсивности в максимуме линии, лучевой скорости максимума и полуширины линии Hα вдоль разрезов 1 и 2, локализация которых показана на рис. 4а (спектр 1 и спектр 2).

Прежде всего, этот рисунок является независимым тестом корректности обработки данных двух программ наблюдений: как видим, согласие и лучевых скоростей, и полуширин линий по интерферометрическим и спектральным данным достаточно

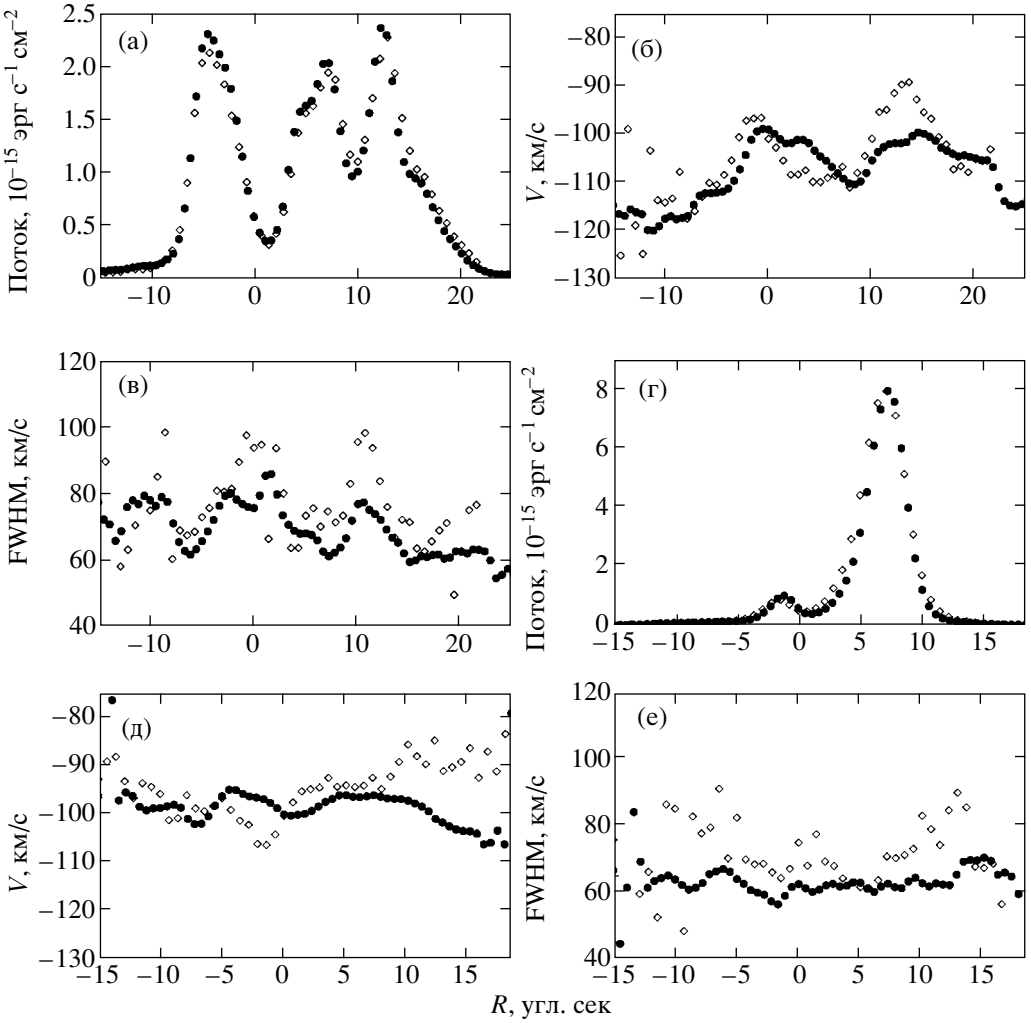

Рис. 6. Сравнение результатов спектральных (незакрашенные символы) и интерференционных (черные кружки) наблюдений: изменение интенсивности, лучевой скорости в максимуме и полуширины линий Hα вдоль двух разрезов, соответствующих положению щели спектрографа, показанному на рис. 4а: спектр 1 (а,в,д) и спектр 2 (б,г,е).

хорошее. При этом, как отмечено выше, в ярких областях HII не видно уширения линии в центре, что ожидалось для оболочек, расширяющихся со скоростью 50–70 км/с. Напротив, явное уширение линии (от FWHM $\simeq$ 60–70 км/с до FWHM $\simeq$ $\simeq$ 80–120 км/с) наблюдается в слабой области диффузного ионизованного газа между яркими областями HII N4 и N2 и между областями N3 и N2. На втором разрезе, пересекающем области N1 и N5, этот эффект тоже есть, но выражен слабее.

Сходное уширение линии в области слабой диффузной эмиссии по сравнению с яркими областями HII выявлено нами и по наблюдениям в линии [OIII]. В работе Туан и др. (1987) также отмечалось, что яркие области HII характеризуются медианными значениями лучевой скорости, а минимальные и максимальные скорости линии Hα наблюдаются в слабом диффузном излучении между ними.

Крупномасштабная кинематика нейтрального газа в области звездообразования выявляет отчетливый градиент лучевой скорости максимума радио линии 21 см (см. рис. 20 в работе Туан и др., 2004). В направлении с северо-востока на юго-запад скорость плавно растет от -110 км/с до $-95-$ -85 км/с в обоих облаках HI, вытянутых в этом же направлении. Природа этого градиента не ясна, авторы работы говорят о возможном вращении газа в центральной области вдоль большой оси галактики. Мы попытались выявить такой же градиент в распределении скоростей ионизованного газа в регионе. Для этого по данным наших Hα наблюдений с ИФП были построены P/V-диаграммы в направлениях, полностью идентичных направлениям P/V-диаграмм для HI в работе Туан и др. (2004). Эффект сходного

плавного градиента лучевой скорости линии Hα мы не обнаружили.

ОБСУЖДЕНИЕ

Полученные изображения центральной области галактики в линиях (Hα + [NII]), [SII] и [OIII] свидетельствуют, что крупномасштабная структура области звездообразования в этих линиях идентична. Все идентифицированные ранее области HII видны как самые яркие эмиссионные детали на наших снимках во всех указанных линиях (см. рис. 1, 2, 4а). Кроме них мы обнаружили большое число новых более слабых эмиссионных деталей, как компактных, так и протяженных диффузных, дуговых и линейных структур. Выделенное в работе Силича и др. (2002) гигантское кольцо удалось разделить на несколько отдельных дуговых структур разной яркости и с разным радиусом кривизны. За его пределами на севере можно выделить еще одну слабую внешнюю дугу. Все яркие эмиссионные детали наблюдаются на фоне слабого диффузного излучения ионизованного газа.

Наша оценка Hα-светимости галактики оказалась значительно ниже значения, полученного Силичем и др. (2002), и хорошо согласуется с ранними оценками Линдс и др. (1998) и Мартин (1998).

Согласно нашим наблюдениям с щелевым спектрографом, представленным выше, и предварительным данным работы Лозинской и др. (2006) относительная интенсивность линий [NII] λ6548, 6583/Hα в VII Zw 403 составляет около 0.03–0.035; сходное значение 0.03 было получено Мартин (1997). Соответственно приведенная в табл. 3 светимость в линиях (Hα + [NII]), найденная по более глубокому изображению с широким фильтром, дает $L(\mathrm{H}\alpha) = 1.86 \times 10^{39}$ эрг/с.

Используя формулу для оценки темпа звездообразования по величине Hα-светимости: SFR $(M_\odot$ год$^{-1}) = 7.9 \times 10^{-42} L(\mathrm{H}\alpha)$ (Кенникутт, 1998), по найденной светимости $L(\mathrm{H}\alpha) = (1.49\text{–}1.86) \times \times 10^{39}$ имеем SFR $= 0.012\text{–}0.015 M_\odot$ год$^{-1}$ для интервала масс от 1 до $100 M_\odot$.

По данным интерферометрических Hα наблюдений построены распределения лучевой скорости максимума линии и полуширины линии в центральной области галактики с угловым разрешением 2″.2. Полуширина линии Hα в области звездообразования заключена в пределах от 60–70 км/с до 100–120 км/с. Скорость ионизованного газа в области звездообразования от −120 км/с до −90 км/с хорошо согласуется с измеренной в работе Туан и др. (2004) скоростью нейтрального газа в двух совпадающих с ней плотных облаках HI.

Расширение ярких сферически-симметричных HII областей со скоростью 50–70 км/с, о котором сообщается в работе Линдс и др. (1998), нами не обнаружено. На наш взгляд, наиболее вероятная причина различий между результатами Линдс и др. (1998) и нашими состоит в том, что авторы этой работы использовали щель шириной 2″, что явно несколько больше характерного размера звездных изображений на обсерватории KPNO. В случае относительно широкой щели когеррентные структуры, напоминающие "эллипсы скоростей" быстро расширяющихся оболочек на спектрах Линдс и др., могут быть вызваны изменением яркости объекта поперек щели, так что на выходе спектрографа смешиваются пространственная и спектральные детали. К сожалению в упомянутой статье нет данных о качестве изображений и мы не можем проверить это предположение. Отметим также, что Hα наблюдения Туан и др. (1987) с ИФП и наблюдения Мартин (1998) с эшелле-спектрографом со спектральным разрешением, соответствующим 11 км/с, также не выявили движений газа со столь высокими скоростями нигде в галактике.

Скорость расширения оболочки N4 размером 6.5–8″ (140–180 пк) мы оценили как 15–20 км/с по наблюдаемому уширению линии к центру.

Соответствующий кинематический возраст оболочки в стандартной модели МакКрэй, Кафатос (1987) составляет около 3–4 млн. лет. OB-ассоциация № 5, ответственная за формирование этой оболочки, содержит 28 голубых O-звезд ГП и сверхгигантов; возраст ассоциации составляет 5–6 млн. лет (Линдс и др., 1998).

Верхняя граница скорости расширения остальных ярких областей HII оценена нами по полуширине линий Hα, Hβ и [OIII] как $V_{\text{расш}} \leq$ $\leq$ 15–20 км/с. Соответствующий кинематический возраст оболочек достигает 3–4 млн. лет или более. Это существенно ближе к возрасту компактных OB ассоциаций, ответственных за их формирование, чем кинематический возраст оболочек около 1 млн. лет, найденный Линдс и др. (1998) в рамках той же стандартной модели при высокой скорости расширения.

Возраст самой богатой ассоциации № 1, связанной с оболочкой N1, по оценке Линдс и др. (1998) составляет 4–5 млн. лет. Ассоциации № 2, 3, 4 и 6 значительно беднее № 1 и 5 и также связаны с яркими компактными областями HII: ассоциация № 3 связана с HII областью N6; ассоциация № 4 – с областью N3; ассоциация № 6 – с областью N5.

Кроме этих сравнительно "компактных" ассоциаций голубые звезды высокой светимости обнаружены по наблюдениям с HST во всем центральном поле галактики. В центре области звездооб-

разования выделена более "разреженная" группировка звезд, обозначенная "центр/center" на рис. 2 и рис. 11 в работе Линдс и др. (1998); с ней связана более слабая диффузная оболочка N2 размером 200–240 пк. Эта ассоциация "смешанного" возраста содержит группу голубых сверхгигантов (возраст около 5 млн. лет), совмещенную с более старым населением (не моложе 10 млн. лет), в их числе 20 красных сверхгигантов этого возраста. В полях, обозначенных "север/north" и "юг/south", также наблюдаются две популяции звезд, возраст которых составляет 5 млн. лет и 10 млн. лет или несколько больше (Линдс и др., 1998).

Таким образом, центральная часть галактики выявляет два всплеска звездообразования 5 млн. лет назад и 10 млн. лет назад; межзвездная среда обнаруживает следы двух этих вспышек последнего эпизода звездообразования. С ассоциациями, образовавшимися около 5 млн. лет назад, идентифицированы все упомянутые яркие HII области. Более слабые волокнистые и диффузные области $H\alpha$-эмиссии, которые выделены во всей центральной области, а также гигантское кольцо ионизованного газа и внешнюю дугу за его пределами, по всей вероятности, можно сопоставить с более старым звездным населением, возраст которого достигает 10 млн. лет.

Обнаруженный эффект уширения линии в слабом диффузном излучении ионизованного газа за пределами ярких HII областей, вообще говоря, может быть связан с наложением на луче зрения нескольких слабых "фоновых" областей ионизованного газа, расположенных в толще газового диска галактики и излучающих на разных лучевых скоростях. Однако более интересна другая возможность: наблюдаемое уширение линии может быть обусловлено более эффективным ускорением газа низкой плотности ударными волнами. Последнее предположение допускает наблюдательную проверку по относительным интенсивностям линий в спектре. Как отмечено выше, внутри гигантского кольца в области слабой диффузной эмиссии между яркими HII областями N4 и N2, а также к северу от областей N3 и N2 действительно усилена яркость излучения в линиях [OIII] и [SII] по отношению к $H\alpha$ (см. рис. 2в). Примерно здесь же локализованы области максимальной ширины линии $H\alpha$. Эта часть комплекса звездообразования совпадает с областью сравнительно низкой яркости излучения в линии 21 см между двумя самыми плотными облаками HI, которая тоже характеризуется более высокой, чем в облаках, дисперсией скоростей нейтрального газа (Туан и др., 2004). Все эти факты могут свидетельствовать в пользу существенного влияния ударных волн, инициированных звездным ветром и сверхновыми упомянутого более старого населения, на газ низкой плотности. Возраст 10 млн. лет говорит о том, что если в области звездообразования уже начался уход массивных звезд с главной последовательности и происходят вспышки сверхновых, то именно в этих областях, а не в более молодых компактных ассоциациях, связанных с яркими оболочками.

Вопрос о природе слабой диффузной эмиссии ионизованного газа в неправильных галактиках остается открытым уже в течение нескольких десятилетий. В качестве дополнительного источника возбуждения запрещенных линий действительно рассматривается действие ударных волн. В VII Zw 403 проблема усугубляется тем, что диффузное излучение ионизованного газа аномально слабое в этой галактике. (По этой причине Мартин (1987, 1988), проведя наблюдения 14 ближайших неправильных галактик, вообще исключила VII Zw 403 из рассмотрения при обсуждении природы диффузного ионизованного газа.) Учитывая низкую яркость $H\alpha$ излучения в двух упомянутых диффузных областях, результаты нашей оценки относительных интенсивностей в линиях должны быть подтверждены наблюдениями с панорамным спектрографом. Наблюдения с MPFS нами уже проведены, детальный анализ спектра свечения диффузного ионизованного газа и ярких HII областей в галактике будет представлен в работе Лозинской и др. (2006). Здесь лишь отметим предварительный результат: наблюдения с панорамным спектрографом не противоречат приведенным в настоящей работе данным фильтровых наблюдений.

Тем более требуют подтверждения обнаруженные в самой яркой сверхоболочке N1 очень слабые высокоскоростные крылья линий $H\alpha$ и [OIII]. Такие скорости: до $-200 - -300$ км/с от центра линии [OIII] (по уровню около 5% $I_{\max}$) и слабая широкая "подложка" линии $H\alpha$, соответствующая турбулентным скоростям с FWHM до 630 км/с (т.е. дисперсии скоростей газа до 270 км/с), — обнаружены в галактике VII Zw 403 впервые. Если эти результаты будут подтверждены независимыми наблюдениями, столь высокие скорости являются однозначным доказательством ускорения газа на фронте ударной волны.

Пока отметим, что такая же "двухкомпонентная" кинематика: слабые высокоскоростные детали в медленно расширяющихся оболочках — наблюдалась в ряде галактических сверхоболочек сходного размера и была объяснена действием ветра звезд Вольфа–Райе и/или вспышками сверхновых внутри старых сверхоболочек (см. Лозинская, 1998, и ссылки в этой работе). В ярких HII областях других спиральных галактик также наблюдаются слабые высокоскоростные крылья линии $H\alpha$ (см. Релано, Беккман, 2005, и ссылки в

этой работе). Однако в обоих случаях речь идет о скоростях не более 100–200 км/с от центра линии.

Более интересным является факт обнаружения слабого широкого компонента линии Hα с FWHM = 1000 км/с в центральной области BCD-галактики SBS 0335–052 (Прамский, Моисеев, 2003). При этом относительная интенсивность широкого компонента составила около 2% от узкого, т.е. примерно столько же, сколько и в нашем случае. Учитывая более низкую плотность газа в карликовых галактиках, тот же приток энергии сверхновых или звездного ветра действительно должен инициировать ударные волны, распространяющиеся с большей, чем в спиральных галактиках, скоростью. В качестве примера можно привести недавнюю работу Пустильника и др. (2004), посвященную BCD-галактике HS 0837+4717, в которой обнаружена широкая (FWHM = 1300 км/с) и значительно более контрастная (до 16%) подложка в линии Hα. При этом высокоскоростной компонент характеризуется необычно большим значением Бальмеровского декремента, что авторы связывают как с возбуждением линий электронным ударом, так и с высоким внутренним поглощением в области формирования этого компонента.

Еще одна проблема, которая требует дополнительных исследований, – детальное сопоставление кинематики ионизованного и нейтрального газа в центральной области VII Zw 403. Это представляется важным для установления "генетической" связи области звездообразования с плотным комплексом HI в центре галактики.

ЗАКЛЮЧЕНИЕ

Итак, наблюдая с тем же спектральным разрешением со щелевым спектрографом, а с ИФП с разрешением, втрое превосходящим разрешение спектральных наблюдений Линдс и др. (1998), мы не выявили признаков расширения ярких оболочек со скоростью 50–70 км/с.

Скорость расширения самой протяженной оболочки N4, определенная по уширению линии Hα в центральной области, достигает 15–20 км/с. Верхняя граница скорости расширения остальных ярких областей HII, оцененная по полной ширине линий Hα, Hβ и [OIII], не превышает 15–20 км/с. Соответствующий кинематический возраст ярких оболочек HII: 3–4 млн. лет или более полностью согласуется с возрастом связанных с ними компактных OB-ассоциаций 4–5 млн. лет по оценке Линдс и др. (1998).

В наиболее яркой сверхоболочке N1 вокруг самой богатой и молодой ассоциации № 1 обнаружены очень слабые высокоскоростные крылья линий [OIII] (до -200– -300 км/с от центра линии) и Hα (с FWHM до 600 км/с и полным потоком в широком компоненте до 4% от полной интенсивности). Такие скорости наблюдаются в галактике VII Zw 403 впервые.

Слабые волокнистые и диффузные области эмиссии, которые выделены практически во всей центральной области галактики, а также гигантское кольцо ионизованного газа мы сопоставляем с более старым и более "разреженным" звездным населением последней вспышки звездообразования, возраст которого достигает, по оценке Линдс и др. (1998), 10 млн. лет.

Наша оценка полной Hα светимости галактики ($L_{\mathrm{H}\alpha} = (1.49–1.86) \times 10^{39}$ эрг/с) не подтвердила измерения Силича и др. (2002), но хорошо согласуется с результатами более ранних измерений Линдс и др. (1998) и Мартин (1998).

Работа проводилась при финансовой поддержке Российского фонда фундаментальных исследований (гранты № 04-02-16042 и 05-02-16454). А.В. Моисеев благодарит "Фонд содействия отечественной науке" за частичную поддержку данной работы. Работа основана на наблюдательном материале, полученном на 6-м телескопе САО РАН, финансируемом Миннауки РФ (регистрационный номер 01-43), и частично на данных Хаббловского космического телескопа НАСА/ЕСА, взятых из архива Института космического телескопа, управляемого Ассоциацией университетов для исследований в астрономии на основании контракта с НАСА (NAS 5-26555). Мы также благодарим Н. Подорванюка и М. Якима за помощь в проведении наблюдений на 6-м телескопе.

СПИСОК ЛИТЕРАТУРЫ

1. Афанасьев В.Л., Моисеев А.В., Письма в Астрон. журн. **31**, 269 (2005).
2. Боманс (D. Bomans), Rev. Mod. Astron. **14**, 297 (2001).
3. Бурстейн, Хейлес (D. Burstein and C. Heiles), Astrophys. J. Suppl. Ser. **54**, 33 (1984).
4. Кенникутт (R.C. Kennicutt), Ann. Rev. Astron. Astrophys. **36**, 189 (1998).
5. Линдс и др. (R. Lynds, E. Tolstoy, E. J.O'Neil, and D.A. Hunter), Astrophys. J. **116**, 146 (1998).
6. Лира и др. (P. Lira, A. Lawrence, and R.A. Johnson), MNRAS **319**, 17 (2000).
7. Лозинская Т.А., Письма в Астрон. журн. **24**, 285 (1998).
8. Лозинская Т.А., Моисеев А.В., Авдеев В.Ю., Егоров О.В., готовится к печати (2006).
9. Луз, Туан (H.-H. Loose and T.X. Thuan), *Star-forming Dwarf Galaxies and Related Objects* (Ed. D. Kunth, T.X. Thuan, Tran Thanh Van, Gif-sur-Yvette: Editions Frontieres, 1985), p. 73.

10. МакКрэй, Кафатос (R. McCray and M. Kafatos), Astrophys. J. **317**, 190 (1987).
11. Мартин (C.L. Martin), Astrophys. J. **491**, 561 (1997).
12. Мартин (C.L. Martin), Astrophys. J. **506**, 222 (1998).
13. Моисеев (A.V. Moiseev), Bull. SAO **54**, 74 (2002); astro-ph/0211104.
14. Отт и др. (J. Ott, F. Walter, and E. Brinks), MNRAS **358**, 1423 (2005a).
15. Отт и др. (J. Ott, F. Walter, and E. Brinks), MNRAS **358**, 1453 (2005б).
16. Пападерос и др. (P. Papaderos, K.J. Fricke, T.X. Thuan, and H.-H. Loose), Astron. Astrophys. **291**, L13 (1994).
17. Прамский А., Моисеев А., Препринт САО РАН **188**, 1 (2003).
18. Пустильник и др. (S. Pustilnik, A. Kniazev, A. Pramskij, *et al.*), Astron. Astrophys. **419**, 469 (2004).
19. Релано, Беккман (M. Relano and J.E. Beckman), Astron. Astrophys. **430**, 911 (2005).
20. Силич и др. (S. Silich, G. Tenorio-Tagle, C. Munoz-Tunon, and L.M. Cairos), Astron. J. **123**, 2438 (2002).
21. Туан и др. (T.X. Thuan, J.E. Hibbard, and F. Levrier), Astron. J. **128**, 717 (2004).
22. Туан и др. (T.X. Thuan, T.B. Williams, and E. Malumuth), *Starburst and Galaxy Evolution, Proc. of the 22th Moriond Astrophys. Meeting* (Gif-sur-Yvette: Editions Frontieres, 1987), p. 151.
23. Шулте-Ладбек и др. (R.E. Schulte-Ladbeck, U. Hopp, M.M. Crone, and L. Greggio), Astrophys. J. **525**, 709 (1999a).
24. Шулте-Ладбек и др. (R.E. Schulte-Ladbeck, U. Hopp, L. Greggio, and M.M. Crone), Astron. J. **118**, 2705 (1999б).

Astronomy Letters, Vol. 29, No. 2, 2003, pp. 77–90. Translated from Pis'ma v Astronomicheskiĭ Zhurnal, Vol. 29, No. 2, 2003, pp. 95–110.
Original Russian Text Copyright © 2003 by Lozinskaya, Moiseev, Podorvanyuk.

Detailed Kinematic Study of the Ionized and Neutral Gas in the Complex of Star Formation in the Galaxy IC 1613

T. A. Lozinskaya[1*], A. V. Moiseev[2], and N. Yu. Podorvanyuk[1]

[1] *Sternberg Astronomical Institute, Universitetskiĭ pr. 13, Moscow, 119992 Russia*

[2] *Special Astrophysical Observatory, Russian Academy of Sciences, Nizhnii Arkhyz, 357147 Karachai-Cherkessian Republic, Russia*

Received August 20, 2002

Abstract—We carried out detailed kinematic studies of the complex of multiple H I and H II shells that represent the only region of ongoing star formation in the dwarf irregular galaxy IC 1613. We investigated the ionized-gas kinematics by using Fabry–Perot Hα observations with the 6-m Special Astrophysical Observatory telescope and the neutral-gas kinematics by using VLA 21-cm radio observations. We identified three extended (300–350 pc) neutral shells with which the brightest H II shells in the complex of star formation are associated. The neutral-gas kinematics in the complex has been studied for the first time and the H I shells were found to expand at a velocity of 15–18 km s^{-1}. We constructed velocity ellipses for all H II shells in the complex and refined (increased) the expansion velocities of most of them. The nature of the interacting ionized and neutral shells is discussed. © *2003 MAIK "Nauka/Interperiodica"*.

Key words: *galaxy IC 1613, star formation, gas kinematics*.

1. INTRODUCTION

The giant complex of multiple ionized shells (Meaburn *et al.* 1988) in the northeastern sector of IC 1613 is the most prominent structure in narrow-band images of this Local-Group dwarf irregular galaxy located at a distance of 725–730 kpc (Freedman 1988a, 1988b; Dolphin *et al.* 2001) in the Hα, [O III], and [S II] lines.

Most of the bright H II regions (Sandage 1971; Lequeux *et al.* 1987; Hodge *et al.* 1990; Price *et al.* 1990; Hunter *et al.* 1993; Valdez-Gutierrez *et al.* 2001) and the only known supernova remnant in the galaxy [Lozinskaya *et al.* (1998) and references therein] belong to this complex.

The stellar population of the complex is represented by some twenty young stellar associations and clusters (Hodge 1978; Georgiev *et al.* 1999; and references therein).

This multishell complex and the rich stellar grouping represent the only site of ongoing star formation in the galaxy. This region of violent star formation in IC 1613 can probably be considered as a very young and small superassociation (Lozinskaya 2003).

Recent 21-cm radio observations of the complex have shown that extended neutral shells (supershells in standard terminology) are associated with multiple ionized shells (Lozinskaya *et al.* 2001, 2002; Lozinskaya 2002).

The ionized-gas velocities in the region were first measured by Meaburn *et al.* (1988); five spectrograms for the bright part of the complex with poor spatial coverage were used to determine the characteristic expansion velocities of the H II shells, $\sim$30 km s^{-1}. Valdez-Gutierrez *et al.* (2001) constructed the ionized-gas radial-velocity field in the Hα and [S II] lines and estimated the shell expansion velocities from the splitting of the line profile integrated over each of the objects.

The H I and H II shells close up and partially overlap in the plane of the sky. If their sizes along the line of sight and in the plane of the sky are assumed to be comparable, then they can be assumed to be in physical contact with one another.[1]

Deep narrow-band Hα images revealed a chain of bright compact emission-line objects at the boundary of the two closing shells in the complex. Spectroscopic observations show that the compact objects are early-type giants and supergiants (Lozinskaya

[*] E-mail: lozinsk@sai.msu.ru

[1] The galaxy is inclined at an angle of 30° to the plane of the sky and the gaseous-disk thickness 500–700 pc, as estimated by Afanasiev *et al.* (2000), is comparable to the size of the multishell complex. Therefore, a chance projection of physically unrelated shells located at different distances is unlikely.

1063-7737/03/2902-0077$24.00 © 2003 MAIK "Nauka/Interperiodica"

Table 1. A log of IFP observations for IC 1613

Date of observation	IFP type	T_{exp}, s	Seeing
Nov. 1, 2000	IFP235	32×240	$2''.0$
Sep. 12, 2001	IFP501	36×200	$1''.8$

et al. 2002). The characteristic ionized- and neutral-gas morphology suggests that the H I and H II shells physically interact in the region of the stellar chain (see also Section 3).

Thus, the complex of star formation shows evidence of the possible collision between expanding ionized and neutral shells, the interaction of ionized shells with the surrounding H I shells, and the like. This evidence suggests that the birth of new-generation stars triggered by shell collisions is probable here (Chernin and Lozinskaya 2003). That is why a detailed study of the structure and kinematics of the ionized and neutral gas in the multishell complex is of current interest.

The neutral-gas kinematics in the complex of star formation has not yet been investigated.

Our goal is to study in detail the kinematics of the neutral and ionized gas components in the shells that constitute the complex of star formation with high spatial and spectral resolutions.

To study the kinematics of the ionized shells, we carried out Hα observations with a scanning Fabry–Perot interferometer attached to the 6-m Special Astrophysical Observatory (SAO) telescope. The kinematics of the neutral shells was studied by using VLA 21-cm radio observations.

The techniques for optical and radio observations and for data reduction are described in Section 2. In Section 3, we use our ionized- and neutral-gas observations to analyze the overall structure of the multishell complex in the plane of the sky. The results of our kinematic study for the H I and H II shells in the complex are presented in Sections 4 and 5, respectively. Our results and conclusions regarding the nature of the multishell complex that follow from them are discussed in Section 6.

2. INTERFEROMETRIC Hα AND 21 cm OBSERVATIONS

Fabry–Perot Observations with the 6-m SAO Telescope and Data Reduction

Interferometric Hα observations were carried out at the prime focus of the 6-m SAO telescope using a scanning Fabry–Perot interferometer (IFP). The interferometer was placed inside the SCORPIO focal reducer, so the equivalent focal ratio was (F/2.9). A brief description of the focal reducer is given on the Internet (http://www.sao.ru/~moisav/scorpio/scorpio.html); the SCORPIO capabilities in IFP observations were also described by Moiseev (2002). The detector was a TK1024 1024×1024-pixel CCD array. The observations were performed with 2×2-pixel hardware averaging to reduce the readout time, so 512×512-pixel images were obtained in each spectral channel. The field of view was $4'.8$ for a scale of $0''.56$ per pixel. An interference filter with FWHM = 15 Å centered on the Hα line was used for premonochromatization.

A log of IFP observations is given in Table 1. For our observations, we used two different Queensgate ET-50 interferometers operating in the 235th and 501st orders of interference at the Hα wavelength (designated in Table 1 as IFP235 and IFP501, respectively). IFP235 provided a spectral resolution of FWHM $\approx$ 2.5 Å near the Hα line (or $\sim$110 km s^{-1}). The separation between neighboring orders of interference, $\Delta\lambda = 28$ Å, corresponded to a range of $\sim$1270 km s^{-1} free from order overlapping. The spectral resolution of IFP501 was $\sim$0.8 Å (or $\sim$40 km s^{-1}) for a range of $\Delta\lambda = 13$ Å (or $\sim$590 km s^{-1}) free from order overlapping.

During the exposure, we sequentially took interferograms of the object for various IFP plate spacings. Therefore, the number of spectral channels was 32 and 36 and the size of a single channel was $\delta\lambda \approx$ 0.87 Å ($\sim$40 km s^{-1}) and $\delta\lambda \approx$ 0.36 Å ($\sim$16 km s^{-1}) for IFP235 and IFP501, respectively.

We reduced our interferometric observations by using the software developed at the SAO (Moiseev 2002). After the primary data reduction, the subtraction of night-sky lines, and wavelength calibration, the observational material represents "data cubes" in which each point in the 512×512-pixel field contains a 32-channel or 36-channel spectrum. We performed optimal data filtering—Gaussian smoothing over the spectral coordinate with FWHM = 1.5 channels and spatial smoothing by a two-dimensional Gaussian with FWHM = 2–3 pixels—by using the ADHOC software package.[2]

The accuracy of the wavelength calibration using the calibration-lamp line was less than 3 km s^{-1}. Our radial-velocity measurements of the night-sky λ6553.617 Å line revealed a systematic shift when measuring the absolute values of the radial velocities: -8 ± 3 km s^{-1} for IFP501 and 15 ± 8 km s^{-1}

[2]The ADHOC software package was developed by J. Boulestex (Marseilles Observatory) and is publicly available in the Internet.

for IFP235. It should be noted, however, that these values were most likely overestimated, because the sky-line intensity varied during the scanning time.

The bulk of the observational data used here were obtained with IFP501, which provided a higher spectral resolution. Only when analyzing the observational data for the supernova remnant, where the weak line wings were observed at velocities outside the range free from order overlapping for IFP501, did we additionally use observations with IFP235.

Observations in the 21-cm Line and Data Analysis

Based on VLA 21-cm observations, we mapped the H I distribution with a high angular resolution and studied the neutral-gas kinematics in an extended region of the galaxy that included the complex of star formation. An application for the project to study the neutral-gas structure and kinematics in IC 1613 was made by E. Wilcots; the first results were published by Lozinskaya *et al.* (2001).

The data given in Sections 3 and 4 were obtained by combining VLA observations in configurations B, C, and D; the width of a single channel in radial velocity was 2.57 km s^{-1}. We smoothed the data with the Hunning function. The data were calibrated by the standard method and transformed into maps using the AIPS software package.

The reduced data are presented in the form of a data cube with an angular resolution of $7''.4 \times 7''.0$, which corresponds to a linear resolution of $\sim$23 pc.

To map the integrated 21-cm line intensity distribution, we summed only 40 of the 127 possible spectral channels, because no galactic line emission was detected in the remaining channels.

3. THE OVERALL STRUCTURE OF THE COMPLEX OF STAR FORMATION IN THE PLANE OF THE SKY

Figure 1a shows the monochromatic Hα image of the multishell complex obtained by integrating the emission over all spectral channels (in the velocity range from -2 to -584 km s^{-1}) using our interferometric observations with IFP501. The arrows indicate the objects discussed in Section 5: the chain of early-type giants and supergiants mentioned above, the only Of star in the galaxy identified by Lozinskaya *et al.* (2002), the only known supernova remnant—the nebula S8 (Sandage 1971), and the bright H II region no. 40a, b from the list by Hodge *et al.* (1990). Also shown in the figure are the ionized-shell numbers from the list by Valdez-Gutierrez *et al.* (2001). (Below, we use the notation adopted in this paper for uniformity.)

All of the brightest ionized shells in IC 1613 are concentrated in the complex of star formation (Valdez-Gutierrez *et al.* 2001; Lozinskaya *et al.* 2002). In Fig. 1a, these brightest regions are overexposed to show the faintest H II shells. The faint filamentary structures in shells R6, R7, R8, and R3 are clearly seen in the figure; we also managed to detect weak emission from thin filaments in several other regions of the complex.

The chain of bright early-type stars is located at the bright boundary of the ionized shell R1 adjacent to shell R2. This region falls within square N27 in Fig. 3 from Valdez-Gutierrez *et al.* (2001) and includes the nebulae S10 and S13, according to the classification of Sandage (1971). Association no. 17 from the list by Hodge (1978) [its eastern part is designated as no. 25 in the list by Georgiev *et al.* (1999)] also lies here.

Our 21-cm H I observations in IC 1613 with a high angular resolution allow us to compare the H I and H II distributions in the complex of star formation. The results obtained from these observations are presented in Figs. 1b and 2a. Figure 1b shows the 21-cm image of the northwestern galactic sector obtained by integrating the emission over 40 channels in the velocity range from -279 to -178 km s^{-1} (indicated by shades of gray) superimposed on the monochromatic Hα image (indicated by isophotes). The latter is represented only by the brightest regions. The H I intensity distribution in the entire galaxy is shown in Fig. 2a (see Section 4).

Even the first observations by Lake and Skillman (1989) with an angular resolution of $60'' \times 60''$ showed that the complex of ionized shells is localized in the region of the brightest spot on the H I map of IC 1613. The multishell structure of this bright spot is clearly seen in Figs. 1b and 2a: the three most prominent H I shells in the galaxy surround the chain of bright ionized shells. Below, these bright neutral shells are called I, II, and III for definiteness.

The central coordinates, sizes, and expansion velocities of the shells estimated in Section 4 are listed in Table 2. The third column gives the shell sizes along two axes in arcsec (upper row) and the mean radius in pc determined by them (lower row).

The shells identified in the star-forming region are 300–500 pc in size. These sizes fall within the region of the peak in the size distribution of giant H I and H II shells in the LMC and SMC (see Meaburn 1980; Kim *et al.* 1999; Staveley-Smith *et al.* 1997).

In addition to these three brightest and most prominent H I shells, we identified much larger ring-shaped and arc-shaped structures in IC 1613, with sizes up to 1–1.5 kpc, supergiant shells in the terminology of Meaburn (1980). These are clearly

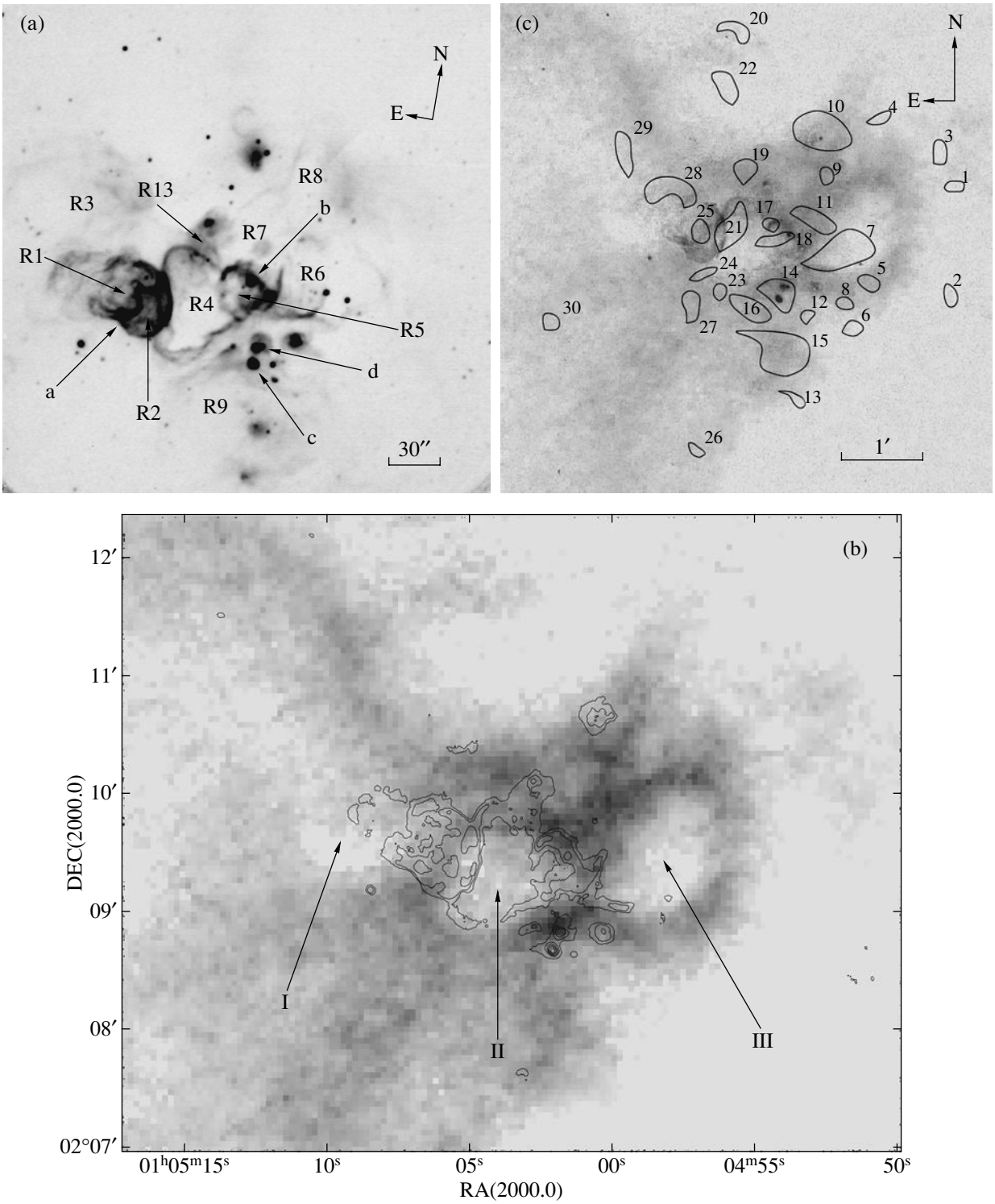

Fig. 1. (a) The monochromatic Hα image of the multishell complex obtained with a Fabry–Perot interferometer on the 6-m SAO telescope. The ionized shells R1–R9 and R13 from the list of Valdez-Guterrez *et al.* (2001) studied here are labeled. The arrows indicate: a—the chain of early-type supergiants at the boundary of shell R1; b—the only Of-type star identified by Lozinskaya *et al.* (2002); c—the only supernova remnant in IC 1613; d—object no. 40a, b from the list of H II regions by Hodge *et al.* (1990). (b) The H I intensity distribution (indicated by shades of gray) superimposed on the monochromatic Hα image of the region (the isophotes corresponding to the brightest regions in Fig. 1a are shown). The Roman numericals I, II, and III mark the three neutral shells investigated here. (c) The boundaries of the OB associations identified by Georgiev *et al.* (1999) superimposed on the intensity distributions in the 21-cm line (indicated by shades of light gray) and in the Hα line (indicated by shades of dark gray) .

Table 2. Parameters of the H I shells in the complex of star formation

Shell	Central coordinates (2000)	Size, arcsec R, pc	V(exp), km s^{-1}	Age, Myr
I	$1^h5^m10^s$	$\sim$97		
	2°9′45″	172		
II	$1^h5^m4\overset{s}{.}5$	73 × 81	12–17	5.6
	2°9′19″	136		
III	$1^h4^m58^s$	73 × 97	16–18	5.3
	2°9′32″	150		

seen in the 21-cm image of the entire galaxy shown in Fig. 2a (see also Section 6).

As follows from Figs. 1a and 1b, a one-to-one correspondence between the neutral and ionized structures in size and localization is observed only in one case: the ionized shell R4 fits well into its surrounding neutral shell II. The remaining bright H II shells are smaller than the neutral shells and are located irregularly: the ionized shell R1 lies within the neutral shell I near its western boundary rather than in the central cavity; R6 lies within shell III near its eastern boundary; the ionized shells R2 and R5 fall on the bars between shells I and II and between shells II and III, respectively. As was shown by Kim *et al.* (1999), the giant H I shells in the LMC are also interrelated differently with H II shells and supershells, which reflects the different evolutionary stages of star formation in the region. This issue is discussed in more detail in Section 6.

The boundary of the ionized shell R1 with the chain of blue giants and supergiants coincides with the thinnest arc-shaped H I bar between the two H I shell structures. The characteristic morphology of the ionized and neutral shells suggests that they are in physical contact: the thin neutral arc adjoins the ionized shell in the region of the stellar chain from the outside and the two shells in this region have the same radius of curvature.

The stellar component of the complex represented by some thirty stellar associations and clusters is superimposed on the Hα and 21 cm images in Fig. 1c. The figure shows the association boundaries that correspond to a new breakdown of the stellar population into separate groups in Georgiev *et al.* (1999). Here, a number of associations from the list by Hodge (1978) were split into several smaller groups.

4. NEUTRAL-GAS KINEMATICS IN THE COMPLEX

The data cube that we constructed from the 21-cm observations allows us to analyze the H I distribution and kinematics in the entire galaxy. The kinematics of the southeastern region of IC 1613 around a WO star was studied previously (Lozinskaya *et al.* 2001). Here, we consider in detail the neutral-gas kinematics in the complex of star formation for the first time.

Our 21-cm observations show that this complex stands out as the dynamically most active region in IC 1613. Velocities of internal neutral-gas motions from $-195\ldots-200$ to $-250\ldots-255$ km s^{-1} are observed in the region of the complex ($\Delta RA = 1^h2^m20^s$–$1^h2^m40^s$, $\Delta D = 1°52'$–$1°55'$) against the background of a smooth systematic variation in the mean H I velocity along the galaxy that was pointed out by Lake and Skillman (1989).

In searching for the possible expansion of the H I shells in the complex, we constructed position–radial velocity diagrams in several bands:

1—in the band that crosses the pair of shells I and II through their centers;

2—in the band that crosses the pair of shells II and III in the same way;

3—in the band that passes through the stellar chain at the boundary of shells I and II;

4, 5, and 6—in the bands that cross each of the three shells I, II, and III, respectively, in the directions perpendicular to scans 1 and 2;

7—in the band that includes scans 15 and 16 in the Hα line (see Section 5) and that passes through the only supernova remnant in IC 1613.

The directions of scans 1–7 on the H I map are shown in Fig. 2a. The position–radial velocity diagrams constructed for these scans are shown in Fig. 2b.

We chose the band width when scanning in such a way that only the central shell region and the two peripheral regions in the direction of each scan fell within this width, which corresponded to 11 pixels or 33″ in the sky.

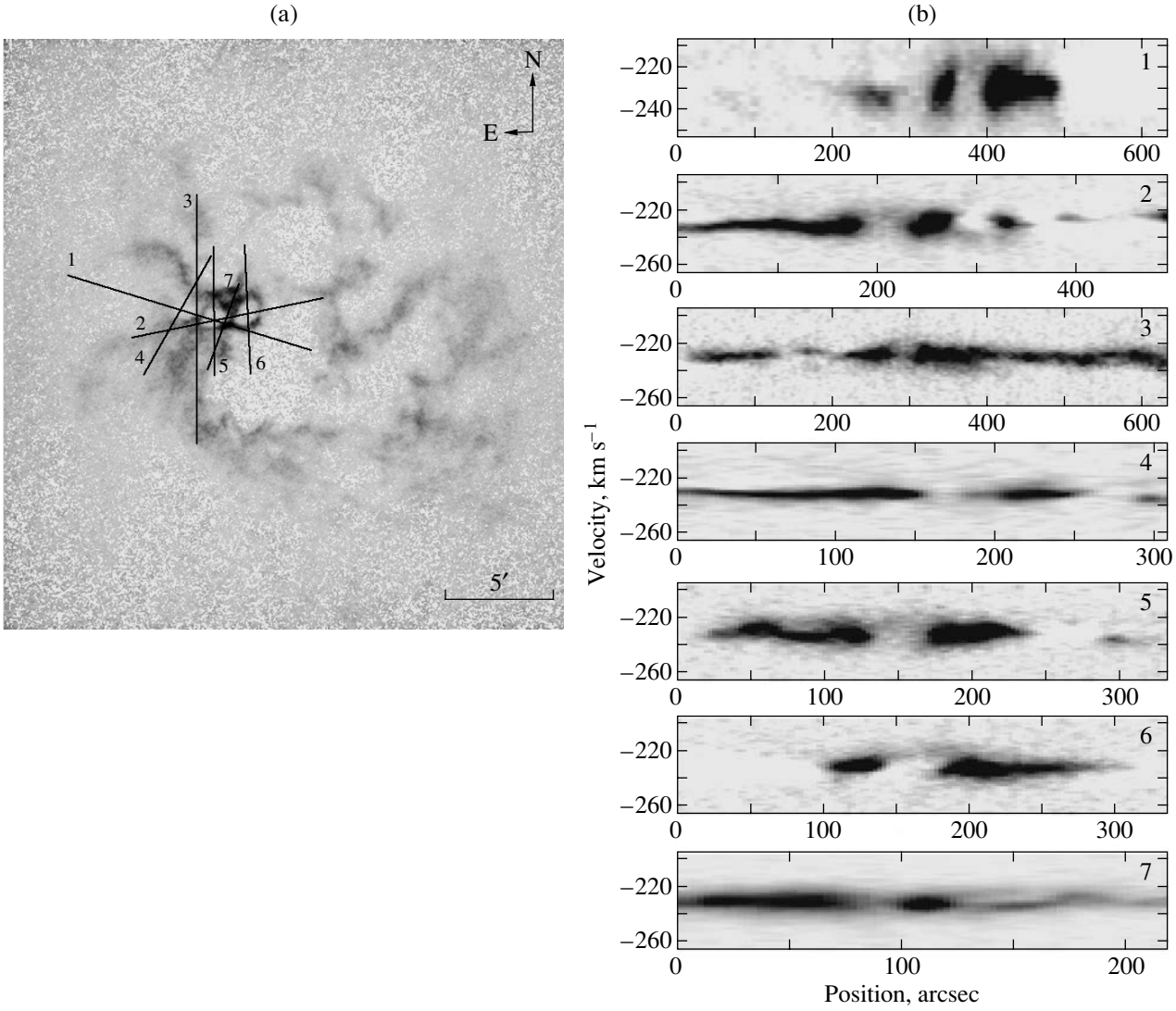

Fig. 2. (a) The localization of scans 1–7 shown in Fig. 2b on the H I map of the galaxy. The numbers are given at the beginning of each scan. (b) The position–H I velocity diagrams for scans 1–7 (the velocity is heliocentric).

The mean H I velocity in the region of the complex that was determined from the emission of "unaccelerated" gas detected on all scans 1–7 outside shells I, II, and III discussed below is $V_{\rm Hel} = -230 \pm 5$ km s^{-1}. This value is in good agreement with the estimate obtained by Lake and Skillman (1989) for this part of the galaxy from low-angular-resolution observations.

Figure 2b shows the radial-velocity variation with distance typical of an expanding shell at least for the two objects denoted by II and III. The characteristic arc-shaped pattern of velocity variation (half of the "velocity ellipse") is seen both on the scans along the pairs of shells I–II and II–III and on the scans that cross each of shells II and III in a perpendicular direction (see Fig. 2b). Evidence of shell-II expansion is seen on scan 1 (370–400 arcsec), scan 2 (180–230 acrsec), and scan 5 (130–170 arcsec). Scan 2 (280–310 arcsec) and scan 6 (140–190 arcsec) exhibit shell-III expansion. In both cases, one side of the expanding shell is clearly seen. The difference between the unaccelerated-gas velocities on the periphery of shell II (from −225 to −230 km s^{-1}) and on its approaching side (from −240 to −242 km s^{-1}) gives an expansion velocity $V(\exp) \sim 12$–17 km s^{-1}. For shell III, we find the expansion velocity from the difference between the unaccelerated-gas velocities on the periphery (from −228 to −230 km s^{-1}) and on the receding side (−212 km s^{-1}) to be $V(\exp) \sim 16$–18 km s^{-1}. The neutral shell I exhibits no distinct expansion.

The inferred expansion velocities of the two H I shells in IC 1613 fall within the region of the peak in

the velocity distribution of neutral supershells in the LMC (Kim *et al.* 1999).

The only supernova remnant in IC 1613 lies at the outer boundary of the densest H I layer in the galaxy that bounds shell II in the south (see Fig. 1). Another, fainter neutral shell in which the supernova remnant is located may adjoin the bright shell II in the south. Scan 7 (120–170 arcsec) shows traces of expansion of this fourth neutral shell. The supernova remnant lies at the inner boundary of this shell (~120 arcsec). This scenario—a supernova explosion inside a cavity surrounded by a dense shell and a collision of the expanding remnant with the shell wall—was suggested by Lozinskaya *et al.* (1998) to explain the peculiarity of this remnant, which combines the properties of young and old objects and which has high optical and X-ray brightnesses.

The region at the boundary between shells I and II where the chain of early-type giants and supergiants is located exhibits high neutral-gas velocities. A deficit of 21-cm brightness is observed in this region on scan 3 (280–310 arcsec). This deficit stems from the fact that emission from only the thin bar between shells I and II is detected here when scanning. However, this weak emission is observed over a wide velocity range, from $\simeq -250$ to $\simeq -210$ km s^{-1} at 20–30% I(max).

Our expansion velocities and the corresponding kinematic ages of the bright neutral shells in the complex of star formation are given in Table 2.

5. IONIZED-GAS KINEMATICS IN THE COMPLEX

To study in detail the kinematics of the ionized shells using our Hα observations with IFP501, we constructed position–radial velocity diagrams for thirty scans, which cover the entire complex of star formation almost uniformly. For each of the chosen directions, we constructed two or three scans of different widths: from 1 to 40 pixels (from 0.5 to 24″). Figure 3a shows the localization of some of these scans. The width of scans 14 and 17 is 21 pixels or 12″; the width of the remaining scans shown in Fig. 3 is 11 pixels or 6″.

The mean velocity of the unshifted feature in the H II emission line in the complex of star formation is from −230 to −240 km s^{-1}. We also observe a smooth velocity variation in the complex between −220 km s^{-1} in the southeast and −260 km s^{-1} in the northwest, in agreement with the results of Valdez-Gutierrez *et al.* (2001).

As was shown in Section 3, the elongated system of the brightest ionized shells, including R1, R2, R4, R5, and R6, is associated with the neutral shells I, II, and III.

Two scans (v1 and v2) cross this chain of bright shells in directions that roughly coincide with scans 1 and 2 over the neutral shells I–II and II–III, respectively (see Section 4).

The two scans clearly show Hα splitting along the entire length of the chain and reveal the characteristic configuration of the velocity ellipse for individual shells and, possibly, for the chain of bright shells as a whole. The typical velocities are about −290 . . . −300 km s^{-1} for the approaching sides of the elongated system of bright shells and about from −190 . . . −200 km s^{-1} for its receding sides. We successively consider all the ionized shells of this system.

Shells R1 and R2 and the Chain of Stars at Their Boundary

Shells R1 and R2 and the region at their boundary where the chain of young stars is located were scanned repeatedly, in different directions, and in bands of different widths. All of the scans passing through the central regions of these shells clearly reveal the characteristic configuration of the velocity ellipse related to their expansion.

The mean velocity of the unperturbed gas at the eastern boundary of shell R1 is −240 km s^{-1}. The local velocity ellipses on scan v2 suggest that the bright western part of shell R1 (45–55 arcsec) expands at a velocity of 50–60 km s^{-1} relative to this unshifted feature: the velocity of the approaching side is −290 km s^{-1}. In shell R2 (55–80 arcsec), the velocities of the bright approaching and faint receding sides are from −280 to −300 and −170 km s^{-1}, respectively. On scan v1 that crosses the same region in a different direction, we see a similar arc structure in region R2 and individual clumps in region R1.

Several scans that cross the system of bright shells in the directions perpendicular to v1 and v2 also clearly reveal an expansion of shells R1 and R2. Scans 3a, 3b, and 4 clearly show that shell R1 expands at a velocity of 60–70 km s^{-1} (up to 100 km s^{-1} in its bright southern part). The bright regions on the shell periphery exhibit the unshifted line component at a velocity of from −230 to −250 km s^{-1}; the velocities of the two sides of the expanding shell are −180 and −320 km s^{-1} (scan 3). Scan 4 also shows that the bright southern part of shell R1 expands faster than does its northern part: the velocity of the approaching side is the same in the entire shell, being about −300 km s^{-1}; the velocity of the receding side is −150 km s^{-1} in the south and −180 km s^{-1} in the north. Scan 2 that crosses the

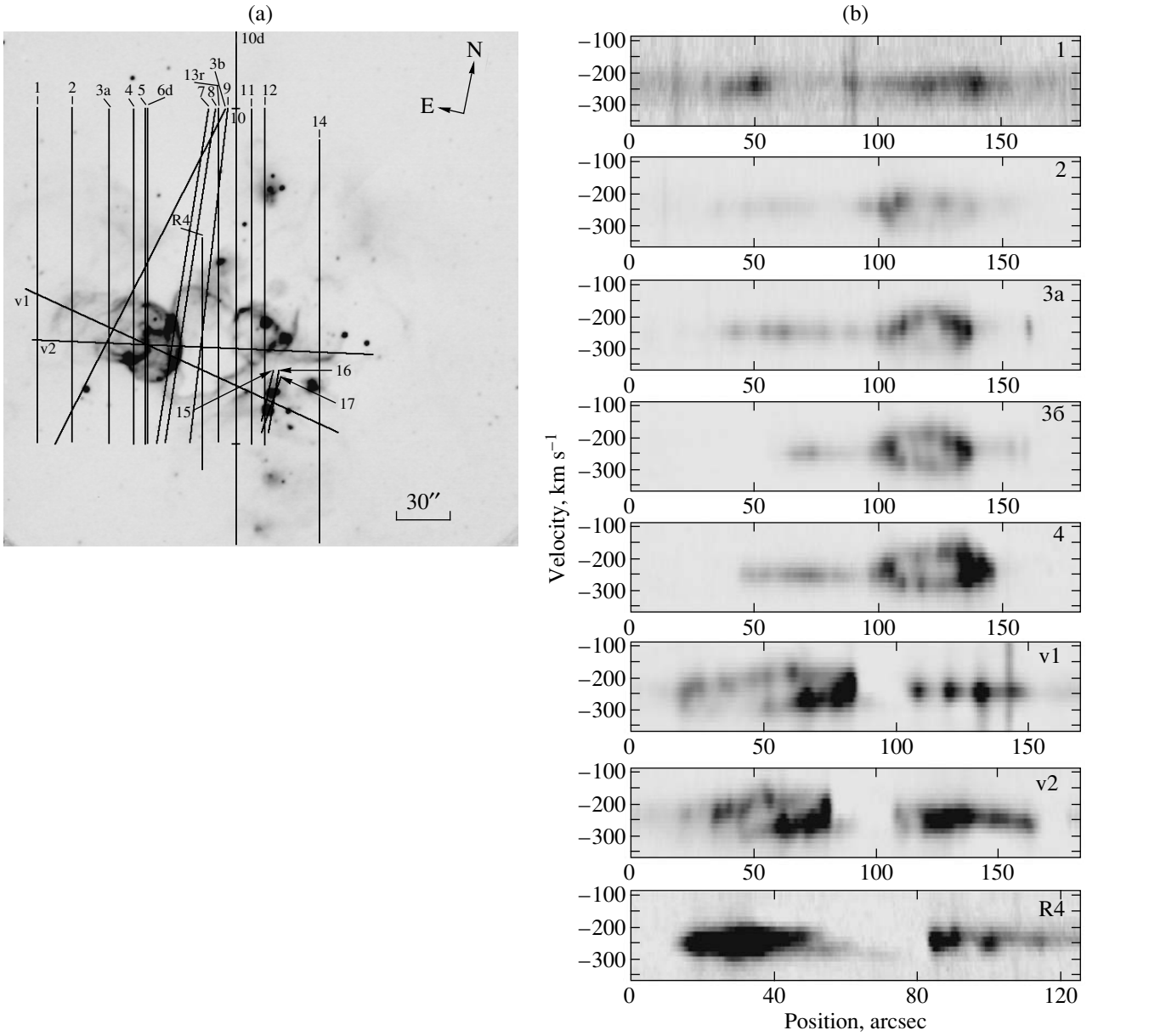

Fig. 3. (a) The localization of the scans shown in Figs. 3b, 3c, and 3d in the Hα image of the complex. The numbers are given at the beginning of each scan. (b) The position–H II velocity diagrams for scans nos. 1, 2, 3a, 3b, 4, v1, v2, and R4 (the velocity is heliocentric). (c) Same as Fig. 3b for scans nos. 5, 6d, 7, 8, 9, 10, and 10d. (d) Same as Fig. 3b for scans nos. 11, 12, 13r, 14, 15, 16, 17.

fainter eastern half of shell R1 also reveals evidence of its expansion. The unshifted features on the shell periphery have a velocity of -240 km s^{-1}, the bright clump in the northern part is observed at a velocity of -215 km s^{-1}, and the faint approaching side has a velocity of -300 km s^{-1}.

Valdez-Gutierrez *et al.* (2001) identified two features in the integrated line profile at velocities of -216 and -274 km s^{-1} in shell R1 and two features at velocities of -244 and -147 km s^{-1} in shell R2. All these values fall within the range determined by the velocity ellipses for these two shells.

The region at the boundary between shells R1 and R2 that, in the 21-cm line, corresponds to the thin bar between the neutral shells I and II, where the chain of early-type stars is located, is represented by scans 5 and 6d. Scan 6d exhibits a bright emission feature in the Hα line at a velocity of about $-270\ldots-280$ km s^{-1}, which corresponds to the bright part of shell R1 with the chain of stars, traces of stellar continuum emission, and a weaker emission feature

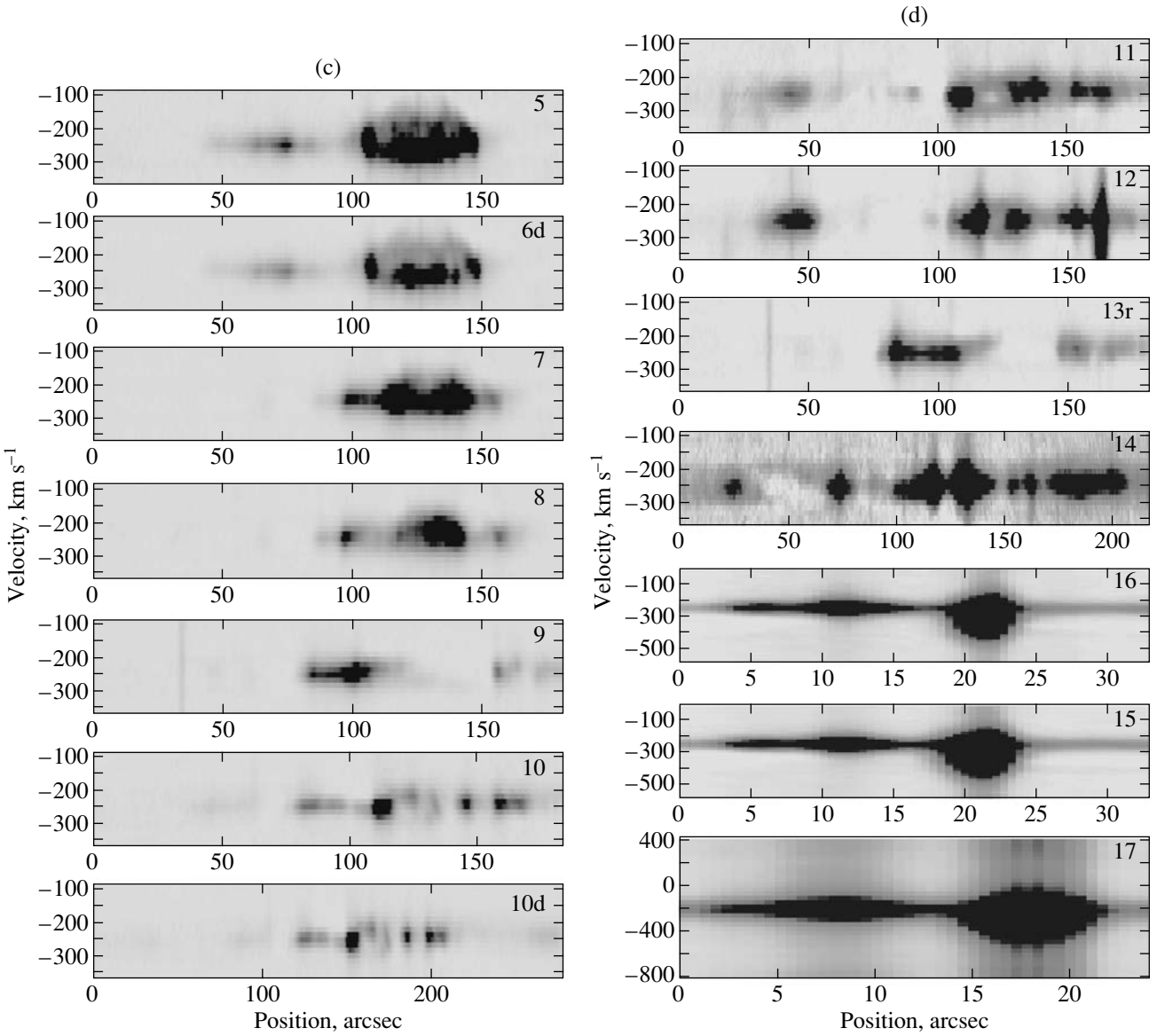

Fig. 3. (Contd.)

in the region of shell R2 at higher velocities, up to $-130\ldots-150$ km s^{-1}. This entire region on scan 6d (105–150 arcsec) widens toward the center, with the dense clumps on the periphery and the gas in the remote part (at 55–85 arcsec) emitting at a velocity of from -240 to -250 km s^{-1}. The observed picture suggests an asymmetric gas expansion in shell R2 at a velocity of about 30 km s^{-1} into a denser medium and at a velocity of about 100–110 km s^{-1} into a less dense medium. We associate this effect with shell R2, because the boundary of the expanding region on scan 6d coincides with the boundary of this shell. Scan 5 also exhibits irregular motions of the receding gaseous clumps up to velocities of from -150 to -160 km s^{-1}; these are probably related to the local action of the wind from the chain stars. The velocity of the near side of shell R2, which is brighter and more regular, reaches from -280 to -290 km s^{-1}. Since the bright clumps on the periphery of the velocity ellipse coincide with the boundaries of shell R2, which is larger than shell R1 here, we believe that the velocity ellipse on scans 6 and 5 also reflects the expansion of shell R2.

Shell R4 and Its Possible Collision with Shell R2

R4 is the most extended shell in the chain of bright shells and the only one that completely fits into the surrounding neutral shell. Its central regions

are characterized by weak emission. Scans R4, 9, v1, v2, and 13r show a deficit of gas in the central cavity and intense emission on the periphery at a velocity of about -240 km s^{-1}. The weak Hα emission features in the central cavity exhibit a blueshift and a redshift relative to this velocity. Weak diffuse emission is observed at velocities up to -200 km s^{-1} (scan R4, 40–55 arcsec; scan 9, 110–120 arcsec) in the north of the cavity and up to -290 km s^{-1} (scan R4, 55–70 arcsec; scan 9, 120–130 arcsec) in the south. The shell expansion velocity determined by these features is $\sim$45 km s^{-1}.

The monochromatic Hα image shows a characteristic lenticular structure at the boundary between shells R2 and R4. This structure can be a manifestation of the dense gaseous ring formed in the region of head-on collision between these shells and oriented almost edge-on to the observer. The formation of this ring follows from three-dimensional numerical simulations of the collision between two expanding shells [see Chernin *et al.* (1995) and references therein].

In the region that corresponds to the eastern boundary of shell R4 (scan 7, 95–115 arcsec), we see no significant deviations from the mean ionized-gas velocity of -240 km s^{-1} in the complex. The inclined ring in the region of collision with shell R2 is observed as two bright unaccelerated clumps and high-velocity motions between them (scan 7, 120 and 140 arcsec) and as a bright structure with high velocities of the internal motions (scan 8, from 120 to 140 arcsec). The velocities of the faint features between the bright clumps are at a maximum; they reach -140 and -340 km s^{-1} at 7% I(max) on scan 7a and -160 km s^{-1} at 10% I(max) on scan 8.

Shell R5

A characteristic arc structure (110–135 arcsec on scan 10 and 150–175 arcsec on scan 10d) is observed at the boundary between shells R4 and R5. This structure may represent the half of the velocity ellipse that corresponds to the receding side of shell R5. We estimated the expansion velocity to be 40–50 km s^{-1}.

Scan 11 (105–135 arcsec) also shows a symmetric expansion of shell R5 at a velocity of about 35–45 km s^{-1}; the velocities of the two sides of the shell are -220 and -310 km s^{-1}.

A compact group of stars with the only Of star identified in the galaxy (Lozinskaya *et al.* 2002) is located on the periphery of shell R5. Scan 12 shows this star in a region of 118 arcsec; the star is surrounded by a bright compact H II region. Given the IFP501 instrumental profile, the line width in the H II region at 0.5I(max) is 50 ± 5 km s^{-1}.

Shell R13 and the H II Region no. 55 from the List of Hodge et al. (1990)

Shell R13, which adjoins shell R4 in the north, consists of two components: a diffuse shell and the bright compact H II region no. 55 (Hodge *et al.* 1990). The bright H II region shows a mean velocity of about $-230 \ldots -240$ km s^{-1} [in agreement with the measurements of Valdez-Gutierrez *et al.* (2001)] and stellar continuum at the center (scan 13r, position 85 arcsec). A group of stars may be located here, because area of the stellar continuum is larger than that in other regions of the same scan. The line width in the bright H II region reaches 57 km s^{-1} at 0.5I(max).

The diffuse shell R13 also exhibits the mean radial velocity of from -230 to -240 km s^{-1} typical of the entire complex. We found no clear evidence of shell-R13 expansion.

Shells R6 and R8

According to our data, the expansion velocity of shell R6 does not exceed 20 km s^{-1}: the velocities of the northern and southern shell boundaries (scan 14, 75 and 120 arcsec, respectively) and the velocity in the central region (about 100 arcsec on the same scan) are about -255 km s^{-1}.

Shell R8 exhibits the characteristic arc-shaped pattern of radial-velocity variation of the far side. The velocity of the bright boundary regions (scan 14, 25 and 75 arcsec) is -255 km s^{-1} and the velocity of the faint far side reaches -190 km s^{-1}, which gives an expansion velocity of about 65 km s^{-1}. We detected no emission from the even fainter near side.

The Bright H II Regions nos. 40a,b and 39 (Hodge et al. 1990)

Valdez-Gutierrez *et al.* (2001) provided the following parameters averaged over the group of object nos. 40a,b and 39: the velocity at the line peak, -239 km s^{-1}, and the velocity dispersion, 10.4 km s^{-1}. We separately scanned the two bright sources no. 40a (scan 16) and no. 40b (scan 15); both also include the emission from the more extended and fainter region no. 39. As follows from Fig. 3d, the velocity at the peak of these three regions is -240 km s^{-1}. The H II region no. 39 is characterized by a narrow Hα line with no wings with the FWHM determined by the IFP501 instrumental profile along the entire length. At the same time, both bright compact H II regions nos. 40a and 40b (scans 16 and 15, respectively) exhibit weak emission at 10% I(max) in the velocity range from -310 to -175 km s^{-1}.

The Supernova Remnant

The bright nebula S8 (Sandage 1971), the supernova remnant, shows emission over the entire velocity range from 0 to −600 km s^{-1} determined by the IFP501 free spectral range (scans 15 and 16, 19–23 arcsec). The remnant emission is observed with IFP235 at least in the velocity range from +200 to −600 km s^{-1} (scan 17). An interfering emission emerges at higher velocities, +400 and −800 km s^{-1}. This emission is probably attributable to an improper allowance for the night-sky 6554-Å line.

This result is in complete agreement with previous observations of Lozinskaya *et al.* (1998) and Rosado *et al.* (2001).

All of the ionized shells in the complex of star formation for which we managed to reliably detect their expansion based on the velocity ellipse are collected in Table 3. For comparison, the fourth column of the table gives the expansion velocities of the same shells determined by Valdez-Gutierrez *et al.* (2001) from line-profile splitting. Since the shell sizes were measured from our deep images, they differ slightly from those of Valdez-Gutierrez *et al.* (2001). It should be noted that, given the irregular shape of most shells, the representation of the observed shells by regular ellipses is arbitrary and subjective in nature.

In estimating the kinematic ages of the shells from their radii and expansion velocities, we used the classical theory of wind-blown bubbles ($t = 0.6\,R/V$). In addition to the age, the mean radius and expansion velocity used for its estimation are given in parentheses (in the form R/V) in the last column of the table. The ages of shells R3 and R6 correspond to the data from Valdez-Gutierrez *et al.* (2001).

Table 3. Parameters of the bright ionized shells in the complex

Shell	Size, pc	V_{exp}, km s^{-1}	V_{exp}(V−G), km s^{-1}	Age, Myr
R1	188 × 138	60–75	29	0.7 (81/67)
R2	145 × 88	50–60	49	0.6 (58/55)
R3	258 × 209		30	1.9 (C–D)
R4	234 × 138	40–45	32	2.2 (93/42)
R5	113 × 113	30–50	38	0.8 (56/40)
R6	226 × 184	≤20	25	2.0 (V–G)
R8	217 × 154	≃65	26	1.7 (185/65)

6. DISCUSSION

The radial-velocity variations with distance from the center of the ionized shells (velocity ellipses) found here are generally in agreement with the observations of Meaburn *et al.* (1988) and Valdez-Gutierrez *et al.* (2001), but they give a clearer picture of expansion. In the latter paper, the conclusions regarding expansion were drawn from integrated line profile splitting in the shells. Since bright peripheral regions or individual bright clumps can give a significant contribution when averaging over the shell or over its separate fields, the expansion velocity determined in this way can be underestimated. The large brightness difference between the approaching and receding sides of the shells can also cause the expansion velocity inferred from line splitting to be underestimated. The constructed velocity ellipses allow these difficulties to be circumvented. The expansion velocity can be determined from the velocity ellipse by taking into account the geometrical projection even if only one shell side is observed, as in the case of R8. Indeed, as we see from Table 3, our estimates of the expansion velocity in most shells gave higher values than those in Valdez-Gutierrez *et al.* (2001).

In several shells, we detected a distinct asymmetry in their expansion: the approaching and receding sides have different velocities.

On scans v1 and v2 crossing the entire chain of the brightest ionized shells, we clearly see that all of them generally have similar velocities but an irregular, clumpy brightness distribution. This irregular brightness distribution may have served as the basis for the conclusion of Valdez-Gutierrez *et al.* (2001) that shells R1 and R2 are at different distances, because they are observed at different radial velocities. These scans show that individual bright clumps on the two sides of these shells actually have different velocities but they all fall within our velocity ellipses. According to our measurements, the approaching and receding sides of the two shells have similar velocities: from −290 to −320 and from −170 to −190 km s^{-1}, as inferred from different scans in R1; from −280 to −300 and −170 km s^{-1} in R2. The far side is brighter in R1 and the near side is brighter in R2. We also noted that the southern part of shell R1 recedes faster ($V = -150$ km s^{-1}) than does its northern part ($V = -180$ km s^{-1}).

Taking into account the structure of R1 and R2 in different velocity ranges, we do not rule out the possibility that these shells generally constitute a single dumbbell-like structure formed on both sides of a dense neutral-gas layer. However, this assumption requires additional observational confirmation.

Valdez-Gutierrez *et al.* (2001) showed that the the energy of the stellar wind from nearby OB associations was enough for most of the ionized shells to be formed. The rapidly expanding shells R1 and R2

constitute an exception. We further increased the expansion velocity of these two objects (see Table. 3) but simultaneously found additional, most intense sources of the stellar wind at their boundary—early-type supergiants and giants (Lozinskaya *et al.* 2002), which removes the problem of the mechanical energy sources.

Recall also that the two mentioned shells R1 and R2 exhibit an intense emission feature in the [S II] 6717/6731 Å lines (see Valdez-Gutierrez *et al.* 2001; Lozinskaya *et al.* 2002), typical of the radiation of the shock waves generated by a supernova explosion.

The neutral shells produced by the combined effect of the wind and supernovae in OB associations are being widely searched for in nearby galaxies (see, e.g., the review article by Brinks 1994; Kim *et al.* 1999; Oey *et al.* 2002 and references therein). In most cases, the 21-cm observations either do not reveal any distinct neutral-gas shell structure around OB associations at all or do not allow the neutral-gas structures to be unambiguously associated with H II shells. The studies of neutral gas in the vicinity of the three well-known ionized supershells in the LMC carried out by Oey *et al.* (2002) serve as a clear example.

The complex of star formation in IC 1613 constitutes a lucky exception. We do not know any other examples of such a distinct interaction between multiple ionized and neutral shells that is observed in the complex under discussion.

Here, we have studied the kinematics of the identified neutral shells I, II, and III for the first time. We have also detected expansion and measured the expansion velocity for the first time.

As was mentioned in Section 3, the derived radii and expansion velocities of the H I shells in IC 1613 fall within the region of the peak in the distribution of neutral shells in the LMC and SMC in size and expansion velocity. The age of the H I shells in the complex of star formation in IC 1613 (5.3–5.5 Myr) is also in complete agreement with the peaks in the age distributions of H I supershells in the LMC (4.9 Myr; Kim *et al.* 1999) and in the SMC (5.4 Myr; Staveley-Smith *et al.* (1997).

We estimated the kinematic ages of the neutral shells II and III in Table 2 from their mean radii and expansion velocities by using the classical theory of a constant stellar wind in a homogeneous medium. This assumes that the mechanical luminosity of the wind from the association stars responsible for the shell formation does not vary with time and that all stars were formed simultaneously. Of course, both assumptions are not valid, although they are universally accepted. Allowance for sequential star formation and for variations in the mass loss rate during the evolution of a rich association as well as for the clumpy structure of the interstellar medium can change the age estimate by a factor of 1.5 to 3 (see, e.g., Shull and Saken 1995; Oey *et al.* 1996; Silich *et al.* 1996; Silich and Franco 1999; and references therein). Nevertheless, we may conclude that the derived ages of shells II (5.6 Myr) and III (5.3 Myr) agree with the ages of the stellar associations in the complex of star formation. Shell I, whose expansion we failed to detect, is similar in size to shells II and III and is most likely similar in age.

The three-color photometry of stars in IC 1613 performed by Hodge *et al.* (1991) gave a minimum age of the stars in their field no. 1, where the neutral shells that we identified are located, equal to 5 Myr. This field includes associations nos. 10, 12, 13, 14, 15, and 17 from the list by Hodge (1978), whose mean and minimum ages were estimated by Hodge *et al.* (1991) to be 17 and 3 Myr, respectively. Recent estimates by Georgiev *et al.* (1999) yielded similar results: the age of the youngest nearby associations nos. 10 and 14 is about 5 Myr and the age of the oldest associations (nos. 12, 19, and 19) reaches 20 Myr.

The mechanical wind luminosity that is required for the neutral shells observed in the complex to be formed and that is determined by using the classical model (with all of the reservations made above) is 5×10^{38}, 5×10^{37}, and 5×10^{36} erg s^{-1} in a medium with an initial density of 10, 1, and 0.1 cm^{-3}, respectively. These values seem reasonable enough for the stars found in the region—the sources of a strong stellar wind (see Valdez-Gutierrez *et al.* 2001; Lozinskaya *et al.* 2002). It should be emphasized, however, that the spectra of bright stars in the region are required to adequately discuss the sources of mechanical energy. Lozinskaya *et al.* (2002) obtained the spectra of stars only in three small fields of the star-forming complex and detected stars with strong winds, blue supergiants and Of stars, in two of them.

Despite the "suitable" age and input of mechanical energy, we do not consider it possible to unequivocally associate the formation of neutral shells with the action of the stellar wind from the OB associations identified by Georgiev *et al.* (1999) for the following reasons.

First, most of the H I supershells identified in the LMC, the SMC, and other Local-Group galaxies are several-fold younger than the corresponding OB associations (see, e.g., Kim *et al.* 1999; Staveley-Smith *et al.* 1997, and references therein). Therefore, it may well be that the H I shells that we detected in IC 1613 were also formed by an older population that the groups of young stars shown in Fig. 1c.

As follows from Table 3 and from similar estimates by Valdez-Gutierrez *et al.* (2001), the ages of most of the ionized shells in the complex lie within the range from 0.6 to 2.2 Myr. These ages are much younger

than the ages of the OB associations that could be responsible for their formation. Such a situation is observed in most galactic and extragalactic ionized shells and supershells. In general, to explain this mismatch, either noncoeval star formation is assumed or the shells are assumed to be formed only by stars at a late evolutionary stage—WR, Of, and BSG with a short-duration, but intense wind. The situation in the complex under consideration is more complicated, because the bright ionized shells are localized inside or at the boundary of the older neutral shells and their evolution differs significantly from the standard theory.

In addition, a number of observed facts actually suggest noncoeval star formation in the complex.

Figure 1c suggests that all of the young OB associations in the region are localized not at the center but in the dense peripheral parts of the H I shells [the only association no. 7 from the list by Georgiev *et al.* (1999) is partly located inside shell III). In general, this picture may provide evidence for the formation of these associations in dense H I shells. We emphasize that the new association boundaries delineated by Georgiev *et al.* (1999) split the associations of Hodge (1978) into smaller groups, which are believed to be the young nuclei of the corresponding associations. The scenario for triggered star formation in expanding shells was considered by many authors [see, e.g., Elmegreen *et al.* (2002) and references therein].

Comparison of the ages and mutual localizations of the ionized and neutral structures in the complex also suggests noncoeval star formation. All the ionized shells are several-fold younger than the neutral shells. As was pointed out in Section 3, most of the bright ionized shells are located in the dense peripheral parts of the H I shells. The only exception is shell R4, which completely fits into the neutral shell II from the inside. According to our measurements, this ionized shell is oldest and all the young nuclei of the OB associations are located in its boundary regions (see Fig. 1c).

However, these arguments for sequential or triggered star formation, which refer to the neutral shells of the complex studied in detail here, are speculative, because the age difference between the H I and H II shells is small.

The multishell complex itself, which represents the only region of violent ongoing star formation in IC 1613, may have been produced by the collision of two older and more massive giant neutral supershells (Lozinskaya 2002, 2003). Indeed, in addition to the three bright and relatively small H I shells considered here, a giant H I ring south of the star-forming complex and a giant arc structure in the north, which probably also represents part of the neutral supershell, can be identified in Fig. 2a. The characteristic size of the two structures is ~1–1.5 kpc. The complex of ongoing star formation lies at their common boundary, where the collision of these two giant supershells could trigger violent star formation. We are planning to consider this scenario in detail.

7. CONCLUSIONS

We studied in detail the structure and kinematics of the neutral and ionized gas components in the only known complex of star formation in the irregular dwarf galaxy IC 1613.

To study the kinematics of the ionized shells, we carried out Hα observations with a scanning Fabry–Perot interferometer attached to the 6-m SAO telescope. The monochromatic Hα image of the multishell complex obtained from our interferometric observations reveals new faint filamentary structures in several regions of the complex.

We constructed position–radial velocity diagrams, which cover the entire complex of star formation almost uniformly. The characteristic velocity variation with distance from the center, the velocity ellipse, was used to refine (increase) the expansion velocities of most ionized shells in the complex estimated by Valdez-Gutierrez *et al.* (2001). The expansion in several shells was found to be asymmetric: the approaching and receding sides of the shells have different velocities.

Based on our VLA 21-cm observations, we have studied the neutral-gas kinematics in the complex of star formation for the first time. The mean H I velocity in the complex is $V_{\rm Hel} = -230 \pm 5$ km s^{-1}, in good agreement with the estimate obtained by Lake and Skillman (1989) for this part of the galaxy from low-angular-resolution observations.

We identified three extended (300–350 pc) neutral shells with which the brightest ionized shells in the complex of star formation are associated. The two H I shells were found to expand at a velocity of 15–18 km s^{-1}.

The sizes, expansion velocities, and kinematic ages of the neutral shells in the complex fall within the regions of the peaks in the corresponding distributions for giant shells in the LMC and SMC.

We identified an incomplete H I shell with the only known supernova remnant in the galaxy located at its inner boundary. This confirms the scenario for a supernova explosion inside a cavity surrounded by a dense shell and a collision of the remnant with the shell wall suggested by Lozinskaya *et al.* (1998) to explain the peculiarity of this remnant, which combines the properties of young and old objects.

We found evidence of the physical interaction between the H I and H II shells in the region of the chain

of stars, early-type giants and supergiants, detected by Lozinskaya *et al.* (2002). The region at the boundary of the two shells where the stellar chain is located was shown to be the dynamically most active part of the star-forming complex. The highest H II and H I velocities are observed here.

The relative positions and ages of the H I and H II shells and OB associations in the complex suggest sequential or triggered star formation in the expanding neutral shells.

In addition to the three brightest and most prominent H I shells, we found supergiant arches and ring structures in the galaxy whose sizes are comparable to the gaseous-disk thickness. These may be assumed to be the traces of preceding starbursts in IC 1613.

ACKNOWLEDGMENTS

This study was supported by the Russian Foundation for Basic Research (project nos. 01-02-16118 and 02-02-06048mas), the Federal Central Research Program (contract 40.022.1.1.1102), and CONACYT (Mexico, project 36132-E). The observational data were obtained with the 6-m SAO telescope financed by the Ministry of Science of Russia (registration number 01-43). We are grateful to the 6-m Telescope Committee for allocating observational time. The National Radio Astronomy Observatory (NRAO) is operated by the Association of Universities Inc. under a contract with the NSF. We wish to thank S.A. Silich for helpful remarks.

REFERENCES

1. V. L. Afanas'ev, T. A. Lozinskaya, A. V. Moiseev, and E. Blanton, Pis'ma Astron. Zh. **26**, 190 (2000) [Astron. Lett. **26**, 153 (2000)].
2. E. Brinks, in *Violent Star Formation from 30 Doradus to QSOs,* Ed. by G. Tenorio-Tagle (Cambridge Univ. Press, Cambridge, 1994), p. 145.
3. A. D. Chernin, Yu. N. Efremov, and P. A. Voinovich, Mon. Not. R. Astron. Soc. **275**, 313 (1995).
4. A. D. Chernin and T. A. Lozinskaya, Astron. Astrophys. Trans. **21** (3) (2003).
5. A. Dolphin, A. Saha, E. D. Skillman, *et al.*, Astrophys. J. **550**, 554 (2001).
6. B. G. Elmegreen, J. Palous, and S. Ehlerova, Mon. Not. R. Astron. Soc. **334**, 693 (2002).
7. W. Freedman, Astrophys. J. **326**, 691 (1988a).
8. W. Freedman, Astron. J. **96**, 1248 (1988b).
9. L. Georgiev, J. Borissova, M. Rosado, *et al.*, Astron. Astrophys., Suppl. Ser. **134**, 21 (1999).
10. P. W. Hodge, Astrophys. J., Suppl. Ser. **37**, 145 (1978).
11. P. Hodge, M. G. Lee, and M. Gurwell, Publ. Astron. Soc. Pac. **102**, 1245 (1990).
12. P. W. Hodge, T. R. Smith, P. B. Eskridge, *et al.*, Astrophys. J. **369**, 372 (1991).
13. D. A. Hunter, W. N. Hawley, and J. S. Gallagher, Astron. J. **106**, 1797 (1993).
14. S. Kim, M. A. Dopita, L. Staveley-Smith, and M. S. Bessell, Astron. J. **118**, 2797 (1999).
15. G. Lake and E. D. Skillman, Astron. J. **98**, 1274 (1989).
16. J. Lequeux, N. Meysonnier, and M. Azzopardi, Astron. Astrophys., Suppl. Ser. **67**, 169 (1987).
17. T. A. Lozinskaya, Astron. Astrophys. Trans. **21** (3) (2003).
18. T. A. Lozinskaya, *Proceedings of Conference "Seeng Through the Dust: The Detection of HI and the Exploration of the ISM of Galaxies," Penticton, Canada, 2001,* Ed. by R. Taylor, T. Landecker, and T. Willis (2002) (in press).
19. T. A. Lozinskaya, O. K. Silchenko, D. J. Helfand, and M. W. Goss, Astron. J. **116**, 2328 (1998).
20. T. A. Lozinskaya, A. V. Moiseev, V. L. Afanas'ev, *et al.*, Astron. Zh. **78**, 485 (2001) [Astron. Rep. **45**, 417 (2001)].
21. T. A. Lozinskaya, V. P. Arkhipova, A. V. Moiseev, and V. L. Afanas'ev, Astron. Zh. **79**, 19 (2002) [Astron. Rep. **46**, 16 (2002)].
22. I. Meaburn, Mon. Not. R. Astron. Soc. **192**, 365 (1980).
23. J. Meaburn, C. A. Clayton, and M. J. Whitehead, Mon. Not. R. Astron. Soc. **235**, 479 (1988).
24. A. V. Moiseev, Preprint SAO RAN No. 166, 1 (2002).
25. M. S. Oey, Astrophys. J. **467**, 666 (1996).
26. M. S. Oey, B. Groves, L. Staveley-Smith, and R. C. Smith, Astron. J. **123**, 255 (2002).
27. J. S. Price, S. F. Mason, and C. A. Gullixson, Astron. J. **100**, 420 (1990).
28. M. Rosado, M. Valdez-Guterrez, L. Georgiev, *et al.*, Astron. Astrophys. **122**, 194 (2001).
29. A. Sandage, Astrophys. J. **166**, 13 (1971).
30. J. M. Shull and J. M. Saken, Astrophys. J. **444**, 663 (1995).
31. S. A. Silich, J. Franco, J. Palous, and G. Tenorio-Tagle, Astrophys. J. **468**, 722 (1996).
32. S. A. Silich and J. Franco, Astrophys. J. **522**, 863 (1999).
33. L. Staveley-Smith, R. J. Sault, D. Hatzidimitriou, *et al.*, Mon. Not. R. Astron. Soc. **289**, 225 (1997).
34. M. Valdez-Gutierrez, M. Rosado, L. Georgiev, *et al.*, Astron. Astrophys. **366**, 35 (2001).

Translated by V. Astakhov

Astronomy Reports, Vol. 46, No. 1, 2002, pp. 16–26. Translated from Astronomicheskiĭ Zhurnal, Vol. 79, No. 1, 2002, pp. 19–30.
Original Russian Text Copyright © 2002 by Lozinskaya, Arkhipova, Moiseev, Afanas'ev.

Observations of Stellar Objects at a Shell Boundary in the Star-Forming Complex in the Galaxy IC 1613

T. A. Lozinskaya[1], V. P. Arkhipova[1], A. V. Moiseev[2], and V. L. Afanas'ev[2]

[1]*Sternberg Astronomical Institute, Universitetskiĭ pr. 13, Moscow, 119899 Russia*
[2]*Special Astrophysical Observatory, pos. Nizhniĭ Arkhyz, Karachai–Cherkessia, Russia*

Received May 7, 2001

Abstract—The single region of ongoing star formation in the galaxy IC 1613 has been observed in order to reveal the nature of compact emission-line objects at the edges of two shells in the complex, identified earlier in Hα line images. The continuum images show these compact objects to be stars. Detailed spectroscopic observations of these stars and the surrounding nebulae were carried out with an MPFS spectrograph mounted on the 6-m telescope of the Special Astrophysical Observatory. The resulting stellar spectra were used to determine the spectral types and luminosity classes of the objects. Of star we identified the only object of this spectral type in IC 1613. The results of optical observations of the multishell complex are compared to 21-cm radio observations. The shells harboring the stars at their boundaries constitute the most active part of the star-forming region. There is evidence that shocks have played an important role in the formation of the shells. © *2002 MAIK "Nauka/Interperiodica".*

1. INTRODUCTION

Irregular galaxies provide unique opportunities for studies of star formation triggered by the combined effect of stellar winds and supernova explosions in rich stellar groupings. Due to the absence of spiral density waves in these galaxies, the formation of giant multishell complexes around stellar groupings can proceed unhindered, enabling completion of the full ecological cycle of interaction between the stellar and gaseous components of giant molecular clouds. For the same reason, irregular galaxies display the longest scale lengths and time scales on which supernovae and stellar winds play a dominant role in the formation of new-generation stars.

IC 1613, a faint dwarf galaxy of the Local Group, provides one of the most striking examples of a giant multishell complex around a group of young stellar associations. The northeastern sector of IC 1613 harbors a prominent giant complex of ionized shells and supershells surrounding several dozen young stellar associations and star clusters. This complex is the sole site of contemporary star formation in the galaxy (see [1, 2] and references therein). The complex also includes the only known supernova remnant in the galaxy (see [3] and references therein). Comparison of the optical and 21-cm brightness distributions showed that the shells of HII are surrounded by extended shells of HI [4]. The shells of ionized and neutral gas are close to each other and partially overlap in the plane of the sky. If the sizes of the shells along the line of sight and in the plane of the sky are comparable, this indicates that these shells and supershells are in physical contact with each other. It is currently thought that collisions of massive expanding shells with each other and/or with giant molecular clouds can serve as triggers of gravitational instability and fragmentation in the collision region, leading to the formation of new-generation stars.

Narrow-band Hα images of the region considered, taken in 1995 with the 4-m telescope of the Kitt Peak National Observatory (KPNO), revealed chains of bright, compact emission-line objects located exactly at the edge of the two shells in the complex. The same region hosts association no. 17 from the list of Hodges [5] (the eastern part of this feature was later catalogued as association no. 25 in the list [2]). However, in our analysis in 1995, we were not able to establish a one-to-one relationship between compact objects and stars. Moreover, the fact that the stellar objects are located exactly along a thin shell-like structure is of considerable interest on its own. This work was motivated primarily by the desire to study the emission spectra and nature of the chain of objects and their possible relationship to triggered star formation.

With this aim in view, we performed photometry and spectroscopy of this region. Section 2 describes the instruments, observations, and data reduction

1063-7729/02/4601-0016$22.00 © 2002 MAIK "Nauka/Interperiodica"

technique employed. Section 3 describes the overall structure of the multishell complex derived from optical and (21-cm line) radio observations and identifies regions that are of greatest interest for detailed spectroscopy. Based on our photometric observations, we show that the compact emission objects in question are stars. Section 4 reports the results of spectroscopic observations of three selected fields made with the MPFS spectrograph mounted on the 6-m telescope of the Special Astrophysical Observatory of the Russian Academy of Sciences. We obtained the spectra of individual stars located at the shell boundaries and estimated their spectral types and luminosity classes. We have determined the distribution of the intensity ratios of the principal lines in the spectra of the surrounding gaseous nebulas and constructed the gas radial-velocity field based on Hβ and [SII] line measurements. Section 5 discusses our main results and conclusions.

2. OBSERVATIONS AND DATA REDUCTION

Photometry

The shell complex was imaged in two filters on October 4–5, 2000 with the 1-m Zeiss-1000 telescope of the Special Astrophysical Observatory of the Russian Academy of Sciences in the process of testing the new SCORPIO focal reducer. A description of the reducer and transmission curves of the interference filters used can be found at `http://www.sao.ru/~moisav/scorpio/scorpio.html`. The reducer is mounted at the Cassegrain focus of the telescope ($F/13$), and the total focal ratio of the system is $F/9$. The spectrograph uses a TK1024 1024×1024 CCD as a detector. The system has an angular resolution of $0.52''$/pixel and a field of view of $8.'9$. We obtained images in two intermediate-band interference filters. The filter with a central wavelength of $\lambda_c = 6620$ Å and a passband halfwidth of $\Delta\lambda = 190$ Å coadded the emission in the Hα and [NII] lines and in the continuum.

To obtain continuum images, we used a filter centered on $\lambda_c = 6060$ Å with a passband halfwidth of $\Delta\lambda = 170$ Å. The total exposure in each filter and the seeing during the observations were 1800 s and $1.5''$, respectively.

After performing standard procedures for CCD frame reduction (offset frame subtraction, flat-field correction, cosmic-ray removal), we reduced the images to an absolute energy scale using images of the spectrophotometric standard star BD+25°4655 taken on the same night. The reduction to equatorial coordinates was based on field stars whose positions were adopted from the digital version of the Palomar Sky Survey (`http://stdatu.stsci.edu/dss/dss-form.html`).

Table 1. Log of MPFS spectroscopic observations

Field	Center coordinates		$T_{\rm exp}$, s	z, deg
	R.A. (2000.0)	DEC (2000.0)		
Field I	$01^{\rm h}05^{\rm m}6\overset{\rm s}{.}1$	$+02°09'34''$	2700	42
Field II	$01^{\rm h}05^{\rm m}5\overset{\rm s}{.}2$	$+02°09'47''$	2700	43
Field III	$01^{\rm h}05^{\rm m}1\overset{\rm s}{.}8$	$+02°09'35''$	2700	48

Spectroscopy

The spectroscopic observations were made on October 23–24, 2000, using the Multipupil Panoramic Field Spectroscope (MPFS) mounted at the primary focus of the 6-m telescope of Special Astrophysical Observatory. A description of the spectroscope can be found at `http://www.sao.ru/~gafan/devices/mpfs/mpfs_main.htm`.

The new spectrograph has a larger field of view, wider spectral range, and higher quantum efficiency than the earlier version of the MPFS [6]. The spectrograph uses a TK1024 1024×1024 CCD as a detector and enables the spectra of 240 spatial elements (in the form of square lenses) to be taken simultaneously, forming a 16×15 array on the sky. The angular size of an image element was $1''$. A spectrum of the night-sky background $4.'5$ from the center of the field of view is taken simultaneously. We obtained spectra with a resolution of 8 Å in the range 4350–6850 Å. The seeing was about $2''$. We observed three areas in the region of the giant shells, whose positions are shown in Fig. 2. Table 1 gives the equatorial coordinates of the field centers, the total exposure times $T_{\rm exp}$, and the mean zenith angles z at the time of observation.

The spectroscopic observations were reduced using IDL-based software developed at the SAO Laboratory for Specroscopy and Photometry of Extragalactic Objects. The preliminary data reduction included offset-frame subtraction, flat-field correction, cosmic-ray removal, extraction of the individual spectra from the CCD images, and wavelength calibration using the spectrum of an He–Ne–Ar calibration lamp.

We then subtracted the night-sky spectrum from the linearized spectra and converted the observed fluxes to an absolute energy scale using observations of the spectrophotometric standard star Feige 110 (taken immediately before observing the program objects at a zenith distance of $z = 50°$). We adopted the parameters for this standard from the public database `http://www.eso.org/observing/standards/spectra`. Our air-mass corrections were based on the mean spectral atmospheric-extinction curve for the Special Astrophysical Observatory given in [7].

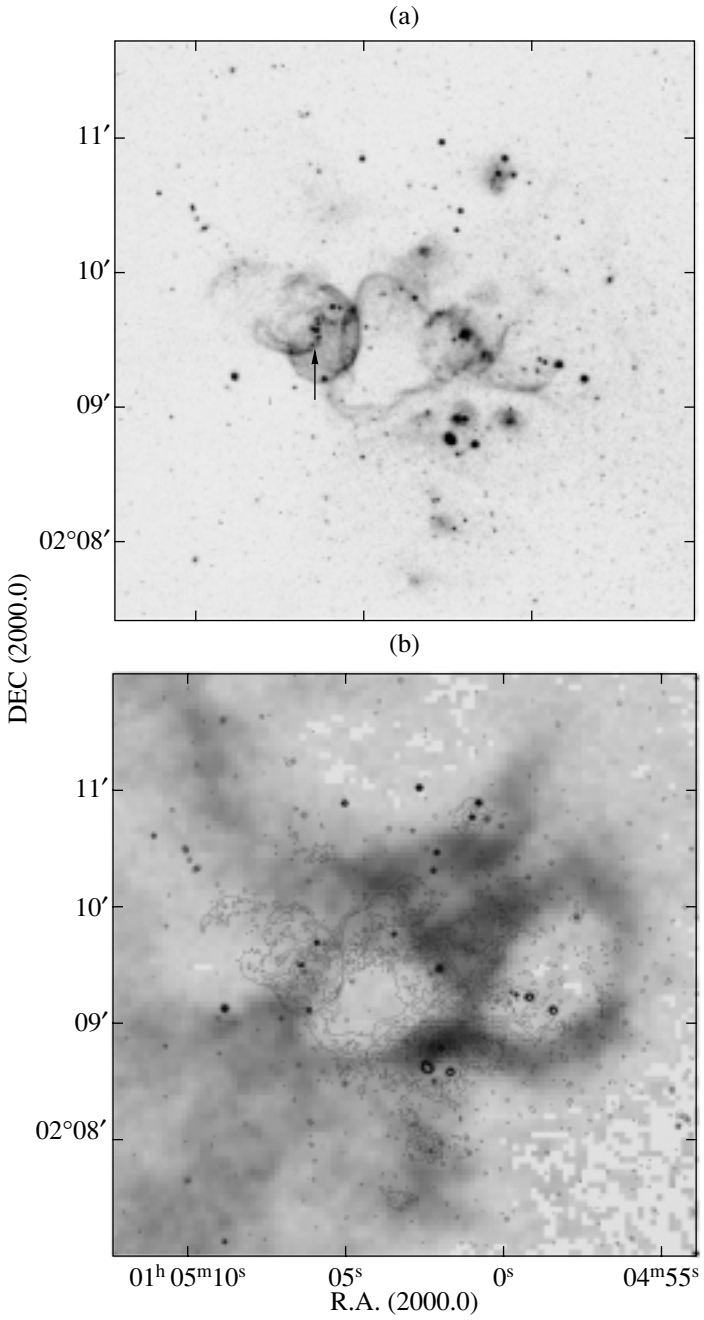

Fig. 1. (a) Hα image of the multishell complex taken with the 4-m telescope of the Kitt Peak National Observatory. The arrow shows the chain of bright, compact emission objects at the shell boundary. (b) HI brightness distribution (shades of gray) superimposed on a narrow-band Hα image of the same area (isophotes) for the northeastern sector of the galaxy IC 1613 (fragment of a chart published in [4]).

In the course of our work, we compared the Hα and [NII] line fluxes measured using the MPFS data with those derived from images of star-free shell regions taken with filters. The two methods (spectrophotometric and photometric) yielded line fluxes that agreed to within about 20%, providing an independent estimate of the actual accuracy of our observations.

3. OVERALL STRUCTURE OF THE MULTISHELL COMPLEX IN THE STAR-FORMING REGION

The multishell complex in the northeastern sector of IC 1613 is the most prominent structure seen in narrow-band Hα images of the galaxy [8–12]. This is the place where the overwhelming majority of the galaxy's bright HII regions, shells, and supershells

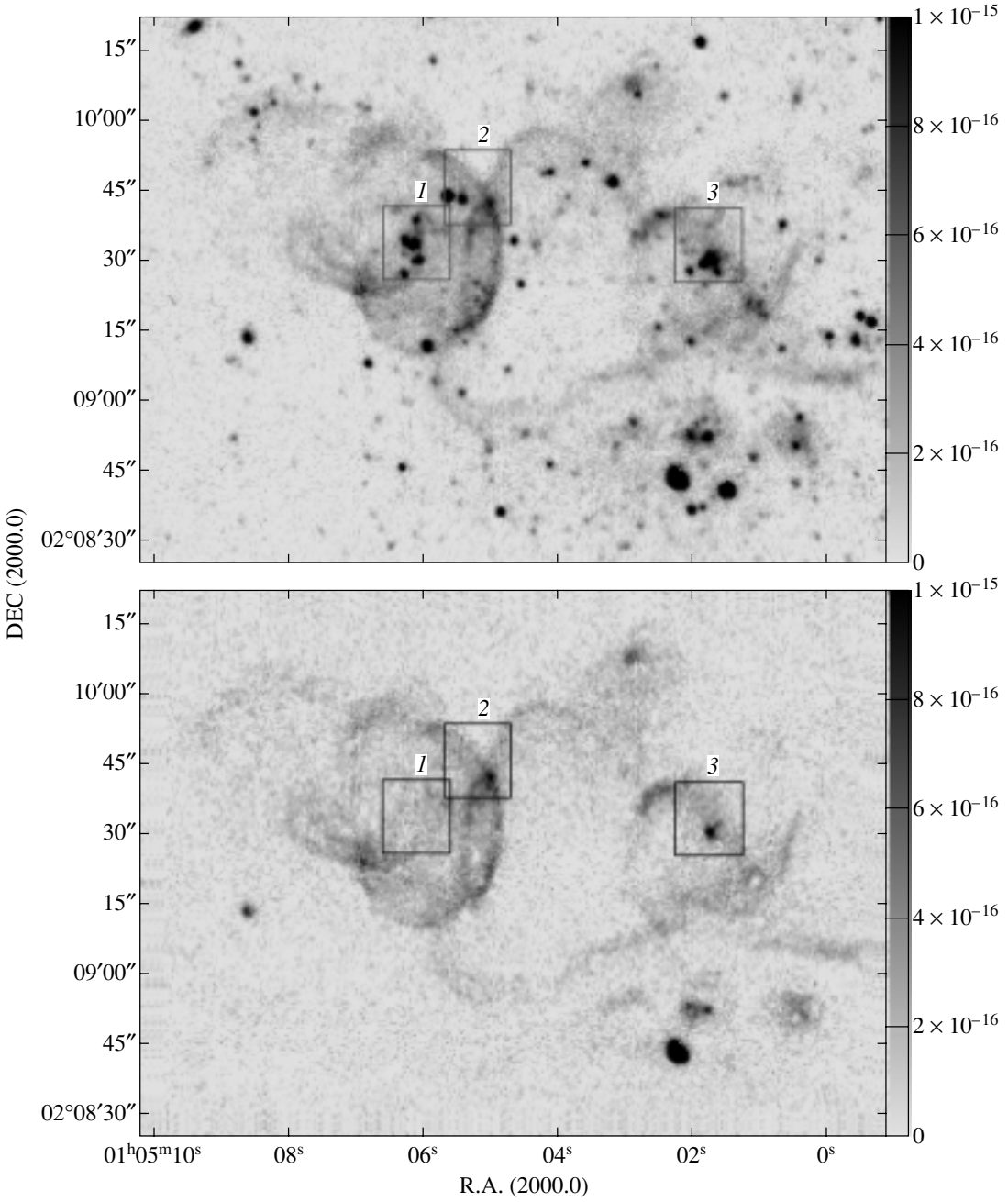

Fig. 2. Image of the complex of ionized shells taken with the Zeiss-1000 telescope equipped with the SCORPIO focal reducer. The scale is in erg/(s cm^3 arcsec). Top: image taken with a filter centered on 6620 Å and a passband halfwidth of 190 Å coadding emission in the Hα and [NII] lines and the continuum. Bottom: emission-line image (continuum subtracted). The rectangles indicate regions observed with the SAO 6-m telescope using the MPFS.

are concentrated. The stellar component of the complex is represented by about twenty stellar associations and star clusters [2, 5].

Figure 1a shows an Hα-line image of the multishell complex taken in 1995 with the KPNO 4-m telescope. The chain of bright, compact emission-line objects located exactly at the bright rim of the shell (indicated by an arrow) and several compact objects at the edges of other shells are clearly visible.

The two shells with compact objects at their boundaries correspond to objects R1 and R2 in the list of shells [12]. Both shells are located within square N27 in Fig. 3 of [12] and include the nebulae S10 and S13 in the classification of Sandage [13].

Meaburn *et al.* [1] were the first to analyze the

kinematics of the complex of ionized shells. Their five spectrograms densely covered the bright part of the complex, enabling determination of the characteristic shell expansion velocities, which proved to be about 30 km/s. Valdez-Gutierrez *et al.* [12] constructed the line-of-sight velocity field of the entire complex in the Hα and [SII] lines and estimated the expansion velocities of its constituent shells and supershells. HI observations of IC 1613 [14] showed that the complex is located in the region of the brightest "spot" in the 21-cm radio emission.

Lozinskaya *et al.* [4] were the first to make a detailed comparison of the Hα and 21-cm radio brightness distributions of the complex. Figure 1b shows a fragment of the map of the northeastern sector of the galaxy published in [4], with the HI brightness distribution superimposed on the Hα line image shown in Fig. 1a.

An HI map with a high angular resolution of $7.''4 \times 7.''0$ (corresponding to a linear resolution of $\sim$25 pc) was constructed using 21-cm VLA observations (part of a large project to analyze the structure and kinematics of the neutral gas in IC 1613 [15]).

We identified the chain of compact emission-line objects and a number of other compact objects at the edges of the shells shown in Fig. 1a in our Hα line image. These compact emission-line features could be either stars located inside compact HII regions or dense clumps of gaseous shell material at the initial stage of gravitational fragmentaion and/or shock-induced compression. To elucidate the nature of these compact objects, we performed photometry of the multishell complex using the Zeiss-1000 telescope equipped with the SCORPIO focal reducer.

The upper part of Fig. 2 shows the image of the complex obtained through a filter centered at 6620 Å with a halfwidth of 190 Å. This image coadds the emission in the Hα and [NII] lines and the continuum. The lower part of Fig. 2 shows the same image after subtraction of the stellar continuum. To determine the continuum level, we used a filter with maximum sensitivity at 6060 Å and a bandpass halfwidth of 170 Å; the shape of the filter transmission curve was rectangular rather than Gaussian. We chose the coefficient for continuum subtraction to ensure the best subtraction of foreground stars. Since the central wavelengths of the two filters differ by almost 600 Å, the fact that the slope of the continuum differs from star to star becomes important. This is why many young stars inside the shell complex appear oversubtracted, due to the appreciable slopes of their continua (see Section 4). The corresponding locations are masked in Fig. 2.

A comparison of Figs. 1 and 2 suggests that the compact objects can be neither purely gaseous clumps nor stars located inside the parent cocoon.

The squares in Fig. 2 indicate Fields I, II, and III for which the spectroscopic observations reported in the next section were made. Figures 3, 4, and 5 show enlargened images of Fields I, II, and III, respectively, obtained with the same SCORPIO focal reducer with a filter centered on 6060 Å and a passband halfwidth of 170 Å. These continuum images of the three fields indicate that the compact, emission-line objects in question are stars.

We can see 13 stars in Field I, two of which are at the edge of the field. The stars in Field I belong to association no. 25 in the list of [2] (the eastern part of association no. 17 from [5]). The brightest of these stars are indeed located along the bright rim of the shell. We can also see two star-like objects at the boundary of the ionized shell in Field II. Part of association no. 17 from [5] is located in this same place. Field III contains stars from association no. 13 from the list of Hodge (1978) (no. 18 in [2]).

Below, we report the results of spectroscopic observations of the brightest of these stars made with a spectrograph mounted on the 6-m telescope of the Special Astrophysical Observatory.

4. RESULTS OF SPECTROSCOPIC OBSERVATIONS

Analysis of Field Spectroscopy

We fitted Gaussians to emission-line profiles to construct a series of monochromatic images of the fields in the Hα and Hβ lines and in the [OIII] 5007 Å and [SII] 6717, 6731 Å forbidden lines. All the line profiles can be adequately fitted by a single Gaussian, without any systematic deviations. Note, however, that our spectral resolution (350–450 km/s) substantially exceeds the expected velocities of relative gas motions [12]. In addition, we also constructed images of the program fields in the stellar continuum at wavelengths $\Delta\lambda = 4600$–4800 Å. Comparison of these data with the continuum images obtained with the Zeiss-1000 telescope enabled us to coadd the spectra from the spatial elements corresponding to individual stars.

Figures 3–5 show the results obtained for Fields I, II, and III, respectively (continuum and emission-line field images and the spectra of individual stars with their surrounding nebulae).

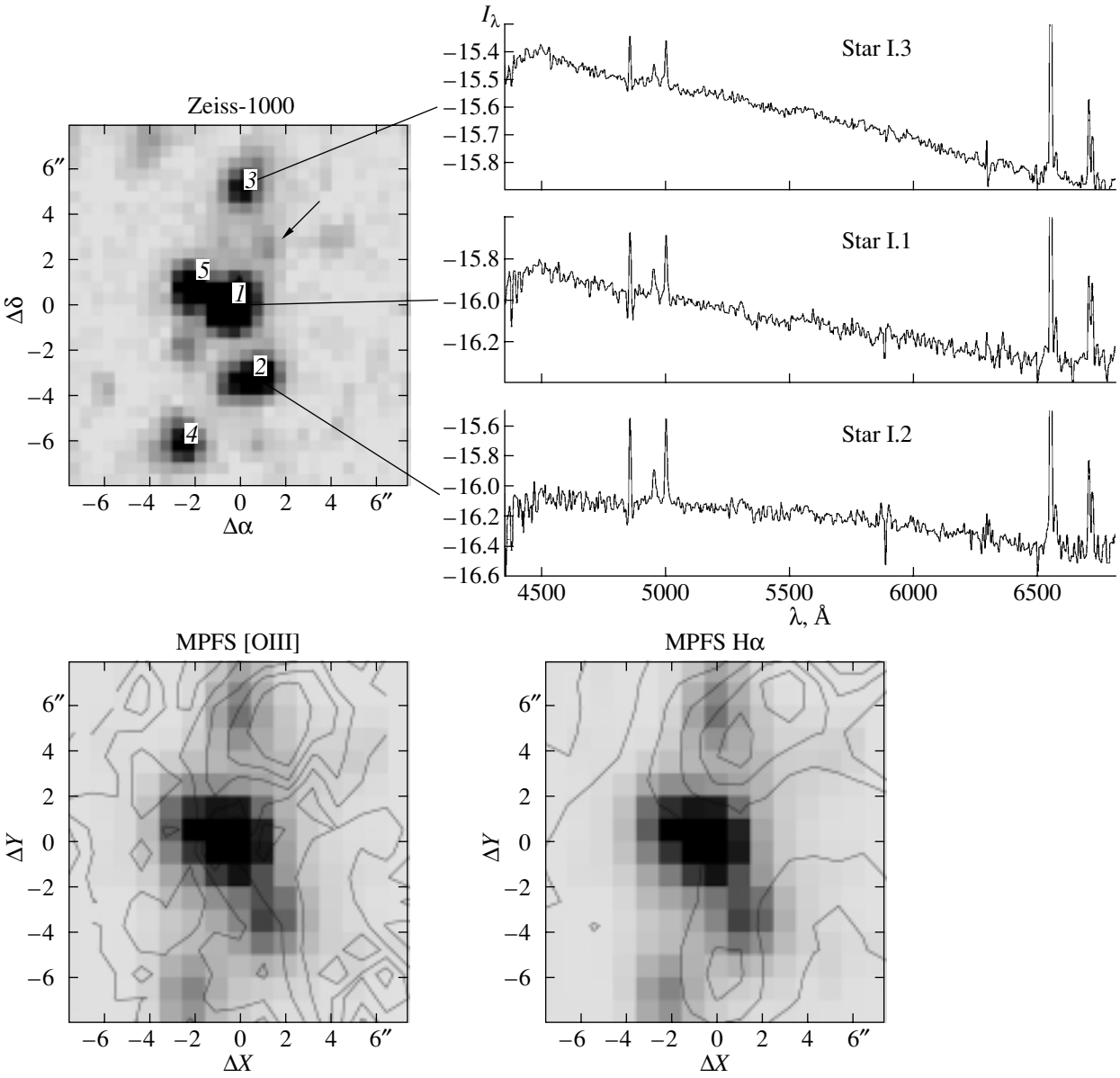

Fig. 3. Top left: Continuum image of Field 1 taken with the Zeiss-1000 telescope through a filter centered on $\lambda_c = 6060$ Å with a passband halfwidth of $\Delta\lambda = 170$ Å. The star numbers are indicated; the arrow marks the hot star that cannot be seen in the MPFS data (see text). Top right: Spectra of the three brightest stars in the field. Bottom: Isophotes of [OIII] (left) and Hα (right) line images superimposed on the 4600–4800 Å continuum images (MPFS data).

Field I

We analyzed the spectra of five stars in Field I to estimate their spectral types. Unfortunately, the low resolution and fairly low signal-to-noise ratio prevented us from reliably detecting all spectral features. In addition, superimposed emission lines from ionized gas in the vicinity of the stars can be seen in all the spectra.

Star I.1 can be classified as an O supergiant, judging from the HeII 4541, 4686 Å and SiIII 4552 Å lines in its spectrum.

Star I.2 is evidently much hotter than star I.1, since it exhibits well defined SiIV 4631, 4654 Å lines; the intensity of its HeII 4686 Å line indicates that the star is a giant rather than a supergiant.

No clearly detectable absorption lines could be found in the spectra of stars I.3 and I.4.

The spectrum of star I.5 exhibits a strong HeII 4686 Å line, indicating the it is an O star of luminosity class III–V.

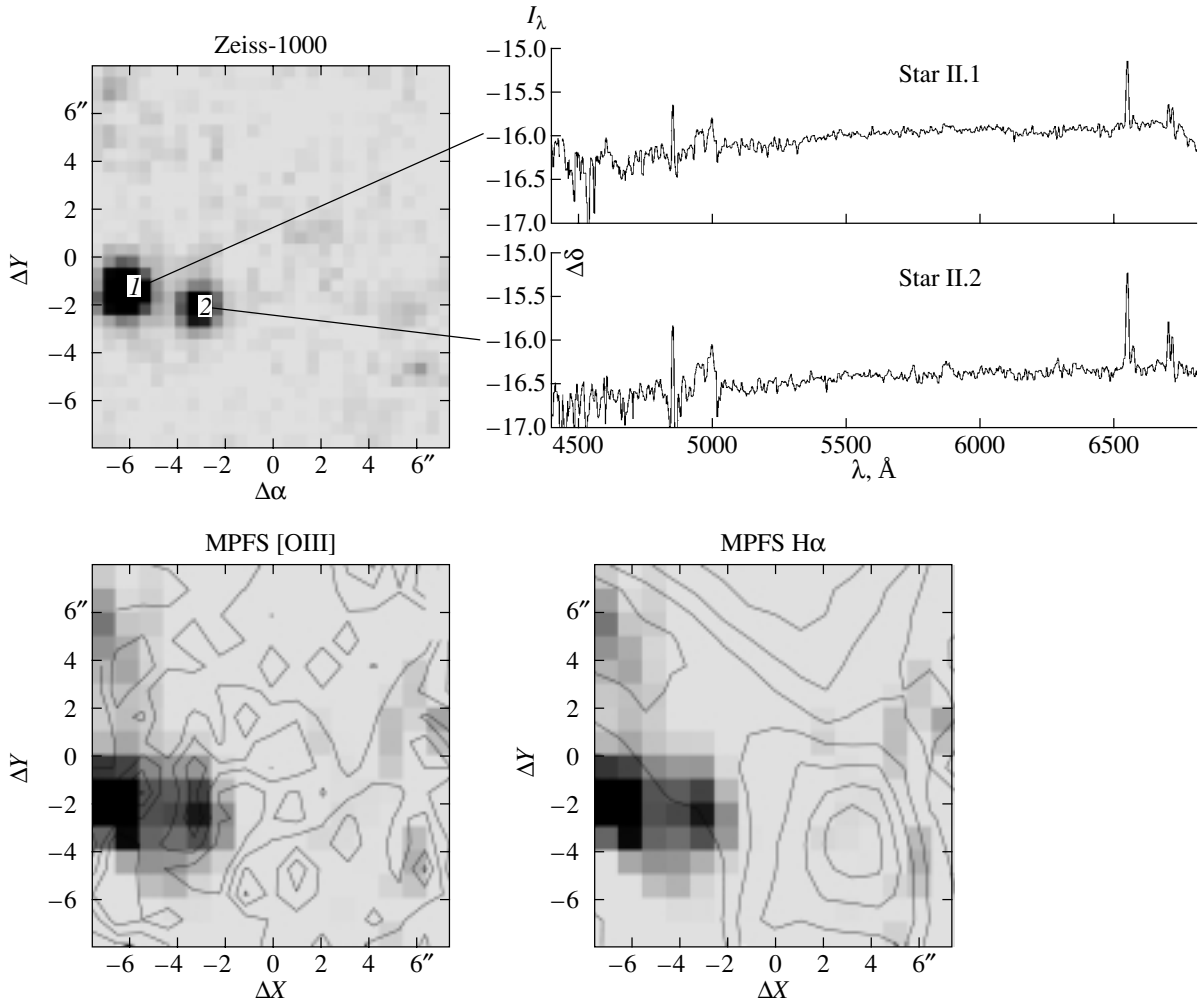

Fig. 4. Same as Fig. 3 for Field II.

We estimated the B and V magnitudes of the stars in the UBV system from their absolute spectral energy distributions, based on the calibration of [16]. The results are summarized in columns 1–3 of Table 2. Column 4 gives the $E(B{-}V)$ color excesses of the stars derived from the Hα/Hβ Balmer decrements of the nearest HII regions located within Field I. Columns 5–7 give the $(B-V)_0$ color index, absolute magnitude M_v, and the spectral type estimated from $(B-V)_0$, taking into account the luminosity classes estimated directly from the spectra.

All estimates in this paper are based on the adopted distance modulus of $(M-m)_0 = 24.31$, corresponding to a distance of 730 kpc, in accordance with the new determination [17].

The hottest star in Field I appears to be star I.5.

The emission-line spectra of the gaseous environments of each star are typical of HII regions. The emission-line ratios in the neighborhoods of stars I.1, I.2, I.3, and I.4 are I([OIII]5007/Hβ) = 0.8; the relative intensities of the same lines for star I.5 yield a ratio of 1.05, confirming the higher temperature of this star.

Note that all five stars in Table 2 show appreciable interstellar extinction.

There is another hot star with coordinates $\Delta X = -5''$, $\Delta Y = +2''$ between stars I.1 and I.3. This star does not show up against the bright nebular background emission in images of Field I based on MPFS data. The [OIII] 5007 Å and Hα brightness maps (see Fig. 3) show a well defined emission maximum at this location. The star can be seen on the KPNO plate as a compact clump of Hα emission and is clearly visible on the Zeiss-1000 plate. This star has $V = 21.3^m$; the extinction estimated from the Balmer decrement is low, and its temperature is high: the line intensities are I([OIII]5007)/I(Hα) $\simeq 0.3$ and I([SII])/I(Hα) $\simeq 0.2$. We therefore conclude that the excitation of the HII region surrounding the star is radiative, and not associated with shocks. The star is responsible

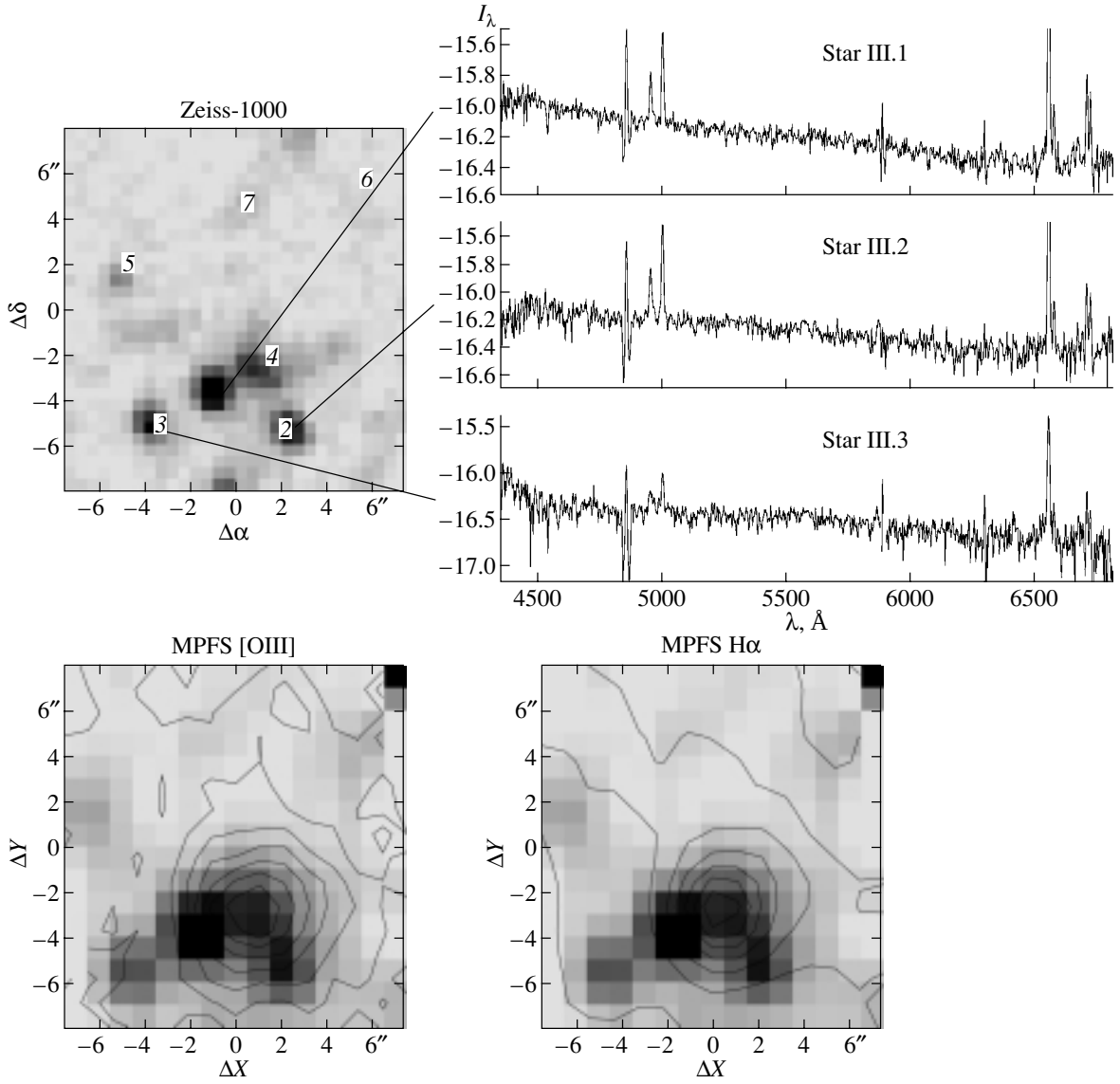

Fig. 5. Same as Fig. 3 for Field III.

for exciting both its own surrounding gas and the gas in the vicinity of the cooler star I.3.

We used the Zeiss-1000 images to estimate the V magnitudes of fainter stars in Field I relative to star I.4 (for which Table 2 gives $V = 19.8^m$). The V magnitudes of these stars are 20.9^m, 21.5^m, 21.6^m, 21.3^m, 21.5^m, and 21.8^m in order of decreasing brightness.

Field II

Our spectra of the two brightest stars in Field II show that these objects are yellow supergiants. We used the same method as for Field I to compute the parameters of these stars presented in Table 3, based on their absolute spectral energy distributions.

The well localized Hα and [SII] line emission maxima can be seen to the west of star II.2, in the region with $\Delta X = 0$, $\Delta Y = +6''$. It is here that the main source of ionizing radiation must be located. However, the emission spectrum of this region is by no means typical of an HII region ionized by an O star: the relative line intensities are $I([\mathrm{OIII}]\,5007)/I(\mathrm{H}\alpha) < 0.2$ and $I([\mathrm{SII}])/I(\mathrm{H}\alpha) \approx 0.35$. Such parameters are typical of cooling gas behind a shock front.

The electron density of the gas component in this region is low, as indicated by the [SII] intensity ratio of $I(6717)/I(6731) \simeq 1.7$, corresponding to $N_e < 100\ \mathrm{cm}^{-3}$.

Based on the 4600–4800 Å continuum intensity in this region, we estimate the upper limit of the V

Table 2. Parameters of stars in Field I

Star	V	$B-V$	$E(B-V)$	$(B-V)_0$	M_v	Sp
1	2	3	4	5	6	7
I.1	17.94	+0.02	0.33	−0.31	−7.4	OI
I.2	19.18	−0.10	0.18	−0.28	−5.7	OIII
I.3	19.32	+0.37	0.18	+0.19	−5.5	A7 III
I.4	19.80	+0.10	0.18	−0.08	−5.0	B8 II
I.5	19.80	−0.05	0.29	−0.30	−5.4	O8III or O4V

Table 3. Parameters of stars in Field II

Star	V	$B-V$	$E(B-V)$	$(B\text{-}V)_0$	M_v	Sp
II.1	18.94	+1.33	0.08	+1.25	−5.6	G8−K0 II
II.2	20.04	+1.53	0.18	+1.35	−4.8	K0−K2 II−I

Table 4. Parameters of stars in Field III

Star	V	$B-V$	$E(B-V)$	$(B-V)_0$	M_v	Sp
III.1	19.40	+0.01	(0.3)	−0.29	(−5.8)	OIII
III.2	19.62	+0.07	0.3	−0.23	−5.6	O−B
III.3	20.17	-0.06	0.3	−0.36	−5.0	Of ?
III.4	19.69	+0.14	(0.4)	−0.26	−5.8	OIII
III.5	21.2	<0?				Possibly O
III.6	21.24	Red				
III.7	21.07	Red				

magnitude of the possible ionizing star to be 19.3^m. This candidate exciting star can be seen at Δ X = 0, Δ Y = $+8''$ on the map obtained with the Zeiss-1000 telescope.

Note that the line-intensity ratio is $I([\mathrm{SII}])/I(\mathrm{H}\alpha) \approx 0.35$ virtually throughout the whole of Field II, as is typical of shock excitation. The same field contains part of the shell R2.

Field III

We obtained the spectra of seven stars in Field III. Table 4 summarizes the results of our photometric and spectral analysis for these stars. The color indices were determined from the Balmer decrements of HII regions surrounding the stars.

The spectrum of star III.1 appears to show the HeII 4541 Å line, whereas the HeII 4686 Å line cannot be identified. We conclude that this star is not an O supergiant but instead a star with luminosity class III. We cannot, however, rule out the possibility that this might be an early O main-sequence star.

The spectrum of star III.2 exhibits a strong [OIII] 5007 Å nebular line: $I([\mathrm{OIII}])/I(\mathrm{H}\alpha) \simeq 0.4$. This may indicate a high temperature for the exciting star ($T \geq 3 \times 10^4$ K). On the other hand, the spectrum of star III.2 may contain HeI 4713 Å line absorption, as is typical of early B stars. This star could well be binary.

The spectrum of star III.3 shows a well defined emission band at 4640−4650 Å, typical of WR and Of stars. However, the absence of other lines characteristic of WR stars leads us to conclude that III.3 should be classified as an Of star.

The spectrum of star III.4 shows well defined HeII 4541 and 4686 Å lines, and possibly SiIV 4630 and 4656 Å lines as well. We classify III.4 a an O7−O8 star of luminosity class III.

Following are the only conclusions we can draw about the three fainter stars in Table 4.

Star III.5 must be blue: its spectrum exhibits well defined traces of an He 4686 Å absorption line, and its estimated $B-V$ color index is indicative of a high temperature.

Stars III.6 and III.7 must be red, judging from their spectral energy distributions.

The main sources of gas excitation in Field III are stars III.1 and III.4, and probably also III.2 and III.3. The Hα line emission is concentrated primarily between stars III.1 and III.4, closer to III.4. The [OIII] line emission surrounds star III.4, suggesting that this is the hottest star in the region. According to our estimates, the size of the [OIII] emission region is no less than 6″, corresponding to a linear radius of $R = 10$ pc. The radius of the Hα emission-line region is also about 10 pc.

The [SII] line intensity ratio in this region is $I(6717)/I(6731) \simeq 1.5$, corresponding to $N_e \leq 100$ cm^{-3}.

We thus conclude that all four bright stars in Field III are O stars, without a single supergiant among them. In contrast to Field I, all stars in Field III are giants according to their luminosity classes.

Ionized Gas Velocities

Our spectroscopic observations in the Hα, [SII], and [OIII] emission lines can be used to construct the line-of-sight velocity fields of the ionized gas in Fields I, II, and III. The spectral resolution of our observations is 350–450 km/s, much lower than that of interferometric observations [12]; we therefore do not discuss the results of our velocity measurements in detail here, pointing out only our main conclusions. We found systematic deviations on the order of 20–40 km/s from the mean value of $V(\mathrm{Hel}) \sim -246$ km/s in each of the three fields. The velocities based on the hydrogen, sulfur, and oxygen line measurements made in the same region vary within the same range. The velocity variations within the regions studied do not go beyond the interval $V(\mathrm{Hel}) \simeq -200$ to -300 km/s. (Note that, here, we refer to the velocities of the line maxima, not those of weak features, as in Section 5).

All the velocity variations in Fields I, II, and III indicated above are in full agreement with the results of interferometric observations of the complex [12].

5. CONCLUSIONS

We obtained new observations of the only complex with ongoing star formation in the galaxy IC 1613 to elucidate the nature of the chain of compact emission-line objects we had identified earlier at the peripheries of two shells of the complex in our analysis of deep Hα images. Our new continuum images obtained with the Zeiss-1000 telescope have shown that these compact objects at the boundaries of two shells are stars.

We performed spectroscopy of selected fields in the region of the complex using the MPFS spectrograph mounted on the 6-m telescope of the Special Astrophysical Observatory. We obtained spectra of the stars forming the chains and estimated their spectral types and luminosity classes. The stars in question are at different evolutionary stages.

Four of the stars forming the chain in Field I at the boundary of the shell R1 are OB stars (with luminosity classes I, II, and III), while one is a cooler object of spectral type A7 III. The position of this last star deviates somewhat from the regular chain structure; we believe that this A7 star is unlikely to be a member of the chain and is simply projected onto the region.

The two brightest stars in Field II lie at the boundary of the shell R2. Our spectra show that these are yellow supergiants. The two stars do not belong to associations identified in the galaxy.

The stars in Field III do not form any clear chain but are coincident with the brightest clump of emission at the boundary of shell R5. The four brightest stars of the seven whose spectra we obtained are O stars. The luminosity classes of all these stars indicates that they are giants, with no supergiants among them, in contrast to what we found in Fields I and II. We assigned a spectral type of O to star III.3. This star, with coordinates R.A. (2000) $= 1^{\mathrm{h}}05^{\mathrm{m}}2.^{\mathrm{s}}2$, DEC (2000) $= +02^{\circ}09'28.6''$, is the only star of this type identified in IC 1613 (its cordinates have been measured to within an accuracy of 1″).

One of the three fainter stars must also be of type O; the other two appear to be cooler.

We have identified sources of ionization of the ambient gas in each of the fields considered.

The shells R1 and R2, at whose boundaries the chain in Field I and two stars of Field II are located, stand out among other objects of the multishell complex in a number of ways.

(1) These two shells partially overlap in the sky, and form the brightest emission-line region in the entire complex (see Fig. 1). According to estimates made in [12], the Hα luminosities of the two shells are $\log L(\mathrm{H}\alpha) = 37.51$ and $\log L(\mathrm{H}\alpha) = 37.77$ erg/s, respectively. The same shells appear to be the brightest in suflur lines—see Fig. 1 in [12] and Section 4 of this paper. We estimate the line intensity ratio in Field II to be $I([\mathrm{OIII}]\,5007)/I(\mathrm{H}\alpha) < 0.2$, $I([\mathrm{SII}])/I(\mathrm{H}\alpha) \approx 0.35$, typical of cooling gas behind a shock front.

(2) The expansion velocity of shell R2 (50 km/s) is the highest in the entire complex; the expansion velocity of R1 is 30 km/s [12]. Note that Valdez-Gutierrez *et al.* [12] measured both velocities as

the mean separation between the two maxima in the double-humped integrated Hα line profiles of the corresponding shells. In fact, images of the complex in hydrogen and sulfur lines in various velocity intervals show both shells to display very complex kinematics. The fact that the brightness of both objects is high even at the extremes of the velocity interval covered (-272 and -177 km/s) means that the velocities of internal motions within the shells substantially exceed the typical expansion velocities indicated above. Two faint symmetric features in the integrated line profile of shell R2 with maxima at velocities of -50 and about -370 km/s are also immediately apparent (see Fig. 9 in [12]).

By analogy with the results that one of us (TAL) obtained by studying the kinematics of supernova remnants and shells surrounding OB associations, we suggest that these weaker high-velocity line features are closer to the shock-front velocity than brighter low-velocity features. In this case, the shock velocity in the shell should be at least 100 km/s. It is possible that we observe here the same "two-component" gas kinematics as in the Galactic shell surrounding Cyg OB1, Cyg OB3, and a number of other Galactic objects [18], namely the coexistence in a single shell of bright emission at low velocities and weak emission at higher velocities.

Such high internal velocities also reflect the substantial role played by shocks in the formation of both shells at whose boundaries the stellar chains are located.

(3) Comparison of the 21-cm and Hα-line brightness observations in Fig. 1b indicates that the part of the ionized shell R1 where the stellar chain is located falls in the thinnest neutral-gas bridge connecting the two neutral shell-like structures. The characteristic morphology of the ionized and neutral gas shells indicates that they are in physical contact: the neutral bridge is closely pressed up against the ionized shell R1 from outside in the region of the stellar chain, and the two shells in this region have the same radii of curvature. This morphology could be the result of the expanding shell R1 colliding with the neutral bridge located between the two HI shells.

All the facts listed above suggest that the shells R1 and R2 are located in the most dynamically active part of the star-forming complex. This is indeed where new-generation stars are most likely to be born. We plan further detailed high spatial- and spectral-resolution studies of the kinematics of the neutral and ionized gas components in this region.

6. ACKNOWLEDGMENTS

This work was supported by the Russian Foundation for Basic Research (project no. 01-02-16118) and the Astronomy State Science and Technology Program (project 1.3.1.2). We are grateful to E. Blanton for providing an Hα-line image of IC 1613 taken upon our request with the 4-m telescope of the Kitt Peak National Observatory, to V. N. Komarov for his assistance with the observations at the Zeiss-1000 telescope, and to the Program Committee of the 6-m telescope for providing observing time.

REFERENCES

1. J. Meaburn, C. A. Clayton, and M. J. Whitehead, Mon. Not. R. Astron. Soc. **235**, 479 (1988).
2. L. Georgiev, J. Borissova, M. Rosado, *et al.*, Astron. Astrophys., Suppl. Ser. **134**, 21 (1999).
3. T. A. Lozinskaya, O. K. Silchenko, D. J. Helfand, *et al.*, Astron. J. **116**, 2328 (1998).
4. T. A. Lozinskaya, A. V. Moiseev, V. L. Afanas'ev, *et al.*, Astron. Zh. **78**, 485 (2001) [Astron. Rep. **45**, 417 (2001)].
5. P. W. Hodge, Astrophys. J., Suppl. Ser. **37**, 145 (1978).
6. V. L. Afanas'ev, V. V. Vlasyuk, S. N. Dodonov, *et al.*, Preprint No. 54, SAO RAN (1990).
7. T. A. Kartashova and N. M. Chumakova, Astrofiz. Issled. (Leningrad) **10**, 44 (1978).
8. J. Lequeux, N. Meysonnier, and M. Azzopardi, Astron. Astrophys., Suppl. Ser. **67**, 169 (1987).
9. P. Hodge, M. G. Lee, and M. Gurwell, Publ. Astron. Soc. Pac. **102**, 1245 (1990).
10. J. S. Price, S. F. Mason, and C. A. Gullixson, Astron. J. **100**, 420 (1990).
11. D. A. Hunter, W. N. Hawley, and J. S. Gallagher, Astron. J. **106**, 1797 (1993).
12. M. Valdez-Gutierrez, M. Rosado, L. Georgiev, *et al.*, Astron. Astrophys. **366**, 35 (2001).
13. A. R. Sandage, Astrophys. J. **166**, 13 (1971).
14. G. Lake and E. D. Skillman, Astron. J. **98**, 1274 (1989).
15. E. Wilcots *et al.* (2002) (in press).
16. V. Straizys, *Multicolor Stellar Photometry* (Mokslas, Vil'nyus, 1977; Pachart Publ. House, Tucson, 1992).
17. A. Dolphin, A. Saha, E. D. Skillman, *et al.*, Astrophys. J. **550**, 554 (2001).
18. T. A. Lozinskaya, Pis'ma Astron. Zh. **24**, 285 (1998) [Astron. Lett. **24**, 237 (1998)].

Translated by A. Dambis

Astronomy Reports, Vol. 45, No. 6, 2001, pp. 417–427. Translated from Astronomicheskiĭ Zhurnal, Vol. 78, No. 6, 2001, pp. 485–497.
Original Russian Text Copyright © 2001 by Lozinskaya, Moiseev, Afanas'ev, Wilcots, Goss.

Interstellar Medium Surrounding the WO Star in the Galaxy IC 1613: New Optical and Radio Observations

T. A. Lozinskaya[1], A. V. Moiseev[2], V. L. Afanas'ev[2], E. Wilcots[3], and W. M. Goss[4]

[1]*Sternberg Astronomical Institute, Universitetskiĭ pr. 13, Moscow, 119899 Russia*

[2]*Special Astrophysical Observatory, Nizhniĭ Arkhyz, Zelenchukskiĭ raĭon, Karachaevo-Cherkessia, 357147 Russia*

[3]*Department of Astronomy, University of Wisconsin–Madison, 475 N. Charter St., Madison, WI 53706 USA*

[4]*National Radio Astronomy Observatory, P.O. Box O, 1003 Lopezville Road, Socorro, NM 87801 USA*

Received September 30, 2000

Abstract—Observations of the nebula S3 associated with the WO star in the galaxy IC 1613 and of an extended region surrounding S3 are reported. The star and bright core of the nebula were observed with a multipupil fiber spectrograph mounted on the 6-m telescope of the Special Astrophysical Observatory of the Russian Academy of Sciences. Images in the principle spectral lines and integrated spectra of the star and three compact clumps were obtained, and the radial-velocity field constructed. An extended region of the galaxy was observed with the Very Large Array at 21 cm. A giant ring or H I shell enclosing a large fraction of the stellar population in IC 1613 was discovered. The WO star and associated bipolar nebula, which we discovered earlier, lie at the inner edge of the H I ring. A local H I deficiency and two arclike H I ridges were also detected for the first time and probably represent the neutral component of the bipolar shell surrounding the WO star. The two arclike ridges may also have been produced by the collective stellar wind (and supernova explosions?) in OB association No. 9 from the list of Hodge. A scenario for the formation of the extended bipolar feature is discussed, based on the new data. © *2001 MAIK "Nauka/Interperiodica".*

1. INTRODUCTION

Only six WR stars of more than five hundred such objects in the Local Group of galaxies belong to the rare WO class, which represents a very brief final evolutionary stage of massive stars approaching the naked CO-core stage (see [1, 2] and references therein). WO stars are characterized by powerful stellar winds (with terminal velocities reaching ≈5000 km/s [1, 3–5]), and their effective temperatures can be as high as 10^5 K [4, 6–8]. One of these six stars was discovered by D'Odorico and Rosa [9] (see also [10, 11]) in the dwarf irregular galaxy IC 1613. The star was identified by the specific wide bands it produces in the spectrum of the core of the bright emission nebula S3 from the list of Sandage [12]—a giant $29'' \times 9''$ (93×30 pc) H II region. Throughout this paper, we adopt the distance 660 kpc for IC 1613, as derived by Saha *et al.* [13]. The central region of S3 shows a bright He II 4686 Å emission [9, 14, 15]. A detailed spectral analysis of the nebula and a discussion of its chemical composition are presented by Garnett *et al.* [15] and Kingsburgh and Barlow [16]. The nebula S3 was found to be a source of thermal radio emission [17]; the full size at half-maximum intensity of the radio source ($19'' \times 14''$) corresponds to a bright region of the optical nebula visible on deep Hα images taken by Hodge *et al.* [18] and Hunter *et al.* [19].

Our observations made with a scanning Fabry–Perot interferometer mounted on the 6-m telescope of the Special Astrophysical Observatory (SAO) and narrowband Hα and [O III] images taken with the 4-m telescope of the Kitt Peak National Observatory resulted in the discovery of a faint external bipolar feature (hereafter called the bipolar shell) extending far beyond the bright nebula S3 [20, 21]. The sizes of the two external components—the southeastern and northwestern shells—are $35'' \times 24''$ (or 112×77 pc) and $\simeq 60'' \times 70''$ (or $\simeq 190 \times 220$ pc), respectively. Radial-velocity measurements at the maximum and the Hα line halfwidths provide evidence for expansion of the bipolar shell, with the lower limits to the expansion velocities of the southeastern and northwestern shells being 50 km/s and at least 70 km/s, respectively.

Afanas'ev *et al.* [21] proposed a scenario for the formation of the unique bipolar feature by the stellar wind of the WO star, which is embedded in a dense layer at the boundary of a supercavity in the galaxy's H I distribution. We identified this supercavity by analyzing the H I column density distribution in IC 1613 published by Lake and Skillman [22]. At that time, we hypothesized the presence of a dense shell surrounding the supercavity and a physical association with the WO star but were not able to prove that this was the case.

In the current paper, we report the results of new observations of the nebula associated with the WO star in the galaxy IC 1613. We observed the bright core of the nebula S3 using the MPFS multipupil fiber spectrograph mounted on the SAO 6-m telescope (Section 2).

1063-7729/01/4506-0417$21.00 © 2001 MAIK "Nauka/Interperiodica"

We obtained integrated spectra of individual compact clumps in the central bright region and reconstructed the radial-velocity field from our Hβ and [O III] 5007 Å measurements. We also obtained observations of a large sector of IC 1613 at 21 cm with the Very Large Array (VLA; Section 3). We derived a detailed image of the neutral-gas distribution, which revealed a giant dense ring or H I shell surrounding the supercavity, and showed that the WO star does indeed reside in this dense ring and is physically interacting with it. We also found a local H I deficiency and two extended features, testifying to the presence of a neutral gas component associated with the ionized bipolar shell. In Section 4, we discuss the results of the observations and analyze a possible scenario for the formation of the extended bipolar feature.

2. SPECTROSCOPIC OBSERVATIONS OF THE WO STAR AND NEBULA S3

2.1. Observations and Data Reduction

The spectroscopic observations were made on November 29 and 30, 1999, using the new MPFS panoramic multipupil fiber spectrograph mounted at the primary focus of the SAO 6-m telescope. A description of the spectrograph can be found at the webpage http://www.sao.ru/~gafan/devices/mpfs_main.htm.

Compared to the earlier version of the MPFS [23], the new spectrograph has a larger field of view, wider spectral range, and higher quantum efficiency. The spectrograph uses a 1024×1024 CCD as a detector and allows a set of spectra to be taken simultaneously from 240 spatial elements ("micropupils") forming a 16×15 array in the plane of the sky. The angular size of an image element can be varied from $0.5''$–$1.0''$. A spectrum of the sky background $4.5'$ from the center of the field of view is taken simultaneously. Table 1 gives a log of the MPFS observations.

These observations were reduced using IDL-based software developed by the SAO Laboratory for Spectroscopy and Photometry of Extragalactic Objects. The preliminary data reduction included offset frame subtraction, flat-field correction, cosmic-ray removal, extraction of individual spectra from the CCD images, and wavelength calibration using the spectrum of a He–Ne–Ar lamp. We then subtracted the night-sky spectrum from the linearized spectra and used a number of spectrophotometric standards observed at the same zenith angle as IC 1613 to convert the observed fluxes to an absolute energy scale. We used the same standards to derive the seeing estimates given in Table 1.

Analysis of the observations showed that the data obtained on November 29 and 30, 1999, yielded consistent values for the main parameters measured (line fluxes and velocities). Therefore, we will consider further only the November 30, 1999, data, since they had a higher angular resolution compared to the data of November 29, 1999.

Figure 1a shows an [O III] line image of the central region of the nebula S3 surrounding the WO star from the data of [21], together with the boundaries of the field of view of our new MPFS observations.

2.2. Analysis of the Field Spectroscopy Results

The WO star

We obtained the integrated spectrum of the WO star by co-adding 24 individual spectra, which exhibited the broad emission bands characteristic of Wolf–Rayet stars.

During the flux measurements, we fitted the emission lines using superpositions of two to six Gaussians; the resulting flux and equivalent-width estimates are summarized in Table 2. Note that the errors quoted in this table do not include uncertainty in the continuum level, which could contribute systematic errors to the equivalent widths. For comparison, this table also gives the fluxes and equivalent widths of the corresponding lines from [16].

We observed a narrower spectral interval than Kingsburgh and Barlow [16]; it is clear from Table 2 that the two sets of observations do not show significant discrepancies. The differences between the equivalent widths are due primarily to the different methods used to determine the continuum level (unlike Kingsburgh and Barlow [16], we did not take into account the nebular continuum component). Our flux estimates are higher than those of [16] for most of the lines. This is likely due to the fact that our panoramic detector collected all the light from the star, whereas a long slit whose width ($1''$) was comparable to or smaller than the image size was used in [16]. To test this hypothesis, we integrated the spectra of the star only over the lenses lying within a $1'' \times 5''$ rectangle aligned along PA = 55°, i.e., in the direction of the slit used in [16]. The resulting WO-star line fluxes, indeed, proved to be a factor of 1.5–2 lower, on average, than the fluxes listed in Table 2. Moreover, as we show below, the emission-line bright-

Table 1. Log of MPFS observations

Date	Size of micropupil	Field of view	Spectral interval, Å	δλ, Å	Exposure, s	Seeing
Nov. 29, 1999	$1''$	$16'' \times 15''$	4450–7050	8	7200	$2''.7$
Nov. 30, 1999	0.75	12×11.3	4450–7050	8	7200	1.8

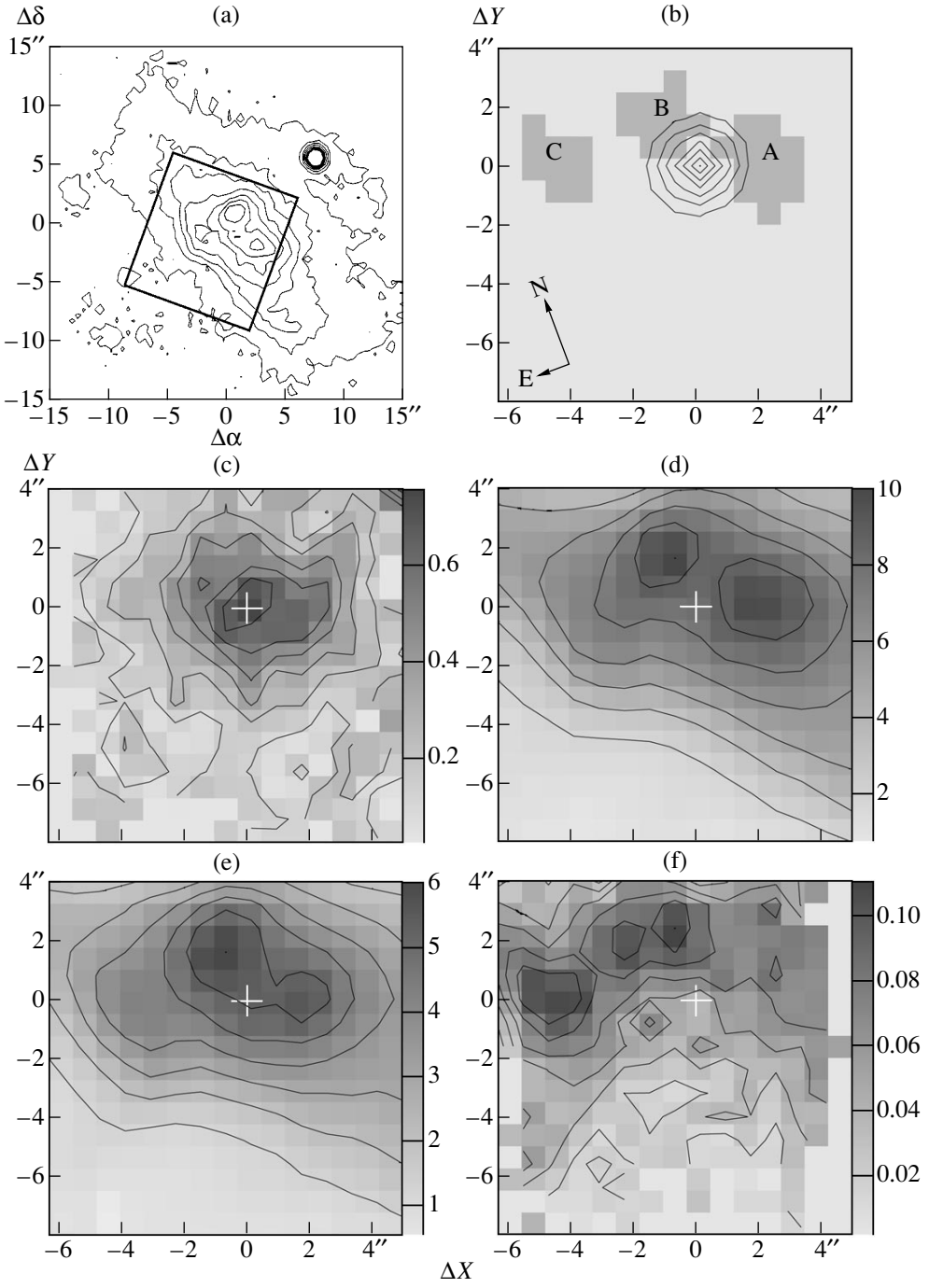

Fig. 1. (a) [O III] image of the nebula surrounding the WO star, adopted from [21]. The frame shows the MPFS field of view for the observations described in this paper. (b) MPFS observations. Isophotes show the brightness distribution in the C IV 5801 Å line emitted by the WO star. Also indicated are the positions of emission clumps. (c), (d), (e), and (f): Images and isophotes of the nebula in the He II 4686 Å, [O III] 5007 Å, Hα, and [S II] 6717 + 6731 Å emission lines, respectively. The cross indicates the position of the WO star. Surface brightness is in units of 10^{-15} erg cm^{-2} s^{-1} arcsec^{-2}.

ness peak in the nebula does not coincide with the position of the star. This could have led to an offset during the positioning of the narrow slit on the star in [16], resulting in further underestimation of the line fluxes.

We constructed images in the C IV + He II 4659 Å, O V 5590 Å, and C IV 5801 Å emission lines by integrating the spectra over the intervals 4600–4725, 5535–5653 and 5735–5850 Å, after subtraction of narrow nebular line components blended with the WO-star lines. The centroids of all the images agree to within ±0.05″ and also agree with the centroid of a continuum image made in the vicinity of 6100 Å. We estimate the

Table 2. Fluxes and equivalent widths of emission lines in the spectrum of the WO star

λ, Å	Line	F, erg cm^{-2} s^{-1}		EW, Å	
		this paper	[16]	this paper	[16]
4659	C IV + He II	2.56×10^{-14}	1.48×10^{-14}	360 ± 25	330 ± 20
5290	O VI	9.50×10^{-16}	1.26×10^{-15}	13 ± 2	55
5411	He II + C IV	1.28×10^{-15}	5.5×10^{-16}	17 ± 2	30
5470	C IV	3.46×10^{-16}	4.2×10^{-16}	4 ± 1	20
5590	O V	4.04×10^{-15}	2.46×10^{-15}	62 ± 11	120
5801	C IV	2.10×10^{-14}	1.41×10^{-14}	420 ± 97	690 ± 40

FWHM of these emission-line images of the WO star to be 1.85 ± 0.05″, 1.84 ± 0.09″, and 1.67 ± 0.03″, respectively, consistent with the seeing estimate of 1.″8 obtained for the standard star (Table 1). Note that, due to certain specific features of the spectrograph, the images constructed from the micropupil array are slightly elongated (1:1.15) along the *x*-axis (Fig. 1b). Therefore, all our FWHM estimates are based on measurements in the *y*-direction.

The continuum image of the WO star was somewhat more extended (FWHM = 2.2″ ± 0.15″) and exhibited a faint base. (This could indicate the presence of a compact cluster made up of several stars, but firm conclusions require further observations.)

Structure and Emission Spectrum of S3

We constructed an entire series of monochromatic images of the bright core of the nebula in the He II 4686 Å, [O III] 5007 Å, [S II] 6717 + 6731 Å, and Hα lines by obtaining Gaussian fits to the emission lines. The results are shown in Figs. 1c–1f. All the line profiles are fit well by single Gaussians and do not show any systematic deviations. Note, however, that the expected relative gas velocities (up to 100 km/s in the bright core [21]) are appreciably lower than the spectral resolution of our data (FWHM = 350–450 km/s).

It is evident from Fig. 1 that the morphology of the nebula is appreciably different in different lines. For example, the He II brightness peak is coincident with the position of the WO star; the He II brightness decreases with distance from the star, and the full size of the emission region is 10″ × 9″. The situation is quite different in the brighter [O III] and Hα lines and also in the [S II] lines: the corresponding images exhibit several bright clumps 2″–3″ from the star (Fig. 1). The [O III] and Hα images show two well-defined bright clumps north and northwest of the star (marked A and B, respectively, in Fig. 1b) and a more extended clump northeast of the star (clump C in Fig. 1b). This extended clump is especially prominent in the [S II] images, where clump A cannot be seen at all.

We discovered the clumpy structure of the S3 core in our earlier study [21], based on uncalibrated [O III] and Hα images of the region. However, having no emission spectra for the clumps, we mistook the WO star for a clump (clump *2* in [21]). (Clumps A and B from our new observations correspond to clumps *3* and *1*, respectively, from [21]; clump C, which can be confidently identified only in the [S II] lines, was not discovered earlier in the [O III] and Hα images.)

We obtained the integrated spectra of clumps A, B, and C; the positions of the image elements whose spectra were co-added in each clump are shown in Fig. 1b. Table 3 gives the relative line intensities for the three clumps, corrected for selective extinction. We assumed $c(\mathrm{H}\beta) = 0.1$ and E(B–V) = 0.069, in accordance with [16]. For comparison, Table 3 also presents the data of [16] for the integrated spectrum of the central region of S3.

2.3. Ionized Gas Velocities in the Core of S3

We used the resulting spectra to construct the radial-velocity field for the central part of the nebula S3. We determined the velocity fields from measurements made in the main spectral lines from Gaussian fits to the corresponding line profiles. Analysis of the night-sky spectrum showed that, after linearization of the spectra, there remained systematic velocity variations in the night-sky lines across the field of ±0.1–0.15 channels, i.e., about 15 km/s. We corrected our emission-line velocity fields for this systematic offset; Fig. 2 shows the results.

We used the resulting velocity fields to estimate the mean velocities in various lines for clumps A, B, and C and for the nebula region projected onto the WO star. In this last case, we used the same set of lenses used when co-adding the spectrum of the star (see Section 2.1). The results are summarized in Table 4, where the quoted errors correspond to the velocity dispersion within individual spatial elements.

The resulting mean clump velocities are consistent with the mean velocity of the nebula S3 as a whole derived from our Fabry–Perot interferometric measurements ($V_{\mathrm{hel}} = -216 \pm 1$ km/s) [21] (taking into account possible systematic absolute calibration errors of 15–20 km/s for the interferometric observations) and are in full agreement with the measurements of Tomita *et al.* [24], based on a single spectrogram of S3: $V_{\mathrm{hel}} = -235$

Table 3. Line intensities for clumps A, B, and C

λ, Å	Line	$I/I(H_\beta)$, %			
		A	B	C	[16]
4686	He II	31.1 ± 0.7	28.3 ± 0.8	12.2 ± 0.8	23.1
4711	[Ar IV]	7.1 ± 0.7	7.9 ± 0.8	3.1 ± 0.8	4.5
4740	[Ar IV]	6.3 ± 0.7	6.5 ± 0.7	5.8 ± 0.8	5.62
4861	Hβ	100.0	100.0	100.0	100.0
4959	[O III]	174 ± 5	168 ± 8	164.0 ± 2	188
5007	[O III]	519 ± 13	511 ± 20	489 ± 6	–
5876	He I	4.1 ± 0.3	4.6 ± 0.7	5.4 ± 0.8	7.1
6542	[N II]	1.4 ± 0.2	1.8 ± 0.3	2.3 ± 0.3	–
6563	Hα	273 ± 4.0	283 ± 10	273 ± 5	276
6583	[N II]	2.4 ± 0.2	2.8 ± 0.4	4.6 ± 0.3	6.4
6717	[S II]	8.9 ± 0.3	10.2 ± 0.2	15.2 ± 0.9	8.73
6731	[S II]	6.9 ± 0.3	7.6 ± 0.2	10.4 ± 0.8	5.78
		$(I)\,H\beta \times 10^{-14}$, erg cm^{-2} s^{-1}			
		1.5	1.2	7.7	

to –230 km/s. We show below (see Section 3) that the velocities of the densest H I clouds in the vicinity of S3 are ≈ –230 km/s or differ from this value by less than 10 km/s.

Two cone-shaped regions where the velocities are systematically different from the mean are immediately apparent in Fig. 2. Our [O III] line measurements enable identification of the region where the velocities differ from the mean value by 40–50 km/s. Both deviations from the mean velocity agree with the velocity variations in the central part of the bright nebula S3 presented in [21], based on interferometric Hα measurements. Note that the cone-shaped regions originate at the position of the star, a pattern that, generally speaking, might indicate an asymmetric stellar wind. However, firm conclusions require further observational evidence, since such velocity variations could also be a consequence of the inhomogeneous structure of the interstellar medium in the near environment of the star.

3. RADIO OBSERVATIONS IN THE 21-CM LINE

3.1. Observations and Data Reduction

We constructed a high angular resolution VLA H I map covering an extended region of the galaxy IC 1613, including the WO star and the associated bipolar shell (this was part of a larger project to investigate the neutral-gas structure and kinematics in IC 1613 [25]). The maps shown below were constructed from combined B-, C-, and D-array VLA observations with a velocity resolution of 2.57 km/s. The data were Hanning smoothed, subjected to the usual calibration procedure, and made into maps using the AIPS package.

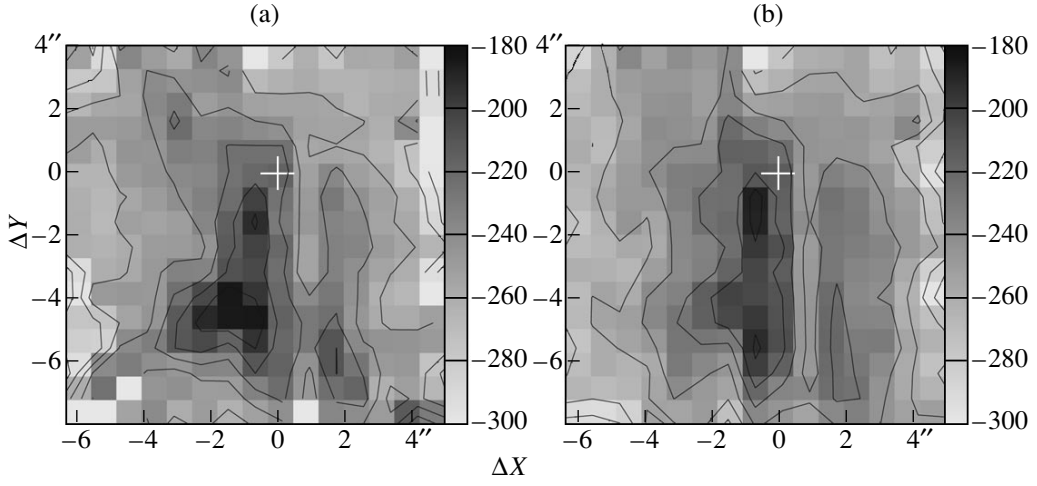

Fig. 2. Ionized gas velocity field in the (a) Hβ and (b) [O III] 5007 Å lines based on the MPFS observations. The cross indicates the position of the WO star. The velocity scale is in km/s.

Table 4. Mean velocities for clumps A, B, and C and toward the WO star

λ, Å	Line	V_{hel}, km/s			
		A	B	C	WO
4686	He II	−213 ± 14	−227 ± 22	−186 ± 30	−214 ± 21
4861	Hβ	−250 ± 10	−242 ± 13	−252 ± 7.	−231 ± 18
4959	[O III]	−247 ± 11	−241 ± 13	−257 ± 6.	−230 ± 18
5007	[O III]	−241 ± 8.	−238 ± 17	−253 ± 10	−225 ± 18
6563	Hα	−246 ± 6.	−248 ± 5.	−242 ± 4.	−251 ± 6.
6717	[S II]	−247 ± 23	−225 ± 13	−224 ± 11	−253 ± 26
Mean		−241 ± 6	−237 ± 4	−236 ± 11	−234 ± 6

The results are represented in the form of a data cube with angular resolution $7\farcs4 \times 7\farcs0$, which corresponds to a linear resolution of ~23 pc.

Figure 3 shows the H I distribution for the eastern sector of the galaxy constructed using these data. A well-defined giant cavity (supercavity) surrounding a large fraction of the stellar population of IC 1613 is immediately apparent. This giant, low surface brightness region of 21-cm emission is also visible on the map of Lake and Skillman [22]. Earlier [21], we suggested that this region was deficient in neutral gas because it had been swept out, implying that the supercavity should be surrounded by a dense, wind-blown shell. Figure 3 shows that such a shell or ring of neutral gas does, indeed, exist and that the WO star resides in a dense gas layer near its inner edge.

The angular size of the supercavity is about 5′, corresponding to a linear size of 1 kpc. The characteristic thickness of the shell is $\Delta R \simeq 1'$–$2'$, or 200–350 pc.

A sketch of the bipolar ionized shell surrounding the WO star and its relative position with respect to the H I supercavity are shown on an enlarged scale in Fig. 4, which presents the southeastern sector of the H I ring.

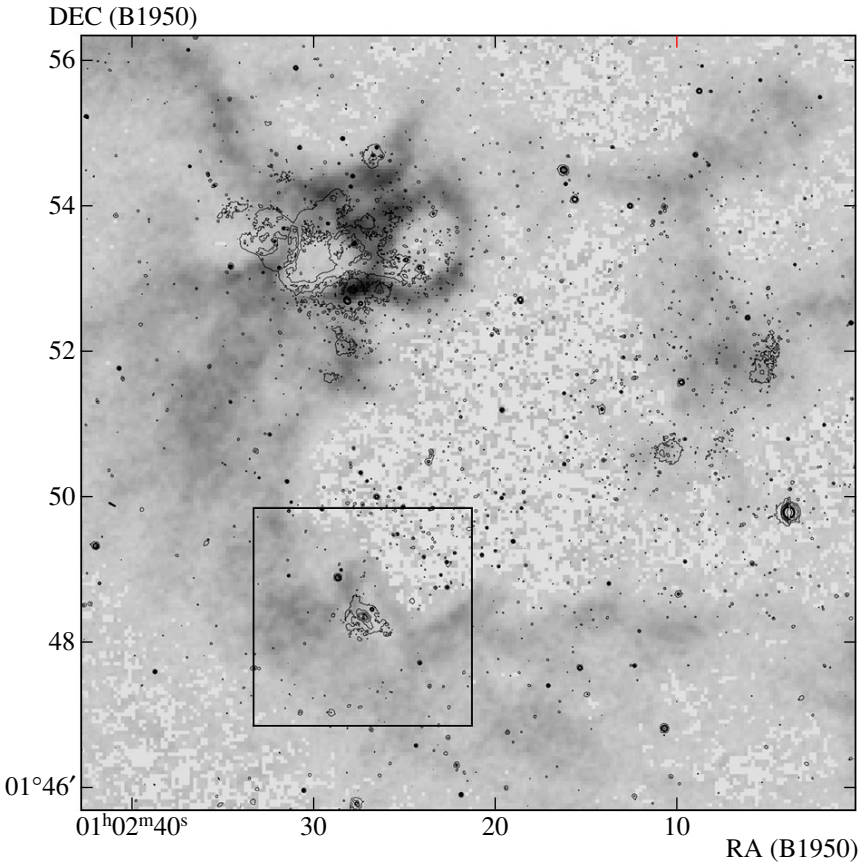

Fig. 3. Eastern sector of the galaxy IC 1613: brightness distribution in the 21-cm line from the VLA data (gray scale) and Hα isophotes (based on the observations made with the 4-m KPNO telescope). An enlarged-scale version of the framed region surrounding the nebula S3 and WO star is shown in Fig. 4.

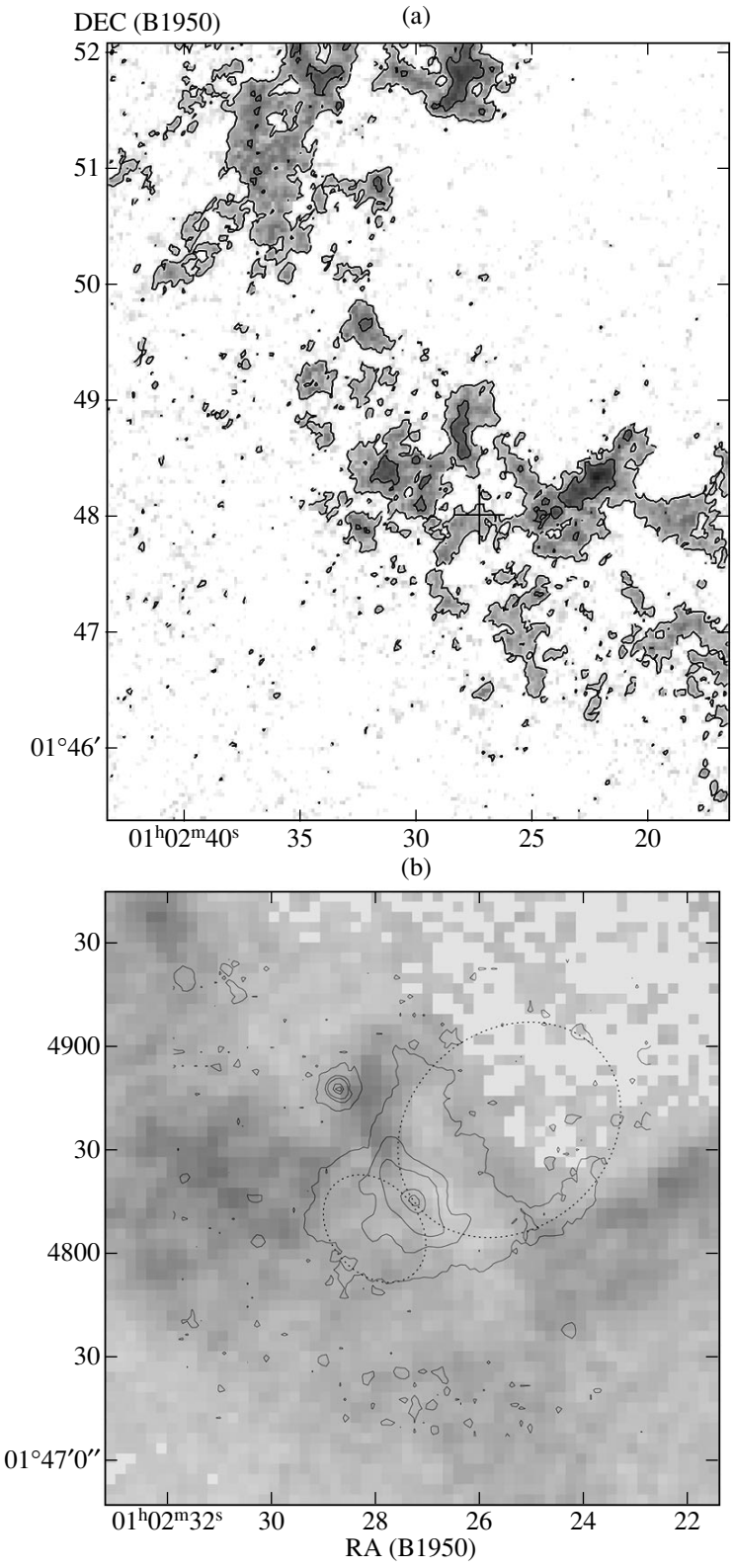

Fig. 4. (a) Southeastern sector of the dense H I ring (including the framed region in Fig. 3). The contours correspond to H I column densities of $N(\mathrm{H\ I}) = (2, 6, 18) \times 10^{20}$ cm^{-2}. The cross indicates the position of the WO star. (b) Sketch of the bipolar ionized shell associated with the WO star (isophotes adopted from [21]); the Hα isophotes correspond to brightness levels of 0.028, 0.2, 0.4, 1.0, and 2.0×10^{-15} erg cm^{-2} s^{-1} arcsec^{-2}. The H I distribution is superimposed as a gray-scale image.

Table 5. Parameters of H I clouds in the vicinity of the bipolar shell

Cloud	RA (B1950)	DEC (B1950)	N(H I), 10^{20} cm^{-2}	M, $10^4 M_\odot$
a	1 2 28	1 47 55	5	~4
b	1 2 31.5	1 48 20	8	~3
c	1 2 21–24	1 48 08	20	10
d	1 02 26	1 48 20	7	2
e	1 02 28	1 48 30–60	9	6

This figure shows that the elongated core of the ionized bipolar shell (previously known as S3) and its bright southeastern component are located in a dense region of the ring, whereas the extended, faint northwestern component is in the low-density medium inside the supercavity.

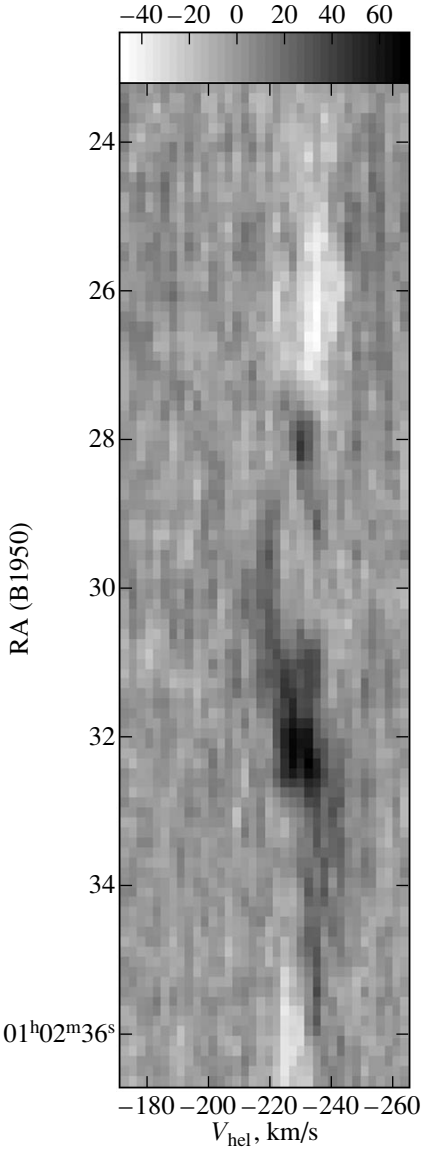

Fig. 5. H I radial-velocity variations in a right-ascension band from the VLA observations (see text). The fluxes are in mJy/beam.

Figure 4 clearly shows a local decrease in the 21-cm brightness, filled by the ionized gas of the core and southeastern component. We can also see two prominent, extended H I features just on the outside of the two sides of the northwestern component of the ionized shell, which reproduce the shape of the shell. This structure probably provides evidence for a local neutral shell surrounding the bipolar shell.

The parameters of the most prominent H I clouds forming the local neutral shell surrounding the ionized bipolar feature are summarized in Table 5, which presents the central coordinates, total mass, and maximum column density of each cloud.

3.2. Neutral Gas Velocities

In order to reveal the possible effect of the expansion of the local neutral shell, we constructed the radial-velocity distribution within a right-ascension band passing through the WO star (Fig. 5). The band is 200″ wide and therefore includes all clouds H I making up the local shell. This distribution clearly demonstrates velocity variations with distance from the star that are typical of an expanding shell (the so-called "velocity ellipse") at right ascensions from $01^h02^m28^s$ to $01^h02^m31^s$. This region corresponds to the part of the local H I shell that is east of the WO star; the characteristic radius of this "half-shell" is 100–140 pc. The velocity difference between the two sides of the neutral shell is ~20 km/s, suggesting an expansion velocity of ~10 km/s. The velocities of the densest "unaccelerated" H I clouds in a large region surrounding the WO star are $V_{hel} = -230 \pm 5$ km/s.

4. DISCUSSION

The results of spectroscopic observations of the WO star and the central region of the nebula S3 reported in this paper are in full agreement with earlier observations, within the errors limits, when the different slit locations are taken into account. The spectra of the compact clumps identified in this paper do not differ significantly from the those of the nebula S3 (see [15, 16] and references therein). The relative line intensities listed in Table 3 are suggestive of a typical H II region ionized by a star with a high effective temperature. The observed differences between the spectra of the three clumps could be due to different excitation conditions: distance from the exciting star and electron density. No shock signatures were found either in the emission spectra (the [N II] and [S II] lines are weak) or in the mean velocities of the bright clumps. The ionized gas velocities of the clumps in the central core of the nebula agree with velocity measurements of neutral gas clouds in the vicinity of the bipolar shell.

Electron Density and He Abundance in the Nebula Core

The relative intensities of the [S II] 6717/6731 Å doublet can be used to estimate the electron density in the three bright clumps identified in this paper. We determined the electron densities in clumps A, B, and C using formulas adopted from [26], assuming that the electron temperature of the nebula is T_e =17000 K (as determined in [16] from the [O III] 4959/4363 Å line intensities). The resulting values are listed in Table 6.

We derived the He abundance in the nebula from He I and He II line intensities of individual clumps using the diagnostic relations and recombination coefficients for hydrogen and helium from [27]. At T_e = 17000 K we determined the relative helium abundances $N(He^+)/N(H)$ and $N(He^{++})/N(H)$ and the total helium abundances $N(He)/N(H)$ (in number) of the clumps. The results are given in Table 6, which also lists data adopted from [16]. We can see that our abundances coincide with those of [16] and are in good agreement with the estimate of [10]: $N(He)/N(H) = 0.073 \pm 0.009$. (In both [10] and [16], the He abundances were obtained from the spectrum of the entire bright core of the nebula without subdividing it into individual clumps.)

Table 6. Electron density and He abundances of clumps A, B, and C

Parameter	A	B	C	[16]
n_e, cm^{-3}	170	80	≤30	100
$N(He^+)/N(H)$	0.051	0.057	0.067	0.057
$N(He^{++})/N(H)$	0.028	0.025	0.011	0.025
$N(He)/N(H)$	0.079	0.082	0.078	0.082

Velocity of the Stellar Wind of the WO star

One of the major parameters determining the structure and kinematics of the interstellar medium at large distances from WR stars is the stellar-wind velocity. Kingsburgh *et al.* [2] have shown (see also [16]) that the halfwidth of the C IV 5801 Å line at zero intensity is a good estimator of the terminal wind velocities of WR stars. The C IV line halfwidth at zero intensity measured from our spectra for the WO star yields a terminal wind velocity of V_w = 2910 km/s, which is virtually coincident with the value 2850 km/s obtained in [16], given that the accuracy of our measurements is determined by the width of the spectral channel (~130 km/s). We thus confirm the conclusion of Kingsburgh and Barlow [16] that the terminal wind velocity of the WO star in IC 1613 is the lowest among the six objects of this class currently known in the Local-Group galaxies.

Large-Scale Structure of the Interstellar Medium

In principle, the giant H I ring shown in Fig. 3 could be the projection onto the plane of the sky of a shell or torus. A torus could be the result of the wind-blown supercavity breaking out of the gaseous disk of the galaxy. In both cases, the neutral gas ring surrounding the supercavity displays a characteristic filamentary structure. The filamentary system making up the H I ring bifurcates at its southeastern end. A system of arclike filaments with characteristic lengths of 1′–1.5′, or 200–300 pc, is also apparent. This filamentary pattern undoubtedly testifies to the action of dynamically active processes that are responsible for the formation of the supercavity and the surrounding dense ring or shell. This large-scale structure apparently formed as the result of a burst of star formation in the region. However, determining the nature of this burst is a separate problem which lies beyond the scope of this paper. Of interest to us here is the very existence of such a dense shell or torus surrounding the supercavity, since we consider this large-scale mass distribution to be responsible for the unique bipolar structure of the extended ionized shell associated with the WO star.

Lozinskaya [20] suggested that the bipolar structure of the ionized shell surrounding the WO star might be the result of a strong stellar wind breaking out of the dense gas layer. Earlier [21], we associated this dense layer with a hypothetical wind-blown shell, which we suggested should surround the giant H I-deficient region in IC 1613 seen on the map of Lake and Skillman [22]. However, only in this paper have we finally been able to provide some evidence supporting this hypothesis. The following factors form our principal arguments.

(1) One piece of evidence is the relative orientation of the bipolar ionized shell with respect to the H I supercavity. It is clear from Fig. 4 that the bright core of the nebula is extended along the boundary of the dense H I ring; the smaller southeastern component of the ionized bipolar shell lies inside a dense neutral gas layer, and the extended northwestern component lies in the low-density medium inside the supercavity.

(2) Afanas'ev *et al.* [21] showed that the southeastern component is brighter than the northwestern component and also has a lower expansion velocity.

(3) The local cavity and extended H I features whose discovery is reported in this paper testify to the presence of a neutral shell surrounding the ionized bipolar shell, providing direct evidence for a physical association of the WO star and the ionized bipolar shell with the supercavity and dense H I ring (the only alternative being a chance projection).

The gas density in the clouds making up the local H I shell surrounding the bright central and southeastern components of the ionized nebula can be derived from our maximum column density and total mass estimates, assuming that the clouds have the same sizes in the line-of-sight and transverse directions. The clouds that make up the local neutral H I shell have irregular structures. Clouds a, c, and e in Table 5, which make up the

expanding part of the H I half-shell, have lengths in the plane of the sky ranging from 40 to 120 pc. For a column density of (5–9) $\times 10^{20}$ cm^{-2}, this yields a characteristic density of $n_{\rm H\,I} \simeq 1.5$–7.5 cm^{-3}.

For comparison, we present estimates of the average density of ionized gas in this nebula: Davidson and Kinman [10] found $n_e = 8.5$ cm^{-3} based on the Hβ emission of the central 6″ of the nebula S3; Kenicutt [28] reports $n_e \simeq 1$ cm^{-3} based on a study of the integrated Hα emission of the bright nebula; and Goss and Lozinskaya [17] found $n_e = 3.5$ cm^{-3} from their analysis of its thermal radio emission.

If the H I clouds surrounding the bright central and southeastern components of the bipolar ionized shell are, indeed, parts of a shell of neutral gas blown out by the stellar wind, the radius and expansion velocity of the expanding section east of the WO star should be 100–140 pc and about 10 km/s, respectively (see Section 3). In the standard model [29, 30], we find the kinematic age of the wind-blown neutral shell to be $t = (6$–$8) \times 10^6$ yr. (Note that this estimate depends neither on the stellar wind power nor on the density of the surrounding gas.) This age substantially exceeds the duration of the final WO stage and corresponds to the main-sequence lifetime of a massive star ($M \geq (30$–$40 M_\odot)$). We thus conclude that the local neutral shell surrounding the bright southeastern and central components of the ionized nebula could have been produced by the stellar wind of the WR progenitor when it was still a main-sequence star. Note that, earlier [21], we concluded that the ionized bipolar shell was blown out by the successive action of the stellar wind from the central star, first at the WR and then at the WO stage.

Our estimates indicate that the terminal velocity of the stellar wind of the WO star reaches 3000 km/s (see Section 2); a mass-loss rate of $2.9 \times 10^{-5} M_\odot$/yr was derived in [16] based on the relation between the He II line luminosities and the mass-loss rates for two WO stars. Accordingly, the power of the stellar wind of the WO star in IC 1613 is $L_w \simeq 10^{38}$ erg/s. In all likelihood, the wind power was a factor of two to three lower during the earlier WR stage (WR stars typically have terminal velocities of 2000 km/s), but the duration of the WR stage ($\simeq 5 \times 10^5$ yr) is at least an order of magnitude longer than that of the WO stage. The power of the stellar wind of the main-sequence progenitor could have been two orders of magnitude lower than at the final Wolf–Rayet stage, however, the main-sequence lifetime was at least an order of magnitude longer than the Wolf–Rayet stage.

The formation of the wind-blown shell is determined by the standard relation $R = 28\,(L_{36}/n_0)^{1/5} t_6^{3/5}$, where L_{36} is the power of the stellar wind in units of 10^{36} erg/s, n_0 is the density of the surrounding gas, R is the radius in pc, and t_6 is the time in units of 10^6 yr [29, 30]. We can easily see that, although the mechanical energy inputs from the massive star during the WR and WO stages are comparable, the stellar wind produced during the main-sequence stage is capable of creating a larger shell than the powerful but short-lived stellar wind at the final stage. Therefore, this latter wind serves as an additional source of mechanical energy in an already formed, slowly expanding shell.

Our results for the two extended arclike H I clouds surrounding the northwestern component of the ionized shell are much less conclusive. On the one hand, these formations could be the result of the stellar wind of the WO star and its progenitor breaking into the tenuous gas inside the supercavity. Our measurements, indeed, indicate that the H I surface density inside the supercavity is at least an order of magnitude lower than in the clouds listed in Table 5. The thickness of the emitting gas layer can be taken to be twice that of the supershell in the plane of the sky, i.e., about 3′–4′ (600–700 pc), according to Fig. 3. Accordingly, we find the mean gas density in the supercavity to be $\simeq 0.04$–0.05 cm^{-3}. If the observed ring-shaped H I distribution is the projection of a thick torus rather than a shell, the size of the emission region should be even larger, so that the above estimate should be considered an upper limit to the gas density inside the supercavity. The same standard relation yields a radius of $R \simeq 180$ pc for a shell blown out in the tenuous medium of the estimated density over the time $t = 7 \times 10^6$ yr found above. This agrees with the observed size of the northwestern part of the local shell outlined by two extended arc-like H I clouds in Fig. 4.

On the other hand, the formation of such an arc-like structure outlined by these extended H I clouds could be the result of the collective stellar winds (and possible supernova explosions) from association No. 9 of the list of Hodge [31], which is adjacent to and inside the supercavity. (This association is the largest in size and the richest in the galaxy.) In this case, the stellar wind and ionizing radiation of the WO star act inside this already formed arc-like feature.

We plan a detailed analysis of the kinematics of the ionized and neutral gas components in this region and a comparison with the stellar population. This study should lead to unambiguous conclusions about the nature of the arclike formation and the possible genetic relation between the WO star and the association.

5. CONCLUSIONS

We have observed the central part of the nebula S3 surrounding the WO star (field spectroscopy with the 6-m telescope) and an extended surrounding region several kpc in size (21-cm VLA observations). We have mapped the brightness of the central nebula in the main spectral lines and constructed the radial-velocity distribution based on Hβ and [O III] 5007 Å line measurements.

We identified three compact clumps and determined their integrated spectra, mean velocities, and electron

densities. Our spectroscopic data for both the WO star and the central region of S3 are in agreement with previous observations (see [15, 16] and references therein). The relative line intensities in the spectrum of the nebula are indicative of pure recombination emission from a highly excited H II region.

We analyzed the structure and kinematics of the neutral gas in an extended region around IC 1613 that includes the WO star and the associated ionized bipolar shell. A giant, dense shell or toroidal formation of neutral gas about 1.5 kpc in size surrounds the H I supercavity. This giant structure was very likely produced by bursts of star formation in this region.

We also discovered for the first time a local deficiency in the brightness of the 21-cm line and two extended H I features, providing evidence that the extended ionized bipolar shell associated with the WO star [20, 21] is, in turn, surrounded by a local shell of neutral gas. The mass and expansion velocity of this shell indicate that it was blown out by the stellar wind of the WO progenitor when it was still a main-sequence star.

Our new observations support a scenario in which the extended bipolar structure was produced by the stellar wind of the WO star residing in the dense "wall" of the supercavity. The arclike structure of the extended H I clouds just outside the faint northwestern component of the ionized shell might have been shaped by the collective stellar wind (and supernova explosions?) of Hodge's [32] association No. 9. In this case, the wind and ionizing radiation of the WO star act inside this previously formed arclike structure.

ACKNOWLEDGMENTS

This work was supported by the Russian Foundation for Basic Research (project no. 98-02-16032) and the Astronomy State Science and Technology Program (project no. 1.3.1.2). The National Radio Astronomy Observatory is a facility of the National Science Foundation operated under cooperative agreement with Associated Universities, Inc. We are grateful to E. Blanton for sharing the Hα line image of IC 1613 taken at Kitt Peak National Observatory, E.E. Gerasimenko for supporting the observations at the 6-m telescope of the Special Astrophysical Observatory of the Russian Academy of Sciences, and the Program Committee of the 6-m telescope for providing the observing time for this project.

REFERENCES

1. M. J. Barlow and D. C. Hummer, in *Wolf–Rayet Stars: Observations, Physics, and Evolution (IAU Symposium 99)*, Ed. by C. W. H. Loore and A. J. Willis (D. Reidel, Dordrecht, 1982), p. 387.
2. R. L. Kingsburgh, M. J. Barlow, and P. J. Storey, Astron. Astrophys. **295**, 75 (1995).
3. A. V. Torres, P. S. Conti, and P. Massey, Astrophys. J. **300**, 379 (1986).
4. M. A. Dopita, P. J. McGregor, T. A. Lozinskaya, and S. J. Rawlings, Astrophys. J. **351**, 563 (1990).
5. V. F. Polcaro, R. Viotti, C. Rossi, and L. Norci, Astron. Astrophys. **265**, 563 (1992).
6. A. Maeder and G. Meynet, Astron. Astrophys. **210**, 155 (1989).
7. J. Melnik and M. Heydari-Malayeri, in *WR Stars and Interrelations with Other Massive Stars in Galaxies (IAU Symposium 143)*, Ed. by K. A. van der Hucht and B. Hidayat (Kluwer, Dordrecht, 1991), p. 409.
8. V. F. Polcaro, F. Giovanelli, R. K. Manchanda, *et al.*, Astron. Astrophys. **252**, 590 (1991).
9. S. D'Odorico and M. Rosa, Astron. Astrophys. **105**, 410 (1982).
10. K. Davidson and T. D. Kinman, Publ. Astron. Soc. Pac. **94**, 634 (1982).
11. T. E. Armandroff and P. Massey, Astrophys. J. **291**, 685 (1985).
12. A. R. Sandage, Astrophys. J. **166**, 13 (1971).
13. A. Saha, W. L. Freedman, J. G. Hoessel, and A. E. Mossman, Astron. J. **104**, 1072 (1992).
14. H. E. Smith, Astrophys. J. **199**, 591 (1975).
15. D. R. Garnett, R. C. Kennicutt, Y.-H. Chu, and E. D. Skillman, Astrophys. J. **373**, 458 (1991).
16. R. L. Kinsburgh and M. J. Barlow, Astron. Astrophys. **295**, 171 (1995).
17. W. M. Goss and T. A. Lozinskaya, Astrophys. J. **439**, 637 (1995).
18. P. Hodge, M. G. Lee, and M. Gurwell, Publ. Astron. Soc. Pac. **102**, 1245 (1990).
19. D. A. Hunter, W. N. Hawley, and J. S. Gallagher, Astron. J. **106**, 1797 (1993).
20. T. A. Lozinskaya, Astrophys. Space Sci. **252**, 199 (1997).
21. V. L. Afanas'ev, T. A. Lozinskaya, A. V. Moiseev, and E. Blanton, Pis'ma Astron. Zh. **26**, 199 (2000) [Astron. Lett. **26**, 153 (2000)].
22. G. Lake and E. D. Skillman, Astron. J. **98**, 1274 (1989).
23. V. L. Afanas'ev, V. V. Vlasyuk, S. N. Dodonov, and O. K. Sil'chenko, Preprint SAO, 1990, no. 54.
24. A. Tomita, K. Ohta, and M. Saito, Publ. Astron. Soc. Jpn. **45**, 693 (1993).
25. Wilcots *et al.* (2000) (in press).
26. M. M. De Robertis, R. J. Dufour, and R. W. Hunt, J. R. Astron. Soc. Can. **81** (6), 195 (1987).
27. A. F. Kholtygin, Astron. Astrophys. Trans. **12** (2–3), 85 (1997).
28. R. C. Kennicutt, Astrophys. J. **287**, 116 (1984).
29. J. Castor, R. McCray, and R. Weaver, Astrophys. J. Lett. **200**, L107 (1975).
30. R. Weaver, R. McCray, J. Castor, *et al.*, Astrophys. J. **218**, 377 (1977).
31. P. W. Hodge, Astrophys. J., Suppl. Ser. **37**, 145 (1978).

Translated by A. Dambis

Astronomy Letters, Vol. 26, No. 3, 2000, pp. 153–161. Translated from Pis'ma v Astronomicheskiĭ Zhurnal, Vol. 26, No. 3, 2000, pp. 190–199.
Original Russian Text Copyright © 2000 by Afanas'ev, Lozinskaya, Moiseev, Blanton.

A Giant Bipolar Shell around the WO Star in the Galaxy IC 1613: Structure and Kinematics

V. L. Afanas'ev[1], T. A. Lozinskaya[2]*, A. V. Moiseev[1], and E. Blanton[3]

[1] *Special Astrophysical Observatory, Russian Academy of Sciences, Nizhniĭ Arkhyz, Stavropolskiĭ kraĭ, 357147 Russia*
[2] *Sternberg Astronomical Institute, Universitetskiĭ pr. 13, Moscow, 119899 Russia*
[3] *Columbia University, New York, USA*

Received May 10, 1999

Abstract—Observations of the nebula associated with the WO star in the galaxy IC 1613 are presented. The observations were carried out with a scanning Fabry–Perot interferometer in Hα using the 6-m Special Astrophysical Observatory telescope; narrow-band Hα and [O III] images were obtained with the 4-m KPNO telescope (USA). The monochromatic Hα image clearly reveals a giant bipolar shell structure outside the bright nebula S3. The sizes of the southeastern and northwestern shells are 112×77 and $(186–192) \times (214–224)$ pc, respectively. We have studied the object's kinematics for the first time and found evidence for expansion of both shells. The expansion velocities of the southeastern and northwestern shells exceed 50 and 70 km s^{-1}, respectively. We revealed a filamentary structure of the shells and several compact features in the S3 core. A scenario is proposed for the formation of the giant bipolar structure by the stellar wind from the central WO star located at the boundary of a "supercavity" in the galaxy's H I distribution. © *2000 MAIK "Nauka/Interperiodica"*.

Key words: *interstellar medium, stellar wind, WR stars*

1. INTRODUCTION

Among more than five hundred WR stars in the Local-Group galaxies, only six objects belong to a rare group of "oxygen" Wolf–Rayet (WO) stars. According to Barlow and Hummer [1], they can be considered as a separate sequence in the WN–WC–WO chain, which represents a very short final evolutionary stage of massive stars close to a bare CO core. The WO stars are characterizes by a "superwind" (with a velocity up to 5000–6000 km s^{-1}; see [1–4]) preceded by the wind at the MS and WR stages. The WO effective temperature reaches 10^5 K [3, 5–7].

Of the six WO stars in the Local-Group galaxies, three were identified in our Galaxy, one in the LMC, one in the SMC, and one in the irregular dwarf galaxy IC 1613; only two of them are associated with bright nebulae, including WO in IC 1613.

Our interest in the latter object also stems from the fact that WO is the only WR star identified in IC 1613, although the number of WO stars cannot exceed ≈1% of the WR population because of their short lifetime.

D'Odorico and Rosa [8] and Davidson and Kinman [9] identified the WO star in IC 1613 by broad lines typical of this class of stars in the spectrum of the core of the bright emission nebula S3 [10]. The star's coordinates, RA(1950) = $1^h02^m27^s.3$ and D(1950) = +01°48′17″, are known with a 1″ accuracy [11].

The central part of S3 is characterized by intense He II 4686 emission [8, 12, 13]. A detailed spectral analysis and a discussion of the chemical composition of the bright nebula are presented in [13, 14]. Narrow-band Hα images revealed regions of weaker emission predominantly southeast of the previously known bright, elongated nebula S3 [15, 16].

Thermal radio emission was detected from S3; the sizes of the radio source at half maximum intensity are $19'' \times 14''$, and the radio image faithfully reproduces the shape of the bright optical nebula [17].

In this paper, we present our Hα observations of the nebula with a Fabry–Perot interferometer on the 6-m Special Astrophysical Observatory (SAO) telescope, as well as narrow-band Hα and [O III] images of the region obtained with the 4-m KPNO telescope.

For the first time, we have clearly revealed a weak outer bipolar shell structure far outside the bright nebula S3 and studied the kinematics of the object.

In Sect. 2, we provide basic parameters of the instruments and describe the observing and reduction techniques; the interferometric observations with the 6-m SAO telescope and the observations with the 4-m KPNO telescope are presented in Sect. 3. The origin of the unique bipolar shell structure of the nebula around the WO star is discussed in Sect. 4.

2. OBSERVATIONS AND DATA REDUCTION

2.1. Interferometric Observations

The interferometric Hα observations were carried out with a scanning Fabry–Perot interferometer at the prime focus of the 6-m SAO telescope with a focal

* E-mail address for contacts: lozinsk@sai.msu.su

reducer (the equivalent focus is *F*/2.4). The interferometer is described in [18]. The pre-monochromatization was performed by using an interference filter with FWHM $\Delta\lambda$ = 15 Å centered on Hα and tilted at an angle of 6°.5.

We used a Fabry–Perot etalon operating in the 235th order at the Hα wavelength; the separation between adjacent orders $\Delta\lambda$ = 27.9 Å corresponded to the 1274 km s^{-1} range free from order overlapping. The detector was a TK1024 1024 × 1024-pixel CCD array. The observations were carried out with a 2 × 2-pixel instrumental binning to reduce the readout time. We obtained 522 × 522-pixel images in each spectral channel, with the pixel size corresponding to 0″.68.

The size of the spectral channel was $\delta\lambda$= 1.16 Å or 53 km s^{-1} in Hα. The actual instrumental profile of the interferometer was determined from night-sky lines (6568.8, 6577.2/6577.4, 6562.8 Å, and Hα); the profile width was ≃3 Å or ≃140 km s^{-1}.

We performed the observations on August 31, 1998, at a 2.5–3″ seeing at the zenith distance z = 51°–54°. A total of 24 interferograms were obtained for various interferometer plate spacings. The time of a single exposure was 240 s.

The He I (6678.15 Å) line of a calibration lamp was used for the phase shift measurement. After the observations, we made several accumulations of the images of the caps of the 6-m primary mirror uniformly illuminated by a lamp of continuous light. This allowed us to make a correction for nonuniform detector sensitivity (flat fielding) and simultaneously to adjust the filter passband.

The observational data were represented as 522 × 522 × 24-pixel "data cubes"; i.e., a 24-channel spectrum corresponded to each image element.

The data reduction (correction for the phase shift, subtraction of the night-sky spectrum, construction of the velocity field and the emission-line and continuum images) was carried out by using the ADHOC software package developed by Boulesteix [19].

Using star images from the Digital Palomar Sky Survey Atlas (DSS), we rotated the original images to coincide with the correct orientation (α – δ) and then averaged a 2 × 2 element, so that the resulting pixel size was 1″.34.

To increase the signal-to-noise ratio, we performed an optimal filtration of the cube of observational data: spectral smoothing by Gaussians with FWHMs of 1.5 channels and spatial smoothing by Gaussians with FWHMs of the order of the seeing. After the smoothing, the resulting spatial resolution was 4″.

Although the actual spectral resolution for the etalon in the 235th order of interference was 130–150 km s^{-1} in Hα, the accuracy of measuring the velocity from the line centroid (or from the Gaussian fit) in the case of a symmetric profile is considerably higher and is determined by the accuracy of phase calibration. The actual accuracy of a single measurement was checked by using a comparison spectrum and was 8–10 km s^{-1}.

The tie-in to the absolute velocity was checked by using night-sky lines. The possible systematic shift did not exceed 15–20 km s^{-1}.

2.2. Narrow-Band Images

The narrow-band Hα and [O III] images of the nebula were obtained with the 4-m Kitt Peak National Observatory (KPNO) telescope. Interference filters centered on the Hα (λ = 6562 Å, FWHM $\Delta\lambda$ = 29 Å) and [O III] (λ = 5009 Å, $\Delta\lambda$ = 45 Å) lines were used. The detector was a 2048 × 2048-pixel CCD array with the pixel size corresponding to 0″.47.

The observations were carried out on December 29 and 30, 1995; the angular resolution determined from star images was 1″.2 in Hα and 1″.4 in [O III].

3. RESULTS OF THE OBSERVATIONS

3.1. Monochromatic Hα Image

Figure 1 shows the monochromatic Hα image of the region obtained by integrating the emission over all spectral channels of the line. For comparison, the image of the same region in continuum in the immediate vicinity of Hα is indicated by isophotes; here, foreground stars in the field of view are clearly seen.

The absolute brightnesses were determined by comparison with the brightness from [15] for several nebular regions. Sources 37b, c, e, and g in the list of these authors were used for the flux calibration, i.e., the brightest and faintest regions were excluded.

Constructing the monochromatic image allowed us to clearly distinguish regions of weak Hα emission from the background far outside the bright nebular core. As a result, we have been able for the first time to clearly show that these outer weak regions form a giant bipolar shell structure around the WO star and the bright S3 core. The two shells forming this bipolar structure are indicated by the dashed line in Fig. 1.

According to our measurements, the sizes of the three components (the bright core and the two outer shells) are the following: angular sizes of 26″ × 20″ or linear sizes of 83 × 66 pc for the bright nebula S3; 35″ × 24″ or 112 × 77 pc for the outer southeastern shell; and (58–60)″ × (67–70)″ or (186–192) × (214–224) pc for the outer northwestern shell.

We give the sizes along the major and minor axes of each structure for a distance of 660 kpc, as inferred by Saha *et al.* [20].

3.2. Narrow-Band Hα and [O III] Images

Figure 2 shows the Hα (Figs. 2a, 2b) and [O III] (Figs 2c, 2d) images of the nebula obtained with the

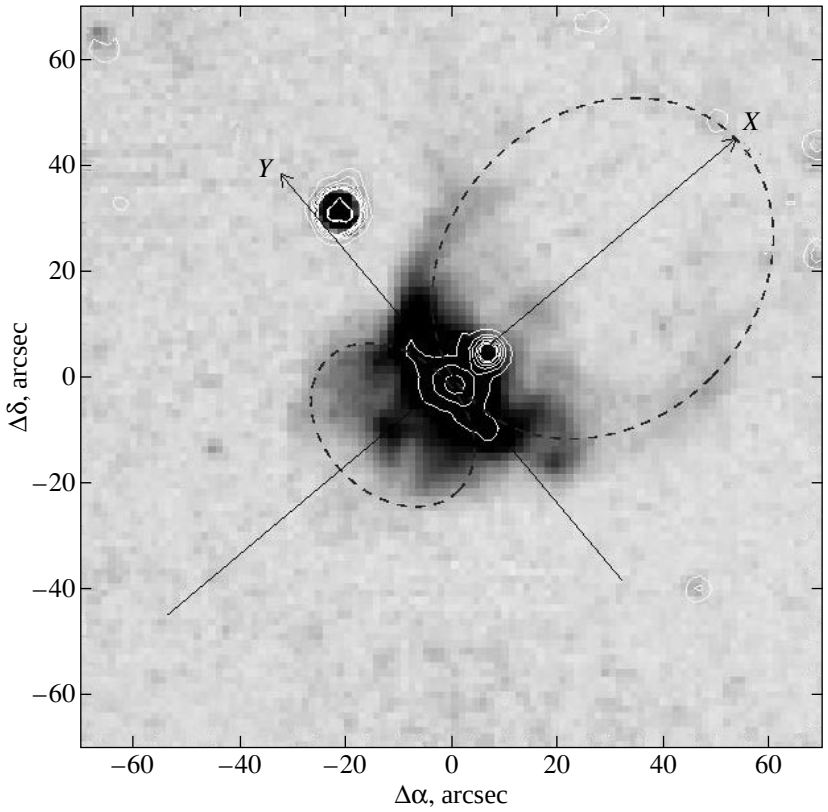

Fig. 1. The monochromatic Hα image of the region obtained by integrating the emission over all spectral channels of the line. The image of the same region in continuum near Hα is indicated by isophotes. The dashed line represents the giant bipolar shell.

4-m KPNO telescope. The southeastern outer shell and part of the northwestern shell at the very "base" near the bright nebular are seen in these figures. Both shells exhibit a distinct filamentary structure; in general, the filaments in the two lines are morphologically identical.

Three compact features unresolvable in the 6-m telescope monochromatic image because of the poor seeing on the observing night are clearly seen in the region of the bright S3 core. In all probability, the brightest of them (N1 in Fig. 2) is the WO star. The remaining features are most likely compact knots of gas, because, as follows from a comparison of Figs. 2b and 2d, their relative brightnesses in the two lines are different (N2 is brighter than N3 in Hα and weaker than the latter in [O III]). To elucidate the nature of these compact sources requires spectroscopic observations at a sufficiently good seeing.

3.3. Kinematics

Figure 3 shows the measured velocities at the line peak and the line FWHMs as inferred from our Fabry–Perot interferometric observations. In the data reduction, the line was fitted by a Gaussian; the line width was corrected for the instrumental profile width by assuming that the latter was also Gaussian. In order to find evidence for expansion of the outer bipolar shell, we constructed the distributions of line velocity and FWHM along two cuts designated, respectively, *X* and *Y* in Fig. 1. The band along the *X* axis is 60″ wide, so the entire bipolar structure falls within it; the (15″ wide) band along the *Y* axis covers predominantly the bright central S3 core and, in part, the weaker emission at the bases of the two outer shells.

A comparison of the line velocities and FWHMs along the two cuts leads us to the following conclusions:

(1) The scatter of velocities of the line peak is systematically larger in both outer shells than that in the central bright S3 core. Indeed, the velocities in the central region (–10″ … +10″) along the *X* axis in Fig. 1 vary in the range from –190 to –255 km s^{-1}; the velocities in the southeastern shell vary in the range from –165 to –295 km s^{-1}; and the range of velocities in the extended northwestern shell is largest: from –150 to –300 km s^{-1}.

As we see from the cut along the *Y* axis in Fig. 3b, the scatter of velocities in the bright S3 core is even smaller: velocities from –200 to –230 km s^{-1} are observed in a band within ±13″ of the center (in accordance with the core size; see Fig. 1). At larger distances from the center, the scatter increases because of the

contribution of emission from the bases of both outer shells.

(2) The line width in both shells also exceeds appreciably the line width in the central core. As we see from Fig. 3c, the line width in the same central region (±10″) is no larger than 240 km s^{-1}; in the southeastern shell, it reaches 330 km s^{-1}; and the broadest line up to 390 km s^{-1} is observed in the northwestern shell.

The two observed patterns of behavior suggest the presence of systematic high-velocity motions in the outer bipolar shell structure. Based on these data, we may take an expansion velocity ≥50 km s^{-1} for the southeastern shell and ≥70 km s^{-1} for the northwestern shell as a rough estimate. The two values are a lower limit; the underestimate can be more significant for the northwestern shell, because here we observe mainly the emission from the periphery, where the effect of geometrical projection reduces the observed radial velocities.

Evidently, observations with a higher spectral and angular resolution are desirable to accurately estimate the expansion velocity. It should be borne in mind, however, that such an "erratic" velocity distribution—from slow bright knots to the most rapid weak features—is observed in most expanding supernova remnants and nebulae around the sources of strong stellar wind, which were studied with a high angular and spectral resolution [21, 22]. Indeed, the nebulae are irregular in shape and clumpy in structure; accordingly, the effect of geometrical projection changes erratically the observed radial velocity. During the passage of a shock wave, the gas of dense bright knots accelerates weakly, while the gas of lower density accelerates more strongly. For these reasons, the entire set of radial velocities, ranging from the gas at rest to the shock velocity, is commonly observed in real expanding shells. Higher resolution observations of the nebula around the WO star in IC 1613 could therefore reveal the same erratic distribution of line velocities and FWHMs.

According to our measurements, the mean velocity of the bright part of the nebula, where the expansion effect is marginal, is $V(\mathrm{Hel}) = -216 \pm 1$ km s^{-1}. Given a possible systematic tie-in error of the absolute velocity measurements within 15–20 km s^{-1} (see Sect. 2), this value is in agreement with the measurements by Tomita [23] $V(\mathrm{Hel}) = -235 \ldots -230$ km s^{-1}, as inferred from one spectrogram of S3, and with the measurements by Lake and Skillman [24] in the 21-cm radio line: the mean velocity $V(\mathrm{Hel}) = -232$ km s^{-1} in the near galactic region.

4. DISCUSSION

The existence of an outer bipolar structure outside the bright core of the nebula S3 in IC 1613 was first suspected by one of us (T.A.L.) back in 1988 on the basis of trial narrow-band [O III] images obtained by M.A. Dopita at her request with the 2.6-m MSSS ANU telescope, which have not been published. This suspicion was completely confirmed in this study.

Lozinskaya [25] suggested the break of a strong stellar wind in two directions out of the dense gas layer forming the "main body" of the nebula, as a possible explanation for the bipolar structure of the outer shells. Not only the morphology of the nebula, but also its orientation relative to the extended region of H I deficiency, which is clearly seen in the distribution of the 21-cm H I line emission obtained by Lake and Skillman [24], argue for this model. The center of this "supercavity" in the H I distribution has the following coordinates: RA = $1^h2^m20^s$ and D = 10°51′; its size is 2′–3′ (40–600 pc). The formation of such a supercavity may be associated with the preceding activity of stars in the region. If the H I deficiency is assumed to be caused by the sweeping up of gas, then the orientation of the nebula's main body along the boundary of the hypothetical swept-up H I "supershell", the southeastern shell in the region of a denser medium, and the extended weak northwestern shell in the medium of lower density inside the supercavity, can be explained naturally.

The bipolar shell structure associated with the WO star in IC 1613 and its location relative to the H I supercavity are schematically shown in Fig. 4.

The analogy with an extensively studied galactic object also argues for the break out of a strong stellar wind into the region of reduced gas density: the bright shell swept up by the wind in a dense cloud and the "blister" produced by the wind burst through the cloud into a tenuous medium are also observed in the nebula G2.4+1.4 associated with the star of the same type, WR 102 [3, 26].

An analysis of the parameters of the two shells associated with the WO star in IC 1613 yields the rough estimates that are in best agreement with the standard model of wind effect on the interstellar medium. The size of both shells ($R_1 \simeq 56$ pc and $R_2 \simeq 110$ pc) is actually the only parameter that was reliably determined from observations. However, the fact that the ages of the two shells must be the same in the proposed model constraints significantly the range of possible values for the parameters.

The wind mechanical luminosity for the WO star in IC 1613 is $L_w \simeq 10^{38}$ erg s^{-1} [14]. This estimate is rather crude, because only the wind velocity ($V_w = 2850$ km s^{-1}) was determined from observations, while the mass-loss rate (2.9×10^{-5} $M_\odot$ yr^{-1}) was estimated indirectly from the relation between the He II-line luminosity and the outflow rate for two WO stars.

The typical density of the interstellar medium in the vicinity of the star can be estimated with the same uncertainty.

First, based on the H_β emission from the brightest central part of S3 6″ in size, Davidson and Kinman [9] found the core density to be $N_e = 8.5$ cm^{-3}. Second,

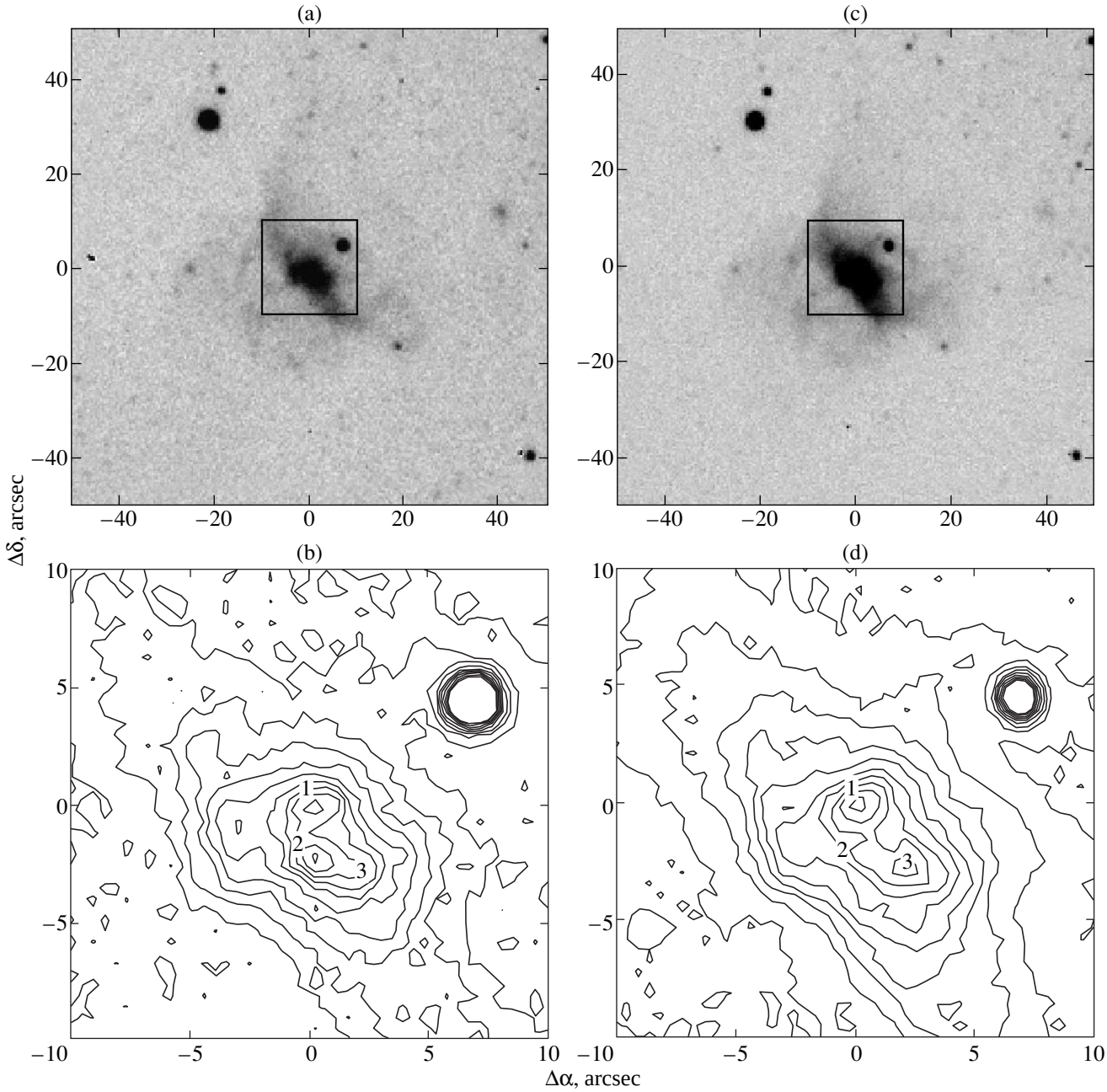

Fig. 2. The narrow-band Hα (a, b) and [O III] (c, d) images of the nebula obtained with the 4-m KPNO telescope. The numbers denote three compact sources; source 1 is most likely the WO star. The square encloses the region whose isophotes are shown below.

using the total Hα emission from the entire bright nebula, Kennicutt [27] obtained a mean $N_e \simeq 1$ cm^{-3}. Third, Goss and Lozinskaya [17] estimated the mean density in the bright nebula S3 from the flux density of thermal radio emission to be $N_e = 3.5$ cm^{-3}.

Given the dense knots that we detected in the central core, all three estimates give a lower limit on the density in the bright nebula. These estimates refer to the densest region of the central nebula, where, judging by the radial-velocity field presented above, the gas was not accelerated by the stellar wind because of the high density.

The mean ambient gas density in a large region around the WO star can be obtained from the 21-cm observations by Lake and Skillman [24]. Their map of the H I column-density distribution gives N(HI) ≃ (2–4) × 10^{20} cm^{-2} for the region of interest. For a thickness of the galactic gas disk of 500–800 pc, this value corresponds to a mean density of ≃0.1 cm^{-3}. We estimated the gas-disk thickness from the following considerations. According to the optical *B* surface-brightness

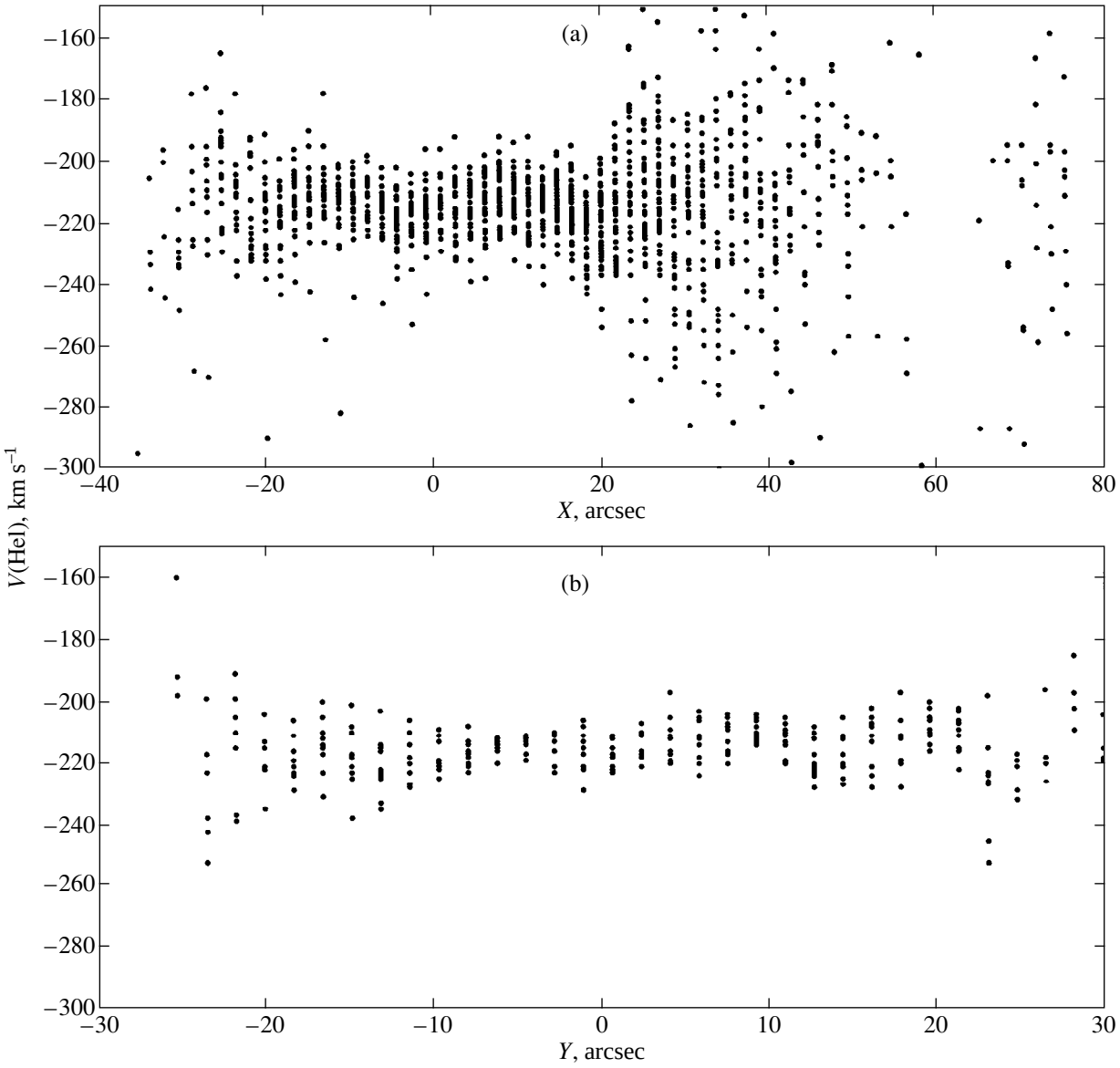

Fig. 3. The measured velocity at line peak and the line FWHMs as inferred from our Fabry–Perot interferometric observations: (a) V(Hel) in a 60″ wide band along the X axis (see Fig. 1); (b) V(Hel) in a 15″ wide band along the Y axis; (c) and (d) the line FWHMs in the same bands along the X and Y axes, respectively.

profile given in the above paper, the stellar surface density at a distance $R \approx 6'$ from the center is $\sigma_* \approx$ 2.5–3 $M_\odot$ pc^{-2}, while the total surface density of stars and gas is $\sigma_T \approx$ 3.5–4 $M_\odot$ pc^{-2}. The thickness of the gas disk can be roughly assumed to be $h_0 \sim 1/\sqrt{\sigma_T}$ (see, e.g., [28]). Since $\sigma_T \approx$ 50–70 $M_\odot$ pc^{-2} at a gas-disk thickness of ≈200 pc in the solar neighborhood, we obtain $h_0 \approx$ 500–800 pc in the WO region for IC 1613.

All these estimates are rather crude, but they show that the initial density in the vicinity of the WO star is unlikely to fall outside the range from 0.01 to 5 cm^{-3}.

The expected ages (in units of 10^6 years) and expansion velocities for the two outer shells in the standard model of a wind-blown bubble [29, 30] are given in the table for various initial densities n_0 at $L_w = 10^{38}$ erg s^{-1} and $R_1 \simeq 56$ pc and $R_2 \simeq 110$ pc derived above.

As we see from the table, similar age estimates for the two shells, depending on the radius, provided that the expected expansion velocity is close to the observed values $v_1 \geq 50$ km s^{-1} and $v_2 \geq 70$ km s^{-1}, are obtained at an initial gas density $n_0 \simeq$ 1–0.1 cm^{-3} for the brighter southeastern shell and $n_0 \simeq$ 0.1–0.01 cm^{-3} for the weaker extended northwestern shell. These ranges of ambient gas densities seem quite reasonable. The ratio of ambient gas densities in the two shells swept up by the wind is determined from the ratio of their sizes

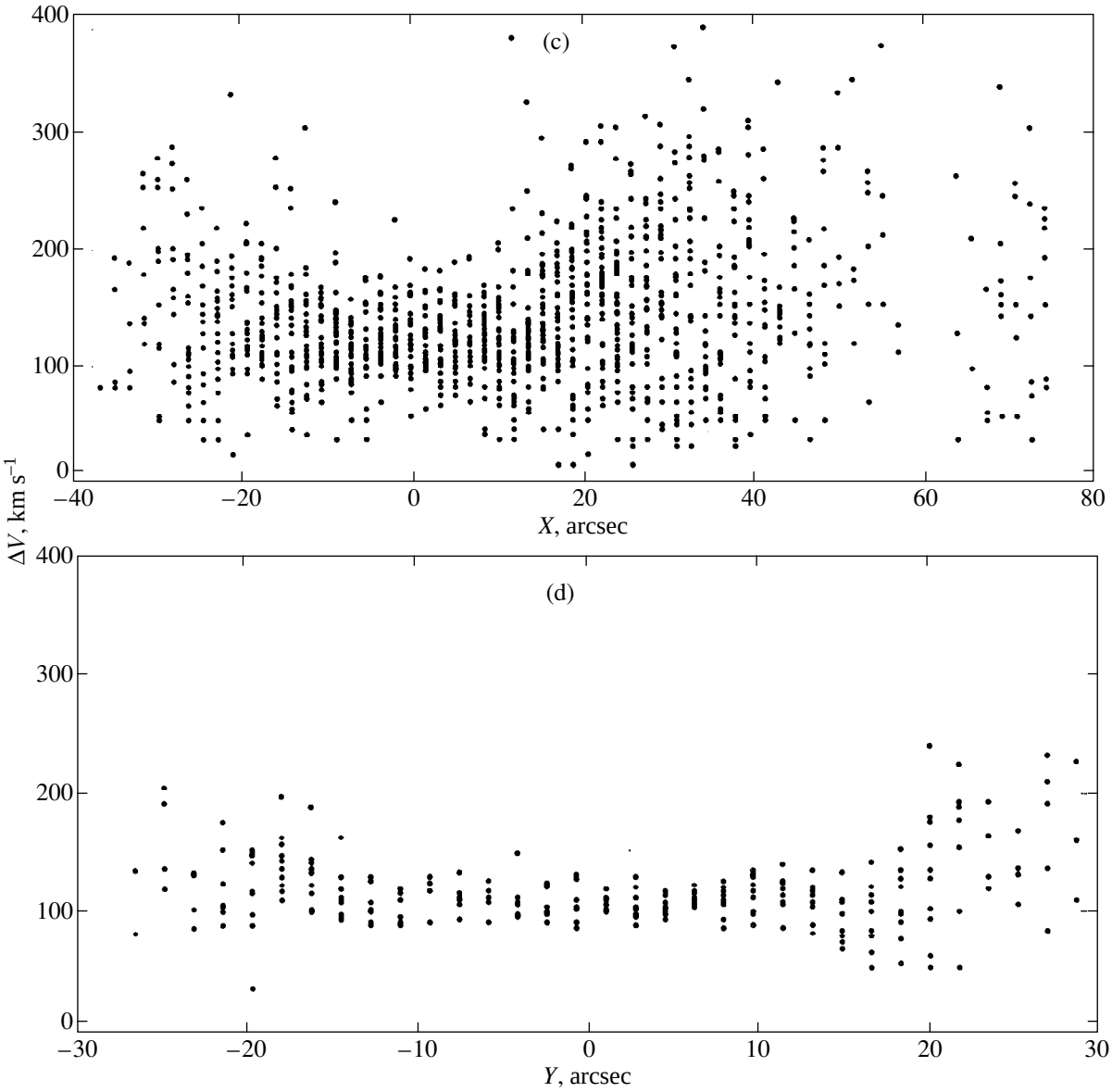

Fig. 3. (Contd.)

more accurately than the density itself: $n_{0,1}/n_{0,2} = (R_2/R_1)^5 \simeq 20$.

The inferred age of the bipolar shell structure, $t_1 \simeq (0.3–1) \times 10^6$ years, is close to the lifetime of a massive WR star and exceeds appreciably the duration of the final WO stage. Note that the age was estimated for the WO wind intensity. The wind intensity at the preceding WR stage was most likely lower, which increases still further the age estimate for the shell. Thus, we conclude that the unique bipolar structure was most likely produced by the wind from the central star at the stage preceding WO. The WO superwind, which switches on inside the previously formed structure, is an additional source of energy. Since the shock wave triggered by the strong WO wind propagates in a medium of very low density inside the existing bipolar shells, the "secondary" shells swept up by them rapidly reach the denser regions at the boundary. The additional compression of gas by the shock wave triggered by the superwind gives rise to a filamentary structure, which is clearly seen in Figs. 3a and 3b in the southeastern shell and at the base of the northwestern shell.

The expected ages and expansion velocities of the two outer shells in a medium of various densities

n_0, cm^{-3}	5	1	0.1	0.01	0.001
$t(R_1)$, 10^6 years	1.2	0.7	0.3	0.15	0.07
v_1, km s^{-1}	28	46	100	218	460
$t(R_2)$, 10^6 years	3.6	2.1	1.0	0.45	0.2
v_2, km s^{-1}	18	30	63	140	300

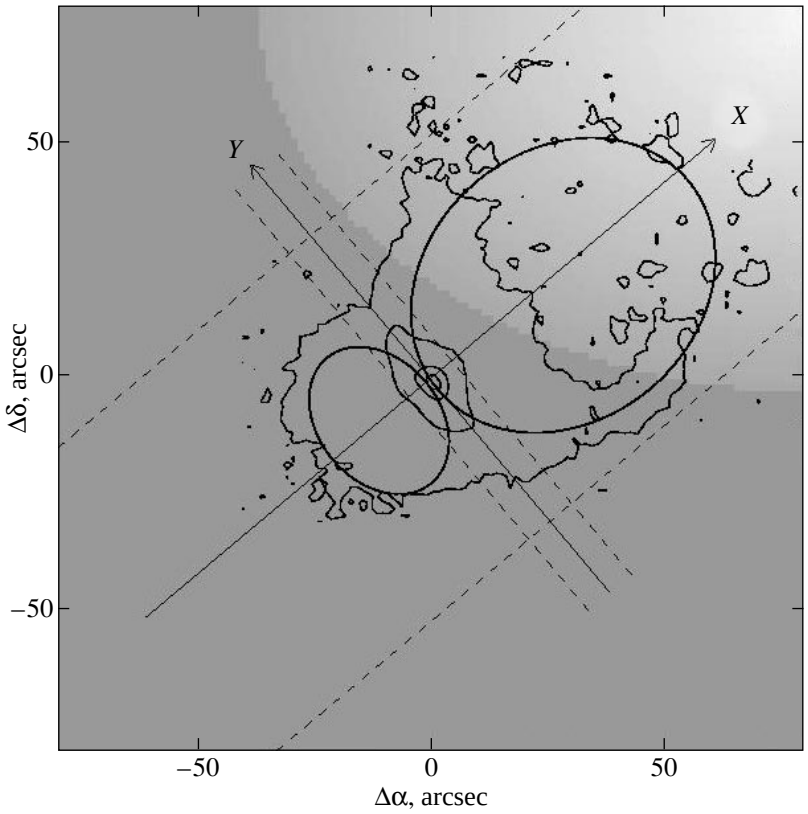

Fig. 4. A scheme for the bipolar shell structure associated with the WO star and its location relative to the H I supercavity. The bipolar shell is represented by two ellipses. The dashed lines indicate the boundaries of the cuts along the *X* and *Y* axes (see Fig. 3). The Hα isophotes as constructed from the 6-m telescope observations correspond to 0.025, 0.4, and 1.0×10^{-15} erg cm^{-2} s^{-1} arcsec^{-2}. The shades of gray indicate the distribution of H I column density (the fit to the data from [24]). The transition from white to gray corresponds to column densities from 0.4 to 2×10^{20} cm^{-2}.

5. CONCLUSION

Our Hα observations of the nebula associated with the WO star in the galaxy IC 1613 using a scanning Fabry–Perot interferometer on the 6-m SAO telescope clearly revealed a giant bipolar shell structure outside the bright nebula S3. The sizes of the shell southeast of the bright nebula are 112 × 77 pc; the northwestern shell is twice as large: (186–192) × (214–224) pc. The object's kinematics has been studied for the first time. We found evidence for expansion of both shells; the possible expansion velocities of the southeastern and northwestern shells are no less than 50 and 70 km s^{-1}, respectively. Using the 4-m KPNO telescope (narrow-band Hα and [O III] images), we detected a filamentary structure of both shells and several compact features in the S3 core.

We propose a self-consistent model for the formation of the giant bipolar structure by the wind from the central WO star located at the boundary of a supercavity in the galactic H I distribution.

ACKNOWLEDGMENTS

This study was supported by the Russian Foundation for Basic Research (project no. 98-02-16032) and the Program "Astronomy" (project no. 1.3.1.2). We wish to thank M. Dopita, who provided unpublished [O III] images of the region, J. Boulesteix for the opportunity to use interference filters, and the 6-m SAO telescope committee for allocating observing time.

REFERENCES

1. M. J. Barlow and D. C. Hummer, *Wolf–Rayet Stars: Observations, Physics, and Evolution*, *IAU Symp. 99*, Ed. by C. W. H. de Loore and A. J. Willis (Reidel, Dordrecht, 1982), p. 387.
2. A. V. Torres, P. S. Conti, and P. Massey, Astrophys. J. **300**, 379 (1986).
3. M. A. Dopita, P. J. McGregor, T. A. Lozinskaya, *et al.*, Astrophys. J. **351**, 563 (1990).
4. V. F. Polcaro, R. Viotti, C. Rossi, *et al.*, Astron. Astrophys. **265**, 563 (1992).
5. A. Maeder and G. Meynet, Astron. Astrophys. **210**, 155 (1989).
6. J. Melnik and M. Heydari-Malayeri, *WR Stars and Interrelations with Other Massive Stars in Galaxies, IAU Symp. 143*, Ed. by K. A. Van der Hucht and B. Hidayat (Kluwer, Dordrecht, 1991), p. 409.
7. V. F. Polcaro, F. Giovanelli, R. K. Manchanda, *et al.*, Astron. Astrophys. **252**, 590 (1991).

8. S. D'Odorico and M. Rosa, Astron. Astrophys. **105**, 410 (1982).
9. K. Davidson and T. D. Kinman, Publ. Astron. Soc. Pacif. **94**, 634 (1982).
10. A. R. Sandage, Astrophys. J. **166**, 13 (1971).
11. T. E. Armandroff and P. Massey, Astrophys. J. **291**, 685 (1985).
12. H. E. Smith, Astrophys. J. **199**, 591 (1975).
13. D. R. Garnett, R. C. Kennicutt, Y.- H. Chu, *et al*., Astrophys. J. **373**, 458 (1991).
14. R. L. Kinsburgh and M. J. Barlow, Astron. Astrophys. **295**, 171 (1995).
15. P. Hodge, M. G. Lee, and M. Gurwell, Publ. Astron. Soc. Pacif. **102**, 1245 (1990).
16. D. A. Hunter, W. N. Hawley, and J. S. Gallagher, Astron. J. **106**, 1797 (1993).
17. W. M. Goss and T. A. Lozinskaya, Astrophys. J. **439**, 637 (1995).
18. S. N. Dodonov, V. V. Vlasyuk, and S. V. Drabek, *Fabry–Perot Interferometer. User's Guide* (Special Astrofiz. Obs., Nizhniĭ Arkhyz, 1995).
19. J. Boulesteix, *ADHOC Reference Manual* (Observatoire de Marseille, Marseille, 1993).
20. A. Saha, W. L. Freedman, J. G. Hoessel, *et al*., Astron. J. **104**, 1072 (1992).
21. T. A. Lozinskaya, *Supernovae and Stellar Wind: Interaction with Galactic Gas* (Nauka, Moscow, 1986).
22. T. A. Lozinskaya, *Supernovae and Stellar Wind in the Interstellar Medium* (AIP, New York, 1992).
23. A. Tomita, K. Ohta, and M. Saita, Publ. Astron. Soc. Jpn. **45**, 693 (1993).
24. G. Lake and E. D. Skillman, Astron. J. **98**, 1274 (1989).
25. T. A. Lozinskaya, Astrophys. Space Sci. **252**, 199 (1997).
26. M. A. Dopita and T. A. Lozinskaya, Astrophys. J. **359**, 419 (1990).
27. R. C. Kennicutt, Astrophys. J. **287**, 116 (1984).
28. A. V. Zasov, *Physics of Galaxies* (MGU, Moscow, 1993).
29. J. Castor, R. McCray, and R. Weaver, Astrophys. J. Lett. **200**, L107 (1975).
30. R. Weaver, R. McCray, J. Castor, *et al.*, Astrophys. J. **218**, 377 (1977).

Translated by V. Astakhov

THE ASTRONOMICAL JOURNAL, 116:2328–2340, 1998 November
© 1998. The American Astronomical Society. All rights reserved. Printed in the U.S.A.

RESOLVING THE SOURCE OF X-RAYS IN THE LOCAL GROUP DWARF IC 1613: X-RAY, RADIO, AND OPTICAL OBSERVATIONS OF A LUMINOUS SUPERNOVA REMNANT

T. A. LOZINSKAYA AND O. K. SILCHENKO
Sternberg State Astronomical Institute, Moscow State University, Universitetskij Prospect 13, 119899 Moscow, Russia
D. J. HELFAND
Department of Astronomy, Columbia University, Box 46, Pupin Hall, New York, NY 10027
AND
W. M. GOSS
National Radio Astronomy Observatory, P.O. Box O, 1003 Lopezville Road, Socorro, NM 87801
Received 1997 September 25; revised 1998 July 31

ABSTRACT

A high-resolution X-ray image of the Local Group dwarf IC 1613 reveals that the principal source of X-ray emission in this direction arises in a background cluster of galaxies, as first suggested by Eskridge. In addition, however, we find a bright X-ray source coincident with the only known supernova remnant in this galaxy, S8. Extensive ground-based follow-up observations in the radio and optical regimes are reported. We confirm the nonthermal radio spectral index of the source and measure its extent to be $\sim 3''$ at 20 cm. Imaging spectrophotometric observations taken with the multipupil spectrograph of the Special Astrophysical Observatory allow us to determine the density and velocity distribution of the gas in the remnant. The simultaneous presence of luminous X-ray and optical emission suggests a relatively young remnant in which the outward-moving shock has recently encountered dense material. We note that many of this object's properties are similar to those of the brightest optical remnant in the Large Magellanic Cloud, N49.

Key words: galaxies: individual (IC 1613) — Local Group — radio continuum — supernova remnants — X-rays

1. INTRODUCTION

IC 1613, located at a distance of ~ 725 kpc (Freedman 1988), is the faintest dwarf irregular galaxy in the Local Group. Recent star formation is concentrated in its northeast quadrant, where a number of bright H II regions have produced a complex of giant shells (Meaburn, Clayton, & Whitehead 1988). The only supernova remnant (SNR) known in the galaxy, a bright compact emission nebula designated S8 in Sandage's (1971) survey of IC 1613's H II regions and No. 49 in the list by Hodge, Lee, & Gurwell (1990), is located at the southern edge of this complex. The object was first classified as a remnant by D'Odorico, Dopita, & Benvenuti (1980) based on Smith's (1975) optical spectrum in which strong [S II] lines were apparent. Subsequent detailed spectrophotometry led D'Odorico & Dopita (1983) and Peimbert, Bohigas, & Torres-Peimbert (1988) to conclude that S8 was an evolved SNR; the line ratios in these spectra were best modeled as shock-heated gas with an inferred shock velocity of 130–160 km s^{-1} and an ambient density of 6–20 cm^{-3}. The measurement of a nonthermal radio spectral index $\alpha = -0.9 \pm 0.3$ by Dickel, D'Odorico, & Silverman (1985) confirmed the SNR identification.

A Wolf-Rayet (W-R) star candidate, WR 8, was identified at the northeast edge of this nebula by Armandroff & Massey (1985) using narrowband filter imaging. However, spectra of WR 8 obtained subsequently (Azzopardi, Lequeux, & Maeder 1988; Massey, Conti, & Armandroff 1987; Armandroff & Massey 1991) did not confirm the W-R identification. These spectra did reveal an H II $\lambda 4686$ line that was much broader than the nebular lines, a number of [Fe II] and [Fe III] lines unusually strong for a SNR, and apparent continuum emission. An inspection of an east-west spatial cut through the knot's spectrum led Massey et al. (1987) to the conclusion that the He II $\lambda 4686$ and [Fe II] $\lambda 5159$ lines were pointlike and centered on the strong continuum source, while the [O III] and Hβ emission were extended. In summary, the early optical spectra of S8 suggested a peculiar object combining properties of a normal radiative SNR evolving in dense interstellar gas superposed on a "pointlike" object (presumably a SNR's knot responsible for the He II), very strong [Fe II], [Fe III], and "strong continuum" emission (Massey et al. 1987).

IC 1613 was observed by the *Einstein Observatory* X-ray imaging proportional counter (IPC) in 1979 July for 6900 s. Despite revealing a moderately bright and marginally extended source of emission detected $\sim 5'$ from the galaxy's centroid, these data languished in the archives until Eskridge (1995) analyzed them, concluding that the most likely interpretation for the source was emission from a background cluster of galaxies at $z \sim 0.2$. Prior to the publication of that work, however, two of us (D. J. H. and T. A. L.) noted the proximity of the X-ray source to an oxygen W-R star (WO [IC 1613]; Goss & Lozinskaya 1995), one of only five such stars in the Local Group, and proposed to observe the field with the *ROSAT* high-resolution imager (HRI) in order to investigate the possible association of the X-ray source with the star or its surrounding wind-driven bubble.

In this paper, we present the *ROSAT* observations, which (1) confirm the background cluster interpretation for the bulk of the X-ray emission, (2) set a limit on X-rays from the WO star; and (3) detect for the first time a luminous X-ray source associated with the IC 1613 SNR S8. We have also undertaken additional observations of the remnant at centimeter wavelengths using the VLA, in narrowband filters using the KPNO 4 m telescope, and, to generate a spectro-

TABLE 1

X-RAY SOURCES IN THE IC 1613 FIELD

Source Number	R.A. (J2000.0)	Decl. (J2000.0)	Count Rate (10^{-4} counts s^{-1})	Extent	ID
1.....	01 05 02	02 01 30	290 ± 20	$3' \times 4'$	Cluster $z \sim 0.2$
2.....	01 05 02.27	02 08 41.4	22 ± 4	$5'' \times 10''$	SNR S8
3.....	01 04 40.74	02 01 08.6	18 ± 3	$<5''$	None
4.....	01 05 16.06	01 59 11.7	13 ± 2	$<5''$	Star; $m_v = 11.4$

photometric image, with the multipupil field spectrograph on the 6 m Special Astrophysical Observatory (SAO) telescope of the Russian Academy of Sciences. The X-ray data are presented in § 2, followed by the radio, optical imaging, and spectroscopic data in the subsequent three sections. Section 6 contains a discussion of the properties of the remnant derived from these observations; we summarize our conclusions in the final section.

2. HIGH-RESOLUTION X-RAY OBSERVATIONS OF IC 1613

Observations using the *ROSAT* HRI were obtained for a 35′ field of view centered at R.A. = $01^h05^m02^s$, decl. = 02°04′12″ (J2000.0); a useful exposure time of 22,600 s was obtained. The data are recorded in $0''.5 \times 0''.5$ pixels, although the effective spatial resolution of the HRI is approximately 3″. The image is dominated by a large region of diffuse emission approximately 4′ in extent and centered at R.A. = 01^h05^m02, decl. = 02°01′30″. In addition, there are three significant compact sources of emission; source parameters are summarized in Table 1.

The absolute astrometry of HRI images can be uncertain by up to 10″. We have used the X-ray detection of an $m_v = 11.4$ mag star (source 4 in Table 1) to verify that any offset in this case is considerably smaller: the Guide Star Catalog position for this star differs by $+2'' \pm 2''.2$ and $-3''.8 \pm 2''.1$ in right ascension and declination, respectively, where the errors include both the statistical errors in the X-ray position and an uncertainty of $\pm 1''$ in the GSC coordinates. As we show below, the positional agreement between the X-ray and radio coordinates of the SNR are even better; thus we use the nominal coordinates of the X-ray image as derived from the standard processing system.

Owing to the high internal background of the HRI, the surface brightness sensitivity of the instrument is limited, and the diffuse emission exceeds the background only over a region $\sim 4'$ across, which should be regarded as a lower limit to the extent of the source. Over a region of 13 arcmin^2, the background-subtracted photon excess is 660 ± 50 counts, yielding a rate of $(2.90 \pm 0.2) \times 10^{-2}$ counts s^{-1}. For a thermal bremsstrahlung temperature of 3 keV and the measured foreground absorbing column density of $N_H \sim 2.8 \times 10^{20}$ cm^{-2}, this yields an X-ray flux of 1.9×10^{-12} ergs cm^{-2} s^{-1} in the 0.1–10 keV band (consistent with the IPC flux reported by Eskridge 1995, which suggests the measured HRI diameter does include most of the source flux). At the redshift obtained by Eskridge (1995) for a galaxy in the cluster coincident with this X-ray emission ($v \sim 59{,}000$ km s^{-1}), this implies a total X-ray luminosity (for $H_0 = 50$ km s^{-1} Mpc^{-1}) of $\sim 4 \times 10^{44}$ ergs s^{-1}, consistent with that of a moderately rich cluster.

The second brightest X-ray source in the field is a slightly extended source located at R.A. = $0.1^h05^m02^s.27$, decl. = 02°08′41″ (J2000.0), less than 4′ from the center of the field of view (see Fig. 3). Using the raw data binned in $2''.0$ pixels, a two-dimensional Gaussian fit to this source yields a size of $10'' \times 6''$ with a major-axis position angle at 80° (measured east of north). Adopting an intrinsic HRI point-spread function FWHM of 3″ yields intrinsic source dimensions of $\sim 10'' \times \sim 5''$; although the relatively small number of source counts leads to substantial statistical errors on these dimensions, the source is clearly more extended than source 4, which has a stellar counterpart, and we conclude it is indeed resolved at 3″ resolution.

The count rate, derived from a 15″ diameter circle centered on the source (with background taken from the surrounding $4' \times 5'$ region), is $(2.2 \pm 0.4) \times 10^{-3}$ counts s^{-1}. Using the Galactic foreground absorption column density of $N_H = 2.8 \times 10^{20}$ cm^{-2} and a range of models including thermal bremsstrahlung, power law, and Raymond-Smith thermal plasma with reasonable parameters ($1 < \alpha < 3$ for the power-law index and 0.5 keV $< kT <$ 5 keV for the temperatures), this implies a flux in the 0.1–2.4 keV band of $\sim (6 \pm 2) \times 10^{-14}$ ergs cm^{-2} s^{-1}. Including the total local mean neutral hydrogen column density in IC 1613 in the vicinity of S8 ($N_H = 1.7 \times 10^{21}$ cm^{-2} [§ 6.2]) raises the inferred intrinsic flux of the remnant by $\sim 10\%$. For our adopted distance of 725 kpc, the source has a luminosity of $(4 \pm 1) \times 10^{36}$ ergs s^{-1} in the 0.1–2.4 keV band and up to twice this value in the 0.1–20 keV band, depending on the model assumptions.

Finally, we have derived an upper limit to the X-ray flux from the oxygen W-R star (Goss & Lozinskaya 1995) that motivated our observation: the excess within a 24″ diameter circle centered on the star is 1 ± 4 counts, implying a 3 σ upper limit of 2×10^{-14} ergs cm^{-2} s^{-1} or $L_X < 10^{36}$ ergs s^{-1}. In addition, no diffuse emission is detected from the windblown bubbles surrounding this object.

3. RADIO OBSERVATIONS OF THE SNR S8

The galaxy IC 1613 was observed for a period of 5 hr in 1993 at a frequency of 8.4 GHz with the National Radio Astronomy Observatory's Very Large Array (VLA)[1] in the D configuration. Unfortunately, the SNR was situated at the edge of the 5′ field since the target of the observations was the W-R star and its nebula S3 (see Fig. 7 in Goss & Lozinskaya 1995). Nonetheless, the SNR was detected, and the flux density is given in Table 2.

The VLA archive was used to obtain flux densities of the SNR at lower frequencies. Data obtained by J. Meaburn and collaborators in the D (in 1988) and C (in 1989) configurations, plus earlier data obtained by F. Israel in the C configuration (in 1985), were used to derive a 5 GHz flux density. The 1.46 GHz intensity was obtained from data

[1] The National Radio Astronomy Observatory is a facility of the National Science Foundation operated under cooperative agreement by Associated Universities, Inc.

TABLE 2

VLA Radio Observations of S8

Frequency (GHz)	Noise (mJy beam^{-1})	Beamwidth (arcsec)	Flux Density (mJy)	Position (R.A., Decl., J2000)
8.4	0.1	8	0.97 ± 0.2	01 05 02.45 ± 0.07, 02 08 42.4 ± 0.7
4.8	0.026	15	0.96 ± 0.05	01 05 02.40 ± 0.02, 02 08 42.8 ± 0.1
1.4	0.056	5 × 4.5	1.9 ± 0.1	01 05 02.42 ± 0.02, 02 08 42.8 ± 0.2

collected by F. Israel (1984) and by J. Dickel (1985) in the B configuration, plus D-configuration data from Meaburn et al. (1988). The instrumental parameters for all of these observations, as well as the flux densities and positions obtained for the SNR, are summarized in Table 2.

The implied spectral index is $\alpha = -0.57 \pm 0.054$ (consistent with, but more accurate than, that obtained by Dickel et al. 1985). The position of the radio source agrees well with that of the optical nebula S8 (Hodge et al. 1990) and with our X-ray source position. Figure 1 displays the radio image of the SNR at 1.4 GHz. The source is resolved with a deconvolved FWHM angular size of $2''.9 \pm 0''.5$. The VLA image also hints at a ridge of emission running along the eastern edge of the bright source.

4. DEEP OPTICAL IMAGES

We obtained optical images at the KPNO[2] 4 m telescope on 1995 December 29 and 30. Narrowband filters centered on Hα ($\lambda = 6562$ Å; $\Delta\lambda = 29$ Å FWHM) and [O III] ($\lambda = 5009$ Å; $\Delta\lambda = 45$ Å) were used. Astrometry using 10 GSC stars in the images allowed us to register the images to about $\pm 1''$. Figure 2*a* displays the $3'$ region around the SNR in Hα, illustrating the complex of shells and bubbles in this region of active star formation; Figure 2*b* shows the close correspondence between the Hα and [O III] images of the remnant. Two-dimensional Gaussian fits to the object in comparison with the bright star $10''$ to the west show clearly that it is extended in both bands at a position angle of $\sim 60°$ and with dimensions $3'' \times 2''$ FWHM (by comparison, the stellar images are $\sim 1''.1 \times 1''.1$ in [O III] and $1''.4 \times 1''.3$ in Hα). In Figure 3, we show the 1.49 GHz position of the SNR together with the *ROSAT* image and [O III] optical image at the same scale. Within the combined astrometric uncertainties of $\sim 1''$–$2''$, the sources are coincident in all three wavelength regimes, making the identification unambiguous.

5. IMAGING SPECTROSCOPY

Imaging spectrophotometric observations of the SNR were carried out during the period 1996 October 9–11 using the multipupil field spectrograph of the 6 m telescope at the SAO (Nizhnij Arkhyz, Russia); for a description of the spectrograph, see Afanasiev et al. (1990). The frame consists of 8×16 square elements $1''.3$ on a side. Thus, during one exposure, we obtained simultaneously 128 spectra from an area $11'' \times 21''$ centered on the SNR. A total of three 1 hr exposures were collected: one in the blue-green spectral range (4000–5800 Å) and one in the red spectral range (5600–7500 Å) with dispersions of 1.6 Å pixel^{-1} (spectral resolution of 2.5 Å in the red and 5 Å in the green), plus one exposure covering the entire band at 3.16 Å pixel^{-1}. As a spectrophotometric standard, we used the sdO star Feige 110. The seeing during the observations was $1''.6$–$1''.7$. The detector used was a 1040×1160 pixel CCD. Standard reduction procedures including cosmic-ray cleaning, linearization, and spectrum extraction were performed using software developed at the SAO (Vlasyuk 1993). We then produced surface brightness distributions for each emission line and for the continuum, maps of line intensity ratios, and the two-dimensional gas velocity field over the SNR and the surrounding field. In the following subsections, we consider the morphology of the nebula in different emission lines, the velocity information, and the spectrophotometric data.

5.1. *Surface Brightness Distributions*

The resulting maps generally yield similar images in all emission lines, although the northeast-southwest elongation of the nebula is more evident in [O I], [O III], and [S II] than in hydrogen. The image in [Fe II] looks the most unusual: it consists of two elongated pieces, almost orthogonal to each other. There is also a clear continuum signal in the 4300–6900 Å band (although new observations are needed to evaluate its full extent and intensity). Figures 4*a*–4*e* display the images in the lines [O I], [S II], [Fe II], and [N II] and in the continuum, overlaid on the Hα image from the 4 m telescope.

5.2. *The Velocity Field*

The spectra we have obtained with the multipupil spectrograph allow us to construct a velocity field with $1''.3$

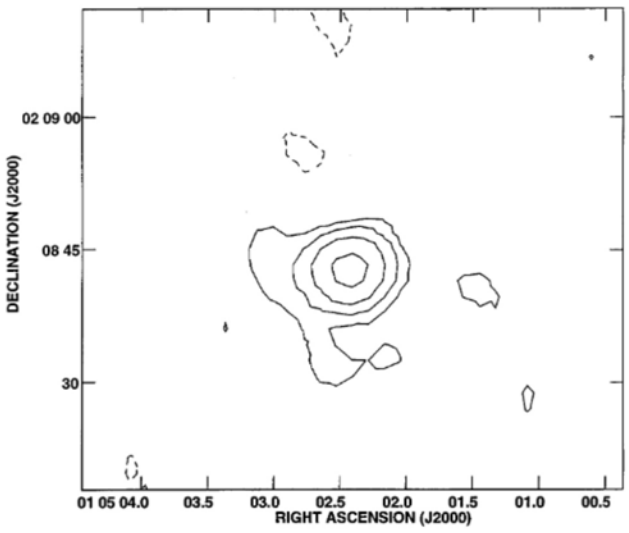

FIG. 1.—Radio image of the SNR at 1.4 GHz obtained with the VLA. The CLEANed image was convolved with a $6''$ circular beam; contour levels are -1 (*dashed*), 1, 2, 4, and 8×0.15 mJy beam^{-1}.

[2] Kitt Peak National Observatory, National Optical Astronomy Observatories, is operated by the Association of Universities for Research in Astronomy, Inc., under cooperative agreement with the National Science Foundation.

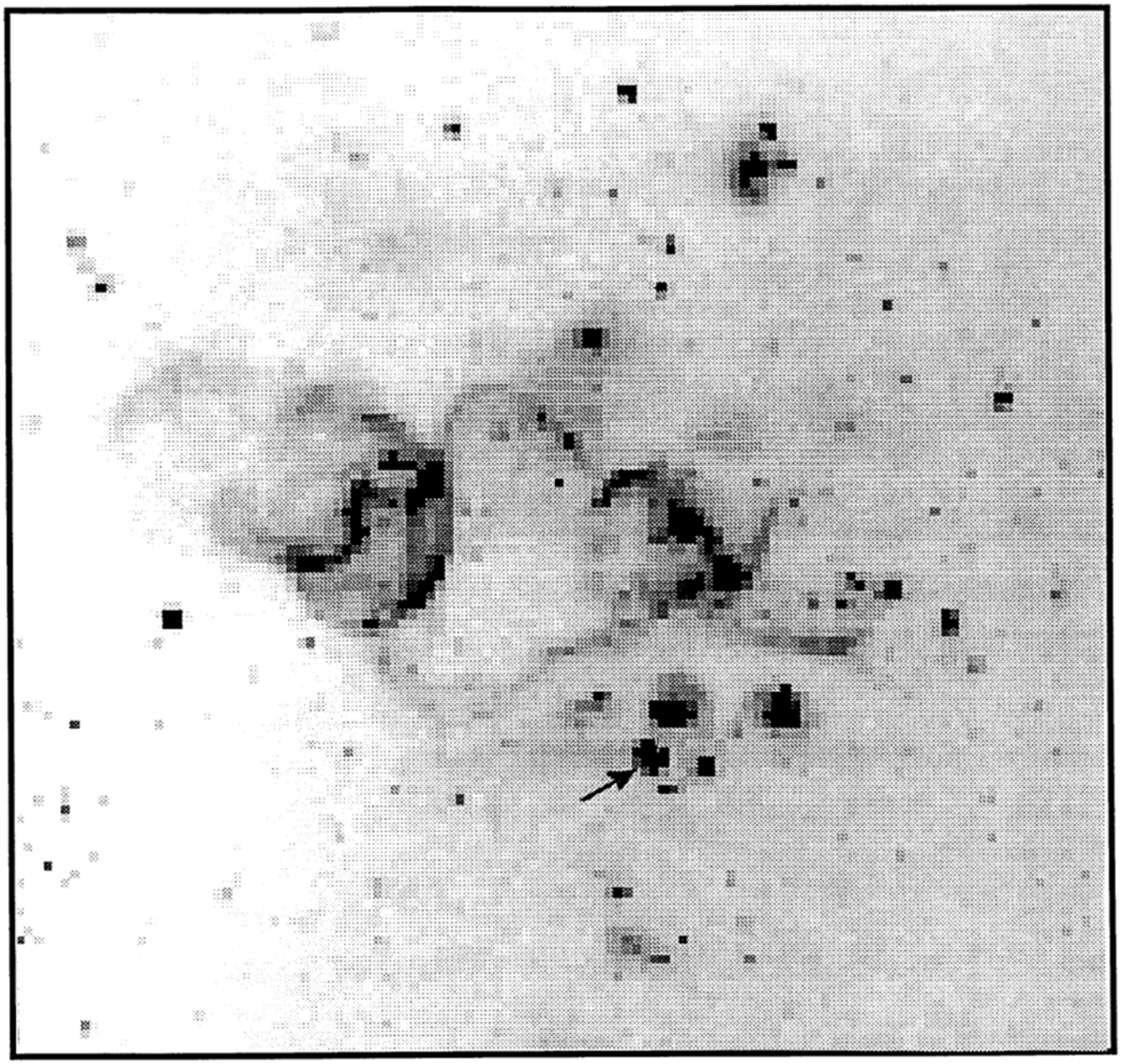

FIG. 2a

FIG. 2.—(*a*) The 3′ region around the SNR in Hα. Pixel size is 0.″47. The source corresponding to S8 is marked with an arrow. (*b*) A gray-scale representation of the remnant in Hα overlain by contours from the [O III] image.

resolution over the entire nebula. The principal results from this exercise are summarized here and in the associated figures:

1. *Mean velocity.*—The mean heliocentric velocity of IC 1613 has been determined to be -231 km s^{-1} (see the Lyons-Meudon Extragalactic Database). The local gas velocities in the vicinity of the remnant are similar: from Figures 1 and 3 in Meaburn et al. (1988), we find the Hα emission at $v \sim -225$ to -230 km s^{-1} over an area 10′ to 20′ in extent surrounding the nebula. For the remnant itself, however, our measurements indicate velocities of -309, -273, and -299 km s^{-1} from the centroids of the Hα, [O I] λ6300, and [S II] lines, respectively. Within the systematic uncertainties of ± 10 km s^{-1}, we conclude that the mean radial velocity of the SNR is -50 to -75 km s^{-1} with respect to the local medium.

2. *Velocity gradient.*—In Figure 5, we display isovelocity contours derived from the main component of the Hα line overlaid on the Hα image of the nebula. A systematic velocity gradient from -290 to -340 km s^{-1} (east to west) is apparent. We discuss the kinematics of the nebula further below.

3. Hα.—The mean FWHM of the main component of the Hα line is 270 ± 3 km s^{-1}. There is no indication that the line width increases from the edge of the nebula toward

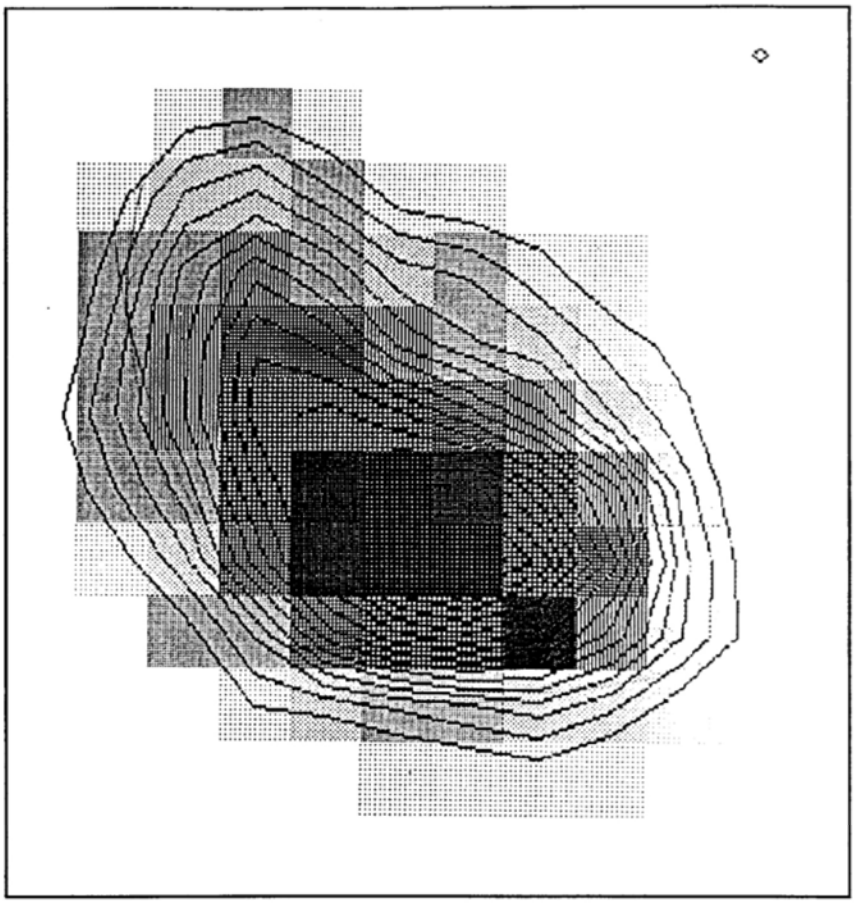

FIG. 2*b*

the center, as would be expected in an expanding shell geometry.

4. *High-velocity features.*—A single Gaussian line profile does not provide a good fit to the Hα emission feature. Allowing multiple Gaussians suggests additional weak features in the red and blue wings of the line. The velocity shifts of the centroids of these features compared with that of the main line vary over the face of the remnant from $+145 \pm 14$ to $+295 \pm 19$ km s^{-1} and -150 ± 36 to -423 ± 13 km s^{-1} for the red and blue components, respectively. The blue component is prevalent in the northeast portion of the nebula, while the red component is strongest in the southwest, indicating an asymmetry in the distribution of this fast-moving gas. The velocities of all three Hα components as a function of position along an east-west cut through the remnant center are displayed in Figure 6.

5.3. *The Integrated Spectrum and Its Comparison with Shock Models*

In Figure 7, we display the integrated spectrum of the remnant accumulated from all pixels in the spectrograph that lie within the confines of the emission nebula. Though of higher signal-to-noise ratio, the spectrum is in general consistent with those published previously (Smith 1975; D'Odorico & Dopita 1983; Peimbert et al. 1988).

In Table 3, we present the observed line intensities alongside those reported by the above-cited authors; the published values have had reddening corrections of $C(\mathrm{H}\beta) = 0.05$, 0.5, and 0.6, respectively, removed for comparison with our observed values. One significant difference we find is for the [O I] λ6300 line; this, along with smaller discrepancies from the published work, are probably a consequence of the fact that previous authors have used a single long slit to accumulate their spectra, whereas we have summed the emission from the entire nebula, which, as we show below, displays significant spectral differences in different regions.

The average intensity ratio of the [S II] lines, λ6717/λ6731 = 0.80 ± 0.05, corresponds to a mean electron density in the emitting plasma of $n_e \sim 1300$ cm^{-3} (Robertis, Dufour, & Hunt 1987). The variation in density over the face of the remnant using this line diagnostic is displayed in Figure 8; significant density changes in the range $n_e \sim$ 600–400 cm^{-3} are apparent, as is a very dense knot ($n_e \sim 2400$ cm^{-3}) at the northern edge of the nebula.

There is also a clear gradient in the Hα/Hβ ratio along the long axis of the remnant (Fig. 9). This ratio, coupled with predicted values from a shock model, is commonly used to derive reddening corrections for SNRs. Large uncertainties can arise, however, from the use of different models: Peimbert et al. find $C(\mathrm{H}\beta) = 0.05$ using model H of Raymond (1979), while D'Odorico & Dopita (1983) obtain $C(\mathrm{H}\beta) = 0.6$ and Smith (1975) reported $C(\mathrm{H}\beta) = 0.50$.

To avoid problems arising from the unknown abundances in the remnant, we use single-element line ratios in comparing our data with extant shock models: [O I]/

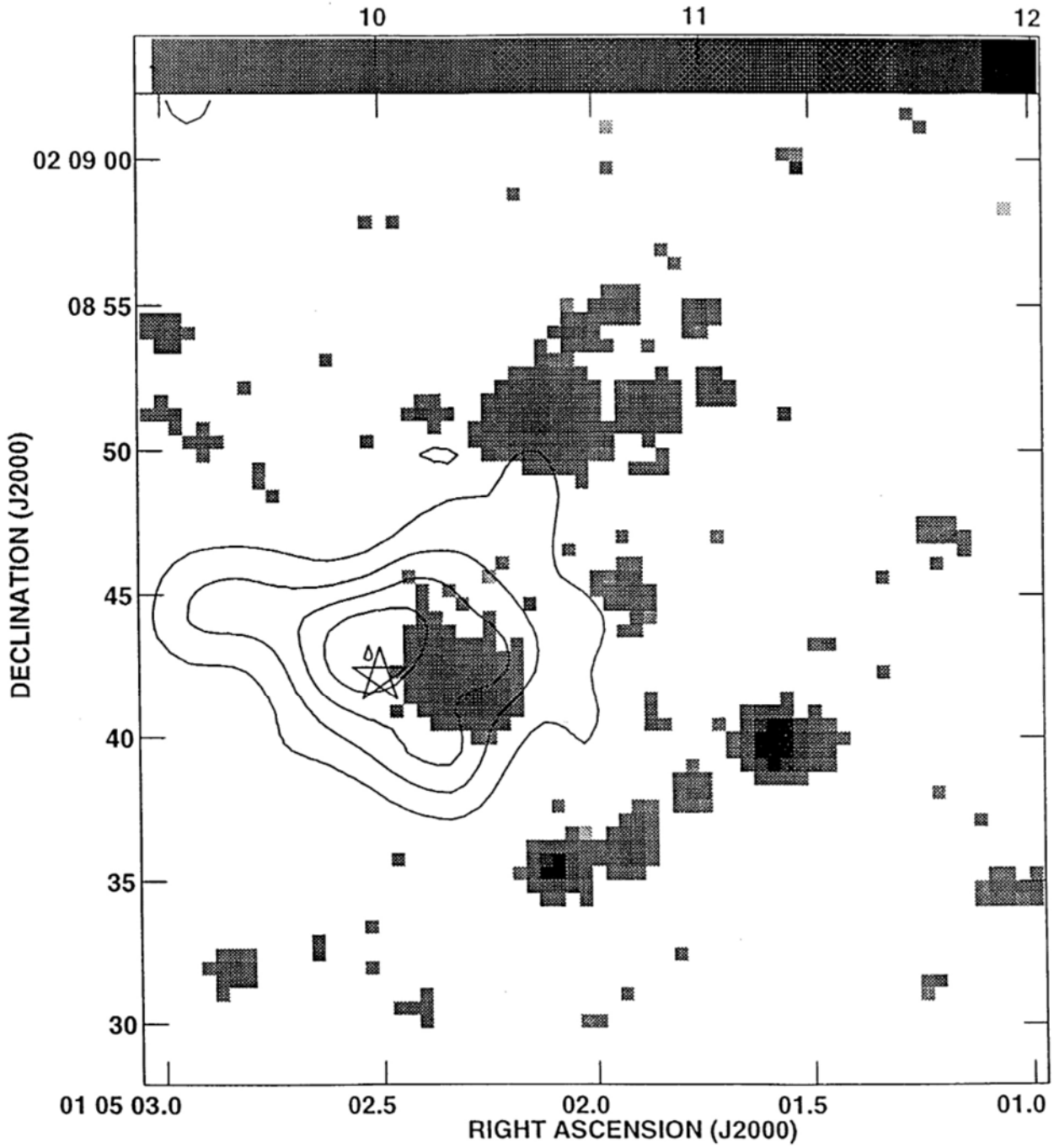

FIG. 3.—X-ray contours from the smoothed HRI image of S8 plotted over a gray-scale image of the [O III] emission; the centroid of the radio source is indicated by a star.

[O II]/[O III], He I/He II, and Hα/Hβ. We also allow for a range of possible reddening values, 0.05–1.0, to cover fully the range of values found previously. Models published by Sutherland & Dopita (1996), Raymond (1979), and Shull & McKee (1979) were considered; the range of parameters explored included 80 km s^{-1} < v_s < 500 km s^{-1}, 1 cm^{-3} < n_0 < 100 cm^{-3}, and, for models including magnetic fields, 0 μG cm$^{-3/2}$ < $B/n^{1/2}$ < 2 μG cm$^{-3/2}$. The best fits are obtained for values in the range 150 km s^{-1} < v_s < 250 km s^{-1}, 1 cm^{-3} < n_0 < 10 cm^{-3}, and a reddening $C(\mathrm{H}\beta)$ = 0.2–0.4. Table 4 lists the model predictions along with our observed line ratios.

A principal reason for the discrepancy is almost certainly the low metallicity of IC 1613 (D'Odorico & Dopita 1983; Dopita et al. 1984). Other factors include the presence, as indicated by our Hα line fitting, of multiple shock velocities and the fact that recently shocked plasma will not be in ionization equilibrium. For example, it is reasonable to postulate that a slow shock in a dense medium is responsible for the high Hα/Hβ ratio and the strong Fe lines seen in the spectrum, while a high-velocity shock gives rise to the He II and [O III] emission (as well as heating the X-ray gas). Such a superposition of slow and fast shocks has been introduced by Vancura et al. (1992) to explain the observed spectrum of

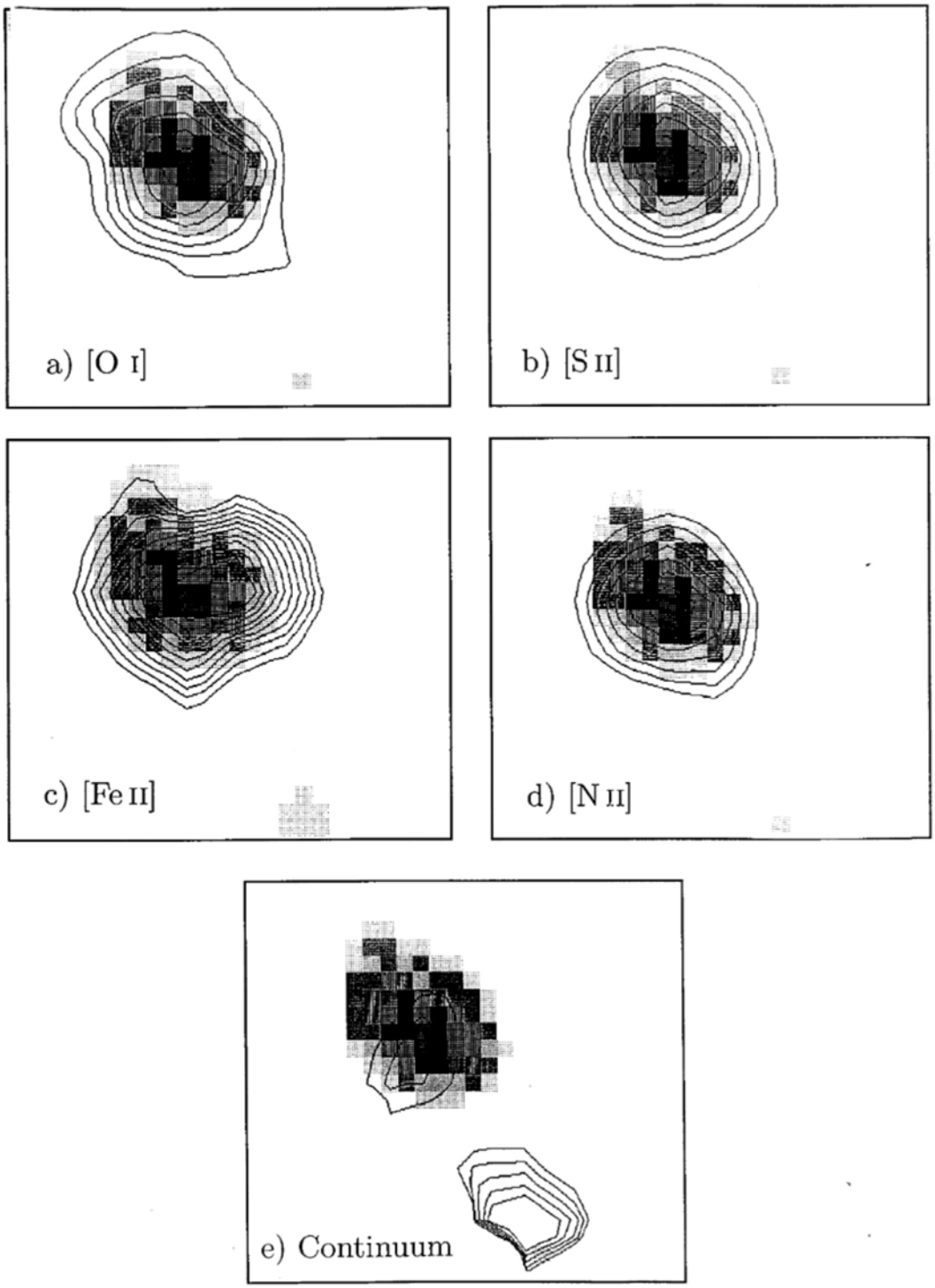

FIG. 4.—Images in the lines of (*a*) [O I], (*b*) [S II], (*c*) [Fe II], and (*d*) [N II] and (*e*) in the continuum (4300–6900 Å), obtained with the multipupil field spectrograph on the 6 m telescope, overlaid on the Hα image obtained with the 4 m telescope. Note the star southwest of the remnant in several of the images. Each field is 30″ on a side.

the Large Magellanic Cloud SNR N49. The recent encounter between the main supernova shock and a dense cloud can help explain the coexistence of bright X-ray and optical line emission (and would guarantee the existence of non-equilibrium conditions). New models incorporating multiple velocities and densities in low-abundance gas are required for quantitative modeling of remnants such as S8, and we are pursuing such efforts.

6. DISCUSSION

The FWHM angular size of the SNR in the optical and radio bands is 3″ › 2″, corresponding to an extent of 10 pc › 7 pc at the adopted distance of 725 kpc. The full-width at zero-intensity extent in our Hα and [O III] images (Fig. 2) is ~ 8″ › 6″.5, consistent with the size quoted by Hodge et al. (1990) and with our (poorly constrained) X-ray size; this

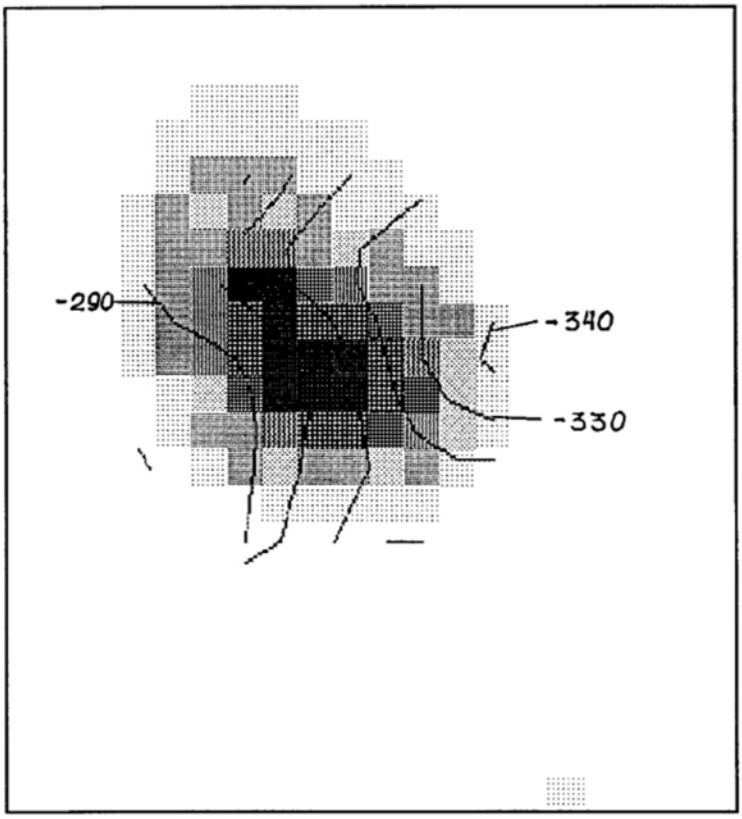

FIG. 5.—Isovelocity contours of the main component of the Hα line overlaid on the Hα image of the nebula

suggests a maximum remnant extent of 28 pc > 23 pc.

We do not confirm the report of a peculiar knot rich in iron (Massey et al. 1987) and bright in He II λ4686. Our [Fe II] image (Fig. 4) is clearly extended and is centered on the Hα nebula. The weak continuum source seen is consistent with the image of a faint superposed star in the south-central portion of the remnant. The He II line, while too weak to derive a high-quality image, is seen throughout the remnant. The n_e distribution is consistent with a high-density region in the northeast quadrant of the remnant, although the overall spectrum here is not significantly distinct from that of the rest of the object. We proceed, then, to interpret the observations reported above in the context of a normal remnant evolving in a structured interstellar medium (ISM).

6.1. *Ambient Gas Structure*

The size of the remnant alone (10–30 pc) does not allow us to distinguish between a young remnant evolving in a diffuse ISM and an older object embedded in a denser medium. A rough estimate of the ambient gas density can be obtained from the 21 cm maps of Lake & Skillman (1989), which show a large H I complex in the northeast quadrant of IC 1613, where the majority of the galaxy's H II regions and giant shells are concentrated (Meaburn et al. 1988). This complex extends for ~ 500 pc in the plane of the sky with a typical column density of $\sim 17 > 10^{20}$ cm^{-2}, whereas the mean H I column density in this part of the galaxy is only $(1–2) > 10^{20}$ cm^{-2}. Adopting a similar dimension for the cloud along the line of sight yields a mean number density of $n \sim 1$ cm^{-3}, roughly 30 times higher than the mean ISM density in the galaxy (Epstein 1964).

The $C(H\beta)$ reddening value for the remnant of 0.2–0.4 that we obtained in § 5.3 corresponds to $E(B-V) = 0.12–0.23$, whereas the mean reddening in the galaxy is ~ 0.04 (Freedman 1988). For this low-metallicity galaxy, we apply the relation $N(\text{H I}) = 8.7 > 10^{22} E(B-V)$ obtained for the Small Magellanic Cloud (Fitzpatrick 1985), and derive an implied $N_{\text{H}} = (1–2) > 10^{22}$ cm^{-2}, an order of magnitude above the mean value for the H I complex as a whole. In Figure 9, we show how the Hα/Hβ Balmer decrement varies significantly over the face of the remnant, increasing from north to south. This gradient, along with the high inferred local gas density, suggests that the excess reddening (and accompanying high-density medium) is local to the remnant. The alternative explanation for the Balmer decrement gradient—that the shock velocity is lower in the southern half of the object—also requires placing a high-density cloud on the southern boundary to decelerate the shock.

6.2. *The Remnant Structure*

The elongated optical appearance of S8 suggests a crescent opening to the northwest; as we have shown in § 5, there are kinematic, density, and Balmer decrement asymmetries along the northwest-southwest axis as well. We have, however, been unable to construct a dynamical model for the remnant structure that incorporates all of the available data.

The observed FWHM of the Hα line is much higher than the expected thermal width and is clearly indicative of bulk motion in the gas with $v_{\text{exp}} \sim 200$ km s^{-1}. However, we reiterate that there is no direct indication of the line

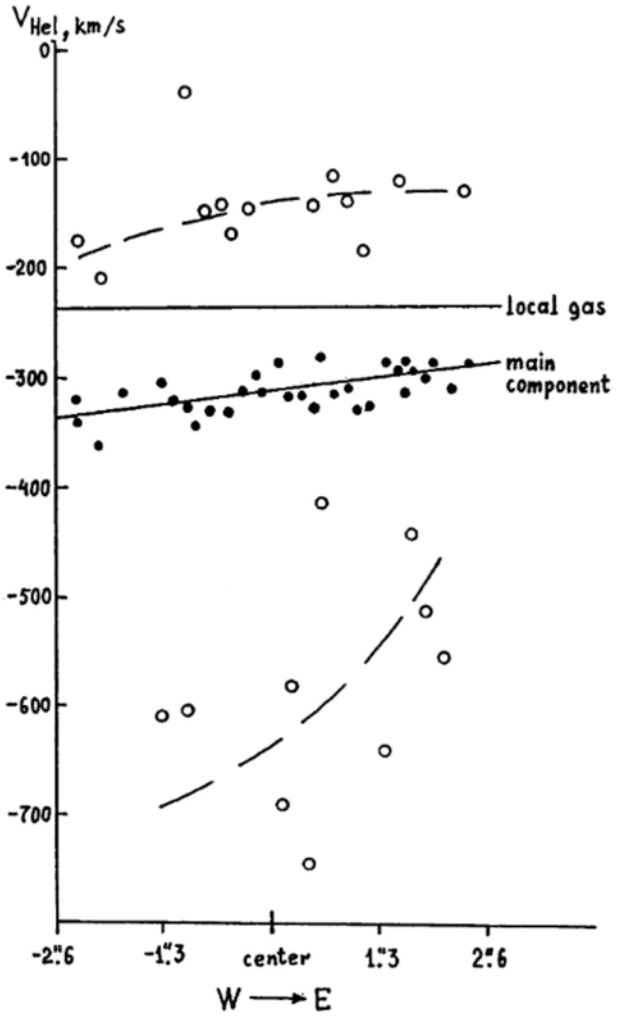

FIG. 6.—Velocities of the main component (*filled circles*) of Hα and of the high-velocity components (*open circles*) vs. the distance from the eastern edge of the nebula.

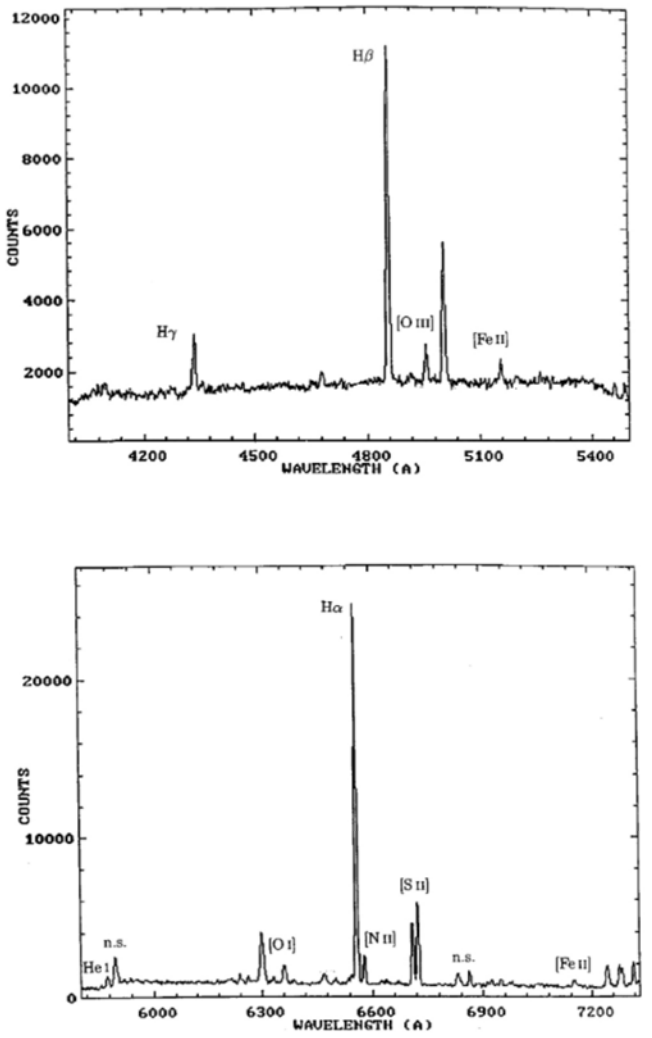

FIG. 7.—Summed spectrum of the whole nebula S8 derived from the multipupil field spectrograph data.

broadening from the periphery to the center of the elongated nebula as would be expected for an expanding shell. If the crescent shape of S8 represents a bright sector of a shell with a center of expansion shifted from the center of symmetry of the nebula, then its expansion velocity may be even higher because of projection effects.

The systematic velocity shift of the main component across the short axis of the elongated nebula may be interpreted in one of two ways: as an expanding annulus inclined to the line of sight or as a bright sector of an expanding shell oriented nearly face-on to the observer. The velocity shift of the bright main component of the Hα line indicates a bulk expansion velocity of less than 100 km s^{-1} in either scenario.

There is also evidence in our spectral data for faint, fast-moving gas that manifests itself as weak blue and red wings on the Hα line at a level 10%–20% of the peak line intensity. These faint features correspond to velocities of at least 200–300 km s^{-1} before accounting for projection effects (Fig. 6).

The coexistence of slow-moving, bright optical filaments and high-velocity faint optical emission is typical of well-

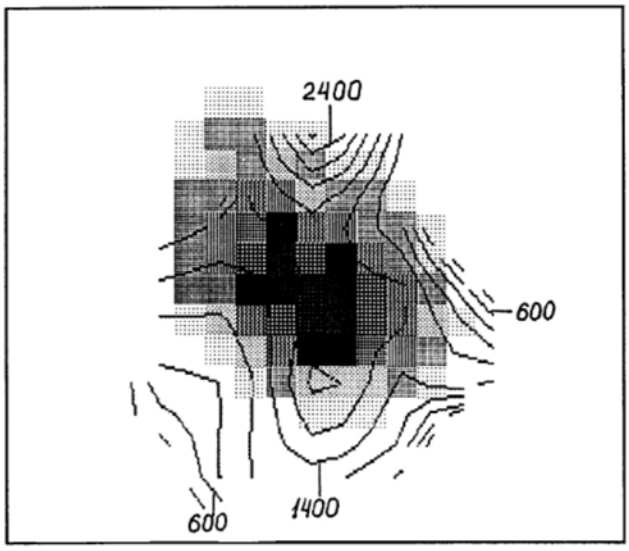

FIG. 8.—Distribution of mean density over the SNR as derived from the [S II] doublet ratio.

TABLE 3

LINE STRENGTHS IN THE INTEGRATED SPECTRUM OF S8

Line	Wavelength (Å)	P[a]	S[b]	DD[c]	This Work
$C(H\beta)$[d]		0.05	0.50	0.60	
O II	3727 + 3729	1.36[e]	...	1.07	...
H9	3835	0.07	...	...	...
Ne III	3869	0.08	...	...	...
He I + H8	3889	0.18	...	...	...
Ca II	3933	0.1	...	...	...
Ne III + Ca II + H7	3937 + 68 + 70	0.24	...	...	...
S II	4068 + 76	0.17	...	0.15	...
$H\delta$	4102	0.245	...	0.18	...
$H\gamma$	4340	0.45	...	0.35	0.38 ± 0.02
O III	4363	0.04	...	0.02	0.05 ± 0.01
Fe II	4415	...	...	0.03	0.04 ± 0.01
He I	4471	0.04	...	...	0.020 ± 0.003
He II	4686	0.05	...	0.03	0.048 ± 0.006
$H\beta$[e]	4861	1.00	1.00	1.00	1.00
[Fe III]	4658	...	...	...	...
O III	4959	0.12	...	0.12	...
O III	5007	0.37	0.42	0.35	0.373 ± 0.008
Fe II	5158	0.07	...	0.06	0.065 ± 0.003
N I	5199 + 5200	...	...	0.02	0.028 ± 0.003
[Fe II]	5261	...	...	...	0.017 ± 0.002
[Fe III]	5270				
He I	5876	0.10	0.12	0.12	0.119 ± 0.004
O I	6300	0.35	...	0.45	0.68 ± 0.04
O I	6364	0.10	...	...	...
$H\alpha$	6563	3.09	4.14	4.17	3.95 ± 0.06
N II	6583	0.22	0.62	0.32	0.311 ± 0.037
S II	6717	0.53	0.70	0.60	0.645 ± 0.023
S II	6731	0.68	0.84	0.74	0.796 ± 0.026
Fe II	7155	0.06	...	0.05	0.090 ± 0.010
Ca II	7291	0.2	...	0.24	0.147 ± 0.011
O II + Ca II	7320 + 23 + 30	0.22	...	0.16	...
Ca II	7323	...	...	...	0.133 ± 0.009
O II	7320 ± 30	0.09	...	0.015	...
log $I(H\beta)$ (ergs cm^{-2} s^{-1})		− 13.40			− 13.19

[a] Peimbert et al. 1988.
[b] Smith 1975.
[c] D'Odorico & Dopita 1983.
[d] All values from the literature have been converted to observed line strengths from the reported dereddened values using these reddening coefficients.
[e] All line strengths are relative to the $H\beta$ line.

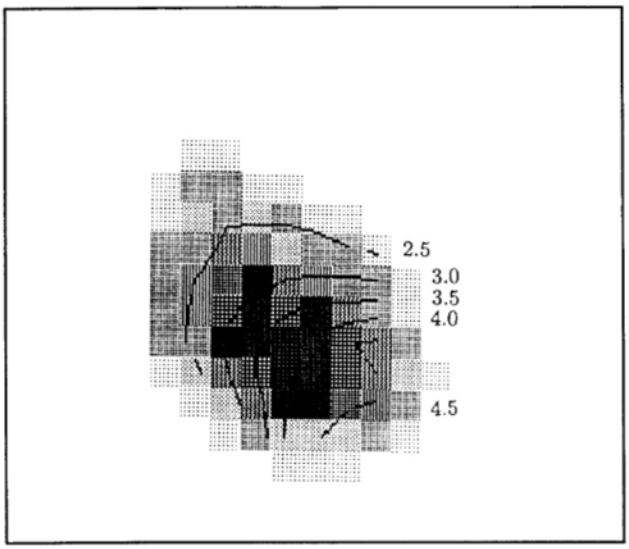

FIG. 9.—Isophotes of the ratio $I(H\alpha)/I(H\beta)$ overlaid on the $H\alpha$ image of the remnant.

studied Galactic SNRs such as the Cygnus Loop and IC 443 (Lozinskaya 1992). Such observations are usually understood either as a shock traveling in a two-component cloud/intercloud medium or in a model of emission from rippled sheets as suggested by Hester (1987). For an inclined annulus, the weak, high-velocity components may represent gas from both sides of the annulus behind the shock (i.e., from the surfaces of two weak "bubbles"). The signs of asymmetry in the distribution of the high-velocity component along the long axis of the nebula, as well as the similar trend in the $H\alpha/H\beta$ ratio, need an explanation. An inclination of the long axis of a bipolar bubble (with the northeast end closer to the observer) might be responsible for the asymmetry of high-velocity gas. One can also expect to detect weak emission from a fast reflected shock if the main blast wave has just hit dense material. Such spatial models of the SNR must be taken as illustrative exercises given the spatial resolution available. We note only that the similar object SNR N49 in the LMC also shows asymmetry in its high-velocity emission on a scale comparable to the remnant radius (see Fig. 5 in Vancura et al. 1992). Our only

TABLE 4

COMPARISON OF OBSERVED LINE STRENGTHS FROM S8 WITH VARIOUS SHOCK-EXCITATION MODELS

Line	Wavelength (Å)	$C(H\beta)$								Models for Different v_s (km s^{-1})				
										DS: S12[a]			R:H[b]	V[c]
		0.05	0.10	0.20	0.30	0.40	0.50	0.70	0.90	150	200	250	160	60+120
O II	3727+29[d]	1.41	1.46	1.57	1.69	1.82	1.96	2.26	2.62	6.17	5.66	6.74	...	...
Ne III.....	3869[d]	0.08	0.08	0.09	0.09	0.10	0.11	0.12	0.14	0.31	0.31	0.31	...	...
O II	4363	0.05	0.05	0.05	0.05	0.06	0.06	0.06	0.07	0.18	0.12	0.08	0.28	...
He II	4686	0.05	0.05	0.05	0.05	0.05	0.05	0.05	0.05	0.05	0.05	0.06	0.05	...
O III.....	5007	0.37	0.37	0.37	0.37	0.36	0.36	0.36	0.35	1.79	1.20	0.93	3.8	1.06
He I	5876	0.12	0.11	0.11	0.10	0.10	0.09	0.08	0.08	0.07	0.15	0.19	0.11	0.07
O I	6300	0.66	0.64	0.60	0.56	0.52	0.49	0.43	0.38	0.38	0.8	1.46	1.6	0.88
Hα	6563	3.80	3.66	3.39	3.13	2.90	2.69	2.30	1.97	3.09	3.02	2.97	2.9	3.08
N II	6583	0.30	0.29	0.27	0.25	0.23	0.21	0.18	0.15	1.28	1.81	2.65	2.2	0.51
S II	6717	0.62	0.59	0.54	0.50	0.46	0.42	0.36	0.30	0.80	1.12	1.28	0.83	0.48
S II	6731	0.76	0.73	0.67	0.62	0.57	0.52	0.44	0.37	0.57	0.81	0.96	0.77	0.67
O II	7320+30[d]	0.09	0.08	0.07	0.07	0.06	0.06	0.05	0.04	0.27	0.19	0.16	...	0.22

[a] Model S12 of Dopita & Sutherland 1996 for three different shock velocities.
[b] Model H of Raymond 1979 for $v_s = 160$ km s^{-1}.
[c] Model of Vancura et al. 1992 incorporating two separate shock velocities.
[d] Data from Peimbert et al. 1988; all other line strengths are from this work.

definitive conclusions are that the nebula is asymmetric and that the velocity of the gas is 50–100 km s^{-1} for the bright emission and 200–300 km s^{-1} for the faint emission, consistent with the results of our comparison of the remnant's optical line ratios with models for radiative shocks.

6.3. *The Evolutionary State of S8*

The crescent shape and central brightening of the nebula make a determination of the shock front's radius problematic. Thus, we evaluate parameters for the SNR for a conservative value $R = 10$ pc (established from the photograph by Sandage 1971) and use $R = 5$ and 14 pc (the FWHM and zero-intensity levels) as lower and upper limits.

An adiabatically expanding blast wave relaxes toward a Sedov solution when $M_{\rm swept\ up} \sim 10 M_{\rm ejecta}$. For typical SN parameters ($M_{\rm ejecta} = 1\ M_\odot$ to several $M_\odot$, $E_0 \simeq 10^{51}$ ergs, and $n_0 \simeq 1$ cm^{-3}), $M_{\rm swept\ up} \simeq 100\ M_\odot$, implying S8 is already in the Sedov stage. However, the local gas density in the immediate neighborhood of the SNR may differ significantly from the average value because of the inhomogeneity apparent in the multishell structure of the parent gas complex. Ignoring magnetic fields, pressure equilibrium between the postshock density n_c and the density given by the [S II] ratio ($n_{\rm S\,II} = 1300$ cm^{-3}) gives an ambient preshock density $n_{\rm S\,II} = 45 n_c [V_s/(100\ {\rm km\ s^{-1}})]^2$ cm^{-3} (Dopita 1979), or 7 to 3 cm^{-3} for shock velocity $V_s =$ 200–300 km s^{-1} and 100 to 25 cm^{-3} for $V_s = 50$–100 km s^{-1}.

It is clear from the high surface brightness of the remnant in various forbidden lines that at least some of the shocked gas is already at the radiative stage. According to Dopita & Sutherland (1996), the Hβ intensity behind a shock scales with the shock velocity and the ambient density: $I(H\beta) = 7.44 \times 10^{-6} [V_s/(100\ {\rm km\ s^{-1}})]^{2.41} n_0$ ergs cm^{-2} s^{-1} (different authors give different exponents near 2); for $V_s =$ 200–300 km s^{-1} and $n_0 = 3$–7 cm^3, the predicted flux through the shock is around $F(H\beta) \sim 4 \times 10^{-4}$ ergs cm^{-2} s^{-1}. For a spherical shock wave, the expected luminosity is 4 times higher than for a plane-parallel shock (Dopita 1979). For a sphere of $R = 10$ pc, the predicted luminosity [$L(H\beta) = (1$–$2) \times 10^{37}$ ergs cm^2 s^{-1}] is several times higher than the value observed by Peimbert et al. (1988) and in this work, suggesting values for n_0 and V_s on the low side of their quoted ranges.

One more piece of evidence for radiative emission from the SNR is the [Fe II] and [Fe III] lines in its spectrum. SNRs that display strong Fe lines include the Crab Nebula, Kepler's (van den Bergh 1980; Leibowitz & Danziger 1983), Cas A (Chevalier & Kirshner 1978; Leibowitz & Danziger 1983), the Cygnus Loop (Fesen, Blair, & Kirshner 1982), RCW 86, RCW 103, IC 443, and Vela (see Leibowitz & Danziger 1983) in the Galaxy, and N49, N63A, N103B, and N132D in the LMC (Danziger & Leibowitz 1985; Morse, Winkler, & Kirshner 1995; Vancura et al. 1992). In both Cas A and N132D, strong Fe lines have been detected only in the quasi-stationary flocculi (typical electron densities of from 2000 to 10,000 cm^{-3}, preshock densities of $\sim$300 cm^{-3}, and typical velocities of $\sim$200 km s^{-1}). Bright knots in Kepler's SNR also result from shock propagation in a dense medium of about 300 cm^{-3} for a shock velocity of 100 km s^{-1} (Dennefeld 1982). In the older SNRs, including N49 in the LMC, [Fe II] and [Fe III] lines have been detected in bright filaments with spectral characteristics of high-density cooling gas behind a radiative shock.

The X-ray data provide further information useful in the determination of the remnant's evolutionary stage. The HRI observations presented above conflict with the early notion (based on the assumption that the optical emission arises behind the main blast wave) that S8 is an evolved remnant in the late adiabatic or radiative phase with an age of about 22,000 yr (D'Odorico & Dopita 1983; Peimbert et al. 1988): the X-ray luminosity is too high. For a sphere of $R = 10$ pc and an X-ray emissivity of 4.0×10^{-23} ergs cm^3 s^{-1} (Hamilton, Sarazin, & Chevalier 1983) we obtain a number density in the hot X-ray plasma $n_{\rm X} = 0.9$–4 cm^{-3} ($n_{\rm X} = 7$–128 for $R = 5$ pc and $n_{\rm X} = 0.3$–1.7 for $R = 14$ pc) for the inferred X-ray luminosity $L(0.1$–$20) = (4$–$10) \times 10^{36}$ ergs s^{-1}; the larger sizes are both consistent with the apparent X-ray extent and with the required density for a Sedov remnant expanding in a medium with $n_0 = 1$ cm^{-3}.

The coexistence of high X-ray luminosity and very bright optical emission can be understood in terms of a two-

component cloud/intercloud model for the ambient interstellar gas. The bright optical emission arises in regions where the main shock has encountered gas in which the density is high enough for the shock to become radiative. Assuming equilibrium between the pressure driving the main blast wave and the cloud shock, we have $\beta n_i V_s^2 = n_c V_c^2$ for a shock of velocity V_c driven into a cloud of density n_c (McKee & Cowie 1975), where β is a dimensionless parameter of order unity; for strong shocks the limiting value is $\beta = 3.15$. For a radiative shock velocity 150–250 km s^{-1} (a conservative value from our Hα line profile and from the comparison of optical line ratios with the shock radiative models), a preshock cloud density of about 10 cm^{-3}, and $n_i = 0.2$–1 cm^{-3}, the implied main blast-wave velocity ranges from about 600 to 1300 km s^{-1}. The post–blast-wave temperature $T = 14V^2$ for the case of fully ionized preshock gas corresponds to $T_e = 5 \times 10^6$ to 2×10^7 K. An adiabatic (Sedov) SNR of $R = 10$ pc for a standard explosion energy $E_{51} = 1$ and $n_i = 0.2$–1 cm^{-3} yields a current main blast-wave velocity $V_s = 700$–1500 km s^{-1}, thus demonstrating the consistency of our preliminary scenario. The inferred Sedov age for S8, then, is $t = (3$–$6) \times 10^3$ yr for a radius of 10 pc.

The high luminosity of S8 in both the X-ray and optical bands could also be explained if the SNR were expanding within a large-scale shell, the dense boundary of which has recently been encountered by the shock. The SNR is located in a region of active star formation, at the edge of the giant complex of neutral gas, ionized shells, and supershells surrounding seven young OB associations. The existence of such an external massive shell alters the appearance of a SNR. Before entering the dense shell, the supernova blast wave expands within a rarefied cavity with little deceleration. The interaction with the shell then slows the primary shock considerably as it attempts to traverse the shell, generating reflected shocks that prevent the evacuation of the interior region (Tenorio-Tagle et al. 1990). Densities in the walls of a shell can be high enough for shocks to become radiative, leading to bright optical emission, while the lower density gas is shocked to X-ray temperatures. In addition, as the calculations by Tenorio-Tagle et al. (1990) show, this scenario can explain how the Hβ luminosity is comparable to, or higher than, the X-ray luminosity, something otherwise unexpected in a young SNR.

The SNR N49, the brightest optical and third-brightest X-ray SNR in the LMC, also shows very strong Fe lines and might be a well-studied analog to S8. According to Vancura et al. (1992), a combined analysis of the *IUE* and optical spectra of N49 indicates a range of radiative shock velocities from 40 to 270 km s^{-1} propagating in a high-density interstellar gas (preshock densities of 20–940 cm^{-3}) while nonradiative, X-ray–emitting shocks with velocities $\gtrsim 400$ km s^{-1} propagate in a gas with a preshock density ~ 1 cm^{-3}. The N49 nebula also appears as a bright filamentary crescent, although at lower intensities the optical emission is more extended. Echelle spectra of the object clearly show broad, large-scale bands of emission shifted both relative to the axis of the nebula and to the rest velocity of the bulk of the nebular material. N49 is 5–10 times brighter in the Hβ line than predicted by shock-wave models fitted to its forbidden line ratios. The similarities between these two remnants are summarized in Table 5. Vancura et al. (1992) explain this combination of features as arising from the interaction of a ~ 5000 yr old remnant with a dense molecular cloud; the location of S8 at the edge of a giant shell complex suggests a similar explanation is plausible.

7. SUMMARY AND CONCLUSIONS

Our high-resolution image of the dwarf galaxy IC 1613 has resolved the origin of its X-ray emission. Most of the flux arises from a background cluster of galaxies, as first suggested by Eskridge (1995). In addition, however, we detect the only SNR known in this galaxy at an X-ray luminosity $L(0.1$–2.4 keV$) = 4 \times 10^{36}$ ergs s^{-1}, making it one of the more luminous thermally emitting remnants in the Local Group. VLA observations of the source provide a precise spectral index ($\alpha = -0.57 \pm 0.05$) and a radio size at 1.4 GHz of $2''.9 \pm 0''.5$. Narrowband optical imaging in Hα and [O III] yields a similar FWHM and a FWZI of $\sim 8''$ $\times$ $6''.5$. Our multipupil spectrometer observations using the 6 m SAO telescope generally display similar images in the Balmer lines of hydrogen, [S II], [O I], [O III], [N II], and [Fe II], with an evident asymmetry in the O and Fe images. There is also extended continuum emission in the range 4300–6900 Å, although new observations are needed to evaluate its full extent and intensity. We do not confirm the pointlike object previously known as WR 8 seen at the northeast edge of S8 and later suspected of being an SNR knot with an unusual spectrum; there is a density enhancement on the northeast edge of the nebula, but its spectrum does not differ radically from that of the nebula as a whole.

The similarities of the properties of this remnant to the brightest optical SNR in the LMC, N49, are noted (as is P. Hodge's prescience in giving this source the same number in his 1990 IC 1613 catalog). The coexistence of the bright X-ray emission from a hot plasma and very bright optical emission from high-density material can be understood if the SNR is expanding within a shell and the main shock has recently encountered the swept-up gas at the edge of the shell or is just encountering a dense interstellar cloud. The SNR's location at the periphery of a complex of multiple expanding shells makes the first suggestion plausible.

TABLE 5

COMPARISON OF THE PROPERTIES OF N49 IN THE LMC AND S8 IN IC 1613

Property	S8 in IC 1613 SNR	N49 in the LMC
R (pc)	10	9
V (km s^{-1}; bright optical)	50–100	<140
V (km s^{-1}; faint optical)	200–300	300–270
n_e (cm^{-3} from [S II])	1300	1000–1800
L(Hβ) (10^{37} ergs s^{-1})	0.4	1
L_X (10^{37} ergs s^{-1})	0.4 (0.1–1.0)	1.9 (0.1–4.5)
V_s (km s^{-1})	700–1500	≥ 400
Sedov age (yr)	3000–6000	5400

Higher resolution observations of this remnant in both the optical (with *HST*) and the X-ray (with *AXAF*) could provide confirmation of our suggested picture for S8 and yield important quantitative data on the evolution of SNRs in an inhomogeneous interstellar medium.

Imaging analysis for this work was performed in large part using the IRAF package. The analysis of the two-dimensional spectra was accomplished using software developed in the SAO of the Russian Academy of Sciences (Vlasyuk 1993) and with the package ADHOC at the Marseille Observatory. We thank Karl Forster and John Morse for their assistance in obtaining the IRAF images from *ROSAT* data, A. Chatterjee for work on the X-ray and optical analyses, and Elizabeth Blanton for obtaining the narrowband optical images. We thank the astronomers of the SAO, V. L. A. Afanasiev and V. V. Vlasyuk, who conducted the observations at the 6 m telescope, which is operated with the financial support of the Science Department of Russia (registration number 01-43). We have also used the Lyons-Meudon Extragalactic Database (LEDA) supplied by the LEDA team at the CRAL–Observatoire de Lyons (France) for obtaining basic information on IC 1613. This work was supported in part by NASA under grant NAG 5-2916 and in part under a grant from the Russian Foundation of Basic Research. T. A. L. thanks the astronomy department of Columbia University for hospitality during her visit. This work is contribution number 645 of the Columbia Astrophysics Laboratory.

REFERENCES

Afanasiev, V. L., Dodonov, S. N., Silchenko, O. K., & Vlasyuk, V. V. 1990, preprint (Spec. Astrophys. Obs., No. N54)
Armandroff, T. E., & Massey, P. 1985, ApJ, 291, 685
———. 1991, AJ, 102, 927
Azzopardi, M., Lequeux, J., & Maeder, A. 1988, A&A, 189, 34
Chevalier, R. A., & Kirshner, R. P. 1978, ApJ, 219, 931
Danziger, I. J., & Leibowitz, E. M. 1985, MNRAS, 216, 365
Dennefeld, M. 1982, A&A, 112, 215
Dickel, J. R., D'Odorico, S., & Silverman, A. 1985, AJ, 30, 414
D'Odorico, S., & Dopita, M. 1983, in IAU Symp. 101, Supernova Remnants and Their X-ray Emission, ed. J. Danziger & P. Gorenstein (Dordrecht: Reidel), 517
D'Odorico, S., Dopita, M., & Benvenuti, P. 1980, A&AS, 40, 67
Dopita, M. A. 1979, ApJS, 40, 455
Dopita, M. A., Binette, L., D'Odorico, S., & Benvenuti, P. 1984, ApJ, 276, 653
Dopita, M. A., & Sutherland, R. 1996, ApJS, 40, 455
Epstein, E. E. 1964, AJ, 69, 490
Eskridge, P. B. 1995, PASP, 107, 561
Fesen, R. A., Blair, W. P., & Kirshner, R. P. 1982, ApJ, 262, 171
Fitzpatrick, E. L. 1985, ApJS, 59, 77
Freedman, W. L. 1988, ApJ, 326, 691
Goss, W. M., & Lozinskaya, T. A. 1995, ApJ, 439, 637
Hamilton, A. J. S., Sarazin, C. L., & Chevalier, R. A. 1983, ApJS, 51, 115
Hester, J. J. 1987, ApJ, 314, 187
Hodge, P., Lee, M. G., & Gurwell, M. 1990, PASP, 102, 1245
Lake, G., & Skillman, E. D. 1989, AJ, 98, 1274
Leibowitz, E. M., & Danziger, I. J. 1983, MNRAS, 204, 273
Lozinskaya, T. A. 1992, Supernovae and Stellar Wind in the Interstellar Medium (New York: AIP)
Massey, P., Conti, P. S., & Armandroff, T. E. 1987, AJ, 94, 1538
Meaburn, J., Clayton, C. A., & Whitehead, M. G. 1988, MNRAS, 235, 479
McKee, C. F., & Cowie, L. L. 1975, ApJ, 195, 715
Morse, J. A., Winkler, P. F., & Kirshner, R. P. 1995, AJ, 109, 2104
Peimbert, M., Bohigas, J., & Torres-Peimbert, S. 1988, Rev. Mexicana Astron. Astrofis., 16, 45
Raymond, J. C. 1979, ApJS, 39, 1
Robertis, M. M., Dufour, R. J., & Hunt, R. W. 1987, JRASC, 81, 195
Sandage, A. R. 1971, ApJ, 166, 13
Shull, J. M., & McKee, C. 1979, ApJ, 227, 131
Smith, H. E. 1975, ApJ, 199, 591
Tenorio-Tagle, G., Bodenheimer, P., Franco, J., & Różyczka, M. 1990, MNRAS, 244, 563
Vancura, O., Blair, W. P., Long, K. S., & Raymond, J. C. 1992, ApJ, 394, 158
van den Bergh, S. 1980, A&A, 86, 155
Vlasyuk, V. V. 1993, Astrofiz. Issled., 36, 107